THÈSE

En vue de l'obtention du

DOCTORAT DE L'UNIVERSITÉ DE TOULOUSE

Délivré par : *l'Université Toulouse 3 Paul Sabatier (UT3 Paul Sabatier)*

Présentée et soutenue le *13/02/2014* **par :**

Stanislas GUILLEMANT

Etude et Simulations des Phénomènes d'Interactions Satellite/Plasma et de leurs Impacts sur les Mesures de Plasmas Basses Énergies

---

JURY

François FORME	Professeur d'Université	Président du Jury
Dominique DELCOURT	Directeur de Recherche	Rapporteur
Vincent GÉNOT	Astronome Adjoint	Directeur des travaux
Alain HILGERS	Directeur de Recherche	Examinateur
Bertrand LEMBÈGE	Professeur d'Université	Examinateur
Philippe LOUARN	Directeur de Recherche	Directeur de thèse
Richard MARCHAND	Professeur d'Université	Rapporteur
Jean-Charles MATÉO-VÉLEZ	Ingénieur de Recherche	Directeur des travaux

---

École doctorale et spécialité :
SDU2E : Astrophysique, Sciences de l'Espace, Planétologie
Unité de Recherche :
Institut de Recherche en Astrophysique et Planétologie (UMR 5277)
Directeur(s) de Thèse :
Philippe LOUARN, *Vincent GÉNOT* et *Jean-Charles MATÉO-VÉLEZ*
Rapporteurs :
Richard MARCHAND et *Dominique DELCOURT*

Résumé :

Les satellites scientifiques en vol sont immergés dans divers environnements spatiaux, entourés par différents types de plasmas qu'ils sont supposés analyser, en utilisant les instruments appropriés de types détecteurs de particules. La simple présence de cette structure dans le plasma conduit à une variété connue d'interactions satellites/plasma qui sont complexes, inter-corrélées, et difficilement considérées dans leur ensemble. L'environnement spatial influence la structure du satellite (courants, charge électrostatique, radiations, *etc*) qui, en retour, affecte son environnement proche (émission de particules, attraction / répulsion du plasma ambiant, *etc*). Finalement les instruments scientifiques embarqués sur les satellites mesurent un environnement local perturbé et il peut être difficile de distinguer le signal naturel des mesures biaisées.
Le but de cette thèse et d'étudier et d'améliorer la compréhension des interactions satellite/plasma, au moyen de simulations numériques multi-échelles effectuées avec le logiciel Spacecraft Plasma Interaction System (SPIS). Notre attention est portée sur le domaine des basses énergies (en dessous de la centaine d'électronvolts) puisque ce sont ces particules qui sont les plus affectées par les perturbations locales. Le but final est d'établir une méthodologie de configuration et de simulation des différentes problématiques liées aux satellites immergés dans des environnements spatiaux, permettant une analyse correcte des mesures plasma en identifiant l'environnement naturel non perturbé parmi les données d'instruments polluées et biaisées.
Pour atteindre cet objectif nous effectuons en premier lieu une étude paramétrique des interactions ayant lieu entre la sonde Solar Probe Plus et le plasma ambiant dans un environnement proche du soleil. Nous présentons les phénomènes ainsi générés tels que les gaines de plasma constituant des barrières de potentiel pour toutes les particules émises par le satellite et le potentiel électrostatique négatif de la sonde résultant, et expliquons leurs origines.
Le deuxième axe est l'extension de notre modèle Solar Probe Plus à des distances héliocentriques plus éloignées, permettant l'étude de la formation des gaines de plasma et des barrières de potentiel entre 0,044 UA du soleil et l'orbite terrestre. Cette étude permet de conclure qu'au périhélie de sa mission, à 0,28 UA du soleil, la mission Solar Orbiter sera concernée par des barrières de potentiel locales et de fortes perturbations au niveau de son instrument Electron Analyser System (EAS).
Troisièmement, nous procédons à une étude paramétrique d'un détecteur de particules soumis à diverses perturbations, et comparons les résultats avec les mesures théoriques attendues. Cette méthode fournit une première quantification des différentes problématiques perturbatrices de mesures (comme les potentiels non nuls et les particules parasites).
Pour finir nous présentons des simulations avancées de notre modèle Solar Orbiter et de son instrument EAS dans divers environnements, ainsi que les quantifications des biais produits par les interactions Solar Orbiter / plasma sur les mesures simulées d'électrons. Un autre cas concernant le satellite Cluster et son détecteur d'électrons embarqué est également détaillé, avec la comparaison des mesures simulées à des données réelles en vol. Le bon accord des deux jeux de données confirme la validité de notre méthode de simulation des interactions satellite/plasma.

Mots clés: Plasma du vent solaire, Structures électrostatiques, Charges de satellites, Instruments plasma, Simulations numériques

Abstract:

In-flight scientific spacecraft are immersed in various space environments, surrounded by different types of plasma they are meant to analyse, using dedicated instruments such as particle detectors. The simple presence of a structure in a plasma leads to various known spacecraft/plasma interactions which are complex, inter-correlated, and difficult to consider globally. The space environment influences the satellite structure (currents, electrostatic charging, radiations, *etc*) which in turn affects its near environment (particle emission, attraction / repulsion of the ambient plasma, *etc*). Finally the spacecraft scientific instruments measure a disturbed local environment and it might be difficult to distinguish the natural signal from the biased data.

The objective of this thesis is to study and improve the understanding of the spacecraft/plasma interactions, through multi-scale numerical simulations performed with the *Spacecraft Plasma Interaction System* (SPIS) software. The focus is on the low energy domain (below a hundred of electron-volts) as those particles are the most affected by local disturbances. The final aim is to establish a methodology of configuring and simulating the various issues related to satellites immersed in space environments, allowing to analyse properly plasma measurements by identifying the natural undisturbed environment from biased and polluted instrument outputs.

To achieve this goal we first perform a parametric study of the Solar Probe Plus/plasma interactions in a near-Sun environment. We present the generated phenomena which are the plasma sheaths representing potential barriers for all spacecraft emitted particles and the associated negative equilibrium potential of the probe, and explain their formation.

The second axis is the extension of our Solar Probe Plus model to farther heliocentric distances, allowing the study of the plasma sheaths and potential barriers formation between 0.044 AU from the Sun to the Earth orbit. This allows to state that the Solar Orbiter mission at its perihelion (0.28 AU) will be affected by local potential barriers and strong disturbances in the vicinity of its electron instrument: the *Electron Analyser System* (EAS).

Third, we proceed to a parametric simulation study of a particle detector subjected to various disturbing phenomena, and compare the measurements with the analytical outputs, expected when considering only the electrostatic potential of the instrument. This method provides a first quantification of the different data polluting issues (such as non null potentials and parasite particles).

Finally advanced simulations of our Solar Orbiter model and its on-board instrument EAS in various environments are presented, with quantifications of the simulated electron measurements biases due to the Solar Orbiter/plasma interactions. Another case considered is the Cluster spacecraft and its on-board electron detector is also detailed, with a comparison of simulated measurements to real in-flight data. The good agreement between the two datasets confirm the validity of our methodology of simulating multi-scale satellite/plasma interactions.

Keywords: Solar wind plasma, Electrostatic structures, Spacecraft charging, Plasma instruments, Numerical simulations

Acknowledgments

I wish to thank first my co-financers: the Centre National d'Etudes Spatiales (CNES) and the Région Midi-Pyrénées, for putting their trust in me. I also thank my two host laboratories. The *Institut de Recherche en Astrophysique et Planétologie* (IRAP), directed by Martin Giard, where I worked in the department *Géophysique Planétaire et Plasmas Spatiaux* (GPPS - directed by Michael Toplis). As for the *Toulouse centre of the Office National d'Etudes et de Recherches Aéronautiques* (ONERA), where I worked in the Department of *Environnement Spatial et Effets* (DESP - directed by Jean-François Roussel), within the *Charge Spatiale et Effets* team (CSE - led by Virginie Inguimbert). Those two institutions gave me all the means to accomplish my PhD study. I also thank the *Ecole Doctorale "Sciences de l'Univers, de l'Environnement et de l'Espace"* (SDU2E) from the *Université de Toulouse*, for managing this study.

I sincerely thank my jury for accepting to evaluate my work and especially the reviewers, Richard Marchand and Dominique Delcourt, for their precious advices and recommendations on this manuscript.

My immense gratitude goes to my directors: Vincent Génot (IRAP/GPPS) and Jean-Charles Matéo-Vélez (ONERA/DESP), who brilliantly supervised me from the beginning of this PhD work until its end. Your guidance, advices, availability and encouragements were not only helpful but essential for my work. During our various think tanks, organized or not, on the studies performed during those three years, you taught me well the art of developing and extending my intuitions on my results. This led to various investigations on what could appear at the beginning as uncertain tracks but which finally occurred to be interesting and convincing results. Our team work allowed me to publish two articles and one report for ESA, which I didn't expect at the very beginning of this PhD study. Again I wish to thank you for your patience and your help on my numerous physics and numerical interrogations, providing me the necessary knowledge on those specific aspects of spacecraft/plasma interaction physics and computation. And I also thank you for your multiple assiduous proofreading of this manuscript and of my other papers. I also appreciated the many other physics-disconnected moments spent together talking about everything else.

I wish to sincerely acknowledge my other PhD director Philippe Louarn (IRAP / GPPS) for his interest in my work and his support, as Jean-Yves Prado, my technical manager at CNES. I warmly thank Pierre Sarrailh (ONERA / DESP) for his helpful guidance on overpowering the multiple subtleties of the SPIS code. He prevented me from several nervous breakdowns when configuring complex simulations on the previous code versions, sometimes a little bit too much sensitive for my rough settings. By the way I address my grateful regards to the Artenum team (Julien Forest, Benoît Thiébault and all others) for their brilliant job on developing and improving the SPIS User Interface. I hope my few suggestions were not too idealistic and difficult to implement. Thanks for answering all my questions about the interface, and all our discussions when meeting together, for work sessions and/or tourism. I am also deeply grateful to Alain Hilgers (ESA) for our numerous discussions on my simulations and associated publications. His precious rigour permitted to bring exactness to my numerical studies and to my reports. Alain gave me important advices on and apart from my work, which I really appreciated especially during the late meetings in Uppsala, Bern, Kitakyushu, *etc.* Concerning the ESA study collaboration I would also like to thank Anders Eriksson and Thomas Nilsson (Swedish Institute of Space Physics - IRF Uppsala) for the precious inputs they provided me concerning my Cluster simulations, and their compliments on my presentations.

I greatly salute all my colleagues. Thank you for your interest in my work and for enlight-

ening me on my various interrogations concerning specific aspects of spacecraft charging issues. Benoît Lavraud (IRAP) for suggesting me the context of my second article, and for our late intense working sessions at the 5^{th} Solar Orbiter Workshop in Brugge, together with Milan Maksimovic and Arnaud Zaslavsky (LESIA). I deeply appreciated the exchanges we had with Milan on the Solar Orbiter spacecraft and the Kappa distribution functions of thermal electrons in the Solar wind, which allowed us to implement SPIS with new capabilities of modelling non Maxwellian environments and to greatly improve my satellite geometry model. I furthermore thank Filippo Pantellini (LESIA) for our sharing of geometry modules of the various elements of Solar Orbiter, without forgetting Emmanuel Guilhem (ALTRAN) for revealing me the mysteries of Solar Orbiter structure. I sincerely acknowledge Andrew Fazakerley and Christopher J. Owen (Mullard Space Science Laboratory - MSSL) for all the informations they kindly provided on the Solar Orbiter and Cluster instruments: the SWA and PEACE detectors. I hope our work gave you interesting points of view on your projects. Many thanks also to Mohamed Belhaj and Thierry Paulmier (ONERA/DESP) for answering my questions about the secondary electron emission and the various material properties used in my simulations, and to my colleagues: Nicolas André, Gabriel Fruit and all others.

I greatly appreciated the interactions with the International Space Science Institute (ISSI) team: Interaction of Satellites with Space Environment, led by Richard Marchand (University of Alberta). Our discussions on spacecraft/plasma interaction issues have been extremely enriching and provided me with plenty of ideas and tracks for my PhD study.

Getting back in time, I address my true acknowledges to all my professors, from the *Faculté des Sciences de Limoges* and the *Université Paul Sabatier* of Toulouse for comforting me into my passion for astrophysics and space engineering, all over these years. My best regards go also to all my training directors: Natalie Webb, Emmanuel Caux and Michel Blanc (IRAP) for the hope they placed in me, Jean-Charles Marty (CNES) and a very special thought to my greatest professor Christophe Peymirat (IRAP). Christophe was the first to instil me the beauty of plasma physics, and supervised me carefully during my training on the electrodynamics of Saturn's rings, with Michel Blanc few years ago. I will never thank him enough for all the discussions we had on plasmas, studies and life in general. Thank you again for your precious friendship and sharing so much with me.

I would hardly have achieved this work without the presence of all my dearest friends. Thank you so much guys for your support and those marvellous moments spent together, which considerably helped me hanging on and put things into perspective during the hard times I went through. My infinite gratitude goes to my parents, for absolutely everything they provided me with: love, attention, education and support during all these years, and also for encouraging me to re-enter into studies for this last academic degree. Thanks also to all my family members for their support. Finally, I wish to express my endless gratitude to my dearest love.

Study and Simulations of Spacecraft/Plasma Interaction Phenomena and their Effects on Low Energy Plasma Measurements

Contents

1 Introduction **1**
- 1.1 Introduction générale en français . . . 1
- 1.2 English introduction: Principle of in flight plasma measurement . . . 5
  - 1.2.1 Past and future scientific missions aiming at analysing low energy plasma 6
  - 1.2.2 Description of particle instruments . . . 8
- 1.3 Sources of perturbations . . . 10
- 1.4 Measurements analysis methods . . . 12
  - 1.4.1 Partial consideration of perturbations . . . 12
  - 1.4.2 Grey areas for a quantitative measurement . . . 14
- 1.5 Interest of numerical simulations . . . 14
  - 1.5.1 Anticipating the problems: help to design spacecrafts and instruments . . 14
  - 1.5.2 Analysing in-flight measurements . . . 15
- 1.6 Objectives of this work . . . 16
- 1.7 Plan and sum up . . . 17

2 The Solar wind plasma **19**
- 2.1 Plasma physics . . . 19
  - 2.1.1 Distribution functions . . . 19
  - 2.1.2 Plasma scales: Debye length and plasma frequency . . . 22
  - 2.1.3 Magnetic field . . . 23
- 2.2 The Solar wind . . . 25
  - 2.2.1 Properties and observations . . . 25
  - 2.2.2 Interaction with the magnetic field: the magnetospheres . . . 29

3 Interactions with a satellite **33**
- 3.1 Equilibrium potential and currents . . . 33
- 3.2 Differential charging . . . 36
- 3.3 Space charge effects and ambient current estimations: probe theory . . . 38
  - 3.3.1 The Boltzmann factor . . . 38
  - 3.3.2 The thick sheath regime . . . 39
  - 3.3.3 The thin sheath regime . . . 41
  - 3.3.4 Concluding remark . . . 44
- 3.4 Ideal collected distribution functions . . . 44
- 3.5 Secondary electron emission / electron impact: SEEE . . . 47
  - 3.5.1 SEEE Principle . . . 47
  - 3.5.2 SEEE Modelling . . . 50
- 3.6 Secondary electron emission under proton impact: SEEP . . . 53
- 3.7 Photoemission . . . 54
- 3.8 Ion wake . . . 56
- 3.9 Potential barriers . . . 59
- 3.10 Viewing factor . . . 61
- 3.11 Other phenomena . . . 63

4 Numerical simulation of Solar wind/satellite interaction 65
4.1 The SPIS numerical code . . . 66
4.1.1 Presentation of the software . . . 66
4.1.2 SPIS basic principles . . . 67
4.1.3 Utility of the SPIS code for simulations . . . 79
4.2 Illustration of Solar wind impacts on spacecraft . . . 80
4.2.1 Article 1: Solar wind plasma interaction with Solar Probe Plus spacecraft 80
4.2.2 Article 2: Simulation study of spacecraft electrostatic sheath changes with the heliocentric distances from 0.044 to 1 AU . . . 89
4.2.3 Possible effects on plasma measurements . . . 100

5 Numerical particle instruments 103
5.1 Definition of scientist's needs . . . 103
5.2 The SPIS-SCI Instruments . . . 105
5.3 Measurement principle . . . 108
5.4 Measurement of a undisturbed Maxwellian plasma: Case 1 . . . 110
5.5 Measurement of a disturbed Maxwellian plasma . . . 112
5.5.1 Positive potential effect: Case 2 . . . 112
5.5.2 Negative potential effect: Case 3 . . . 115
5.5.3 Photoemission: Case 4 and 5 . . . 117
5.5.4 Secondary electron emission: Case 6 . . . 122
5.5.5 Combined effect of SEEE and photoelectrons: Case 7 . . . 125
5.6 Undisturbed non isotropic Maxwellian plasma: Case 8 . . . 127
5.7 Conclusion . . . 130

6 Applications 133
6.1 Solar Orbiter . . . 134
6.1.1 Solar Orbiter simulations: configurations . . . 134
6.1.2 Results analysis of SOLO at 1 AU . . . 144
6.1.3 Results analysis of SOLO at 1 AU with a Fast Solar Wind . . . 159
6.1.4 Results analysis of SOLO at 0.28 AU . . . 164
6.1.5 Solar Orbiter cases conclusion . . . 174
6.2 Cluster . . . 175
6.2.1 Cluster simulation: configuration of the CLUS@1 AU case . . . 177
6.2.2 Results analysis of CLUS@1 AU . . . 185
6.2.3 Cluster simulation conclusion . . . 197
6.3 Conclusion on scientific applications and engineering . . . 197

7 Conclusion and perspectives 199
7.1 Achievements (English) . . . 199
7.2 Critical analysis of this PhD and Perspectives (English) . . . 200
7.3 Conclusion générale (français) . . . 203

A Appendix 209
A.1 Physical and Geophysical Constants . . . 209
A.2 Basic concepts of the distribution function . . . 209
A.3 Cluster in-flight data . . . 210

A.4 Article 1 - Guillemant et al. (2012): Solar wind plasma interaction with Solar Probe Plus spacecraft 212
A.5 Article 2 - Guillemant et al. (2013): Simulation study of spacecraft electrostatic sheath changes with the heliocentric distances from 0.044 to 1 AU 231

Bibliography **245**

Chapter 1

Introduction

Contents

1.1 Introduction générale en français 1
1.2 English introduction: Principle of in flight plasma measurement 5
1.2.1 Past and future scientific missions aiming at analysing low energy plasma . 6
1.2.2 Description of particle instruments 8
1.3 Sources of perturbations 10
1.4 Measurements analysis methods 12
1.4.1 Partial consideration of perturbations 12
1.4.2 Grey areas for a quantitative measurement 14
1.5 Interest of numerical simulations 14
1.5.1 Anticipating the problems: help to design spacecrafts and instruments . . . 14
1.5.2 Analysing in-flight measurements 15
1.6 Objectives of this work 16
1.7 Plan and sum up 17

1.1 Introduction générale en français

La nature de l'environnement spatial a depuis toujours éveillé la curiosité de l'esprit humain. De nombreuses théories ont émergé pour expliquer les objets célestes visibles, au départ, à l'œil nu : soleil, lune, planètes, voie lactée et étoiles, fixes, dansantes, filantes, *etc.* L'humanité a par la suite été confrontée directement aux aspects microscopiques du milieu spatial lors de ses premières incursions au-delà du ciel, et notamment via le satellite américain Explorer 1 (lancé en 1958) qui permit à Van Allen et son équipe de mettre en évidence des ceintures toroïdales de protons et d'électrons énergétiques autour de la Terre. Par la suite les phénomènes d'érosion des matériaux dans l'espace, de charge électrostatique des satellites menant à des décharges électriques fatales pour ces structures ou pour leurs composants électroniques intégrés, ont rapidement été identifiés et étudiés pour éviter autant que possible ces phénomènes et prolonger la durée de vie de missions de plus en plus ambitieuses.

D'un point de vue scientifique, la volonté de comprendre et connaitre l'environnement spatial mène à l'utilisation de différents types d'instruments embarqués sur les satellites, afin de procéder à des analyses sur la plus grande gamme d'éléments possible. Il ne s'agit pas seulement d'identifier quels types de particules peuplent l'environnement spatial, mais aussi de caractériser en détail les distributions de ces particules, et d'être ainsi capable de représenter leurs partitionnement en énergie, densité, *etc*, en fonction de la localisation spatiale. Des détecteurs spécifiques sont élaborés afin d'analyser des particules neutres ou chargées, des champs électriques, magnétiques, des flux électromagnétiques. Mais ce travail de thèse se focalisera sur les instruments

à plasma, et plus spécifiquement sur les détecteurs de particules qui permettent l'analyse des éléments chargés constituant les plasmas.

Un plasma peut être rapidement défini comme un état de la matière constitué d'un ensemble de particules chargées présentant un comportement collectif, dominé par des interactions électromagnétiques. Ces particules chargées répondent à la présence d'un satellite parmi elles via des interactions diverses qui rendent leur analyse complexe et trompeuse, avec des mesures de particules plus ou moins biaisées. Ces interactions sont particulièrement fortes dans le domaine des basses énergies (considérées ici comme étant en deçà de la centaine d'électronvolts), c'est pourquoi cette étude est menée sur ce domaine énergétique spécifique.

De nombreuses missions spatiales scientifiques ont été dédiées ou mises à contribution à l'étude de l'environnement spatial dans les basses énergies. Trois missions, en cours ou à venir, nous intéressent en particulier dans cette thèse. Tout d'abord Solar Probe Plus, un projet de la NASA consistant à étudier l'environnement proche du soleil, à seulement 0,044 Unités Astronomiques (UA) de notre étoile d'ici à 2021, pour comprendre les phénomènes de chauffage de la couronne solaire et d'accélération du vent solaire (ce flux de particules, variable, émis par cet astre dans toutes les directions et dans lequel baignent l'ensemble du système solaire et des satellites lancés par l'Homme). Dans ces conditions extrêmes la sonde sera soumise à des flux intenses de protons et d'ions énergétiques, ainsi qu'à une température intense qui influeront sur la charge des matériaux, non sans conséquences sur la qualité des mesures de plasma effectuées par les instruments embarqués. La mission Solar Orbiter (Agence Spatiale Européenne, lancement prévu en 2017) naviguera à son périhélie à 0,28 UA du soleil (jusqu'à 1,4 UA à son aphélie), et portera à son bord l'ensemble d'instruments Solar Wind Analyser (SWA), comportant notamment l'Electron Analyser System (EAS) pour effectuer des mesures de ces particules, y compris dans les basses énergies. Enfin la mission Cluster (NASA/ESA), lancée en 2000 qui fournit depuis des données de mesures in-situ de la magnétosphère terrestre au moyen de quatre satellites identiques volant en formation. Ces analyses simultanées révèlent les phénomènes tridimensionnels variant spatialement et temporellement. Les sondes Cluster, en rotations à 15 tours/min, ont embarqué les ensembles Plasma Electron And Current Experiment (PEACE), comprenant les High/Low Energy Electron Analyser (HEEA/LEEA), scannant les électrons plus ou moins rapides de leur environnement.

Toutes ces missions seront indubitablement confrontées aux phénomènes problématiques des interactions satellite/plasma, dont nous pouvons énumérer les principales ci-après :

- **Charge du satellite**
  Une structure immergée dans un plasma spatial va collecter des particules chargées et donc verra son potentiel électrostatique modifié. Le plasma environnant sera plus ou moins affecté par le (ou les) potentiel(s) du satellite en fonction : des charges, de l'énergie moyenne des particules et des niveaux de potentiels, menant à divers degrés de perturbations des observations de plasma.

- **L'émission de particules parasites**
  A la suite des impacts de particules sur la structure du satellite, des électrons de basses énergies (quelques électronvolts) sont relâchés par les couches externes de la structure avec des taux variant en fonction du plasma et des propriétés de ces matériaux. Cela ajoute de nouvelles populations dans l'entourage de la sonde et de nouveaux courants sur ses surfaces. Ces populations ainsi générées sont composées d'électrons secondaires par les impacts d'électrons ou de protons, et les électrons émis suite à l'irradiation ultra violette des surfaces par le rayonnement solaire (appelés photoélectrons). Toutes peuvent être

collectées par les surfaces du satellite et/ou par les détecteurs de particules, polluant ainsi les mesures.

- **Les effets de charge d'espace**
  Sur une échelle assez large un plasma à l'équilibre est électriquement neutre. A des échelles inférieures et plus précisément au niveau des surfaces d'un satellite : la quasi-neutralité du milieu n'est plus valable. Cette région, issue de la présence d'un ou de plusieurs potentiels non nuls sur le satellite et à des densitées non négligeables de particules secondaires est appelée gaine de plasma.

- **Le facteur de vue**
  Chaque détecteur de particules possède un champ de vue spécifique potentiellement limité et donc restrictif pour l'interprétation de son environnement. Si l'instrument observe les 4π stéradians autour de lui, alors des éléments du satellite le véhiculant à travers l'espace apparaissent nécessairement dans son champ de vision ce qui induit des mesures erronées. De plus chaque détecteur de particules possède ses propres caractéristiques techniques (avec des gammes d'énergie couvertes et des résolutions en énergie limitées, des fréquences d'échantillonnage variées, *etc*) rendant une vision partielle du plasma mesuré.

- **Le sillage d'ions**
  Le flux de plasma combiné à la vitesse du véhicule spatial peut générer dans la direction résultante une dépression d'ions qui pourra probablement augmenter les perturbations à proximité de la sonde.

- **Les barrières de potentiel**
  Lorsque les particules émises par le satellite (électrons secondaires et photoélectrons) sont générées en quantités importantes elles peuvent s'accumuler localement à proximité des surfaces et dominer la charge d'espace. Cela résulte localement en des potentiels électrostatiques négatifs pouvant constituer des barrières de potentiel pour les particules de basses énergies, en particulier celles émises par le satellite. Ces dernières risquent donc d'être repoussées par les barrières vers le satellite ou son détecteur de particules. D'autres sources de barrières sont par exemple les potentiels élevés de certaines surfaces d'un véhicule par rapport à d'autres surfaces.

- **Autres phénomènes**
  Le dégazage des matériaux, les poussières chargées ou encore la propulsion des satellites sont d'autres éléments pouvant influer sur la condition d'une structure et de son environnement, avec de possibles implications sur les données en vol.

Cet ensemble d'interactions résulte en une variété de perturbations de mesures du plasma basse énergie, de différentes origines et intensités. Dans une situation idéale, il devrait être possible de distinguer l'environnement naturel parmi les données totales fournies par les instruments et d'identifier les sources et les proportions de chaque biais de mesures.

Même si des modèles analytiques combinés à des solveurs numériques existent et donnent des estimations cohérentes des biais de mesures du plasma, ils ne sont valides qu'en ne considérant que quelques perturbations induites par les interactions satellite/plasma. Les éléments clés nécessaires à la compréhension totale de l'environnement spatial via les résultats des instruments sont encore négligés, étant donné que leur modélisation analytique est difficile. Ces modèles sont par ailleurs nécessairement contraints par diverses approximations et simplifications limitant

leurs portées, et ils considèrent souvent les différentes interactions indépendamment les unes des autres. Les modèles analytiques les plus complets sont rapidement dépassés par la considération de plusieurs phénomènes perturbants, notamment pour raisonnements en trois dimensions.

Les simulations numériques, même effectuées après que le satellite eut été conçu, sont essentielles aux physiciens des plasmas. Elles leurs permettent d'abord de concevoir des instruments spécifiques aux environnements à étudier, mieux adaptés aux différents contraintes liées aux plasmas et au satellite portant ces détecteurs. Tant au niveau du champ de vision de l'instrument que de ses caractéristiques techniques telles que les gammes d'énergies étudiées, la résolution en énergie, les fréquences de mesures, voire le positionnement ou l'orientation de l'instrument par rapport au reste de la structure. Mais Les simulations peuvent également aider à anticiper les perturbations sur les instruments en vol et améliorer la compréhension des mesures effectuées (comme par exemple déterminer l'origine d'un flux temporaire de particules dans telle gamme d'énergie).

L'objectif de cette thèse est donc d'étudier et de simuler les phénomènes d'interactions satellite scientifiques/plasma et d'étudier l'impact de ces phénomènes sur les mesures de plasma dans le domaine des basses énergies. L'idée est de développer une méthodologie visant à modéliser correctement ces interactions via des simulations numériques multi-échelles (modélisant des éléments de quelques millimètres jusqu'à plusieurs dizaines de mètres) le tout au moyen du logiciel Spacecraft Plasma Interaction System (SPIS). Il est à noter que ce manuscrit de thèse a été rédigé en anglais.

Pour ce faire, après avoir effectué des rappels historiques et théoriques sur les principes des mesures de plasmas (Chapitre 1), la physique du vent solaire (Chapitre 2), et la présentation physique détaillée des interactions satellite/plasma (Chapitre 3), je présenterai mon outil principal de travail, SPIS, et la méthodologie de simulation. Dans cette même partie (Chapitre 4) je reviendrai sur les deux articles publiés au cours de cette thèse (intégralement disponibles en annexes A.4 et A.5). Nous nous intéresserons en premier lieu à la sonde Solar Probe Plus, et simulerons sa présence à son futur périhélie (à 0,044 UA). Les phénomènes ainsi générés tels que les gaines de plasma constituant des barrières de potentiel ainsi que le potentiel électrostatique négatif de la sonde résultant seront présentés et expliqués. Ensuite, ce modèle de sonde sera déplacé à différentes distances héliocentriques, permettant l'étude de la formation des gaines de plasma et des barrières de potentiel jusqu'à 1 UA. Cette étude paramétrique constitue la deuxième publication et permet par ailleurs de déterminer qu'au périhélie de sa mission (0,28 UA), la mission Solar Orbiter sera concernée par des barrières de potentiel locales et de fortes perturbations au niveau de son instrument EAS. La troisième étape consistera à simuler point par point un détecteur de particules seul dans le plasma soumis à diverses perturbations, et je comparerai les résultats de mesures obtenus avec les mesures théoriques attendues (Chapitre 5). Cette méthode fournira une première quantification des différentes problématiques perturbatrices de mesures (comme les potentiels non nuls et la collection de particules parasites). Enfin je présenterai dans le Chapitre 6 des simulations complexes avancées de mon modèle Solar Orbiter et de son instrument EAS dans divers environnements, ainsi que les quantifications des biais produits par les interactions Solar Orbiter / plasma sur les mesures simulées d'électrons. Un autre cas concernant le satellite Cluster et son détecteur d'électrons embarqué LEEA sera également détaillé, avec la comparaison des mesures simulées à des données réelles. Le bon accord des deux jeux de données confirmera la validité de mon méthode de simulation des interactions satellite/plasma. Ce dernier chapitre fait par ailleurs partie d'un rapport que j'ai fourni à l'Agence Spatiale Européenne dans le cadre d'un contrat pour le développement de l'extension du logiciel SPIS : Spis-Science. Le Chapitre 7 concluera ce travail et en présentera

les perspectives.

1.2 English introduction: Principle of in flight plasma measurement

Hypothesis of space environment nature haunted curious minds since humanity's first light. Putting aside any religious consideration; the Sun and the Moon, Stars and Planets, Aurorae Borealis and Milky Way inspired suppositions, ideas, theories and dreams about this endless and mysterious surrounding horizon. Smaller celestial objects as comets and asteroids, however, fed the fears as their destructive powers have already been assessed on Earth, more or less directly, about 65,000,000 years ago somewhere in central America or more recently in 1911 in the Siberian region of Russia.

Considering now even smaller celestial objects, more precisely microscopic components of the space environment, humans have been consciously confronted to space radiations once Van Allen and his collaborators on *Explorer 1* (an American satellite launched in 1958) discovered near Earth toroidal belts of energetic electrons and protons. This can be considered as the early beginning of spacecraft plasma interactions studies (very soon after the beginning of the space exploration initiated by the Soviet *Sputnik* probe in 1957), since several following missions objectives were to study the Van Allen belts, with many resulting models of the belts and their effects on satellites. The loss of a satellite in the early seventies apparently due to spacecraft charging from the magnetospheric plasma intensified the efforts to understand and anticipate the interactions issues between probes and space environment. The *Spacecraft Charging at High Altitude* program (SCATHA) launched in 1979 was indeed entirely dedicated to this subject. Material erosion and charging, hazardous electrostatic discharges, damages onto integrated electronic components, particle contamination were rapidly identified and studied to avoid as much as possible those phenomena and extend the duration of more and more expensive space missions.

From a scientific point of view, the will to understand the space environment leads to use several instruments on-board satellites, aiming at performing various measurements on the largest span possible. Not only to identify the different particle types that populate the space environment but also to characterize each species distribution in details and thus be able to represent its partitioning of energy. Specific detectors are built to analyse neutral or charged particles, magnetic or electrostatic fields, electromagnetic fluxes, *etc*, but this work will focus on plasma instruments, especially the particle detectors which allow the analysis of the charged particles constituting the plasma.

A plasma can be quickly defined as a state of matter made of a set of charged particles exhibiting a collective behaviour, ruled by electromagnetic interactions (further explanations on plasma physics are reviewed in Chapter 2). Charged particles respond to the presence of a satellite among them through several interactions that make their analyses complex and possibly misleading, with particle measurements more or less distorted. Those interactions are particularly strong in the low energy ranges (considered here as below a hundred of electron-volts), this is why the present study is carried out on this energy span.

Some scientific missions or on-board scientific instruments have been dedicated to the low energy plasma measurements. A review of those missions is presented in the following section.

1.2.1 Past and future scientific missions aiming at analysing low energy plasma

A scientific satellite is a great opportunity for loading on board various instruments, each dedicated to a specific physical interest. Among all past, present or future scientific missions, several carry on-board payload dedicated to low energy plasma measurements.

The NASA *Ranger 1*'s mission, launched in 1961, was to test performance of the new technologies intended for operational Ranger flights and to study the nature of particles and fields in interplanetary space. It carried on-board an electrostatic analyser, but re-entered Earth's atmosphere three days later, because of the loss of its telemetry. The same year its successor *Ranger 2*, with the same objectives, flew only one day, due to a malfunction in its booster rocket.

Pioneer 6, launched in 1965, was the first of four American spacecraft designed to study interplanetary phenomena in space: *Pioneer 7, 8, 9* were respectively launched every year starting in 1966. Each one carried on-board a plasma analyser and constituted the first solar monitoring network. They provided simultaneous scientific measurements at widely dispersed locations in heliocentric orbit.

Helios, a joint German-American deep-space mission, including two twin spacecraft *Helios 1* and *Helios 2* launched respectively in 1974 and 1976, aimed at studying the main solar processes and solar-terrestrial relationship. Its instruments investigated the solar wind, magnetic and electric fields, cosmic rays and dust in regions between Earth's orbit at 1 AU and the closest region from the Sun never reached by any other spacecraft of its generation: 0.29 AU from the Sun. The charged particle experiments covered various energy ranges from 0.15 eV to 1 GeV.

Voyager 1 and *Voyager 2* left the Earth in 1977, aiming at exploring Jupiter and Saturn, thanks to a specific alignment of the outer planets that occurs only once in 176 years. Both spacecraft, still in flight, are carrying among others the following experiments: plasma particles, low-energy charged-particles and plasma wave instruments. In 2013 both orbiters have reached a distance from the Sun greater than 100 AU and are still travelling away at a speed of about 523.6 million km (3.5 AU) per year.

ISEE-3/ICE, launched in 1978, was the third of three *International Sun-Earth Explorers* (ISEE) designed and operated by NASA in cooperation with the European Space Agency. NASA built the first and third spacecraft, while ESA built the second. The three spacecraft were to simultaneously investigate a wide range of phenomena in interplanetary space. Carrying several experiments to study, for example, solar X-rays, solar wind protons and electrons, and plasma composition, it is the first mission to monitor the solar wind approaching Earth. It also detected an impressive plasmoid of electrified gas ejected from Earth's magnetosphere.

The *Ulysses* spacecraft (NASA/ESA), launched in 1990, was equipped with a wide range of scientific instruments. These were able to detect and measure magnetic fields, energetic particles, radio and plasma waves, dust and gas, X-rays and gamma rays. But mainly it carried the *SolarWind Observations Over the Poles of the Sun* (SWOOPS) which measured solar wind ions and electrons in energy ranges between 0.8 and 814 eV [Issautier et al. (2001)]. Ulysses flew above the Sun's southern and northern poles, regions never studied before which allowed the survey of the solar wind from all angles, producing the first three-dimensional picture of the heliosphere.

In 1997, the NASA *Advanced Composition Explorer* (ACE) left the Earth to investigate the matter ejected from the Sun to establish the commonality and interaction among the Sun, Earth, and the Milky Way galaxy. ACE brought many scientific experiments: (SWIMS) so-

lar wind ion mass spectrometer; (SWICS) solar wind ion composition spectrometer; (ULEIS) ultra-low-energy isotope spectrometer; (SEPICA) solar energetic-particle ionic charge analyser; (SIS) solar isotope spectrometer; (CRIS) cosmic-ray isotope spectrometer; (SWEPAM) solar wind electron, proton, and alpha monitor; (EPAM) electron, proton, and alpha particle monitor; (MAG magnetometer) and (RTSW) real-time solar wind experiment. This mission is still in progress and keeps providing space weather reports (*i.e.* about the changes of environmental conditions in near-Earth space) and warnings of geomagnetic storms that might disrupt communications on Earth and harm astronauts in space.

The sample return mission *Genesis*, launched by NASA in 2001, collected during almost three years 0.4 milligrams of solar wind dust, before returning them to Earth, as the first extraterrestrial materials brought since the Apollo Moon missions. The spacecraft also carried an ion and electron monitor.

The NASA sponsored program *Global Geospace Science Program* (GGS), a part of the *International Solar Terrestrial Physics* (ISTP) program, aims at extending the knowledge of the behaviour of the solar-terrestrial system. ISTP is a cooperation between the United States, Japan, Russia, the Czech Republic and ESA, including the *Wind, Geotail, Polar, SOHO,* and *Cluster* missions.

Solar and Heliospheric Observatory (SOHO), still operating since its launch in 1995, is a project of international cooperation between ESA and NASA to study the Sun, from its deep core to the outer corona, and the solar wind. SOHO uses the CELIAS instrument (designed to study the composition of the solar wind and of solar and interplanetary energetic particles).

The *Wind* spacecraft carries eight instruments (including one from France and one from Russia) to investigate the solar wind's encounters with Earth's magnetosphere and ionosphere in order to determine the origins and three dimensional characteristics of the solar wind. Among those instruments there are the Hot Plasma and Charged Particles (3DP); Plasma and Radio Waves (WAVES); Solar Wind Experiment (SWE); Solar Wind and Suprathermal Ion Composition Studies (SWICS/STICS). The mission began in 1994 and is still in progress.

The still operating *Solar TErrestrial RElations Observatory* (STEREO), launched in 2006, is the third mission in NASA's *Solar Terrestrial Probes* program (STP). The mission consists of two space-based observatories - one ahead of Earth in its orbit, the other trailing behind. With this new pair of viewpoints, it is possible to trace the structure and evolution of the flow of energy and matter from the Sun to Earth as well as reveal the 3D structure of *Coronal Mass Ejections* (CME). STEREO has on-board the *In-situ Measurements of Particles and CME Transients* (IMPACT) which samples the 3D distribution and provide plasma characteristics of solar energetic particles and the local vector magnetic field.

Time History of Events and Macroscale Interactions during Substorms (THEMIS) is also a NASA mission (2007) involving five small satellites studying the energy discharges occurring in the terrestrial magnetosphere, causing the polar auroras. Each probe carry an electrostatic analyser (ESA) measuring thermal ions and electrons.

Three missions will be particularly studied in this work. The first one is the NASA *Solar Probe Plus* project, which consists in studying the very close environment of the Sun to understand the heating process of the Sun corona and the acceleration of the solar wind. This spacecraft will approach the Sun as close as 9.5 solar radii above the surface (an heliocentric distance equivalent to 0.044 AU). The launch is planned for 2018 and the first perihelion in 2021. By making direct, in-situ measurements of the region where some of the most hazardous solar energetic particles are energized, this mission should fulfil the following objectives:

- Determine the structure and dynamics of the magnetic fields at the sources of both fast and slow solar wind;
- Trace the flow of energy that heats the corona and accelerates the solar wind;
- Determine what mechanisms accelerate and transport energetic particles;
- Explore dusty plasma phenomena near the Sun and its influence on the solar wind and energetic particle formation;

The second point of interest for this work is the *Cluster II* ESA mission (with a participation of NASA), an in-situ investigation of the Earth's magnetosphere using four identical spacecraft simultaneously, launched in the year 2000. A first launch attempt in 1996, carrying the four satellites Cluster, resulted in the self destruction of the launcher. *Cluster II* now permits the accurate determination of three dimensional and time-varying phenomena with the possibility to distinguish between spatial and temporal variations. The *Cluster* satellites, spinning at 15 rotations per minute, are mapping in three dimensions the plasma structures contained in the following regions: solar wind and bow shock, magnetopause, polar cusp, magnetotail and auroral zone. One of the scientific experiment on-board the mission, and that will be simulated in the work, is the *Plasma Electron And Current Experiment* (PEACE), which looks at all electrons in the space plasma which have low to medium energies, counts them and measures their direction of travel and speed. One part measures faster electrons (*High Energy Electron Analyser* - HEEA), while another part detects slower electrons (*Low Energy Electron Analyser* - LEEA).

Finally the joint ESA/NASA *Solar Orbiter* mission, scheduled for launch in January 2017 and aiming at answering the following questions:

- How and where do the solar wind plasma and magnetic field originate in the corona?
- How do solar transients drive heliospheric variability?
- How do solar eruptions produce energetic particle radiation that fills the heliosphere?
- How does the solar dynamo work and drive connections between the Sun and the heliosphere?

The three-axis stabilized Solar Orbiter will be placed into an elliptical orbit about the Sun with perihelion as close as 0.28 AU. It is equipped with instruments for both in-situ measurements and remote-sensing observations. One of its in-situ device is the *Solar Wind Analyser* (SWA) which consists in a suite of sensors that will measure the ion and electron bulk properties (density, velocity, and temperature) of the solar wind, thereby characterising the solar wind between 0.28 and 1.4 AU from the Sun. One of the sensor, the *Electron Analyser System* (EAS), will be simulated in this work. The next section introduces the concept of on-board particle instruments, their functioning principle and characteristics.

1.2.2 Description of particle instruments

Several scientific experiments allow the analysis and measurements of space ambient plasmas. When the objective is focused on the determination of plasma particle distribution functions, the electrostatic analyser, introduced by [Carlson et al. (1983)], is perfectly adapted. It uses an electric field between two concentric curved plates to guide the flight path of a charged particle

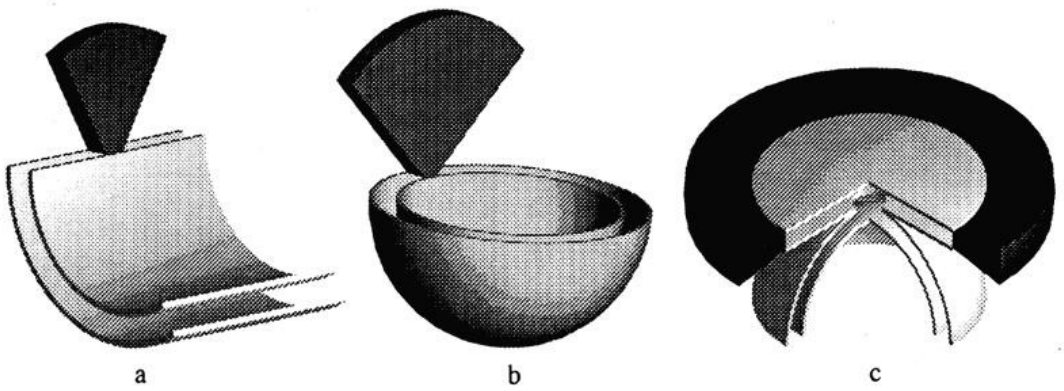

Figure 1.1: Various configurations possibly used for electrostatic analyser geometries: a) cylindrical analyser; b) hemispherical analyser, c) top-hat analyser. The dark areas stand for the instrument type field of view. *Diagram provided by Christopher T. Russell, from the Institute of Geophysics and Planetary Physics / UCLA (http://www-ssc.igpp.ucla.edu/personnel/russell/)*

around a bend to a detector. Few curved plates geometry bases are available for the electrostatic analyser configuration, with various corresponding fan-shaped field of views.

Simplified examples of analysers geometries are given in Figure 1.1, showing a) a pair of cylindrical plates and for b) and c) a pair of spherical plates. Particles enter into the first two detectors (between two electrically biased conducting surfaces) over a limited path length. This length together with the size of the sensor at the end of the curved plate defines a geometric window as illustrated with the dark regions. This field of view (FOV) is characterized by specific acceptance angles proper to each analyser. The top hat analyser on the right hand of Figure 1.1 views a full 360 degrees in azimuth with a narrow fan in the orthogonal direction. This top-hat design has hemispherical plates but the particles enter at the top of the plates and are bent by less than 90 °. The top plate above the entrance helps guide the particles into the slit.

The voltage polarity applied to generate the electric field between the plates, the voltage range and the size of the aperture will determine the particle type, energy and incoming region detected. Indeed the entering particles have to follow the spherical slit of the curved plate analyser, guided by the electric field which exerts a force $q\mathbf{E}$ on the particle that causes it to move in a circle with radius r equal to mv^2/qE. Particles finally end their courses on the segmented *Micro Channel Plates* collector (MCP) at the bottom of the detector, which allows the counting and discretization of incoming particles over the azimuthal field of view (also called the angular resolution).

A representation of a top-hat electrostatic analyser is displayed on Figure 1.2, with a schematic cut of the EESA-High analyser on-board the WIND spacecraft. This is in this case a large electron analyser since deflection plates are mounted just behind the aperture grids and deflect the particle trajectories, and thus the analyser FOV of $\pm$ 45 °. This design allows to overcome the limited field of view of simple hemispherical electrostatic analyser. Finally, combined with a spinning satellite body or a second particle detector on the opposite side of the first one, the instrument configuration can easily provide a coverage of the entire 4π steradians of the particle environment. For instance the EAS analyser mounted on three axis stabilized Solar Orbiter spacecraft is a set of two sensors similar to EESAH, which covers the entire surrounding electron environment.

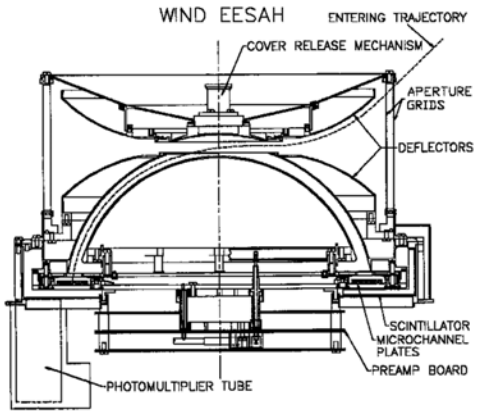

Figure 1.2: Schematic cut of the EESA-High top-hat electrostatic analyser on-board the WIND spacecraft. This analyser is one of the four 3DP instrument detectors, covering high energy electrons from 200 eV to 30 keV (though typical values vary from a minimum of 137 eV to a maximum of 28 keV) in a 32 sample energy sweep, each one covering 11.25 ° of spacecraft spin. EESAH has a 360 ° planar FOV tangent to the spacecraft surface which can be electro statically deflected into a cone up to ± 45 ° out of its normal plane. *Diagram provided by Christopher T. Russell, from the Institute of Geophysics and Planetary Physics / UCLA (http://www-ssc.igpp.ucla.edu/personnel/russell/)*

A complex electronic chain is deployed further to the MCP to amplify and multiply the signal received on the detector. This technical aspect of the detector response conversion and intern processing is not of concern in this study, as the focussing is brought on plasma measurement results correlated with the spacecraft/plasma interaction effects. Those particle detectors provide output that can be integrated over certain durations, over the entire field of view or discretized over the instrument pointing direction. Each electrostatic analyser has its own characteristics such as the FOV, the accepted energy range and resolution, the measurement period, and calibration [McFadden et al. (2005)].

Detailed concepts and descriptions of particle measurement techniques in space plasmas are available in the reference book of [Pfaff et al. (1998)].

1.3 Sources of perturbations

A flying satellite is submitted to several interactions with the environment. The main interactions are summed up on Figure 1.3 and will be briefly enumerated in the following (the detailed descriptions of those phenomena can be found in section 3).

- **Spacecraft charging**
  A satellite immersed in a space plasma will collect charged particles and thus modify its electrostatic potential. The surrounding ambient plasma will be more or less affected by the satellite potential(s), depending on; the charges, the particles mean energy and the potential levels, leading to various ranges of distortions in plasma observations;

- **Parasite particles emission**
  Through particles impacts on the spacecraft structure, low energy electrons are released

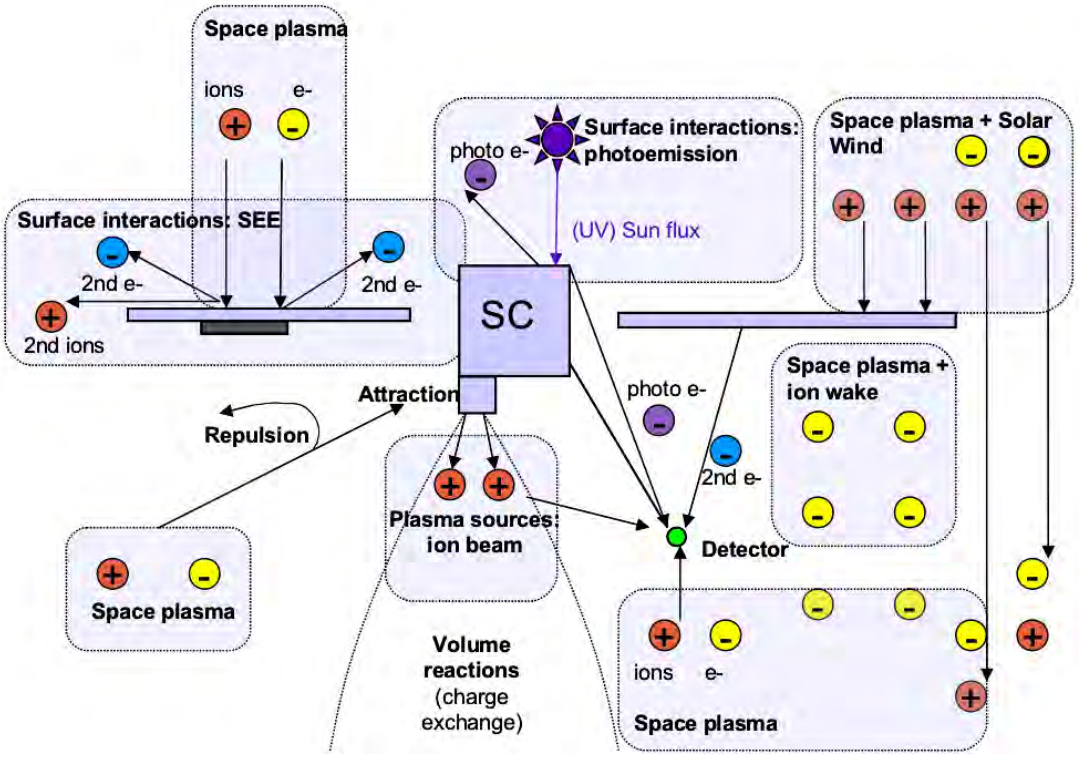

Figure 1.3: Schematic representation of main satellite/plasma interactions

from the covering materials with rates depending on plasma and materials properties, adding new populations in the vicinity of the probe and new currents to its surfaces. Those generated populations (*Secondary Electron Emission under Electron impact* or SEEE, *Secondary Electron Emission under Proton impact* or SEEP, electrons emitted under Solar UV radiations or photoelectrons) may be collected by the particle detectors and affect the measurements;

- **Space charge effects**
  On a large enough scale a plasma at equilibrium is electrically neutral. At smaller scales and especially near the spacecraft surfaces the quasi-neutrality might not be respected. This region is also called the *sheath*;

- **Viewing factor**
  Each particle detector has a specific field of view which can be limited and therefore restrict the interpretation of the environment. If the instrument sees the entire 4π steradians around it, some spacecraft parts appear in the field of view which might induce erroneous measurements. Also particle detectors have their own technical properties (with specific energy ranges and resolutions, sampling, measurement frequencies, *etc*) which give a partial view of the measured plasma;

- **Ion wake**
  The plasma flow combined to the vehicle velocity can generate, in the resultant direction, an ion depletion which will likely increase the disturbances on the near probe environment;

- **Potential barriers**
  When spacecraft-generated particles (secondary and photoelectrons) are emitted in high quantities they might accumulate in regions near from the satellite and dominate the space charge. This results in a negative local electrostatic potential which constitutes a barrier for low energy particles, especially the spacecraft-generated particles. The latter can thus be repulsed by the barrier and return to spacecraft or its plasma instrument. Other sources of barriers are the spacecraft surfaces at high potentials with respect to other surfaces;

- **Other phenomena**
  Material outgassing, plasma dust, propulsion are other elements that might modify the conditions on the satellite and in its near environment, with possible perturbations in the plasma measurements.

This set of interactions disturbs the satellite surrounding environment and thus the associated measurements, resulting in various biases of different origins and intensities. In an ideal situation, one should be able to distinguish the natural environment from the total biased signal and identify the sources and proportions of each disturbance in the in-flight data.

1.4 Measurements analysis methods

1.4.1 Partial consideration of perturbations

Once the previously enumerated various perturbations impacting plasma measurements are understood, it should be possible to apply corrections on output instrument data to get back to the "true" environment characteristics. Various possibilities exist, provided that only few perturbations are taken into account. Some phenomena presented in section 1.3 are indeed highly inter-correlated with each other and, when modelled by simplified considerations, cannot fully explain certain features observed in the plasma instrument outputs.

For instance to explain observations of recollected photoelectrons and secondary electrons on the ATS 6 spacecraft, [Whipple (1976)] proposed a spherically symmetric photoelectron sheath model, including effects of ions, thermal electrons and secondaries to determine whether the potential barrier responsible for the secondaries reflection was originating from those same particles or not. However, a comparison with the spacecraft data showed that the observed barrier of potentials is too large to be explained by their model (*i.e.* a spherically symmetric photoelectron or secondary electron sheath surrounding a uniformly charged spacecraft). The authors concluded that the most probable explanation is that some portions of the ATS 6 surfaces are charged to different potentials.

In the context of instruments for active control of the potential, [Zhao et al. (1996)] proposed an analytical approach to compute the electrostatic barrier and compared to the Geotail spacecraft measurements. However, this analysis is also only relevant in a sheath approximation and does not consider the secondary electronic emission.

[Thiébault et al. (2004)] developed a fully self-consistent analytical model of the plasma around an electron emitting central body in a spherically symmetric geometry, used to analyse the electrostatic sheath around an idealized spacecraft. The aim was to apply their model for cases of conductive spacecraft (like Geotail and Cluster). It was shown by comparison with 3D *Particle In Cell* (PIC) simulations that non-monotonic potential with negative potential

barrier can exist all around a positively charged spacecraft, even in the case of an asymmetric illumination pattern. Yet this model is too simplistic to allow detailed comparisons with observations.

The "perfect" detector concept, introduced in [Song et al. (1997)], considers an ideal spectrometer without any calibration issues which makes the uncertainties in the calculated moments purely caused by the technical constraints (upper and lower cutoffs) and the formation of secondary and photoelectrons from the spacecraft. They predicted that in the presence of the spacecraft potential the cutoff energies should be evaluated as the detector's cutoff energies plus (minus) the satellite potential for ions (electrons), even though the calculations were performed considering a null spacecraft potential.

In [Salem et al. (2001)] the low energy cutoff is considered, and the variable potential of the WIND spacecraft is taken into account to treat the electron measurements obtained from the electron electrostatic analyzer of the three-dimensional Plasma experiment (3DP) and the thermal noise receiver (TNR), which yields unbiased electron density and temperature from the spectroscopy of the quasi-thermal noise around the electron plasma frequency. They derive the analytical relations for the measured electron moments as functions of the real ones. Then using the TNR densities and temperatures as good estimates of the real ones, they fit the coefficients of analytical solution to the data from both instruments. However a limitation of this method is that it is only valid for an isotropic Maxwellian distribution.

Several attempts for correcting the measured moments of a drifted Maxwellian distribution function have been proposed with quite successful results, especially in the published work of [Génot et al. (2004)] and [Geach et al. (2005)]. Indeed the first presents a complete computation of the effect of the spacecraft potential on electron moments. They assume a perfect detector, several plasma regimes and spacecraft potential values, then compute the true moments (which would be measured by the perfect detector) of the distribution function, starting from a biased moment. Their methodology consists in expressing analytically the measured and biased moments (density, velocity and temperature) as functions of the (a priori unknown) true moments of a Maxwellian distribution function in free space, the spacecraft potential, and lower and upper energy cutoffs of the detector. After the numerical inversion of the obtained non-linear system, the algorithm provides the "real" moments. It leads to several estimations of the influence of the spacecraft potential, the detector energy ranges and the environment on the necessary correction rates between measured and real moments.

A direct application of this method is displayed in [Geach et al. (2005)] where the corrected moment data from Cluster's PEACE experiment in different plasma environments are computed. They can correct the electron moments calculated on-board from the effects of potential broadening and energy range truncation, and make comparisons with data from other Cluster instruments, as well as the equivalent ground-based calculations using full 3-D distribution PEACE telemetry. The generic correcting procedure is proved to be efficient, showing that the obtained corrected moments match the ground based calculations and data from other Cluster instruments. This work aimed at demonstrating that on-board calculated moments can be corrected to gain accurate data from plasma detectors, despite the physical limitations of flying such devices in space. Unfortunately the more general approach used in that paper did not integrate the secondary and photoelectrons, which are essential for the low energy plasma measurements [Szita et al. (2001)].

Concerning ion wakes, [Engwall (2006)] performed theoretical analysis and computer simulations to demonstrate an enhanced wake formation process behind a positively charged spacecraft in flowing tenuous plasma. Their model shows good agreement with comparison to observa-

tions from the Cluster satellites. Even though the impact of the wake on PEACE measurements was not the point of this paper, further analysis that would include the wake should be quite interesting to evaluate the associated perturbations on low energy particle measurements.

1.4.2 Grey areas for a quantitative measurement

Even though analytical models combined with numerical solvers exist and provide consistent results in estimating plasma measurement biases, they remain valid for the consideration of only few perturbations induced by spacecraft/plasma interactions. Key elements for a complete space environment understanding through plasma instrument data analysis are still neglected, as their analytical modelling are difficult.

It is shown in the previous section that perturbations induced by all the spacecraft/plasma interactions are obviously a subject of interest for plasma physicists and modellers, but the issues are usually studied independently from each others, despite their inter-correlation. Analytical models are rapidly overwhelmed or more simply impossible to establish when dealing with several interdependent sources of perturbations. Moreover an analytical expression of a complex physical process implies different assumptions and approximations that drastically limit the range and the validity of this formulation. This simplification is of course necessary to set the theory but avoids some critical issues.

A blatant example is the consideration of 3D aspects of the spacecraft/plasma interactions. Considering the particles coming purely radially to the detector (as in [Génot et al. (2004)]) or based on a plane-parallel approximation ([Scime et al. (1994)]) ignores all of the spacecraft relevant aspects of the sheath, solar illumination (shadowing, booms), three dimensioned ion wake, and also different material properties depending on the satellite surfaces considered, *etc.* Particle deflections due to local surface (and eventually differential) potentials can lead to misinterpretations of the local plasma parameters. Authors are perfectly aware of this charged spacecraft focussing issue and admit that the analytical method reached its limits. Global PIC simulations should help analysing the interactions network as they handle 3D geometries with adequate material properties plus the computation of individual particle trajectories.

1.5 Interest of numerical simulations

1.5.1 Anticipating the problems: help to design spacecrafts and instruments

There is no need to harp on about the global advantage provided by computers in the preliminary studies concerning all the possible engineering fields. From the space engineering point of view, numerical simulations are obviously essential to conceive a satellite and anticipate mechanical, thermal, electrostatic, and many other issues in the final probe design. Several powerful softwares are available to compute and solve (more or less independently) these problems and configure efficient and robust satellites for telecommunication, military or scientific use. Simulating a satellite within its expected environment allows the anticipation of the possible charging that can occur (in case of arcing risks between several elements if the potentials reached are hazardous), the rates of secondary emission, the ion wake dimension and orientation, *etc.* If all the problematic interactions aforesaid were modelled through numerical simulations one would have a comprehensive understanding of the complex satellite/environment system.

Numerical studies even when performed after that the satellite has been practically designed are essential to the plasma physicists. Modellers wish to conceive particle detectors that will

analyse specific physical environments, knowing that the instruments themselves will respond to the environment (through secondary emission and charging), in the vicinity of a satellite structure which will also react to the environment. Once a scientific probe orbit has been defined and the expected encountered space environment conditions have been determined, simulations are not only useful to conceive an instrument that will correctly measure the expected ambient plasma (in terms of energy range, scanning frequency, aperture angle, field of view) but also to anticipate the instrument constraints generated by the interacting system "satellite + instrument + plasma".

Some issues have been described in the previous sections and are hardly avoidable but it is still possible to limit the impact of the interactions on plasma measurements by choosing adapted materials at key locations, which can for example emit fewer parasite particles in certain environment conditions, or generate fewer disturbances owing to lower charging potential level. Some technical designs on the satellite are often mandatory and scientists who submit the instrument proposals have no choice but to yield to the constraints imposed by thermal, electrical or mechanical considerations. However there is practically no interest in embedding an instrument that will be blind most of the time. Numerical simulations provide insight on leeways and compromises for optimizing the correlation of the "satellite + instrument + plasma" system and providing more accurate evaluations of the space environment.

In this context the *Spacecraft Plasma Interactions Network in Europe* (SPINE) community has been initiated in 2000 by the *European Space Research and Technology Centre* (ESTEC) in Noordwijk, Netherland. The objective of this network is to share resources and to coordinate efforts in all domains related to the interaction of Spacecraft with the space plasma, including spacecraft charging. The SPINE Web site[1] is an advanced platform for information exchange and collaborative work, a kind of Virtual Laboratory dedicated to studies of spacecraft/plasma interactions. SPINE provides guidance for the SPIS software development and participates to the software development and testing.

Concurrently with this PhD study, I am also a young scientist member of the *Interaction of Satellites with Space Environment* team[2], hosted by the *International Space Science Institute* (ISSI - Bern, Switzerland). The objective of this group is to advance knowledge and understanding in targeted areas in ways that would not be possible without the level of collaboration considered in this team. Research activities concentrate on five basic and interdependent aspects of satellite interaction with the space environment. These are: 1/ charging, 2/ sheath effects, 3/ particle emission from surfaces, 4/ transient responses and 5/ wake dynamics. The group uses a combination of computer models (EMSES, iPic3D, LASP, PTetra and SPIS - references about those numerical codes will be cited in Section 4) and, where possible, detailed measurement results. Different plasma conditions are considered including the ionosphere, Earth magnetosphere and the interplanetary solar wind. Studies are also conducted by considering specific cases or missions of direct interest to group members including for example, Solar Probe, Solar Orbiter, Rosetta, Cluster or Swarm.

1.5.2 Analysing in-flight measurements

Thanks to numerical simulations, some of the disturbances can be modelled ahead of the real in flight measurement, allowing scientist to anticipate certain phenomena aforementioned. For

[1]SPINE community Web site, *http://dev.spis.org/projects/spine/home/spis*

[2]Interaction of Satellites with Space Environment team web site, *http://www.issibern.ch/teams/satspacenv/-index.html*

instance, through a simulation of a specific satellite (considering its appropriate geometry and covering materials in the expected environment) one can predict the pollution rate of secondary and photoelectron within the detected ambient electron population, allowing a better correction of the measured moments. The spacecraft charging level can also be anticipated in order to prepare the measurements operation phases.

Once the satellite is operational and provides data, numerical simulation can allow a better understanding of the instruments responses. For example by predicting the potential distribution on spacecraft surfaces to avoid erroneous interpretation of plasma measurements. This is especially useful when some covering material potentials will disturb the local populations (while those potentials are indicated within the spacecraft telemetry data). The simulated measurements compared with real data enable the verification of a hypothesis, the identification the origin of some unknown measured phenomena origin and the correction of output data.

1.6 Objectives of this work

In this introduction were briefly presented the main issues related to low energy particle measurements through plasma instruments on-board scientific satellites. Sources of perturbations are many, interrelated and intrinsic to the presence of the spacecraft within the same environment it is supposed to analyse. The spacecraft perturbs its close environment which disturbs in return the satellite.

Philosophically speaking, this same concept of inter-correlation between the observer and the studied phenomenon can be found again in many other domains, where the mere fact of doing in-situ passive measurements modifies the subject and misleads the analyst. Few examples can be given in the fields of sociology, where a studied population or remote tribe might change their behaviour in front of ethnologists. Zoologists studying wild animals always keep their distance with the group, conceal their presence and use powerful telephoto lenses to avoid modifying the behaviour of the subjects that they observe. Another analogy can be made: the Lascaux caves (in the Dordogne province in France), one of the most important paleolithic site, had to be identically reproduced just next to the original site so the tourists could continue the visits, as the real cave was eroded by fungus and bacteria brought by archaeologists and visitors. In all these cases the disturbing factors have been identified and taken into account for the studies results, as it is not always possible to avoid those biases.

In the field of space sciences and especially on-board instruments, several laboratories acquired the expertise in conceiving accurate and rigorously calibrated devices. The error margins and necessary corrections intrinsic to the instrument are known, quantified and easily used. However the low energy plasma disturbing effects due to the spacecraft/environment interactions remain largely unquantified, and somehow neglected in the design of spacecraft. Physical principles of each perturbation source (SEEE, SEEP, photoemission, charging, *etc*) are known but their effects on plasma analysis need further investigations. Generally the quantification of disturbances is made a posteriori, when the satellite is already cruising in space providing data and no changes can be made concerning the spacecraft and instrument configuration. As explained in the previous section numerical simulations allow a better understanding of the in-flight measurements, but for example it can also enhance the design and configuration of a probe and its embedded detectors.

The purpose of this thesis is to propose a methodology for evaluating the impact of the main spacecraft/plasma interactions on the satellite itself, on its close environment and fi-

nally on plasma measurements, with a quantitative determination of the induced biases. This methodology should aim to:

- optimise the design and configuration of scientific spacecrafts and their embedded plasma instruments
- enhance the in-flight data analysis of plasma measurements by providing quantitative corrections that will better represent the undisturbed environment.

1.7 Plan and sum up

A simple summary of these spacecraft/plasma interactions overview consists in saying that a spacecraft disturbs its near environment which in return alters the satellite. In this way, the near spacecraft environment results in a combination of a natural ambient environment and a spacecraft generated environment. The first depends on the vehicle position on its orbit and the Solar activity at a given time, the second depends on the satellite structure and on the first environment, through highly synergistic interactions that cannot be considered as linear. This final spacecraft environment (which differs from the natural ambient environment) is the one measured by the mission instruments, and should thus be considered as biased, as for its consecutive measurements.

In Chapter 2, we will first describe the Solar wind (section 2), flowing over all the scientific satellites simulated in this work. The chapter will start with a reminder of a few concepts of plasma physics: defining the particle distribution functions, plasma scales and the magnetic field effect on plasmas, before presenting the Solar wind characteristics, with an introduction of its interaction with a well known space travelling object: the Earth. Some observations and examples of Solar wind measurements will finally be illustrated. Note that the Table A.1 in section Appendix A.1 displays the various physical and geophysical constants used in this work.

Chapter 3 will detail the various plasma interactions with space vehicles, starting with a review of what are the equilibrium electrostatic potentials and consecutive currents balance. The main natural and spacecraft generated particles interactions with a space probe will also be explained, with a presentation of the several analytical methods existing to model those phenomena. Other effects of a spacecraft presence in a plasma will be introduced, such as wakes and potential barriers. The idea is to enumerate the various interactions that can disturb space plasma measurements, and thus present a non exhaustive list of the main issues to be considered by numerical modellers, satellite and plasma instrument designers and plasma physicists processing low energy plasma experiment outputs. This is why this section continues with a description of the measurement biases intrinsically linked to the particle detectors themselves. It finally ends with a brief presentation of other perturbing issues related to spacecraft technical design (particle emitters, Solar arrays structures, outgassing, *etc*).

From this state of knowledge the *Spacecraft Plasma Interaction System* (SPIS), the numerical tool used for all computer simulations performed in this work will be presented (Chapter 4) with a tutorial on the good numerical practices to properly and efficiently model spacecraft/plasma interactions, from the very beginning of the study to the analysis of the simulation results. The presentation will directly jump to the first applications of those methods, by presenting two parametric studies, whose corresponding published articles are joined in the appendix A.4 and A.5. Those papers focus on particular issues linked to the spacecraft plasma interactions: the photoelectron and secondary electron sheaths, the associated potential barrier and its effect on

a simple conducting satellite equilibrium currents and potential. The first paper deals with a simulation set at the Solar Probe Plus satellite at its closest perihelion (at 0.044 AU from the Sun) with a sensitivity study of several physical and numerical parameters on final steady probe potential and currents. The second extends the simplified Solar Probe Plus case to ten heliocentric distances, from 0.044 to 1 AU, in order to observe the evolution of the sheaths, potential barriers and satellite equilibrium potential and currents. The chapter ends with a discussion of the effects of the simulated phenomena on low energy plasma measurements.

Chapter 5 takes on the numerical particle instruments concept and simulations. First defining the scientist's needs, it presents the principle of numerical measurement and the methods. The next sections show a simulation campaign of a single particle detector instrument immersed in a plasma, with step-by-step increments in the complexity of the environment aiming at getting closer to a realistic simulation of satellite/plasma interactions. At each step the simulated plasma measurements are presented and compared with theoretical results. The differences between analytical theory and numerical results are evaluated and discussed.

Chapter 6 enters into more sophisticated and completed SPIS simulations, with detailed geometries of two spacecraft, Solar Orbiter and Cluster, immersed in their natural environment, coupled with their own particle analysers, EAS and LEEA (section 1.2.1). After the presentation of the simulations inputs (geometry, environments, detectors), simulation results for the satellites and the near environment will be displayed and discussed, before presenting the numerical particle measurement outputs and their analysis. The chapter ends with a discussion of the scientific applications and engineering considerations.

Finally, Chapter 7 presents a conclusion of this thesis, and some perspective on possible future work.

Chapter 2

The Solar wind plasma

Contents

2.1 Plasma physics 19
2.1.1 Distribution functions 19
2.1.2 Plasma scales: Debye length and plasma frequency 22
2.1.3 Magnetic field 23
2.2 The Solar wind 25
2.2.1 Properties and observations 25
2.2.2 Interaction with the magnetic field: the magnetospheres 29

2.1 Plasma physics

2.1.1 Distribution functions

The velocity distribution functions are fundamentals of plasma physics. These are the basics of the kinetic phenomena that scientists want to understand in the studied plasma, but also the fundamental inputs to initialise the numerical simulations. In this section are presented the most common velocity distribution functions, especially those used in the simulations performed in this work. Necessary reminders on the concept of the distribution functions are presented in appendix A.

2.1.1.1 Maxwellian distribution functions

Basic theory about the most probable distribution function of a system in thermodynamic equilibrium was introduced by [Vincenti and Kruger (1965)] and [Bittencourt (1986)]. This function is actually the famous Maxwellian equilibrium distribution function.

Considering $\mathbf{u}(\mathbf{x}, t)$ the average macroscopic velocity of the particles:

$$\mathbf{u}(\mathbf{x}, t) = \langle \mathbf{v} \rangle$$

the Maxwellian distribution function is defined as:

$$f(\mathbf{x}, \mathbf{v}, t) = n(\mathbf{x}, t) \left[\frac{m}{2\pi k T(\mathbf{x}, t)} \right]^{3/2} \exp \left[\frac{-m|\mathbf{v} - \mathbf{u}(\mathbf{x}, t)|^2}{2kT(\mathbf{x}, t)} \right] \tag{2.1}$$

where n is the density, $\mathbf{u}$ the average velocity, k the Boltzmann constant, T the characteristic temperature of the plasma and m the mass of the particle considered (m_e for electrons and m_p for protons). See Table A.1 in the Appendix A.1 for the numerical values of the constants. The term $\mathbf{v} - \mathbf{u}$ is the random velocity:

$$\mathbf{c} = \mathbf{v} - \mathbf{u} \tag{2.2}$$

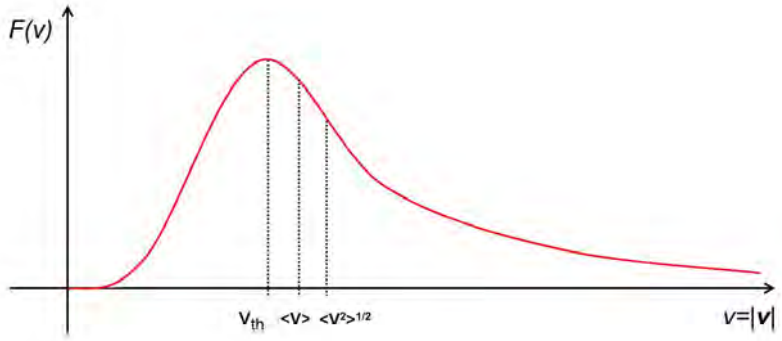

Figure 2.1: Plot of equation 2.8 illustrating the aspect of the Maxwellian distribution function. The thermal, mean and root mean square velocities are identified on the abscissa axis

with $\langle \mathbf{c} \rangle = 0$. Considering the case where $\mathbf{u} = 0$, several properties can be extracted by integration of equation 2.1:
Thermal velocity v_{th} (which is the most probable speed):

$$v_{th} = (2kT/m)^{1/2} \tag{2.3}$$

Mean speed:

$$\langle v \rangle = (8kT/\pi m)^{1/2} \tag{2.4}$$

Root mean square velocity:

$$\langle v^2 \rangle^{1/2} = (3kT/m)^{1/2} \tag{2.5}$$

Most probable energy:

$$E = \frac{1}{2}kT \tag{2.6}$$

Mean energy:

$$\langle E \rangle = \frac{3}{2}kT \tag{2.7}$$

Finally, if the distribution function is isotropic it only depends on the speed $v = |\mathbf{v}|$, and it can be expressed as the reduced distribution function F (after conversion into spherical polar coordinates):

$$F(v) = 4\pi \left(\frac{1}{\pi}\right)^{3/2} (v^2/v_{th}^2) \exp(-v^2/v_{th}^2) \tag{2.8}$$

Equation 2.8 is plotted on Figure 2.1 which gives the known general aspect of the Maxwellian distribution function. The thermal, mean and root mean square velocities are identified on the abscissa axis.

If an electrostatic potential $\Phi(\mathbf{x})$ is present within the plasma, the local density of particles of charge q becomes:

$$n(\mathbf{x}) = n_0 \exp\left(-q\phi(\mathbf{x})/kT\right) \tag{2.9}$$

For an electron: $q = -e =$. The exponential in equation 2.9 is called the Boltzmann factor. In this case the local Maxwellian distribution function can be written as:

$$f(\mathbf{x}, \mathbf{v}, \phi, t) = n_0(\mathbf{x}, t) \left[\frac{m}{2\pi kT(\mathbf{x}, t)}\right]^{3/2} \exp\left(\frac{-\left[m|\mathbf{v}|^2 + q\phi\right]}{2kT(\mathbf{x}, t)}\right) \tag{2.10}$$

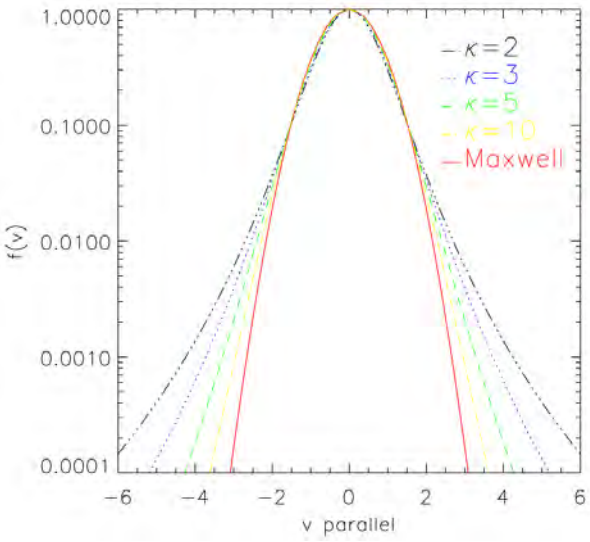

Figure 2.2: The Kappa velocity distribution function for several values of the κ parameter. When $\kappa \to \infty$ the Kappa distribution approaches a Maxwellian. $v_{\parallel}$ is the velocity component parallel to the local magnetic field direction. *Figure taken from* [Pierrard and Lazar (2010)].

2.1.1.2 Kappa distribution functions

The Solar wind plasma at thermal equilibrium is usually modelled through a Maxwellian distribution function. However, other types of distribution functions are useful to describe the Solar wind. Indeed in the plasma particle velocity distribution of the measured Solar wind, observations were made of some non-Maxwellian suprathermal tails [Maksimovic et al. (2005)]. Those non-thermal populations can be well modelled thanks to the so-called Kappa (κ) distribution function, also called generalized Lorentzian, as explained in [Pierrard and Lazar (2010)] and also [Summers and Thorne (1991)]:

$$f_\kappa(v) = \frac{n}{\pi^{3/2}} \frac{1}{\theta^3} \frac{\Gamma(\kappa+1)}{\kappa^{3/2}\Gamma(\kappa-1/2)} \left(1 + \frac{v^2}{\kappa\theta^2}\right)^{-(\kappa+1)} \tag{2.11}$$

with

$$\theta^2 = \left(\frac{2\kappa-3}{\kappa}\right)\left(\frac{T}{m}\right)$$

κ is the parameter that, when approaching infinity, makes the Kappa distribution function approach a Maxwellian (as illustrated on Figure 2.2). Note that $\kappa > 3/2$ and $\Gamma(x)$ is the Gamma function.

According to [Montgomery et al. (1968)], [Feldman et al. (1975)], [Štverák et al.(2009)], the Solar wind electron velocity distribution function can be considered as the sum of three distinct populations (Figure 2.3): an isotropic Maxwellian *Core* plus an isotropic Lorentzian *Halo* plus a drifting isotropic Lorentzian *Strahl*.

$$f(v) = f_c(v) + f_h(v) + f_s(v) \tag{2.12}$$

For the Core electron population (of density n_c and temperature T_c), with the identification of $V_c = (2kT_c/m)^{1/2}$, equation 2.1 can be written as

$$f_c(v) = n_c \frac{1}{\pi^{3/2}} V_c^{-3} \exp\left(-\frac{v^2}{V_c^2}\right) \tag{2.13}$$

For the Halo population (of density n_h and temperature T_h), the velocity V_h is

$$V_h = \left[\frac{2\kappa - 3}{\kappa}\frac{kT_h}{m}\right]^{1/2}$$

which allows to rewrite equation 2.11 as

$$f_{h,\kappa}(v) = \frac{n_h}{2\pi\kappa^{3/2}V_h^3}\frac{\Gamma(\kappa+1)}{\Gamma(\kappa-1/2)\Gamma(3/2)}\left(1+\frac{v^2}{\kappa V_h^2}\right)^{-(\kappa+1)} \tag{2.14}$$

The Strahl population (of density n_s and temperature T_s) is drifted away from the Sun, carrying the heat flux. The drift velocity has three components and can thus be defined in the (x, y, z) basis as $V_D^2 = V_{Dx}^2 + V_{Dy}^2 + V_{Dz}^2$. In this case by defining:

$$u^2 = (v_x - V_{Dx})^2 + (v_y - V_{Dy})^2 + (v_z - V_{Dz})^2$$
$$V_s = \left[\frac{2\kappa - 3}{\kappa}\frac{kT_h}{m}\right]^{1/2}$$

equation 2.11 can be written as

$$f_{s,\kappa}(v) = \frac{n_s}{2\pi\kappa^{3/2}V_s^3}\frac{\Gamma(\kappa+1)}{\Gamma(\kappa-1/2)\Gamma(3/2)}\left(1+\frac{u^2}{\kappa V_s^2}\right)^{-(\kappa+1)} \tag{2.15}$$

2.1.2 Plasma scales: Debye length and plasma frequency

A plasma, sometimes described as the fourth state of matter, is defined as a set of charged particles whose behaviour is ruled by collective particle interactions [Bittencourt (1986)]. Looking on a large enough scale a plasma at equilibrium is electrically neutral. The characteristic length over which the neutrality is established is called "Debye length" and is expressed as:

$$\lambda_D = \sqrt{\frac{\varepsilon_0 kT}{n_0 e^2}} \tag{2.16}$$

with ε_0 being the permittivity of free space, n_0 the plasma density and T the characteristic temperature of the plasma.

The Debye length is thus the scale over which mobile charge carriers (usually electrons) screen out electric fields. It is the distance over which significant charge separation can occur. If a material surface is in contact with a plasma and in the presence of electrical fields: the characteristic thickness of the region in front of the surface is λ_D, and this region is known as the sheath. Inside the sheath charged particles behave as individual particles dominated by electromagnetic forces and the plasma may not be in necessarily locally neutral (especially near the satellite surfaces where particle emission and collection are important). Considering the satellite dimension L_{SC}: if $\lambda_D \gg L_{SC}$ the system "satellite/plasma" is considered as electrically coupled, meaning that a potential on one spacecraft element will be felt all over the satellite.

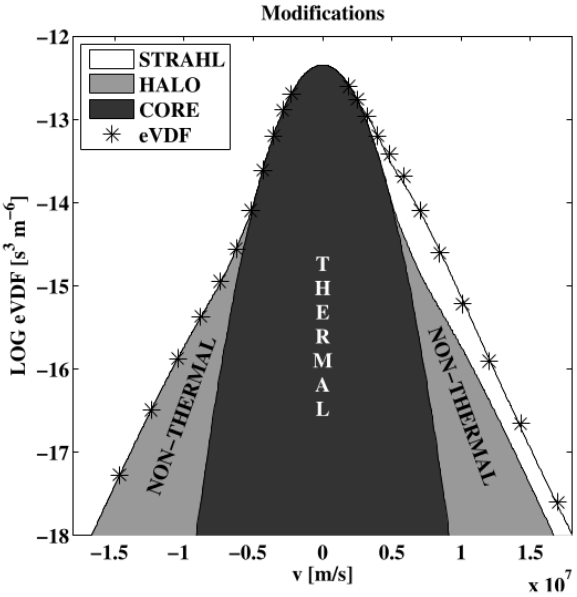

Figure 2.3: Model of the electron velocity distribution function used in [Štverák et al.(2009)], composed of a sum of three distinct components: a thermal Core f_c, a hotter suprathermal Halo f_h and a magnetic field-aligned Strahl f_s.

This corresponds to a situation where the so-called *thick sheath* approximation is valid. On the other hand if $\lambda_D \ll L_{SC}$ the system is electrically uncoupled and each element is only coupled to the surfaces in its near vicinity (unless different satellite components are internally coupled electrically, as for biased probes, or for components interconnected with resistors). In this case the *thin sheath* approximation is used.

Another characteristic property linked to the electromagnetic phenomena occurring in a charged plasma is the fundamental electron oscillation frequency, which is associated to the wave excitation and propagation that occur in a plasma:

$$\omega_{p,e} = \sqrt{\frac{e^2 n_e}{\varepsilon_0 m_e}} \tag{2.17}$$

It can also be calculated for ions ($\omega_{p,i}$) by substituting n_e and m_e with respectively n_i and m_i. This electron plasma frequency can also be expressed, using the Debye length formulation 2.1.2, as

$$\omega_{p,e}^2 = \frac{v_{th,e}^2}{2\lambda_D^2} \tag{2.18}$$

It can be understood as the oscillation frequency of a plasma where thermal fluctuation separates the electrons from the ions by a Debye length.

2.1.3 Magnetic field

The charged particles constituting the space plasma are subject to electromagnetic forces which regroup the electrostatic force

$$\mathbf{F}_E = q\mathbf{E} \tag{2.19}$$

and the magnetic force

$$\mathbf{F}_B = q(\mathbf{v} \times \mathbf{B}) \tag{2.20}$$

with q being the particle charge: $q = Ze$ with Z the charge number on the particle: -1 for an electron, +1 for a proton, +2 for a doubly charged ion, *etc.* $\mathbf{F}_E$ is the electric force and $\mathbf{F}_B$ the magnetic force. Applying the fundamental principle of particle dynamics results in the Lorentz force equation:

$$\frac{d\mathbf{v}}{dt} = \frac{q}{m}(\mathbf{E} + \mathbf{v} \times \mathbf{B}) \tag{2.21}$$

Considering a null electric field and a constant and uniform magnetic field aligned with for example the z direction of a reference Cartesian basis $(\mathbf{e}_x, \mathbf{e}_y, \mathbf{e}_z)$, the magnetic field is defined as $\mathbf{B} = B\mathbf{e}_z$ and the velocity perpendicular to $\mathbf{e}_z$ as $\mathbf{v}_\perp$. Then the equations of motion are:

$$\frac{dv_z}{dt} = 0$$
$$\frac{d\mathbf{v}_\perp}{dt} = \frac{qB}{m}\mathbf{v}_\perp \times \mathbf{e}_z$$

The solution is

$$v_x = v_\perp \sin(\Omega t + \phi)$$
$$v_y = v_\perp \cos(\Omega t + \phi)$$
$$v_z = v_\parallel$$

with $v_\perp^2 = v_x^2 + v_y^2$ and the trajectory

$$x - x_0 = \frac{-v_\perp}{\Omega}\cos(\Omega t + \phi)$$
$$y - y_0 = \frac{v_\perp}{\Omega}\sin(\Omega t + \phi)$$
$$z - z_0 = v_\parallel t$$

If $v_{z0} = 0$ the trajectories are circles in the plane perpendicular to the magnetic field vector. The particles gyrate with the cyclotron frequency Ω of

$$\Omega = qB/m \tag{2.22}$$

The gyro or cyclotron radius of this circular trajectory is

$$r = \frac{v_\perp}{\Omega} = \frac{mv_\perp}{qB} \tag{2.23}$$

If $v_{z0} \neq 0$ the charged particle trajectory is thus a spiral along the magnetic field direction (this spiral corresponds to the combination of the cyclotron motion and the translation along $\mathbf{B}$ imposed by $v_\parallel$). This particle trajectory makes an angle with the magnetic field, called the pitch angle, that is defined by

$$\alpha = \tan^{-1}\frac{v_\perp}{v_\parallel} \tag{2.24}$$

Considering now a finite and time independent electric field $\mathbf{E} = E_\parallel \mathbf{e}_z + E_\perp \mathbf{e}_x$, we can express the zeroth order drift velocity of the particle:

$$\mathbf{v} = \frac{\mathbf{E}_\perp \times \mathbf{B}}{B^2} = \mathbf{v}_d \tag{2.25}$$

Finally the motion of the charged particle in this electromagnetic field is a combination of:

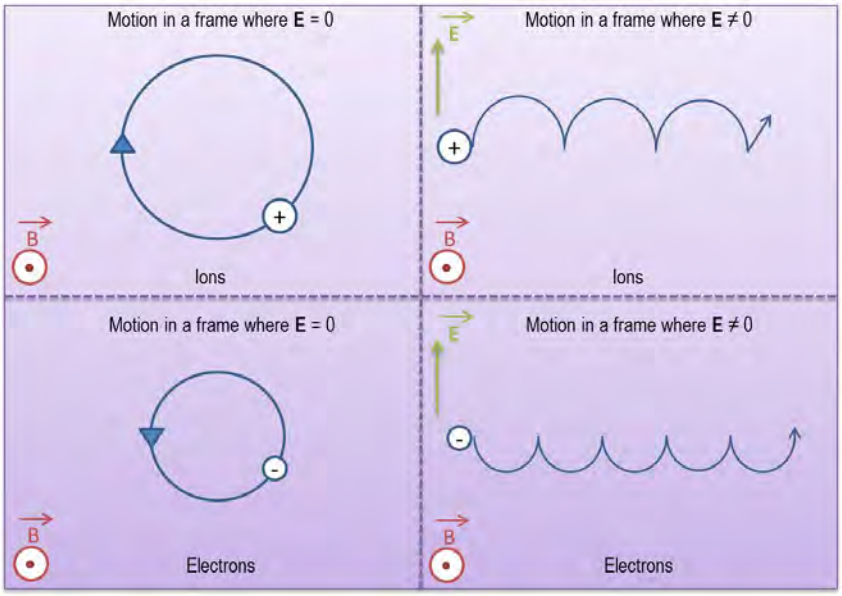

Figure 2.4: Cycloidal trajectories of charged particles in constant electric and magnetic fields

1. gyration around the magnetic field of a radius r and a frequency Ω,
2. translation parallel to the magnetic field (for $\mathbf{E} \cdot \mathbf{B} = 0$) with a velocity $\mathbf{v}_{\parallel}$ and an acceleration along $E_{\parallel}$ $v_{\parallel} = qE_{\parallel}/m$,
3. translation perpendicular to both $\mathbf{E}_{\perp}$ and $\mathbf{B}$ with the drift velocity $\mathbf{v}_d$.

This final drift velocity (equation 2.25) is known as the "*E cross B*" drift velocity. An illustration of the cycloidal trajectories of ions and electrons in an electromagnetic field is presented in Figure 2.4.

2.2 The Solar wind

2.2.1 Properties and observations

The plasma physics presented in the previous 2.1 section apply to the dominant plasma present in the Solar system: the Solar wind. It is the main environment a spacecraft will be exposed to during its journey, especially on interplanetary space. The Solar wind is a plasma composed of ions and electrons, continuously emitted by the Sun (the wind also contains about 4% of Helium nuclei and traces of heavier elements). This plasma flow propagates across the Solar System at velocities which can vary depending on both Solar activity and heliocentric distance. On average at 1 AU, the Solar Wind plasma density is about $5\,cm^{-3}$, the temperature about 10 eV, and it carries a weak magnetic field of 5 nT. But the interplanetary plasma density, temperature and magnetic field increase closer to the Sun. Also the region 0.05 - 0.1 AU from the Sun is a strong acceleration zone of the wind which progressively increases through the solar system (some Solar wind solutions for various coronal temperatures in the Parker model are presented on Figure 2.5 extracted from [Parker (1958)]). Two models are proposed to explain this phenomena: the Parker model with a competition between thermal and gravitational effects, particularly

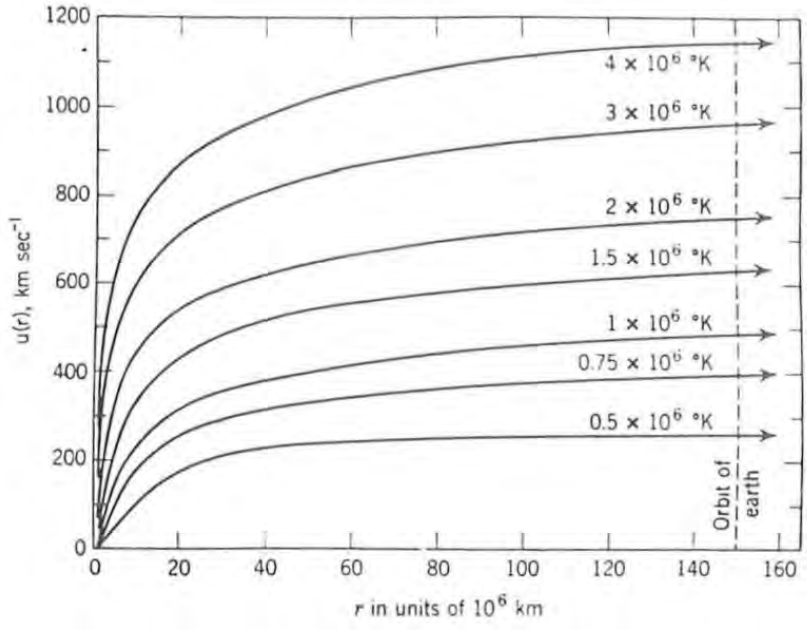

Figure 2.5: Spherically symmetric hydrodynamic expansion velocity $v(r)$ of an isothermal Solar corona (of temperature T_0) plotted as a function of r/a where a is the radius of the corona, taken to be 10^9 m. *Figure taken from* [Parker (1958)]

important near the Sun; and the kinetic model. This last theory states that at equilibrium the electric field in the corona adjusts itself in order to keep the escaping electron flux equal to that of the protons, and thus ensures zero net emitted current. The electron electrostatic energy at the exobase (the lower boundary of the exosphere: the thin volume surrounding the Sun where collisionless molecules are gravitationally bound to that body) must therefore be several times its thermal energy in order to confine most of the electons in the potential well. The corresponding electric field pushes the protons in the opposite direction and since those particles carry most of the mass, a wind is produced [Meyer-Vernet (1999)].

An usual ellipsis consists in presenting two types of Solar winds: the slow one (with velocity < 300 km/s and low density) and the fast one (> 700 km/s and high density). Indeed in time periods when the Sun is highly active, around the Earth orbit at 1 AU, the Solar wind reaches velocities as high as 900 km/s while during a normal activity it is closer to 400 km/s. However thanks to the Ulysses mission, it was discovered that the solar wind varied with solar latitude (see Figure 2.6). The fast wind is basically present throughout the whole 11-year solar cycle and disappears only at solar maximum. At solar minimum (left panel of Figure 2.6) the fast wind fans out from the poles to fill two thirds of the heliosphere, blowing at an average uniform speed of 750 km/s (see arrows), much faster than the wind that emerges from the Sun's equatorial zone at 350 km/s. At solar maximum (right panel of the Figure) the solar wind is more turbulent and irregular. This is why the Solar wind has to be considered as variable. Furthermore, specific Solar events called *Coronal Mass Ejections* (CMEs) occasionally occur and highly disturb the space environment, by ejecting a large magnetized cloud. This phenomenon can propagate to the Earth orbit (at velocities as high as 2500 km/s) and induce strong perturbations on the space systems present in the environment.

Humans have observed the effects of the solar wind for tens of thousands of years with

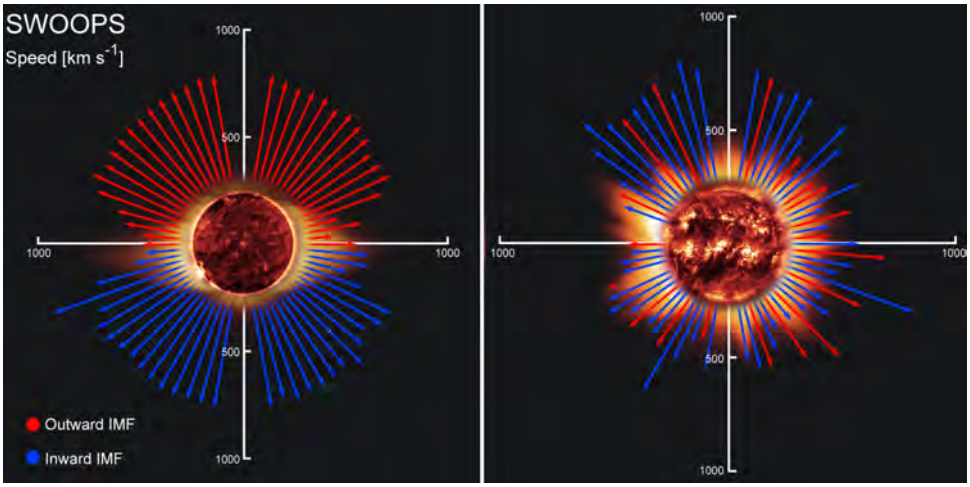

Figure 2.6: Solar wind speeds measured by Ulysses, notably thanks to the *SolarWind Observations Over the Poles of the Sun* (SWOOPS) which measured solar wind ions and electrons in energy ranges between 0.8 and 814 eV. The left panel presents the solar wind velocity measured at minimum solar activity, the right panel is during the maximum activity. It shows the dependence of the velocity on the solar latitude. IMF stands for Interplanetary Magnetic Field. *Figure taken from the ESA website*: http://spaceinimages.esa.int.

the most noticeable manifestation being the *aurorae borealis* that occur in the high latitude regions. Indeed they are caused by the collision of energetic charged particles (originate in the magnetosphere and the solar wind, directed by the Earth magnetic field), with molecules and atoms of the high altitude atmosphere. The first in-situ observation of the solar wind date from 1959, with the Soviet probe Luna 1 which also measured its flux. The data were subsequently verified by the following missions (Luna 2, Luna 3, Venera 1). The first American mission to observe the solar wind arrived three years later through the Mariner 2 spacecraft. Note that the first simulation of the solar wind was performed by [Pneuman and Kopp (1971)], using a model based on magnetohydrodynamics equations.

The *Solar and Heliospheric Observatory* (SOHO), launched in December 1995, and its *Ultraviolet Coronal Spectrometer* (UVCS) instrument on-board helped discover the acceleration region of the fast solar wind emanating from the Sun poles. Observations of the solar wind from high solar latitudes (and not from the ecliptic plane as in previous missions) were provided in 1990 by the *Ulysses* probe (ESA/NASA) which notably allowed a better understanding of the Sun's magnetic field being extending into the solar system. The *Global Geospace Science* (GGS) WIND satellite (NASA) was launched in 1994 to study radio and plasma that occur in the solar wind and in the Earth's magnetosphere. This mission provides complete plasma, energetic particle, and magnetic field input for magnetospheric and ionospheric studies, and investigates basic plasma processes occurring in the near-Earth solar wind. An example of a typical measurement of the solar wind is presented on Figure 2.7, with a dataset provided by WIND in 1995, close to solar activity minimum [Meyer-Vernet (2007)]. In this illustration, the mean proton velocity and the mean electron density show a characteristic pattern of alternate slow and fast streams, with a period that matches the synodic sun equatorial rotation period. The sequence is the following: it starts with the wind speed abruptly doubled (sometimes even more), simultaneously with a density peak of short duration; then the speed decreases slowly

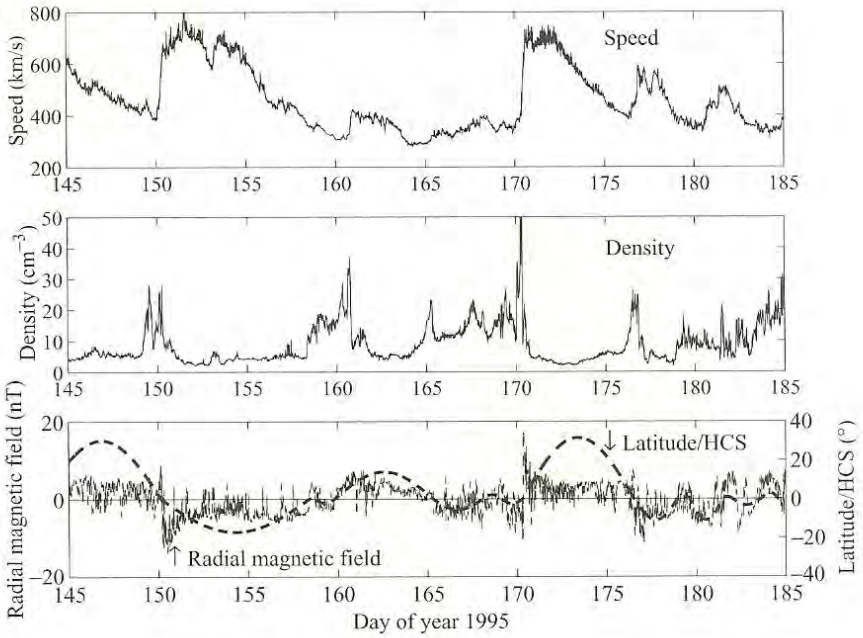

Figure 2.7: WIND spacecraft measurements performed during the minimum solar activity in June 1995, in the ecliptic plane at 1 AU from the Sun. The top panel shows the mean proton velocity, the middle panel shows the mean electron density and the bottom panel displays the Sun-centred **B** radial component and the WIND latitude with respect to the heliospheric current sheet (HCS). (*Figure from* [Meyer-Vernet (2007)]).

until a new burst about one week later, while the density remains low and relatively constant during this period. It also appears on Figure 2.7 that each new pattern of fast solar wind stream corresponds to a change of the radial component of the magnetic field. One should note that this observation, similar to practically all other spacecraft measurements orbiting in this region, is performed within or near the ecliptic plane, where the observer is placed alternately in two opposite magnetic hemispheres due to the Sun's dipolar magnetic field rotation.

Outside the particular ecliptic plane associated with a specific magnetic field configuration, measured data and the consecutive comprehension of the solar wind should vary, as explained in [Meyer-Vernet (2007)]. Indeed, the Ulysses instruments results provided at the same time of the WIND observations (June 1995) but at a different heliolatitude ($\sim 65\,^{\circ}$). Those results, presented in Figure 2.8, do not exhibit any two-state wind patterned solar stream as in the ecliptic plane on Figure 2.7. The speed and the density here remain practically constant with respective values of $\sim$ 750 km/s and 2.5 cm^{-3}. Those two observations show that without any particular event (such as CME or *Corotating Interacting Region* - CIR) the solar wind already varies temporally and spatially, depending on the observer location with respect to the Sun dipolar magnetic field.

Concerning more violent events such as CME: the NASA *Advanced Composition Explorer* (ACE, launched in 1997, and which has enough propellant on board to maintain its orbit until $\sim$2024) studies low energy particles of solar/interplanetary origin and high energy galactic particles. It is also able to warn in the issue approximately one-hour warnings for potentially

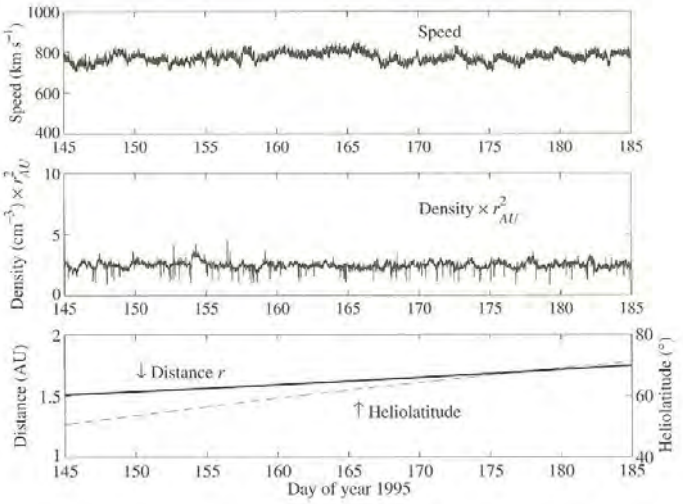

Figure 2.8: Ulysses measurements of the solar wind at the same period that the previous WIND observations, in June 1995. This time the spacecraft is at 1.6 AU from the Sun (but the density measurements have been normalised to the distance of 1 AU) and far from the equatorial plane of the solar magnetic dipole. The top panel shows the mean proton velocity, the middle panel shows the mean electron density and the bottom panel displays the heliocentric distance (thin line) and latitude (dashed line) in solar coordinates. (*Figure from* [Meyer-Vernet (2007)]).

hazardous geomagnetic storms. Figure 2.9 shows an example of solar wind measurements performed by ACE during a CME event. The 24^{th} of October 2003 at 14:49 UT a CME passage has been observed by ACE showing: an abrupt increase of the solar wind velocity from 450 to 600 km/s, holding this velocity for several hours; a progressive increase of the plasma density (from few particles per cm^3 to more than 70 a few few hours later); a brutal income of high energy particles which then slowly decreased in time, while exhibiting large fluctuations. Since 2006 the two satellites constituting the *Solar Terrestrial Relations Observatory* (STEREO) mission are performing stereoscopic images of the Sun and help forecast CMEs. Since the year 2000, four Cluster satellites (flying in formation around Earth on highly elliptical orbits) are collecting three-dimensional information on how the solar wind interacts with the Earth magnetosphere.

Globally, the Solar wind (the plural solar *winds* may actually be more appropriate considering the various possible types of plasma flows ejected by the Sun) can be understood as a magnetized flow of charged particles - variable in intensity, velocity and energy range - that will automatically impact all objects present in the Solar System as it impacts the planetary bodies orbiting around the Sun. A concrete example of this plasma flow/magnetized body interaction is presented in the following section, for the Earth magnetosphere.

2.2.2 Interaction with the magnetic field: the magnetospheres

The Solar wind interacts with any Solar system body endowed with a magnetic field. The structure resulting from the encounter between the Solar wind and the magnetized object is known as the magnetosphere. The Earth, Jupiter, Saturn, Uranus and Neptune own their proper magnetosphere. They can also be found around Mercury, Ganymede (one of the Jupiter's moon), Mars and Venus (those two last planets have induced magnetospheres). The best example to

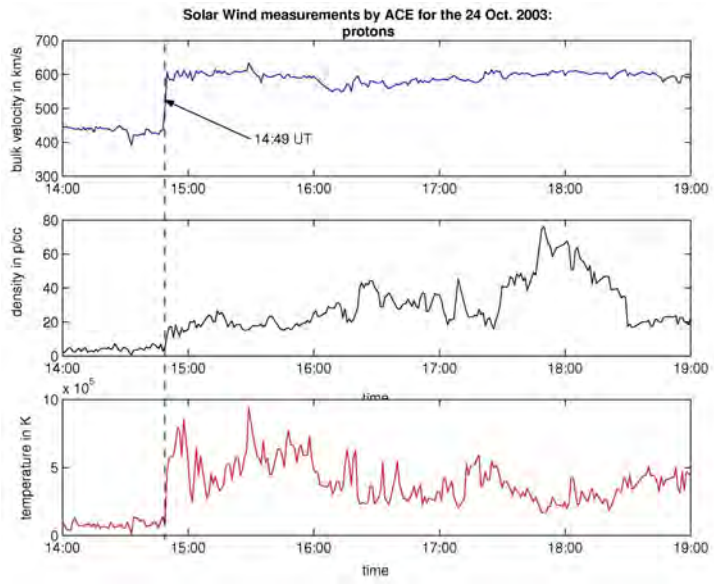

Figure 2.9: Solar wind proton density, velocity and temperature measured by ACE on 24 Oct. 2003 at the $L1$ Lagrangian position. The CME passage was observed at 14:49 UT. Later on the density reached a peak above 70 particles per cm^3, about 15 times the usual value. (*Figure provided by ESA*)

describe the structure that region is the Earth case as its magnetosphere is now well known. Note the magnetosphere environment will not be treated in this work as it focusses on low energy particles and those regions are usually populated with particles well beyond a hundred of eV.

The magnetosphere around Earth is composed of the terrestrial magnetic field lines immersed in the wind. Its configuration is quite deformed: compressed by the flow on the day side, towards the Sun (it extends up to $\sim 10\,R_E$ with R_E being the Earth radius) and highly elongated on the night side (as far as several hundreds of Earth radii). A schematic view of the Earth magnetosphere structure is displayed on Figure 2.10 and its main components are described hereafter:

- The Solar wind is slowed down at the **bow shock**, the outermost layer of the magnetosphere. The magnetic field is increased and some particles are accelerated. It represents the boundary between the magnetosheath and the interplanetary environment;

- Downstream of the bow shock is the **magnetosheath**, mainly formed from shocked solar wind, with high particle energy fluxes and strong variations of the magnetic field;

- The **magnetopause** is the region beneath in which the pressure from the planetary magnetic field is balanced with the pressure from the Solar wind;

- On the night side, the extended region is the **magnetotail**, containing two **lobes**. In the northern lobe the magnetic field points towards the Earth and in the southern tail it points away from Earth. The lobes have a relatively low density ($< 5\,cm^{-3}$) with temperatures of about 100 eV for electrons and 300 eV for ions;

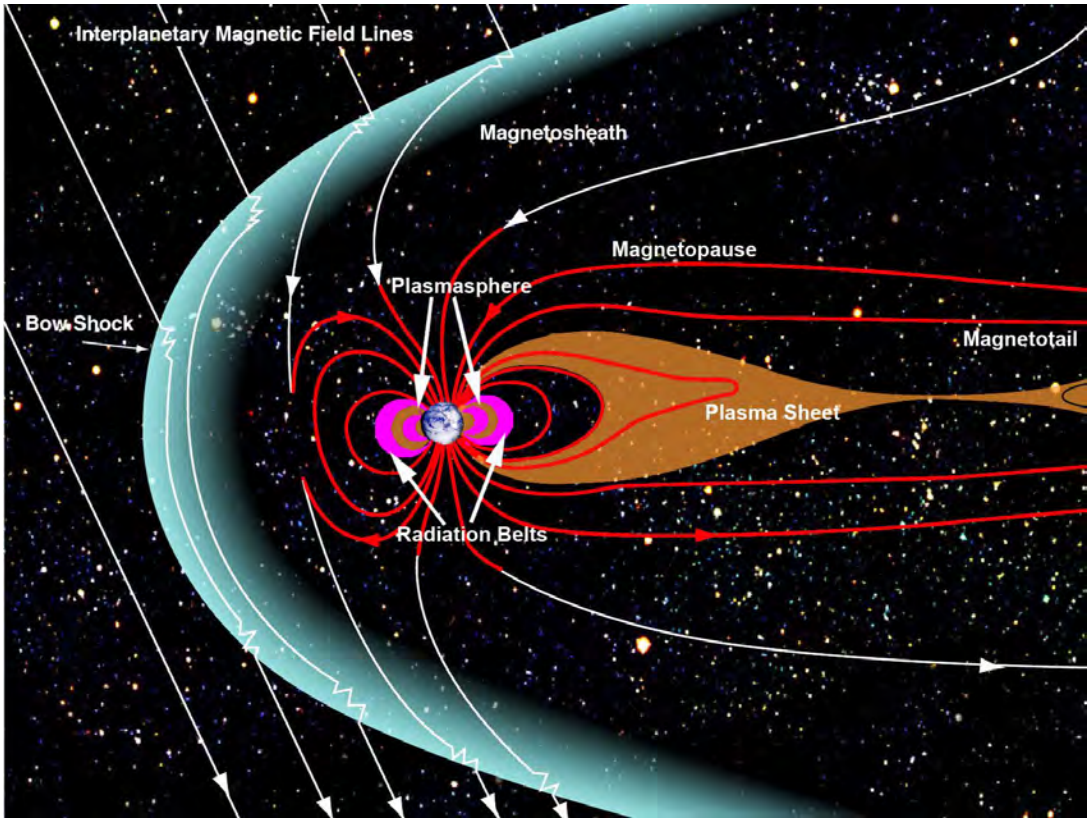

Figure 2.10: Main components of the Earth magnetosphere structure (*Original bitmap from NASA*)

- The **plasma sheet** is the plasma layer surrounded by the lobes, and constitutes the main particle reservoir of the magnetosphere. Its thickness depends on the magnetospheric activity but it ranges between few hundreds to tens of thousands kilometres. In that region, electrons have a temperature of about 0.5 - 1 keV and it raises to 1 - 5 keV for protons. The density is of about 0.1 - 1 cm^{-3}.

- The **radiation belt** is a region populated by energetic particles (E > 10 keV) and extending between 2 and 10 Earth radii. Trapped particles drift slowly around Earth, switching guiding field lines but staying at approximately the same distance. One reason for that drift is that the intensity of B increases as Earth is approached. The gyration around the guiding field line is therefore not a perfect circle, but curves a little more tightly on the side closer to the Earth, where the larger B gives a smaller Gyroradius. This change in curvature makes the belt drifting around the planet with opposite directions depending on the particle charge: electrons are drifting eastward and ions westward. This region is hazardous for artificial satellites which cross the belts to reach the *Low Earth Orbit* (LEO) and further trajectories.

Even though the magnetosphere will not be treated in this study, its configuration briefly mentioned above perfectly illustrates the complexity and diversity of space environments.

Chapter 3

Interactions with a satellite

Contents

3.1 Equilibrium potential and currents 33
3.2 Differential charging 36
3.3 Space charge effects and ambient current estimations: probe theory . 38
3.3.1 The Boltzmann factor 38
3.3.2 The thick sheath regime 39
3.3.3 The thin sheath regime 41
3.3.4 Concluding remark 44
3.4 Ideal collected distribution functions 44
3.5 Secondary electron emission / electron impact: SEEE 47
3.5.1 SEEE Principle 47
3.5.2 SEEE Modelling 50
3.6 Secondary electron emission under proton impact: SEEP 53
3.7 Photoemission 54
3.8 Ion wake 56
3.9 Potential barriers 59
3.10 Viewing factor 61
3.11 Other phenomena 63

3.1 Equilibrium potential and currents

The first issue encountered when placing a satellite in space is its charging. The structure is covered with various materials - such as conducting layers or dielectrics - and can thus charge electrically through the different interactions occurring with its environment. According to [Langmuir (1960)] and [Chen (1965)], a spacecraft structure immersed in a plasma behaves as a Langmuir probe, meaning that it surfaces collect ambient charges and the probe electrostatic potential varies in response to these currents. It is said that the spacecraft potential is floating relative the plasma potential (assumed to be null at an infinite distance from the satellite). Once a satellite begins collecting charges, it is in a general situation of *spacecraft charging*. Different forms of charging are identified:

- **Absolute Charging**
  The structure overall ground potential is different from the plasma potential (assumed to be null far from the satellite). Sometimes the difference can reach thousands of volts;

- **Surface charging**
  The electrical charges are located onto the satellite external surfaces. This charging can lead to a surface electrostatic potential pattern (potentially non uniform over the satellite surface) different from the potential value reached through the *Absolute charging*. It happens if the spacecraft surface elements are electrically separated from the internal circuit or if there are dielectrics on the satellite surface. In this last case the charges can be onto the surface dielectric material or inside the dielectric volume;

- **Differential charging**
  The surface potential discrepancies over the *surface charging* pattern can reach thousands of volts, depending on the different material properties (and eventually a non isotropic environment) with possible destructive surface arcing. The potentials generated over one strongly charged surface material can spread out over less charged spacecraft elements, complicating the surrounding electrostatic environment. A specific section is dedicated to the differential charging (3.2);

- **Internal charging**
  Elements inside the spacecraft body, even shielded, are accessible to highly energetic particles (typically for E $>$ 100 keV) which might penetrate in dielectrics or on isolated conducting surfaces. This charging is potentially hazardous when leading to breakdowns of insulators, or on electrical circuits;

All particle fluxes which are either collected or emitted by the surfaces constitute currents which will bring the system "satellite and near environment" to a certain equilibrium. This steady state can be expressed in equation (3.1) which balances all the net currents interacting with the satellite body. It would be too simplistic assumption to assess that all those net currents depend on an uniform spacecraft potential ϕ_{SC}, and that this equation is verified for a certain value of this single spacecraft potential (as it is usually seen in the literature). Indeed even if the structure is entirely conducting, other phenomena such as potential barriers or ion wakes (see the following sections 3.8 and 3.9) can impose different current flows, not only dependant of ϕ_{SC} but also of the near spacecraft environment (local particle densities and potentials). Considering the different satellite surface potentials and the surrounding local plasma potential values, the reasoning should be consequently done with the set of local potentials (onto and around the satellite), here identified as $\Sigma\phi$. This expression stands for a global electrostatic configuration which can locally adapt to verify equation 3.1, knowing that each net current is a function of the local potentials. The spacecraft potentials can be considered as floating (meaning that there is no active control on the potentials from specific devices such as ion/electron emitters) in which case $\Sigma\phi$ will vary until verifying a null total net current on spacecraft. If the spacecraft potentials are held to constant values then the plasma potentials and currents will adapt to this constraint until cancelling the total net current. In some particular cases (GEO orbits, radiation belts), satellite potentials can reach a few kilovolt order due to fluxes of energetic particles, with possible electrical arcing between the structure components and strong damages to the elements.

$$I_e(\Sigma\phi) + I_i(\Sigma\phi) + I_{se}(\Sigma\phi) + I_{si}(\Sigma\phi) + I_{be}(\Sigma\phi) + I_{ph}(\Sigma\phi) + I_b(\Sigma\phi) + I_s(\Sigma\phi) = I_{net} = 0 \quad (3.1)$$

where

$\Sigma\phi$ = satellite and near environment potentials,
I_e = incident net electron current on satellite surface,
I_i = incident net ion current on satellite surface,
I_{se} = secondary electron net current due to I_e,
I_{si} = secondary electron net current due to I_i,
I_{be} = net backscattered electron current due to I_e,
I_{ph} = net photoelectron current,
I_b = active net current sources (charged particle beams, ion thrusters, ...),
I_s = surface net current to other surfaces or through the surface (conductivity)

The net current I_{net} can also be formulated as:

$$I_{net} = \frac{\partial Q}{\partial t} \tag{3.2}$$

where Q is the surface charge. Considering ϕ_{SC} as the electrostatic potential pattern of the satellite body (with possibly various different local potentials), equation 3.2 has a steady state solution given by $I_{net}(\phi_{SC})=0$. It is possible to determine the time scale for the surface potential to reach the steady state. If ϕ_{SC0} is the steady state solution of $I_{net} = 0$, and $\delta\phi_{SC}$ a small perturbation on the potential as $\phi_{SC} = \phi_{SC0} + \delta\phi_{SC}$ then, considering $Q = C\phi_{SC}$ where C is the surface capacitance with respect to infinity, equation 3.2 can be written as:

$$C\frac{\partial\delta\phi_{SC}}{\partial t} = \frac{dI_{net}}{d\phi_{SC}}\rfloor_{\phi=\phi_{SC0}}\delta\phi_{SC} \tag{3.3}$$

The solution of 3.3 is

$$\delta\phi_{SC} = (\delta\phi_{SC})_0 \exp\left(\frac{-t}{\tau}\right) \tag{3.4}$$

with $\tau = -C/(dI_{net}/dV_S)|_{\phi=\phi_{SC0}}$. Depending on materials and environment condition, charging time scales are typically between the millisecond for conducting materials (absolute charging) and the minute for dielectrics [Whipple (1981)].

As plasma measuring consists in detecting electrically charged particles, any non null potential on the satellite or the detector itself will attract or repulse them, depending on the charge signs and surface potential value, providing a biased measurement. This has been already expressed in equation 2.9 relating the local particle density to the local potential: $n = n_0 exp(-q\phi/kT)$. For instance, when considering a positively charged electron detector, its potential represents an attracting well for ambient electrons and will accelerate them. The instrument response will thus be increased concerning electron flux and energy, leading to a discrepancy in ambient electron population estimated density and energy with respect to the natural (unperturbed) environment. On the contrary, a negatively charged satellite will repel electrons leading to an underestimate in the measured ambient electron population. However this bias effect only concerns particles with energies of the same order as that of the satellite. In particular, a particle at 1 keV will not be affected by a 10 V charged surface. In this study the attention is focused on low energy plasma measurement (below one hundred of electron Volt) meaning that the work is focused on low potentials (below $\pm$ 100 V).

The various currents taking parts in equation 3.1 can be estimated depending on the environment conditions and satellite properties. The first currents to be considered are the ones associated with the collection of ambient plasma. This will be explained in the next section.

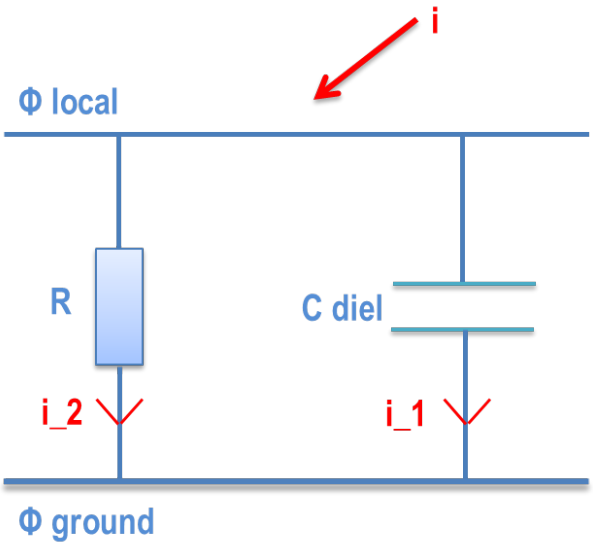

Figure 3.1: Simplified local representation of a dielectric surface: between the outer surface exposed to the plasma and the ground surface, an equivalent resistor R (taking into account the bulk resistivity, surface resistivity and the Radiation Induced Conductivity - RIC) is mounted in series with the dielectric capacitance C_{diel}. The incoming current I is thus divided into I_1 and I_2.

3.2 Differential charging

If the satellite surface has components at different voltages: it is in a situation of differential charging. This can lead to several issues, simply disturbing for the near environment measurements or more hazardous for the structure itself.

Differential charging is mainly due to the presence of dielectric materials over the spacecraft surface. Depending on the impacting particle energies kT, the induced potentials will proportionally vary if the conductivity is negligible. Charging also depends on the material properties, dimension and behaviour under space irradiation. For instance impacting low energy particles will be trapped on the outer dielectric surface layers (at a depth of few μm). The local surface potential then generated depends on the different charging currents and the evacuation of the trapped charges is linked to the material resistivity. The dielectric charging (see the equivalent representation of this surface on Figure 3.1) can be expressed in equation 3.5 as follows:

$$C_{\text{diel}} \frac{d(\Phi_{\text{local}} - \Phi_{\text{ground}})}{dt} = I - \frac{\Phi_{\text{local}} - \Phi_{\text{ground}}}{R} \tag{3.5}$$

With $I = I_1 + I_2$ the collected current on the plasma exposed surface and $\Phi_{\text{local}} = RI_2$ the potential on this outer surface. Its time variation can be expressed as: $d\Phi_{\text{local}}/dt = I_1/C_{\text{diel}}$.

High energy particles, however, directly cross the surface layers and contribute to the internal charging. Through the particle bombardment, the external covering material electrical properties are modified: by ionization of the material with an energy transfer inside its structure. This generates an increase of the apparent surface and bulk conductivity, the so-called

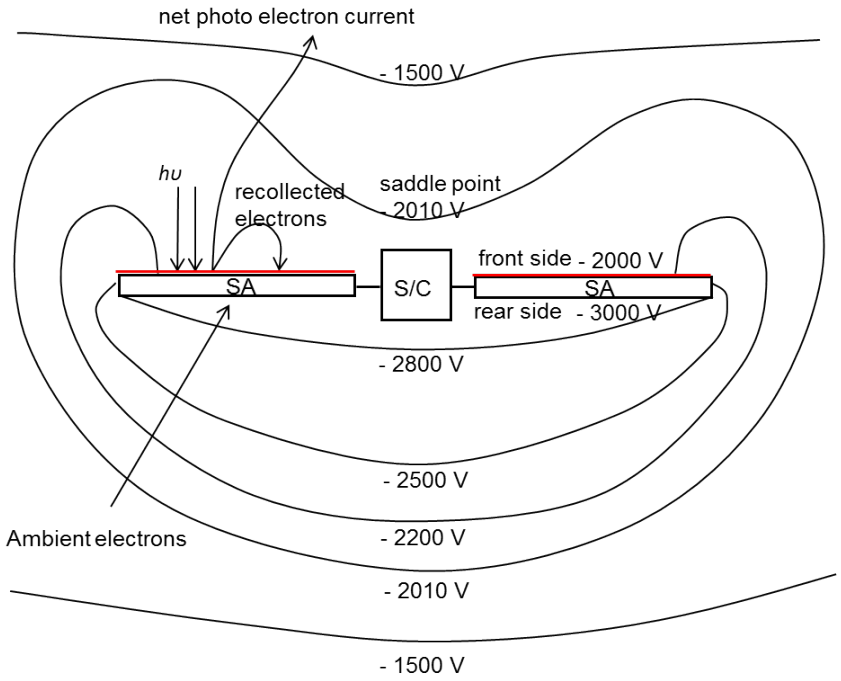

Figure 3.2: Typical situation on a GEO spacecraft: inverted potential gradient (-2000V in sunlight and -3000V in shade on this example) and creation of a potential barrier blocking part of the photoemission. SA = Solar Array; S/C = spacecraft. *Figure taken from the SPIS-GEO tutorial.*

Radiation Induced Conductivity (RIC), as explained in [Paulmier et al. (2009)]:

$$\sigma_{\mathrm{RIC}} = k \left(\frac{dD}{dt} \right)^{\Delta} \tag{3.6}$$

with D [Gy] being the radiation dose, k [Ω^{-1}.m^{-1}.rad^{-1}.s] the coefficient of induced conductivity under radiation (depending on the material) and Δ a parameter (without unit) depending on the material (between 0.5 and 1). The natural conductivity, standing for the natural charge leak, is named *dark* conductivity and is calculated with

$$\sigma(E) = \varepsilon_0 \varepsilon \frac{dV_S/dt}{V_S} \tag{3.7}$$

where ε_0 is the permittivity of vacuum, ε the relative permittivity of the dielectric, E is the electric field and V_S the surface potential.

The total conductivity is the sum of the dark and RIC conductivities. It has to be reminded that electrical conductivity (or specific conductance), in [S.m^{-1}], is the reciprocal of electrical resistivity [$\Omega.m$], and measures a material's ability to conduct an electric current. The resistivity (also known as specific electrical resistance or volume resistivity) quantifies how strongly a given material opposes the flow of electric current. The conductivity of the material can be related to the surface (the lateral conductivity) or the volume (also called bulk conductivity) [Hanna et al. (2011)].

In a differential charging configuration, the potential pattern on and around the vicinity of the satellite can often look like the illustration of Figure 3.2, especially in a GEO environment. When sunlit dielectric charging is controlled mainly by photoemission and conductivity while on the shadowed side the dielectric charge is controlled by the balance between electron and proton current; the secondary electron emission under electron and proton impact; and the conductivity. On this figure the strongest potential pattern on the shadowed side of the spacecraft spreads until the front sunlit side, creating electrostatic blockage of secondary particles (it can be interpreted as a potential barrier because the local Debye length is larger than the spacecraft dimension).

3.3 Space charge effects and ambient current estimations: probe theory

An important aspect of the satellite/plasma interactions is the influence of the charge distributed in a local region, or *space charge* effect. As explained in Section 2.1.2, within the plasma characteristic length λ_D (the Debye length expressed in equation 2.16), the quasi neutrality of the plasma is not established. This sheath constitutes a region where charged particles behave as individual particles dominated by electromagnetic forces. An analogy can be made to illustrate the plasma sheath as a boundary layer of a classic fluid above a surface, and quasi neutrality would be the outer solution of the flow. Depending on the spacecraft dimension R_{SC} compared with the Debye length (greater/lower than), the concept of respectively thin/thick sheath is appropriate, and consecutive analytical solutions to ambient current values and charging equations can be found, on the condition that very simple equipotential satellite geometries are considered.

3.3.1 The Boltzmann factor

For the repelled species s, considering a Maxwellian distribution $f(E)$ at a density n around a charged spacecraft at the potential ϕ, the distribution of particles arriving on the satellite surface would be shifted in energy:

$$f(E + q_s\phi) = f(E) \exp\left(-\frac{q_s\phi}{kT_s}\right) \tag{3.8}$$

The corresponding current collected on the surface area A under these conditions is thus:

$$I(\phi) = J(\phi)A = J(0) \exp\left(-\frac{q_s\phi}{kT_s}\right) A \tag{3.9}$$

With:

$$J = \frac{1}{4} q_s n \langle v \rangle = \frac{1}{4} q_s n \left(8kT/\pi m\right)^{1/2} \tag{3.10}$$

and $I = JA$. Consequently the collected current valid for spherical, cylindrical and plane Langmuir probes [Mott-Smith and Langmuir (1926)] is given by:

$$I(\phi) = I(0) \exp\left(-\frac{q_s\phi}{kT_s}\right) \tag{3.11}$$

The exponential term in equation 3.11 is the Boltzmann factor, already shown in equation 2.9. This factor only applies to the repelled species.

The consideration of the attracted species lead to two different sheath regimes which will be described in the following sections.

3.3.2 The thick sheath regime

In the thick sheath assumption ($\lambda_D \gg R_{SC}$), considering a charged spherical satellite attracting a particle from infinite distance $r = \infty$, the constant sum of the particle kinetic and potential energy is given by

$$mv^2(r)/2 + q\phi(r) = mv_\infty^2/2 \tag{3.12}$$

At infinity, the particle kinetic energy should be the thermal velocity of plasma at equilibrium (equation 2.3), giving

$$mv_\infty^2/2 = kT \tag{3.13}$$

The angular momentum is also conserved for a spherically or cylindrically symmetric potential over the particle trajectory (see Figure 3.3 for a illustrated example with a negatively charged spacecraft and attracted ions):

$$mv_\infty h = mv_a a \tag{3.14}$$

with h being the maximum distance measured from the center of the sphere (of radius a) to the straight line of the trajectory and v_a the particle velocity when it impacts the sphere (h is the largest impact parameter such that the particle trajectory intersects the satellite). Replacing equations 3.13 and 3.14 into 3.12 leads to the expression of the impact distance h:

$$h = a\left(1 - \frac{q\phi}{kT}\right)^{1/2} \tag{3.15}$$

and to the velocity expression at impact ($r = a$):

$$v_a = v_\infty\left(1 - \frac{q\phi}{kT}\right)^{1/2} \tag{3.16}$$

After this single particle picture of the problematic, let us consider the current collection on the plasma scale.

Current collection in spherical geometry

For a spherical spacecraft of potential ϕ in a stationary plasma of density n, the collected current $I(\phi)$ is:

$$I(\phi) = 4\pi h^2 nqv \tag{3.17}$$

The impact distance h formulated in equation 3.15 allows the development of the previous equation into

$$I(\phi) = 4\pi a^2 nqv\left(1 - \frac{q\phi}{kT}\right) \tag{3.18}$$

It can be seen that $I(0) = 4\pi a^2 nqv$ and, posing $Q = -q\phi/kT$ ($Q > 0$ for the attracted species, $Q < 0$ for the repelled ones), equation 3.18 can be written as:

$$I(\phi) = I(0)\,(1 + Q) \tag{3.19}$$

This equation 3.19 is the *thick sheath - orbit limited current collection* formula or *orbit-motion-limited* (OML) formula for a spherical spacecraft, relevant in a orbit-limited regime as explained in [Mott-Smith and Langmuir (1926)]. When taking into account for example both attracted (ions) and repelled (electrons) species, for the negatively charged spherical spacecraft:

$$I(\phi) = I_i(0)\left(1 - \frac{q_i\phi}{kT}\right) - I_e(0)\exp\left(-\frac{q_e\phi}{kT}\right) \tag{3.20}$$

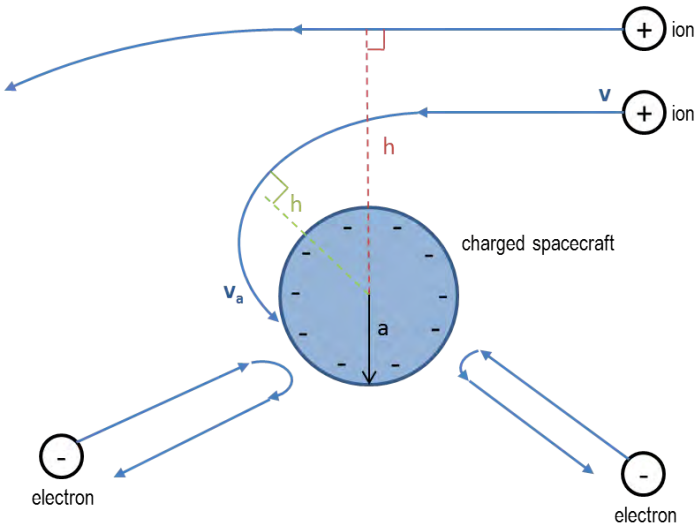

Figure 3.3: Spherically shaped spacecraft (assumed as a Langmuir Probe). In this example the satellite is negatively charged, electrons are repelled and ions are attracted by a central force. Their angular momentum remains constant.

This last equation 3.20, which only considers ions and ambient electrons, remains a simple approximation helpful for determining analytical solutions for simple spacecraft geometries charging, by finding ϕ from the solution of $I(\phi) = 0$.

This illustrates the fact that the low plasma density (and thus the corresponding great value of λ_D regarding the spacecraft dimension) makes the orbital parameters (energy and momentum) of each far field attracted particle influence their eventual collection by the charged surface. On the contrary in the thin sheath approximation the self-consistent space charge in the vicinity of the charged surfaces determine the particle collection, and not the far field plasma properties.

Current collection in cylindrical geometry

Similar calculation for a cylindrical spacecraft (per length L) (in a 2D cylindrical geometry) would give $I(0) = 2\pi anqvL$ and:

$$I(\phi) = I(0)\,(1+Q)^{1/2} \tag{3.21}$$

This equation was firstly obtained by [Mott-Smith and Langmuir (1926)]. A more accurate calculation using an integration over cylindrical coordinates by [Laframboise and Parker (1973)] and [Prokopenko and Laframboise (1980)] yields:

$$I(\phi) = I(0)\left(2/\pi^{1/2}\right)\left[Q^{1/2} + g\left(Q^{1/2}\right)\right] \tag{3.22}$$

With

$$g(s) = \exp\left(s^2\right)\int_s^\infty \exp\left(-t^2\right)dt \tag{3.23}$$

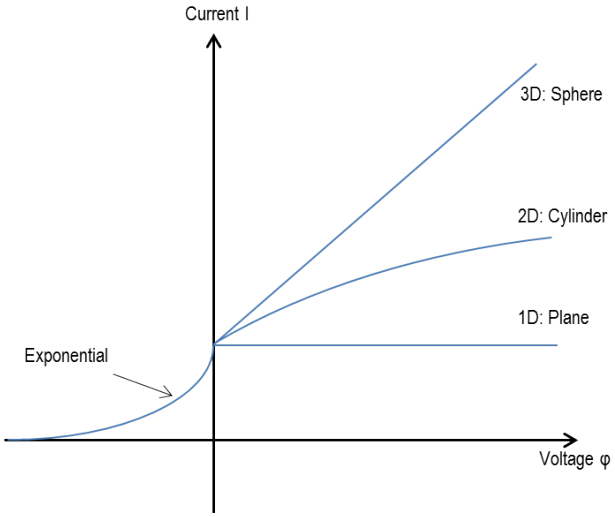

Figure 3.4: Orbit limited current collection: qualitative behaviour of current-voltage curves depending on the one-, two-, and three-dimensional geometries.

Current collection in planar geometry

Finally in a 1D plane geometry for an infinite plane, there is no central force and no angular momentum. The same integration over cylindrical coordinates yields for attracted species:

$$I(\phi) = I(0) \tag{3.24}$$

which is independent of Q. Actually, the planar solution is conceptually equivalent to a thin sheath limit. The consecutive orbit-limited current collection for the three simple geometry shapes are presented on Figure 3.4. It exhibits a qualitative understanding of the currents to the probe evolution with respect to the ratio of the Debye length to the satellite radius: from large ratio values (thick sheath or spherical case) to small values (thin sheath, equivalent to a planar geometry).

3.3.3 The thin sheath regime

Attracted species

If the sheath dimension ($\lambda_D \ll R_{SC}$) S is significantly smaller than the spacecraft characteristic size R_{SC}, the orbit-limited regime is not valid any more. The high local charged particle density (corresponding to a small Debye length) makes the space charge dominate the plasma behaviour. This is the so-called *space charge regime* or *current saturation regime* where the space charge local potentials control the particle flows and no longer the orbital parameters of the far field particles or the spacecraft attracting potential.

Considering only a spherical probe in a thin sheath regime, some previous work detailed in [Langmuir and Blodgett (1924)] and [Parker (1980)] for non-flowing Maxwellian plasma gives the sheath dimension S:

$$\frac{S}{R_{SC}} = \frac{1}{2} + \left(\frac{1}{4} + \frac{D}{R_{SC}}\right)^{1/2} + 0.052\frac{D}{R_{SC}} H\left(\frac{D}{R_{SC}} - 0.2\right), \text{for } \frac{D}{R_{SC}} \leq 19 \tag{3.25}$$

$$\frac{S}{R_{SC}} = \left(1 + \left(\frac{D}{R_{SC}}\right)^{0.753}\right)^{0.752}, \text{for } \frac{D}{R_{SC}} > 19 \tag{3.26}$$

where $H(x)$ is the unit step function: $H(x < 0) = 0$; $H(x \geq 0) = 1$. D is the one dimensional analytic sheath obtained by [Child (1911)] and [Langmuir (1913)]

$$D = 1.26\lambda_D \left(\frac{e(\phi_{SC} - \phi_P)}{kT_e}\right)^{3/4} \tag{3.27}$$

with ϕ_P being the plasma potential. The validity of the Langmuir-Blodgett model (equations 3.25 and 3.26) however remains limited to cases where the orbital motion of particle around the spherical probe is negligible. Any particle penetrating within the sheath will be collected by the probe. So the translation due to thermal velocity must not divert the particle further than the probe characteristic size R_{SC}. This implies:

$$\frac{e(\phi_{SC} - \phi_P)}{kT_i} > \left(\frac{S}{R_{SC}}\right)^2 \tag{3.28}$$

Another approach would consist in neglecting the repelled species. Considering a surface (nearly planar relative to the thin sheath dimension) charged to a potential ϕ_S, the potential $\phi(x)$ at a distance x from this surface can be calculated with Poisson's equation for the attracted species:

$$\frac{d^2\phi(x)}{dx^2} = -\frac{qn(x)}{\varepsilon_0} \tag{3.29}$$

Making the assumption that the attracted particle has a null energy at an infinite distance from the surface and accelerates toward it without collisions, the energy conservation leads to

$$\frac{1}{2}mv^2(x) + q\phi(x) = 0 \tag{3.30}$$

and the current density j can be expressed as

$$j = qn(x)v(x) \tag{3.31}$$

Combining equations 3.30 and 3.31 into 3.29 yields:

$$\frac{d^2\phi(x)}{dx^2} = -\frac{j}{\varepsilon_0\sqrt{2q\phi(x)/m}} \tag{3.32}$$

This last equation can be solved assuming that $\phi(x)$ and $d\phi(x)/dx$ vanish at a distance $x = d$ that corresponds to the sheath thickness and also by making the space charge limited assumption. This means that the space charge over the planar surface is sufficient to shield the electric field originating from the surface. Finally after integration:

$$j = \frac{4}{9}\varepsilon_0 \left(\frac{2q}{m}\right)^{1/2} \frac{\phi^{3/2}(x)}{d^2} \tag{3.33}$$

This equation 3.33 is known as the Child-Langmuir law for space charge limited flow, and relates the current that can flow to a surface at a given potential $\phi(x = S)$ to the size of the sheath d.

From equation 3.33 [Hastings and Garret (1996)] expressed the sheath thickness S as :

$$S = \frac{2}{3}\left(\frac{\sqrt{2}}{K^*}\right)^{1/2} \lambda_D \left(\frac{|q\phi_{SC}|}{kT}\right)^{3/4} \tag{3.34}$$

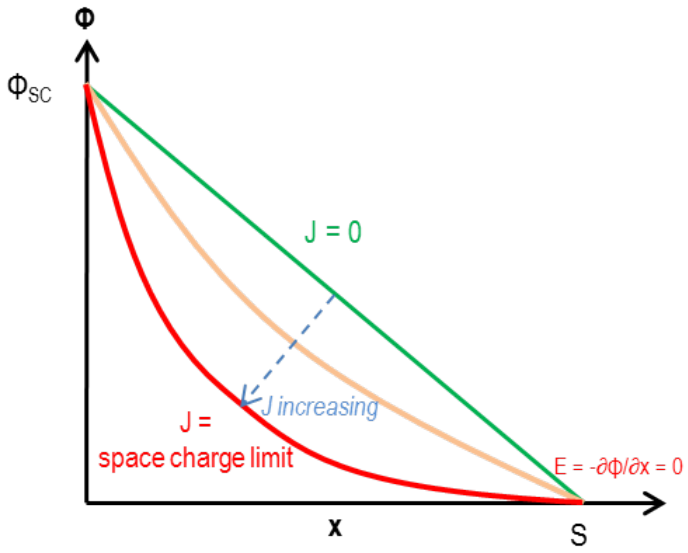

Figure 3.5: Evolution of the monotonic potential profiles $\phi(x)$ with increase of the current density J, considering only the attracted species.

with $1/\sqrt{2\pi} \leq K^* \leq 1$.

In this thin sheath consideration: S is at least of the order of the Debye length, leading to $|q\phi_{SC}/kT| \gg 1$ (the electrostatic potential energy of the spacecraft dominates over the kinetic energy of the particles). The sheath thickness defines the limit under which the present charges are collected, and allows to calculate the maximum current flow to a probe charged at ϕ_{SC}. The local plasma potential profiles $\phi(x)$ are displayed on Figure 3.5, for three representative values of the current density J. At $x = 0$ on the spacecraft surface the potential is ϕ_{SC}, and it vanishes at the sheath limit $x = S$. The profile is initially nearly linear for low current densities. When J increases the potential profile is bended until the space charge limit is reached: the electric field E vanishes at $x = S$ and the current density is given by equation 3.33 (still without considering the repelled species). This space charge limited current is the maximum J that can flow to the surface for the given sheath thickness S. In all those cases the potential profile remains monotonic. Indeed if J were to increase again, $E(x = S)$ would reverse its polarity and become repulsive for the considered current (a non monotonic profile would thus be set, generating a potential barrier for the attracted species).

Attracted and repelled populations consideration

Now, the introduction of the repelled species (identified as r) to the attracted population (named a) in the above system can be done with simplified considerations. Supposing a is cold ($kT_a = 0$) it also has a non null velocity v_0 at the sheath boundary $x = S$ (to allow particles penetrating the attracting region), where quasi neutrality is established ($n_a \approx n_r$). Energy conservation gives:

$$\frac{1}{2}m_a v(x)^2 + q\phi = \frac{1}{2}m_a v_0^2 \tag{3.35}$$

which leads to:

$$v(x) = \sqrt{v_0^2 - \frac{2q\phi}{m_a}} \tag{3.36}$$

After calculations, v_0 can be shown to satisfy the following inequality:

$$v_0 > \sqrt{\frac{kT_r}{m_a}} \tag{3.37}$$

This last condition is known as the Bohm sheath criterion, imposing a inferior limit to the attracted particles velocity arriving on the sheath. This minimum velocity is required for a stable sheath to exist around the surface and is related to the repelled population characteristics. If the condition is not satisfied an oscillating sheath will occur. v_0 implies that the attracted particles have already been accelerated by a potential drop around $y = S$, of the order of the repelled population energy. In this case the previous assumption of a null electric field at the sheath limit is no longer possible: E must still exist beyond the sheath in the quasi neutral plasma (even though at a small level and on a short distance). This concept is known as the *presheath*, and is defined as a region beyond the sheath where ϕ varies between kT_r/q_r (where the repulsed species are blocked) to 0 (boundary of the undisturbed plasma).

3.3.4 Concluding remark

The several assumptions set to establish those analytical solutions are obviously difficult to apply on a real vehicle immersed in natural plasma conditions. But it can be easily understood here that a plasma instrument immersed in a plasma sheath where the spacecraft potential effect is not screened will be affected by disturbances. It is however usually difficult to place the instruments at the end of long booms or wires, in order to be outside the sheath.

Furthermore those ambient current estimations do not take into account the secondary and photoelectrons generated from the satellite surfaces in the vicinity of its structure, and thus modify the local space charge distribution and the sheath properties. Those parasite particles are already taken into account for the charging equation 3.1, their current intensities have now to be estimated and this will be introduced in the further sections. Before that, the implications of equation 3.8 in a simple analytical example will now be presented.

3.4 Ideal collected distribution functions

It has already been mentioned in the previous sections that spacecraft charging may affect the scientific measurements, especially those determining the plasma properties. This is a direct consequence of the previous equation 3.8, describing the modification of a population distribution function arriving on a charged surface. Indeed as a charged spacecraft repels particles of the same sign that its potential and attracts those of the opposite sign, a non neutral sheath formed in its vicinity where the repelled species are logically in lower density than the attracted ones. Consequently the plasma density inside the sheath is different from the ambient plasma outside the sheath. This plasma sheath mean energy is also different, since the charged particles energies are shifted by attraction or repulsion, depending on their respective signs. Therefore the measured distribution function of the local plasma sheath, in which the plasma instrument is immersed, will be altered. A basic approach of charging effects on the measured distribution function will be introduced in the following.

The approached is based on Liouville's theorem which states that along a particle trajectory, the volume defined by the distribution function is conserved in the phase space. This means that if A and B are two points of space and a particle trajectory exists between the points of the phase space (A, V_A) and (B, V_B), then in the absence of collisions:

$$f_A(V_A) = f_B(V_B) \tag{3.38}$$

[Laframboise and Parker (1973)] indicates how an isotropic Maxwellian velocity distribution function is modified by a positive or negative potential, in the Orbit Limited Motion (OML) assumption. Applied to a particle detector measurement of an ambient distribution function, the problem can be analytically formulated as follows.

The detector collecting surface denoted as D is defined as a planar area without any calibration or technical biases (no energy or angular resolution issues, energy cut-off and a full scan of the 2π sr visible by the collecting face of the surface). D is immersed in an isotropic and non collisional plasma and no secondary or photoemission occur. With those assumptions the distribution function collected by the non charged collecting surface is just half of the exact same function describing the ambient environment at infinity ∞ as the detector collects particles only from one face: the measured distribution function and density are thus over 2π sr as mentioned previously. As a consequence it has been set that only positive electron velocities are collected.

On the detector at a potential ϕ_D, using energy conservation, the collected particles have a velocity:

$$V_D = \sqrt{V_\infty^2 - \frac{2q\phi_D}{m}} \tag{3.39}$$

And they can reach the detector only if they satisfy

$$\frac{1}{2}mV_D^2 + q\phi_D \geq 0 \tag{3.40}$$

which means that detected particles have at least the potential energy of the collecting surface. This way, for all particles verifying equation 3.40:

$$f_D(V_D) = f_\infty(V_\infty) = f_\infty\left(\sqrt{V_D^2 + \frac{2q\phi_D}{m}}\right) \tag{3.41}$$

Considering now a Maxwellian plasma, this equation is in accordance with equation 2.10 which describes the local distribution function of a plasma in the presence of a potential $\phi(\mathbf{x})$.

A quick numerical application (feasible with any spreadsheet software) to ambient electrons allows to illustrate their distribution function modification due to the non null detector electrostatic potential.

The electron population velocity distribution function is defined as follow, based on equation 2.1 with a null average macroscopic velocity $\mathbf{u} = 0$ (the plasma is here isotropic):

$$f_\infty(V) = n_\infty\left(\frac{m}{2\pi kT}\right)^{3/2}\exp\left(\frac{-mV^2}{2kT}\right) \tag{3.42}$$

This population properties are arbitrarily set with a density $n_\infty = 10^6\,\mathrm{m}^{-3}$ and a temperature $kT = 10\,\mathrm{eV}$.

Figure 3.6 shows the theoretically measured velocity distribution functions of electrons, depending on the ϕ_D value: 0, 10 and -10 V. It respectively stands for an undisturbed, attracted and repulsed electron population. The velocity range is discretized with corresponding steps of 0.5 eV. The blue curve is the electron population measured by the non charged surface. It corresponds to half of the initial particle distribution function (only the positive normal velocities are collected). When the collecting surface electrostatic potential becomes attracting for electrons ($\phi_D = +10$ V, the red curve) the effect of condition 3.40 is obvious: if $q\phi_D$ is negative than V increases to conserve the particle total energy and no particle with an energy less than the detector potential energy is detected (10 eV), see the corresponding energy distribution functions on Figure 3.7. When ϕ_D is repulsive (-10 V) only the electrons having an initial energy superior to $q\phi_D$ (10 eV) can reach the surface, with a final energy reduced of 10 eV. It consequently eliminates all the electrons from the initial distribution function which were not energetic enough to reach the repulsive plate, as it appears on the measured distribution function with a loss of electronic population.

The isotropic velocity distribution functions can be transformed in energy distribution functions. Considering the density dn, expressed as:

$$dn = f_E(E)dE = f_V(V_x, V_y, V_z)dV_X dV_Y dV_Z = f_V(V)\sin(\theta)d\theta d\phi V^2 dV \tag{3.43}$$

and integrating on the polar coordinates angles θ and ϕ:

$$dn = f_V(V)4\pi V^2 dV \tag{3.44}$$

Knowing that $E = \frac{1}{2}mV^2$ and thus $dE = mVdV$ a combination with the previous equation allows to state that:

$$f_E(E) = f_V(V)\frac{4\pi V}{m} \tag{3.45}$$

The corresponding energy distribution functions are presented on Figure 3.7. The same effects that for the velocity distribution function modifications clearly appears in this Figure. The attracting potential effect on electrons (the red curve for $\phi_D = +10\,V$) is even more visible when considering the energy, because of the V conversion factor in equation 3.45. Numerical integrations on the various distribution functions allow to evaluate other properties of the plasma (also called moments):

$$n = \int_0^\infty 4\pi V^2 f_V(V)dV \tag{3.46}$$

$$J = \pi \int_0^\infty V^3 f_V(V)dV \tag{3.47}$$

$$V_{\text{mean}} = 4\frac{J}{n} \tag{3.48}$$

$$E_{\text{mean, volume}} = \frac{m}{2}\frac{\int_0^\infty V^2 f_V(V)2\pi V^2 dV}{\int_0^\infty f_V(V)2\pi V^2 dV} \tag{3.49}$$

$$E_{\text{mean, surface}} = \frac{m}{2}\frac{\int_0^\infty V^3 f_V(V)\pi V^2 dV}{\int_0^\infty f_V(V)V\pi V^2 dV} \tag{3.50}$$

If f_V is the isotropic undisturbed Maxwellian then $E_{\text{mean, volume}} = 3kT/2$ and $E_{\text{mean, surface}} = 2kT$.

In this present case the integration on the velocity are limited to $0 \longrightarrow +\infty$ as only the positive velocities are considered. Results are presented in Table 3.1. As expected, the null

Potential (V)	Density (m^{-3})	Mean velocity (m/s)	Integrated flux ($m^{-2}.s^{-1}$)	Mean E of DF (eV)	Mean E of surfacic DF (eV)
0	4.99×10^5	2.12×10^6	5.28×10^{11}	15	20
+10	7.92×10^5	2.70×10^6	1.07×10^{12}	22	24.8
-10	1.84×10^5	2.12×10^6	1.94×10^{11}	15	20

Table 3.1: Numerical results of analytical application of the Liouville's theorem: modification of electron Maxwellian population with respect to different surfacic detector electrostatic potential.

potential of the detector allows to find again the Maxwellian electron population, with a reduced density due to the half velocity phase space considered.

It appears that the repulsive potential ($\phi_D = -10\,V$) does not modify the estimate of the distribution function mean energy (15 eV) even though the density is considerably reduced with respect to the 5×10^5 m^{-3} expected (which represents a loss of 63%: indeed in this case $\exp(-q\phi/kT_e) \sim 0.37$). All electrons with an initial energy lower than 10 eV could not reach the surface, which constitutes a true loss of particles and thus a loss of information. Electrons with an initial kinetic energy $E_\infty > 10$ eV are collected with a final kinetic energy $E_D = E_\infty - 10$ eV. The function obtained remains a Maxwellian due to:

$$f(V) = f_0(V) \exp\left(\frac{-q\phi}{kT_e}\right)$$

and the mean energy of the DF does not vary (see Table 3.1.

When the surface potential is attractive the density is highly increased with respect to the assumed environment (7.92×10^5 m^{-3} which is an increase of 58%), and this time the mean energy of the distribution is increased (22 eV). All electrons usually collected at a null ϕ_D are still collected but have been accelerated ($E_D = E_\infty + 10$ eV). This is why the detector seems to be blind below 10 eV: the electrons with $E_\infty \sim 0$ eV are now accounted for electrons at ~ 10 eV, but there is no loss of collected particles compared with $\phi_D = 0$ V, the detected flux is on the contrary highly enhanced (see Table 3.1). The detector collects the OML current (or flux):

$$J = J_0 \left(1 - \frac{q\phi}{kT_e}\right)$$

which in this case leads to $J = 2J_0$, within 1% due to the energy discretization in the spreadsheet. OML is obtained because it is assumed that the only effect is a change in energy. In this analytical case OML predicted results are logically obtained. We will see in a further section 5.5 that numerical simulations can carry out OML theory to its limits.

This first approach limited to a simple application of the Liouville's theorem shows that Maxwellian distributions of particles subjected to non null potential are not simply shifted in energy as it is sometimes mentioned in the literature. The potential effect is not trivial, even in this very idealised case with no other perturbations. This example lets us foresee the complexity of the measured distributions analysis that will arise with the consideration of all other disturbing phenomena described in this Chapter. Further analysis of distribution function modifications enhanced with numerical simulations will be presented in Chapter 5, taking into account other biasing elements that will be introduced in the following sections.

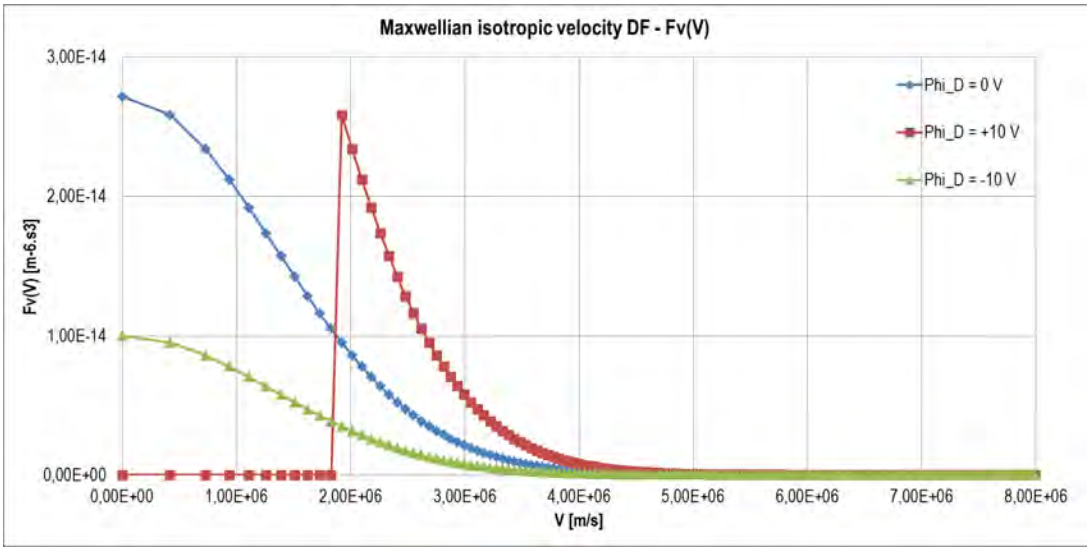

Figure 3.6: Example of analytical modifications of a Maxwellian electron velocity distribution functions (DF) according to Liouville's theorem and depending on detector potential value ϕ_D.

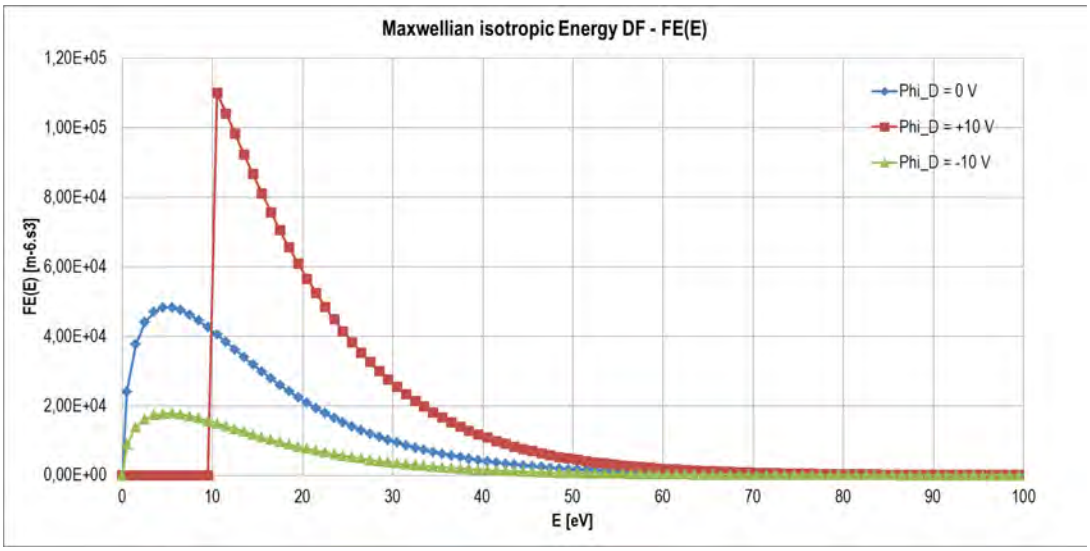

Figure 3.7: Example of analytical modifications of a Maxwellian electron energy distribution functions according to Liouville's theorem and depending on detector potential value ϕ_D.

3.5 Secondary electron emission / electron impact: SEEE

3.5.1 SEEE Principle

The surrounding environment of a satellite interacts with its structure through particle bombardment, partly responsible for charging. As explained in [Whipple (1981)], three possibilities occur when an electron impacts a surface (and is thus called the primary electron). It can be reflected or it can be absorbed which leads to two possibilities. The penetrating electron may collide with several other atoms and get its direction reversed out of the material, in which case it is called a "backscattered" electron (assumed to exit the surface with 1/2 to 2/3 of its initial energy). Or it can lose its energy and transmit it to other electrons present in the material which, through this excitation process, will escape the surface and be thus called "secondary electrons". This last process is known as *Secondary Electron Emission under Electron impact* (or SEEE).

Each incoming primary electron impacting a certain type of surface will eject a number $\delta_e(E, \theta)$ of secondary electrons, equal to the ration of the emitted flux to the collected one, and known as the *secondary electron coefficient* or *Secondary Electron emission Yield* (SEY).

$$\delta_e = \frac{J_{\text{emitted}}}{J_{\text{collected}}} \tag{3.51}$$

This yield is proper to each material and is a function of several parameters:

- the material properties (composition, thickness, cleanliness);
- the primary electron energy at impact E. For each material there is a maximum yield of secondary emission $\delta_{\text{e,max}}(E_{\text{max}}, \theta)$ for a specific primary electron energy E_{max};
- the primary electron incident angle with respect to the surface normal θ. The SEY function rises with the angle of incidence of primary electrons, as formulated in the further equations for SEY modelling.

An accurate modelling of the secondary electron yield is essential for spacecraft charging simulations as a direct impact on the surface emitted electron current. The secondary electrons directly affect the surface potentials, the spacecraft environment and therefore the plasma measurements. This is why many experiments have been carried out to determine $\delta_{\text{e,max}}$ and E_{max} for the most usual materials used on satellite structures [Katz et al. (1977)]. Examples of maximum yields and energy at maximum yield for secondary electron emissions are presented in Table 3.2. In certain conditions some yields can reach values higher than unity, meaning that an ambient electron flux will snatch a greater secondary electron flux from the surface, increasing the material electrostatic potential towards more positive values. Examples of secondary electron measurements in laboratory have been taken from [Balcon et al. (2012)], performed in a facility located at the ONERA center in Toulouse, France. The *Dispositif d'Emission Electronique Secondaire Sous faisceau d'Electrons* (or DEESSE facility, standing for SEE Under Electron Beam Apparatus) is an experimental tool totally dedicated to the characterization of secondary electron emission. [Balcon et al. (2012)] focuses on low-energy SEE measurements on dielectrics and conductors (incident electron energy below 20 eV). The results for several space materials are presented on Figure 3.8 for δ_e measurements depending on the incident electron energy. Figure 3.9 is similar to 3.8, but it focuses on low energies near the cross-over energy. Figure 3.10, on the other hand, illustrates the dependence of δ_e on the incident angle

Material	$\delta_{\text{e,max}}$	$E_{\text{max}}(eV)$
Aluminium	0.97	300
Aluminium oxyde	1.5-1.9	350-1300
Magnesium oxyde	4.0	400
Silicon dioxyde	2.4	400
Teflon	3	300
Kapton	2.1	150
Magnesium	0.92	250

Table 3.2: SEEE: Examples for several materials of maximum yields and energy at maximum yield for secondary electron emissions by primary electrons. *Taken from* [Hastings and Garret (1996)].

of the primary electron for a chrome sample (as shown on Figure 3.12 for the ITO material). The cross-over corresponds to the primary electron threshold energy where δ_e equals to unity. This limit is important as it determines the sign of satellite charging as a consequence of the incoming electron flux. If the SEEY curve crosses unity at the energy threshold E_1, it will cross it again at E_2, meaning that for a certain energy range of primary electrons $E_1 < E < E_2$ the secondary emission phenomenon will act positively on the surface potential, and negatively for E outside this range. Other examples of SEY curves of common materials used on spacecraft are presented in Figure 3.11 from SEY measurements done by [Baglin et al. (2000)] with materials which surfaces have not been treated before the measurements. The figure illustrates the function aspect, in good adequation with [Balcon et al. (2012)] results.

Typical secondary electrons have an energy spectrum assumed to be an isotropic Maxwellian energy distribution function with a mean energy of 2 eV [Whipple (1981)], [Sternglass (1954)]. Emitting materials therefore populate the spacecraft environment with low energy electrons, the ones of interest when measuring the low energy end of the background electron distribution. Once extracted from the materials, those secondary and backscattered electrons might be detected by the particle instruments and be accounted for low as energy ambient electrons.

3.5.2 SEEE Modelling

In [Katz et al. (1977)], a formulation is suggested, aiming at improving the calculation of the secondary electron emission through strong relations with characterized material parameters and possible future enhancement, taking into account new laboratory measurement results. This model is applied in the NASCAP and SPIS software. The secondary emission yield is expressed as follows, considering the range and energy loss rate of incident particles:

$$\delta_{e,\theta} = c_1 \int_0^R \left|\frac{dE}{dx}\right| \exp\left(-c_2 x \cos\theta\right) dx \tag{3.52}$$

where $\delta_{e,\theta}$ remains the number of emitted secondary electron per primary incident at angle θ, and the range and energy loss rate are related by

$$\left|\frac{dE}{dx}\right| = \left(\frac{dR}{dE}\right)^{-1} \tag{3.53}$$

If the range function is known, the above equation can be evaluated with the c_1 and c_2 constants, determined from the energy maximum yield E_{max} and its corresponding yield $\delta_{\text{e,max}}$.

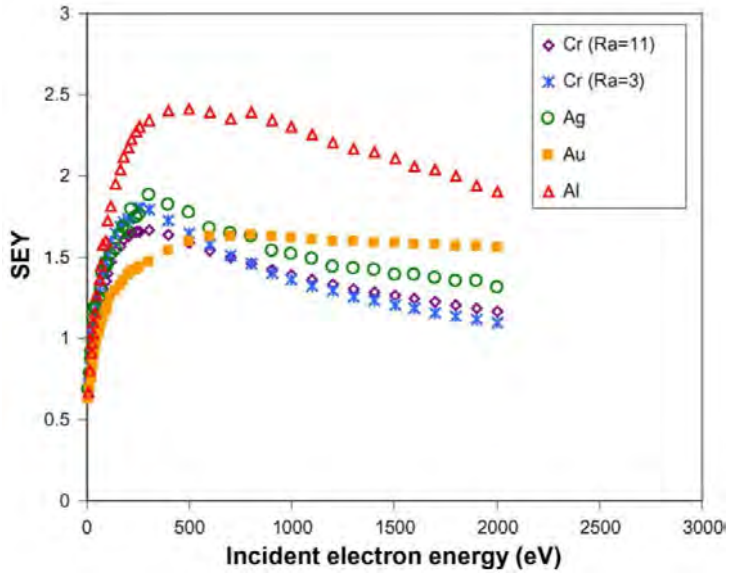

Figure 3.8: SEY curves measured on Aluminium (Al), Gold (Au), Silver (Ag) and Chrome (Cr). *From* [Balcon et al. (2012)].

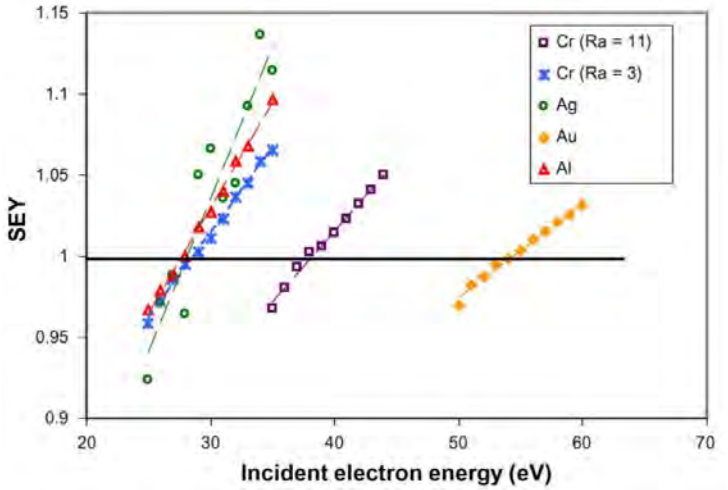

Figure 3.9: SEY of Al, Au, Ag, and Cr as a function of the incident electron energy near the first crossover energy. R_a stands for the roughness of the material (a material less polished than others will present more bumps on its surface and will be considered as rough). *From* [Balcon et al. (2012)].

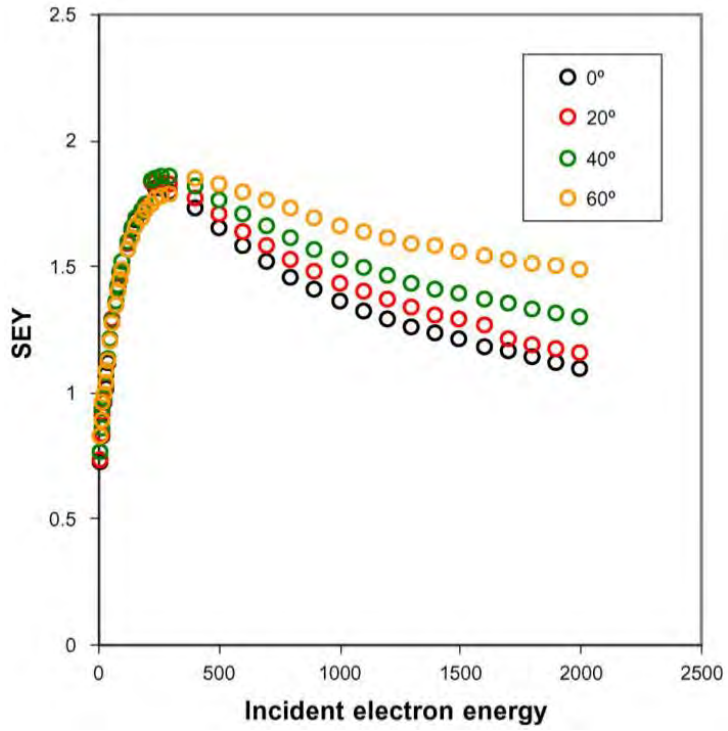

Figure 3.10: SEEE: Effect of the incidence angle on the SEY of a smooth Cr surface (roughness $R_a = 3$). *From* [Balcon et al. (2012)].

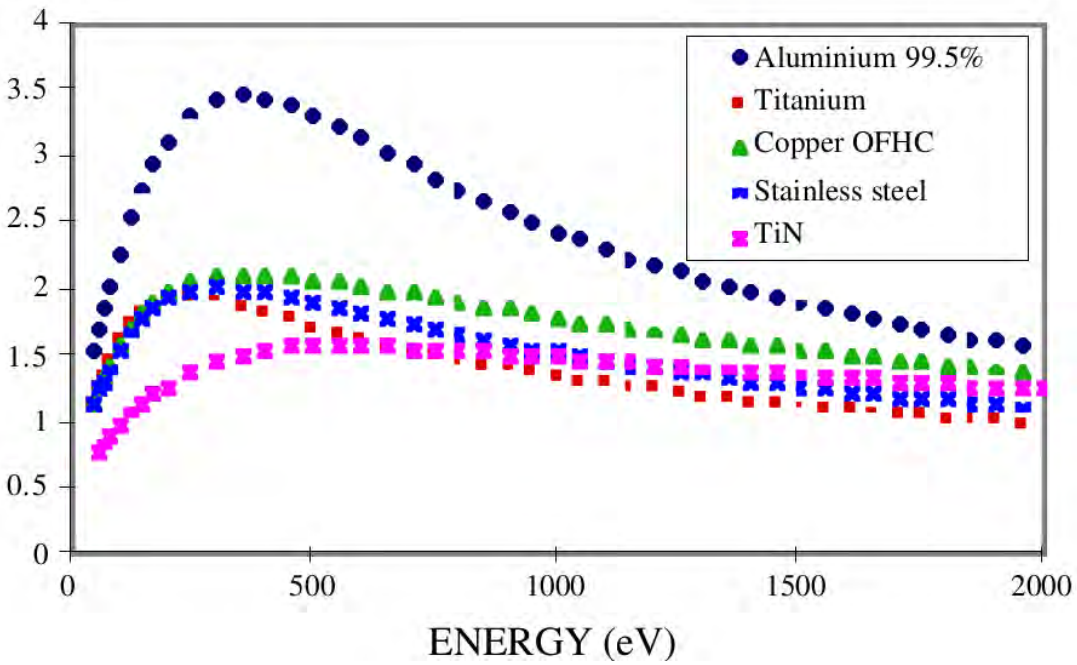

Figure 3.11: SEY of various materials (usually used as satellite covering materials) depending on the primary electron energy. Those materials have not been treated before measurements. *From* [Baglin et al. (2000)].

Otherwise, for a general range expression, equation 3.52 is evaluated assuming dE/dx is constant, and setting the upper limit of equation 3.52 in order to give the correct total energy loss. This leads to:

$$\delta_{e,\theta} = c_1 \int_0^{E\frac{dR}{dE}} \left(\frac{dR}{dE}\right)^{-1} \exp\left(-c_2 x \cos\theta\right) dx \tag{3.54}$$

Posing $Q = c_2 E dR/dE$, the angle average yield becomes

$$\overline{\delta}(E) = 2c_1 E(Q - 1 + \exp(-Q))/Q^2 \tag{3.55}$$

The NASCAP software evaluates equation 3.52 by assuming that dE/dx is linear in x:

$$\frac{dE}{dx} = \left(\frac{dR}{dE_0}\right)^{-1} + \frac{d^2R}{dE_0^2}\left(\frac{dR}{dE_0}\right)^{-3} x \tag{3.56}$$

The range R is represented by the sum of two exponentials:

$$R = r_1 E^{n_1} + r_2 E^{n_2} \tag{3.57}$$

The upper limit R_u is taken as the lesser solution of:

$$\frac{dE}{dx}\rfloor_{R_u} = 0 \tag{3.58}$$

$$\int_0^{R_u} \mid \frac{dE}{dx} \mid dx = E \tag{3.59}$$

Then posing $Q = c_2 R_u \cos\theta$:

$$\delta_{e,\theta} = c_1 \left[R_u \left(\frac{dR}{dE_0}\right)^{-1} \frac{1 - \exp(-Q)}{Q} + R_u^2 \frac{d^2R}{dE_0^2}\left(\frac{dR}{dE_0}\right)^{-3} \frac{1 - (Q+1)\exp(-Q)}{Q^2}\right] \tag{3.60}$$

$$\overline{\delta}(E) = 2c_1 \left[R_u \left(\frac{dR}{dE_0}\right)^{-1} \frac{Q - 1 + \exp(-Q)}{Q^2} + Z R_u^2 \frac{d^2R}{dE_0^2}\left(\frac{dR}{dE_0}\right)^{-3}\right] \tag{3.61}$$

where Q is evaluated at normal incidence and

$$Z = \int_0^1 u du \frac{1 - (Qu+1)\exp(-Qu)}{Q^2 u^2} \tag{3.62}$$

The SPIS and NASCAP software use those expressions to evaluate the constants c_1 and c_2 from user input parameters $\delta_{e,\max}$ and $E_{\max}$. An example of SEY computation from [Katz et al. (1977)] model is presented on Figure 3.12, for Indium Tin Oxyde, for a number of incident angle of the primary electron.

[Whipple (1981)] presents a linearised version of the [Katz et al. (1977)] model, commonly used in computational modelling programs;

$$\delta_e(E,\theta) = \frac{1.114\delta_{e,max}}{\cos\theta}\left(\frac{E_{max}}{E}\right)^{0.35}\left\{1 - \exp\left[-2.28\cos\theta\left(\frac{E}{E_{max}}\right)^{1.35}\right]\right\} \tag{3.63}$$

Furthermore backscattered electrons are added to the parasite electrons emitted by the satellite. Their production process differs from that of SEEE as the backscattered particle is the primary electron, with a direction that has been reversed after several collisions with local atoms. Thus the *Backscattered Electron Coefficient* (or *Backscattered Electron Yield* - BEY) cannot be greater than unity. This yield is more considered as a probability η that the primary electron will come out from the penetrated material. As for SEEY, BEY depends on the material, the primary electron energy and incident angle. However the backscattered electron energy is typically between 1/2 and 2/3 of its initial energy.

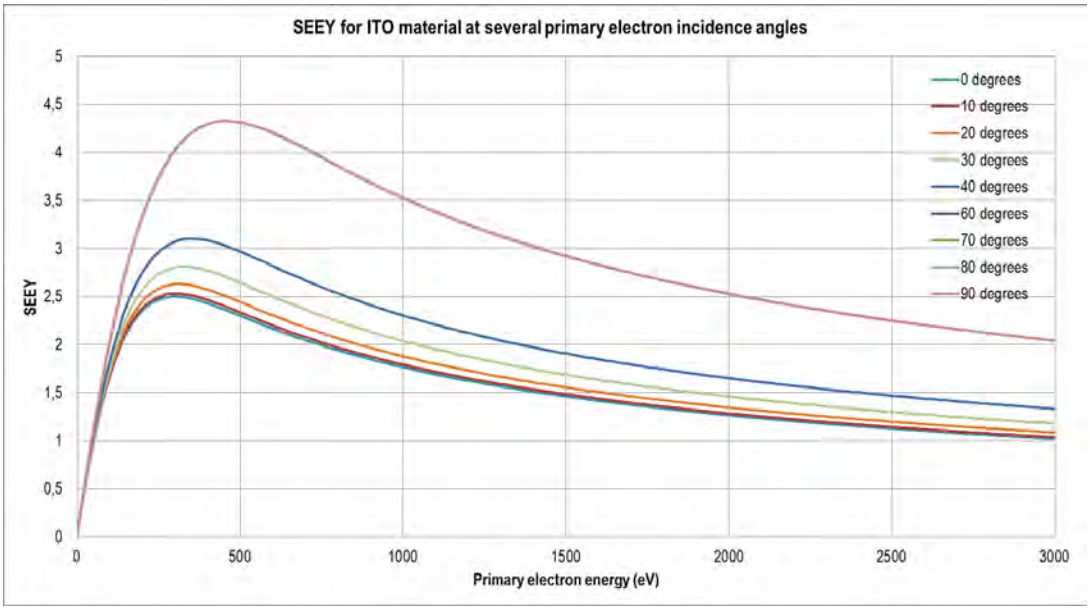

Figure 3.12: SEEE: Influence of primary electron incidence angle θ on the secondary electron yield δ_e for the ITO material.

3.6 Secondary electron emission under proton impact: SEEP

Other impacting particles as ions can generate secondary electrons through a similar process to secondary electron emission under electron impact. For secondary electrons generated by protons it is called *Secondary Electron Emission under Proton impact* (or SEEP). SEEP yields are also specific to the materials and depend on the incident particle energy and angle with respect to the normal surface.

Thanks to experimental measurement campaigns [Whipple (1981)] an empirical expression of the SEEP yield has been developed:

$$\delta_i(E,\theta) = \frac{2\delta_{i,max}\sqrt{E/E_{\max}}}{1+E/E_{\max}}\sec\theta \tag{3.64}$$

For impacting protons with energies lower than 10 keV, the yields of SEEP are inferior to unity [Hastings and Garret (1996)]. For example protons impacting Aluminium can release $\delta_{\mathrm{i,max}} = 4.2$ electrons only for a $E_{\max}$ as high as 90 keV. The emitted population also corresponds to an isotropic Maxwellian with a mean energy of few electron volts.

In NASCAP and SPIS, the secondary electron emission under proton impact is treated with the same empirical formulas as for secondary electron under electron impact [Katz et al. (1977)]. However with protons, the energy loss is parameterised by:

$$\frac{dE}{dx} = \frac{cE^{1/2}}{1+\dfrac{E}{E_{\max}}} \tag{3.65}$$

with $E_{\max} \sim 90\,\mathrm{keV}$.

Material	Work function (eV)	$\lvert j_{ph0}\rvert$ ($\mu A/m^2$)
Aluminium oxyde	3.9	42
ITO	4.8	30
Gold	4.8	29
Stainless steel	4.4	20
Vitreous carbon	4.8	13
Graphite	4.7	4

Table 3.3: Photoelectron current density at 1 AU for several materials. The work function is the minimum thermodynamic work (*i.e.* energy) needed to remove an electron from a surface. *Taken from* [Hastings and Garret (1996)].

3.7 Photoemission

In addition to secondary electrons resulting from electron and ion impact, photoelectrons are emitted by surfaces exposed to the sunlight *UV*. The photoelectron current created depends on the *UV* Solar flux, the Solar incident angle, the material properties (taking into account the material reflectance R) and the surface potentials [Lucas (1973)] considering their action on the photoelectron recollection. According to laboratory and space experiments emitted photoelectrons have an isotropic Maxwellian energy distribution function, but depending on the literature the corresponding mean energy is 1-3 eV [Whipple (1981)], or a double Maxwellian of temperatures 2.7 eV and 10 eV (with emission rates of respectively 95% and 5%) [Pedersen (1995)]. Extensive studies are in progress in the ONERA facilities to strengthen our knowledge on the photoemission process.

Considering a situation where the photoemitting surface has zero or negative potential (without any potential barrier), all photoelectrons will escape. The corresponding photoelectron current density is given by:

$$j_{ph0}(R) = -\int_0^\infty f_S(E) Y(E,R) dE \tag{3.66}$$

with $f_S(E)$ being the incoming solar flux (function of the energy E) and $Y(E,R)$ the photoelectron yield per incident photon (depending on the material reflectance R, which is also a function of E).

Some photoelectron emission characteristics of usual satellite surface materials are presented in Table 3.3. The reference photoelectron current density $|j_{ph0}|$ at 1 AU is comprised between 4 and 42 $\mu A/m^2$ (an average value of about 20 $\mu A/m^2$ is usually considered).

All spacecraft surfaces are potentially emitters, even the particle detector surfaces, as it occurs on any vehicle sunlit face. It leads to a complex 3 dimensional charging effect, which anisotropy is further complicated if the satellite structure does have a spin. A shadowed element will not photoemit but might still release secondary electrons. All those particles are considered as parasites as they remain electrons independently of their origin. They thus create additional currents to the spacecraft and in a more troublesome way they can be collected by electron detectors, thus introducing aberrations in the measurements. This last phenomenon is worsen by a positively charged detector, even if it is only at few volts, as those particles are emitted with low energies and are easily influenced by local potentials. Some particles originating from the tail of the Maxwellian distribution function have higher energies and a higher probability to escape, or reach negative spacecraft surfaces.

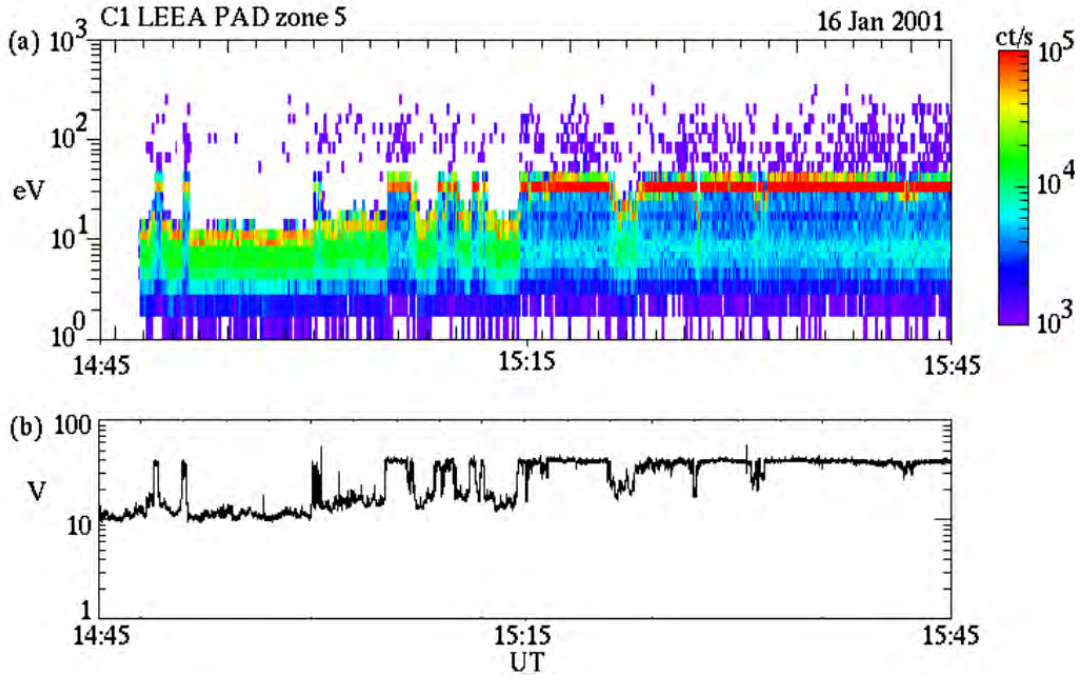

Figure 3.13: Cluster Spacecraft 1 data (16 January 2001) showing spacecraft electrons in a low density environment (a) PEACE LEEA data (b) EFW data showing spacecraft potential. *Taken from* [Szita et al. (2001)].

An example taken from [Szita et al. (2001)] shows the detection of secondary and photo-electrons (Figure 3.13). The top illustration Figure 3.13-a shows the count rate data of the instrument *Low Energy Electron Analyzer* (LEEA) when the Cluster spacecraft was inside the northern magnetosphere in a region of low plasma density. The spectrogram is dominated by spacecraft electrons, and no thermal electrons can be detected with a temperature below the spacecraft potential (see equation 3.40). Thus all electrons with energies below this threshold have been generated by the satellite itself. Figure 3.13-b shows the result of the *Electric Field and Wave experiment* (EFW) which makes measurements of electric field and spacecraft potential fluctuations using four probes on ∼50 m long booms. The spacecraft potential for this period ranges between 10 V and 40 V. The variations are apparently not due to electrons in the PEACE energy range, but may be due to a varying flux of higher energy electrons or ions. The highest values of the count rate are seen in a single energy bin at or near the top edge of the spacecraft electron spectrum. This is a commonly seen feature, and is often strongest in the middle (spin plane) anodes. The energy of this feature closely correlates with the spacecraft potential determined by EFW.

3.8 Ion wake

The combined velocity of the spacecraft and the crossed ion flow generates an ion wake in the resulting direction of the two velocities, as a boat travelling through water. A wake essentially concerns ions rather than electrons as the thermal velocity $v_{th} = (2kT/m)^{1/2}$ (see equation 2.3) is inversely proportional to the root square particle mass, which is much greater for ions.

Therefore, at equal temperature, the thermal velocity of electrons will make them repopulate much faster the depleted region than the ions. An ion wake is thus a region dominated by electrons, with practically no positive charges, which makes the plasma quasi-neutrality rule violated and the local potential negative. In worse cases, [Wang et al. (1994)] demonstrated that under certain ionosphere environment (nightside auroral electron conditions), a severe charging zone would exist in the near wake of a large plate with a floating potential.

[Engwall (2006)] proposes schematic views of positive ion wakes behind a positively charged spacecraft, for two different contexts. They are displayed on Figure 3.14. In case a) the ion flow energies are much higher than the spacecraft potential V_{sc}: the wake has the typical transverse size of the spacecraft and is called "narrow wake". In case b) the ion flow energy is below V_{sc}: ions scatter off the positive electrostatic potential from the spacecraft, creating an "enhanced wake". Another wake type is also possible if the satellite potential is negative (and thus attracts ions) and the ion flow energy is below V_{sc}: this situation is represented in the c) in Figure 3.14 and corresponds to what can be seen as a "reduced wake".

An evaluation of the highest absolute potential inside an ion wake is possible but requires several approximations. The obtained estimations of local potentials remain rough but give an idea of the wake potential level that can be expected and its influence in the vicinity of the spacecraft.

Starting from the Poisson-Boltzmann equation, where ϕ is the electrostatic potential, ρ the charge density ($\rho = -en_e$), and knowing that the electric field $\mathbf{E}$ = -$\nabla\phi$:

$$\triangle\phi = -\frac{\rho}{\varepsilon_0} = -\nabla\mathbf{E} \tag{3.67}$$

Then using the Gauss theorem to determine the electric field ($\mathbf{E}$) flux across a surface S (boundary of a volume V):

$$\oiint_S \mathbf{E}\cdot d\mathbf{S} = \iiint_V (\nabla\cdot\mathbf{E})\,dV = \iiint_V \frac{\rho}{\varepsilon_0} dV, \tag{3.68}$$

assuming that n_e is uniform, the electrostatic potential within simple volume geometries can be approximated.

Cylindrical narrow ion wake

Considering case a) in Figure 3.14 with the narrow wake, the charges distribution behind the vehicle can be seen as a cylinder with a density n_e of electrons. If a cylinder of radius r and length L is chosen as Gauss' surface, equation 3.68 gives (knowing that the scalar product ($\mathbf{E}$·d$\mathbf{S}$) vanishes for the two circular faces of the cylinder):

$$2\pi r E(r) L = \pi r^2 L \frac{\rho}{\varepsilon_0}$$

which leads to:

$$E(r) = \begin{cases} \dfrac{\rho r}{2\varepsilon_0} & \text{if } r \leqslant L, \\ \dfrac{\rho L^2}{2\varepsilon_0 r} & \text{if } r \geqslant L. \end{cases} \tag{3.69}$$

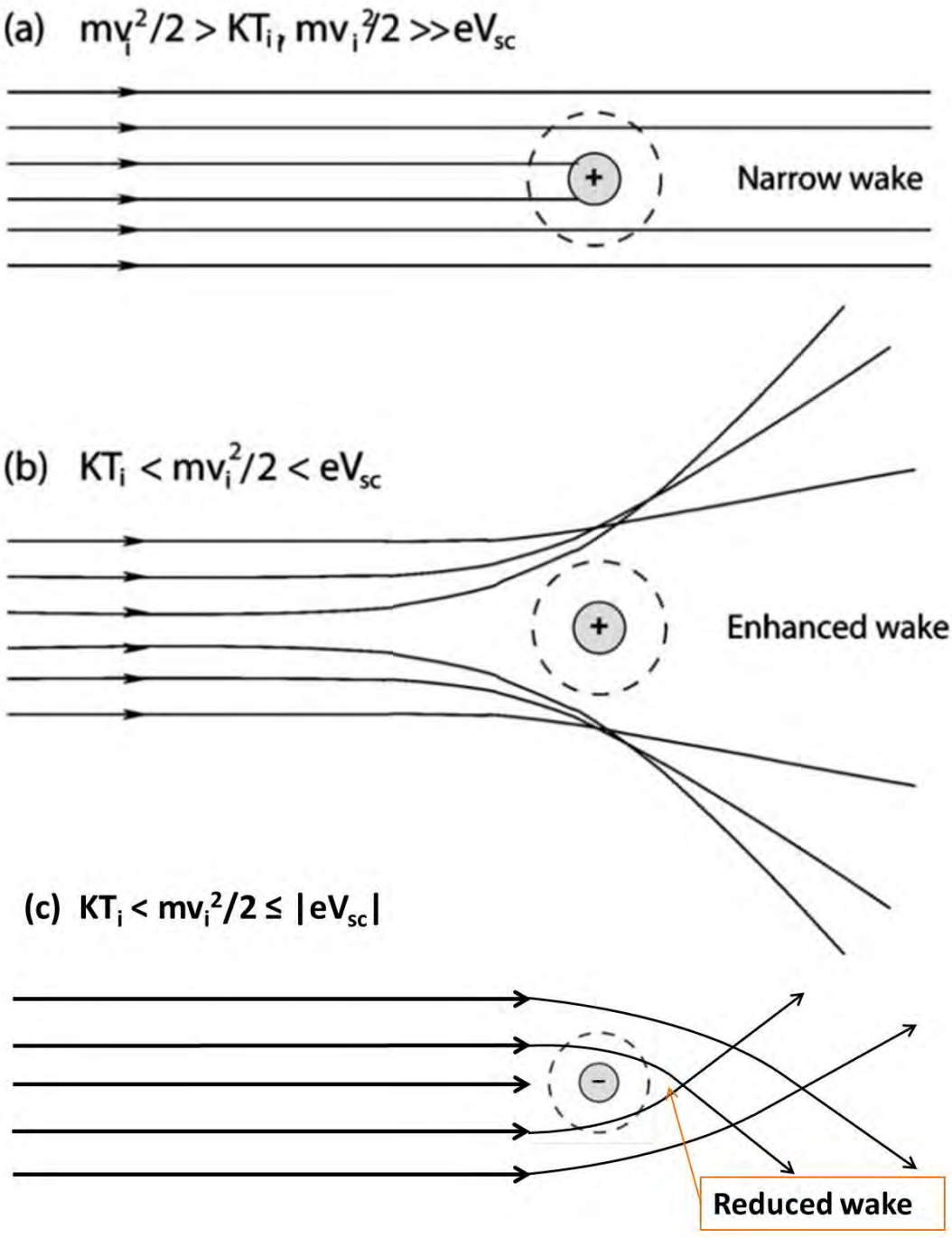

Figure 3.14: Possible ion wakes configurations for various ion flow energies and satellite potentials. The two firsts sketches are taken from [Engwall (2006)], and correspond to positively charged spacecraft with: (a) a narrow wake configuration and in (b) an enhanced wake. (c) illustrates a possible reduced wake associated to a negatively charged satellite.

It allows to go back to the expression of the electrostatic potentials after integration:

$$\phi(r) = \begin{cases} \dfrac{-\rho r^2}{4\varepsilon_0} + A & \text{if } r \leqslant L, \\ \dfrac{-\rho L^2}{2\varepsilon_0} \ln(r) + B & \text{if } r \geqslant L. \end{cases}$$

A and B are constants that can be determined assuming the wake is limited by a boundary where ϕ is zero; that is where quasi-neutrality is established with $n_e = n_i$. It finally gives:

$$\phi(r) = \begin{cases} \dfrac{\rho}{4\varepsilon_0} \left(L^2 - r^2\right) & \text{if } r \leqslant L, \\ \dfrac{\rho L^2}{2\varepsilon_0} \ln\left(\dfrac{L}{r}\right) & \text{if } r \geqslant L. \end{cases} \tag{3.70}$$

The interest is the potential at the center of the wake cylinder ($r = 0$) which can also be expressed in terms of λ_D (equation 2.16) by:

$$\phi(r = 0) \sim -\frac{1}{4} \frac{kT_e}{e} \left(\frac{L}{\lambda_D}\right)^2 \tag{3.71}$$

Spherical reduced ion wake

In the same manner it is possible to approximate the potential within a reduced wake as for situation c) of Figure 3.14. To do this the wake can be considered as a spherical region of radius L, void of ions. It is true that the handmade sketch on Figure 3.14-c does not make the wake look like a sphere, but it will be showed later that for some numerical simulations under certain conditions and satellite geometry, the ion wake can be assimilated to a sphere. In this case the previous calculations adapted to the sphere lead to:

$$E(r) = \begin{cases} \dfrac{\rho r}{3\varepsilon_0} & \text{if } r \leqslant L, \\ \dfrac{\rho L^3}{3\varepsilon_0 r^2} & \text{if } r \geqslant L. \end{cases} \tag{3.72}$$

After integration the constants can be solved for $\phi = 0$ at an infinite distance r from the sphere. Finally:

$$\phi(r) = \begin{cases} \dfrac{\rho}{2\varepsilon_0} \left(L^2 - \dfrac{r^2}{3}\right) & \text{if } r \leqslant L, \\ \dfrac{\rho L^3}{3\varepsilon_0 r} & \text{if } r \geqslant L. \end{cases} \tag{3.73}$$

At the sphere center ($r = 0$) and using λ_D, the electrostatic potential is obtained as:

$$\phi(r = 0) \sim -\frac{1}{2} \frac{kT_e}{e} \left(\frac{L}{\lambda_D}\right)^2 \tag{3.74}$$

Equations 3.71 and 3.74 have to be considered as rough numerical approximations of the electrostatic potential inside ion wakes. The important characteristic to be remembered is that this potential is proportional to $kT_e(L/\lambda_D)^2$ (with a factor 1/2 or 1/4 depending on the geometry of the wake (*i.e.* respectively spherical or cylindrical).

One should note that ion wakes do not only appear behind the satellite platform but also behind any other element facing the ion flow. Large Solar panel arrays can perfectly generate ion depletions and thus create local disturbances in the plasma potential around the spacecraft.

Therefore some plasma measurements perturbations are conceivable. As explained above an ion wake is negatively charged in its center, which also appears in the previous equations. Under certain conditions the potential can be negative enough to repulse low energy electrons, especially the secondary and photoelectrons emitted from the satellite. The deviated particles can thus be collected by the surfaces and/or a particle detector.

3.9 Potential barriers

The section 3.3 presented the issues related to space charge effects and sheath region surrounding a space probe. It was also mentioned that local densities of ambient electrons might be increased by secondary and photoelectron populations. Indeed as explained in sections 3.5 and 3.7 those parasite particles are emitted with relatively low mean energies of few eV, meaning that they will not be necessarily ejected out of the sheath. In this usual case, the local potential associated with the dense localized electron plasma is dug until reaching negative values, enough to compensate the multiple types of electron flows and equilibrate the current system.

The sheath is therefore going along with a potential well, locally or entirely facing the satellite surfaces, depending on the emission rates and localization of surfaces producing secondary and photoelectrons. This negative potential, created by accumulation of low energy secondary and photoelectrons, might often become strong enough to repel other parasite particles back to the spacecraft. The local potential well is thus named "potential barrier" for the spacecraft generated particles, modifying the existing currents to the surfaces, and consequently their equilibrium potential. Even though for simple potential barrier geometries, analytical expressions of the potential profiles can be found [Sherman et al. (1971), Besse et al. (1980)], the charging equation 3.1 can be highly disrupted and lead to new solutions, quite difficult to derive analytically because of the extremely inter-correlated equation parameters.

Following observations of recollected photoelectrons and secondary electrons on the ATS 6 spacecraft, [Whipple (1976)] developed a theory for a spherically symmetric photoelectron sheath, including the effect of ions, thermal electrons and secondaries. The aim was to determine whether the potential barrier responsible for the secondaries reflection was caused by those same particles or not. However, a comparison with the spacecraft data showed that the observed potential barrier is too large to be explained by the model (*i.e.* a spherically symmetric photoelectron or secondary electron sheath surrounding a uniformly charged spacecraft), and the authors concluded that the most probable explanation was that some portions of the ATS 6 surfaces are charged to different potentials.

Referring to the Helios spacecraft, a paper [Isensee (1977)] presents particle-in-cell simulations of the plasma environment of a spacecraft in the Solar wind, at 0.2 AU from the Sun. With a conducting spacecraft, the consideration of 1 eV mean energy photoelectrons and the expected Solar wind conditions, the author obtained a slightly positively charged satellite (+2.9 V) surrounded by negative plasma potentials in the wake and in the ram. In front of the sunlit face, due to very high densities of photoelectrons, the local potential reached -1.4 V and in the ion wake behind the probe: -4.5 V. The 1 eV emitted photoelectrons are thus recollected by the surfaces of the probe. The rest of the paper focusses on the consequences in distortions of measured electron distribution functions. Such simple simulations of photoelectron clouds and their effects on spacecraft charging were already of interests for the understanding of plasma measurements disturbances. However in these simulations, the secondary electronic emission was not modelled.

[Thiébault et al. (2004)] studied the potential barrier in the electrostatic sheath around a magnetospheric spacecraft, for cases of conductive spacecraft like Geotail and Cluster. A fully self-consistent analytical model of the plasma around an electron emitting central body in a spherically symmetric geometry was used to analyse the electrostatic sheath around an idealized spacecraft. It was shown by comparison with 3D PIC simulations that a non-monotonic potential with negative potential barrier can exist all around a positively charged spacecraft (with Debye length of the order of the central body radius or more) even in the case of an asymmetric illumination pattern.

In the Solar Probe Plus context at 0.044 AU from the Sun, simulation results provided in [Ergun et al. (2010)] show that a negatively charged satellite is obtained using a PIC code and a simplified geometrical model. High potential barriers for emitted photoelectrons and secondary electrons appear in the ram and the wake sides of the probe, due to their high densities in these regions, and make those low energy particles recollected by the spacecraft. Current balance is obtained for a negative spacecraft potential.

Other sources of potential well generation have been introduced in section 3.8. Analytical calculations of electrostatic potential in heart of the different ion wake configurations have been presented, showing that negative values are ubiquitous in positive ion depletions. Usually facing the shadowed faces of the spacecraft (depending on the vehicle, ion drift velocities and Sun direction configuration), the electrostatic potential inside the wake can also reach negative values sufficient to repel the other spacecraft emitted particles onto the shadowed faces: mainly secondary and more rarely backscattered electrons. This wake thus constitutes a potential barrier for those low energy electrons, and eventually for the wandering photoelectrons that would access this area.

From the outside "spacecraft and sheath" system, the potential wells do not automatically represent electrostatic barriers for ambient particles. Indeed thermal electrons usually have higher energies than secondary particles and are thus able to cross the few negative volts inside the sheaths. Small energy shifts or particle trajectory deflections might be observed in ambient plasma measurements, but the potential profile along an electron trajectory coming from the far field is not necessarily monotonic, which complicates the interpretation of the detected electron energy distribution functions. Drifting ions however are less affected by the sheaths potential values due to their heavy mass and drift velocity, making their kinetic energy large enough to cross those potentials and hit the satellite surfaces.

Finally, as mentioned in section 3.2, differential charging can generate strong electrostatic potential patterns that spread from a localized region on a satellite surface element to nearby regions (see Figure 3.2). The extended potential isocontour profiles can constitute potential barriers for secondary particles, especially if the Debye length is important compared to the spacecraft dimension.

A more detailed analysis of potential barriers will be presented in section 4.2.

3.10 Viewing factor

Each particle detector has a specific field of view, defining the regions from which incoming particle trajectories will be accepted within the detector entrance and thus be counted for the measured population. For some configurations the instrument is able to cover completely the 4π steradians around it, this is for instance the case of the EAS instrument on-board Solar Orbiter which owing to its two combined sensors can scan simultaneously in all directions. However in

those configurations the instrument will automatically look also in the spacecraft direction.

The satellite therefore constitutes a physical obstacle to particle detection, especially for heavy particles such as ions with a thermal velocity much smaller than that of electrons. Moreover if the satellite body is electrically charged it represents an electrostatic bias to particle detection: the geometrical obstacle of the structure will be enlarged or reduced depending on the potential signs on the surfaces and the charge of the measured particles. It was already mentioned in section 3.1 that the satellite potential can attract or repulse the ambient populations depending on the combined potentials and particle charges, thus biasing particle measurements by increasing or decreasing the detected fluxes. This also modifies the interpretation of the configuration of the incoming fluxes made through the detector result analysis. Indeed considering one viewing direction of the instrument, the detector could collect particles with a velocity orientation practically opposed to the pointing direction. If those collected charges travelled near the electrostatic configuration of the spacecraft however, their trajectories might have been bent, depending and the potentials and the particles energies, so the original incoming region is different from the instrument pointing direction.

Furthermore a spacecraft element directly in the field of view of an instrument might contribute efficiently to secondary or photoelectron detection. Other types of particle detectors have a limited instantaneous field of view but use the satellite spin to cover the 4π steradians of the environment. This is for example the case for PEACE/LEEA on-board the Cluster spacecraft, where no satellite elements are directly in the sight of the detector, apart from antennas.

Finally, even though an instrument does not directly look onto any satellite element it is possible that its field of view does include an ion wake structure generated upstream by a satellite component. As the ion depletion structure is not neutral but negatively charged, it might repulse electrons with energy comparable or inferior to the most negative potential inside the ion wake. The corresponding deviation of particle trajectories will affect, in proportions that still have to be evaluated, the measured fluxes. An example of particle deviations is given in Figure 3.15, for a non charged satellite and particle detector, but with a near spacecraft environment disturbed by local negative electrostatic potentials. Considering a negative ion wake (on the rear side of the probe) and a negative plasma sheath in the ram due to a photoelectron cloud, incoming ambient electrons are more or less deflected depending on their initial energy, only because of the near probe environment. It results in a misinterpretation of the velocity directions.

The instrument intrinsic technical characteristics such as the observed energy range, the resolution, the measurement sampling period, the scanning frequency, have obviously a direct impact on the studied plasma analysis. Instrument properties ill-adapted to an environment might cause information losses (fast plasma frequency fluctuations, temporary density pikes, *etc*). However those issues do not rely directly on spacecraft/plasma interactions but have to be anticipated in advance as part of the plasma instrument design and conception.

The combined factors of the particle detector field of view, the electrostatic potentials on the satellite and the instrument and instrument technical properties have to be taken into account for plasma measurement analyses.

3.11 Other phenomena

The extreme low pressures in space make the spacecraft materials outgass neutral atoms, molecules or ions, called contaminants. Some contaminants can also come from the space environment, and will orbit around the satellite or adsorb on it surfaces. Furthermore the

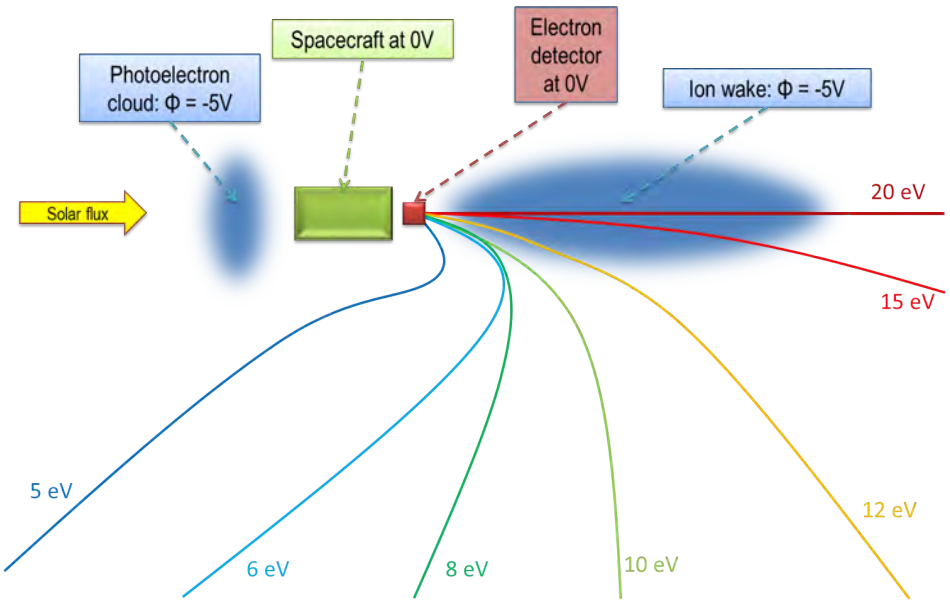

Figure 3.15: Examples of electrons trajectories arriving at a probe. The given values denote the energy corresponding to the plotted trajectory, as a simple qualitative estimation. It highlights the electron deflection due to local negative potentials: an ion wake and a local high density of photoelectrons in the ram.

propulsion and attitude control systems operate by emitting gases as narrow oriented plumes, but some particles might deviate from the nozzle exit and impinge the surrounding surfaces. All those volatile species are considered as contaminants as they can condensate on critical surfaces and degrade their properties or modify the material characteristics, for instance the associated yields of secondary and photoemission. Besides the chemical propulsion systems (solid rocket motors, bipropellant or monopropellant thrusters), satellites can also embed plasma thrusters which also release neutral gas in the plume as the efficiency of ionization of those thrusters is only of a few percent: it produces low energy ions from charge exchange reactions between ions and slow neutrals produced by the imperfect thrusters. These low energy ions can be deflected towards the spacecraft elements.

Other types of microscopic or macroscopic particles can disturb the satellite, more or less violently depending on their size and velocity. The closer to the previously cited plasma is the "dusty plasma" which is an electron-ion set also containing charged dust grains (of sizes between nanometres and millimetres) and neutral atoms. The grains (metallic, conducting or made of ice particles) highly increase the system complexity [Shukla and Mamun (2002)].

In order to control the satellite potential, ion or electron emitters are often embedded on the structures. These devices aim at swinging the spacecraft potential towards more negative or positive values by emission of respectively positive ion or electron beams. It is possible that those beams are less energetic than the potential energy of the some charged spacecraft elements and thus return back to the structure. This generation of new currents to the satellite will affect the equilibrium and, add to the space charge effect in the plumes. The satellite environment risks to become hardly predictable with a considerable injection of charged particles within the ambient plasma. In addition, emitters discharge the spacecraft absolute potential, and not necessarily dielectric coatings. Particle measurements should be definitely affected by those

phenomena.

Some of the satellite external surfaces are quite complex, such as the solar panel with several areas of different natures, particularly suitable for conditions of differential charging. At equilibrium, all connected conductors have a global null net current (but some areas can collect positive currents while others gather negative currents) and all dielectrics satisfy local current balance (zero net collected current), taking into account the conductivity as the leakage current. Therefore some parts of the solar arrays (or spacecraft) will collect electrons and other parts will collect ions, meaning that local potentials will be respectively positive and negative relative to space. Concerning the current collection from the solar panels, it will occur at any place where conductors (or semiconductors) are exposed to the ambient plasma, which is the case for solar cell edges and metallic inter-connectors between cells. Solar cell surfaces themselves are covered with dielectric layers: the cover glass. To reach current balance the dielectric surface has several options of steady surface potentials. First it can charge negatively enough to repeal most of incoming electrons (the balance is thus between incoming ions and electrons). Secondly it can emit secondary electrons enough to balance the incoming primary electrons and outgoing secondary electrons. Finally it can conduct current to the ground. Those secondary particles will be recollected by the surrounding conductors (if positively charged with respect to the dielectrics) [Hastings and Chang (1989)]. The resulting potential distribution on the solar array might lead to a complex variable and pattern with the formation of potential barriers. Such potential structures might disturb the satellite environment and consequently its measurements. One should finally note that the important discrepancies between close local potentials can generate destructive electrostatic discharges (ESD), potentially hazardous for the mission.

Chapter 4

Numerical simulation of Solar wind/satellite interaction

Contents

4.1 The SPIS numerical code 66

4.1.1 Presentation of the software 66

4.1.2 SPIS basic principles 67

4.1.3 Utility of the SPIS code for simulations 79

4.2 Illustration of Solar wind impacts on spacecraft 80

4.2.1 Article 1: Solar wind plasma interaction with Solar Probe Plus spacecraft . 80

4.2.2 Article 2: Simulation study of spacecraft electrostatic sheath changes with the heliocentric distances from 0.044 to 1 AU 89

4.2.3 Possible effects on plasma measurements 100

The objective of this chapter is to present the main numerical tool used in this study. The *Spacecraft Plasma Interaction System* (SPIS) will thus be introduced in a first section, with a brief historical review and an overview of its main principles. In the next section the first applications of the SPIS software to this study will be detailed, through two papers published during those three years.

Several numerical codes are however also dedicated to *Particle-In-Cell* (PIC) simulations and are able to model the interaction of satellites with space environment while accounting for detailed payload and instrument geometry, and for a broad set of relevant physical processes. We briefly cite them hereafter:

- **EMSES**: an electromagnetic particle simulation code for studying spacecraft plasma interactions [Miyake and Usui (2009)]
- **iPic3D**: a *C++* code fully electromagnetic 3D PIC code for multi-scale plasma simulations, (a full review of iPic3D can be found in [Markidis et al. (2009)]
- **LASP**: an IDL based code, including a time-stationary solver using ballistic ions and fluid electrons [Ergun et al. (2010)]
- **PTetra**: a simulation code written in Fortran 90, described in detail in [Marchand (2012)]. PTetra treats all particle species fully kinetically using the PIC approach.

4.1 The SPIS numerical code

4.1.1 Presentation of the software

The *Spacecraft Plasma Interaction System* (SPIS) project aims at developing a software toolkit for spacecraft-plasma interactions and spacecraft charging modelling. It was started in December 2002, first released in March 2004, and has become today the European standard for modelling of spacecraft plasma interactions. Initiated by ESA including CNES support and following an open-source approach in the frame of the *Spacecraft Plasma Interactions Network in Europe* (SPINE) community (see Section 1.5.1), SPIS knows today a real and dynamic community life (SPINE counts more than 600 registered members and an active forum with more than 70 messages per month). It is developed in an Open Source approach and oriented towards a future community-based development

SPIS is a simulation software based on a numerical kernel, called SPIS-NUM, an electrostatic 3D unstructured Particle-In-Cell plasma model (PIC) consisting in a Java-based highly modular Object Oriented library. SPIS is designed to be used for a broad range of industrial and scientific applications. The simulation kernel is integrated into a complete modular pre-processing / computation / post-processing framework, called *SPIS User Interface* (SPIS-UI), allowing a high degree of integration of external tools, such as CAD modellers, meshers and 2D/3D visualization tools.

Originally designed to focus on scientific applications, the scope of SPIS is largely wider now and is regularly extended to new engineering applications or domains of physics. This includes, for instance, modelling of electrical propulsion systems, ESD prediction on solar arrays or link with radiation models through deep charging phenomena. Owing to its modularity and the implemented models representing the present state-of-the-art in plasma/satellite interactions, SPIS is currently probably the best basis to address these issues in a self-consistent manner. A specific version of SPIS, called SPIS-GEO/MEO, is dedicated in modelling Geosynchronous Earth Orbit (GEO) and Medium Earth Orbit (MEO) missions (simplifying its usage in an engineering context). SPIS-GEO/MEO has been developed in consortium by Artenum (SPIS-UI) and ONERA (SPIS-NUM) [Roussel et al. (2008-a)], evaluated and validated by OHB-Sweden and ASTRIUM-France with the support of the European Space Agency (ESA) in the frame of the contract Nr 4000101174 - Order Nr AO/1-6218/09/NL/AT). SPIS-UI is based on the general Integrated Modelling Environment (IME) Keridwen, developed by Artenum[1].

Recent enhancements have consisted in improving multi time scale and multi physics capabilities [Roussel et al. (2010)]. Before that SPIS has been successfully used for several scientific applications. One first paper on a real engineering application, SMART-1 [Hilgers et al. (2006)], studied the electrostatic potential variation of the probe and the first SPIS validations by comparison with theoretical models are presented in [Hilgers et al. (2008)]. The effect of in-orbit plasma on spacecraft has been modelled in a wide range of configurations: geosynchronous (GEO) spacecraft charging [Roussel et al. (2010)], electric propulsion [Roussel et al. (2008-b)], barrier of potential at millimetre scale [Roussel et al. (2008-a)] and electrostatic discharge onset on GEO solar panels [Sarrailh et al. (2010)]. The ONERA plasma chamber, named JONAS, was simulated and the results compared to experiments in [Matéo-Vélez et al. (2008)]. It has also been compared with other numerical models [Roussel et al. (2010), Matéo-Vélez et al. (2012)].

In addition, scientific tools were added by ONERA and ARTENUM to SPIS (The Computational tools for spacecraft electrostatic cleanliness and payload accommodation analysis:

[1] Artenum's Keridwen Web site, *http://www.artenum.com/EN/Products-Keridwen.html*

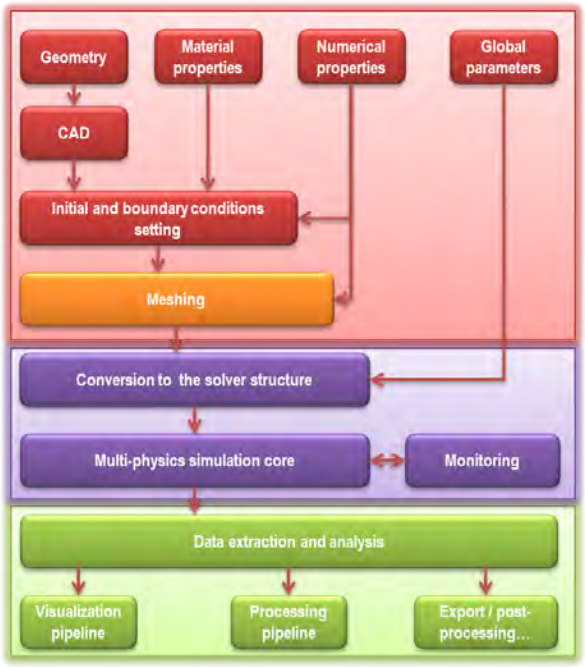

Figure 4.1: Schematic modelling chain of the SPIS software. The first red section indicates the phase of simulation configuration which is user defined and critical. Inside this section: the orange meshing step stands for the 3D unstructured mesh construction process, which is initially user configured but finally computer generated. The purple box contains all steps performed by the software itself, based on the user inputs. The green section gathers the output extraction and analysis. *Figure taken from the SPIS user manual.*

SPIS-SCIENCE or SPIS-SCI) in order to answer SPINE community needs in term of accuracy, performance and advanced scientific capabilities, evaluated and validated by IRAP-France and IRFU-SWEDEN, in the frame of the SPIS-SCI ESA contract Nr 4000102091/10/NL/AF - Order AO/1-6368/10/NL/AF). SPIS-GEO/MEO and SPIS-SCI activities were based on the version 5.0 of the main branch of SPIS, which is maintained in the frame of the SPINE open-source community.

4.1.2 SPIS basic principles

The goal of this chapter is to describe the basic principles of SPIS functioning: the main processes necessary to configure and launch a simulation, plus SPIS solver main methods. For conciseness, this section will not enter into the details of the SPIS numerical architecture, or all the possibilities. The SPIS simulation process requires the different steps illustrated on Figure 4.1. From the user point of view, the simulation configuration procedure is represented on the simple sketch (Figure 4.2), and each step will be presented in the following sections.

4.1.2.1 Project creation methodology

If one wishes to simulate a specific situation of spacecraft/plasma interactions, the first step consists in configuring a *quick simulation test*, avoiding an immediate heavy simulation (with

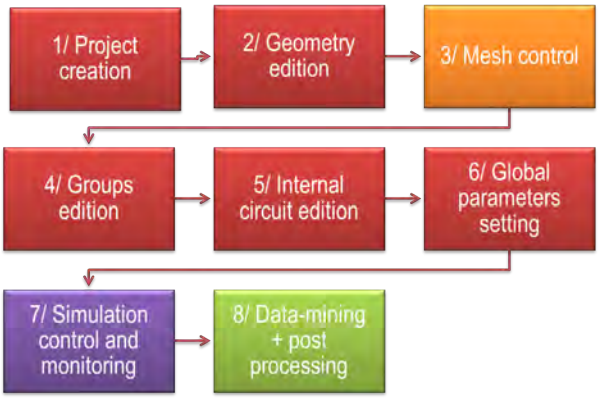

Figure 4.2: SPIS simulation configuration procedure from the user point of view. The colors used in Figure 4.1 corresponding to the different levels of user implication are also used here. The meshing phase cannot be totally user controlled. *Figure taken from the SPIS user manual.*

detailed geometry and refined mesh, small time steps, large number of particles, *etc*) costly in CPU time of computation and memory. The objective of this first simulation is to prepare the study by:

1. Identifying the geometrical elements of the satellite in need of a focused interest: small elements, angles and corners, thin elements, shadowed or wake exposed surfaces, and the verification of the simulation box dimension which has, if possible, to contain the entire sheath of the satellite, including an eventual ion wake;

2. Identifying the corresponding location of necessary mesh refinement and optimization: to adapt the grid size to small areas, ensure a progressive mesh enlargement, avoid degenerate tetrahedra, and provide a maximum mesh size element corresponding to half of the local Debye length, in case of full *Particle In Cell* (PIC) simulations;

3. Ensuring that the simulation duration is long enough to obtain a null total net current. The satellite ground and surface potentials have to be at equilibrium by the end of the simulation. The plasma has also to be stationary over the entire simulation box. The time steps inputs used for particle pushing and electrical circuit solving can also be optimized depending on the results;

It is greatly recommended to fill in and keep up-to-date a sort of simulation library containing for each simulation launched its main properties (inputs main parameters, real duration, observations) and archive the simulation folders containing both inputs and outputs. Although some projects can rapidly reach important sizes, experience shows that saving entirely SPIS projects is helpful for eventual further and future post-processing studies.

4.1.2.2 Geometry edition

This phase is performed through the GMSH software[2] (a 3D finite element grid generator with a build-in CAD engine and post-processor). Combining the interactive graphical user interface

[2]GMSH software web page: *http://geuz.org/gmsh/*

or ASCII text files using Gmsh's scripting language, the user generates *.geo* file(s) that will be used by SPIS for the simulation. The geometry should contain:

- The external boundary, corresponding to *a priori* the undisturbed plasma and made of one closed surface;
- The computational volume corresponding to the surrounding plasma;
- The inner boundary which stands for the spacecraft structure, defined by one or several closed surfaces.

The user has to define within the geometry what the *physical elements* are that SPIS will have to deal with, such as the external boundary, the computational volume, the different physical surfaces of the satellite and finally the instrument surfaces corresponding to the particle detector entrances.

4.1.2.3 Mesh control

Within the Gmsh phase of geometry construction, the user defines the meshing grid size on each point of the satellite structure. The mesh dimension also has to be defined on the external boundary. One particular specification of the meshing for SPIS is that the size of any surface cell or volume element must be inferior to half of the local plasma Debye length (meaning that near the satellite the eventual secondary and photoelectron populations should be taken into account for the Debye length estimations). Furthermore meshing on spacecraft or instrument surfaces should contain more than one cell per surface. This seems obvious but it is necessary to obtain a correct modelling of particle/surfaces interactions, with an acceptable local resolution of current balance. This might thus generate an impressive total number of cells when the geometry contains very small elements. Indeed some particle detector have aperture gaps no larger than few millimetres, forcing the local meshing to be smaller than 10^{-3} m, while on the external boundary of the simulation box it can reach several meters. This is clearly the "multi-scale" aspect of this PhD study.

Based on the various local grid size imposed on each geometry point by the user, Gmsh then generates the 3D unstructured mesh (exported in a *.msh* file). As explained in the above section the resulting mesh has to be inspected by the user to avoid eventual elongated cells or brutal variations in local cell dimension structuring. This might happen near the satellite elements corners or edges and it would result in a degradation of the particle statistics and a decrease in reliability of the results. In order to avoid this type of issue it is possible to define intermediate surfaces within the computational volume containing specific indications of meshing dimension values. It allows a better control of the cell size expansion within the volume. This intermediate boundary has no physical existence and remains transparent to the plasma. Another option is to use thin elements rather than 3D objects. Indeed SPIS handles specific spacecraft components defined as thin elements: thin wires to model antennas or thin panels to represent solar arrays. For those singular geometries the radius or edges cannot be meshed without generating degenerated elements. These modelling possibilities enhance the mesh quality in the vicinity of complex elements, avoiding issues such as degenerate tetrahedra near corners and edges of the usual 3D elements (a thin wire is a 1D object and thin panels are 2D elements). Note that it is also possible to act directly on mesh elements through the Gmsh interface, by picking and splitting manually the distorted cells and tetrahedra. However this method can be tedious and complex in case when large number of optimisations is needed.

Group type		Property type	Description
Spacecraft surface group	*Mandatory Properties*	*S/C Plasma population BC*	Define all characteristics related to the plasma model on the boundary defined by the S/C surface.
		Electrical node model	Select the electrical node for the present group. Please notice, that this property care shared with other groups.
		S/C conductivity model	Define all characteristics related to the conductivity model.
		S/C electric field	Define all characteristics related to the electric field model on the present S/C surface boundary.
		S/C macroscopic characteristics	Define all macroscopic characteristics, including thickness and temperature .
		S/C thin elements	Set if the present group corresponds to a thin element or not. See the corresponding section.
		S/C sources and interactors	Defined all characteristic related to the interactions models and sources.
		S/C material	Select the material for the present group.
		S/C mesh properties	Define all characteristics of the mesh model for the inner boundary defined by the S/C surface.
	Optional Properties	*S/C instrument support*	Set if the present group correspond to an instrument on the S/C surface or not. This option is not supported on all SPIS versions.
External boundary group	*Mandatory Properties*	*Ext. Bound. Plasma Population BC*	Define all characteristics of the plasma model on the external boundary defined by far plasma.
		Ext. Bound. Electric field BC	Define all characteristics of the electric field model on the external boundary defined by far plasma.
		Ext. Bound. mesh properties	Define all characteristics related to the mesh model the external boundary defined by far plasma.
	Optional Properties	*N/A*	N/A
Computational volume group	*Mandatory Properties*	*Volume plasma model*	Define all characteristics related to the plasma model on the external boundary defined by far plasma.
		Volume mesh properties	Define all characteristics related to the mesh model the external boundary defined by far plasma.
	Optional Properties	*N/A*	N/A

Figure 4.3: SPIS groups and properties types. SC = spacecraft, BC = Boundary Conditions. *Figure taken from the SPIS user manual.*

Finally the meshing phase demands a user controlled mesh initialization and, once the mesh is generated, a detailed check of the mesh quality with eventually localized grid refinements for meshing optimization.

4.1.2.4 Groups edition

Once the mesh is entered in the SPIS project, the next step consists in identifying the different physical groups of the mesh (lines, surfaces and volumes) with the specific associated properties. These correspond to the local parameters used to define the model. This includes material, physical and numerical properties. The aim of this pre-processing part is to attribute these properties to each specific part of the spacecraft or to the computational domain, and convert them into fields (*i.e.* DataFields) mapped on the mesh that the numerical model can use as input. The different types of physical groups and the associated properties are presented in Figure 4.3.

Materials can be attributed to spacecraft surface groups. In the SPIS context materials gather numerical attribution flags and physical characteristics. Catalogues of material are automatically pre-loaded with a large set of predefined materials (including NASCAP-2K based materials) but each characteristic can be edited (secondary emission yield, thickness, resistivity,

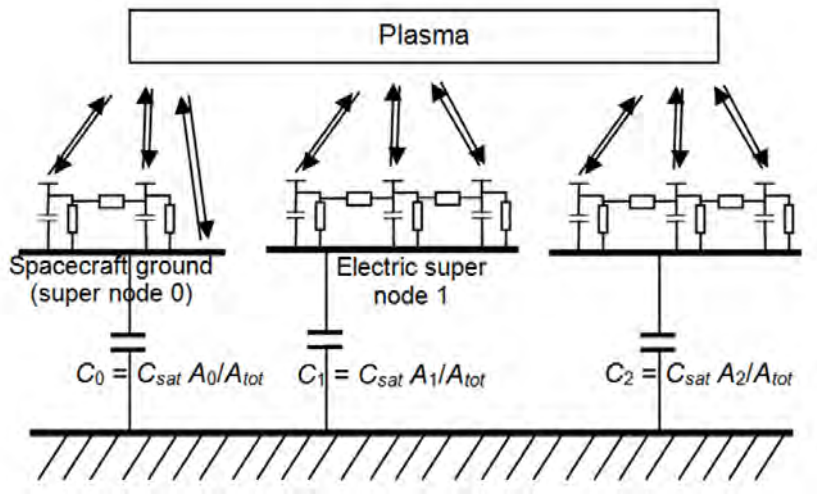

Figure 4.4: Spacecraft potential calculation modelling. In the present example, all separate *Electrical Super Nodes* (ESN) are floating with each other. They are linked to the undisturbed plasma potential through the local absolute capacitance (ratio of ESN surface area with respect to total spacecraft area). *Figure taken from the SPIS user manual.*

etc). New materials have recently been added.

More specifically concerning resistivity, dielectrics are modelled as a capacitor in parallel with a resistor between the dielectric top surface facing the plasma and the back conducting surface, in order to model bulk conductivity. Surface resistivity is modelled by a resistor between adjacent dielectric top surfaces. Plasma spacecraft current exchanges (collection/emission) are achieved on all spacecraft surface groups, so-called *Electrical Super Nodes* (ESN), which can be conductors or dielectrics (in this last case the ESN should be understood as the underlying ground common to all dielectrics facets). Absolute potential is calculated using the absolute spacecraft capacitance C_{sat} with respect to undisturbed plasma. Differential charging is calculated using the dielectric capacitance and resistivity.

The collection of the properties information will lead to the construction of DataFields deployed on the mesh with the corresponding values.

4.1.2.5 Internal circuit edition

SPIS supports the description of the spacecraft structure with several macro electrical nodes, in order to model differential charging and real time dynamics transient evolution. By default, macro electrical nodes are floating with respect to undisturbed plasma with no connection between each other (Figure 4.4). The use of an internal circuit allows a better control of internally connected elements, such as in Figure 4.5. Electrical Super Nodes can be connected through resistors (R), capacitances (C) or voltage generators (V). The internal RCV circuit can be simply edited with any text editor (or the one provided within the SPIS-UI) and the corresponding data are saved in a simple ASCII "circuit.txt" file in the project repository.

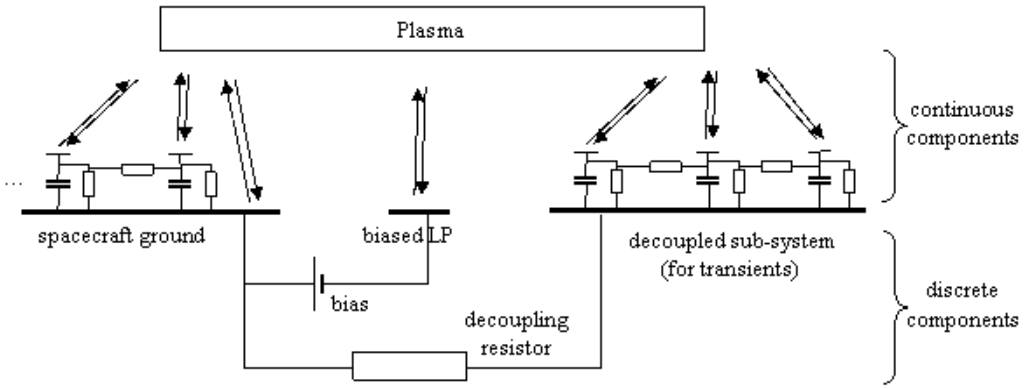

Figure 4.5: Example of internal circuit connections. Here, the ESN are not floating with respect to the plasma. A potential bias is imposed between spacecraft ground and the *biased LP* (LP = Langmuir Probe). A resistor is imposed between the ground and the group on the right. The absolute capacitance is applied to the full spacecraft (not separated between ESNs). *Figure taken from the SPIS user manual.*

4.1.2.6 Global parameters setting

These parameters correspond to the global physical values of the space environment (such as the plasma populations temperatures, densities, *etc*) or numerical values (simulation duration, time steps) that are general to the simulation and don't have to be deployed locally on the mesh. Global parameters are subdivided into many categories and are available through several indices and tables.

The global parameters setting phase is critical to obtain a consistent simulation with reliable results. In addition to a correct configuration of the plasma parameters, corresponding to the environment to be simulated, an adequate time steps used by the SPIS numerical core to solve densities in volume and currents on satellite surfaces are essential, and have to be configured at this level. This can be done automatically (letting SPIS decide what durations should be taken for the different loops of simulation, see Figure 4.6) or manually (requiring a user pre-evaluation of the different time steps, depending on the plasma properties and the characteristic response times of the simulated materials to the charging currents).

Time steps

The simulation cycles (also called loops) are presented in Figure 4.6. It shows that SPIS simulations can be divided in three levels of control:

- At simulation level: interaction between the satellite and the plasma (calculation of spacecraft potentials as a function of collected and emitted currents on spacecraft)
- At plasma level: resolution of the particle transport coupled with Poisson equation
- At particle populations level: particle trajectories in the electric and magnetic fields, weighting algorithm to calculate densities in volume and currents on surfaces.

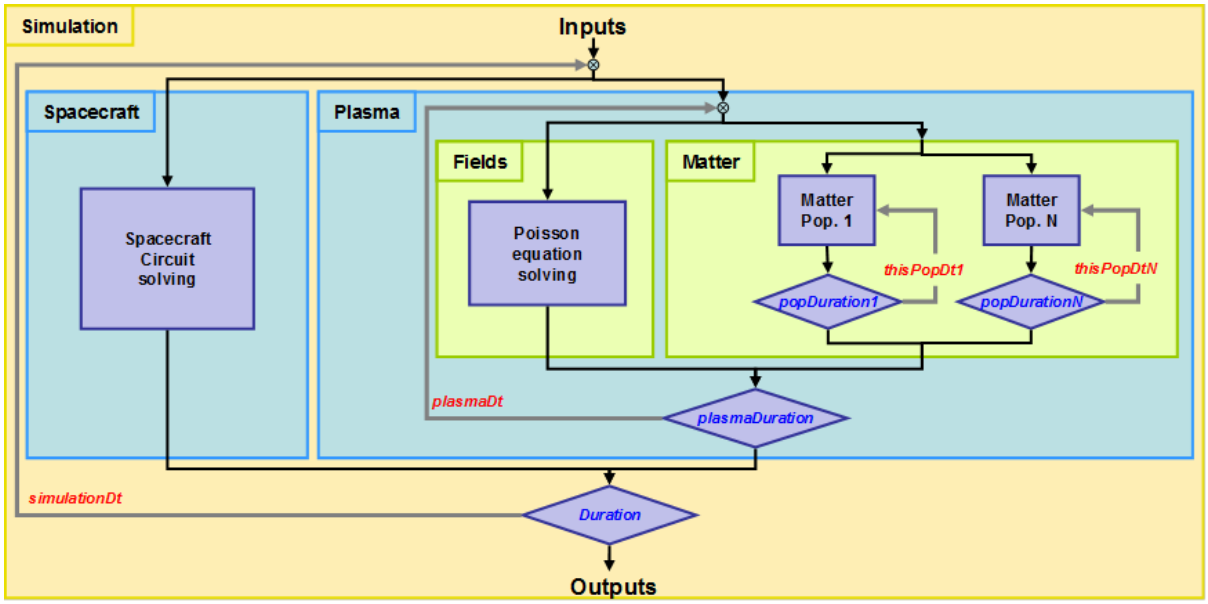

Figure 4.6: Hierarchical structure of a SPIS simulation. The nested boxes reflect the object structure of the code (what may the basic user not care about) while the arrows represent the time evolution of a simulation (what does he need to be aware of). *Figure taken from the SPIS user manual.*

For each level of control, a duration of integration (xxxDuration) and a time step (xxxDt) can be defined to control the integration process during the simulation. The ratio of the duration over the time step is the number of sub-cycling at this level (xxxLoopNb). The three nested levels can be controlled: Simulation, Plasma and Matter.

In the most general case, all the components of the simulation are resolved in real time, the duration of integration of one level is equal to the time step of the upper level (for example $popDuration\# = plasmaDt$, where # is the index of the population) and *plasmaDt* is a fraction of the plasma period. Nevertheless, in certain cases, the characteristic time of two processes can be very different. In such a case, the simulation may be sped up by considering that the fast process dynamics is quasi-static as compared to the slow one. Thus the stationary state of the fast process can be attained without integrating over the complete duration of the upper level time step. Consequently, it could be useful to define an integration duration different from the upper level time step (for example $popDuration\# < plasmaDt$). Two examples taken from the SPIS user manual can be cited:

1. This Example 1 considers the time evolution of the plasma compared to the spacecraft differential charging. In certain cases, the satellite potential evolution can be very slow (in the order of seconds) compared to the plasma dynamic (in the order of micro-seconds to nanoseconds). Plasma can thus be considered as stationary at the large time scale of surface potential dynamics (to be checked by the user in each case). In such a case, it is not useful to integrate the plasma evolution over the complete duration of the simulation time step. The *plasmaDuration* may be set by the user to a value several orders of magnitude lower compared to the *simulationDt* (the choice of this value is the responsibility of the users as a function of possible physical assumptions in each case). An illustrative

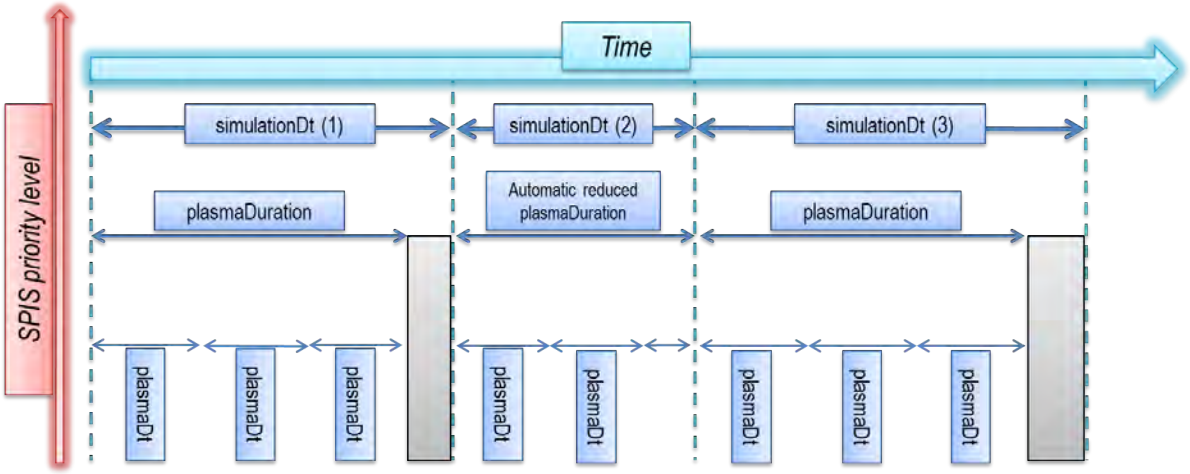

Figure 4.7: Time step series illustrating the Example 1 of a simulation with numerically accelerated plasma integration with respect to simulation loop.

diagram of time steps and integration duration for this first example is given on Figure 4.7. The simulation time step is automatically adapted by the numerical kernel during the simulation, in order to prevent large potential variations between two time steps. The plasma duration is kept constant, but still lower than the current simulation time step. The same paradigm prevails for the plasma/particle loop.

2. In an Example 2: two populations can have very different velocities. It is actually quasi-systematically the case between ions and electrons in plasma due to the mass ratio, but it can also be the case between two populations which have very different energies. In such a case, the efficiency in term of calculation velocity can be substantially increased by selecting appropriate integration duration for both populations. For the slow population, the integration duration should be *popDuration1* = *plasmaDt* (*i.e.* real time calculation) and for the fast population *popDuration2* $\ll$ *plasmaDt* (i.e. quasi-stationary state) taking into account the velocity ratio. A second illustrative diagram is given in Figure 4.8 for Example 2. The electron population does not need to be computed in the same footing as ions since electrons can reach local steady-state much faster.

In the frame of this project, I came to propose basic recommendations to initiate a simulation through the time global parameters. The different durations and time steps are enumerated hereafter in the following order:

1. Plasma - spacecraft loop

   - **duration** = the estimated time to reach stable steady-state equilibrium. There are two characteristic times: the absolute charging duration and the differential charging duration (usually the longest one), with two different capacities (*resp.* C_{sat} and C_{diel}). The duration can be estimated by:

$$\text{duration} = \frac{C_{\text{diel}}\Delta\Phi}{I_{\text{initial}}} \tag{4.1}$$

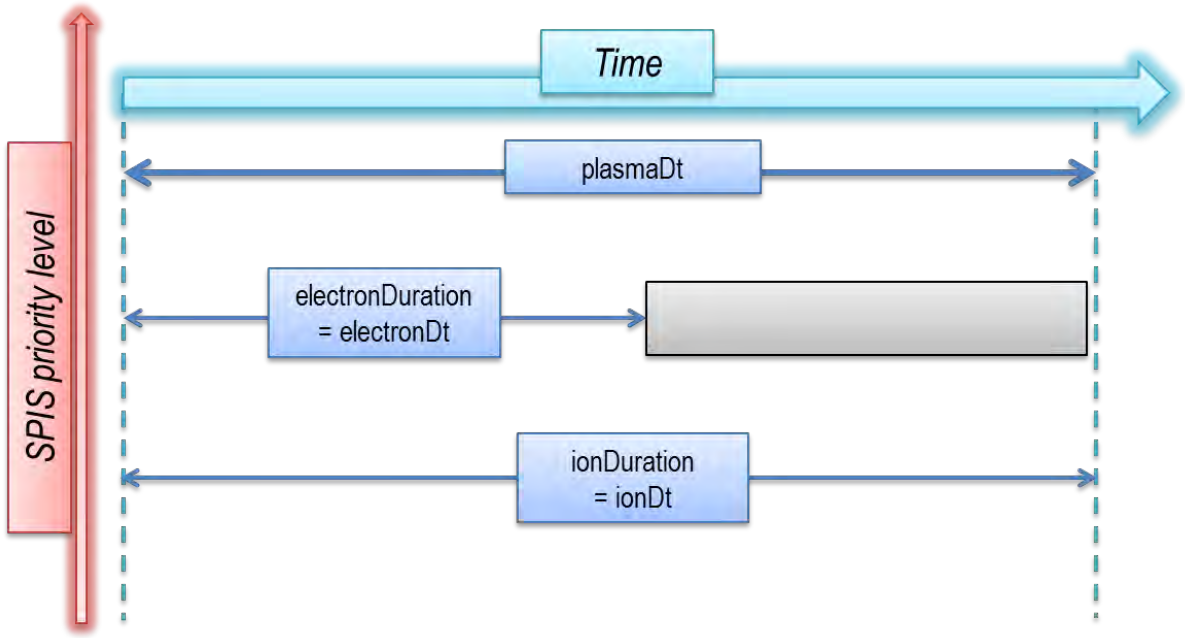

Figure 4.8: Time step series illustrating the Example 2 of a simulation with numerically accelerated electron population integration with respect to plasma loop.

I_{initial} is the estimated initial current of thermal electrons to the spacecraft, *i.e.* $J_{0,e}A$, A being the spacecraft area exposed to the plasma and $J_{0,e}$ the initial flux of thermal electrons (see equation 3.10). Within the scope of this PhD the different voltage variations encountered $\Delta\Phi$ in the various simulations are globally between +20 V and -kT_e/e V.

- **simulationDt** is the simulation time step. It is recommended to have at least simulationDt $\leq$ duration/100
- **simulationDtInit** stands for the initial simulation time step, set as $\leq$ duration/1000. It will progressively increase until a maximum value of *simulationDt* is reached.

2. Population loop

   - **popDt** = **popDuration** = time for each plasma population *pop* to cross the entire simulation box. It thus has to be set as the size of the box over the mean *pop* velocity.

3. Plasma loop

   - **plasmaDt** represents the time step for global plasma dynamics. We recommend to set it as a fraction of the plasma period for the PIC plasma modelling stability: *plasmaDt* $\leq 0.2 \times 2\pi/\omega$ (see equation 2.17).
   - **plasmaDuration** is the integration duration of the plasma dynamics. It has to last at least for two *plasmaDt* times steps and contain all the *popDurations*. Technically it can be translated as: *plasmaDuration* $\geq \max(2 \times \text{plasmaDt}; \max(\text{popDuration}))$ which can provide large plasma duration in case of slow population (often ions), leading to strong increase in CPU time. It is recommended to use *plasmaDuration*

> $2\times$ *plasmaDt* and verify that the slow population steady state is achieved at the end of the simulation. If one can neglect the impact of this population during the transient phase (which is often the case when considering ions, in the present work), even the transient phase may be quite realistic.

Each time step will obviously depend on the plasma population characteristic time scales, which depend on the configured environment.

Environment

Concerning the environment: SPIS now provides users with means to define their own distribution functions for ambient and secondary particles, extending the legacy Maxwellian distributions. An unlimited number of distributions can be defined through the global parameter list and using tabulated ASCII files. However the usual distributions are still predefined: several possibilities exist but the main environments are cited hereafter.

- *GlobalMaxwellBoltzmannVolDistrib*: describes analytically a particle population as a global thermal equilibrium distribution (Maxwell-Boltzmann) and is usually valid when no attractive potential or potential barrier exists (density increase is limited to a linear variation for positive potential).

- *UnlimitedGlobalMaxwellBoltzmannVolDistrib*: similar Maxwell-Boltzmann distribution but density increase is not limited for positive potential (remains exponential).

- *PICVolDistrib*: simulates this population dynamics (*Particle In Cell* or *PIC* modelling) which is much more costly in computation time and memory.

- *BackTrackingVolDistrib*: computes currents onto spacecraft surface through backtracking (but does not compute densities) and follows the Liouville's theorem described in section 3.4 to calculate the particles weight.

- *BacktrackingBoltzmannCompositeVolDistrib*: computes currents onto spacecraft surface through backtracking and densities through Boltzmann distribution.

- *BacktrackingPICCompositeVolDistrib*: computes currents onto spacecraft surface through backtracking and densities through PIC modelling of populations dynamics.

Concerning the *Backtracking* process, cited in the three last modelling methods, it rises from the practical review of the PIC modelling which presents a lack of statistics on the small satellite elements. Two possibilities are offered to overcome those issues. The first is to increase the number of particles within the computational volume, which might become extremely costly. The second is to follow the numerical particles "backward in time": 1/ particles are emitted randomly from the satellite; 2/ the software follows their trajectories backward until the external boundary; 3/ if the distribution function of the population on the boundary is known, Liouville's theorem can be used to assign a weight and thus a contribution to the current of this particle. This sequence is repeated N times. The limitation of this simple backtracking process is that this is possible for the currents on surfaces but not the density in volume. Otherwise the last *BacktrackingPICCompositeVolDistrib* combines backtracking and PIC to solve *resp.* the currents onto spacecraft surfaces and the volume densities.

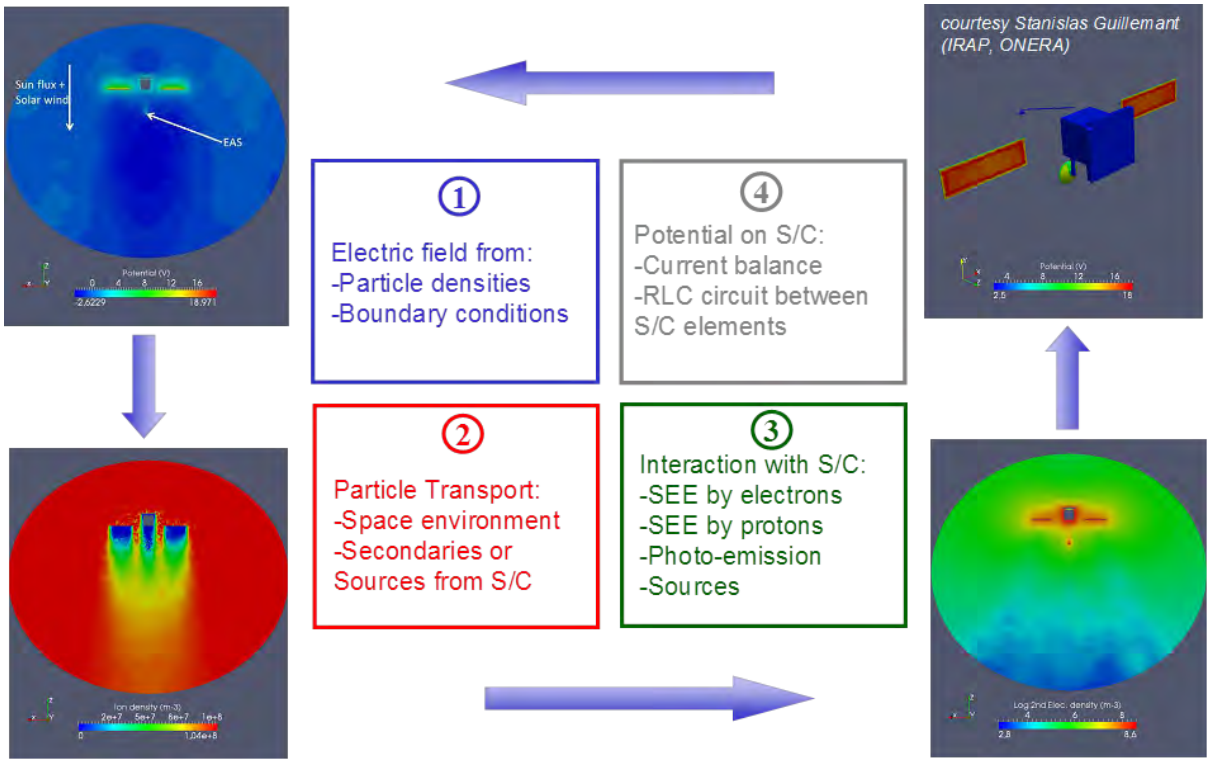

Figure 4.9: The SPIS numerical simulation principle. *Figure taken from the SPIS user manual.*

For each plasma population the user configures the desired distribution and the appropriate parameters (density and temperature, plus a possible average drift velocity). Other main parameters are the magnetic field (constant and uniform during the simulation), Solar flux (intensity and orientation), (de)activation of secondary and photoemission, *etc.* Depending on the plasma parameters, the time steps will be adapted to respect the plasma period ($2\pi/\omega_p$, see equation 2.17) or the gyrofrequency if a magnetic field is considered (see equation 2.23).

4.1.2.7 Simulation control and monitoring

The SPIS numerical simulation principle is presented in Figure 4.9. It can be divided into 4 domains:

1. Fields: electric and magnetic field
2. Matter: electrons, ions, artificial sources, *etc*
3. Spacecraft surface interactions: photoemission, secondary emission, erosion
4. Spacecraft surface potential: conductivities, bias potentials, *etc*

Concerning fields, the Poisson equation finite element solver follows a preconditioned conjugate gradient method. The boundary conditions can either be Dirichlet, Neumann or a mix of them (known as Robin or Fourier), which allows a better modelling of pre-sheath conditions. Non linear Poisson equation (*i.e.* Poisson including a Boltzmann distribution for electrons) can also be solved with an implicit method. The singular geometries (thin wires or plates) are

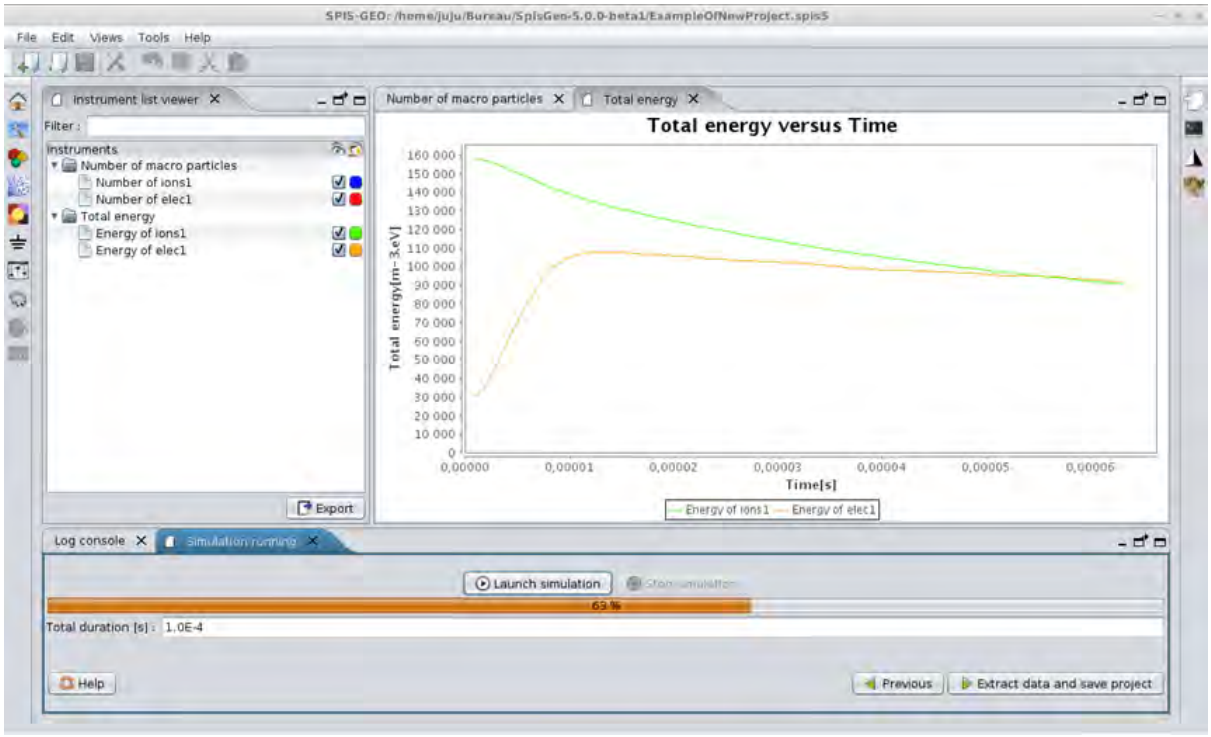

Figure 4.10: The SPIS simulation control panel.

handled through the analytical subtraction of the singular part of the potential field resulting from the geometrical singularity (as $\phi_{\text{sing}}(x) = \ln(x)$), and then by solving the regular part (this splitting is transparent for the user).

For the matter domain, the main models are: a Particle-In-Cell (PIC) solver of Vlasov equation, and a Boltzmann distribution to describe the thermal equilibrium distribution of electrons. The surface interaction models cover the following phenomena: secondary electron emissions under electron impact (accordingly to equation 3.60, proton impact (same method) and the backscattered electrons (released with 2/3 of the primary electron energy in a reversed direction), photoemission (see equation 3.66), radiation induced conductivity and erosion.

The spacecraft surface interactions considered are secondary electron emission under electron, proton and photon impact. Yields are calculated automatically within SPIS depending on macroscopic material properties defined by the user. For instance the yield of true electron emission under electron impact is computed using the maximal yield and the energy of the maximum (see section 3.5.2). Distribution functions are Maxwellian in volume.

Finally, the spacecraft surface potential evolution involves the equivalent satellite circuit, taking into account coating capacitances and conductances (surface and volume conductivities), plus the eventual user-defined "discrete" components (extra resistors, biases or capacitors added between subsystems). The spacecraft circuit implicit solver handles issues with very different time scales through physics predictors of the plasma current variations in reaction to potential changes.

The Simulation Running and Control panel (illustrated in Figure 4.10) allows to follow and check the evolution of the simulation in real time. Monitors are automatically updated during the simulation evolution.

4.1.2.8 Data mining and post-processing

The SPIS Data Miner allows to visualize within SPIS and extract the simulation results, for further data analysis and post-processing. This is done through the Post-processing panel. It is possible to visualize within the SPIS software both 2D and 3D data with the embedded *Cassandra* software[3]. This generic 3D scientific data viewer based on the *Visualization Toolkit* (VTK)[4], renders 2D and 3D fields of data (DataFields) deployed on the mesh.

Depending on the data type, several renderings are possible and/or are pre-selected as follows:

- Time series and $y = f(x)$ type data: 2D plots (histograms, *etc*)
- Surface data: 3D surface view, with various rules regarding the cell trans-typing (*i.e.* conversion of the localization on cells): computed on nodes, faces or edges.
- Volume data: 3D volume view, with the different rules for the cell trans-typing (computed on nodes, faces, cells or edges).

Note that the simulation output analysis is essential not only to assess the final values of potentials, currents or instrument measurements, but to verify the adequate configuration of the simulation itself. Sometimes, in-depth studying of data can reveal several issues, such as for instance a lack of resolution on certain spacecraft surfaces with secondary electron emission, too coarse a spatial resolution above some satellite elements, strong fluctuations in current collection which might reveal erroneous time steps, *etc*. This usually involves a new simulation with corrected and optimized parameters, followed by a verification that new results are qualitatively and quantitatively improved compared to the old ones. For simulations with long durations it might take several iterations to obtain the optimized final simulation results, especially in case of a parametric study aiming at determining the optimal parameters (time steps, conductivity, instrument output frequency, *etc*).

4.1.3 Utility of the SPIS code for simulations

Issues related to the spacecraft/plasma interactions cannot be completely avoided but through numerical simulations of spacecraft/plasma interactions they can be anticipated and reduced for an optimized scientific satellite system. On the long term plasma instrument design can also be enhanced, which will lead to a better understanding of the true ambient space environment. The simulations have to be as complete as possible and take into account the most important phenomena involved in the near satellite environment generation. This implies complex multi-scale numerical simulations which require:

- in-depth analysis of the system that has to be simulated (spacecraft geometry, electrical circuit and surface materials; plasma instruments geometry, detector materials and technical properties; expected ambient environment characteristics and main interactions to be considered). This requires extensive studies, sometimes for a few additional assumptions, and the corresponding adequate configuration of the numerical simulation,
- in-depth study of the simulation results, with possible output post-processing. Some unexpected phenomena might be discovered at the very end of the results analyses and imply further specific and adapted simulations.

[3]Cassandra Web site, *http://dev.artenum.com/projects/cassandra*
[4]VTK web page: *http://vtk.org/*

After this description of the SPIS code capabilities, in terms of physical and numerical properties, the following section 4.2 will present the first applications performed with this software during this PhD, following this simulation methodology. They illustrate slow Solar wind impacts on spacecraft and an approach on secondary and photoemission, potential barriers and wake effects on charging in various environments.

4.2 Illustration of Solar wind impacts on spacecraft

Issues related to spacecraft charging in the Solar Wind and the apparition of electrostatic potential barriers around a satellite have been introduced in section 3. The two following sections refer to two articles published during this study, presenting SPIS simulations of satellite charging in the Solar wind at different heliocentric distances. The software version used for the performed simulations at that time was SPIS-v4.3.

4.2.1 Article 1: Solar wind plasma interaction with Solar Probe Plus spacecraft

During the early beginning of this project and the training period on the SPIS software, a scientific space mission appeared of interest for studying certain aspects of spacecraft/plasma interactions: the Solar Probe Plus spacecraft, a NASA probe approaching the Sun at less than 9.5 Solar radii (R_S) (as close as 0.044 AU), in an extremely hot and dense environment. A previous paper [Ergun et al. (2010)] based on a simplified Solar Probe Plus spacecraft geometry (a perfectly conducting cylinder), predicted a negative floating potential for the spacecraft at perihelion. At first sight this result might seem contradictory when considering the high photoemission rate occurring so close to the Sun, and the associated local hot and dense environment leading to high secondary emission rates from surfaces exposed to the plasma. Those electron emissions should a priori push the probe potential to positive values.

This configuration was reproduced through the SPIS software and a parametric study had thus been initiated ([Guillemant et al. (2012)], see Appendix A.4). Several cases were generated with SPIS, using all available numerical capabilities of the software, each simulation testing the influence of varying parameters, one at a time, on the final results. It let to a better understanding of spacecraft/near-Sun environment interactions to an enhanced mastery of the software.

The article is attached in Appendix A.4. The main results are presented hereafter.

4.2.1.1 Nominal Simulation $S1$

The spacecraft is simulated as a fully conducting cylinder of 1 m in radius and 2 m in length, at the center of a simulation box, which itself, is a: a cylindrical domain of dimension 6 m in radius (R) and 12 m in length (X), with a progressive coarsening of the mesh refinement (from 5 cm on the sunlit face of the cylinder until 2 m all over the domain limits). The characteristic cell size on the boundary is in this case larger than the Debye length for thermal electrons but a further simulation (presented in Section 4.2.2.1) with a meshing more adapted to the physical constraints will however validate the results obtained in this present case. The whole meshed volume contains $\sim$158 000 tetrahedra. Figure 4.11 shows the Gmsh model for the satellite. The environment corresponding to this heliocentric distance is described in Table 4.1. Those parameters are used for the initial nominal simulation $S1$.

Parameter	Value
Thermal electron density n_e	$7 \times 10^9\,\mathrm{m}^{-3}$
Thermal electron temperature T_e	85 eV
Ion type	H^+
Ion density n_i	$7 \times 10^9\,\mathrm{m}^{-3}$
Ion temperature T_i	82 eV
Ion velocity	$V_Z = -300\,\mathrm{km\,s}^{-1}$
Ion and electron modelling	PIC
Backscattered electron	Active
Photoelectron temperature T_{ph}	3 eV
Photoelectron current density J_{ph}	29 $\mathrm{mA/m}^2$
SEEE temperature T_{se}	2 eV
SEEE distribution	Maxwellian
Debye length for thermal electrons λ_{the}	0.8 m
Material	ITO, conductive
Meshing	from 5 cm to 2 m
Number of tetrahedrons	$\sim 158\,000$
External boundary conditions	Fourier: $1/r^2$ decrease of potential
Magnetic field	Not considered

Table 4.1: Parameters used for the nominal simulation S1.

The electron numerical modelling is performed through a full PIC method. It must be noticed that the Maxwell-Boltzmann distribution also available is exact when the satellite potential is negative and if no potential barrier exists. The Boltzmann model (see equation 2.9 in section 2.1.1) is only approximate if a potential barrier exists and is more negative: the less energetic electrons should not be able to cross this barrier, so the Boltzmann model is overestimating the particles arriving at the satellite. It becomes completely wrong if potential barriers are large or if the spacecraft is significantly positive. For the ions, the PIC model is used to inject particles at the domain boundary following a Maxwellian distribution with an energy of $T_i = 82\,\mathrm{eV}$ and a drift velocity of $-300\,\mathrm{km\,s}^{-1}$ in the Z direction. The magnetic field is not considered: the thermal electron gyroradius is of 15 m (and for ions 640 m), greater than the simulation box dimension. For secondary electrons, the gyroradius is of about 3 m. To simplify the problem the magnetic field is neglected. Indeed the expected equilibrium potential is about -10 to -20 V, leading to electrostatic forces much greater than magnetic ones. Furthermore the strong expected potential barriers should repel most of the secondaries back to the probe before the particles drift velocity becomes visible.

The surface material assumed for Solar Probe Plus model is a conductive layer with properties similar to *Indium Tin Oxide* (ITO). Its yields of secondary emission are presented in Figure 4.12. In particular for thermal electrons at 85 eV, the backscattering yield of ITO for an isotropic incident flux is 0.18 and the δ_e yield (or SEEY) for an isotropic incident flux equals 1.63. No secondary electron emission under ion impact was modelled. For photoelectrons and secondary electrons, Debye lengths are expected to be smaller than 5 cm. These conditions dictate the choice for the mesh parameters: (1) the smallest grid spacing possible on the sunlit side of the cylinder to compute properly these populations with a PIC model and (2) the

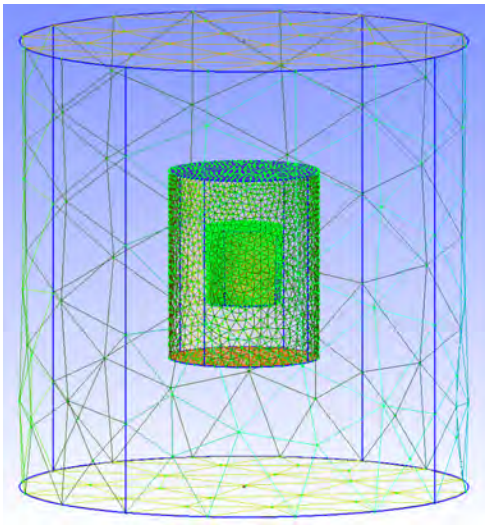

Figure 4.11: The GMSH model of the simplified Solar Probe Plus spacecraft used in SPIS simulations with the associated surface grid. The Z axis described in the text is the vertical axis in this figure. The intermediate meshing cylinder, used to control the progression of the mesh resolution, is located between the spacecraft (inner cylinder) and the outer boundary.

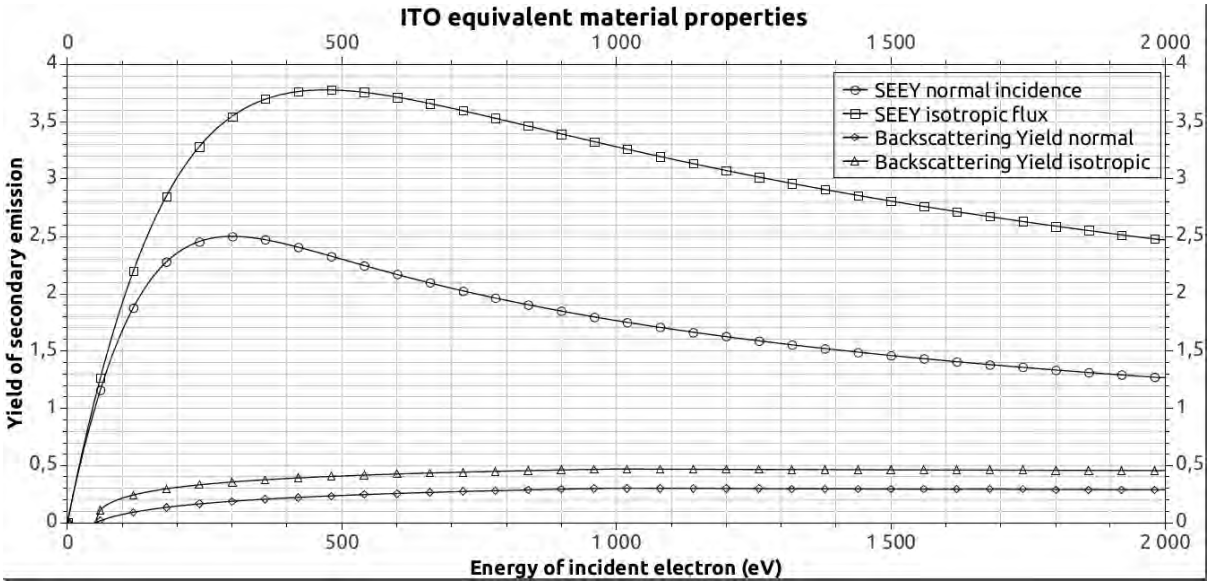

Figure 4.12: Secondary electron emission yield (SEEY) and the backscattering yield of ITO material (used in parametric study) vs. incident electron energy (with a normal or isotropic incident flux).

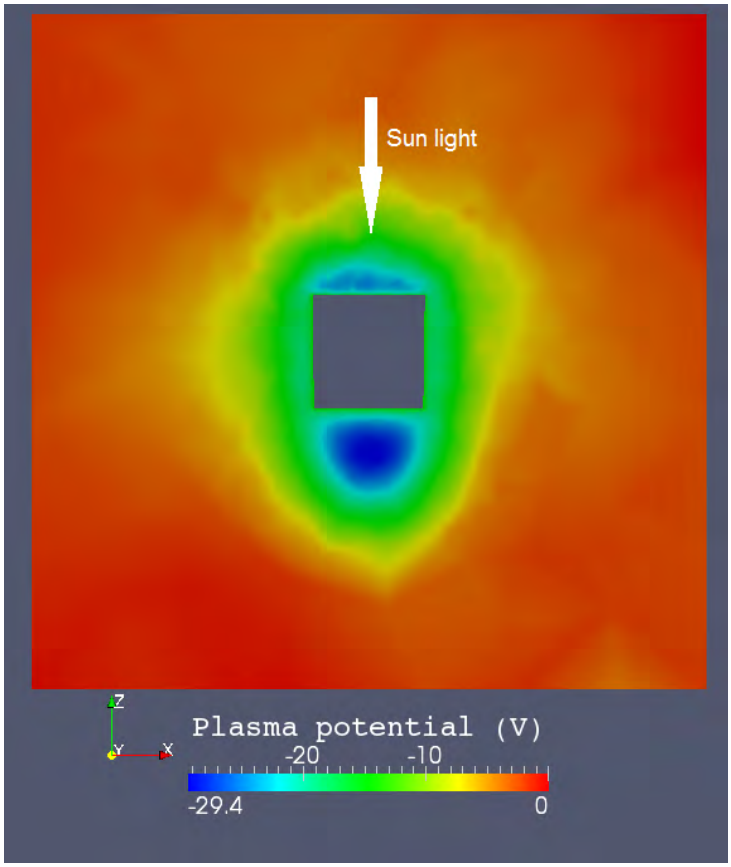

Figure 4.13: Simulation S1: map of the plasma potential in a $X - Z$ plane.

intermediate meshing cylinder at 1 m around the satellite (larger than λ_{the}).

The floating spacecraft potential at steady state in this S1 case sets around -14.5 V (the plasma potential map is represented in Figure 4.13). Once the potential is in steady state 76 % of emitted secondary electrons are recollected and this ratio goes up to 92 % for photoelectrons (see Table 4.3). The surrounding sheath with local potential values between -25 V (in the ram) and -30 V (in the wake), represents thus a potential barrier of -10 to -15 V for secondary and photoelectrons (with their 2-3 eV of mean kinetic energy). Most of the thermal electrons ($kT_e \sim$ 80 eV), however, can cross the sheath, impact the surfaces and generate other trapped SEEE. The sheath therefore forms a small electrostatic barrier from the ambient electron point of view.

The maps in a $X - Z$ plane of the particle densities obtained through the S1 simulation are displayed on Figure 4.14. The thermal electron density is almost constant over the simulation box except near the satellite where it reaches $3.16 \times 10^9\,\text{m}^{-3}$. The rear wake dimension is relatively short, despite the strong ion bulk velocity, due to the thermal velocity of these particles and also to ion focusing by the negative probe potential. Local striations of the ion density plot at the front are due to statistical noise in the ion PIC approach caused by a reduced number of superparticles per cell in this region (this quantity decreases below 5 per cell because super particles cross region of increasing number of cells). However, that does not impact the results since the space charge is ruled by photoelectron density in the sheath. In addition, the space charge used in the Poisson solver is computed using charge deposit of ions along their trajectory and not at the end of each time step, which reduces the statistical noise. Photoelectrons are

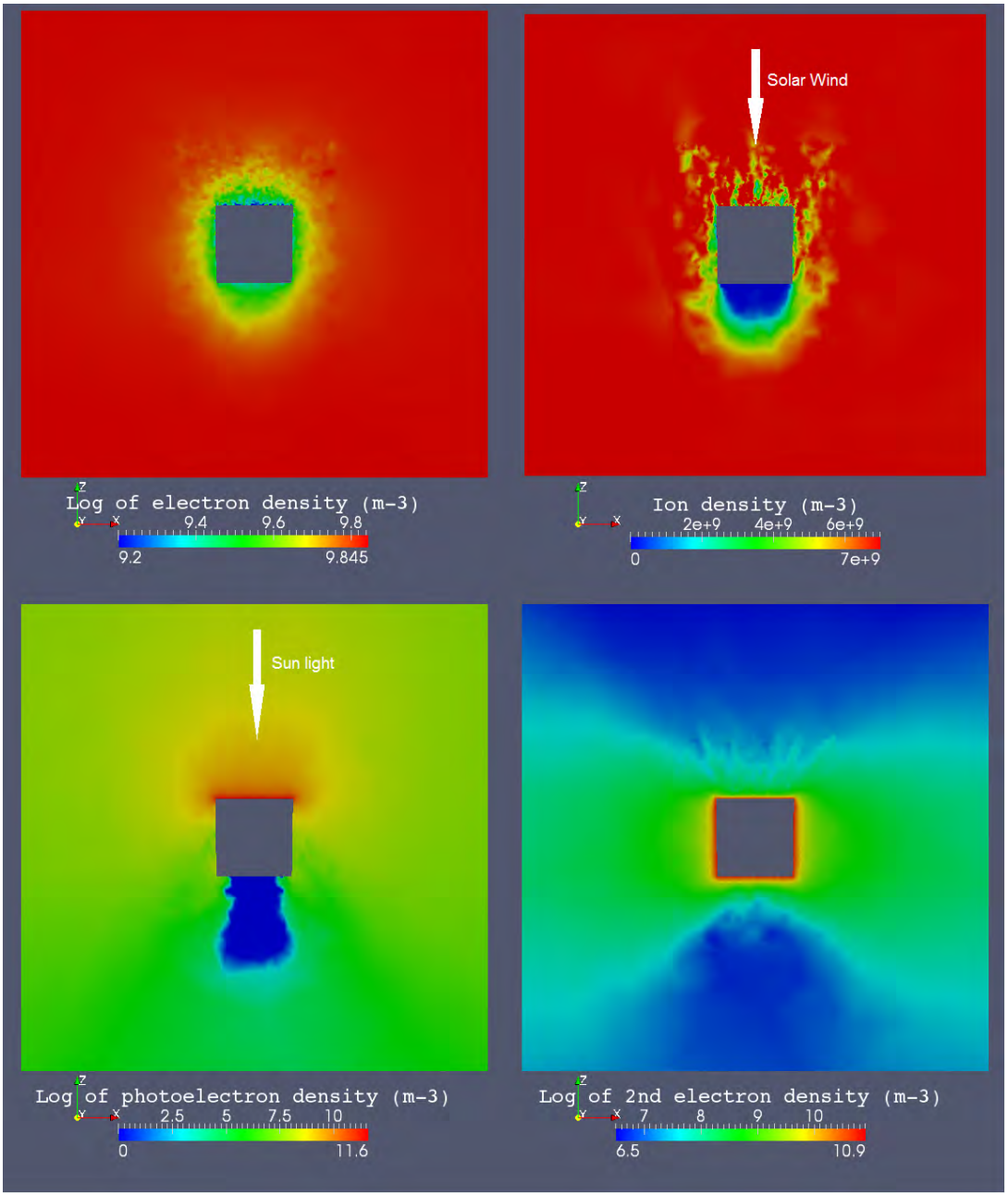

Figure 4.14: Simulation S1 population density maps in the $X - Z$ plane: **(a–d)** from the upper left figure to the lower right figure. **(a)** Thermal electrons, **(b)** Ions, **(c)** Photoelectrons, **(d)** Secondary electrons.

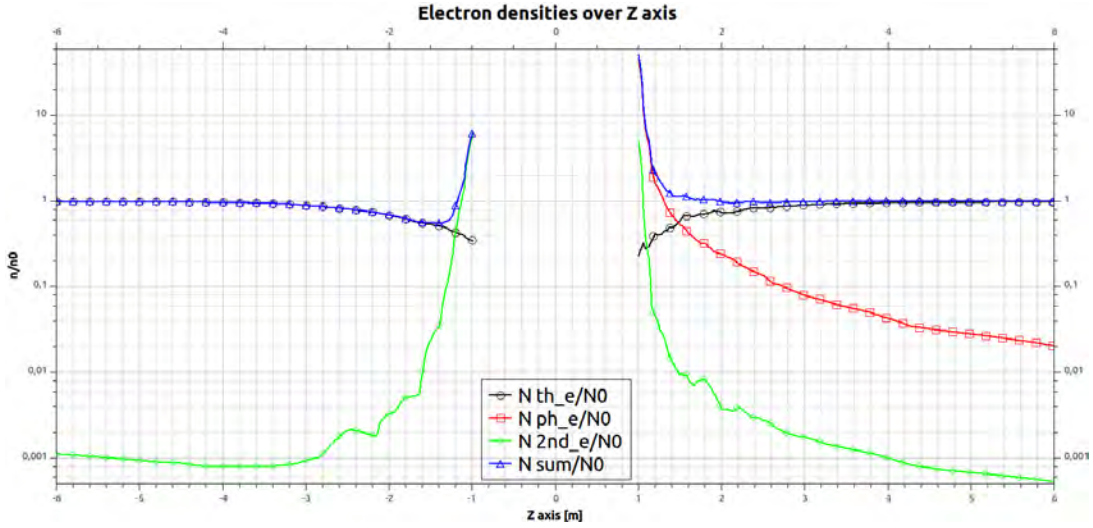

Figure 4.15: Simulation S1: normalized electron density along the z-axis ($n_0 = 7 \times 10^9\,\mathrm{m}^{-3}$).

responsible for the largest electron densities in the entire simulation domain. They are emitted from the sunlit face at densities of about $10^{11}\,\mathrm{m}^{-3}$ and they are spreading around down to the wake zone. The photoelectron wake is also visible on the rear side of the cylinder, and the highly negative potential present there prevents photoelectrons from penetrating this area and from being recollected on this face. Secondary electrons are highly present over all surfaces of the spacecraft. The potential barrier has an important influence by preventing secondary electrons from escaping the front and the back faces of the spacecraft.

Figure 4.15 shows the relative densities of thermal (black), photo (red) and secondary (green) electrons densities over the plasma density ($n_0 = 7 \times 10^9\,\mathrm{m}^{-3}$), the blue curve being the sum of those contributions. Photoelectrons and secondary electrons dominate over thermal electrons in the ram, with a higher density of photoelectrons over secondary electrons. Thermal electrons are predominant over secondary electrons $\sim 10\,\mathrm{cm}$ further from the front face and over photoelectrons $\sim 50\,\mathrm{cm}$ further. On the back side of the cylinder, photoelectrons are not visible because of their extremely low densities with respect to the scale of the plot. Secondary electrons are dominant over thermal solar wind electrons by $\sim 25\,\mathrm{cm}$.

Actually, the ion wake configuration (4.14-b) in S1 is a typical example of the theoretical reduced ion wake illustrated in section 3.8, In panel (c) of Figure 3.14. The reduced wake dimension is due to the assumed ion temperature and the fact that they are treated kinetically. The deflection of their trajectories makes them spread more efficiently and faster repopulate the wake. The reduced wake increases the final probe potential. This ion configuration occurs when $kT_i < mv_i^2/2 \leq |eV_{SC}|$. However this condition did not considered any sheath potential but only the satellite potential. In this case local potential extrema exist and influence particle fluxes. The exact expression should thus consider $|eV_{max}|$ instead of $|eV_{SC}|$. Indeed the numerical application done with the most negative potential around the spacecraft for S1 (around $-30\,\mathrm{V}$) gives:

$$(kT_i = 1 \times 10^{-21} J) < (mv_i^2/2 = 7 \times 10^{-17} J) \simeq (|eV_{max}| = 5 \times 10^{-17} J)$$

As $mv_i^2/2$ is of the same order than $|eV_{max}|$, the reduced ion wake condition can be considered as satisfied in S1.

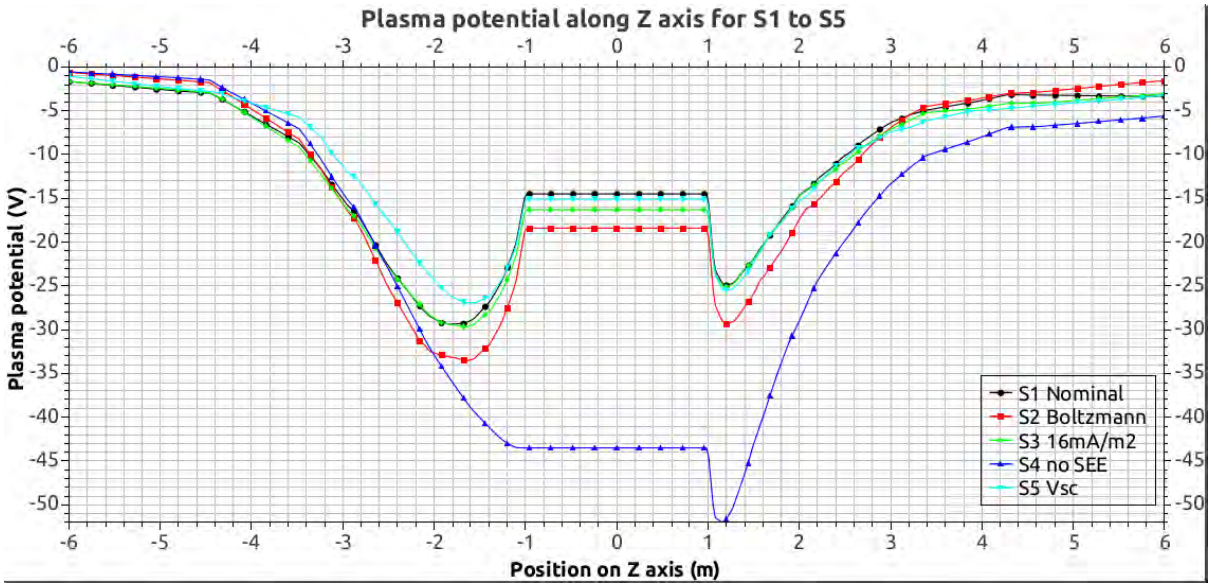

Figure 4.16: Plasma potential along the Z axis for all SPIS simulations (parametric study). The Sun is on the $+Z$ side of the axis, the ion wake on the $-Z$ side. Note that for S5 the Z axis is not aligned with the ion wake as a spacecraft speed component perpendicular to the solar wind speed has been added.

Assuming then that this reduced ion wake is spherical, equation 3.74 should give an estimate of the minimum expected potential at its center. According to Figure 4.16, the wake potential extrema is located at a distance of 80 cm (the Debye length) from the rear face of the cylinder. On Figure 4.15 the local density of the dominant thermal electrons at this point is $0.6 \times n_0$, which allows an estimate of the local Debye length to $\lambda_D = 1.0$ m. Equation 3.74 thus gives the local potential at the center of this assumed spherical ion wake of ~ -40 V while the numerical simulation reads a value of ~ -30 V. This 10 V difference is simply due to: 1) the simulated ion wake is not perfectly spherical; 2) the local density is not uniform in the wake. However the rough estimate provides a good idea of the expected local perturbation.

4.2.1.2 Results from other simulations

Other SPIS simulations are described in [Guillemant et al. (2012)] (Appendix A.4), each one varying one specific parameter. The description of all varying input values is displayed in Table 4.2 and all results are summed up in Table 4.3. For instance with S2 the thermal electron population is treated as a Boltzmann fluid instead of being treated kinetically in the PIC formalism. S3 tests the effect of a half UV Solar flux while S4 considers a situation without any secondary electron emission. Finally S5 investigates the effect of a spacecraft velocity component perpendicular to the solar wind velocity to verify the effects of an side-shifted wake behind the spacecraft. This corresponds to one part of the predicted orbit of Solar Probe Plus at this distance from the Sun. The potential profiles along the Z axis for each simulation is plotted on Figure 4.16. All simulations are analysed in detail in [Guillemant et al. (2012)] (Appendix A.4), but the main results are that in this near Sun environment, photoemission rate and the characteristic emission temperature of photoelectrons are highly important, as for the secondary emission yield which has a great influence on the spacecraft and surrounding plasma potential.

Case	Description	Electron model	Ion velocity	J_{ph} (mA/m^2)	SEEE
S1	Nominal	PIC	V_Z = -300 km/s	29	*Active*
S2	Boltzmann	Boltz. fluid	V_Z = -300 km/s	29	*Active*
S3	$J_{ph} = 16$	PIC	V_Z = -300 km/s	16	*Active*
S4	No SEE	PIC	V_Z = -300 km/s	29	*Disabled*
S5	Ion drift	PIC	V_Z = -300 km/s	29	*Active*
			V_X = -180km/s		

Table 4.2: Specific inputs for the parametric study.

I (mA)	Value	S1 Nom.	S2 Boltz.	S3 $J_{\mathrm{ph}}/2$	S4 No SEE	S5 V_{sc}
Ions	Col	2.1	2	1.3	1.7	1.7
Electrons	Col	−26.7	−25.5	−26.2	−19.2	−26.5
Photoelec.	Col	−84.1	−85.2	−44.3	−72.4	−83.8
	Emit	−91.1	−91.1	−50	−91.1	−91.1
	Net (%)	7 (92 %)	5.9 (93 %)	5.7 (88 %)	18.7 (79 %)	7.3 (92 %)
2nd elec.	Col	−52.3	−49.1	−49.4	0	−52.8
	Emit	−68.6	−65.6	−67.2	0	−68
	Net (%)	16.3 (76 %)	16.5 (75 %)	17.8 (74 %)	0	15.2 (78 %)
All pop	Col	−161	−157.8	−118.6	−89.9	−161.4
	Emit	−159.7	−156.7	−117.4	−91.1	−159.1
	Net	−1.3	−1.1	−1.2	1.2	−2.3
ϕ(V)	SC	−14.5	−18.4	−16.3	−43.5	−15.1
	Ram	−25	−29	−25	−52	−25.5
	Wake	−29.5	−34.5	−29.5	−43.5	−31
	Ram bar	−10.5	−10.6	−8.7	−8.5	−10.4
	Wake bar	−15	−16.1	−13.2	0	−15.9

Table 4.3: Final currents and potentials for all S cases. Potential barriers are calculated for secondary particles emitted from the spacecraft (photoelectrons and secondary electrons). *Coll* stands for Collected, *Emit* for Emitted, *bar* for barrier.

4.2.1.3 Conclusion of the parametric study

[Guillemant et al. (2012)] (Appendix A.4) highlighted the near-Sun environment effects. The main phenomenon achieved is that the spacecraft structure tends to have a negative floating potential (typically -10 to -20 V), due to the surrounding presence of electrostatic barriers. These originate from secondary electrons and photoelectrons which reflect the secondary particles back to the spacecraft. Furthermore the parametric study emphasized the importance of key parameters that heavily affect the final Solar Probe Plus potential and the surrounding plasma potential near the probe. The three controlling parameters that require more investigation are (1) the photoelectron temperature, (2) the secondary electron emission yield (which depend on the coating materials) and (3) the orientation of the wake (potentially modifying plasma measurements depending on the position of the instruments with respect to the ion flux). It is necessary in this case to account at least for the full PIC modelling and good models of photoelectron and SEEE to obtain reliable simulation results. Secondary particle recollection is problematic for plasma instruments, especially the secondary electrons recollection which can occur all around the spacecraft, as it was demonstrated in this parametric study. Final negative spacecraft potentials will definitely affect low energy plasma measurements, preventing electrons below this absolute potential from reaching the probe and its instruments.

For instance, the analysis of case $S1$ could be compromised by three distinct sheaths formed and linked to each other, completely surrounding Solar Probe Plus:

- the ram region in front of the sunlit face of the cylindrical probe, intensively emitting photoelectrons and secondary electrons. A local thin sheath is established, there with a one dimension barrier;

- the region around the sides of the cylindrical probe, where the material is only emitting secondary electrons (the Sun incidence is tangent to the surface normal and no photoemission occurs here). A secondary electron cylindrical sheath (with few photoelectrons arrived from the front face) prevents other of those particles from escaping from the satellite sides;

- the ion wake behind the shadowed face of the cylindrical probe, associated with a strong negative potential region (due to the lack of ions and the high densities of ambient and secondary electrons) blocking all other secondary electrons on the back face of the cylinder.

Figure 4.17 shows a simple but informative schematic view of the negative charging process caused by the SEEE. Indeed on step 1) a quantity N of ambient electrons impacts the probe and deposits Ne negative charges on the surface. With this incoming primary electron energy of 80 eV, the SEEY for this ITO material is between 1.5 and 2.5. Considering an average value of $\delta_e = 2$, the second step (2) is the emission of $2Ne$ charges, bringing the surface potential to positive values with $+Ne$ charges. Finally, due to the potential barriers, the simulations show that the majority of the emitted secondary current is repelled back to the probe: the recollection of 75 % of the $2Ne$ charges brings back $1.5Ne$ to the surface. Therefore the assessment is that N primary electrons collected lead, with the combined effect of secondary emission and potential barriers, to a collection of $-0.5Ne$ charges.

So close to the Sun, even the high photo-emitted current (necessarily positive in the balance) can not compensate this negative charging. As it appears in Table 4.3: the recollection of photoelectrons is between 80 and 90 % leading to a net current (of 7 mA for S1) which remains inferior to the sum of the thermal and net secondary electron currents (-10.4 mA for S1).

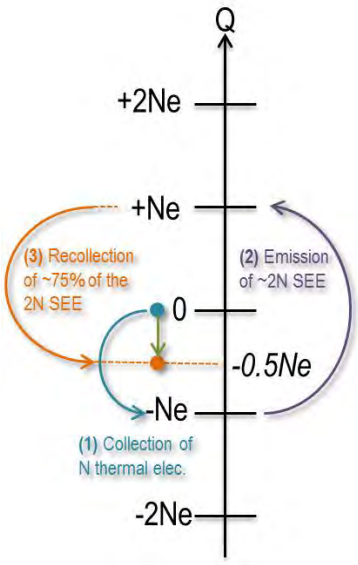

Figure 4.17: Sketch of negative charging process from ambient electron collection with SEEE and potential barriers

4.2.2 Article 2: Simulation study of spacecraft electrostatic sheath changes with the heliocentric distances from 0.044 to 1 AU

[Guillemant et al. (2012)] (Appendix A.4) showed in detail how secondary and photoelectrons sheaths can occur in a near Sun environment, and the consequences for a conducting probe which finally charges at a negative uniform potential. Knowing that at 1 AU satellites are generally positively charged, one of the obvious question that arises from the previous simulations is: getting closer to the Sun, from what heliocentric distance will this spacecraft swing to a negative potential ? This then leads to the question of the potential barrier formation and evolution, depending on the heliocentric distance. Evidently the exact location of the potential transition depends on the spacecraft covering materials, geometry and any active potential control systems. This is why this kind of study should be initiated keeping the same geometry and materials for all simulations at different distances.

This work has been performed in the paper [Guillemant et al. (2013)] (see Appendix A.5). Based practically on the same probe configuration that [Guillemant et al. (2012)] (Appendix A.4 using the same SPIS-v4.3 version), the environment has been changed for each simulation to reproduce the conditions assumed at ten different specific heliocentric distances, between 0.044 AU as in the previous case and 1 AU. In each case a summary of the potential values (on and around the probe), the balance of currents, the sheath and the wake aspects is presented. The article is attached in Appendix A.5. The main findings of this paper are summarised below.

The heliocentric distances selected for this parametric study are given in Figure 4.18. This table gathers the essential physical environment parameters that have to be considered for such simulations. Plasma characteristics at main positions are derived from Helios data (V. Krasnoselskikh and M. Maksimovic, private communications), other environments at intermediate locations are interpolated. The solar wind velocity is discretized for all positions based on the model of [Parker (1958)].

The spacecraft geometry model used for all simulations is based on the previous paper

PLASMA	Earth	Venus	Merc. Aph	Merc. Peri	SO peri	SP+ 1st Peri	0,11 UA	SP+ Sci ops	0,067 UA	SP+ Last Peri
Distance (AU)	1	0,72	0,46	0,3	0,25	0,162	0,11	0,093	0,067	0,044
Distance (Rs)	215	154,8	98,9	64,5	53,75	34,83	23,65	19,995	14,405	9,46
Sun Flux (#1AU)	1,00	1,93	4,73	11,11	16,00	38,10	82,64	115,62	222,77	516,53
Ne = Ni (m-3)	6,9E+06	1,4E+07	3,7E+07	8,9E+07	1,2E+08	3,1E+08	8,0E+08	1,1E+09	1,9E+09	7,0E+09
Te (eV)	8,14	10,41	14,52	19,80	22,95	31,77	41,50	48,33	59,25	84,47
Ti (eV)	8,00	11,21	17,00	25,00	30,76	39,90	49,00	55,82	67,00	87,25
V ram H+ (km/s)	430	430	400	395	401	366	355	350	335	300
J_ph emit (ITO) (A/m2)	3,2E-05	6,2E-05	1,5E-04	3,6E-04	5,1E-04	1,2E-03	2,7E-03	3,7E-03	7,2E-03	1,7E-02
J_the coll (A/m2)	5,3E-07	1,2E-06	3,7E-06	1,1E-05	1,5E-05	4,7E-05	1,4E-04	2,1E-04	4,0E-04	1,7E-03
J_ion coll (A/m2)	4,8E-07	9,3E-07	2,4E-06	5,6E-06	7,6E-06	1,8E-05	4,6E-05	6,4E-05	1,0E-04	3,4E-04
Mach number	15,53	13,11	9,91	8,07	7,39	5,92	5,18	4,79	4,18	3,28
λ_D (m)	8,06	6,52	4,67	3,51	3,27	2,38	1,69	1,53	1,30	0,82
λ_D photoelec (m)	0,98	0,71	0,45	0,29	0,25	0,16	0,11	0,09	0,07	0,04
SEEY (at Te)	0,28	0,35	0,45	0,65	0,7	0,95	1,2	1,32	1,55	1,92
The. Gyrorad (m)	1,7E+03	1,1E+03	4,8E+02	2,7E+02	2,4E+02	1,2E+02	5,5E+01	4,9E+01	1,9E+01	1,5E+01
H+ Gyrorad (m)	7,0E+04	5,0E+04	2,2E+04	1,3E+04	1,2E+04	5,8E+03	2,6E+03	2,3E+03	8,6E+02	6,4E+02
Magnetic field (T)	5,8E-09	9,7E-09	2,7E-08	5,5E-08	6,7E-08	1,6E-07	4,0E-07	4,8E-07	1,4E-06	2,1E-06

Figure 4.18: Summary of SPIS simulations for the parametric study in [Guillemant et al. (2013)] (Appendix A.5). Shaded lines give input parameters entered in SPIS. In the table, *Peri*, *Aph* and *Sci ops* refer respectively to *perihelion*, *aphelion* and *science operations orbit*.

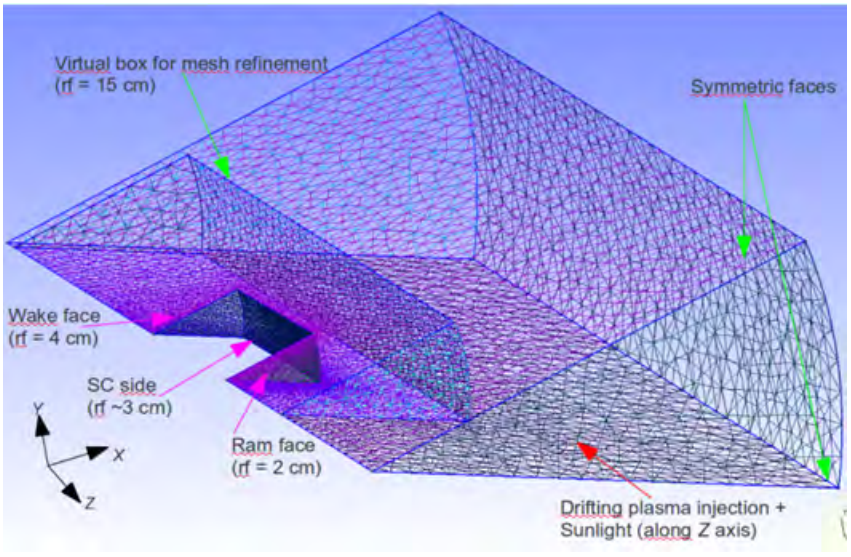

Figure 4.19: Geometry cut model of the cylinder (covered with ITO material) and the simulation box + the associated mesh ("rf" = mesh refinement).

[Guillemant et al. (2012)] (Appendix A.4): the same cylinder (1 m radius and 2 m long) in a cylindrical simulation box. The whole system thus presents a symmetry of revolution around the Z axis. As SPIS handles the symmetries of fluxes and electric field, and for a gain in CPU time, a cut geometry model with a 30 ° angle around the Z axis can be used. The domain is finally a 5 m (in X) × 10 m (in Z) pie chart (30 ° angle), containing the satellite portion, with an unstructured mesh with a spatial resolution of 2 cm on the sunlit face of the satellite, 4 cm on the rear side and 50 cm on the edges of the simulation box (Figure 4.19). The external boundary conditions are set to a "Fourier" type (a $1/R^2$ decrease of potential, R being the distance to the spacecraft surface) where particles are injected and to a "mirror" type for the two symmetric faces (see Figure 4.19) which means that particles cannot cross those faces and are reflected into the simulation box.

The varying parameters between the simulations are: plasma properties (densities, temperatures, solar wind velocity), the sun flux (it varies as $1/r_s^2$, r_s being the distance to the Sun) and the time steps to compute every plasma population transport loops. To solve the equivalent electrical circuit representing the satellite the spacecraft capacitance is estimated at $C = 1.9 \times 10^{-10}$ Farad for a surface entirely covered with the conducting Indium Tin Oxide (ITO) material. The value of this parameter is however not important in this study since we are interested here in the steady state, rather than the transient phase.

All species (protons, thermal electrons, secondary electrons and photoelectrons) are treated kinetically using the PIC formalism. In Table 4.18 the values in gray are the input parameters. The satellite orbital velocity is neglected; that is, at rest in the solar inertial frame of reference. Only the proton population speed (that depends on the distance to the Sun) is simulated. This velocity is considered to be only along the $-Z$ axis as we neglect the spacecraft orbital motion. The magnetic field is not taken into account, as proton and electron gyroradii are much greater than the simulation box, even at 0.044 AU (Table 4.18).

In the following section I present results for the model at 0.044 AU from the Sun. In the next section, results of the same geometrical model near Solar Orbiter perihelion at 0.25 AU will be summarized. Concerning particles, for both cases the software has generated approximately the following numbers of elements:

- electrons = 1200000
- ions = 510000
- photoelectrons = 350000
- secondary electrons = 250000

4.2.2.1 Results at 0.044 AU: Solar Probe Plus at perihelion

The present simulation has the same inputs that the previous $S3$ case performed in my first article [Guillemant et al. (2012)] (Appendix A.4). The main difference is in the geometry. Other cases of the previous article used a high photoemission yield of 29 $\mathrm{mA/m^2}$, instead of ∼16 in the present case and S3. Finally this run allows to validate the cut geometry model, a quite useful way to gain time of computation, refine the meshing and the results. The compared results between those two simulations give an accuracy better than 1 V (see the Table 2 in [Guillemant et al. (2013)] (Appendix A.5).

In this case, the satellite potential converges to -16.2 V. Figure 4.20 is a plot of the plasma potential map and the population densities (thermal electrons, ions, photoelectrons and sec-

ondary electrons) around the spacecraft. Looking at the potentials, the lowest in the ram is at -25.4 V. With respect to the satellite it corresponds to a potential barrier for photoelectrons and secondary electrons of -9.2 V. In the ion wake a minimum of -31 V is reached, which corresponds to a potential barrier for all secondaries of about -15 V. On the side of the cylinder a -3 V barrier also forces the recollection of a fraction of secondaries. Those barriers are generated through the high densities of photoelectrons and secondary electrons in the front, and the high densities of secondary electrons added to the lack of ions at the rear. Looking at the positions of those plasma potential minimum values, in the ram it is located at 0.23 m from the sunlit face, which corresponds to 5 times the Debye length of photoelectrons ($\lambda_{ph} = 0.04$ m). In the wake the minimum is at 0.84 m which corresponds to the thermal electron and secondary electrons Debye length (0.8 m), which are predominant at this location. The height of the potential barrier in the ram is of the same order as the photoelectron temperature.

An important parameter is the ratio between the dimension L (∼0.8 m) of the wake and the Debye length λ_D: if $L \sim \lambda_D$, the potential may be scaled at a fraction of $\sim k_B T_e/e$ in the wake. Indeed using both Poisson's equation and Gauss's flux theorem, two minimum potentials can be obtained in the wake. Depending on the wake geometry, perfectly spherical or cylindrical, these minima are respectively $\phi = (0.5 \text{ or } 0.25)\ (L/\lambda_D^2)\ (-k_B T_e/e)$ (see the corresponding equations 3.74 and 3.71 in section 3.8). We have in this case ϕ between -40 V and -20 V. This simulation gives a wake minimum of -31 V which seems like an intermediate case between the "spherical reduced wake" and the "cylindrical wake".

The potential surrounding the satellite is between -25 V and -31 V. Those barriers represent about 1/3 of the thermal electron temperature of 85 eV so it affects their densities close to the spacecraft, as only 30% of the initial thermal electron density ($n_0 = 7 \times 10^9$ m^{-3}) populates the region close to the spacecraft (see the thermal electron map). The ion wake is clearly visible and varies between no particles near the rear face of the cylinder (in the wake) and n_0 near the boundary. The ion vacuum is reduced by the thermal diffusion of these particles and by ion focusing through the negative ϕ_{SC}. Local disturbances of the ion density at the front are due to statistical noise in the full PIC approach (the figure is not averaged enough through post-processing treatment such as to reduce noise). However, that does not impact the results the system is mainly driven by the photoelectron density in the sheath. The most dense plasma populations is still that of photoelectrons, emitted from the sunlit face at densities of about 10^{11} m^{-3} before spreading around in the volume. Photoelectron depletion is also visible on the rear side of the cylinder, because highly negative potential present there prevents photoelectrons from penetrating this area. Secondary electrons are dense over all surfaces of the spacecraft. The potential barriers have a great influence by preventing secondary electrons from escaping the front and the back faces of the spacecraft.

Table 4.18 shows all net currents on SP+ for all simulations. Concerning this first case, the total thermal electron current arriving on the spacecraft I_{the} reaches 24.6 mA and for ions it is 1.5 mA. Assuming that thermal electrons are treated as a fluid, as in the Maxwell-Boltzmann statistics equilibrium approximation, theoretical net I_{the} should reach $J_{\text{the},0} \times S_{SC} \times \exp(e\phi_{SC}/(k_B T_e)) = 26.8$ mA (according to $J_{\text{the},0}$ in Table 4.18 and the spacecraft total surface of $S_{SC} = 18.9$ m^2). Of the 51.9 mA of photoelectron current emitted, -45.2 mA is collected, for a net current of 6.7 mA (87% of recollection). For secondary electrons: 61.4 mA are emitted and -46.2 mA are collected, leading to a net current of secondaries of 15.2 mA (75% of recollection, all over the spacecraft surfaces). Plots of all potentials (SC and barriers) are presented on Figure 4.24.

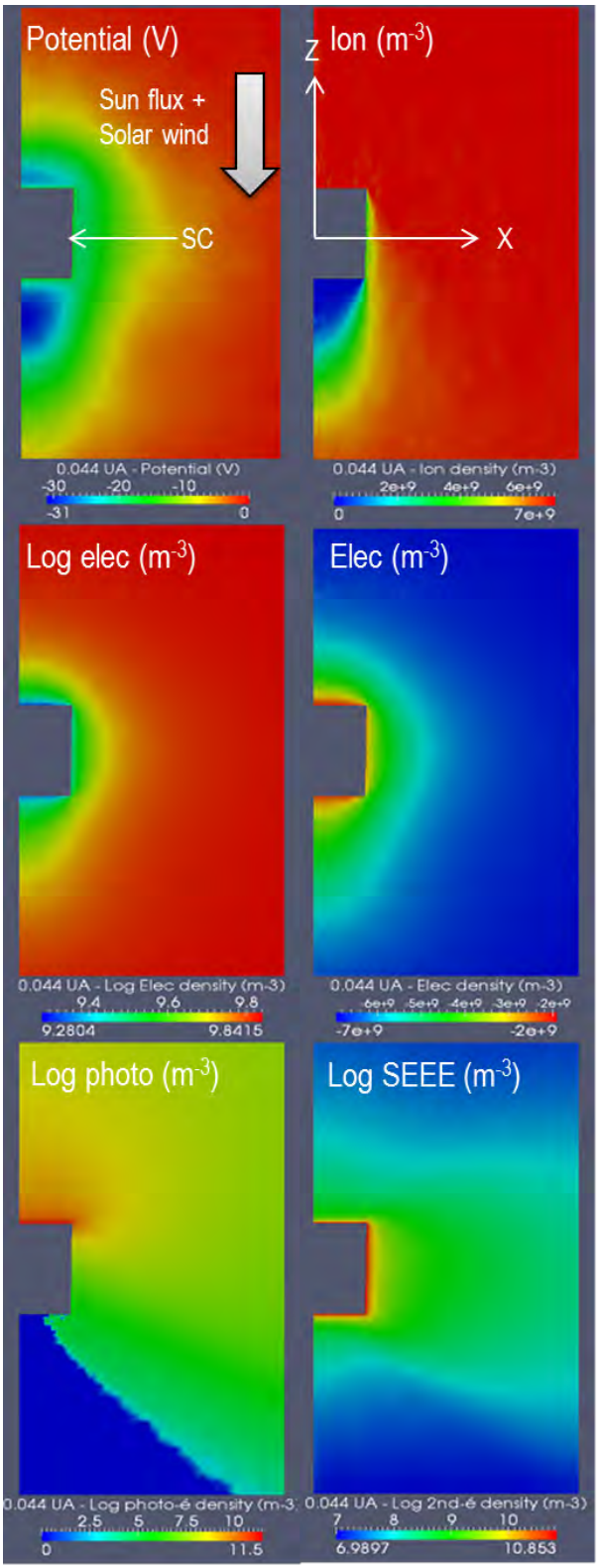

Figure 4.20: Simulation results (potential and population densities) for the 0.044 AU case (Solar Probe Plus - SP+ perihelion) in a $X-Z$ plane. The Solar wind and Sun flux are flowing along the $-Z$ direction.

4.2.2.2 Results at 0.25 AU: Solar Orbiter spacecraft at perihelion

The case with Solar Orbiter closest perihelion at 0.25 AU from the Sun is now considered. Results for plasma potential and population densities are presented on Figure 4.21. The final ϕ_{SC} is now found to be +6.30 V. This is due to the larger Debye length of photoelectrons: the barrier has changed from a 1D geometry at 0.044 AU (thin sheath) to a 3D geometry here (thick sheath). The recollection is thus less important and mainly due to the positive satellite potential. However, negative potential values are still present around the spacecraft: -1.1 V at 1.6 m in front of the sunlit face in the ram (at ∼6 times the photoelectron Debye length of 0.25 m), and -1 V at 2.9 m of the rear face in the wake (close to λ_{the} which equals 3.27 m for ambient electrons). For secondary and photoelectrons, it represents respectively -7.4 and -7.3 V barriers, added to the positively charged satellite which will thus attract them more efficiently. Incoming thermal electrons from the solar wind encounter a -1 V barrier (∼4% of their mean kinetic energy of 23 eV) so they are not as much repelled as previously. However the distribution at the spacecraft surface is truncated at $\phi_{SC} = +6.30$ V: electrons have at least a 6.30 eV energy on spacecraft.

Concerning the cylindrical ion wake obtained here, the minimum potential expected at its center (using equations 3.74 and 3.71 with $L \sim 1$ m and $\lambda_{\text{D,the}} = 3.27$ m) should be between -1.2 V and -0.6 V. This is consistent with the value of -1 V obtained in the simulation..

Looking at plasma population densities, the major difference with the former simulation is the plasma potential structure around the cylinder. In the 0.25 AU case it is more symmetric around the satellite body, less disturbed by the ion wake. This wake is more elongated along the Z axis than before, as the ion speed is increased by ∼100 km/s, T_i is reduced by 4, and there is no focusing of those particles as ϕ_{SC} is now positive. As $\lambda_{the} = 3.27$ m (larger than the spacecraft dimension) the space charge in the wake only slightly modifies the potential (by about 1/10 of V). The global behaviour of photoelectrons and secondaries is the same as in the first case, except that they are less dense than previously and they can spread farther from the cylinder because of the reduced potential barriers. The recollection of secondary electrons reaches 80.8% and practically the same (78%) for photoelectrons (Table 4.27). Here the recollection of secondaries, which is the condition for equilibrium, is achieved with a positive ϕ_{SC} , and a small potential barrier due to space charge. At 0.044 AU collected photoelectrons represented 40% of all collected currents on spacecraft, and the same proportion was reached for secondaries. At 0.25 AU the collected photoelectron current is now 60% of all collected currents while secondaries represent ∼20%. This is due to the lower SEEY at 23 eV with respect to the SEEY at 85 eV: a lower emission leads to a lower recollection.

4.2.2.3 Results between 0.044 AU and 1 AU

The same simulation was performed for several additional distances from the Sun, using the input parameters in Table 4.18. All the corresponding results (currents and potentials values) are displayed in Table 4.27. Plasma potential profiles along Z and X axis are displayed on respectively Figures 4.22 and 4.23. Values of satellite potentials are plotted in Figure 4.24, the location of minimum potentials is plotted on Figure 4.25.

Looking at the plasma potential profiles along the Z axis, Figure 4.22 shows that for this type of model, below ∼0.3 AU from the Sun, a non-monotonic evolution of potential is obtained, due to secondary electron and photoelectron space charge. Farther from the sun, the space charge is less important. The transition between negative and positive satellite equilibrium potential is reached between 0.093 and 0.11 AU, but it has to be emphasized that this situation depends

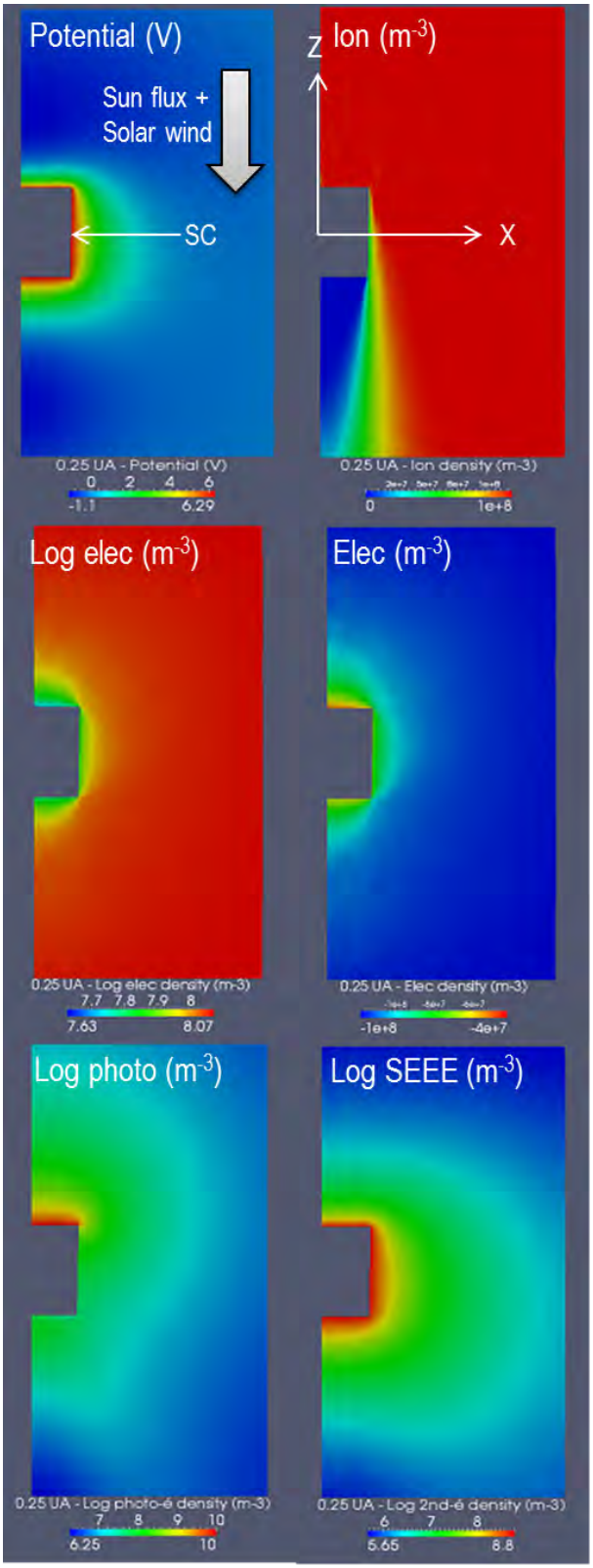

Figure 4.21: Simulation results (potential and population densities) for the 0.25 AU case (Solar Orbiter at perihelion) in a $X - Z$ plane. The Solar wind and Solar UV are flowing along the $-Z$ direction.

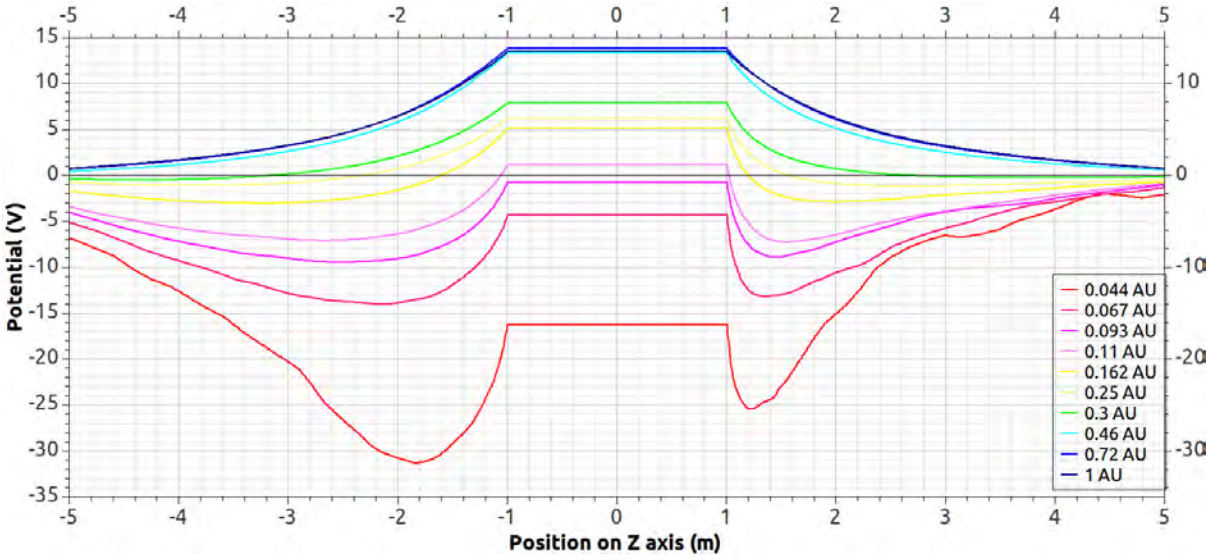

Figure 4.22: Plasma potential along the Z axis for all simulations. The spacecraft potential is monotonically increasing with heliocentric distance.

on the total spacecraft surfaces exposed to the environment and the type of covering materials. The farther from the Sun, the farther the ram and wake minimum potential positions are located from the spacecraft surfaces. Beyond 0.3 AU the plasma potential profile is decreasing monotonically away from the cylinder. This is visible for the cases at 0.46, 0.72 and 1 AU to the Sun. Thus recollection of secondary particles in these regions is simply due to the spacecraft positive potential. It can be seen from Figure 4.24 that the limit of the sheath reaches the boundary of the simulation box in each case. The plots of ram and wake minimum potentials should reach 0 V far enough from the body beyond 0.3 AU, but they are slightly larger the fact that the sheath then extends up to the simulation box boundary. This restriction was necessary for reasons of CPU time consumption, and it slightly affects the potential profiles in the surrounding plasma.

The transition between positively and negatively charged spacecraft is linked to the geometry of the sheath. It changes from a 3D thick sheath far from the Sun (farther than 0.11 – 0.093 AU, where thermal and photoelectrons Debye lengths are long) to a thin 1D sheath closer to the sun, where the photoelectron Debye length is shorter. Far from the Sun, with no blocking from a potential barrier, the current balance is reached for a positive spacecraft potential (it is easier for photoelectrons to escape a 3D sheath with a small depth). In the second case, the limitation from space charge is a 1D phenomena: the photoelectron recollection is extremely efficient (the net current being approximately given by the Child-Langmuir's law, expressed in equation 3.33 in Section 3.3) and we can obtain the current balance with a negative spacecraft potential.

On Figure 4.25, we notice a difference in positions of the minimum plasma potentials: below ∼0.3 AU the wake potential barrier is farther from the spacecraft than the ram barrier. Beyond 0.3 AU the positions of the barriers regarding the facing surfaces are similar in the ram and in the wake. This also corresponds to regions where the potential along Z axis evolves non monotonically. More precisely Figure 4.25, suggests that below 0.093 AU the ram barrier position on the sunlit face follows the photoelectron Debye length (which is much smaller than λ_{the}). Indeed when closer to the Sun than 0.093 AU the extreme near Sun UV flux generates

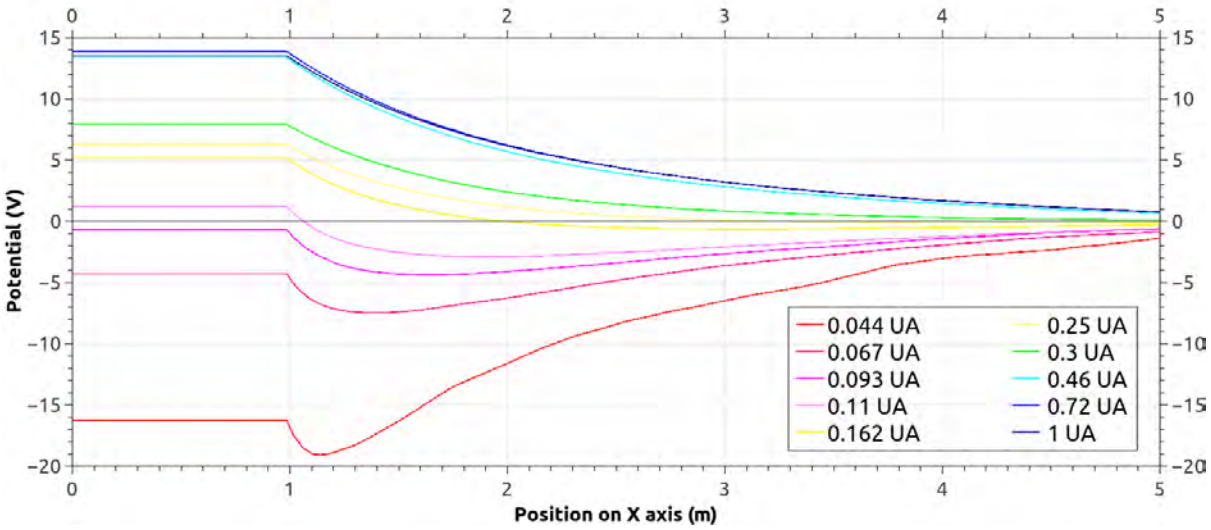

Figure 4.23: Plasma potential along the X axis for all simulations. The spacecraft potential is monotonically increasing with heliocentric distance.

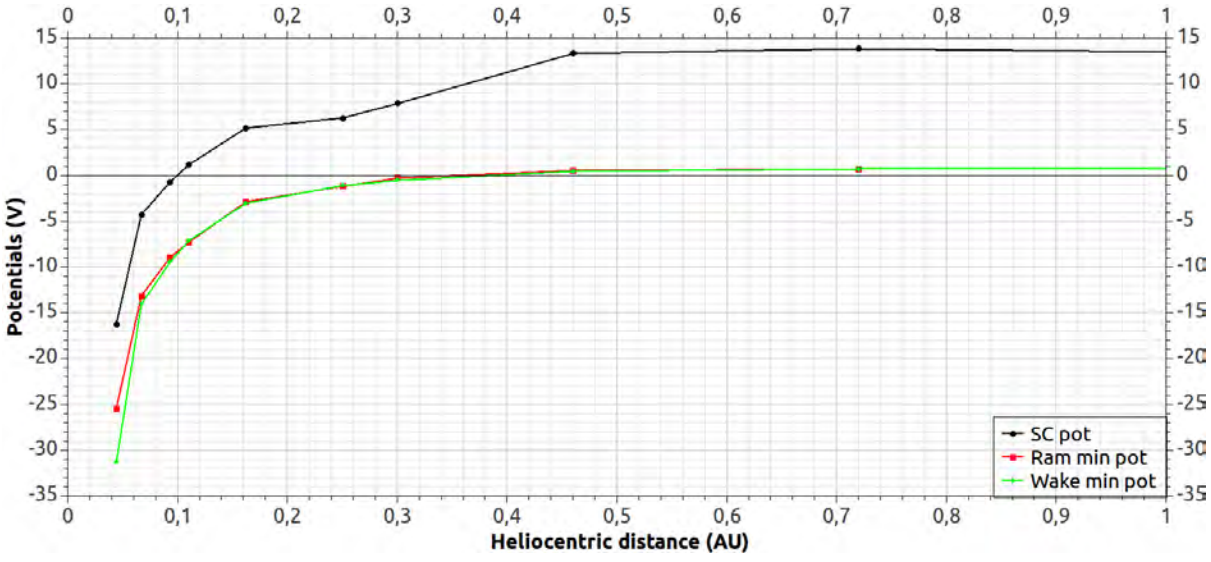

Figure 4.24: Potentials versus heliocentric distance.

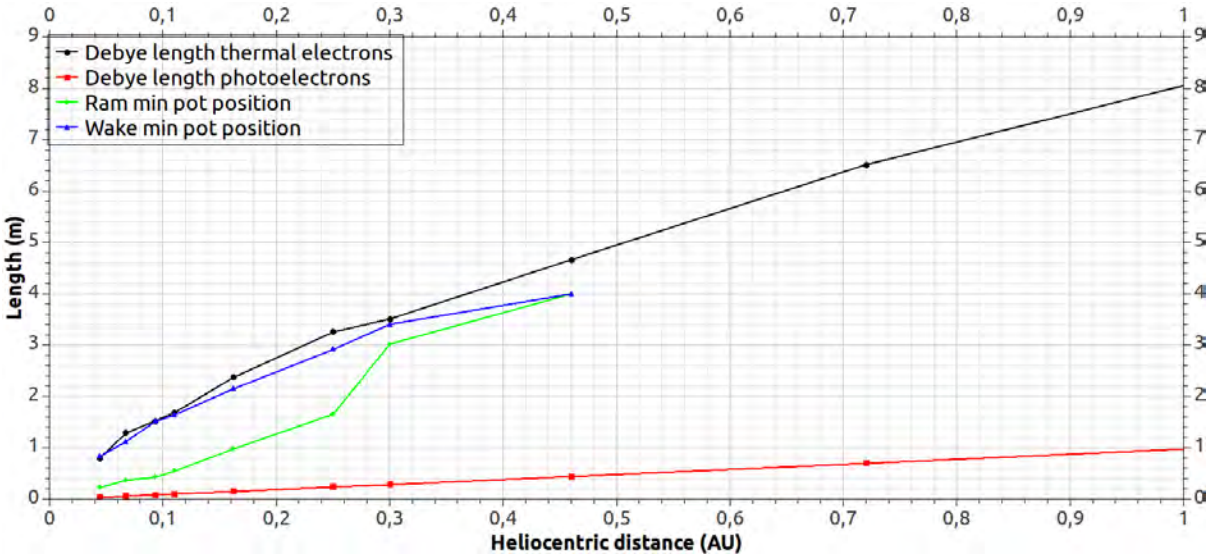

Figure 4.25: Comparison of Debye lengths and locations of potentials minima in plasma versus heliocentric distance.

high densities of photoelectrons that seem to influence most the plasma behavior in the ram region. Up to 0.25 AU the ram barrier position is at about 5 – 6 times λ_{ph} from the sunlit face. Beyond that, as it appears in Figure 4.25, the ram barrier distance to spacecraft is similar to the wake barrier distance and it is comparable to the thermal Debye length. Within 0.25-0.3 AU the emitted secondary electron current becomes lower than the collected thermal current. Still on Figure 4.25 photoelectron and thermal electron Debye lengths as a function of heliocentric distance appear to be the two asymptotes between which are contained the ram and wake barrier position curves. As in the wake the plasma seems to be more influenced by thermal and secondary electrons, which have similar densities. The potential barrier there is controlled by the thermal electron Debye length and temperature, the spacecraft size and the ion Mach number.

Figure 4.26 clearly shows the part of secondary particles (both photoelectrons and SEEE) among collected electrons on the spacecraft. In each case, between 0.044 and 1 AU, those non environmental particles represent ∼80% of the collection. Photoelectrons are increasingly more important in the recollection farther from the Sun. This seems paradoxical but can be understood as the SEEE is highly reduced with increasing distance to Sun. This is because of the decreasing mean energy of the thermal electrons, which reduces the secondary emission rate. From a plasma detector point of view, photoelectron recollection occurs essentially on the sunlit face and it will affect the detector entrance areas less than secondary electrons will.

4.2.2.4 Conclusion of the parametric study

The simulations performed in [Guillemant et al. (2013)] (Appendix A.5) showed the variation of space charge potential barriers around a spacecraft depending on its distance to the Sun. At less than 0.3 AU for this model geometry, the plasma potential around the spacecraft decreases non monotonically. Potential barriers for secondary and photoelectrons thus appear and force their recollection to lower ϕ_{SC} (even at negative values below 0.11 AU to the Sun). The barriers are created by high densities of secondary particles that control the surrounding plasma and

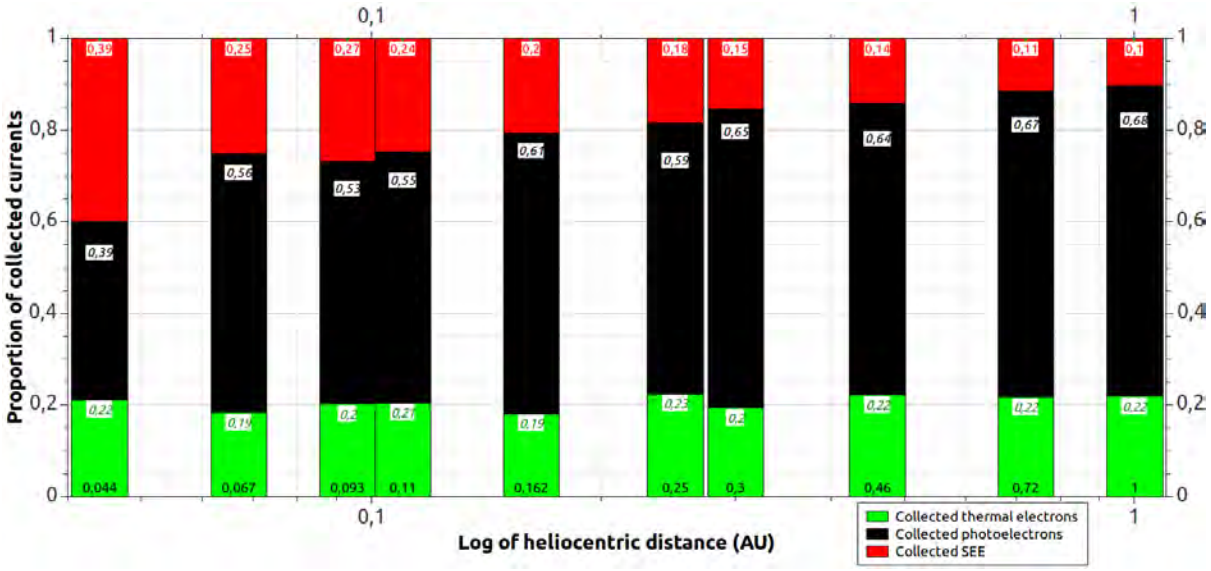

Figure 4.26: Proportion of particles among collected electrons versus heliocentric distance.

are dominant in the collected particles.

The specific case studied at 0.25 AU showed that Solar Orbiter near its perihelion may be affected by those phenomena, even if they are less pronounced than at 0.044 AU as for the Solar Probe Plus perihelion environment. Measurement errors on low energy plasma measurements are possible but depend on the size of the spacecraft and its covering materials which will control secondary particles emission. At Solar Orbiter perihelion low energy plasma measurements will be disturbed: high rates of secondary particles recollection can still occur and potential barriers still affect the surrounding plasma. A small fraction of incoming thermal electrons (with energies $\leq$ 1 eV) will be filtered and particles emitted from the satellite surfaces might be measured as noise by the onboard detectors, and thermal electrons arriving on the detectors will be accelerated (as $\phi_{SC} > 0$) to 6.3 eV

A reliable prediction of space-environment condition effects on Solar Orbiter would require more detailed simulations. These would include the effect of detailed geometry, and material properties (solar panels materials, heat shield properties, taking into account thin wires and locations of plasma instruments...) and possibly electrical properties (equivalent resistors and capacitors inside the spacecraft and between the electrical nodes). The geometric model used here is quite far from the real Solar Orbiter geometry, but this simulation gives a first hint of the plasma reaction to a satellite crossing this region, as Solar Orbiter will be travelling this far. Actually, given the size of the real Solar Orbiter probe, sunshield and solar arrays, the created ion wake should be bigger and the corresponding potentials more negative, thus increasing the potential barriers and the biasing phenomena. However the electron instrument (SWA/EAS) is located at the end of a 4-5 m boom, behind the spacecraft, which might limit the influence of ϕ_{SC}. Moreover, the exposed covering materials (conductors and dielectrics) will generate different level of secondary particles. More complete simulations of the ESA mission will be performed in Chapter 6.

PLASMA	Earth	Venus	Mercury Aph	Mercury Peri	SO peri	SP+ 1st Peri	0,11 UA	SP+ Sci ops	0,067 UA	SP+ Last Peri
CASE (AU)	1	0,72	0,46	0,3	0,25	0,162	0,11	0,093	0,067	0,044
CURRENTS on SC (A)										
The net	-2,5E-05	-5,0E-05	-1,3E-04	-2,7E-04	-4,8E-04	-9,4E-04	-2,6E-03	-3,8E-03	-6,4E-03	-2,5E-02
H+ net	1,5E-06	3,1E-06	8,1E-06	2,1E-05	2,9E-05	6,6E-05	1,7E-04	2,4E-04	4,0E-04	1,6E-03
Photoelectrons										
Coll	-7,9E-05	-1,5E-04	-3,7E-04	-9,0E-04	-1,3E-03	-3,2E-03	-7,0E-03	-9,9E-03	-2,0E-02	-4,5E-02
Emit	1,0E-04	1,9E-04	4,8E-04	1,1E-03	1,6E-03	3,8E-03	8,3E-03	1,2E-02	2,2E-02	5,2E-02
Net	2,2E-05	4,1E-05	1,0E-04	2,2E-04	3,5E-04	6,7E-04	1,3E-03	1,7E-03	2,8E-03	6,8E-03
SEEE										
Coll	-1,2E-05	-2,6E-05	-8,2E-05	-2,1E-04	-3,9E-04	-1,1E-03	-3,2E-03	-5,0E-03	-8,7E-03	-4,6E-02
Emit	1,4E-05	3,2E-05	1,0E-04	2,4E-04	4,8E-04	1,3E-03	4,2E-03	6,7E-03	1,3E-02	6,1E-02
Net	2,3E-06	6,0E-06	2,0E-05	2,9E-05	9,3E-05	1,9E-04	1,1E-03	1,7E-03	4,1E-03	1,5E-02
All pop.										
Coll	-1,1E-04	-2,3E-04	-5,8E-04	-1,4E-03	-2,1E-03	-5,1E-03	-1,3E-02	-1,8E-02	-3,4E-02	-1,1E-01
Emit	1,1E-04	2,3E-04	5,8E-04	1,4E-03	2,1E-03	5,1E-03	1,3E-02	1,8E-02	3,5E-02	1,1E-01
Net	-3,6E-09	-1,8E-07	1,3E-07	-1,6E-06	-2,5E-07	-1,0E-05	-8,7E-05	-7,7E-05	9,1E-04	-1,1E-03
Recoll. (%)										
Photoelec	78,4	79,1	78,5	80,6	78,0	82,4	84,4	85,1	87,6	87,0
SEEE	84,0	81,2	80,4	88,1	80,8	85,1	74,6	74,3	67,7	75,2
POTENTIALS										
SC (V)	13,5	13,9	13,4	7,9	6,3	5,2	1,2	-0,7	-4,3	-16,2
Ram min pos. (m)	NA	NA	NA	3,0	1,7	1,0	0,6	0,4	0,4	0,2
Wake min pos. (m)	NA	NA	NA	3,4	2,9	2,2	1,7	1,5	1,1	0,8
Ram min val (V)	NA	NA	NA	-0,2	-1,1	-2,8	-7,2	-8,9	-13,1	-25,4
Wake min val (V)	NA	NA	NA	-0,5	-1,1	-3,0	-7,1	-9,4	-14,0	-31,3
Potential barriers for secondaries (V)										
Ram	13,5	13,9	13,4	-8,1	-7,4	-8,1	-8,5	-8,2	-8,9	-9,2
Wake	13,5	13,9	13,4	-8,4	-7,4	-8,2	-8,3	-8,7	-9,8	-15,1
OTHER VALUES										
Rate 2nd-emit/the-coll	-0,6	-0,6	-0,8	-0,9	-1,0	-1,3	-1,6	-1,8	-2,0	-2,5
Coll-The/Coll-ALL (%)	22,2	22,0	22,5	19,7	22,8	18,4	20,9	20,5	18,7	21,5
Coll-2nd/Coll-ALL (%)	10,4	11,4	14,2	15,6	18,6	21,0	25,0	27,2	25,4	40,4
Coll-photo/Coll-ALL (%)	68,8	67,9	64,7	66,3	60,0	61,9	55,5	53,6	57,1	39,5

Figure 4.27: Parametric study results, main output values. Coll = Collected, Emit = Emitted, Pos = Position.

4.2.3 Possible effects on plasma measurements

The two articles [Guillemant et al. (2012)] (Appendix A.4) and [Guillemant et al. (2013)] (Appendix A.5) illustrate the complexity of spacecraft/plasma interactions, even though the spacecraft geometry is relatively simple (considered as an entirely conducting cylinder). Their various effects on the satellite itself (potential and collected/emitted currents) and on its near environment (plasma sheaths, potential and barriers) point to the multiple biases that local plasma measurements would suffer from.

The parametric study highlighted the strong dependence of the global spacecraft/plasma relation with the considered environment. Indeed the variation of the heliocentric distance entails a variation of the plasma parameters (temperature, density, ion velocity, Solar flux) and consequently a modification of the secondary and photoemission yields. The simple satellite goemetry used in [Guillemant et al. (2013)] (Appendix A.5) leads to the following results: the probe is negatively charged below 0.1 AU from the Sun, the plasma potential in the near environment of the probe is non-monotonic below 0.3 AU. It has to be recalled, however, that those "threshold" heliocentric distances might vary with any modification of the probe geometry, dimensions, covering materials or internal circuit.

Concerning low energy plasma measurements, several phenomena exhibited in those papers will definitely affect the plasma instrument outputs. The negative potential around the probe should repel low energy ambient electrons (as it has already been demonstrated in section 3.4). The potential barriers around the probe should force the recollection of secondary particles. The ion depletion behind the satellite should lower the local potential and act like another barrier (see the analytical approach presented in section 3.8). The question raised here is: in which proportion will those phenomena pollute the measurements, quantitatively speaking ? In the following Chapter 5, numerical simulations of the main phenomena created through satellite/plasma interactions will be performed with a single particle detector instrument floating in space (and thus considered as the satellite), in order to estimate quantitatively the misinterpretation of the instrument outputs compared with theoretically expected undisturbed environment.

Chapter 5

Numerical particle instruments

Contents

5.1 Definition of scientist's needs . . . 103
5.2 The SPIS-SCI Instruments . . . 105
5.3 Measurement principle . . . 108
5.4 Measurement of a undisturbed Maxwellian plasma: Case 1 . . . 110
5.5 Measurement of a disturbed Maxwellian plasma . . . 112
5.5.1 Positive potential effect: Case 2 . . . 112
5.5.2 Negative potential effect: Case 3 . . . 115
5.5.3 Photoemission: Case 4 and 5 . . . 117
5.5.4 Secondary electron emission: Case 6 . . . 122
5.5.5 Combined effect of SEEE and photoelectrons: Case 7 . . . 125
5.6 Undisturbed non isotropic Maxwellian plasma: Case 8 . . . 127
5.7 Conclusion . . . 130

In this Chapter is presented the numerical particle instrument concept. First the definition of the user's needs and the design principle of numerical particle detectors are presented, owing to this study and IRAP contribution. Secondly the description of numerical instrument measurement method and outputs is given. Finally, the best illustration of numerical particle measurement: a parametric study of a simple set of detectors alone in the plasma and subjected to various perturbations is described and analysed in detail. This allows a quantitative analysis of the main disturbing phenomena on ideal particle measurements.

5.1 Definition of scientist's needs

Concerning simulations of particle measurements by electrostatic analysers on board satellites, investigators's expectations are:

- modelling an instrument at its proper location on the spacecraft, with its own geometry, covering materials and technical properties, to reproduce as faithfully as possible a response of the instrument in the appropriate conditions of the satellite environment;
- obtaining precise plasma measurement outputs to anticipate a future mission scientific results or compare actual existing data to simulated ones.

The idea is to help investigators not only simulate but also understand measurements. As enumerated in section 1.3 and detailed in section 1.4.2 and chapter 3: perturbations due to spacecraft/plasma interactions on plasma measurements are various, grey areas for particle data

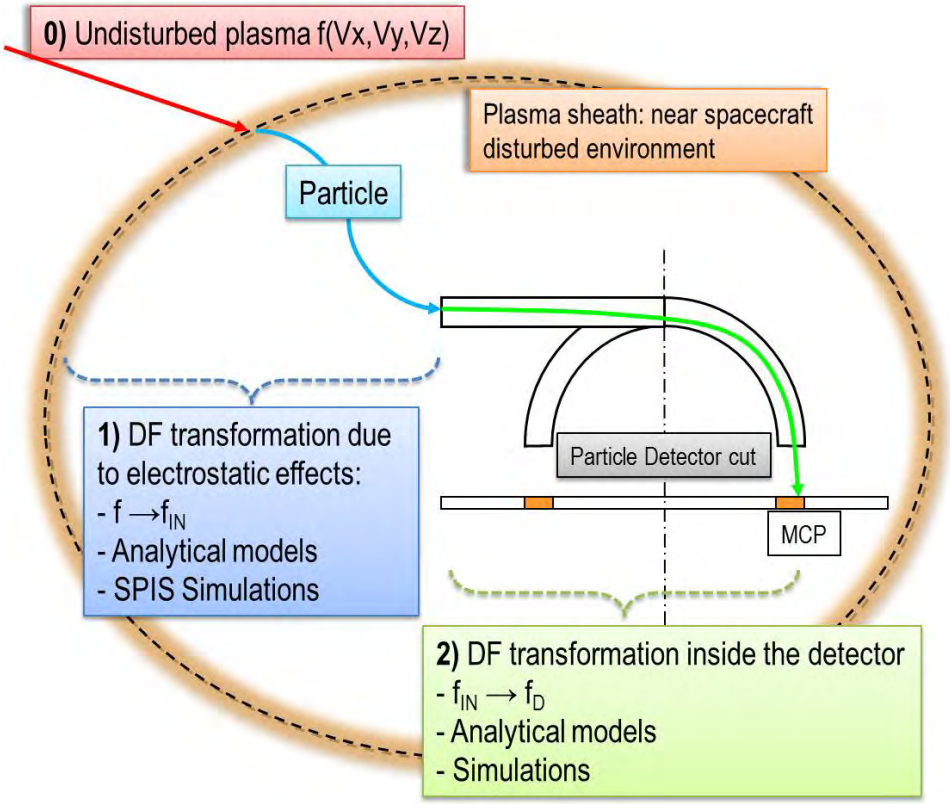

Figure 5.1: Illustration of numerical particle measurements setup. The focus can be made on the undisturbed plasma (0), outside the sheath until the particle arrival at the detector entrance (1), after the DF modification inside the disturbed environment, or the interest can be carried out on the particle DF transformation inside the detector (2). Both phenomena cannot be modelled within the same simulation with presently available simulation codes.

analysis remain. Each perturbation has a particular effect on measurements, so the combined perturbations generate a complex and convoluted bias that should be dealt with.

In the frame of the SPIS-SCI project it is possible to configure instruments, through a generic instrument interface, called SPIS Instruments. One specific contribution of this PhD and IRAP laboratory within this SPIS-SCI project was the definition of instrument models, outputs and their validation. Some of the simulation results will be presented in Chapter 6.

Two possibilities are offered to the SPIS user to model particle measurements as explained on Figure 5.1. The first one, that has been used here, is the addition of the particle detector within the satellite and environment simulation, and modelling the ambient particles outside the detector until they reach its entrance (between steps 0 and 1 on this figure). The detector gap constituting the entrance of the top hat analyser, usually covered with a grid, is not generated as a slit but modelled as a simple physical surface that effectively collects particles. The computed fluxes of particles onto those collecting surfaces, their velocity distribution functions and the corresponding currents constitute the base of the instrument outputs. The other option is to simulate the inside of the electrostatic analyser (step 2 on Figure 5.1). The simulation box boundary would thus stand for the inner lining of the instrument, and the numerical plasma volume would be the slit guiding the particles from the entrance to the MCP. However, even

though this is perfectly possible with SPIS (indeed several studies performed with this software deal with the modelling of plasma chambers, see for example [Matéo-Vélez et al. (2008)]), this simulation would be decoupled from the spacecraft/surrounding plasma interactions context, which is beyond the scope of this PhD. It is presently not practical to model both the satellite immersed in its near environment and the inside of the scientific instrument within the same simulation. Those two issues have to be computed separately: the outside simulated fluxes arriving on the detector entrance modelled in a first step become the input particle fluxes injected within the detector path in a second inner simulation. Considering the points of interest in the present study, however, the computation work is focused on the outside of the analyser to introduce and understand the main concepts of satellite/plasma interactions biasing effects on low energy plasma measurements.

The contribution has been carried out on particle detectors. Based on the classical geometry of a top-hat analyser (see Figure 1.1). The idea is to discretise the particle entrance of the detector (usually circular or semi-circular) into several relatively flat sections, constituting together the collecting ring aperture of the instrument. Note that even though the sections are full surfaces and not holes, SPIS will handle those collecting faces as entrances of the particle detector. Their flatness allows to ensure a correct definition by the user of the acceptance angles for each surface, with respect to the user-defined detector basis proper to each section. Combining all sections acceptance solid angles, it is thus possible to recreate the entire field of view of the instrument. An example of the modelling method of a top-hat electrostatic analyser covering 360° in azimuth (AZ) and 45° in elevation (EL) is displayed on Figure 5.2. Note that this cylinder ring can be defined as set of truly flat surfaces (an hexagon or octagon, depending on the precision level desired). However instrument measurement computation and the gathering of the detectors output files might become lengthy when dealing with 8 sets of particle detector outputs. This compromise remains the user's choice.

More details about the detectors basis definition will be presented in a further section, but in the following the focus is made on the different available particle detector types in SPIS-SCI, the various outputs provided and the computational method used.

5.2 The SPIS-SCI Instruments

Thanks to the SPIS-SCI capabilities, extended studies can be performed and intensively post-processed to investigate the most important specificities of plasma measurements and biasing effects in the near spacecraft environment. The numerical instruments allow performing advanced measurements inside the whole computational domain and/or on the spacecraft surface. The objective of the instruments is to provide the user with specific information on the simulation outputs.

The results provided depend on the sub-type of instruments. The instruments are configured just before launching the numerical simulation. There are currently three main categories of instruments:

1. The Particle Detectors category including:

    - Particle detectors themselves, providing mainly the particle distribution functions on dedicated spacecraft surfaces. They basically rely on a *Test Particle* (TP) method which consists of calculating the particle trajectories in a frozen electromagnetic field, by a series of forward and backward tracking using Liouville's theorem.

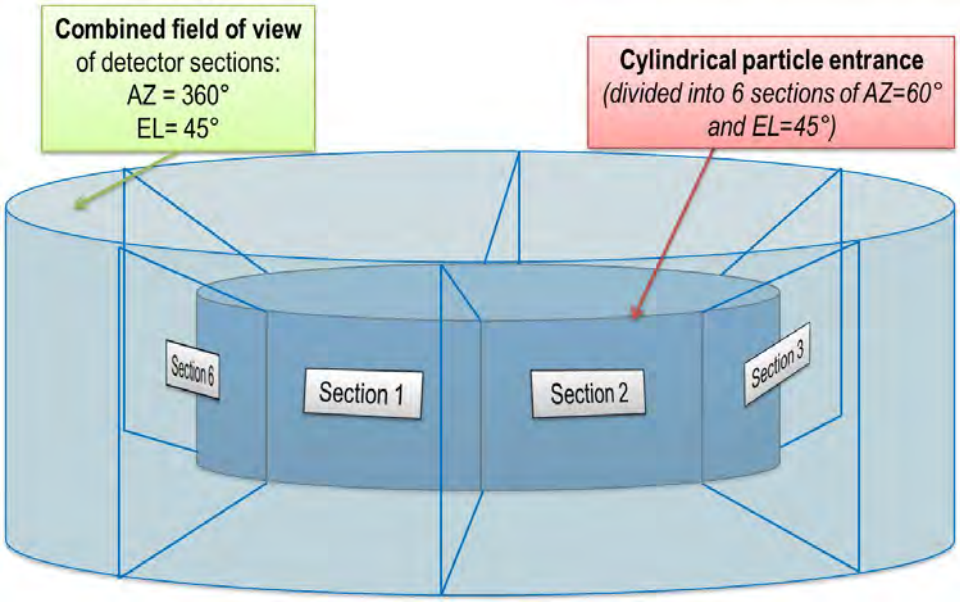

Figure 5.2: Example of the discretisation of a top-hat electrostatic analyser. Each of the 6 chosen sections has, regarding its normal, an acceptance Azimuth (AZ) of ±30° and Elevation (EL) of ±45°. The combined sections cover together 360° in AZ and 45° in EL.

- Langmuir probe instruments which extend the Particle Detector class by introducing *Intensity-Voltage* (IV) sweep measurements coupled with TP.

2. The Virtual Particle Detectors category providing the same information as real particle detectors (defined on spacecraft surfaces) but on a surface independent from the spacecraft. They do not interact with the plasma and spacecraft dynamics. They are used to estimate currents flowing through a virtual surface immersed in the computational volume.

3. Plasma sensors that perform simple and quick diagnostics in the plasma volume. They do not interact with the plasma and spacecraft dynamics. Within the course of the SPIS-SCI activity, diagnostics of values positioned on spacecraft surfaces were also developed and considered in this category. So "plasma sensors" should be understood by users as a Live Monitoring of the simulation.

Outputs from Instruments can be:

- Data fields of local data deployed on the grid (e.g. maps of potential, current density at detection and injection);

- Distribution function as a function of the energy. It is performed at detection on the instrument and at injection (on boundary for ambient populations and on spacecraft for secondaries);

- Slices of the distribution function at a given energy as a function of elevation (EL) and azimuth (AZ) angles user-defined (defined at detection and injection), for each particle detector;

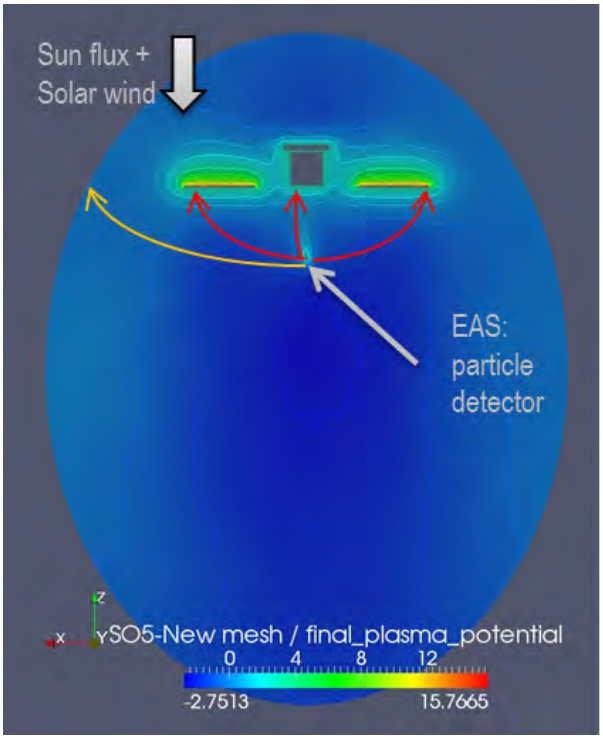

Figure 5.3: Backtracking principle of SPIS-SCI particle detector instruments (example of the Solar Orbiter spacecraft at 0.28 AU from the Sun). It represents a top view of the plasma potential around the satellite. Particle detectors are located at the end of the rear boom (the *EAS* instrument). The backtracked trajectories of particles are plotted in orange for thermal electrons and in red for secondary electrons.

- Times series, including spectrograms of the energy distribution function versus time (at detection and injection)

- A useful file named here "ParticleList" constituting the list of detected particle on the detector in the output frame. There is one line per particles with successively the position on the detector (X_D, Y_D, Z_D), the velocity at the detector (Vx_D, Vy_D, Vz_D), the flux weight of the particle on the detector (W_{FD}), the position on the particle source (X_E, Y_E, Z_E), the velocity at the particle source (Vx_E, Vy_E, Vz_E), the flux weight of the particle on the particle source (W_{FE}) and the statistical weight of the particle in volume (W) which is conserved in Liouville's theorem. This file allows various possibilities of post-processing instrument data, such as filtering the incoming particle directions depending on the energy ranges, particle deflection angles, *etc.* Some possibilities developed during this PhD will be presented in Chapter 6.

Settings are defined through the pre-processing information such as global parameters and geometrical description.

One important aspect is that statistics are relatively poor on small satellite elements. As the objective of the instruments is to provide precise and refined distribution functions (or any other outputs), a specific numerical method has been implemented.

The advanced algorithm used to compute fine distribution of particles crossing detector

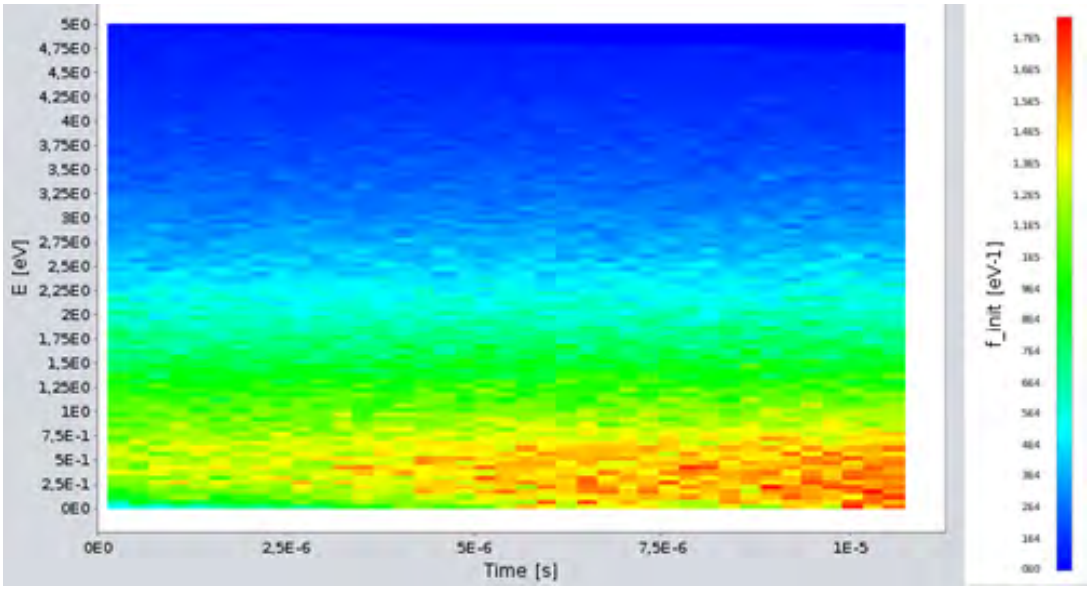

Figure 5.4: Example of 2D data field result from a SPIS-SCI particle detector instrument: here the energy distribution function of secondary electrons (at injection, *i.e.* on the satellite at particle emission) versus time.

surface relies on a Test Particle approach. Particle trajectories are computed in backward mode (also forward mode during initialization) where particles are tracked from the detector surface back to the point of origin (see Figure 5.3). It helps significantly in reducing statistical noise on spacecraft surfaces designed as instruments, which size can be very small compared to other satellite elements (and which only collect a few super particles in classical forward mode). The distribution is optimized by using an *OcTree* algorithm permitting to refine the 3D velocity distribution in domains of interest. For each detector the user can specify what particles will be tracked, and with what precision. In addition, 2D data (current density at detection and injection) are generated in order to clearly identify where the detected fluxes come from (see Figure 5.4).

Results of SPIS-SCI instruments obtained during this study will be presented in the following parametric study, as well as in Chapter 6 with the modelling of future and existing electron detectors.

5.3 Measurement principle

As the total understanding of space environment requires a complete knowledge of the biases on plasma analysis: a reference case study of particle detector response to perturbations must be established. The straightforward method consists in modelling initially a simple instrument alone in a plasma, without any disturbing phenomena, and then get back to the expected ambient environment as it was injected in the simulation box through the simulated measurement outputs. This first preliminary simulation might be seen as a calibration of the numerical instrument. The focus is on low energy electrons, easily influenced by small perturbations, and possibly originating from the spacecraft (or the instrument) itself.

The chosen environment for this sequential study is the one of Solar Orbiter at 0.28 AU from

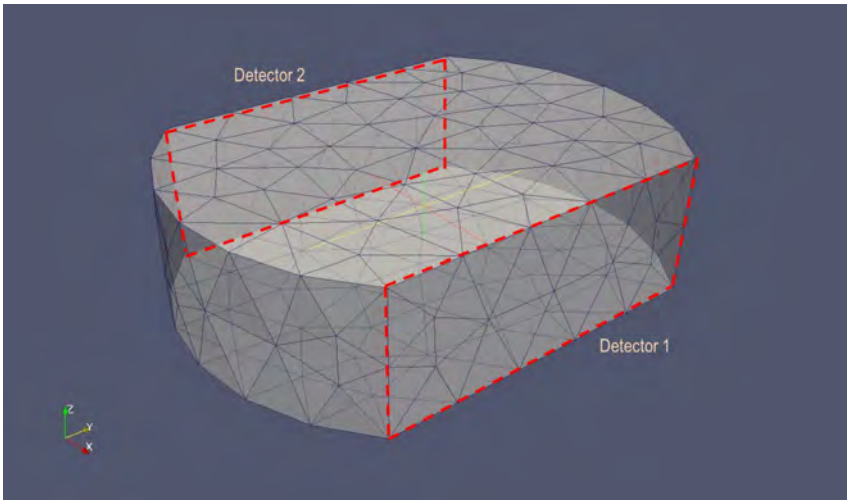

Figure 5.5: The GMSH model of the electrostatic analyser used for basic particle measurement simulations. The collecting surfaces, encompassed by the dashed red lines and normal to the X axis, constitute the detectors. The foreground Detector 1 accepts all incoming electrons with $V_x < 0$. On the other side and visible by transparency, Detector 2 collects all arriving electrons with $V_x > 0$. The meshing is also visible on the entire instrument.

the Sun (see Table 4.18, data at 0.28 AU are interpolated between parameters from 0.25 and 0.3 AU): a plasma population with a density n_0 of 1.036×10^8 m^{-3} and an electron temperature of $kT_{e,0} = 21.37$ eV, with the same density and a temperature of 27 eV for the protons. The instrument geometry (see Figure 5.5) is based on a flat parallelepiped of dimensions (X, Y, Z): 5 cm × 5 cm × 2 cm, with on the edges two opposite flat sides constituting the particle detector entrances (normal to the X axis), the two other faces being curved. The top and bottom faces of the instrument (normal to the Z axis) remain flat. It is placed at the center (0, 0, 0) of a 5 m radius spherical simulation box, and also at the center of an intermediate 0.3 m radius spherical boundary (which has no physical existence, it is only generated to control the meshing enlargement in the vicinity of the detector). The mesh size varies between 70 cm on the external boundary to 5 cm on the intermediate boundary and finally to 1 cm on the detector surfaces. The instrument covering material is Indium Tin Oxyde (ITO) which properties concerning SEEE are presented in section 5.5.4, when the secondary emission will be activated. Details about the photoemission yield are given in section 5.5.3.1.

Each of the two flat collecting surfaces has an open field of view, meaning that it accepts all incoming electrons having a non zero V_x component towards the inside of the surface. Detector 1 (on the positive section of the X axis) accepts all particles having $V_x < 0$, and Detector 2 (on the negative section of the X axis) accepts all particles having $V_x > 0$. This open field of view is more easily represented through the angle of acceptance of incoming trajectories onto the surface. Based on a spherical system of coordinates with origin at the center of the instrument (0, 0, 0) in the (X, Y, Z) reference frame of the GMSH model, two angles common to both detectors are defined. Considering the velocity vector $\mathbf{V}$ of the particle at its arrival on one of the detector surface, the first θ angle describes the direction of $\mathbf{V}$ in the (X, Y) plane: θ is included between the interval $[-\pi/2; \pi/2]$ and is defined as the azimuth (AZ) of the detected incoming particle trajectory. The second angle ϕ corresponds to the elevation (EL) of $\mathbf{V}$, as the

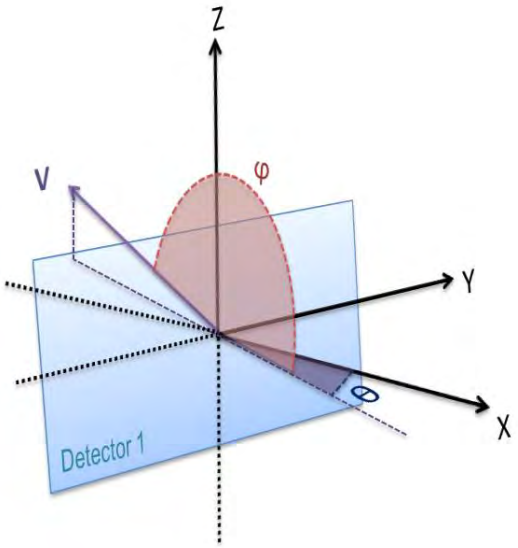

Figure 5.6: Sketch of the θ and ϕ angles definition. Regarding the present Detector 1, the incoming electron here detected has a velocity $\mathbf{V}$ which spherical coordinates are approximatively $\theta \sim -\pi/6$ and $\phi \sim 3\pi/4$

angle between the direction defined by θ and the vector $\mathbf{V}$. ϕ is included between the interval $[-\pi;\pi]$. An illustration of the angles definition is displayed on Figure 5.6 for Detector 1.

This way Detector 1 can collect incoming particles which velocity vector coordinates on the surface are: $\theta \in [-\pi/2;\pi/2]$ and $\phi \in [-\pi;-\pi/2] \cup [\pi/2;\pi]$. Detector 2 sees the incident particle velocity vector coordinates as: $\theta \in [-\pi/2;\pi/2]$ and $\phi \in [-\pi/2;\pi/2]$. Each Detector sees 1/2 of the 4π steradians of the environment, and the simple superposition of both fields of view covers the entire solid angle within the spherical simulation box.

From this state, each following simulation will address a specific perturbation mechanism, whose own impact on measurement results will be analysed. The biases generated by the combination of several perturbations should be investigated thereafter. This kind of parametric study can rapidly generate an extremely wide grid of cases, through various combinations of perturbing phenomena. The grid of cases used here has however to be limited to relatively basic problems. In the following, the main measurement disturbances will be simulated and studied, starting with the detection of an undisturbed Maxwellian plasma.

5.4 Measurement of a undisturbed Maxwellian plasma: Case 1

This first simulation is close to the Liouville's theorem application performed analytically in section 3.4, with a zero instrument potential and no secondary or photoelectrons. This time particles are simulated through the PIC method.

The zero plasma potential around the instrument is illustrated on Figure 5.7. This picture is zoomed on the instrument location but the entire volume has a zero electrostatic potential. Figure 5.8 simply shows that both detectors 1 and 2 see the same type of environment: each one detects half of the ambient electron population. Noise appears on those measurements, due to the high energy resolution assumed for the detectors.

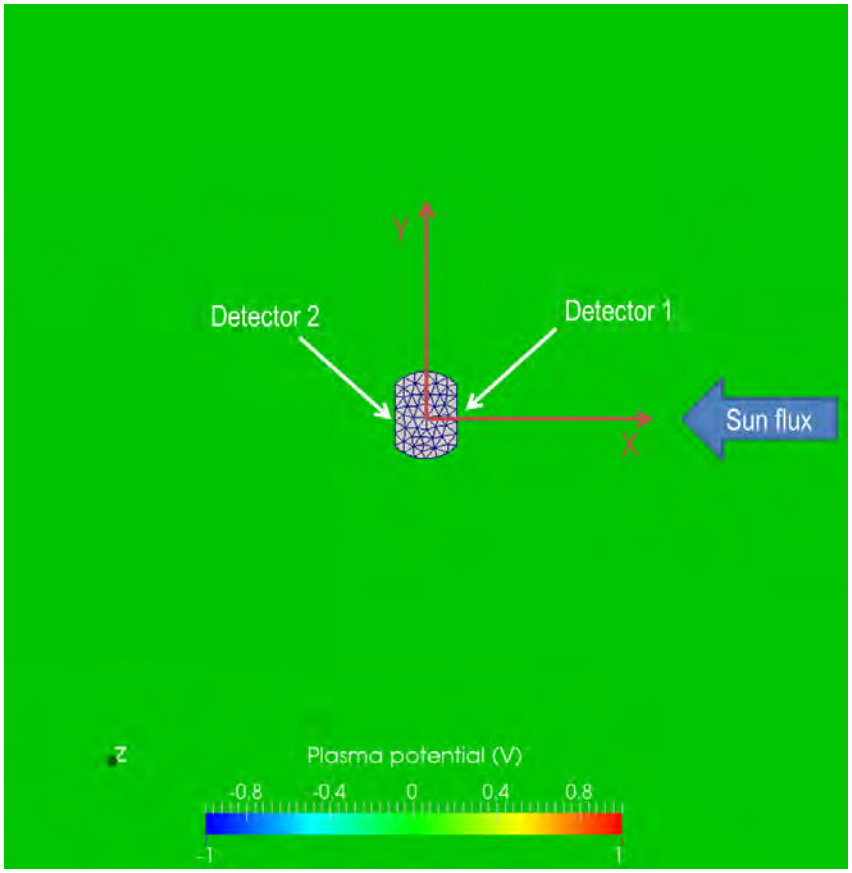

Figure 5.7: Case 1: plasma potential around the instrument at $\phi_D = 0\,\mathrm{V}$ (top view) in the $X - Y$ plane. The entire volume has a null plasma potential at equilibrium.

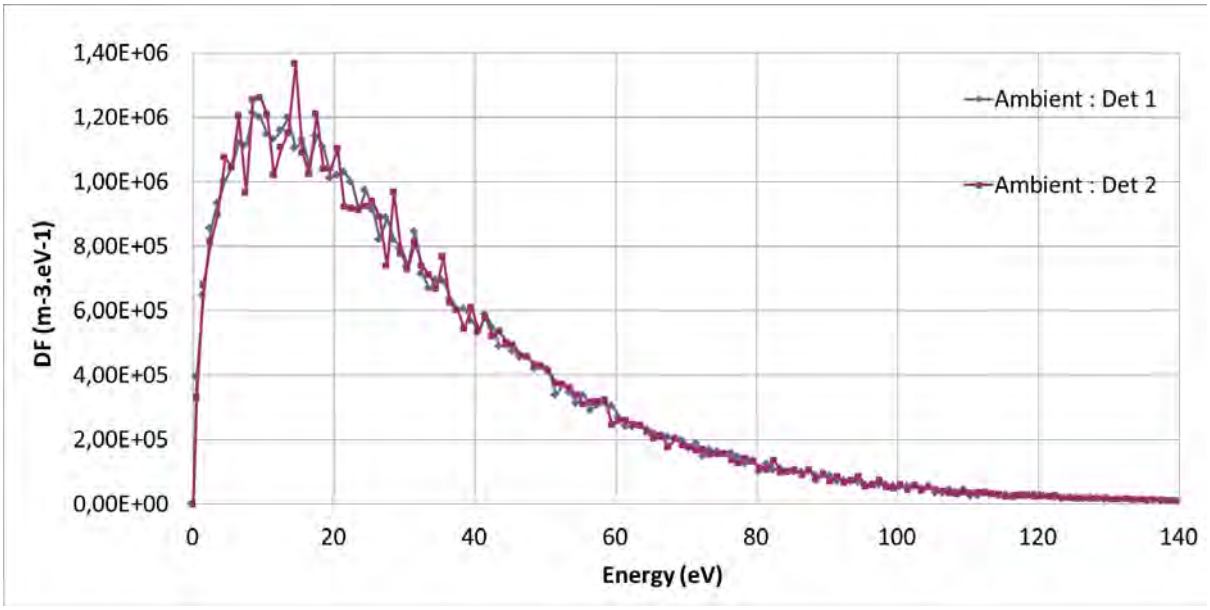

Figure 5.8: Case 1: measured energy distribution functions of ambient electrons (energy resolution of 1 eV).

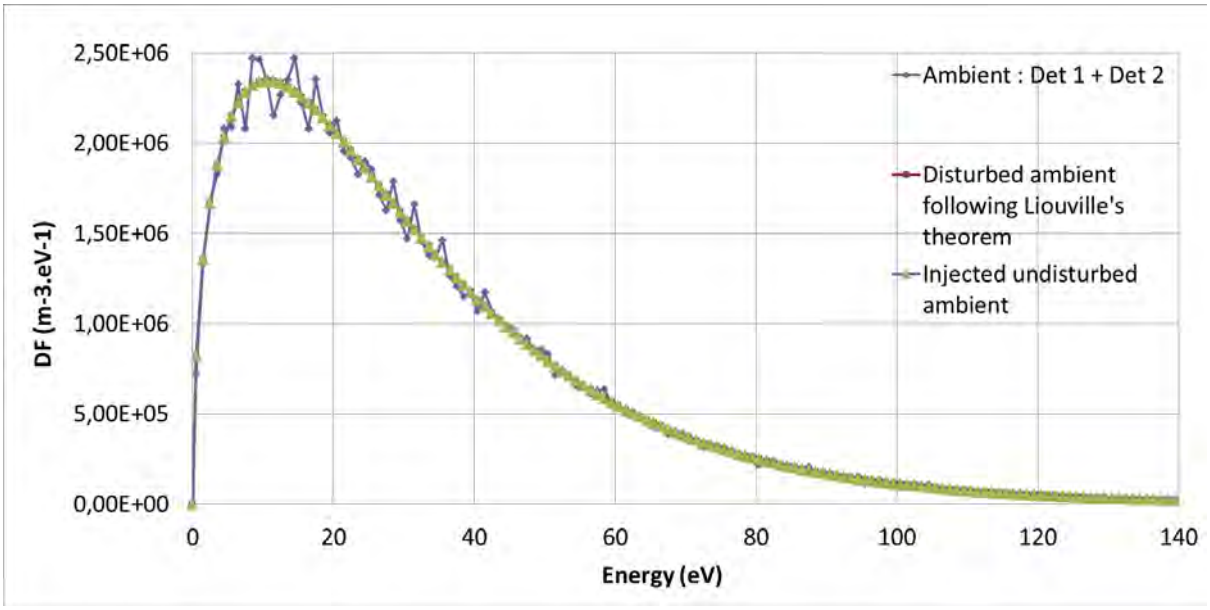

Figure 5.9: Case 1: measured and theoretical energy distribution functions of ambient electrons (energy resolution of 1 eV). The red and green curves are identical.

In Figure 5.9 the sum of the two previous detector measurements is plotted (blue curve), due to this instrument configuration the basic combination of the two detector surfaces covers the entire environment. This superposition allowed to recover the Maxwellian undisturbed distribution injected as an input in the simulation volume (green curve), with an almost perfect fit between the two curves, apart the remaining discretisation noise. This injected Maxwellian environment is completely merged with the expected distribution function (red curve) as no disturbing potential exists. The lack of parasite particles (secondary or photoelectrons) maintains a correct evaluation of the low energy natural environment.

Concerning numerical values, the expected electron population has a density n_0 of $1.036 \times 10^8\,\mathrm{m}^{-3}$ and a temperature of $kT_{e,0} = 21.37\,\mathrm{eV}$. The integration of the measured energy distribution function (blue curve on Figure 5.9) gives a density estimation of $1.038 \times 10^8\,\mathrm{m}^{-3}$ which is different by only 0.2% with respect to n_0 (see Figure 5.33). The measured average kinetic energy is 32.06 eV while the theoretical mean energy is $3kT_{e,0}/2 = 32.05\,\mathrm{eV}$. This value comparison (theory *vs* measurements) shows that this first simulation is well calibrated and constitutes a solid reference case to progressively add disturbances.

5.5 Measurement of a disturbed Maxwellian plasma

5.5.1 Positive potential effect: Case 2

This Case 2 simulation is the same that Case 1 with an electrostatic potential of the instrument ϕ_D set constant at +10 V.

This case is close to the one simulated in section 3.4: it is the same value of positive potential although the environment is now the one for a satellite at 0.28 AU, *i.e.* hotter and denser than the plasma considered in section 3.4. The ϕ_D value of +10 V should thus here be less disturbing than in the analytical case. The potential distribution on the instrument and in its vicinity is

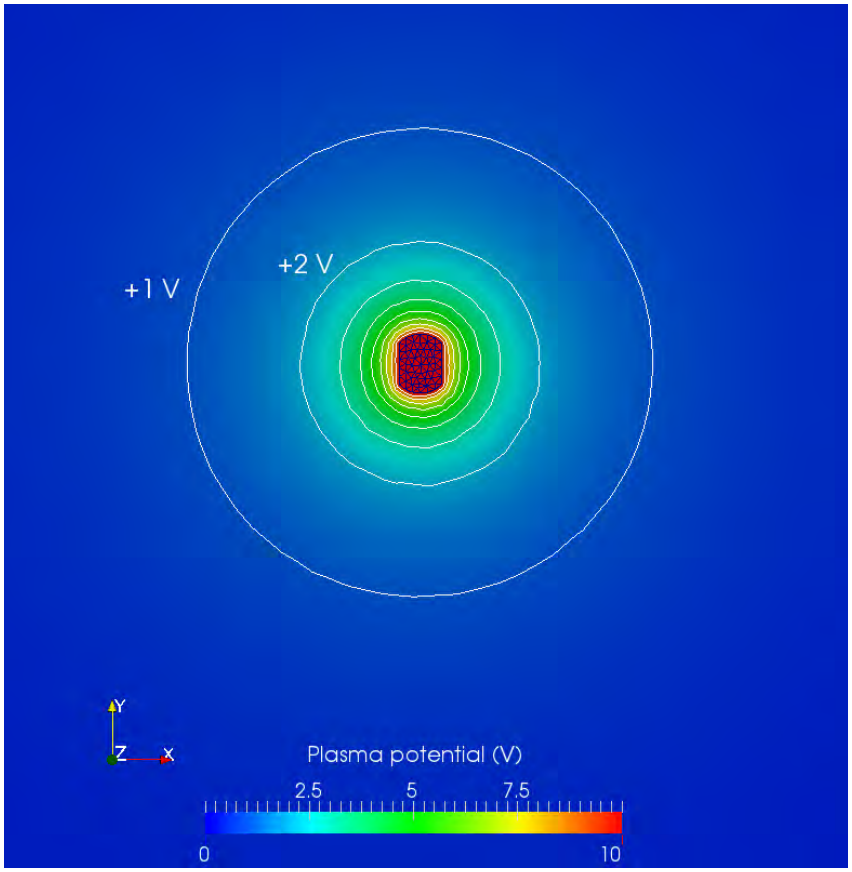

Figure 5.10: Case 2: plasma potential around the instrument (at $\phi_D = +10\,\mathrm{V}$) in the $X - Y$ plane. Potential isocontours are also represented.

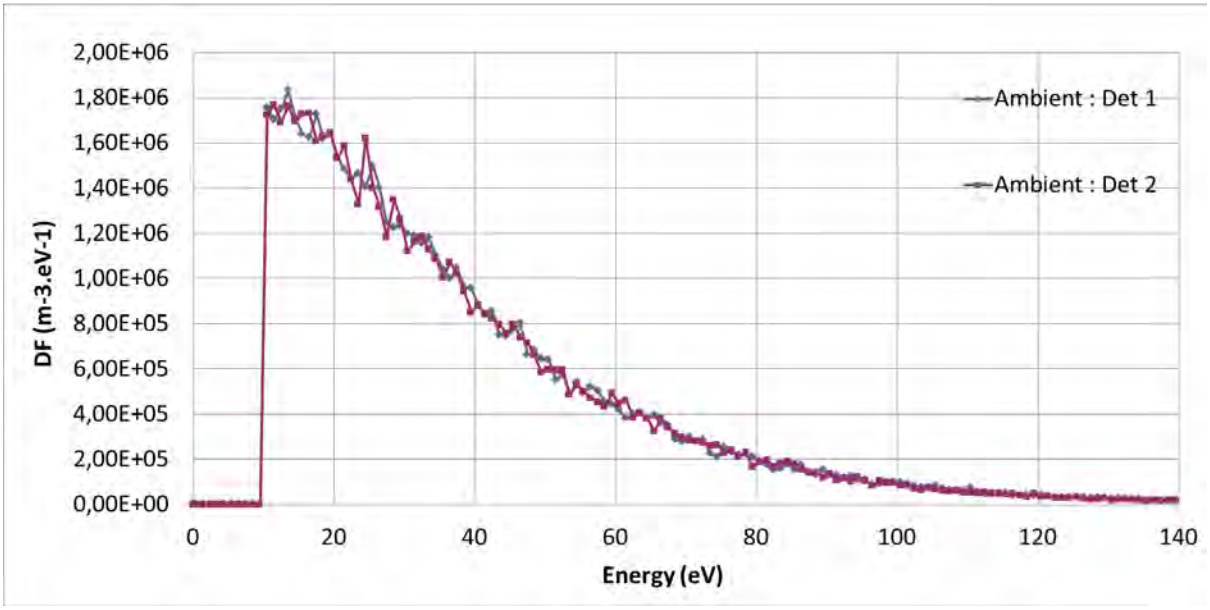

Figure 5.11: Case 2: measured energy distribution functions of ambient electrons (energy resolution of 1 eV).

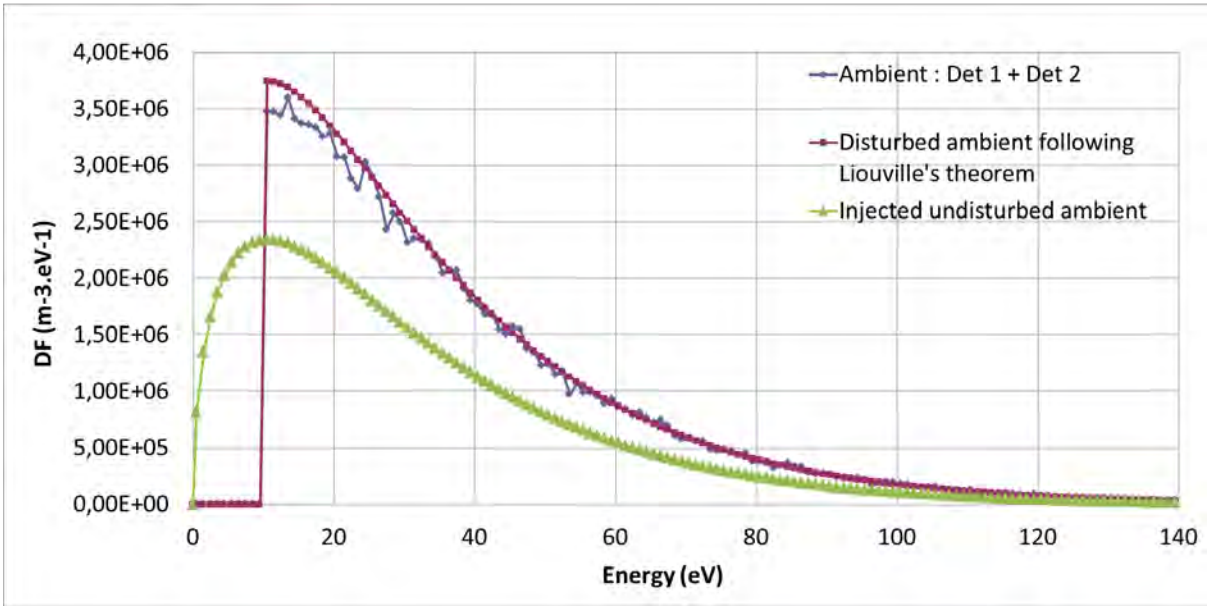

Figure 5.12: Case 2: measured and theoretical energy distribution functions of ambient electrons (energy resolution of 1 eV).

illustrated on Figure 5.10.

The resulting measured energy distribution functions plotted on Figure 5.11 show as expected the threshold due to the 10 V of positive charging on the detector surfaces, and the functions remain symmetric. On Figure 5.12 the transformation of the injected environment (green curve) to the expected analytical function following Liouville's theorem (red curve), assuming that all impacting velocities on the detectors correspond to an existing trajectory coming from the undisturbed and isotropic plasma, is identical to what has already been presented in section 3.4. Compared with the ambient density n_0, the integration of the theoretical red curve gives an increased density of $1.35 \times 10^8\,\mathrm{m}^{-3}$: about 30% higher than n_0. In section 3.4 where the attracting detector potential was of the same order (+10 V) as that the electron energy (10 eV) the computed density increase compared with the actual density n_0 was calculated to be as high as 58%. In this Case 2 the attracting potential represents only half of the electron temperature $kT_{e,0} = 21.37\,\mathrm{eV}$, which explains why the density increase is less important.

A first gap between the expected and the measured functions appears on this last Figure 5.12. A discrepancy is visible when comparing the expected measurement (red curve) and the effective measured one (blue curve): between 10 and ∼40 eV the measured function is lower than expected. The gap is confirmed by the density comparison between those two functions (Liouville and measured) giving respectively 1.35×10^8 and $1.31 \times 10^8\ \mathrm{m}^{-3}$, which is a difference of 3.3%. The reason is that the Liouville's estimation of the collected distribution function is valid for a single charged collecting surface alone in the plasma, while in this study it is an instrument box with a 3D geometry, with several surfaces between the two detector plates. When the instrument box is entirely positively charged, its attracting potential for electrons makes all the surfaces (and not only the two plane detectors performing the measurements) attract the particles. Thus the currents collected by the top, bottom and side surfaces, just behind each detector face (see figure 5.5), are lost and not accounted in the measurements. The position of the non detecting faces combined with their positive potential make them collect

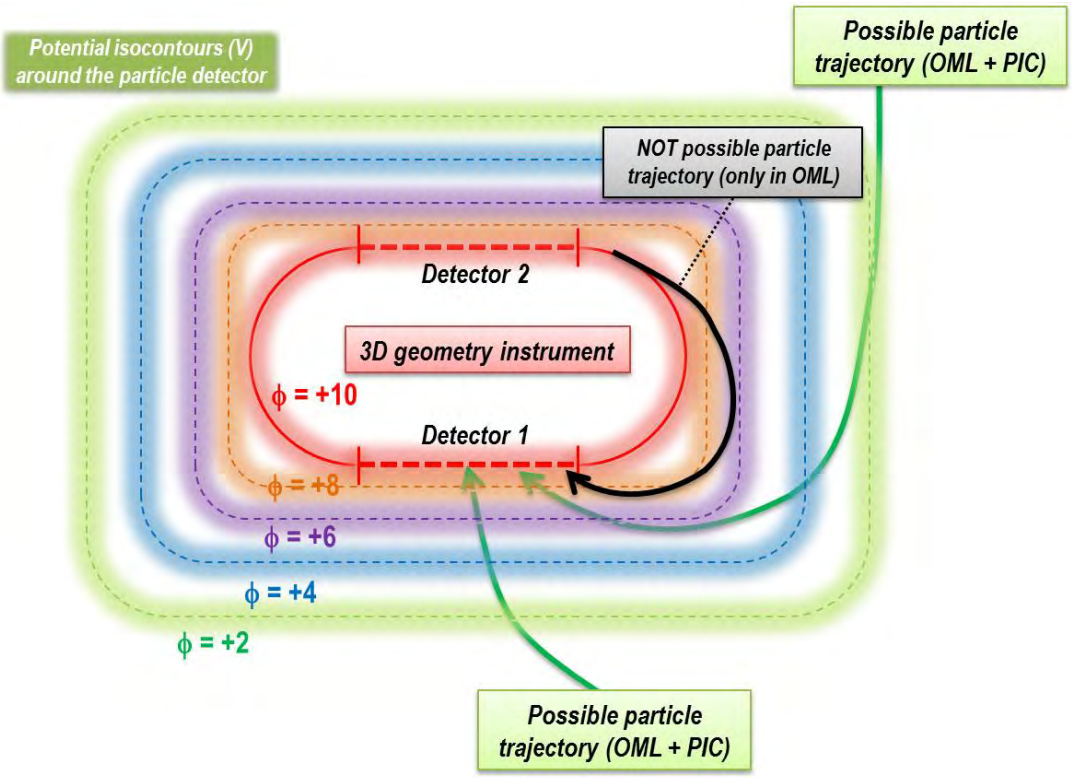

Figure 5.13: Case 2: Sketch illustrating the approximate OML theory for this simple 3D situation. In this top view of the instrument charged at +10 V, some trajectories (green lines) are possible in both OML theory and PIC simulation but others (as the black line) cannot exist.

the electrons that should have impacted the detector 1 or 2 with their velocity direction nearly tangent to the detecting surfaces. This lack of information clearly appears in the results and especially in the low energy range (below 40 eV in this case) for which electrons are the most easily deflected. Actually the non-detecting surfaces represent a bigger area than the true detector surfaces. This is illustrated in Figure 5.13, showing a top view of the instrument, surrounded by different potential contours between +10 V and 0 V. The black line is a typical example of an electron trajectory, considered in Liouville's theory, that cannot be possible in this 3D geometry with other attracting surfaces. With this geometry model at an attracting potential, the OML theory validity is no longer valid which appears on the measurements by a loss of information.

The measured energy distribution function has a mean energy of 38.3 eV, instead of the ambient $3kT_{e,0}/2 = 32.05$ eV. This phenomenon has already been showed in section 3.4 where the attracting potential of a single detector analytically shifts the measured mean energy of the collected distribution function.

5.5.2 Negative potential effect: Case 3

Changing now the null ϕ_D potential of the first Case into a negative -10 V potential, the results are presented on Figures 5.14, 5.15 and 5.16.

This time the measured energy distribution function perfectly fits the expected function

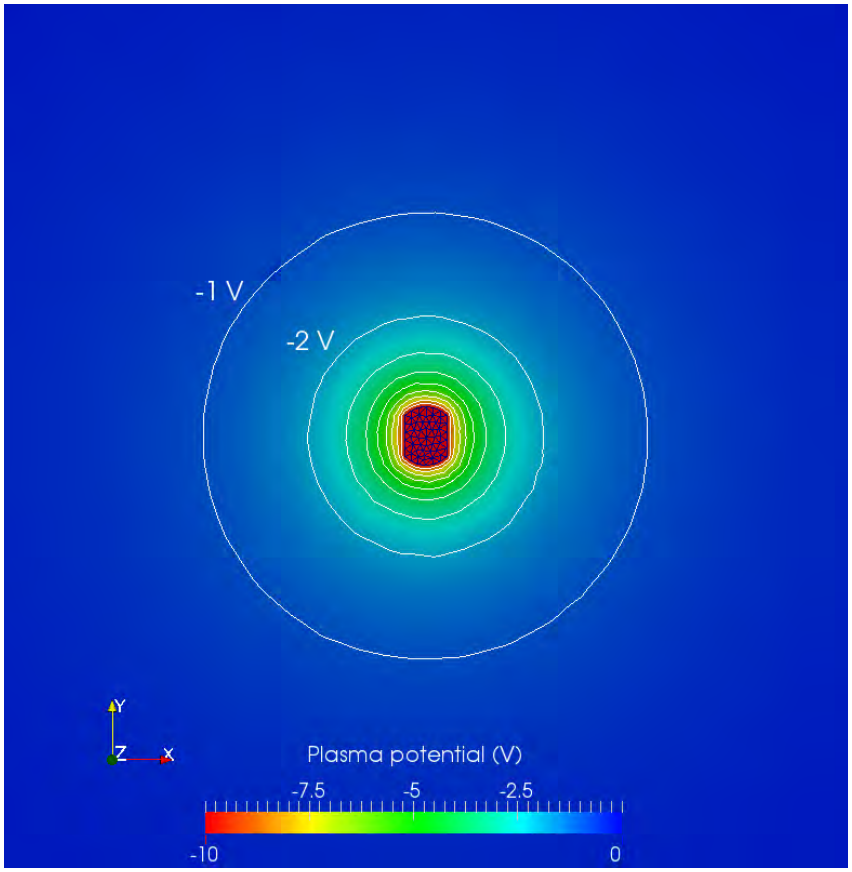

Figure 5.14: Case 3: plasma potential around the instrument (at $\phi_D = -10\,\mathrm{V}$) in the $X - Y$ plane. Potential isocontours are also represented.

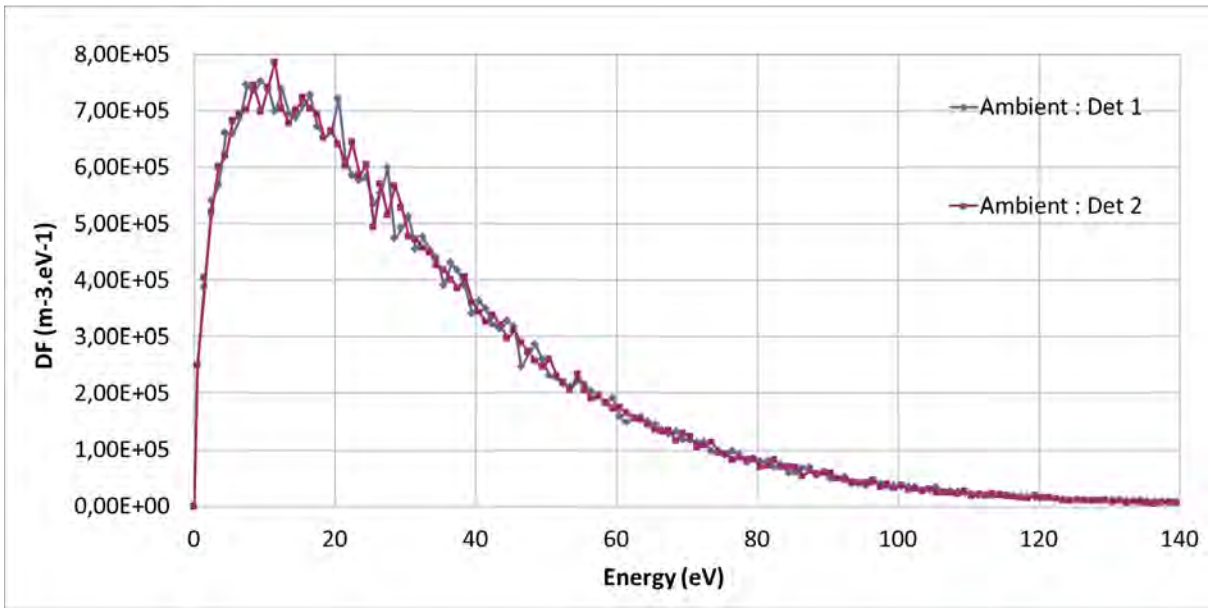

Figure 5.15: Case 3: measured energy distribution functions of ambient electrons (energy resolution of 1 eV).

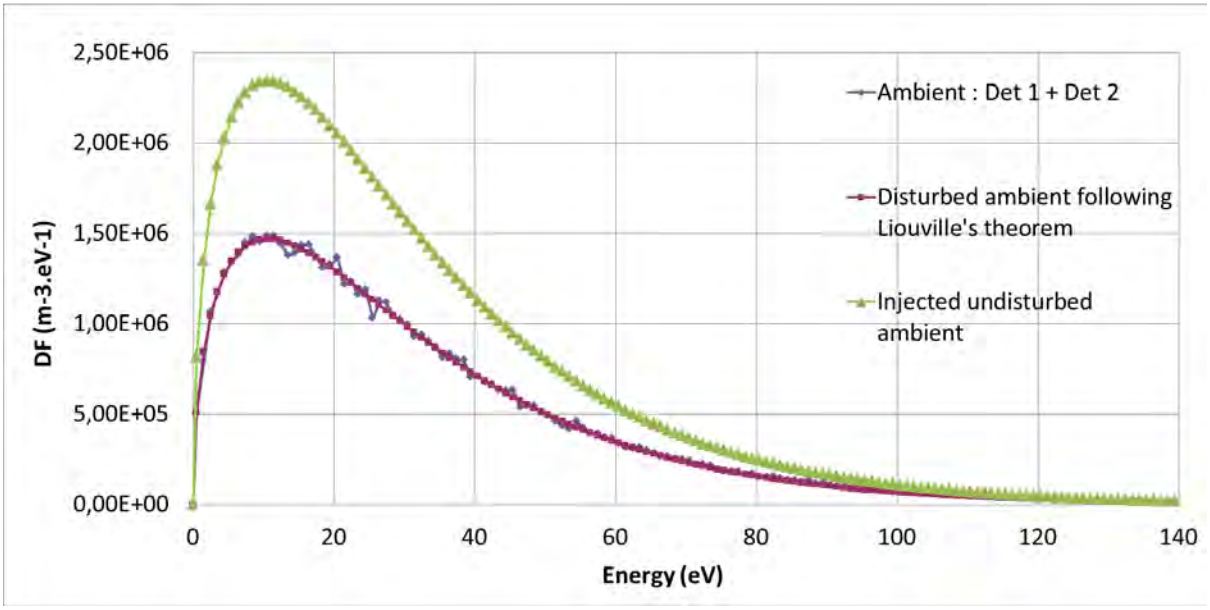

Figure 5.16: Case 3: measured and theoretical energy distribution functions of ambient electrons (energy resolution of 1 eV).

in a repulsive potential (see plot 5.16). The phenomenon exhibited in the previous attracting case and resulting in a lack of measured information does not occur here. Indeed in the present simulation all surfaces of the instrument repel electrons with the same intensity. And the lowest energetic particles (below 10 eV) cannot reach the detector surrounding area. The distribution function of particles as a function of energy shown in Figure 5.16 are lower than what they would be in an unperturbed plasma, due to the repulsive potential ϕ_D that prevents any collection of electrons with energies lower than 10 eV. This low energy population is lost which appears as a density decrease in the measurements: $6.49 \times 10^7\,\mathrm{m}^{-3}$ (as for Liouville's expectation) regarding n_0 (1.036×10^7 m^{-3}), and it constitutes a loss of 37.4%. Particles detected with a final kinetic energy E_D had initially $E_\infty = E_D$+10 eV. The measured particles have a mean energy of 32.05 eV, as for particles in the unperturbed environment. Indeed the Maxwellian is transformed in a Maxwellian with same temperature and multiplied by the Boltzmann factor, see section 3.4. If one of the instrument non detecting surface were charged at a more negative potential that ϕ_D on the detector surface, the measured energy distribution function (blue curve) would have been inferior to the one expected (red curve) because of the increased repelling effect of these surfaces nearby the detectors.

5.5.3 Photoemission: Case 4 and 5

5.5.3.1 Photoemission and attracting potential at +3 V: Case 4:

In this Case 4 simulation the photoemission is activated, with a corresponding solar flux at this heliocentric distance of 0.28 AU thus 12.76 times the flux at 1 AU (it gives a photoelectron current density j_{ph0} of about $260\,\mu A/m^2$). The sun is practically aligned with the X axis, meaning that detector 1 is on the sunlit side and detector 2 is shadowed. The sun direction has been slightly shifted in the $+Z$ direction in order to allow the emission of photoelectrons from the top surface of the instrument box and increase their quantity regarding a test simulation

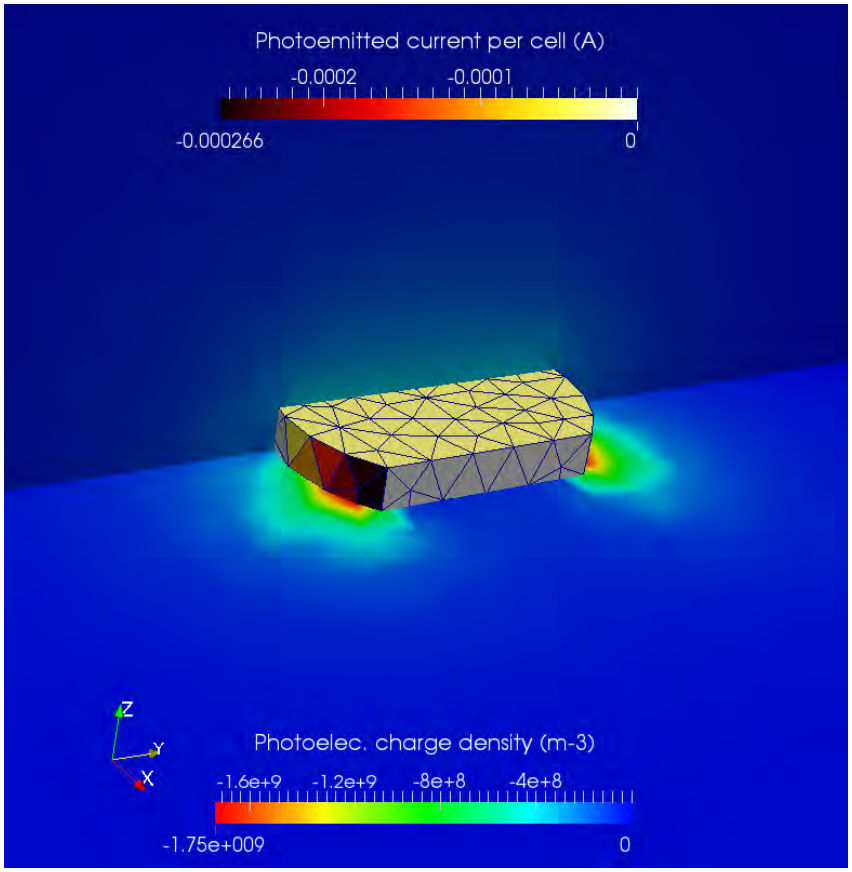

Figure 5.17: Case 4: Photoelectron density in the $X-Y$ and $Y-Z$ planes. The emitted current of photoelectron per instrument cell element is also represented (actually in A/m^2).

with a purely X-aligned Sun direction. No detector surfaces are allowed to emit photoelectrons, they can only collect those particles.

The instrument electrostatic potential ϕ_D has been set at $+3\,\mathrm{V}$, as previous and not reported tests with a zero potential did not allow to recollect any of the photoelectrons on the detectors: all those particles could escape the instrument vicinity owing to their characteristic temperature $kT_{ph} = 3\,\mathrm{eV}$ (and no photoelectrons are emitted from the detectors themselves).

Figure 5.17 displays the photoelectron density in the vicinity of the instrument in the $(X-Y)$ and $(Y-Z)$ planes and the photoelectron current emitted per instrument surface elements (in $\mathrm{A/m^2}$). Only the curved sides of the instrument (and its top face in lower quantity) generate photoelectrons. Depending on their kinetic energy, photoelectrons can escape the instrument vicinity or not. Each time it gets farther from its originating attracting surface, it is slowed down and if finally the velocity becomes tangent to an equipotential, the photoelectron cannot escape farther and gets back to the attractive potential (see the trajectories of collected photoelectrons on Figure 5.18 and the collected distribution functions on Figure 5.19). On this last Figure two sets of distribution functions are plotted. The first set (dashed lines) was configured with a low energy resolution (1 eV), the second with a higher resolution of 0.1 eV, to refine the results and better distinguish the collection peaks. Note that the lower resolution suggests that some particles are collected with kinetic energies as high as 3.5 eV: this is simply an interpolation issue, without any reality. Indeed photoelectrons with an energy greater than 3 eV are all definitely

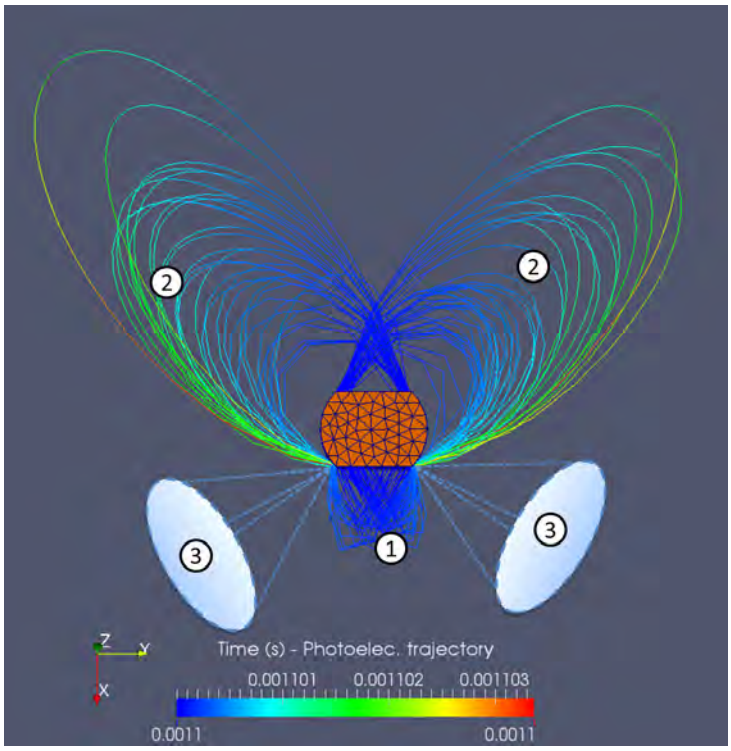

Figure 5.18: Case 4: trajectories of collected photoelectrons (top view). (1): Low energy photoelectrons (below ∼1.5 eV) collected by detector 1. (2): Photoelectrons of higher energies (1.5 - 3 eV) collected by detector 2. (3): loss cone of photoelectrons: if the particle initial velocity is oriented within this range of directions, and is associated to a kinetic energy of at least 3 eV, it can escape the instrument attracting potential.

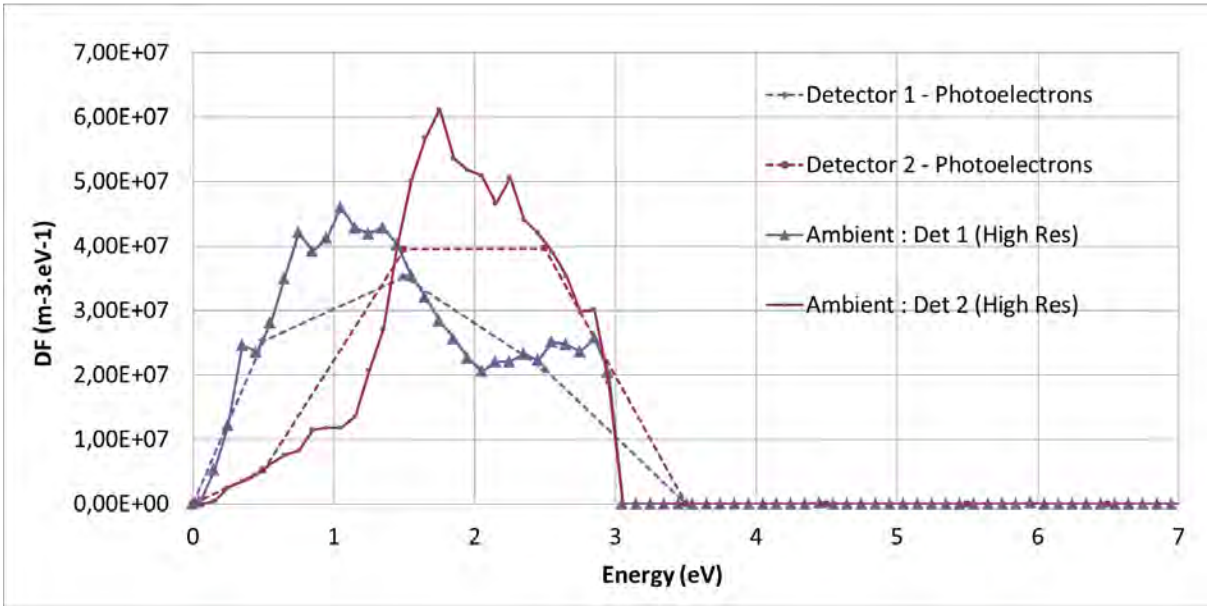

Figure 5.19: Case 4: measured energy distribution functions of photoelectrons. Dashed lines: low energy resolution of 1 eV. Full lines: high energy resolution of 0.1 eV.

ejected, because the instrument potential is not sufficient to attract them and because of the convex shape of the instrument. The integration of the functions for low and high energy resolutions provides the same densities and mean kinetic energies.

The trajectories plotted on Figure 5.18 are those with the most important weight, this is the reason why practically no trajectories come from the top face, as this surface emits less photoelectrons than the instrument angles, due to a tangent incidence of the UV flux. It is also noticeable that detector 2 catches more photoelectrons of higher energies than detector 1. This is explained by the geometrical distance between the location of the most important photoemitting areas and the detectors. The main photoelectron source, on the two curved edges of the instrument (on the $+X$ side), are just next to detector 1 entrance. The lowest energetic photoelectrons will thus be rapidly recollected by detector 1 (below ∼1.5 eV according to Figure 5.19) or on near other surfaces after extremely short trajectories. The few photoelectrons below 1 eV on detector 2 are originating from the top sunlit face. Particles with higher energies have two ways out; 1/ they are ejected out of the edge with inclined velocity vectors regarding the surface normal and might travel over a long parabolic orbit (or over several loops) before impacting detector 2 or another surface; 2/ the initial velocity has a sufficient perpendicular component for crossing the equipotential contours and can escape the attracting system. The fact that shadowed detectors might sometimes collect more photoelectrons that sunlit detectors has to be kept in mind: the electrostatic potential field around a satellite can deviate low energy particles along complex trajectories and thus mislead measurement interpretation.

The analysis of the measured photoelectron population gives a density of 1.67×10^8 m^{-3}, greater than n_0, and a mean kinetic energy of 1.72 eV (corresponding to a measured average temperature kT_{ph} of 1.14 eV). The generated photoelectrons have been initially configured with $kT_{ph,0} = 3$ eV ($3kT_{ph,0}/2 = 4.5$ eV), but the detected ones are those which succeeded in escaping the positively charged surfaces just after their emission. As those particles are emitted by and collected on surfaces at the same potential (+3 V), they keep the same kinetic energy: $E_{\text{emit}} = E_{\text{coll}}$.

The measurements exclusive to ambient electrons are similar to the ones obtained previously with Case 2, except that in Case 4 the attractive potential ϕ_D is limited to +3 V (and not +10 V as in Case 2). This appears on the shifted measured ambient electron distribution function (Figure 5.20). Consecutive estimations of ambient electron density remain consistent with attractive potential situation: the measured density is of 1.13×10^8 m^{-3} (9% of increase regarding n_0) and the mean energy reaches 33.44 eV (instead of 32.05 eV for the injected electron population). The difference between the red and blue curves (which stands for the underestimation of the measured electrons regarding Liouville's theory due to additional attracting surfaces) is still present in this Case 4, even though it is not as strong as in Case 2 due to the lower ϕ_D value in this simulation.

However the addition of the measured photoelectrons highly disturbs the electron signal. In reality photoelectrons are not distinguished from the ambient measured electrons by the detectors as all those particles remain electrons, independently of their origin. The sum of the electron and photoelectron measured populations is displayed on Figure 5.21. Below ∼3 eV, the electron measurement are completely overwhelmed by the photoelectron flux. This low energy peak however stands out visibly from the expected Maxwellian distribution, and can thus logically be considered as a parasite detected population.

Integrating the total measured energy distribution function gives an erroneous density of 2.80×10^8 m^{-3}. The photoelectron population combined with the +3 V attracting instrument potential generates a density overestimation of 170% regarding n_0, but ignoring all electrons

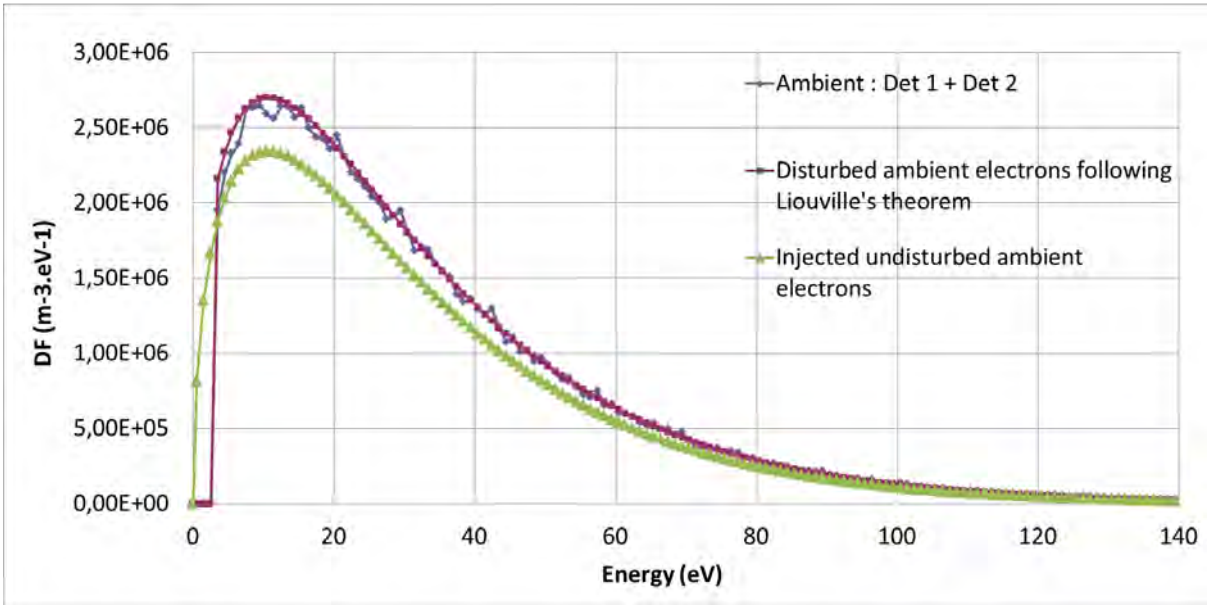

Figure 5.20: Case 4: measured and theoretical energy distribution functions of ambient electrons (energy resolution of 1 eV).

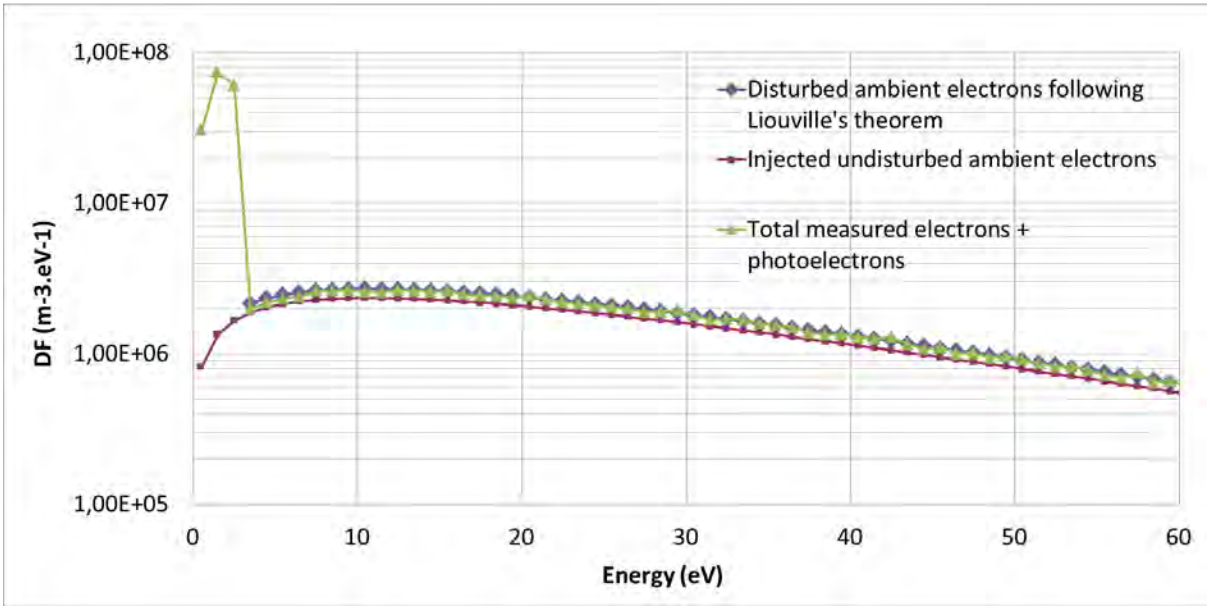

Figure 5.21: Case 4: measured and theoretical energy distribution functions of ambient electron and photoelectron populations (energy resolution of 1 eV). A logarithmic scale has been used here to distinguish all curves.

below 3 eV in the integration allows to get back to the previous 9% of overestimation due to the attracting potential (indeed below 3 eV: no ambient electrons are measured by the detectors). Performing the density and mean kinetic energy calculations on the low or high energy resolution only changes marginally the obtained values (of less than 1%).

5.5.3.2 Photoemission and attracting potential at +10 V: Case 5

The same configuration as Case 4 is used, but now with an attracting potential set constant at +10 V. As it is displayed in Figure 5.22, all the photoelectrons caught by detectors 1 and 2 had initially extremely skimming trajectories. Depending on their kinetic energy at emission and their direction they will reach one of the two detectors as explained in the previous Case 4. In this situation the measured photoelectron spectrum covers the energy range 0-10 eV (see Figure 5.23 with two energy resolutions: dashed curves for the 1 eV and full curves for the 0.1 eV resolution). The asymmetric measurements for detectors 1 and 2 are still present, even though now detector 2 collects fewer photoelectrons than the first surface, since the mean kinetic energy of photoelectrons (4.5 eV) is less than the energy needed to escape the 10 V attractive potential on the instrument. The recollection of photoelectrons by the entire instrument is highly increased here compared with the previous ϕ_D value of +3 V, practically no photoelectron (except the few ones coming from the energetic tail of the emitted distribution function) can escape the system. The measured mean energy of photoelectrons is now raised to 4.77 eV ($kT_{ph} = 3.14$ eV), and the density to 3.16×10^8 m^{-3}. The resulting aberration on the total electron populations measured by the instrument is an increase of 330% compared to n_0 (see Figure 5.24). As expected, no ambient electrons are detected below 10 eV, corresponding to the threshold imposed by $\phi_D = +10$ V. All the particles detected under 10 eV are photoelectrons, and can thus be considered as parasite particles in the data post processing.

5.5.4 Secondary electron emission: Case 6

We now investigate the effect of secondary electron emission (SEEE) instead of photoemission (which is deactivated). The electrostatic potential of the instrument ϕ_D had also to be held constant at a positive potential (+3 V) to recollect some secondary electrons. The detector surfaces 1 and 2 do not emit secondary electrons. Theoretically, both detectors 1 and 2 should measure the same flux of those parasite particles (emitted isotropically with a temperature $kT_{\mathrm{se},0}$ of 2 eV). With this ambient electron environment the secondary electron emission yield δ_{e} for the chosen covering material of the instrument (ITO) is around 0.5 (see Figure 5.25). Results of the measured energy distribution functions are presented in Figures 5.26 for the SEEE and 5.27 for all electrons. The SEEE detection already looks more symmetric compared to the previous photoelectron studies. The measured mean kinetic energy of secondary particles is evaluated at 1.6 eV (compared with the emission model at 3 eV) and the density reaches 8.46×10^7 m^{-3}. The parasite particles represent an increase in the estimated total density of 91% compared to n_0, and of 72% compared to the Liouville's theory of the ambient environment. In this specific environment the secondary electron emission has a lower disturbing effect on electron measurements, compared with the photoemission in the previous cases.

In Figure 5.27 the results obtained by setting ϕ_D at +10 V are plotted with the dashed curves, where the dispersion of the SEEE measured energy distribution function is illustrated with the increase of the attracting potential. The measured density of secondary electrons is in this case of 1.17×10^8 m^{-3} (38% of increase compared with the collected SEEE at +3 V) which

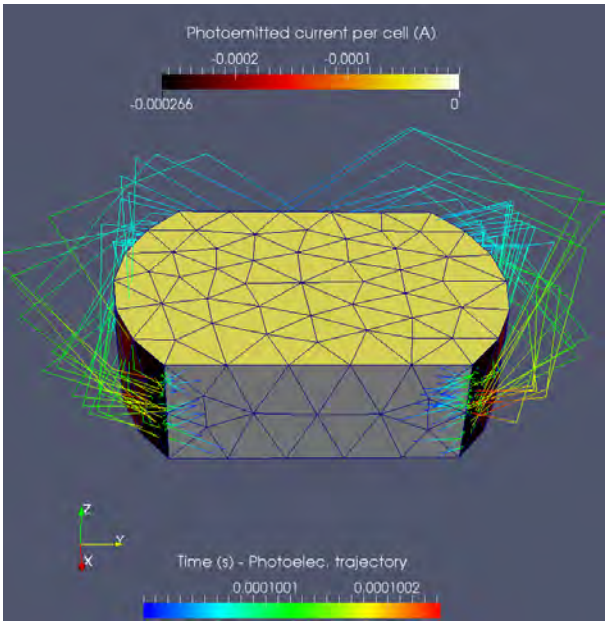

Figure 5.22: Case 5: trajectories of collected photoelectrons. Photoelectrons are confined to the extreme near vicinity of the instrument because of its strong attracting electrostatic potential (+10 V) regarding the mean kinetic energy of emitted particles (4.5 eV). All detected phototelectrons had initially skimming trajectories, as others ejected normally to the surfaces are recollected on the same areas, and practically no photoelectron has a sufficient energy to escape ϕ_D. Note that the tooth-shaped trajectories is only due to the frequency used to output the trajectory points. Computed trajectories are smoother, as in Figure 5.18.

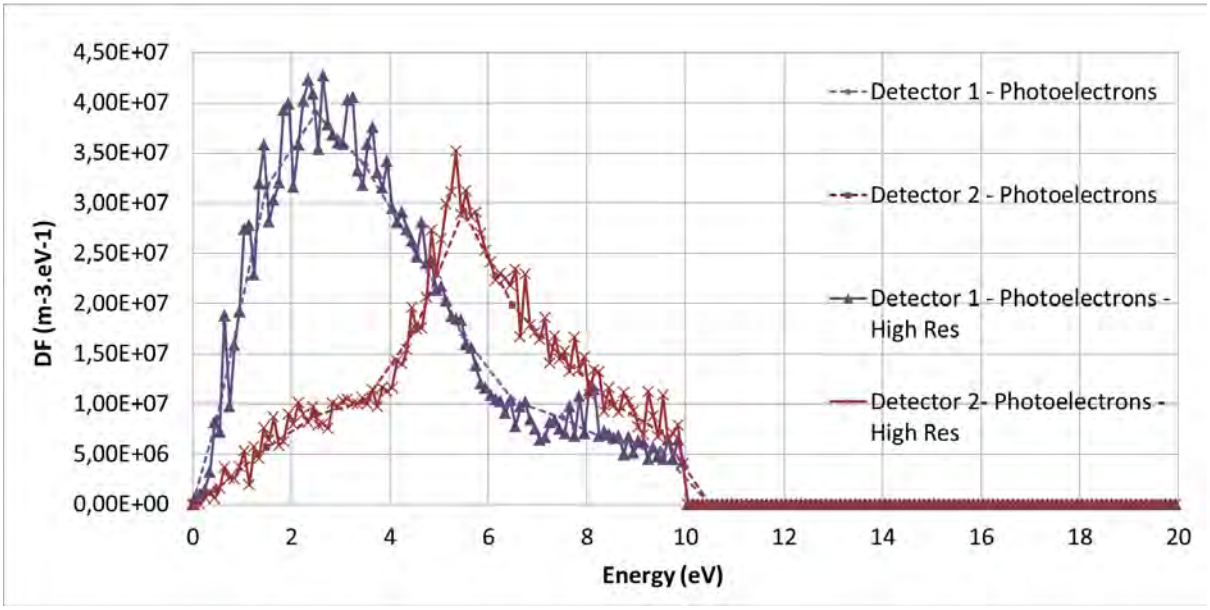

Figure 5.23: Case 5: measured energy distribution functions of photoelectrons. Dashed lines: low energy resolution of 1 eV. Full lines: high energy resolution of 0.1 eV.

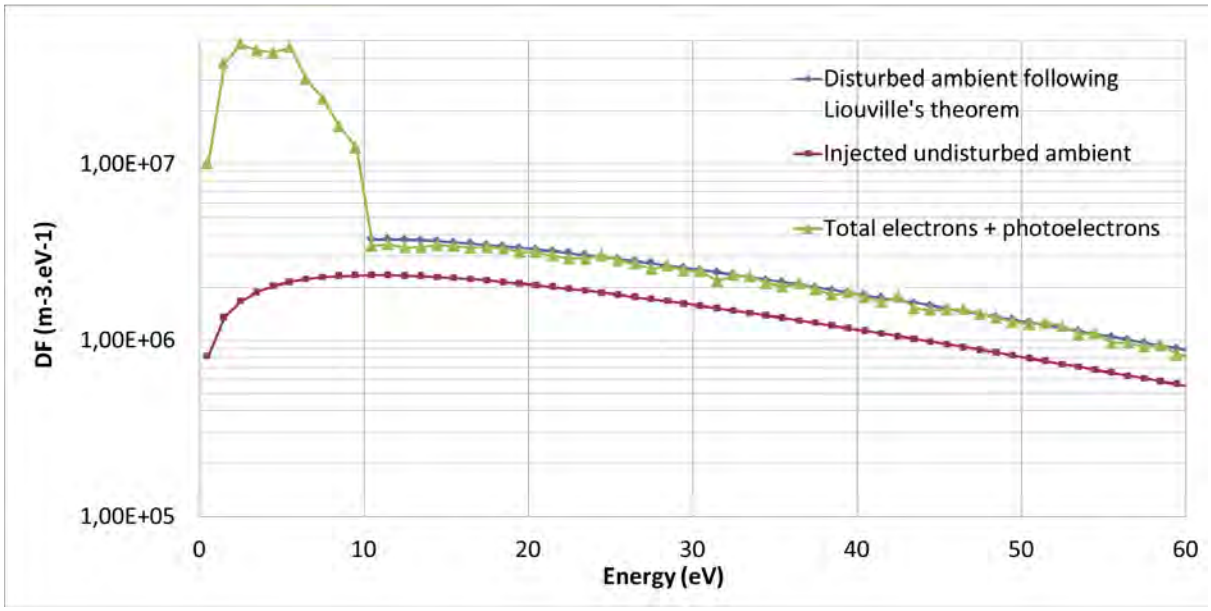

Figure 5.24: Case 5: measured and theoretical energy distribution functions of ambient electron and photoelectron populations (energy resolution of 1 eV). A logarithmic scale has been used here to distinguish all curves.

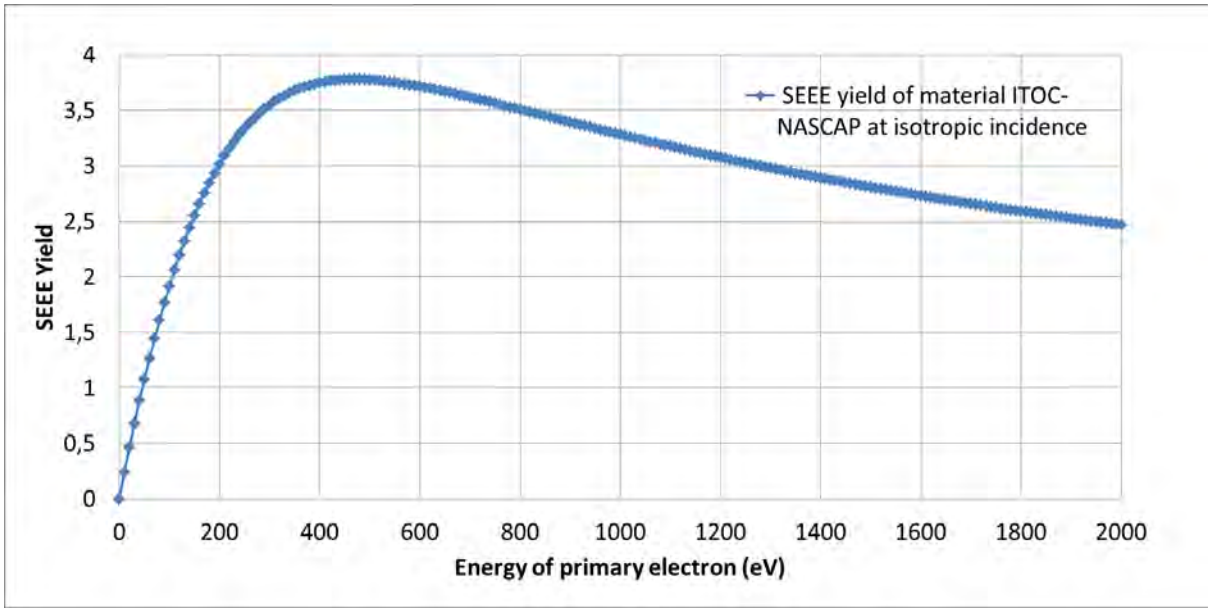

Figure 5.25: Case 6: secondary electron yield δ_e for the ITO material used in the Case 6 simulation.

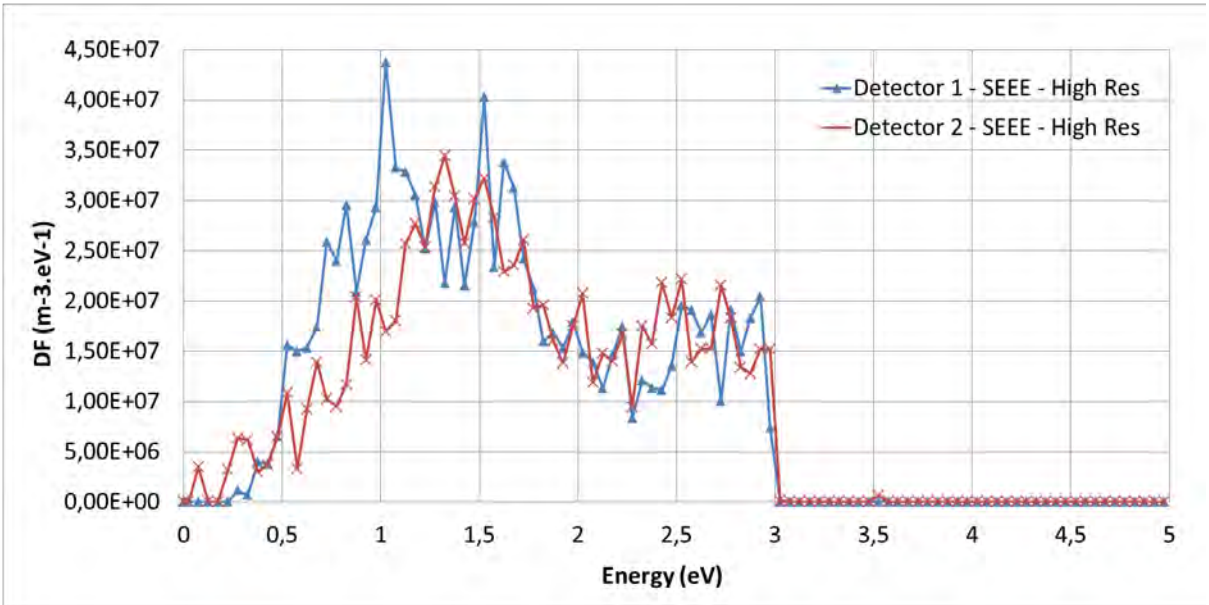

Figure 5.26: Case 6: measured energy distribution functions of secondary electrons. The curves are plotted using a 0.05 eV resolution. The minor differences come from: 1/ the discretisation method of the phase space and 2/ from the current map of SEEE, obtained after the full PIC treatment of the plasma, necessarily noisy due to the mesh refinement in the vicinity of the detectors.

gives a total measured electron density increased of 138% with respect to n_0 (91% when the instrument was set at +3 V). Even at a higher attracting potential, secondary electrons are in this environment less disturbing than photoelectrons.

5.5.5 Combined effect of SEEE and photoelectrons: Case 7

The activation of both secondary electron emission and photoemission is analysed in the present Case 7. The emission models are the same than Cases 4, 5 and 6. The electrostatic potential of the instrument ϕ_D still has to be set positive (at +3 V here) to recollect some the emitted particles.

The results obtained are simply the sum of the previous separated configurations, because there are no effects of space charge that could have modified the potential map. In the presence of a local potential barrier generated by a combination of secondary and photoelectron density, results might be different. The measured energy distribution functions of SEEE and photoelectrons are displayed in Figure 5.28. As showed in the previous Cases : photoelectrons are more abundant than secondary electrons. Same observations can also be made regarding the energy threshold of detection (0 - 3 eV) due to the instrument electrostatic potential. SEEE are still collected symmetrically, contrary to photoelectrons. The total collected distribution functions are plotted in Figure 5.29, and gives a final density of 3.61×10^8 m^{-3}, 248% higher than the initial n_0. When increasing the potential to +10 V (see the dashed curves on the same Figure), the synthetically density exceeds n_0 by about 435%.

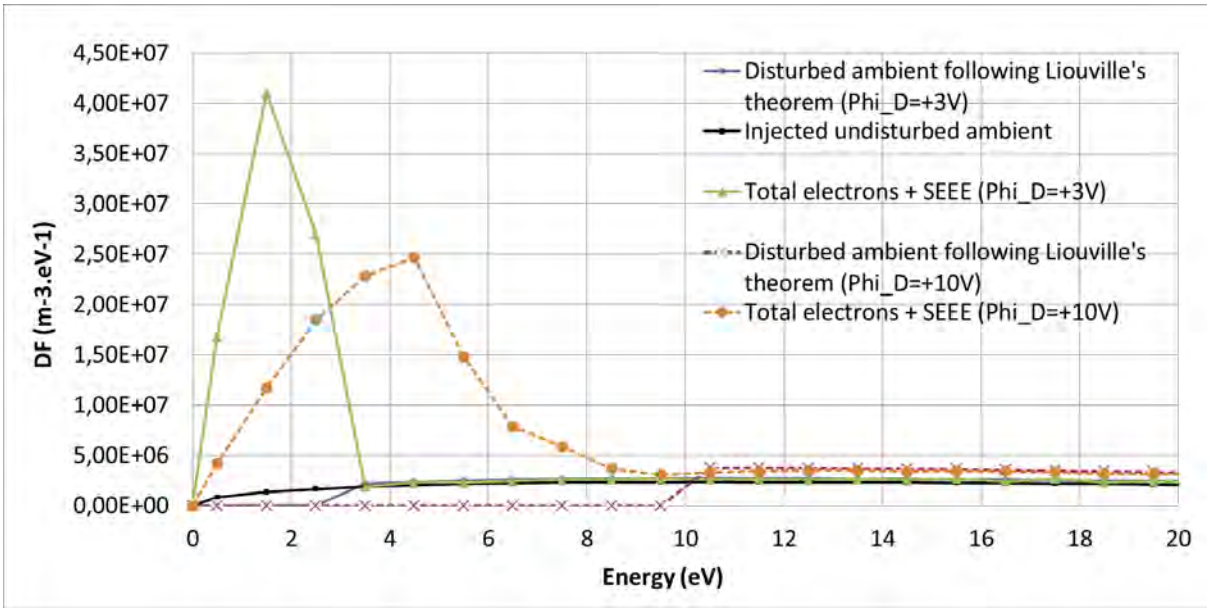

Figure 5.27: Case 6: measured and theoretical energy distribution functions of ambient electron and secondary electron populations, plotted with a resolution of 1 eV, for $\phi_D = +3$ V. Results for $\phi_D = +10$ V are plotted with the dashed curves.

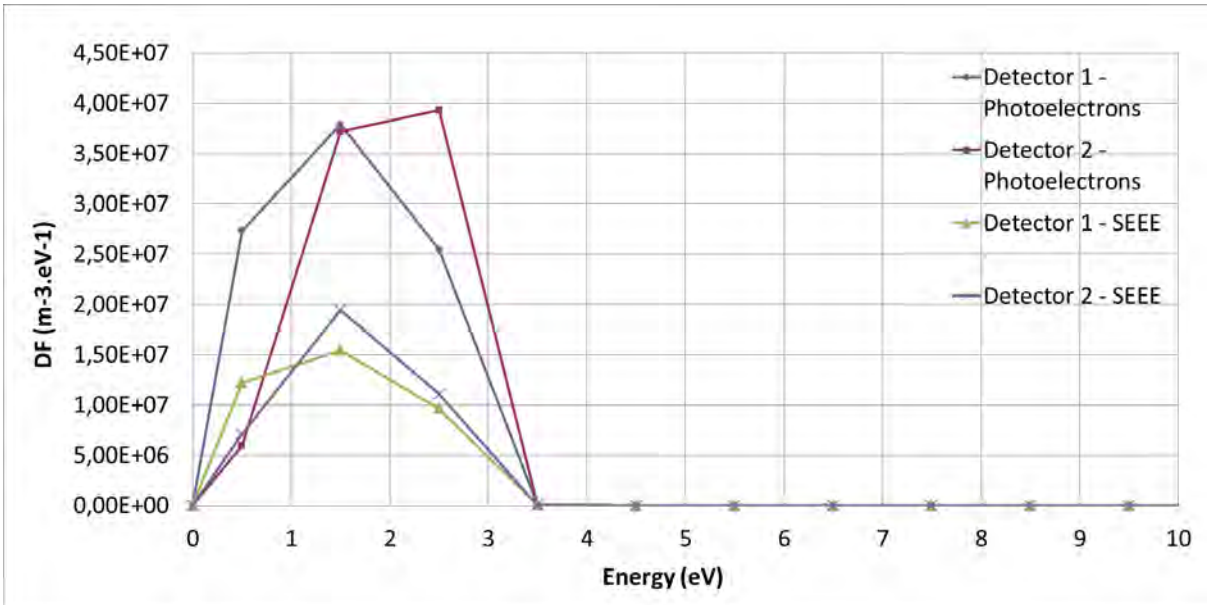

Figure 5.28: Case 7: measured energy distribution functions of secondary and photoelectrons. The curves are plotted using a 1 eV resolution.

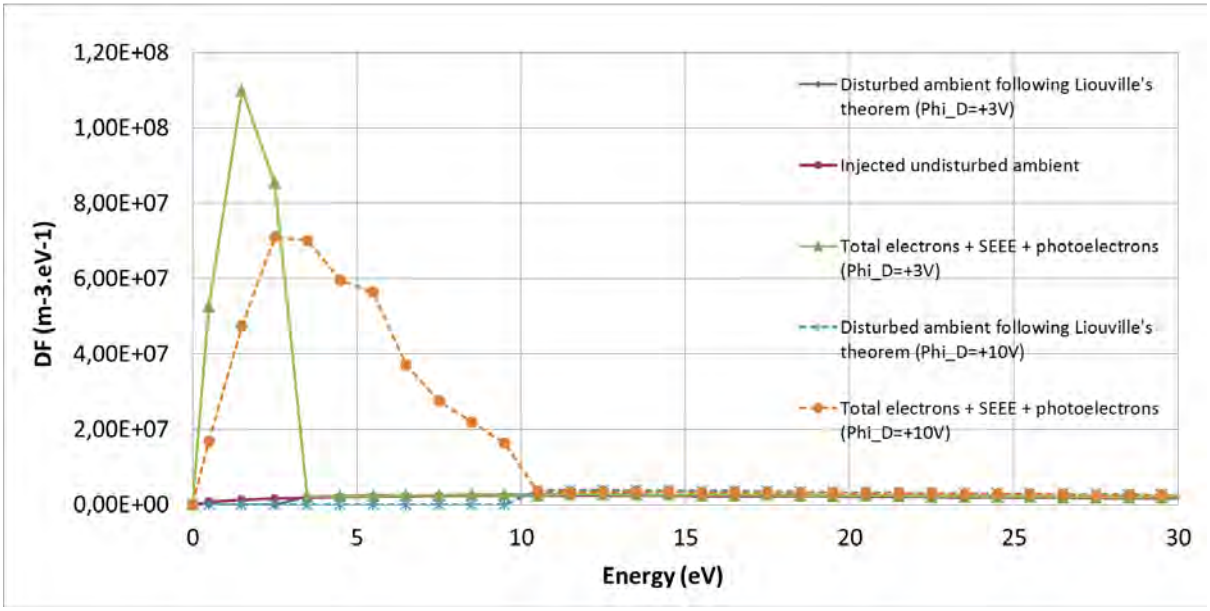

Figure 5.29: Case 7: measured and theoretical energy distribution functions of ambient, secondary and photoelectron populations, plotted with a resolution of 1 eV, for $\phi_D = +3$ V. Results for $\phi_D = +10$ V are plotted with the dashed curves.

5.6 Undisturbed non isotropic Maxwellian plasma: Case 8

In this Case 8 the effect of a drifted Maxwellian electron population - a non isotropic velocity distribution function - is investigated on particle detector measurements. The point of this simulation is not to discuss the realism of this environment at this heliocentric distance, this will be done through a specific Solar Orbiter simulation with a Kappa distribution function for ambient electrons later on (in chapter 6). This is why the simulated environment here remains based on the parameters used in sections 5.4 and 5.5 ($n_0 = 1.036 \times 10^8$ m^{-3} and $kT_{e,0} = 21.37$ eV), but this time a mean electron velocity component has been added to the ambient population. It is simply the application of equation 2.1, setting the mean velocity $\mathbf{u}$ to -2×10^6 m.s^{-1} along the X axis (the ratio between the average and thermal velocities gives $u/v_{th} = 0.73$). This average macroscopic velocity corresponds to a kinetic energy of 11.47 eV. In this configuration detector 1 should measure a stronger electron flux than detector 2, which accepts the incoming electrons with a positive velocity component. This simulation is configured with a null instrument electrostatic potential and without any secondary or photoemission.

One important point is to model the theoretical undisturbed electron distribution function expected on the detectors, to reproduce the type of Figures already used in the previous simulation output presentations. Even though the analytical formula expressed in equation 2.1 gives directly the velocity distribution function for a non zero $\mathbf{u}$ vector, the SPIS instrument outputs are given as functions of energy. The conversion method expressed in equation 3.45, allowing to move from $f_V(V)$ to $f_E(E)$ by multiplying the first function by $4\pi V/m$ is not appropriate if the $\mathbf{u}$ term in $f_V(V)$ is non zero. Indeed in that situation one energy value E might correspond to several velocities $|\mathbf{v} - \mathbf{u}|$. The construction of the matrix $[E, f_E(E)]$ for a non isotropic population has thus to be performed numerically.

The algorithm used is as follows:

1. Creation of:
   - three identical velocity components $V_{X,i}$, $V_{Y,j}$, $V_{Z,k}$, taken here to be from -6×10^6 to 6×10^6 m.s^{-1}, in steps of 2.4×10^5 m.s^{-1}, and with indices $i, j, k \in [1; 51]$
   - the mean X component of the velocity $u_X = -2 \times 10^6$ m.s^{-1}
2. Computation of three dimensioned matrices, each element of which corresponds to a specific ($V_{X,i}$, $V_{Y,j}$, $V_{Z,k}$) triplet:
   - the speed $V_{i,j,k} = |\mathbf{v}| = (V_{X,i}^2 + V_{Y,j}^2 + V_{Z,k}^2)^{1/2}$. The $V_{i,j,k}$ matrix has several identical values for different i, j, k indexes (corresponding to the same speed but with different orientations)
   - the random speed $c_{i,j,k} = |\mathbf{c}| = |\mathbf{v} - \mathbf{u}| = \left[(V_{X,i} - u_X)^2 + V_{Y,j}^2 + V_{Z,k}^2\right]^{1/2}$
   - the kinetic energy $E_{i,j,k} = \frac{1}{2} m V_{i,j,k}^2$. Note that $E_{i,j,k}$ also has several identical values for different i, j, k indexes.
   - the velocity distribution function $f_V(V_{i,j,k})$:
   $$f_V(V_{i,j,k}) = n \left(\frac{m}{2\pi k T}\right)^{3/2} \exp\left(\frac{-m c_{i,j,k}^2}{2kT}\right)$$
   - the energy distribution function $f_E(E_{i,j,k}) = (4\pi V_{i,j,k}/m) f_V(V_{i,j,k})$
3. The next step consists in transforming the previous 3D matrices into 1D vectors in order to plot the requested $[E, f_E(E)]$ curve. It is then necessary to reorder $E_{i,j,k}$ in ascending order:
   - This process generates the new one dimensioned $E2_a$ vector ($a \in [1; 51^3]$) and the associated L_a vector which gives for each $E2_a$ element the corresponding indexes of the associated $E_{i,j,k}$ value. The generated $E2_a$ vector has thus some identical values for several consecutive a indexes.
   - The created L_a vector is the key to reorder the $f_E(E_{i,j,k})$ matrix in accordance with $E2_a$, obtaining correspondingly to each $E2_a$ value the appropriate vector value $f_{E2}(E2_a)$, picked from $f_E(E_{i,j,k})$
   - The calculation of $F_E(E)$ as the average of $f_{E2}(E2_a)$ for the common $E2_a$ values.

As mentioned previously: $E2_a$ has identical values for several consecutive a indexes, leading to multiple f_{E2} values for one energy bin $E2$. This issue is illustrated in Figure 5.30, with the plot of $[E2, f_{E2}(E2)]$ spectra. The average curve of $f_{E2}(E2_a)$ is also represented in this Figure, and stands for the theoretical energy distribution function of the drifted Maxwellian electron population $f_E(E)$ that should be measured by the instrument. The value of the distribution function at a given E is the average of the values obtained for each triplet ($V_{X,i}$, $V_{Y,j}$, $V_{Z,k}$) of energy E., because we set a regular discretisation.

Detector 1 and 2 results are presented on Figure 5.31: the non isotropic characteristic of the drifted electrons clearly appears here. Detector 1 is fully facing the mean velocity $\mathbf{u}$, along the $-X$ direction, generated a more important distribution function than the one measured by detector 2. The first detector gives a measured density of $n_1 = 8.78 \times 10^7$ m^{-3} and a mean kinetic energy of 46.6 eV, while the second measures $n_2 = 1.57 \times 10^7$ m^{-3} and an energy of 26.3 eV. The ratio between the two estimated densities $n_2/n_1 = 0.18$ (while $u/v_{th} = 0.73$). The strong

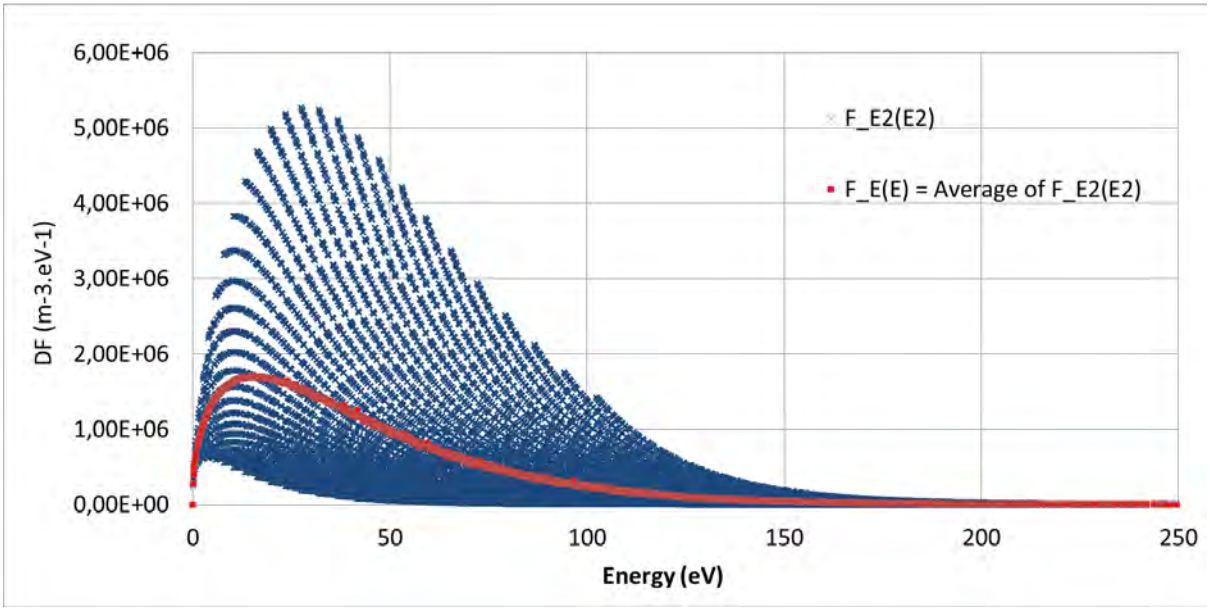

Figure 5.30: Case 8: theoretical energy distribution functions of the drifted Maxwellian electron population. The blue crosses represent the possible EDF values for each energy value (as this distribution is not isotropic: one energy bin generates several distribution function values). The red squares represent the averaged energy distribution function of the drifted Maxwellian.

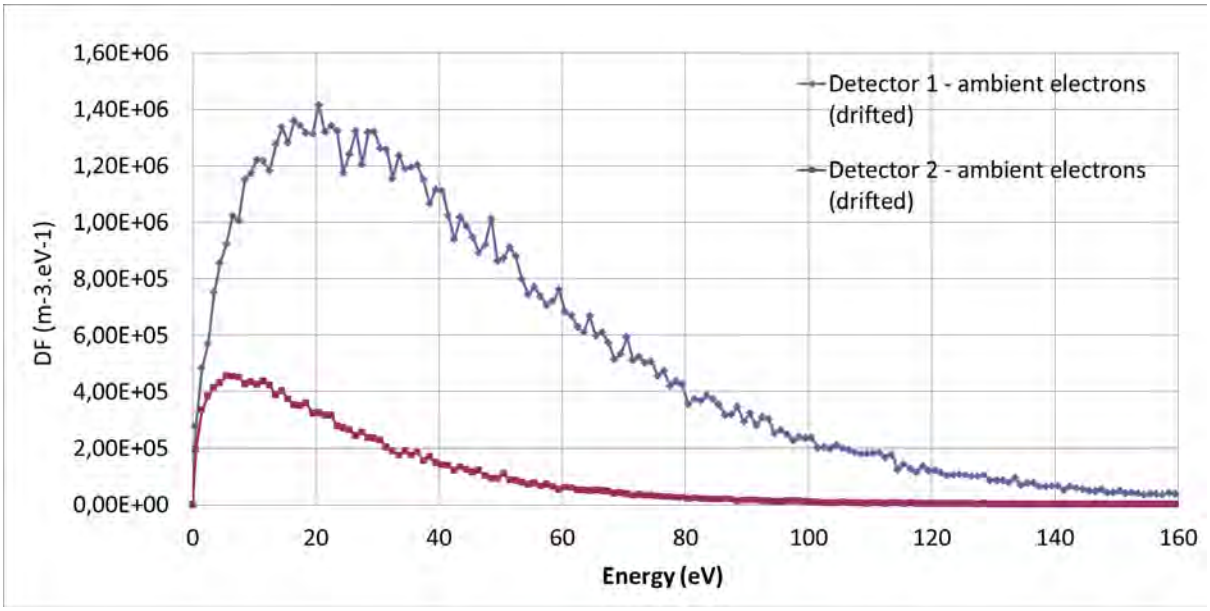

Figure 5.31: Case 8: energy distribution functions of the drifted Maxwellian electron population (measured by detectors 1 and 2), plotted with a resolution of 1 eV, for $\phi_D = 0$ V.

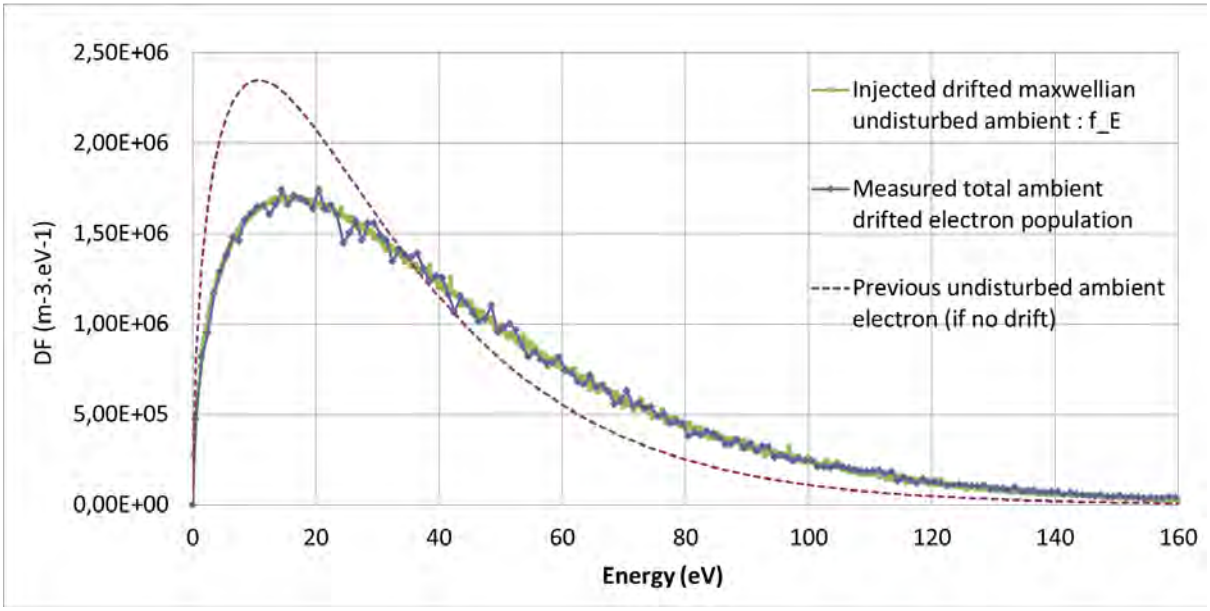

Figure 5.32: Case 8: computed energy distribution functions of the total measured drifted Maxwellian electron population, theoretical non isotropic $f_E(E)$ and a Maxwellian non drifted function, used in the previous Cases (1-7), for $\phi_D = 0\,\mathrm{V}$.

effect of the oriented average macroscopic direction (even if it remains comparable to the particle thermal velocity) on the density estimation discrepancy between the two detectors, demonstrates the importance of a full consideration of the 4π sr of the environment. The cumulated energy distribution function, compared with the theoretical drifted function and the previous isotropic function used in the previous Cases are displayed in Figure 5.32. It shows indeed that the sum of detector 1 and 2 measurements provides a clear match with the environment. The integration of the total measured energy distribution function provides the following outputs: $n = 1.035 \times 10^8$ m^{-3} (less than 0.1% difference compared with the injected n_0 and less than 3% difference compared with the density provided by integration of the theoretical curve). The measured mean kinetic energy gives 36.4 eV (corresponding to $kT_e = 24.3\,\mathrm{eV}$). The measured environment perfectly fits the analytical values obtained through the previous algorithm.

5.7 Conclusion

The effects of the main disturbances of electron measurements have been quantified in this Chapter (see the Table of numerical results on Figure 5.33). Those effects can be summarised as follows (for this chosen initial environment):

1. The attracting potential of the detector increases the measured electron density and temperature, with respect to the ambient environment parameters;

2. The repulsing potential of the detector reduces the measured electron density but does not affect the estimated electron temperature;

3. Below the attracting potential value of the detector: all the measured electrons are originating from the satellite;

Case		1	2	3	4	5	6	6-bis	7	7-bis	8
Phi_D		0	10	-10	3	10	3	10	3	10	0
n x 10^8 m-3	n0 = 1,04	1,04	1,31	0,65	1,13	1,31	1,13	1,31	1,13	1,31	1,04
Population	Density increase (%)										
elec	Liouv. # n0	0,0	30,3	-37,4	10,8	30,3	10,8	30,3	10,8	30,3	0,0
elec	Meas. # n0	0,2	26,0	-37,4	9,1	26,1	9,2	25,8	9,1	25,9	-0,1
elec	Meas. # Liouv.	0,2	-3,3	-0,1	-1,6	-3,3	-1,5	-3,5	-1,6	-3,4	3,0
elec + photo	Meas. # n0				170,2	329,9			176,2	327,4	
elec + SEEE	Meas. # n0						90,9	138,7	81,4	133,9	
All	Meas. # n0								248,6	435,3	

Figure 5.33: All Cases: results of the density measurement increases for all cases. *elec* = thermal electrons, *photo* = photoelectrons and *SEEE* = secondary electrons. *Liouv.* is the density estimation of thermal electrons according to Liouville's theory, *Meas.* is the measured density and $n0$ is the theoretical density injected in the simulation box. The density increases are estimated with and without the additional electron populations (secondary and photoelectrons). For example the above expression "*Meas. # n0 for elec and SEEE*" stands for the increase of the measured density (counting both thermal electrons and SEEE) regarding the injected undisturbed density of ambient electrons.

4. Photoelectrons are the major contaminant particles, with a non isotropic detection, if the detector is exposed to UV radiation and positively charged;

5. Secondary electrons remain isotropically detected (depending on the numerical precision) and less significant than photoelectrons (a different environment condition and/or the presence of other physical emitting objects in the computational volume might change this assertion);

6. A non isotropic Maxwellian electron population can be properly retrieved through particle measurements provided that the entire solid angle of the environment is scanned.

As explained previously, various other possible cases are conceivable, each new simulation complicating a little more the basic reference Case 1. For instance Case 8 with the drifted environment could be developed into various sub-cases including, for example, secondary electron emission (and necessarily a positive instrument charging to allow the SEEE measurements). In this sub-case the non isotropic ambient electron population would have generated a non symmetric secondary emission, contrarily to what have been presented so far with the non drifting environment. Some further simulations would include for instance potential barriers due to high local secondary and photoelectron densities, others some ion wakes (of different types and orientations), and perhaps also a physical obstacle to particle detection, such as a solar panel (which can be electrically charged, with secondary and photoelectron emission).

The possibilities are infinite. Choices had to be made in order to introduce the basic concepts of particle measurement disturbances. This parametric study constitutes a concrete application that will dictate what will be the main disturbing phenomena in complete satellite/plasma interaction simulations, as they will be simulated in the context of the Solar Orbiter and Cluster missions. Those simulations are presented in the following chapter 6.

Chapter 6

Applications

Contents

6.1 Solar Orbiter 134
6.1.1 Solar Orbiter simulations: configurations 134
6.1.2 Results analysis of SOLO at 1 AU 144
6.1.3 Results analysis of SOLO at 1 AU with a Fast Solar Wind 159
6.1.4 Results analysis of SOLO at 0.28 AU 164
6.1.5 Solar Orbiter cases conclusion 174
6.2 Cluster 175
6.2.1 Cluster simulation: configuration of the CLUS@1 AU case 177
6.2.2 Results analysis of CLUS@1 AU 185
6.2.3 Cluster simulation conclusion 197
6.3 Conclusion on scientific applications and engineering 197

In this Chapter, advanced numerical studies performed with the SPIS-SCI software are presented. There are three objectives pursued regarding those simulations: 1/ predict the future Solar Orbiter spacecraft charge within various environments, and the different effects of spacecraft/plasma interactions on low energy plasma measurements of its electron instrument; 2/ Compare simulated electron measurements of the Cluster probe to existing data in one environment; 3/ contribute to the validation of the new SPIS-SCI tools, especially of the numerical instrument module.

This work has been performed during the development and validation phase of the SPIS-SCI extension of the SPIS software. All the new numerical capabilities will be gathered within the SPIS-5 release. The context of this study was thus a European collaboration within the frame of the ESA study, and all simulations presented in this chapter contributed to the validation of the SPIS-SCI tools. The following results are extracted from the Validation Test Report (VTR) - Part I, which I produced as a deliverable expected by the ESA/ESTEC contract in the frame of the IRAP/ONERA partnership. This document (123 pages), delivered and accepted by ESA in June-July 2013, assembles all the validation case results (7 dedicated to Solar Orbiter and 1 to Cluster) but only 4 of them will be partly presented here.

One of the simulations in the VTR-Part 1 deals with a Solar Orbiter case at 0.28 AU immersed in a non Maxwellian plasma. Indeed it has been explained in section 2.1.1.2 that Kappa distribution functions (also called generalized Lorentzian functions) are more adapted to model non-thermal populations [Maksimovic et al. (2005)]. And SPIS has been recently implemented with new functionalities allowing to set as inputs user-defined distribution functions, or predefined Kappa functions, to set the injected environment in the simulation box. A simulation run has thus been performed using the Core (Maxwellian), Halo and Strahl (Kappa) electron ambient populations at 0.28 AU. The aim was at this time to provide numerical tests of those

new functionalities, through a code version still under development. Results are not oriented towards our physical interest here, and time was missing for extending this simulation. This is why we will not present this simulation results in this thesis, but it might be an extremely interesting perspective for future studies.

In the VTR a special attention has been given to show how numerical parameters could influence simulation durations, results, precision and stability, which stands out of the scientific scope presented here. Note that the second Part of the VTR, produced by The Swedish Institute of Space Physics (IRF), is devoted to the study of electric field measurements for the Cluster, Cassini and Rosetta missions.

Three validation cases concerning the future Solar Orbiter mission in different environments will be presented hereafter, plus one simulation concerning the Cluster spacecraft at 1 AU (these are the *SO* cases, for Solar Orbiter and *CL* cases for Cluster). The on-board electron instruments are also integrated to the study. For each validation case, several pre-simulations have been carried out in advance, to ensure the numerical stability according to the methodology presented in section 4.1.2. As this validation phase has been performed within the course of the SPIS-SCI development, this work contributed to the debugging of the code. Finally at least a hundred of simulations have been initiated and launched during the validation campaign.

6.1 Solar Orbiter

The ESA Solar Orbiter mission (also called SOLO in this chapter), scheduled for a launch in 2017-2018 with a NASA participation, is dedicated to solar and heliospheric physics. It has been selected within the ESA Cosmic Vision Programme 2015-2025. Solar Orbiter will study, through a combination of in-situ and remote sensing observations the heliosphere and its magnetic field, the solar wind and solar energetic particles among other phenomena. It will provide close-up, high-latitude observations of the Sun. Solar Orbiter will have a highly elliptic orbit: between 0.9 AU at aphelion and 0.28 AU at perihelion.

6.1.1 Solar Orbiter simulations: configurations

6.1.1.1 Geometry model and materials

The Solar Orbiter structure design projected by ESA (Section 1.2.1) is illustrated in Figure 6.1 (note that now the geometric configuration and the dimensions have low probabilities of changing in the near future). The on-board instruments are briefly described in the following (and located on the satellite body as on Figure 6.2):

For the in-situ measurements:

- EPD: Energetic Particle Detector
- MAG: Magnetometer
- RPW: Radio and Plasma Waves
- SWA: Solar Wind Plasma Analyser, including the *Heavy Ion Sensor* (HIS) and *Proton-Alpha Sensor* (PAS) for ions, *Electron Analyser System* (EAS) for electrons

And for the remote-sensing instruments:

- EUI: Extreme Ultraviolet Imager

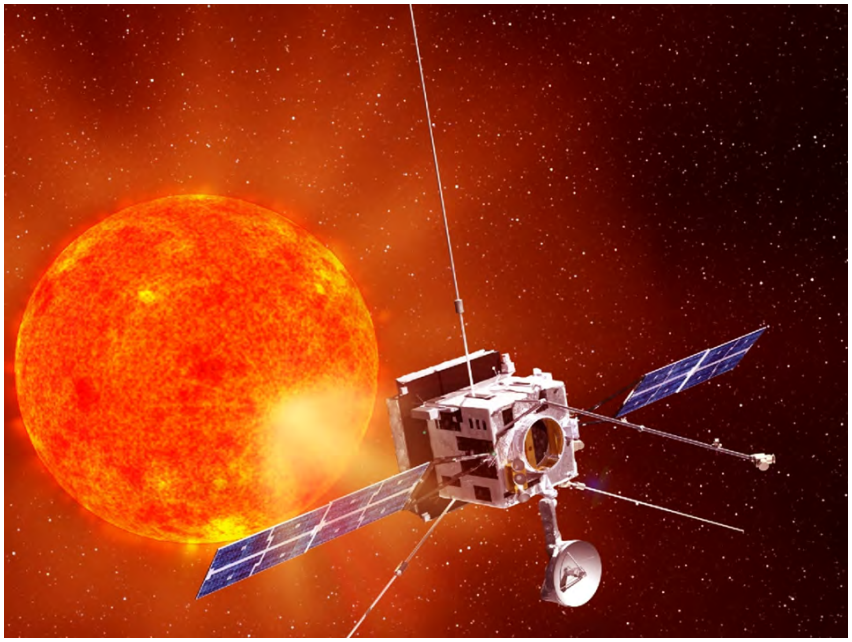

Figure 6.1: The Solar Orbiter spacecraft. *Image credit: ESA*.

- METIS: Coronagraph
- PHI: Polarimetric and Helioseismic Imager
- SoloHI: Heliospheric Imager
- SPICE: Spectral Imaging of the Coronal Environment
- STIX: X-ray Spectrometer/Telescope

The SOLO spacecraft has been modelled with the GMSH software (included in the SPIS package). This geometry model (see Figure 6.3) includes the satellite structure and the SWA/EAS detector. The main dimensions of the spacecraft elements visible on Figure 6.3 are:

- Spacecraft body: 1.68 × 1.68 × 1.80 m
- Sunshield: 2.5 × 2.5 × 0.9 m
- Solar Panels: 3.85 × 1.20 × 0.025 m
- *High Gain Antenna* (HGA): 0.55 m (radius) and 0.22 m (depth) + a support mast: 1.42 m (length) × 0.14 m (width)
- Rear Boom supporting EAS at its rear extremity: 4 m (long) × 0.025 m (radius)
- The *Radio and Plasma Waves* experiment (RPW): 3 antennas of 5.34 m (long) × 0.006 m (radius), electrically connected to the Spacecraft
- SWA/EAS Box: 0.2 × 0.18 × 0.11 m

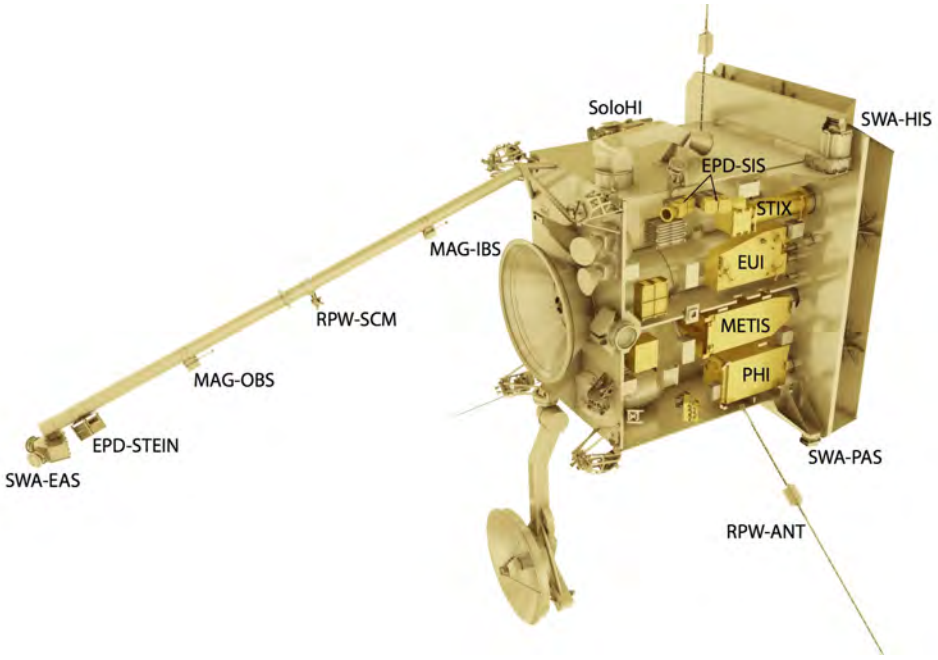

Figure 6.2: Payload accommodation on-board Solar Orbiter. *Image credit: ESA.*

Solar panels interconnectors are neglected. The table in Figure 6.4 presents the covering materials of the Solar Orbiter model (courtesy of Astrium), even though all materials were not definitely settled by the time the SO cases were configured. In Figure 6.5 are presented the different covering materials with their main characteristics for a SPIS simulation, taken from SPIS default material list, except for the "Steel for detectors" and "AlOx for HGA" materials which have been manually configured. AlOx for HGA stands for the dielectric ceramic coating of the HGA (the characteristic data were provided by Astrium) and the Steel for detectors is a simple steel coating which can not emit any particle (to model the fact that there is no surface on the detector gap but only an aperture). Note that this list is probably not definitive and some Solar Orbiter materials might change in the future, but these are the best estimations available during this study.

6.1.1.2 SWA/EAS instrument

The Solar Wind plasma Analyser (SWA), consists of three sensors (EAS, PAS, HIS) that will measure the ion and electron bulk properties (including density, velocity, and temperature) of the solar wind, between 0.28 and 1.4 AU from the Sun. In addition to determining the bulk properties of the wind, SWA will provide measurements of solar wind ion composition for key elements (*e.g.* the C, N, O group and Fe, Si or Mg).

The *Electron Analyser System* (SWA/EAS) consists of a pair of top-hat electrostatic analysers with aperture deflection plates mounted in the shadow of the spacecraft at the end of the instrument boom. Orthogonal mounting of the two sensors and the $\pm 45°$ aperture deflection provides an almost full 4π field of view subject only to minor blockage by the spacecraft and its appendages. The sensor will measure electron fluxes in the energy range from $\sim$1 eV to $\sim$5 keV with the energy resolution $\Delta E/E \sim 10-12\%$ and an angular resolution of 10°. Moments of the electron distribution will be returned with a cadence of 3 s, although the sensor will be capable

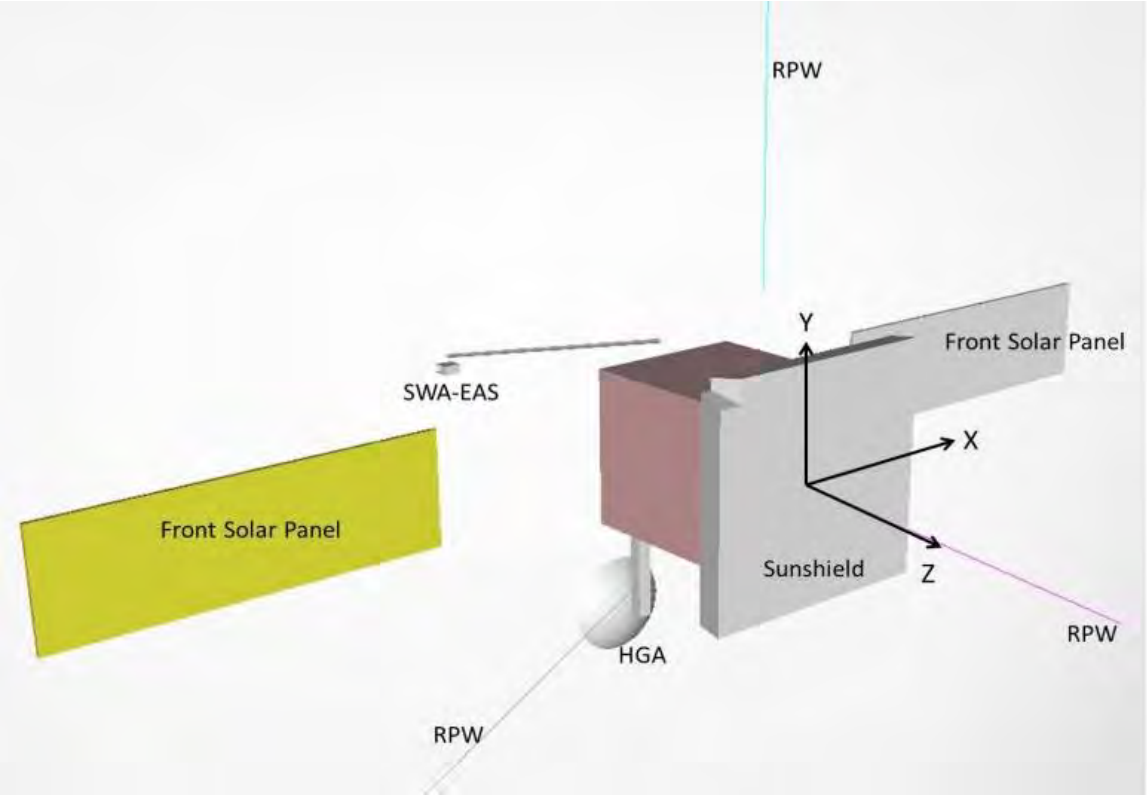

Figure 6.3: Solar Orbiter geometric model (created with the GMSH software). The 3 RPW antennas are modelled as thin wires.

Material	*CFRP*	*Black Kapton*	*CERS*	*Steel*	*Steel for detectors*	*AlOx for HGA*	*Gold*
SC elements covered with this material	- Sunshield - HGA support - Rear boom - SA rear faces and sides	- Solar Orbiter body	- Sunlit sides of SA	- EAS box (without the detectors)	- All detectors of EAS	- HGA	- The 3 RPW antennas

Figure 6.4: Solar Orbiter main elements and materials.

Characteristics		Material						
Name	Description	*CFRP*	*Black Kapton*	*CERS*	*Steel*	*Steel for detectors*	*AlOx for HGA*	*Gold*
BUC	Bulk conductivity (/ohm/m)	N/A	N/A	9.99E-15	N/A	N/A	1.00E-12	N/A
PEE	Primary elec. Energy for max SEEY(keV)	0.30	0.15	0.80	0.25	0.25	0.35	0.80
IPE	Proton energy for max SEEP yield (keV)	135	140	230	140	140	230	135
SRE	Surface resistivity (ohm)	N/A	N/A	9.99E14	N/A	N/A	N/A	N/A
PEY	Photoelectron current at 1AU (A/m2)	7.19E-6	4.99E-6	1.99E-5	1.99E-5	0.00	3.99E-5	2.90E-5
RPR1	Range parameter r1 (Angstrom)	110	71.48	70	70	70	50	88.79
RPR2	Range parameter r2 (Angstrom)	300	312.10	150	150	150	100	53.47
MSEY	Max. SEEY	0.69	2.09	5.50	2.50	0.00	3.50	1.29
SEY	SEEY due to impact of 1keV protons	0.41	0.45	0.24	0.45	0.00	0.24	0.41
RPN1	Range parameter n1	1.89	0.60	0.50	0.60	0.60	0.60	0.92
RPN2	Range parameter n2	1.03	1.76	1.64	1.79	1.79	1.64	1.73
RDC	Relative dielectric constant	1.00	3.50	3.79	1.00	1.00	10.00	1.00
Thick.	Material thickness (m)	1.25E-4	1.25E-4	1.25E-4	1.25E-4	1.25E-4	1.25E-4	1.25E-4

Figure 6.5: Solar Orbiter model - material properties.

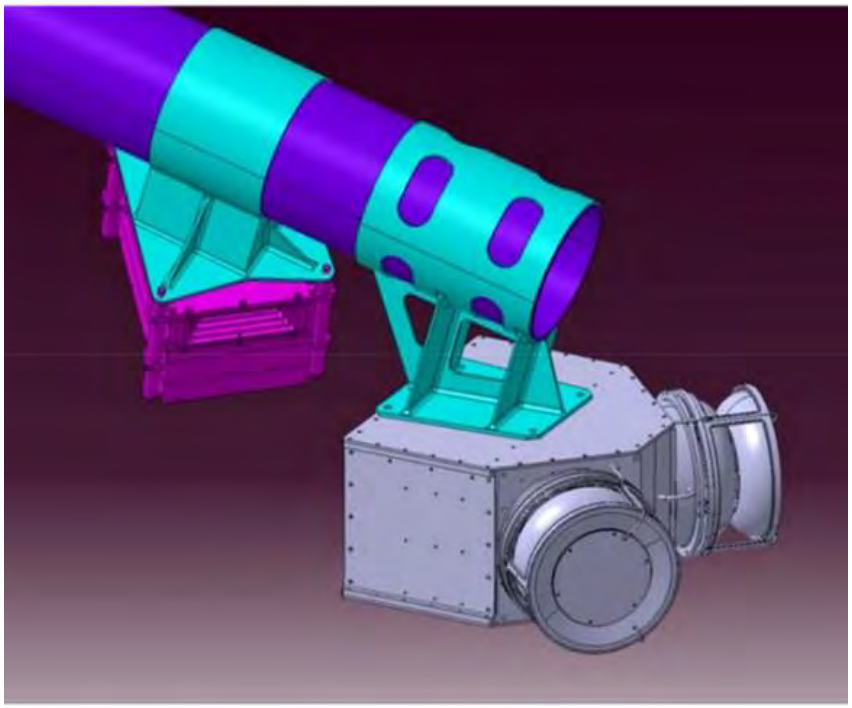

Figure 6.6: SWA/EAS CAD model. *Source: SWA/EAS Instrument Design Report.*

of returning full 3D distributions at lower cadence, and 2D electron pitch angle distributions at ∼0.1 s cadence during short periods of burst mode.

The *Proton-Alpha Sensor* (SWA/PAS) comprises a top-hat electrostatic analyser (EA) designed to measure the full 3D velocity distribution functions of major solar wind species, protons and alpha particles in the energy range $[0.2 - 20]$ keV/q, with $\Delta E/E \sim 7.5\%$, an angular resolution of 2° across a field of view of –17.5° to +47.5° by ±22.5° about the solar direction and a cadence of 3 s. Reduced distribution functions (1.5-D) of the solar wind protons and alpha particles over a similar energy range will be returned at higher cadence (0.1 s) during burst modes.

The *Heavy Ion Sensor* (SWA/HIS) consists of an electrostatic analyser module with ion steering to achieve the required extent of the HIS field-of-view (–33° to +63° × ±18°), coupled with a time-of-flight (TOF) telescope with solid state detectors for total ion energy measurements. HIS will measure five key properties for all ions: mass in the range 2-56 amu/q, charge (q), energy in the range $[0.5 - 100]$ keV/q (for azimuth) and $[0.5 - 16]$ keV/q (for elevation), $\Delta E/E \sim 6\%$ and direction of incidence (θ, ϕ) with 6° × 6° pixel resolution. The time resolution for 3D distribution measurements is 5 minutes for a full scan in normal mode and 30 s for heavy ions or 3 s for alphas in burst mode.

The EAS detector CAD model is presented in Figure 6.6. It is composed of the EAS box (containing electronic hardware) and two sensors which together cover 4π sr of the environment. Some elements of the Solar Orbiter structure as the back faces of the Solar panels are thus in sight of the instrument. The main characteristics of EAS are presented in Figure 6.7.

SPIS-5 can simulate major characteristics of the instrument:

- energy range and resolution

Parameter	Range/Resolution	EAS
Sensors		2 x EA
Mass	Species	Electrons
Energy	Range	1 eV - 5 keV
	Resolution (ΔE/E)	12%
	Analyzer constant (eV/V)	6
Angle	Range (AZ)	360°
	Range (EL)	± 45°
	Range scan (EL)	16 steps
	Resolution (AZ x EL)	11.25° x 3° - 8°
	Pixel Field of view	11.25° x 3° - 8°
Temporal	Resolution – Normal mode	4 s moments – 100 s full 3D vdfs
	Burst mode	0.125 s
Sensitivity	Per pixel (cm^2 sr eV/eV)	Variable < 2.6E-4

Figure 6.7: Main scientific performances of SWA/EAS detectors. *Source: SWA/EAS Instrument Design Report.*

- azimuth (AZ) and elevation (EL) angles of the field of view
- period of measurements
- type of particles detected

We focus the studies on the spacecraft/plasma interaction effects on low energy electron measurements: this is why the entire energy range of electrons $[1-5]$ keV will not be measured but only particles up to a few hundreds of eV. For this type of particle detector, with a particle entrance for each EAS sensor as a circular ring, it was necessary to consider each EAS entrance as the sum of 8 curved surfaces (see Figure 6.8), to limit the curvature of each surface detector. Indeed each surface is considered in SPIS model as a particle detector with a unique local detector basis (X_D, Y_D, Z_D) defined so as the Z_D axis is pointing into the detector, normal to the surface. This definition allows defining properly the acceptance angles for incoming particles in this basis. This is why each particle detector has to remain relatively "flat". The EAS instrument is thus composed in this model of 16 particle detector surfaces, each one providing its own outputs which will have to be combined for a global overview of EAS results. For all cases presented here the acceptance angles are $\pm 90\,^\circ$ in AZ and $\pm 45\,^\circ$ in EL. This way the entire field of view of both detectors covers the 4π sr of the environment. The common basis (X_0, Y_0, Z_0) in which the results of all particle detectors measurements are provided is presented on Figure 6.9. This basis is different from the (X, Y, Z) basis defined in the GMSH model (visible on Figure 6.3) of Solar Orbiter: $X_0 = -X$, $Y_0 = -Z$, $Z_0 = -Y$.

The characteristic dimension of EAS (∼20 cm) and its detectors aperture gaps (1 mm) are extremely small regarding the Solar Orbiter model dimension (∼10 m from one solar panel end to the other), and the simulation box size (40 m). This configuration represents challenging multi-scale numerical simulations.

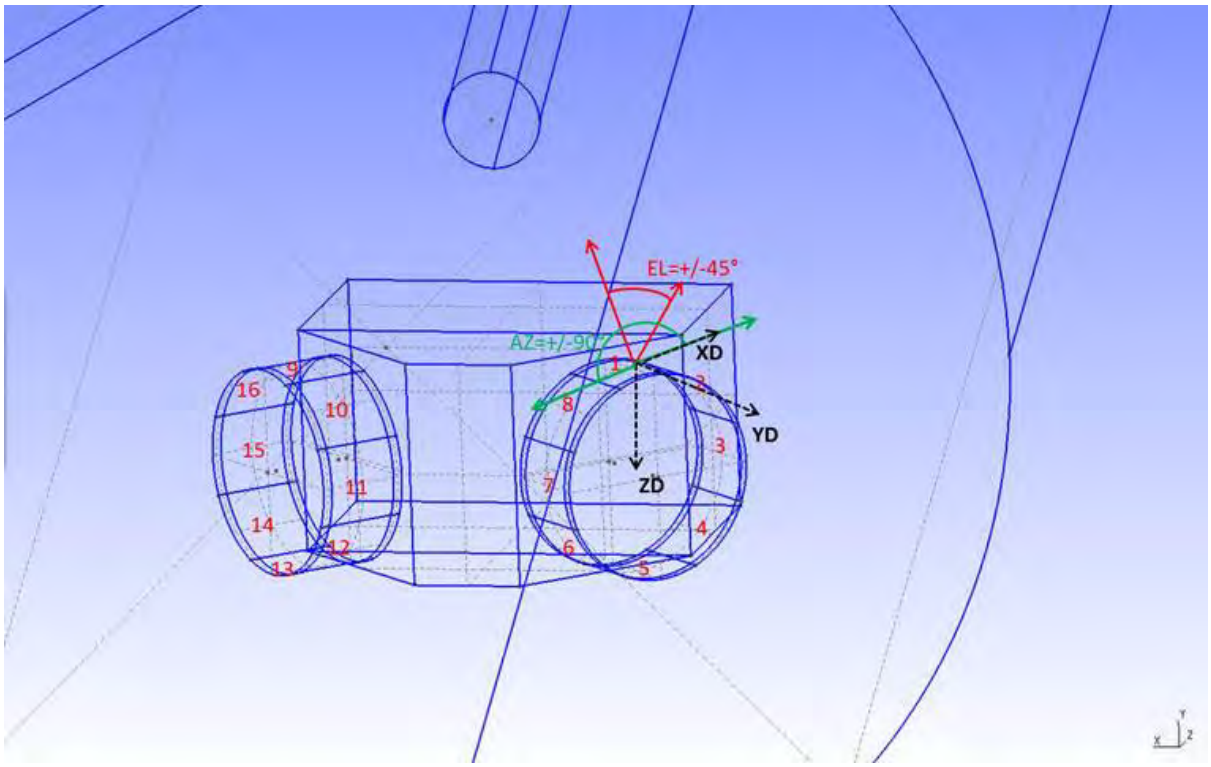

Figure 6.8: GMSH model of EAS for SPIS.

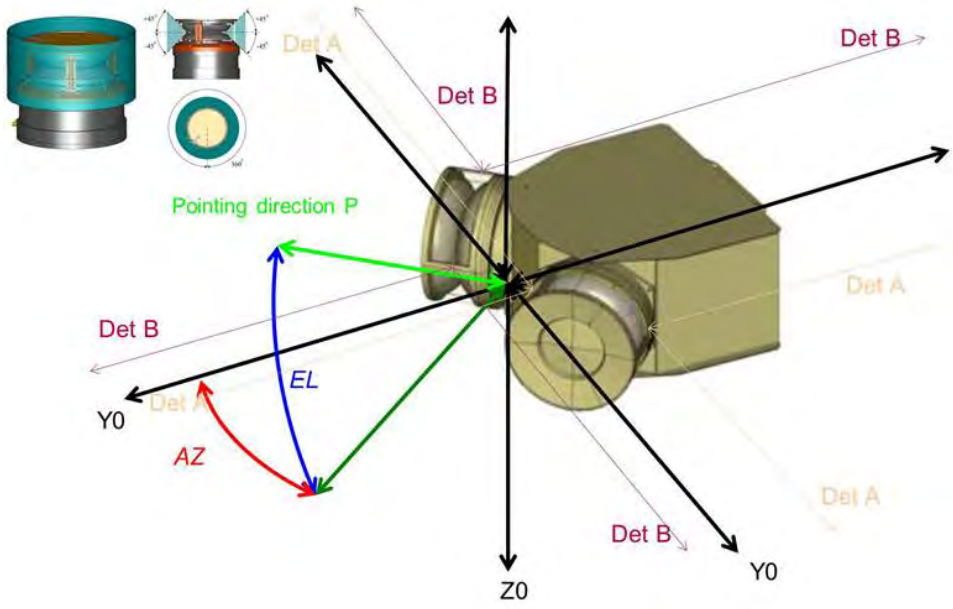

Figure 6.9: EAS outputs reference basis (X_0, Y_0, Z_0) description of Azimuth (AZ) and Elevation (EL) angles.

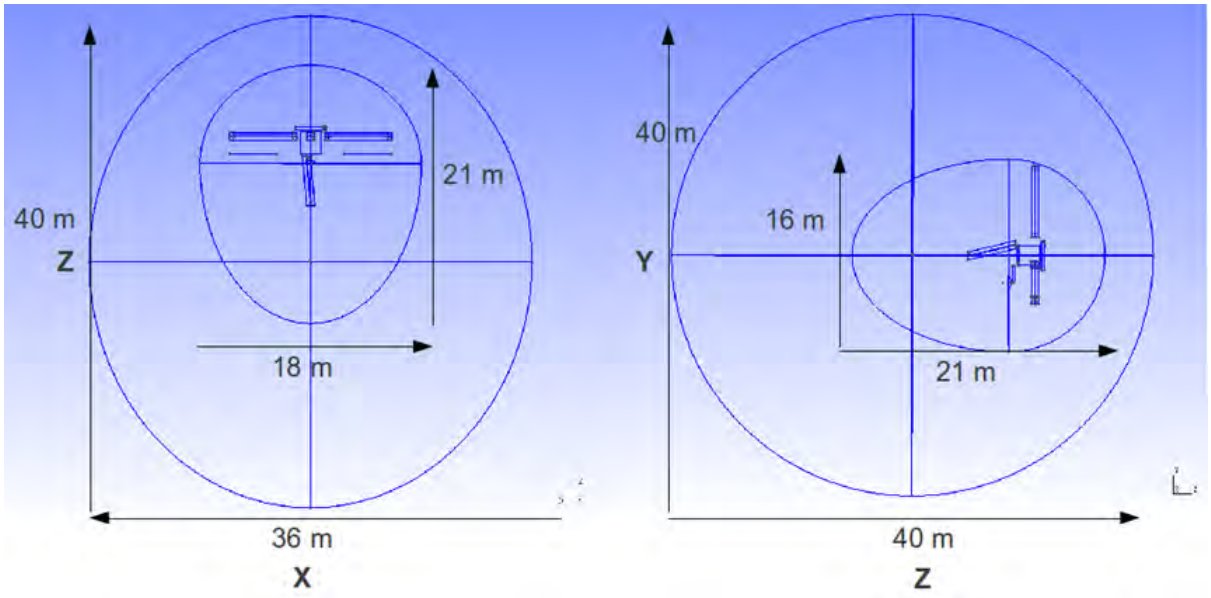

Figure 6.10: Simulation box dimensions for all Solar Orbiter cases.

Concerning the instrument results, the code provides several output ".txt" and ".msh" files which allow various possibilities for post-processing the results. Methods of analysing results depend on what the users need to investigate. Some examples of post-processed outputs are also presented in this manuscript (built using different software tools not provided in the SPIS package). Post-processing methods have been developed gradually with analysing simulation results.

6.1.1.3 Simulation box and meshing

The same geometry model for Solar Orbiter, EAS and simulation box with the same mesh have been used in all SOLO cases. The mesh size varies from 0.005 m on EAS detector surfaces to 3 m on the boundaries of the computational volume. Note that the thin gap of 1 mm constituting the real aperture is not modelled alone but all the surface made by the deflection plates: indeed any electron reaching those plates is supposed to be guided inside the top-hat analyser. The entire volume contains about 205000 tetrahedrons. The dimensions of the simulation domain are presented in Figure 6.10 and the meshing on Solar Orbiter and EAS are respectively illustrated on Figures 6.11 and 6.12. Several refinement mesh boxes appear on those figures. They aim at controlling the meshing size extension in the vicinity of small spacecraft elements (EAS) and also generate the thin wires constituting the 3 RPW antennas (through two planes intersection within those boxes). Note that the simulation box and meshing parameters will be modified for one of the validation case: SOLO@0.28 AU. This will be explained further.

6.1.1.4 Environment

The main global parameters used in the simulations are presented in Table 6.1 (based on Table 4.18). Data at 0.28 AU (the so-called SOLO@0.28 AU case) are interpolated between 0.25 and 0.30 AU while parameters for the SOLO@1 AU-FW case (an extreme case in the context of a fast CME), were obtained from the Wind spacecraft at 1 AU in 2004. Similar conditions may

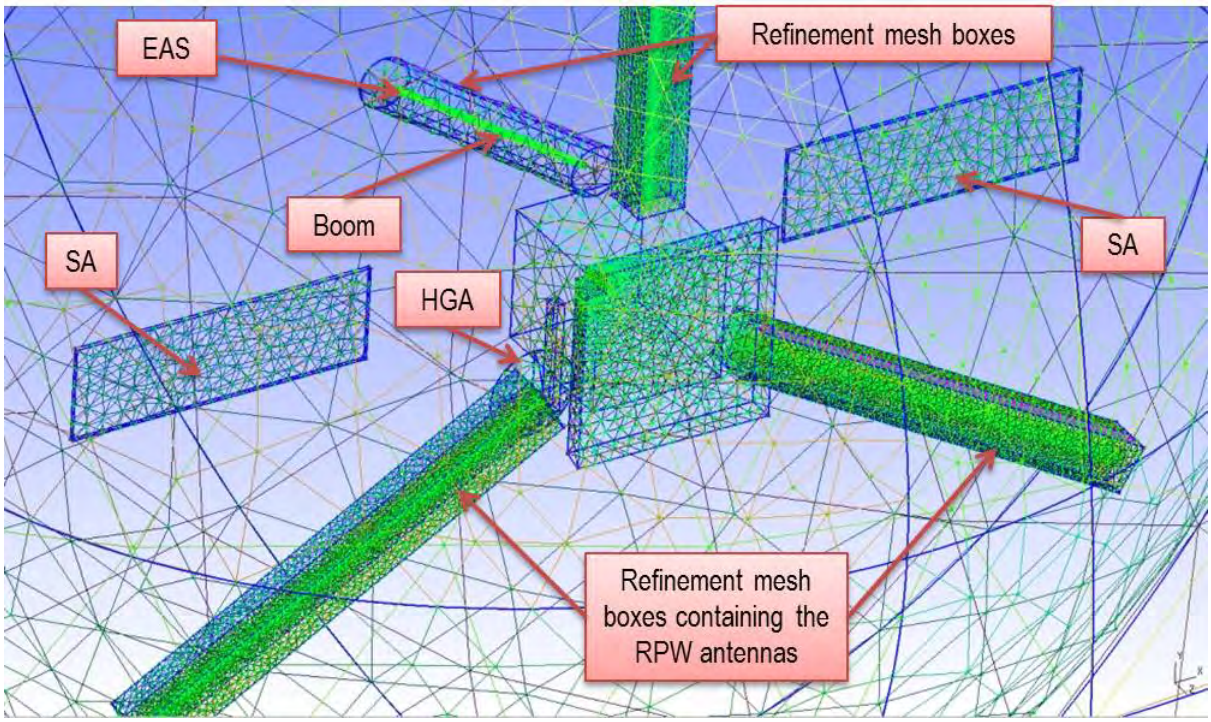

Figure 6.11: GMSH meshing on Solar Orbiter and the simulation box.

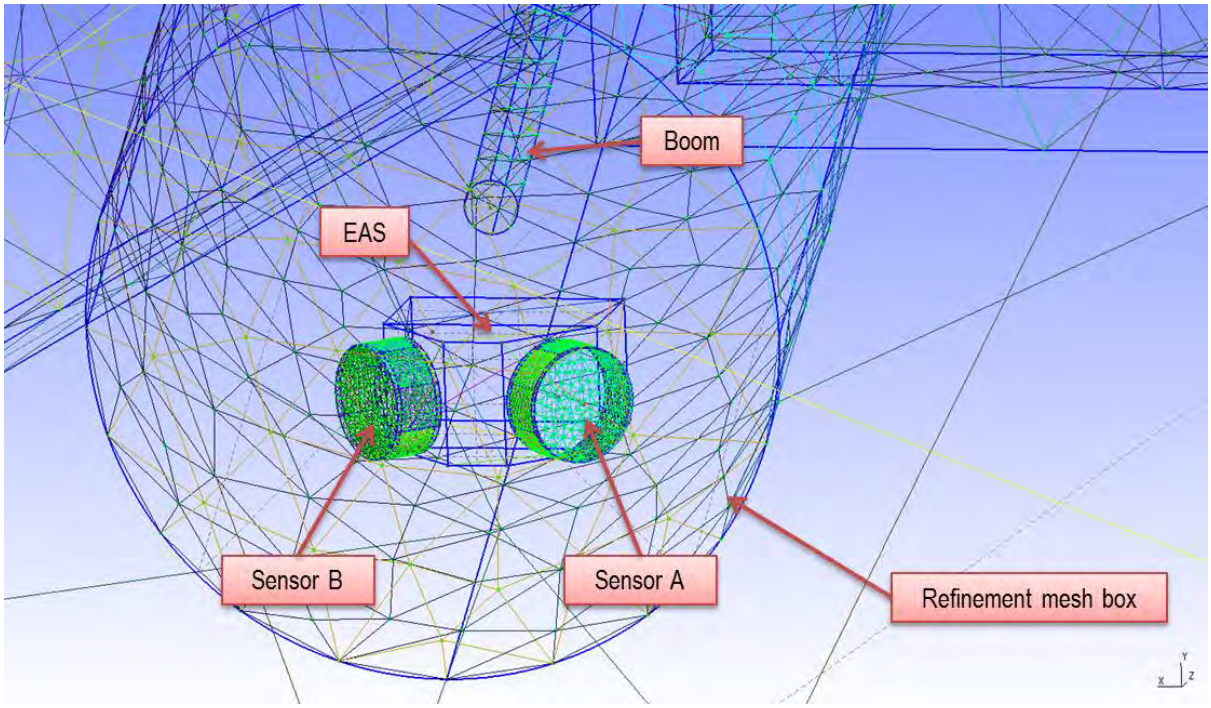

Figure 6.12: GMSH meshing on SWA/EAS.

Simulation ID	SOLO@1 AU	SOLO@1 AU-FW	SOLO@0.28 AU
Distance (AU)	1.00	1.00	0.28
Distance (R_s)	215	215	60.2
Sun Flux (# 1AU)	1.00	1.00	12.76
Elec. density N_e (m^{-3})	6.93×10^6	6.00×10^6	1.04×10^8
Elec. temp. kT_e (eV)	8.14	40.00	21.37
Ion density N_i (m^{-3})	6.93×10^6	6.00×10^6	1.04×10^8
Ion temp. kT_i (eV)	8.0	130.0	27.0
Ion ram speed (km/s) V_Z	430	1060	400
Mach number	15.5	9.5	7.86
Debye length (m)	8.06	19.00	3.38
Debye length photo (m)	0.98	0.98	0.27

Table 6.1: SO cases main parameters for SPIS simulations.

be readily encountered by Solar Orbiter in the declining phase of the solar cycle 24. For all SOLO simulations there are common parameters for the SPIS software:

- Ions: H^+, PIC with Maxwellian distribution and drift (other species could be simulated in other contexts, which was not necessary in this study)
- Electrons: PIC with Maxwellian velocity distribution function
- Photoelectrons: PIC with Maxwellian velocity distribution function, Temperature $kT_{ph} =$ 3 eV
- SEEE: PIC with Maxwell velocity distribution function, Temperature $kT_{\mathrm{SEEE}} = 2$ eV, backscattered electrons with 2/3 of their initial energy
- External boundary conditions: Fourier, $1/R^2$ decrease of potential
- EAS measurements are activated for thermal electrons, SEEE and photoelectrons
- No magnetic field considered (estimated gyroradii are larger than the simulation box in all cases)

As it appears in Table 6.1 the SOLO@0.28 AU case leads to a Debye length for thermal electrons of only 3.38 m, while the meshing size on the simulation box boundaries is set at 3 m. The plasma scale here generates a numerical constraint to respect the meshing rule ("one particular specification of the meshing for full PIC is that the size of any surface cell or volume element must be inferior to half of the local plasma Debye length", see section 4.1.2.3). This is the reason why the simulation box geometry and meshing will be adapted to the last Solar Orbiter case.

6.1.2 Results analysis of SOLO at 1 AU

6.1.2.1 Satellite potential equilibrium

The virtual duration of the simulation SOLO@1 AU, Solar Orbiter at 1 AU, immersed in a slow Solar wind, was set to 7 seconds. This is long enough to reach steady potentials on dielectric

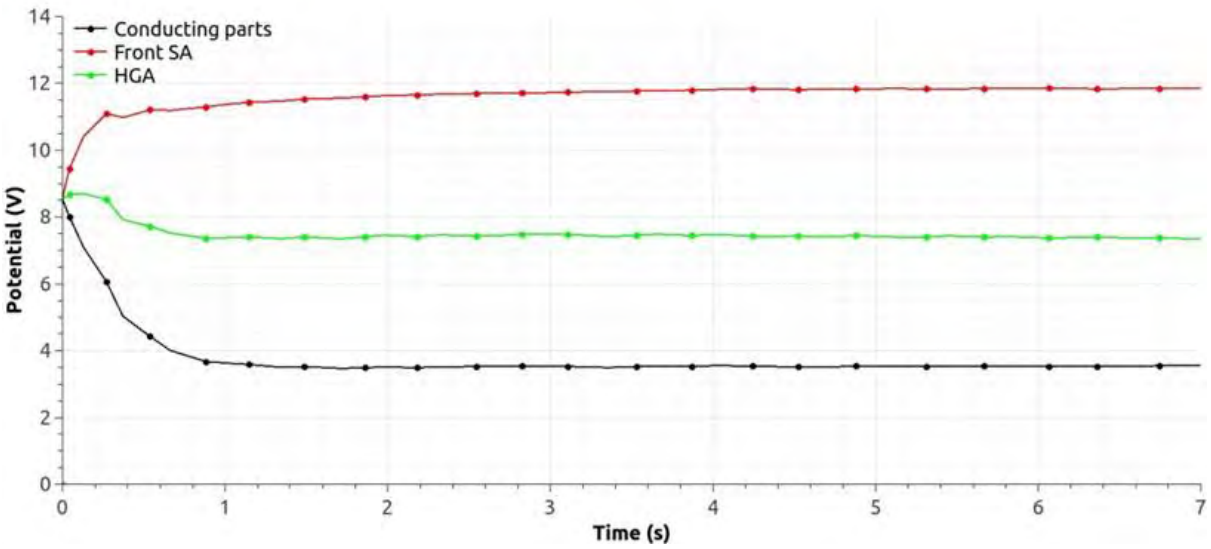

Figure 6.13: SOLO@1 AU - Spacecraft potentials versus time.

surfaces and a stable surrounding plasma. At $t = 7\,\mathrm{s}$, the particle measurements by EAS begins. Once the transitory regime is over (see Figure 6.13, showing the evolution of satellite potentials versus time), the conducting parts of the spacecraft settle at a potential of $+3.6\,\mathrm{V}$ (including EAS detectors), the front faces of the Solar panels charge at +11.9 V and the HGA to +7.4 V. Those positive potentials might accelerate the low energy thermal electrons and thus bias EAS measurements, this will be checked through the analysis of EAS measurements in a further section.

Furthermore to Figure 6.13 which shows that steady electrostatic potentials have been reached by the end of the simulation, the stability of the numerical computation is illustrated on Figures 6.14 (the time evolution of the net currents on spacecraft) and 6.15 (number of superparticles in the simulation box: between 1 and 6 millions for each population). Those figures show that the satellite potentials and the plasma behaviour are at equilibrium at the virtual duration of 7 s (when EAS measurements begin).

This result is consistent with [Guillemant et al. (2013)] (Appendix A.5) which showed that at this distance from the Sun (1 AU) a spacecraft will be positively charged. In the previous work [Guillemant et al. (2013)] the model used was a simple fully conducting cylinder while here the model is much more complex, bigger and includes dielectric surfaces. But these differences do not seem to change the global results for this specific environment.

6.1.2.2 Plasma

The plasma potential is displayed in Figure 6.16, where a monotonic decrease of potential from the satellite surface to simulation box boundaries can be seen. There are no potential barriers for secondary electrons and photoelectrons. All thermal electrons around Solar Orbiter are thus accelerated by the positive potentials on its surfaces. The plasma population densities are plotted in Figure 6.17, Figure 6.18 and Figure 6.19 (*resp.* ions and electrons, photoelectrons, SEEE and SEEP). The ion wake reaches the rear boundary of the simulation box. The electron density map is a bit noisy due to mesh refinement in the vicinity of the spacecraft. However

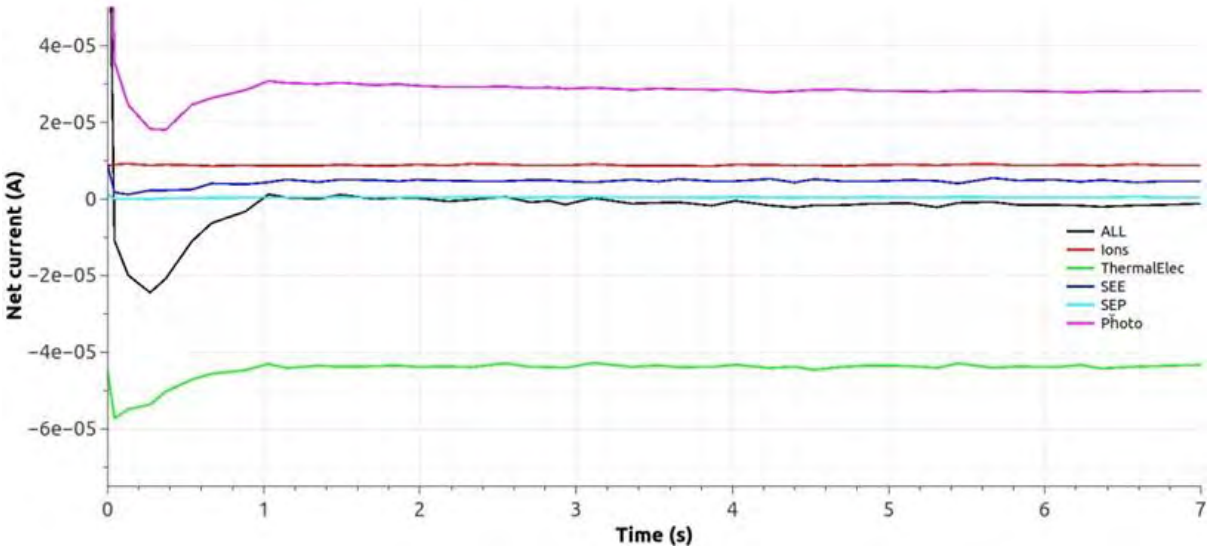

Figure 6.14: SOLO@1 AU - Net currents to spacecraft versus time.

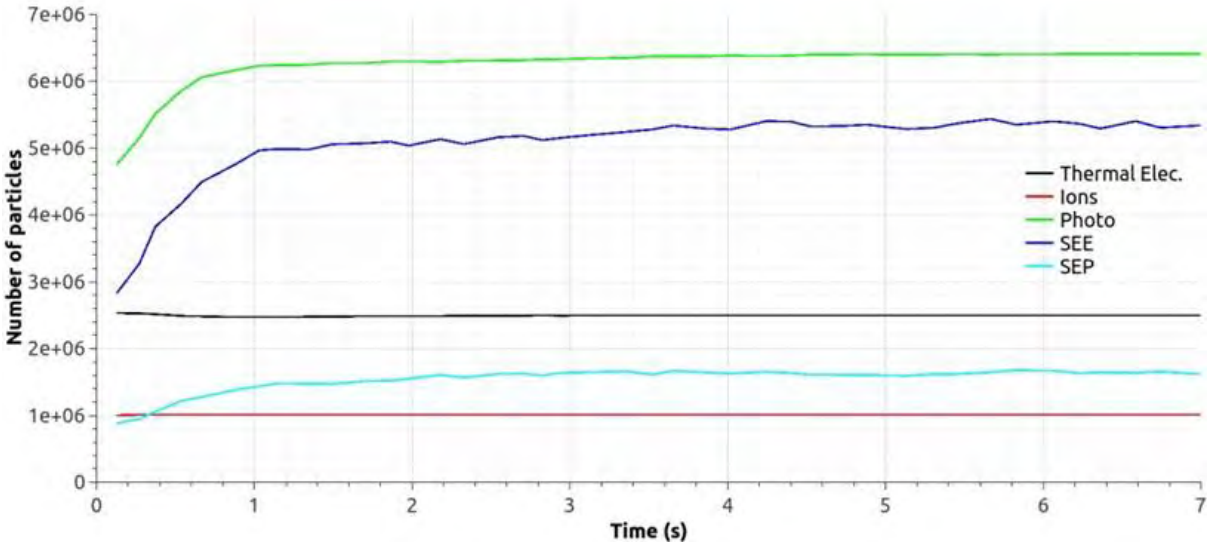

Figure 6.15: SOLO@1 AU - Number of superparticles in the simulation box versus time.

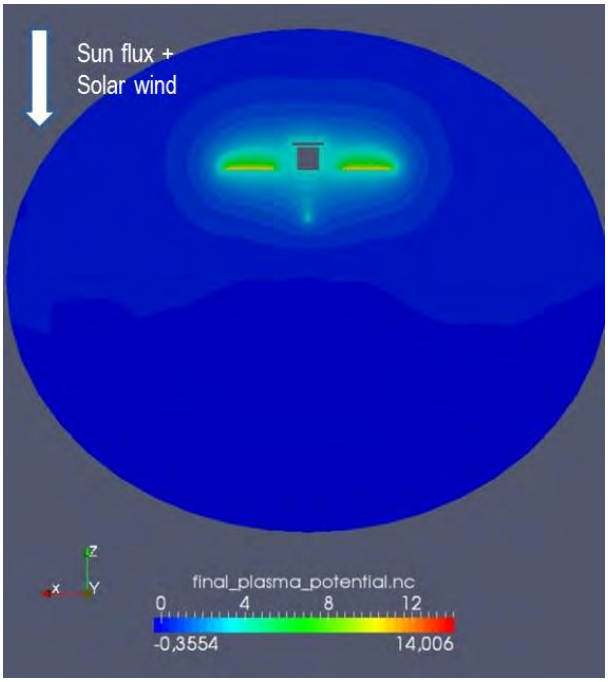

Figure 6.16: SOLO@1 AU - Plasma potential.

as the mesh elements dimension remains smaller than λ_D, it does not produce noise on the potential map. The number of particles in a sphere of radius λ_D corresponds to the correct number even if they are distributed with a lack of uniformity in the cells contained in the sphere. Even if this is not necessary here, the statistics can always be improved through mesh optimisation and an increase in the number of particles within the simulation volume. It might however extend each simulation duration, especially for the further cases including secondary and photoelectrons, highly increasing the number of particles and the memory usage, required in the simulation. Concerning secondary and photoelectrons, SEEE are practically 10 times less dense than the photoelectrons but they surround the structure since they are produced from all surfaces exposed to the environment, while photoelectrons surround faces exposed to UV light. We notice the presence of those particles in the close area of EAS: some secondary and photoelectrons will thus be detected by the instrument.

The recollection rates are important: 89% of photoelectrons and 70% of SEEE are recollected by the satellite structure, and for SEEP it reaches 84%. The net current of SEEP (4.6×10^{-7} A) is below the net currents of SEEE (4.9×10^{-6} A) and photoelectrons (2.8×10^{-5} A). SEEP are of secondary order of magnitude in the establishment of the current balance and the final potentials.

6.1.2.3 EAS measurements

Figure 6.20 shows the Energy Distribution Function (EDF) of thermal electrons for EAS in SOLO@1 AU. This plot presents the results following the same methodology used in Chapter 5.

The *environment* yellow curve is the electron distribution from environment as described in Table 6.1, and the one that EAS should measure if there were no plasma disturbances due to spacecraft/plasma interactions. Thus, the environment is plotted directly from equations

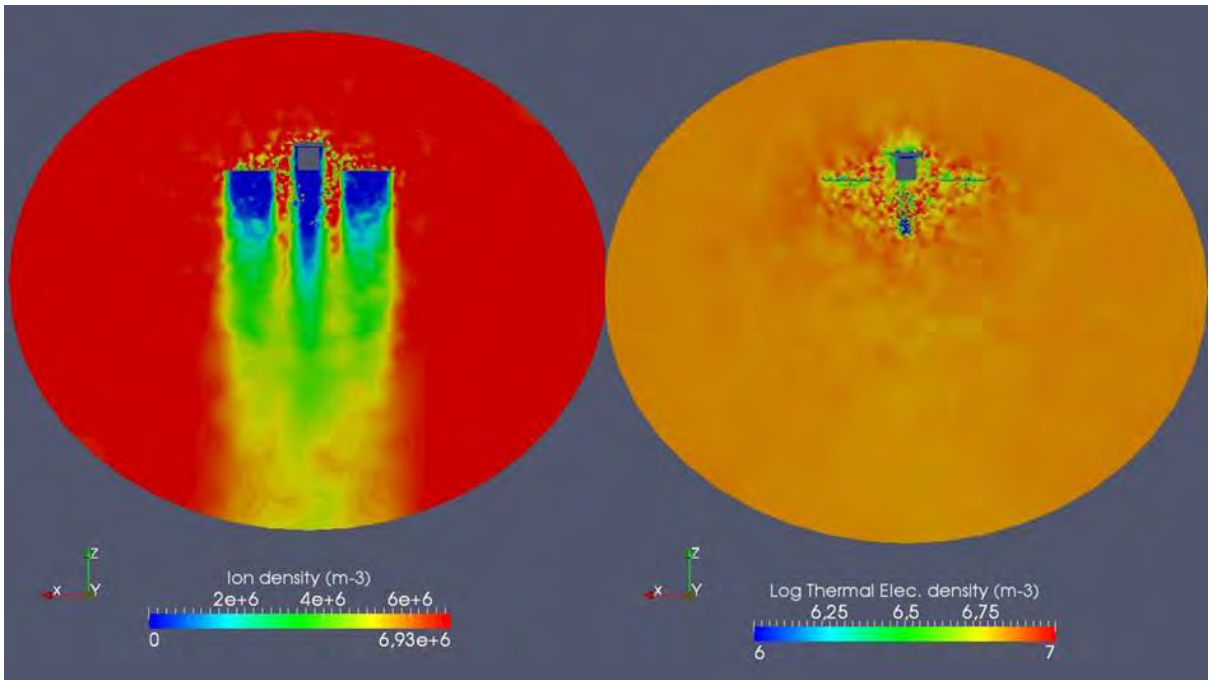

Figure 6.17: SOLO@1 AU - Ions and thermal electrons density (in the $X - Z$ plane).

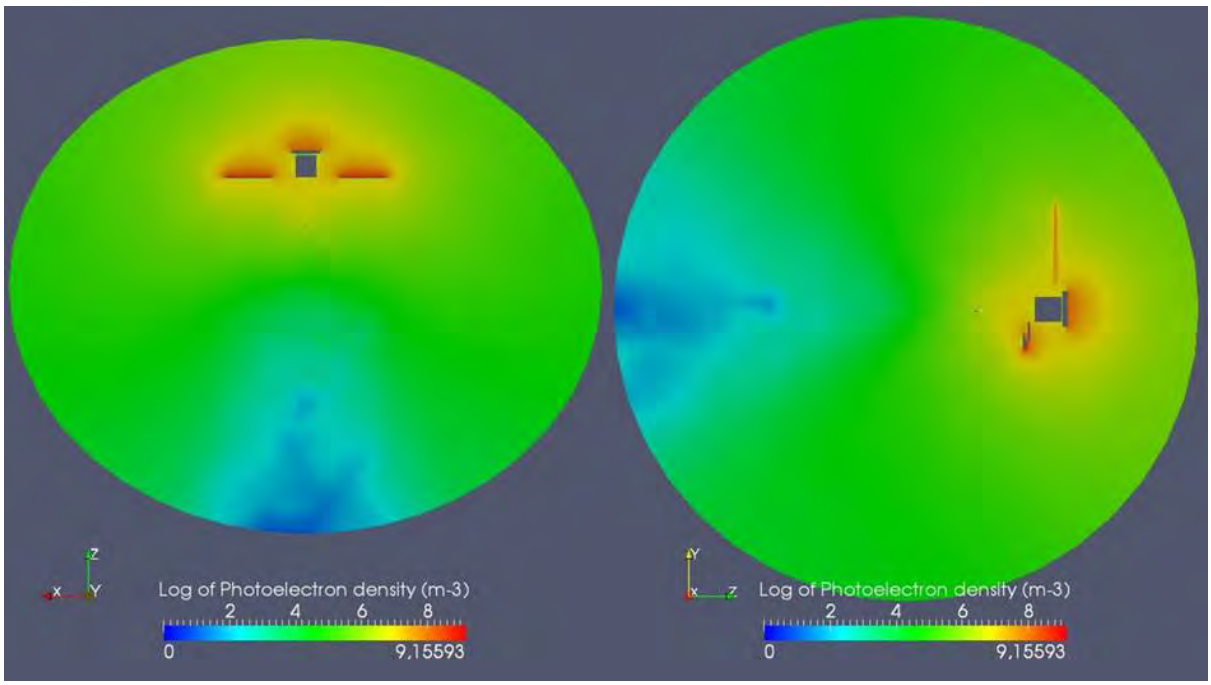

Figure 6.18: SOLO@1 AU - Log of photoelectron density (left: $X-Z$ plane, right: $Y-Z$ plane).

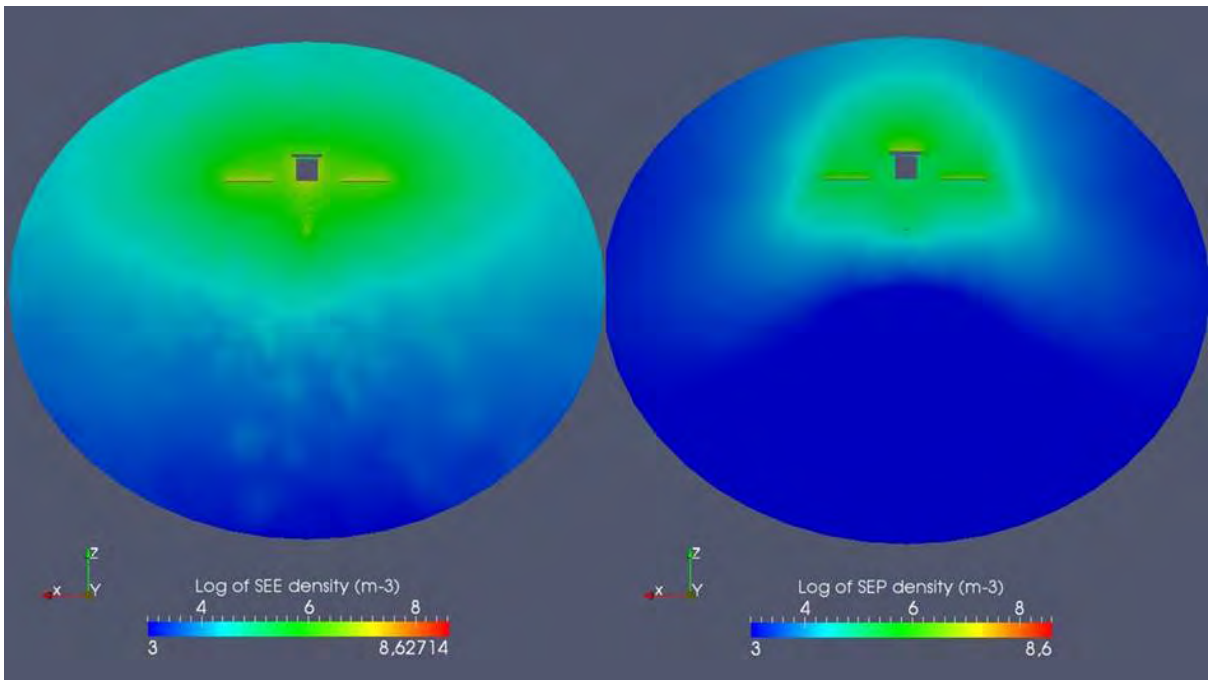

Figure 6.19: SOLO@1 AU - Log of SEEE (left) and SEEP (right) density.

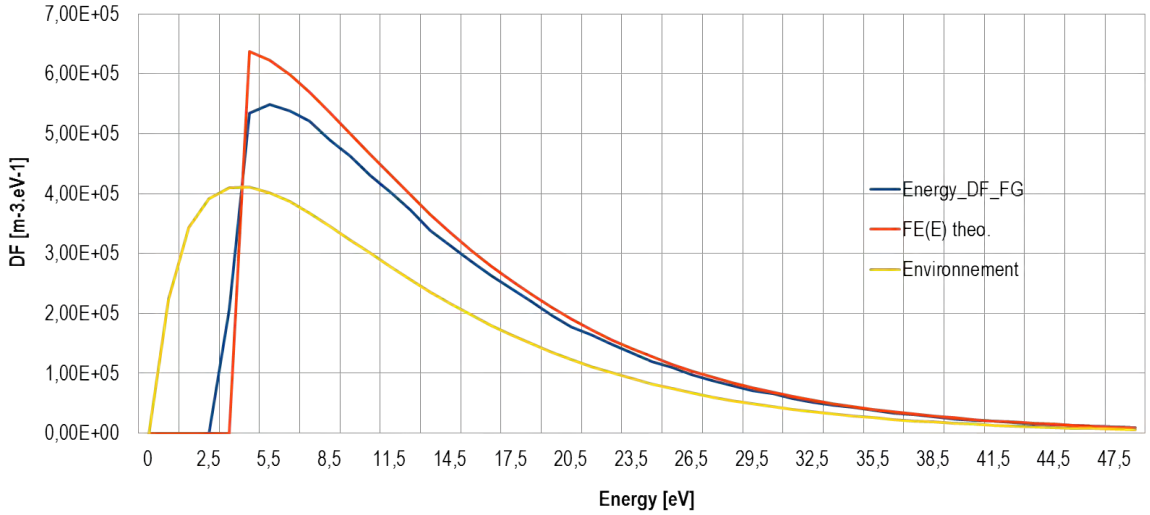

Figure 6.20: SOLO@1 AU - Energy distribution functions of thermal electrons on EAS. The measured DF (blue) starts at 2.5 eV because of a discretisation effect on the spreadsheet table used for this plot.

2.1 and 3.45, with the appropriate input parameters of Table 6.1. The orange curve $F_E(E)$ represents the environment that should be theoretically measured by EAS if there was only this instrument charged at its potential of +3.6 V in the simulation box, with no spacecraft, no wake or any potential barrier. It is calculated analytically using Liouville's theorem (equation 2.10). This distribution function is thus based on the true environment, but shifted of 3.6 eV (indeed no electrons can reach the detector with a potential energy inferior to EAS potential), and increased after 3.6 eV because of the attracting electric potential of EAS.

Finally, the blue curve *Energy DF FG* represents the simulated measurement of thermal electrons. The letters "FG" in the legend stand for "Geometric Factor", meaning that measurements have been corrected by the geometric factor of each surface detector (which naturally sees only 1/4 of the entire phase space volume. The measurement results in a combination between the true environment and the theoretical measure of EAS alone. Here the phenomenon already discussed in section 5.5 is increased. Indeed the analytical modelling using Liouville's theorem assuming all possible trajectories are filled regarding the expected distribution function in a local non zero potential is only valid for a single detector immersed in the plasma. During the previous simulations it has been highlighted that the structure of positively charged instrument box reduced the DF with respect to Liouville's DF (with a few percent of difference). As here the entire Solar Orbiter structure is positively charged (at values that can reach +11.9 V on the Solar panels), many thermal electrons are attracted in those areas and fewer on EAS detectors which results in a lack of information on the low energy electrons in the simulated measures. It can be seen on the difference of amplitude between the maximums of the blue and orange curves. This result is consistent with the ones obtained in section 5.5, using the attracting potentials. The difference relies here in the important spacecraft structure that increases the gap between the expected distribution function and the measured one.

Integrating those DF over energy gives us the corresponding thermal electron densities (Figure 6.20):

- Undisturbed environment (yellow): $N_0 = 6.90 \times 10^6\,\mathrm{m}^{-3}$ for a root density (Table 6.1) of $6.93 \times 10^6\,\mathrm{m}^{-3}$. The difference is due to the truncated integration in injected model
- Theory (orange): $N_{\mathrm{theo}} = 8.58 \times 10^6\,\mathrm{m}^{-3} > N_0$ because of EAS potential (+3.6 V)
- Measurements (blue): $N_{\mathrm{meas}} = 8.10 \times 10^6\,\mathrm{m}^{-3} < N_{\mathrm{theo}}$ because of the spacecraft charged structure and the plasma disturbances (ion wake, solar panels, HGA, *etc*).

The measured density of thermal electrons gives a difference of +17% compared to N_0 (and 5.6% regarding N_{theo}). Adding to those measurements the detected fluxes of photoelectrons, SEEE and SEEP (Figure 6.20) gives a total density of measured electrons (the blue curve) of $N_{\mathrm{total}} = 1.56 \times 10^7\,\mathrm{m}^{-3}$ (125% of difference compared to N_0 and 81.8% to N_{theo}). For plasma physicists, this is a well-known rate of misreading when considering the very low energy electrons, a problem that is confirmed in this work.

The conclusions of Chapter 5 remain practical here. Indeed below the potential energy of 3.6 eV all detected electrons are originating from the satellite itself. There is a strong pollution of measurements in this low energy range ($E < 3.6\,eV$). It is noticeable that in th is case secondary electrons seem to be as disturbing as photoelectrons. This is explained by the fact that in this SOLO@1 AU configuration with the UV flux coming from the $+Z$ direction the EAS instrument is completely shadowed by the satellite body. The few detected photoelectrons have not been emitted by the instrument itself and recollected by the detector entrances as in the

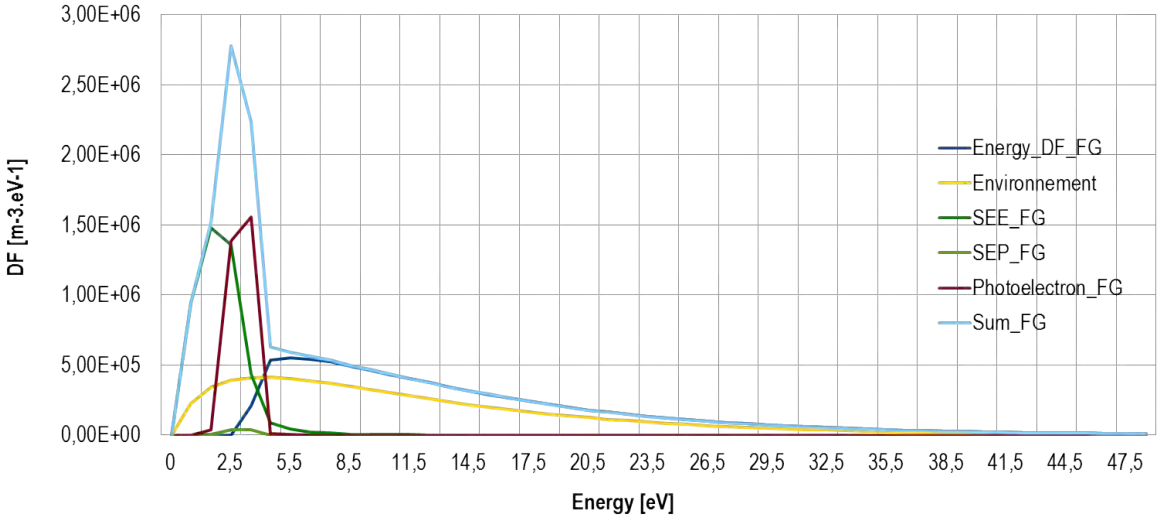

Figure 6.21: SOLO@1 AU - Energy distribution functions for all electrons on EAS.

previous simulations of Chapter 5, but they came from the "far" sunlit faces of the spacecraft and travelled along its body to finally end on the sensors. Secondary electrons are on the contrary still emitted by the instrument box, just next to the particle detectors. Furthermore, as explained in the previous section 6.1.1.2 describing EAS, this instrument has direct lines of view pointing the spacecraft body (especially the rear faces of the Solar panels). The quantity of detected secondary electrons, emitted by all surfaces, is consequently highly increased regarding previous simulations (knowing also that in SOLO@1 AU the total area of surfaces exposed to the plasma is much larger than the single instrument area of Chapter 5).

3D Plots of trajectories for particles measured by EAS are displayed in the next Figures (6.22 for thermal electrons, 6.23 for photoelectrons and 6.24 for SEEE). Actually SPIS computes trajectories and orders them by their weight (using a backtracking modelling, see section 5.2). If a detector is asked by the user to provide 5 trajectories SPIS will generate 5 *vtk* files (one for each 3D plot), numbered from the highest weight (n°1) to the lowest (n°5). Thus some existing trajectories may not be saved by SPIS for visualisation, even if SPIS computed them during the plasma measurements, simply because their weight is inferior to a limit and the user did not ask for enough trajectories. This will be illustrated farther.

The deflection of thermal electrons by the spacecraft positive potentials is clearly illustrated on Figure 6.22. Electron trajectories are primarily deviated by the most positive potentials (+11.9 V) on the front faces of the Solar panels. The HGA (at +7.4 V) and the spacecraft body (at +3.6 V, including the 3 RPW antennas), have less influence but still attract electrons. For photoelectrons, more complex trajectories appear (Figure 6.23 with a multiple loops around the satellite various elements. Some photoelectrons are visibly originating from the RPW thin wires. Figure 6.24 shows that almost all SEEE trajectories computed come from the close vicinity of EAS (from the EAS box itself or from the rear boom). As explained earlier: only the trajectories accounting for the most important weights are visible. EAS, however, does detect secondary electrons from other spacecraft surfaces.

This can be demonstrated using other instrument output files permitting to identify the

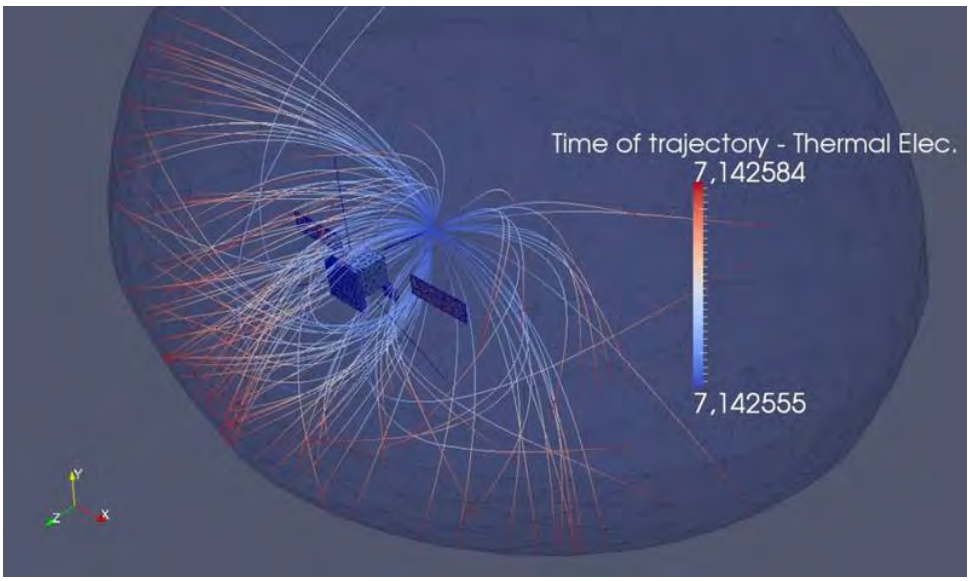

Figure 6.22: SOLO@1 AU - Trajectories of some thermal electrons detected by EAS. Note that the time scale for trajectories, a direct SPIS output, is following the backtracking principle. This is why the earlier time is associated with the "emission" from the particle detector, and the later time with the "arrival" at the boundary. This color coding of time evolution should have been the other way around, but it had not been implemented when these simulations were made. All other trajectory plots make use of this same reversed time scale.

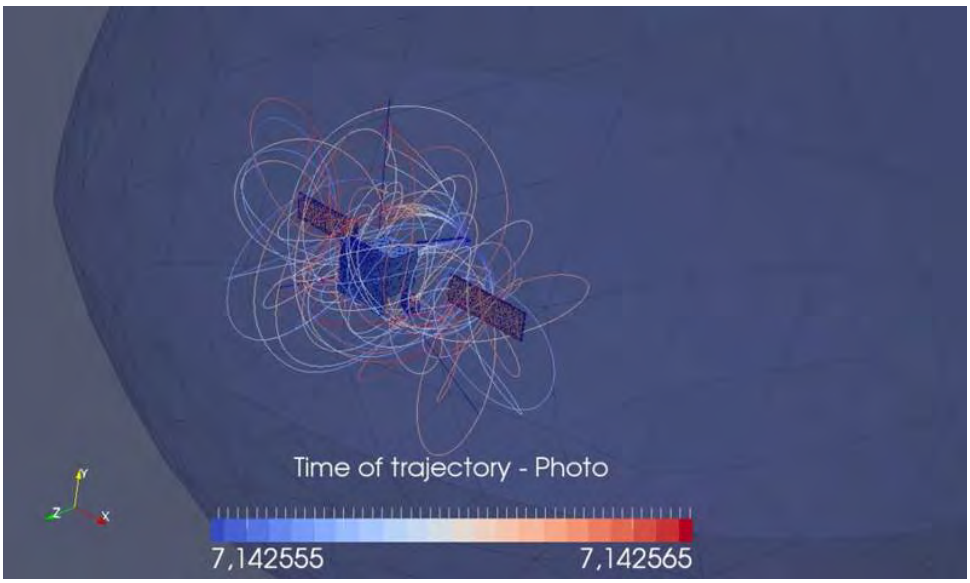

Figure 6.23: SOLO@1 AU - Trajectories of some photoelectrons detected by EAS.

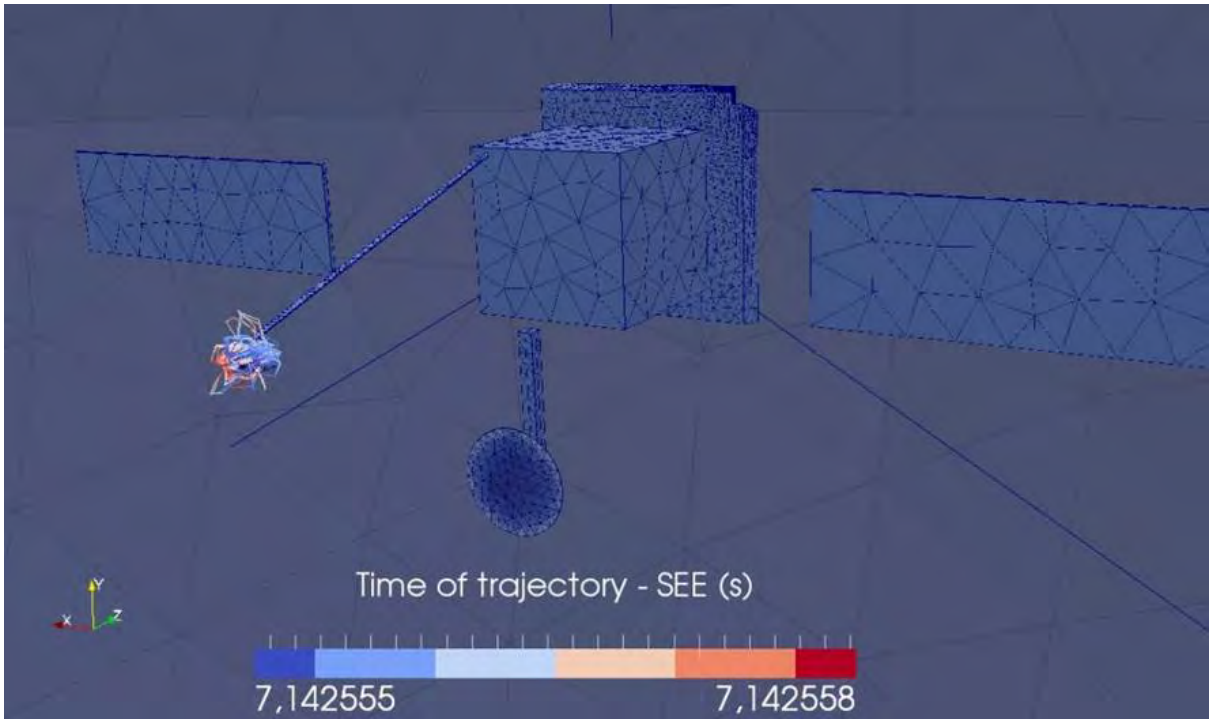

Figure 6.24: SOLO@1 AU - Trajectories of some secondary electrons detected by EAS.

2D surfaces which are sources of currents detected by an instrument. For instance concerning secondary electrons, each particle detector provides a file presenting the detected current value at its originating surface on the spacecraft (for example in this case to identify which part of the satellite surface contributes most to contaminating electrons to EAS). On the other side those outputs are also provided for thermal electrons (or ions, if required), allowing to determine which region of the simulation box boundary contributes the most/less to thermal electron current collection on a particle detector surface.

A SPIS-external post-processing method (easily feasible with the Paraview software) consists of adding the same outputs (for all the 16 particle detector surfaces which together constitute the instrument) to have a global view on the sources of currents for the entire EAS (and not for each particle detector separately). For instance to represent the field of view of EAS concerning thermal electrons we add the *vtk* files of thermal electrons current at the origin for each particle detector constituting the EAS instrument (16 detectors for ambient electrons). In the following example (Figure 6.25) the post-processing method is presented to show the sources of photoelectron current detected by EAS.

On the left part of this screenshot (Figure 6.25) the list of *vtk* files to be added is entered and linked to the *PythonCalculator* filter (a tool embedded in *Paraview* allowing to manipulate *vtk* files values). In the *Object Inspector* window (on the bottom left part of the screenshot) the expression of the *PythonCalculator* is entered as follow (in one single text line):

```
inputs[0].CellData['spis.Util.Instrument.ParticleDetector9_Injection_
On_SC_at_15.027859s.nc']+
inputs[1].CellData['spis.Util.Instrument.ParticleDetector10_Injection_
On_SC_at_15.027859s.nc']+
```

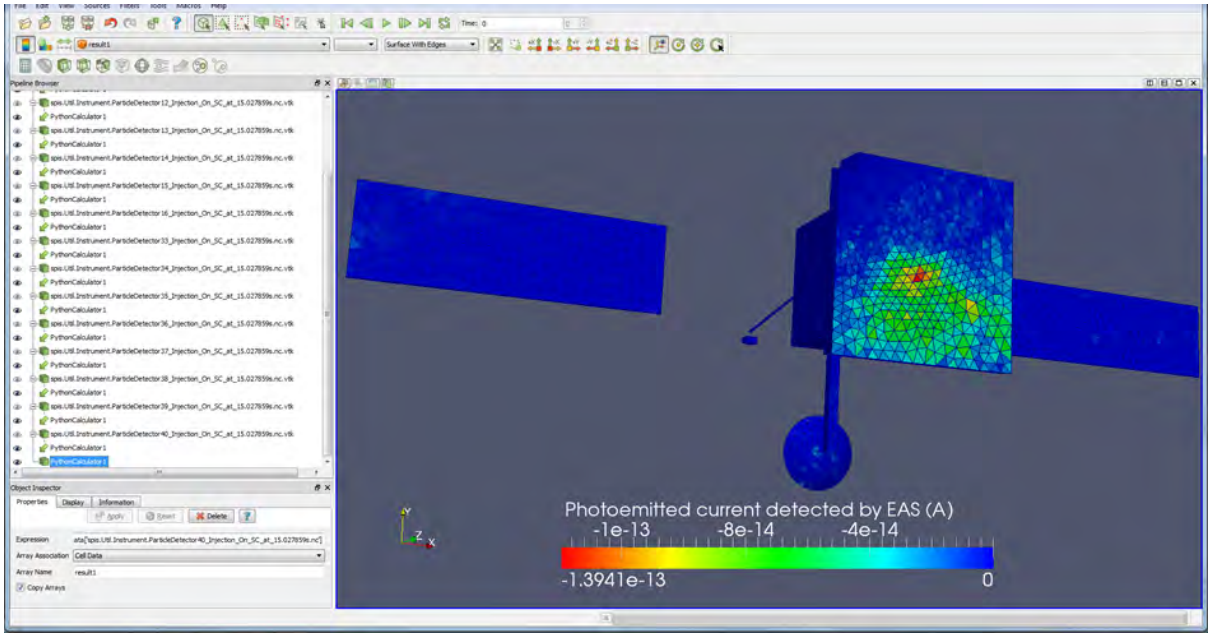

Figure 6.25: Screenshot of the post-processing method that cumulates *vtk* files to represent the source of collected currents detected by EAS (made with Paraview – here for photoelectrons). The data plotted is the current in A.

```
inputs[2].CellData['spis.Util.Instrument.ParticleDetector11_Injection_
On_SC_at_15.027859s.nc']+ ...
```

The file names between [spis.Util...] depend of course on the simulation (the *ParticleDetector#* and the *Time* in *s* have to be changed depending on the *resp.* population followed and the time of instrument measurements). In this example for photoelectrons there are 16 *inputs*[−] to consider all the photo-detectors. The result of the expression is then displayed in the graphic window on the right.

Using the aforementioned methodology, Figure 6.26 represents the source of secondary electrons detected by EAS. The color scale corresponds to the current on each cell and not to the current density (which makes the distribution of the sources look non homogeneous). It shows that almost all secondary electrons come from a confined area on the rear side of the Solar Orbiter body (around the origin of the rear boom) and from the EAS box itself (see Figure 6.27 for a focus on the instrument). We can conclude that a more detailed study on the originating sources of secondary electrons on EAS would thus require a mesh refinement on those specific spacecraft areas.

Figure 6.28 shows the origin of photoelectrons detected by the entire EAS instrument. They evidently come from the sunlit surfaces of the satellite but more precisely by the lower part of the Sunshield (it seems that the positively charged HGA attracts them efficiently towards EAS). But there is also the effect of meshing refinement in this Sunshield corner that reduces the current (displayed in A per cell). Plotting the current per unit area would be much more informative but it had not been implemented when these simulations were made. Only few photoelectrons emitted by the Solar panels are caught by EAS since emitting surface at +11.9 V highly recollect the particles. The HGA also produces some photoelectrons which are measured by the electron

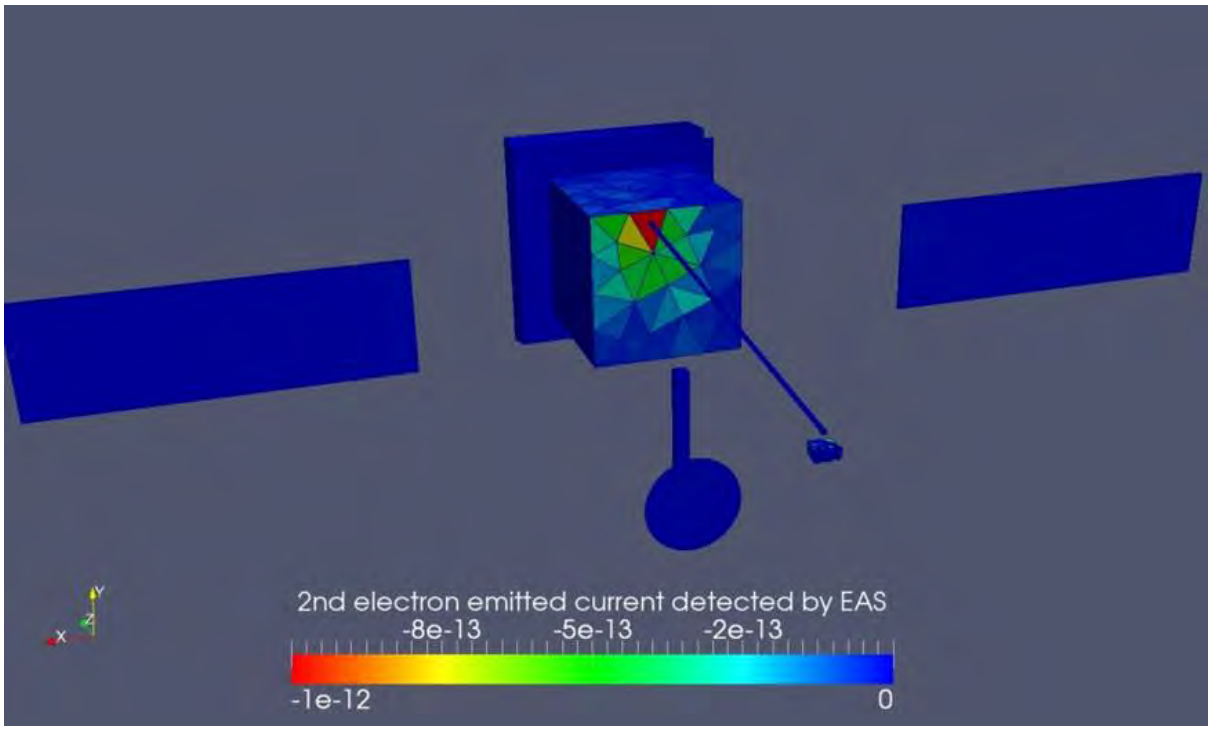

Figure 6.26: SOLO@1 AU - Source of SEEE detected by EAS. The data plotted is the current in A.

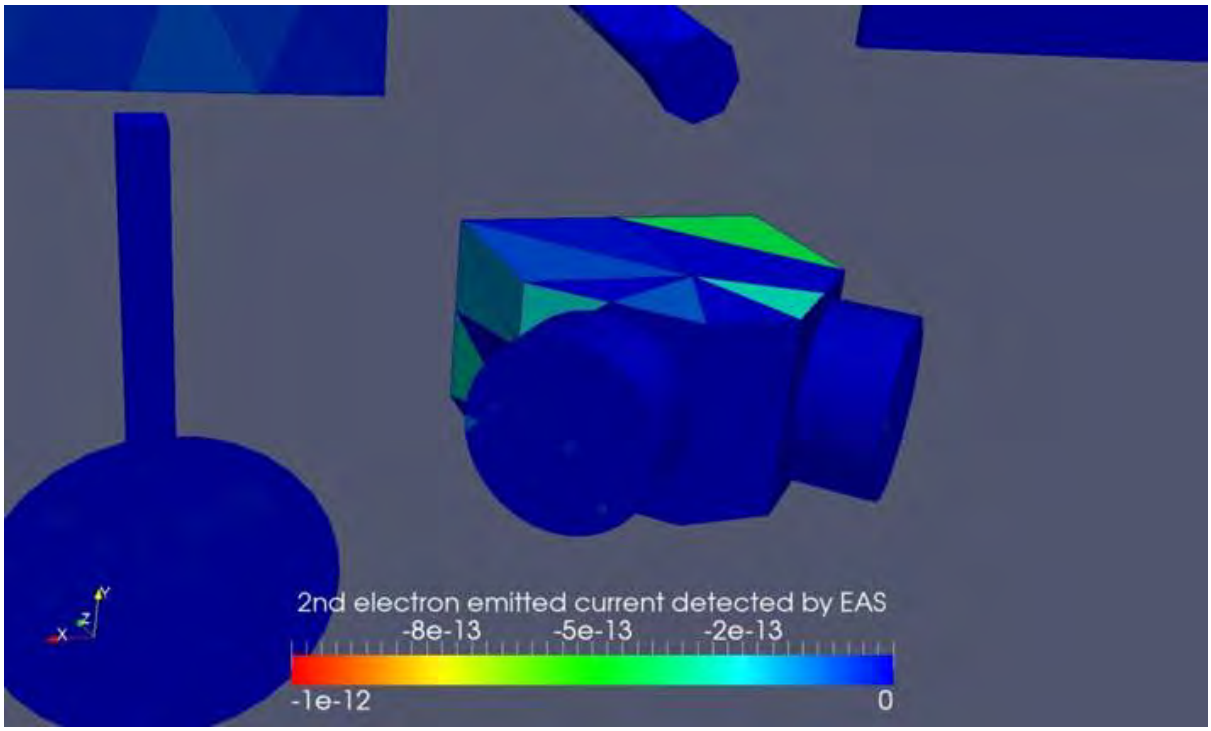

Figure 6.27: SOLO@1 AU - Source of SEEE detected by EAS, with a focuss on the EAS instrument. The data plotted is the current in A.

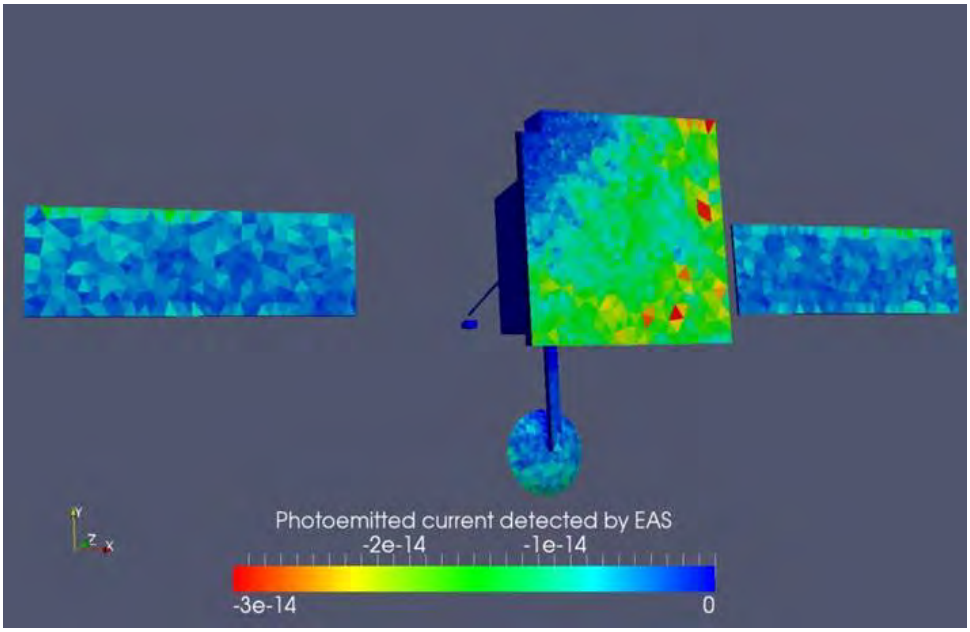

Figure 6.28: SOLO@1 AU - Source of photoelectrons detected by EAS (A) focussed on the EAS instrument. The data plotted is the current in A.

instrument.

Other results produced with post processing the particle detector outputs are the 2D maps of detection of thermal electrons regarding EAS pointing direction. They can provide information regarding the instrument field of view and help answer questions such as: where are the physical or electrostatic obstacles to electron detection and what are the consecutive impacts on measurements, from which directions come the highest/lowest particle fluxes, *etc.* Note that SPIS-SCI can provide directly several maps representing the detected fluxes (in a single user-defined reference basis and for each single particle detector). However the present EAS configuration is made of 16 collecting sections and the results have to be summed up into one map and with one reference basis the results of all detectors, to allow the global viewing of measurements. In this perspective an extended post-processing of the instrument output files and local basis transformation have thus been generated to compute the presented EAS maps. This work is performed outside of the SPIS framework, using a computation routine on the *Scilab* software and providing the desired 2D data tables. This method can also be applied to secondary and photoelectrons, which will be done for the further cases.

The EAS detailed field of view, with definition of pointing angles azimuth (AZ) and elevation (EL), was presented in Figure 6.9. The limits of AZ acceptance when EL = 0° are also represented (with thin purple and orange arrows) to show that both sensors are needed to cover the entire field of view. Figure 6.29 is the counting map of thermal electrons detected by the entire EAS instrument, regarding the pointing direction (AZ and EL angles). In order to compute this map it was necessary to create bins in AZ and EL (10° bins in this case) constituting the angular resolution (and similar to the real EAS angular resolution - see Figure 6.7). Only electrons with less than 15 eV energy have been treated (as low energy electrons are the most disturbed by the spacecraft presence in the environment). Other types of resolution/energy ranges can be of course selected to better fit other requirements. In red are indicated the objects pointed with

the corresponding values of AZ and EL: the Solar Arrays (SA) and the spacecraft body (SC) when looking behind EAS (note that the objects positions are quite approximated). The bin colors (from blue to red) indicate the number of electrons counted in each bin direction.

In the same Figure 6.29 the effect of the physical body clearly blocking particle arrival is manifest. The Solar panels do not visibly affect detection in their specific direction as they are quite thin regarding the bin precision and close to the spacecraft body. At AZ $\sim 90°$ and $\sim 270°$ (and EL $\sim 0°$) there is a lower particle detection due to several causes. First the pointing direction skimming or targeting the charged detectors themselves. Indeed it appears in Figure 6.9 that at AZ $\sim 90°$ and a null elevation, detector B on the left points towards the detector A on the right, charged at $+3.6$ V. Secondly the connection between the two detectors fields of view: indeed at these specific directions one detector begin its acceptance domain while the other ends it, see Figure 6.9, which also explains the loss of particles when both detectors point the null AZ and EL direction. When EL $\sim 0°$ the sensors have no common pointing directions. On the contrary the enhancement of electron detection at high EL values is simply due to a geometric factor: when EL approaches $\pm 90°$, both sensors have common pointing direction, whatever the AZ value considered. It results in an increase in particle counting. The HGA and the two lower RPW antennas have also a blocking effect on electrons (EL $\sim -45°$, AZ $\sim 180°$), this is why EAS collects fewer particles when pointing towards EL $\sim$ -90°, rather than EL $\sim$ $+90°$.

Maps similar to Figure 6.29 but representing this time the value of the particle average deflection angle at its arrival on EAS have also been generated. This angle (represented with the color scale on the Figure) is the difference between the electron velocity vector at injection in the simulation box and this vector at collection on the surface detector. This result (Figure 6.30) completes the counting map above, with a lack of information when pointing towards the rear spacecraft body due the absence of particles in this region. However the electrostatic effect due to the spacecraft positive potentials is obvious when pointing at regions around the satellite. There the average deflection is of nearly $\sim 40°$ meaning that most of them do not originate from those directions but from other areas and were deviated by the spacecraft positive potentials. Above and below the spacecraft elements deflection is thus also increased. Solar Orbiter, owing to its positive charge, acts as a focussing lens to electron detection, which is blatant in this Figure. The high deviations (at null EL) at AZ $\sim 90°$ and $\sim 270°$ correspond to regions where the particle fluxes are reduced (see Figure 6.29). The HGA effect is also visible when pointing in negative elevation ranges, while the top RPW antenna deflects the electrons coming from positive elevations. Electrons coming from the ion wake direction (approximatively null AZ and EL values) are practically not deflected, as no disturbing potentials appear locally in the wake for this S1 case.

6.1.2.4 Conclusion of the SOLO@1 AU simulation

This case showed that it is possible to model completely a spacecraft equipped with its scientific instrument, immersed in a specific environment, and observe the spacecraft/plasma interactions around the probe, on it, and within the particle measurement results. Outputs are consistent with our previous separated simpler studies concerning: 1/ the spacecraft/plasma interactions global behaviour at 1 AU [Guillemant et al. (2013)] (Appendix A.5: at this heliocentric distance: no potential barriers in the plasma sheaths and a positively charged satellite), 2/ the biasing effects on electron measurements (section 5.5.5) on a single instrument submitted to an attracting potential, the secondary electron emission and photoemission.

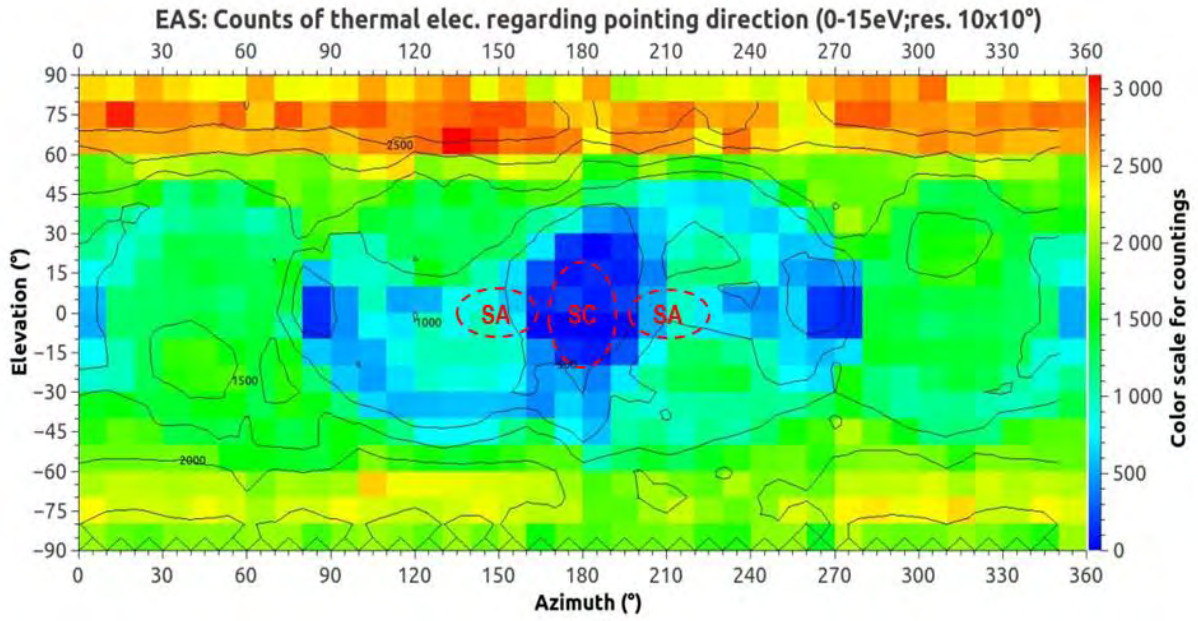

Figure 6.29: SOLO@1 AU - Counting map of thermal electrons detected by EAS. The estimated positioning of the Solar Orbiter elements are indicated with red dashed lines, the colour scale indicates the average number of superparticles collected per angular bins.

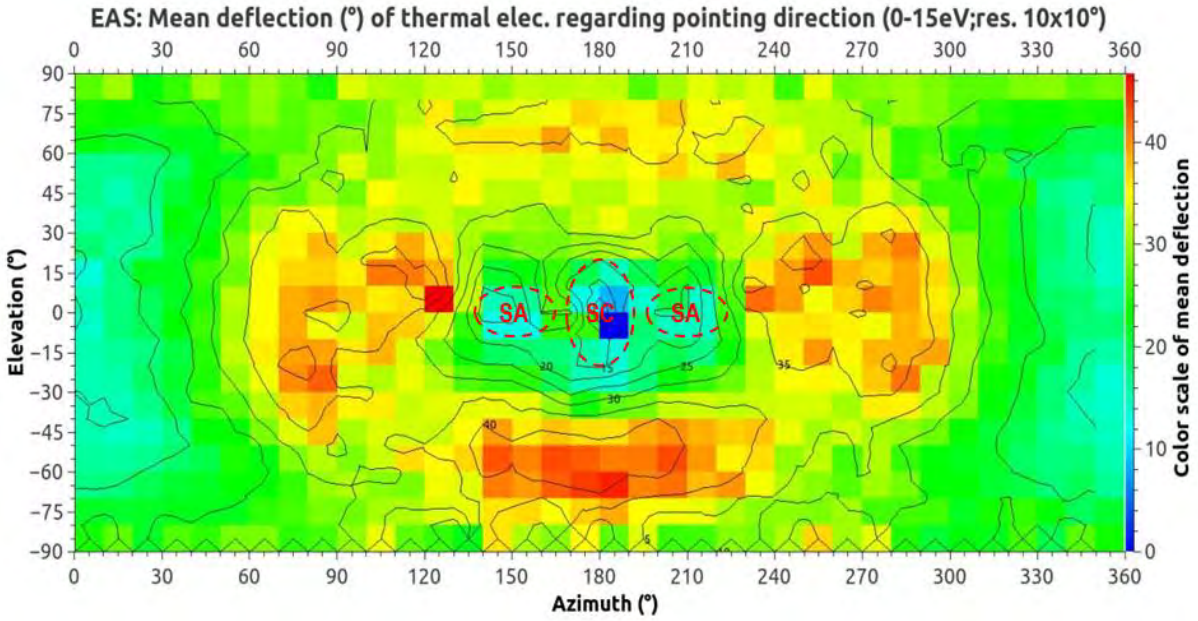

Figure 6.30: SOLO@1 AU - Deflection map of thermal electrons detected by EAS. The estimated positioning of the Solar Orbiter elements are indicated with red dashed lines, the colour scale indicates the average angular deflection (in degrees) of superparticles collected per angular bins.

Obviously the present SOLO@1 AU simulation is highly more complex than the simple combination of the previous separated studies. Both Solar Orbiter and EAS models are widely more developed compared with the previous entirely conducting cylinder and the electron detector made of two flat collecting surfaces. The analysis of this complex case benefited from the simpler studies performed in section 5.5. Obviously other studies could provide other leads of understanding. The ideal method should be the coupling of a global approach and a sequential study where the various perturbations are separated.

6.1.3 Results analysis of SOLO at 1 AU with a Fast Solar Wind

The SOLO@1 AU-FW validation case concerns Solar Orbiter at 1 AU from the Sun in a Coronal Mass Ejection (CME) configuration (faster Solar wind, higher temperatures for ions and electrons). Input parameters are detailed in Table 6.1. The simulation duration has been fixed to 5 s to ensure that steady potentials have been reached by the end of the simulation.

6.1.3.1 Satellite potential equilibrium

In this environment, the following steady potentials are obtained on the satellite:

- Spacecraft body and all conductive parts: +6.4 V
- Front faces of Solar panels: +15.4 V
- HGA: +11.1 V

Compared with SOLO@1 AU, at the same heliocentric distance but with a more energetic environment, SOLO@1 AU-FW showed that this type of CME will make the Solar Orbiter elements gain on average +3 V. This is due to the higher energetic environment in SOLO@1 AU-FW which generates more secondary electrons than in SOLO@1 AU, and thus contributes to more positive charging.

Indeed comparing the average SEEY over the entire satellite surface, for both simulations:

$$\text{For SOLO@1 AU: } \delta = \frac{I_{\text{SEEE,emit}}}{I_{\text{the,coll}}} = \frac{1.64 \times 10^{-5}}{4.38 \times 10^{-5}} = 0.37$$

$$\text{For SOLO@1 AU-FW: } \delta = \frac{I_{\text{SEEE,emit}}}{I_{\text{the,coll}}} = \frac{7.29 \times 10^{-5}}{6.60 \times 10^{-5}} = 1.10$$

The average SEEY in this case greater than unity means that the secondary emission counterbalances the ambient electron collected current, while for SOLO@1 AU the SEEE combined to the electron collection tends to lower the potentials. This is the main explanation for this charging difference as the photoemission yields are identical (same Solar flux at 1 AU), and the thermal electron currents $I_{\text{the,coll}}$ are nearly of the same order. In this fast and more energetic solar wind condition, because of the high surface emission, the potentials rise higher because of SEEE and stabilize once $\Sigma\Phi_{SC}$ are sufficient to attract the secondary electrons and reach the current balance.

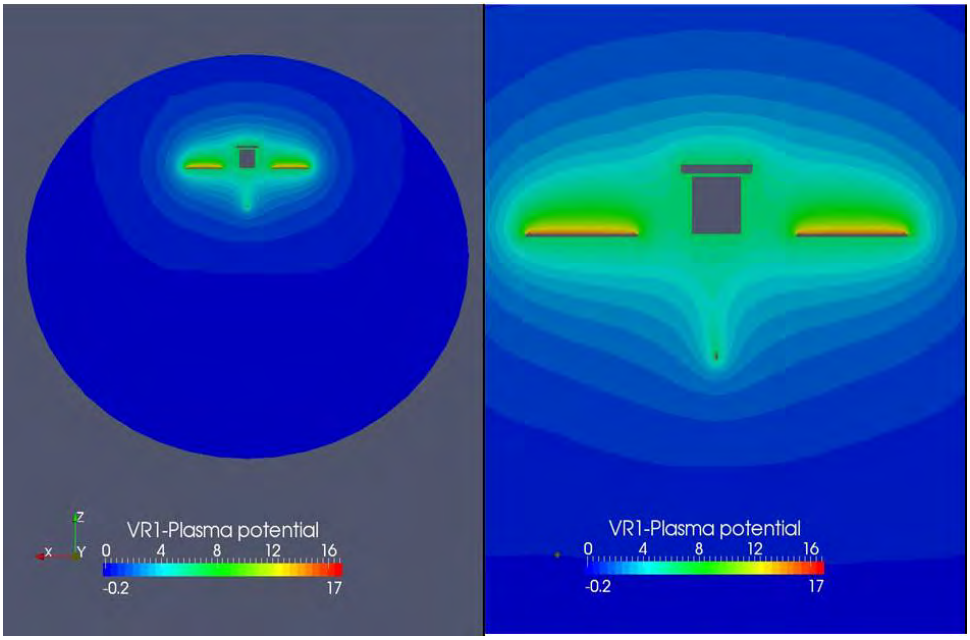

Figure 6.31: SOLO@1 AU-FW - Plasma potential around Solar Orbiter in the $(X - Z)$ plane. Focus on the spacecraft on the right side.

6.1.3.2 Plasma

Plasma potential is displayed in Figure 6.31 and 6.32, the potential decrease from the satellite surface to simulation box boundaries is practically monotonic, except in the region far behind the spacecraft where -0.23 V are reached (weakly repulsive for the 40 eV thermal electrons). There are no potential barriers for secondary electrons and photoelectrons in the vicinity of the satellite. All thermal electrons around are thus accelerated by the positive potentials of Solar Orbiter.

The plasma population densities are plotted on Figure 6.32, 6.33 and 6.34 (*resp.* ions, electrons and photoelectrons, SEEE and SEEP). The ion wake reaches the rear boundary of the simulation box. We observe the same behaviour of photoelectrons and secondary electrons regarding SOLO@1 AU.

This simulation can be compared to SOLO@1 AU (same heliocentric distance but different environment). The recollection rates are close to the ones for SOLO@1 AU: 88% of photoelectrons and 87% of SEEP are recollected, and for SEEE it reaches 79% (more than the 70% for SOLO@1 AU but Solar Orbiter is here more positively charged). The net current of SEEP (1.9×10^{-6} A) is still below the net currents of SEEE (1.47×10^{-5} A) and photoelectrons (3.36×10^{-5} A) but 4 times greater than for SOLO@1 AU as ions are here more energetic (see Table 6.1). Compared with others, SEEP are still of secondary order of magnitude in the establishment of the current balance and the final potentials.

6.1.3.3 EAS measurements

The energy distribution functions of expected environment and measured electrons are displayed in Figure 6.35 for thermal electrons and 6.36 for all electronic populations. In this last Figure the curve representing the measured SEEP energy distribution function appears but it is negli-

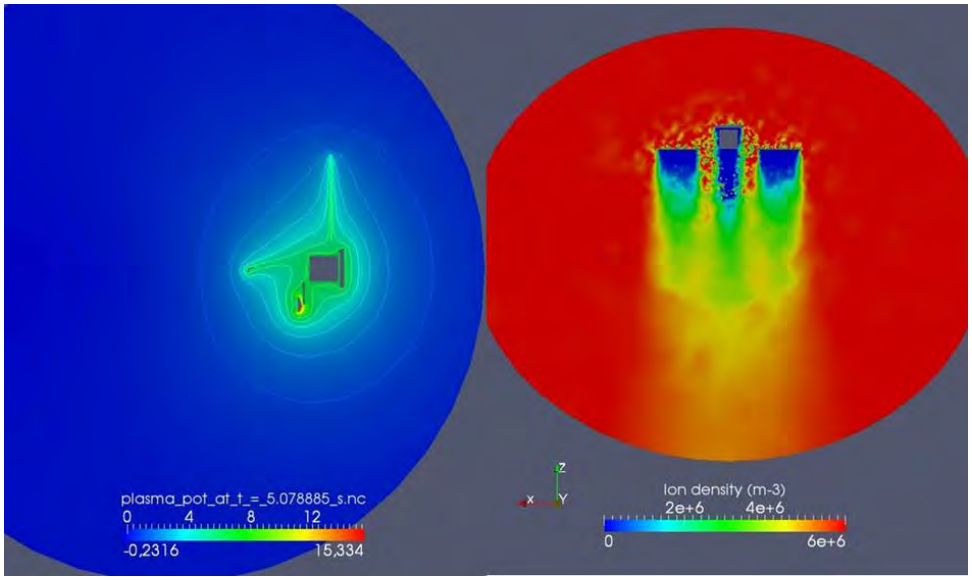

Figure 6.32: SOLO@1 AU-FW - Plasma potential in the $(X - Z)$ plane (left) and ion density in the $(X - Z)$ plane (right).

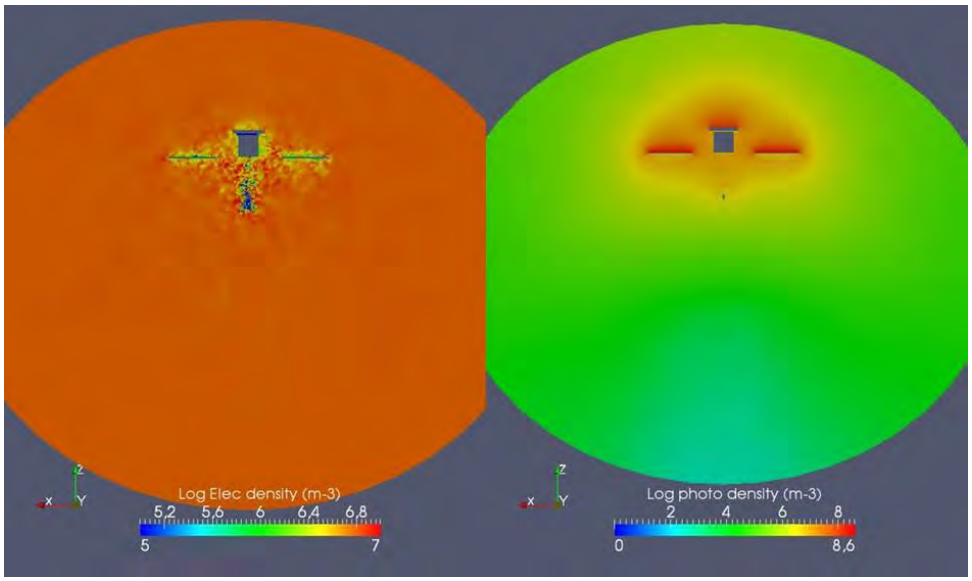

Figure 6.33: SOLO@1 AU-FW - Log of thermal electron density (left) and photoelectrons (right).

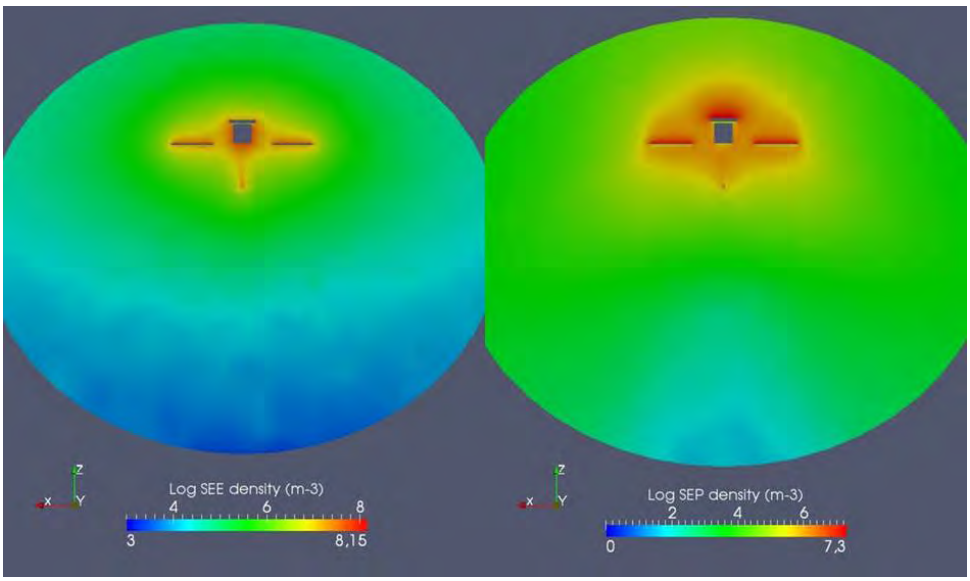

Figure 6.34: SOLO@1 AU-FW - Log of SEEE density (left) and SEEP (right).

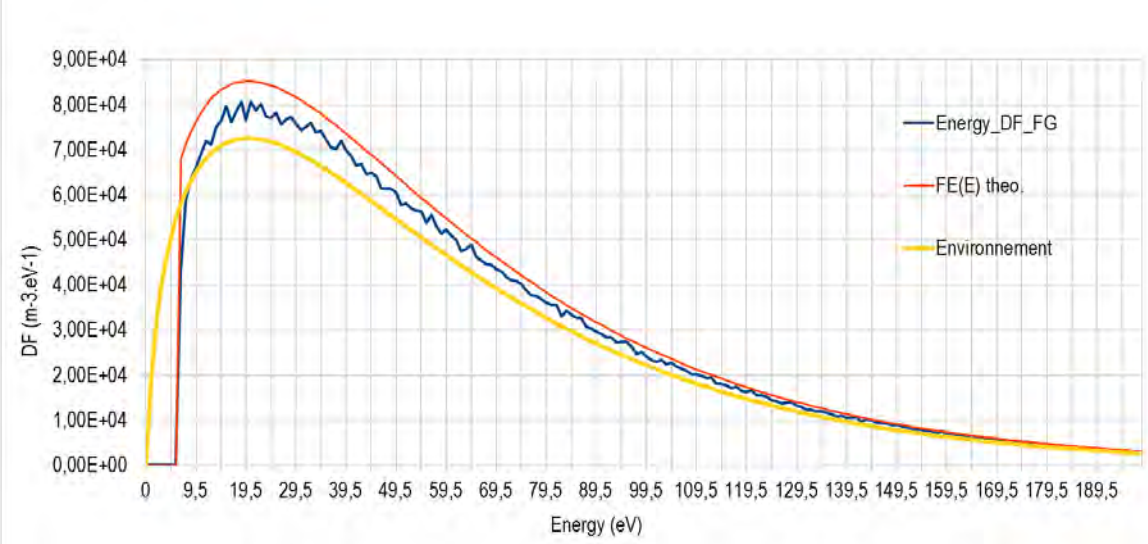

Figure 6.35: SOLO@1 AU-FW - Energy distribution functions of thermal electrons on EAS.

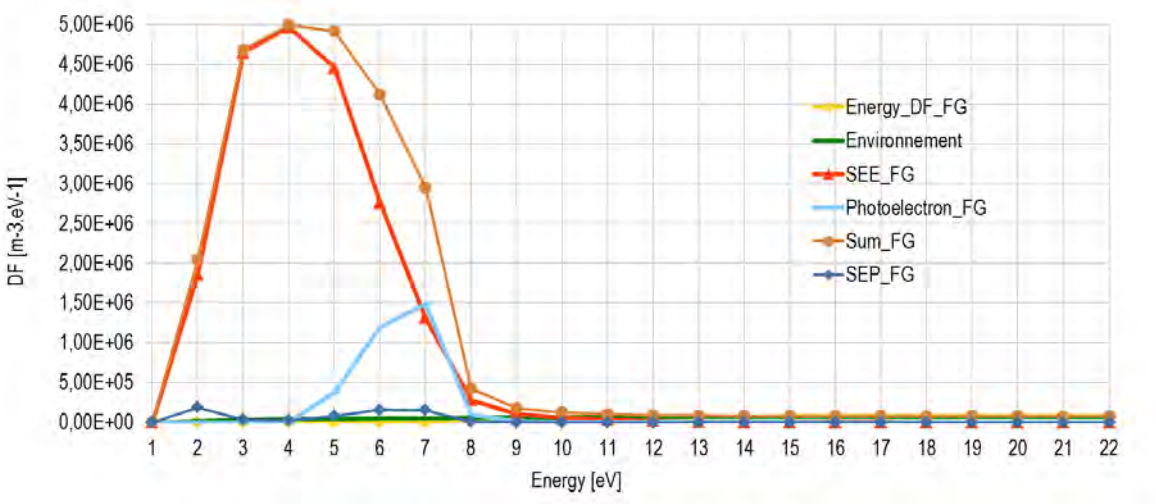

Figure 6.36: SOLO@1 AU-FW - Energy distribution functions of all electrons on EAS.

gible compared with SEEE or photoelectrons. The corresponding densities calculated from an integration of thermal electrons DF (Figure 6.35) are:

- Undisturbed environment (yellow): $N_0 = 5.89 \times 10^6\,\mathrm{m}^{-3}$ for a root density (Table 6.1) of $6.00 \times 10^6\,\mathrm{m}^{-3}$. The difference is due to the truncated integration in the injected model
- Theory (orange): $N_{\mathrm{theo}} = 6.63 \times 10^6\,\mathrm{m}^{-3} > N_0$ because of EAS potential (+6.43 V)
- Measurements (blue): $N_{\mathrm{meas}} = 6.16 \times 10^6\,\mathrm{m}^{-3} < N_{\mathrm{theo}}$ because of the spacecraft charged structure and the plasma disturbances (ion wake, solar panels, HGA, *etc*).

The simulated measurements of thermal electrons give a difference of 4.6% compared to N_0, which is less than obtained for the SOLO@1 AU because here the ambient populations are more energetic and thus less affected by the satellite potentials. Adding to those measurements the detected populations of photoelectrons, SEEE and SEEP (Figure 6.21) gives a total density of measured electrons (the blue curve) of $N_{\mathrm{total}} = 2.74 \times 10^7\,\mathrm{m}^{-3}$ (an increase of 365% compared to N_0). Actually the low energy ranges are overwhelmed by secondaries, which is understandable when noticing that SOLO@1 AU-FW has the most energetic environment among all test runs performed for SPIS-SCI.

The existence of measured secondary and photoelectrons beyond the satellite potential threshold seems contradictory to previous results obtained in Chapter 5, when only the positively charged instrument was considered, alone in the plasma. Indeed in that cases the single instrument collected secondary particles emitted from itself, meaning that those electrons must have been deviated enough to reach the detector surfaces. Only the particles with energies lower that the surface potential could be detected. Higher energy electrons escaped. In the present case, EAS does have other spacecraft elements in his direct field of view: considering the Maxwellian distribution of the satellite emitted electrons, some energetic secondary and photoelectrons could escape the attracting potentials of their emitting surfaces and end their path on EAS.

6.1.4 Results analysis of SOLO at 0.28 AU

In this case SOLO@0.28 AU is based on the Solar Orbiter spacecraft immersed in its closest perihelion environment at 0.28 AU from the Sun (see the plasma parameters in Table 6.1). As explained earlier, the thermal electron Debye length is small compared with the initial meshing size on the boundary surface, which is no longer smaller than $\lambda_D/2$. This is why the previous simulation box used for SOLO@1 AU and SOLO@1 AU-FW has been reset with smaller meshing at its boarders: 1.5 m instead of 3 m (it also led to reduce the simulation box size to keep reasonable computational times). The new domain dimensions are 36 m length × 28 m width (compared with the former 40 m length × 48 m width). The number of tetrahedrons reaches 270000 (instead of 205000 before). This reduction of the box dimension along the X axis will not affect the plasma computation around the satellite as previous simulations show that key locations of plasma issues (ion wakes, secondary or photoelectron sheaths) are not situated in those omitted regions. This is a typical step of geometry optimisation.

In this case, the SPIS software has generated the following number of particles (approximately):

- electrons = 3500000
- ions = 1500000
- photoelectrons = 1400000
- SEEE = 2500000
- SEEP = 600000

6.1.4.1 Satellite potential equilibrium

In this SOLO@0.28 AU environment, the following steady potentials are obtained on the satellite:

- Body and all conductive parts : +3.1 V
- Front faces of Solar panels: +14.1 V
- HGA: +9.0 V

The potential on the spacecraft conducting parts remains stable regarding SOLO@1 AU (also at $\sim +3$ V). The dielectric elements gained around +2 V.

6.1.4.2 Plasma

The plasma potential is displayed in Figure 6.37, the potential decrease from the satellite surface to simulation box boundaries is this time non-monotonic. It reaches -1.25 V in the ram (due to high densities of secondary and photoelectrons) and -2.7 V in the wake (due to the lack of ions and high densities of thermal and secondary electrons). Those barriers have different values regarding incoming particles: for secondary and photoelectrons emitted from the spacecraft, they encounter -4.4 V in the ram and -5.8 V in the wake which might force their recollection (added to the positive spacecraft potential effect). Thermal electrons, however, are coming from outside the sheath and thus face only -1.25 V in the ram and -2.7 V in the wake which is a weak repulsive potential regarding their thermal energy of 21 eV. The thermal electrons

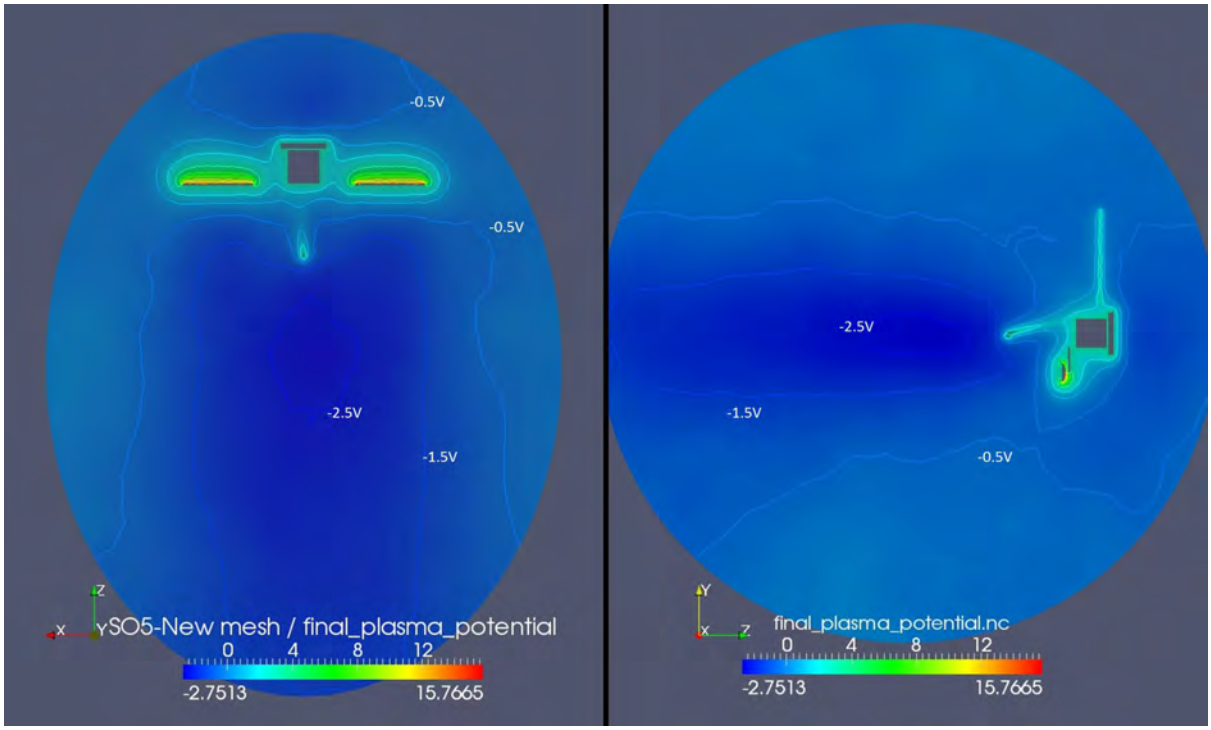

Figure 6.37: SOLO@0.28 AU - Plasma potential (left: $X-Z$ plane, right: $Y-Z$ plane).

measurements by EAS should be somewhat disturbed by the potential barriers, the photo and secondary electrons recollection and the spacecraft positive potentials.

This result is consistent with [Guillemant et al. (2013)] (Appendix A.5) which showed that at this distance from the Sun a spacecraft floating potential will be a few volts positive, despite the presence of potential barriers in the ram and in the wake. In [Guillemant et al. (2013)] the model used was a simple fully conducting cylinder while here the model is much more complex. It is larger in volume and also accounts for conducting surfaces as well as for dielectric surfaces. The global results for this environment however, is not significantly affected by these differences in geometry and material properties. The general plasma behaviour obtained through SOLO@0.28 AU also fits the first estimations made in [Isensee (1977)], where at 0.2 AU from the Sun with a simple spacecraft geometry: a lightly positively charged satellite (+2.9 V) was obtained, surrounded by negative plasma potentials in the wake (-4.5 V) and in the ram (-1.4 V), although the two numerical models and methods used are quite different (see section 3.9).

The plasma population densities are plotted in Figures 6.38, 6.39 and 6.40 (respectively ions, electrons and photoelectrons, SEEE and SEEP). The ion wake reaches the rear boundary of the simulation box. The recollection rates are: 86.5% of photoelectrons and 85% of SEEP are recollected, and for SEEE it reaches 71.7%. The net current of SEEP (3.37×10^{-6} A) is below the net currents of SEEE (1.55×10^{-4} A) and photoelectrons (4.93×10^{-4} A).

6.1.4.3 EAS measurements

Energy distribution functions of expected environment and measured electrons are displayed in Figures 6.41 and 6.42. The corresponding densities calculated through integration of thermal electrons DF (Figure 6.41) are:

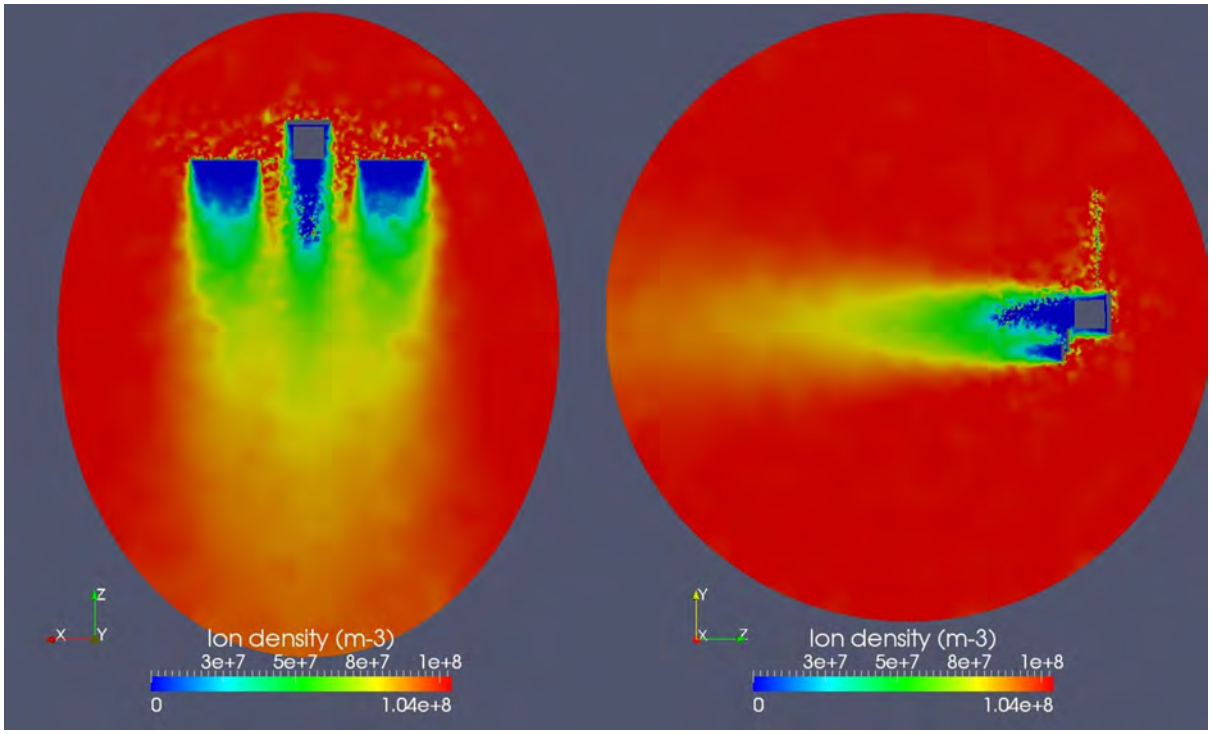

Figure 6.38: SOLO@0.28 AU - Ion density (left: $X - Z$ plane, right: $Y - Z$ plane).

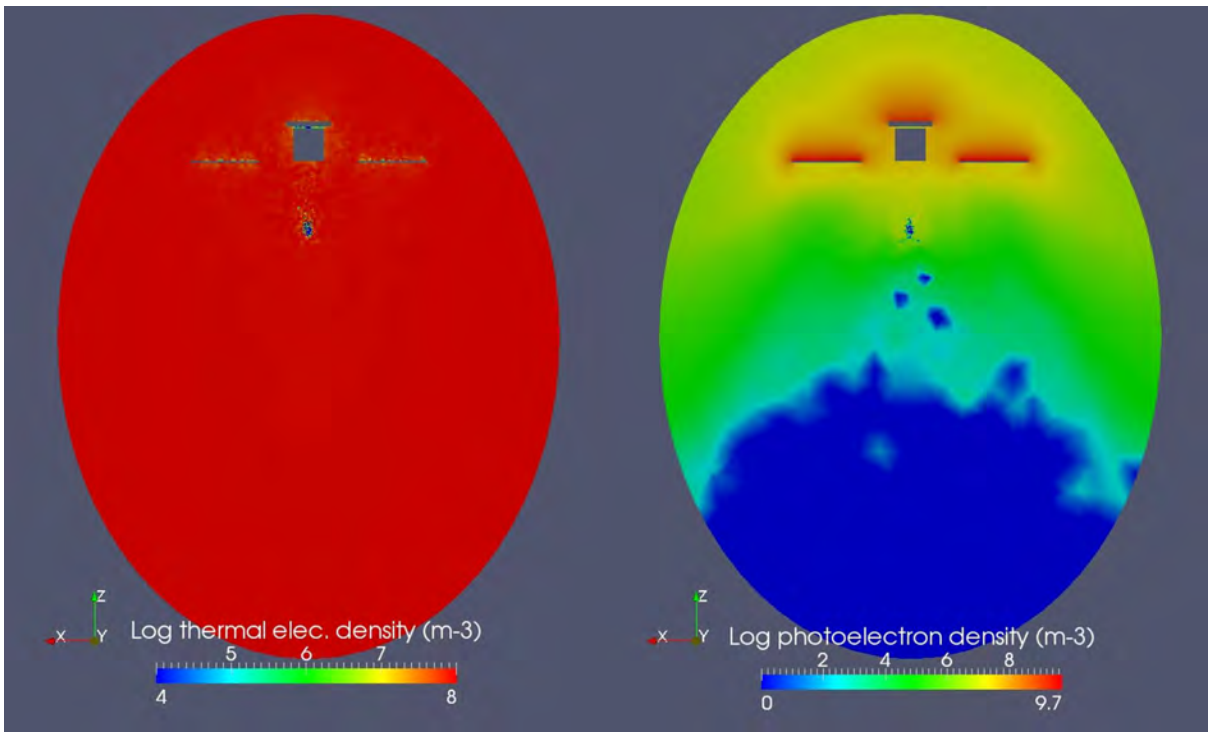

Figure 6.39: SOLO@0.28 AU - Log of thermal electron density (left) and photoelectron density (right).

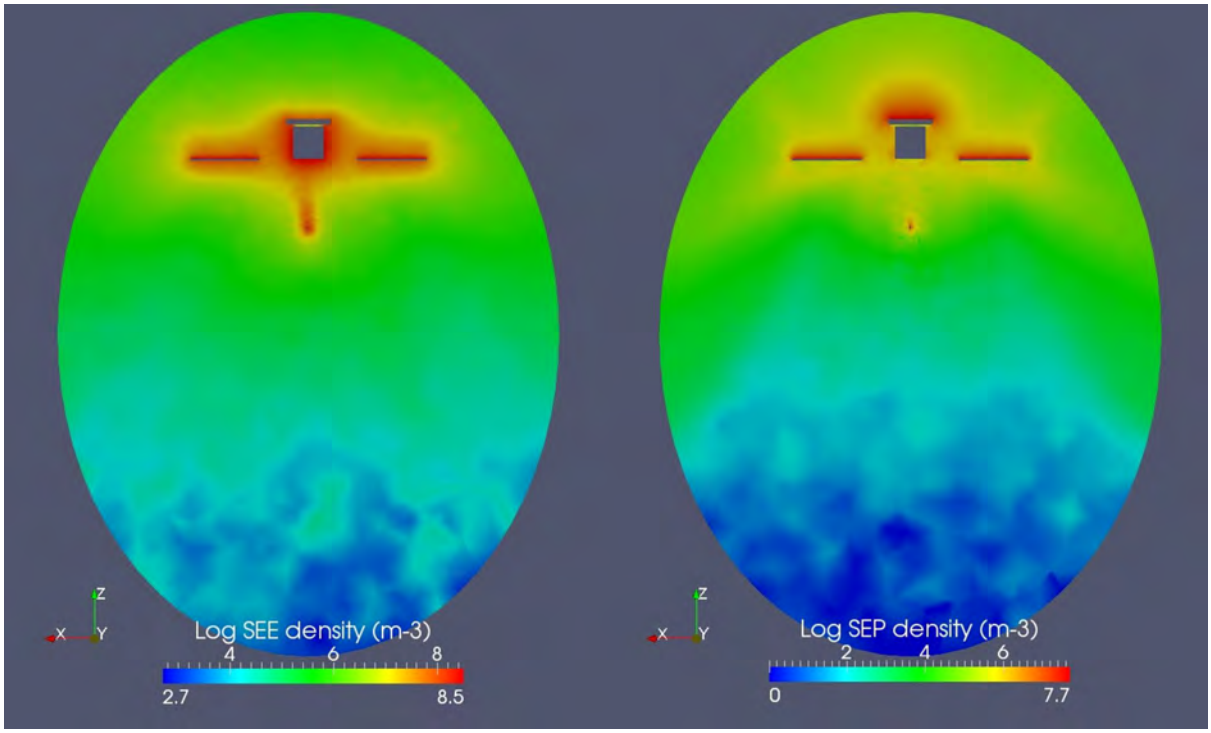

Figure 6.40: SOLO@0.28 AU - Log of SEEE (left) and SEEP (right) density.

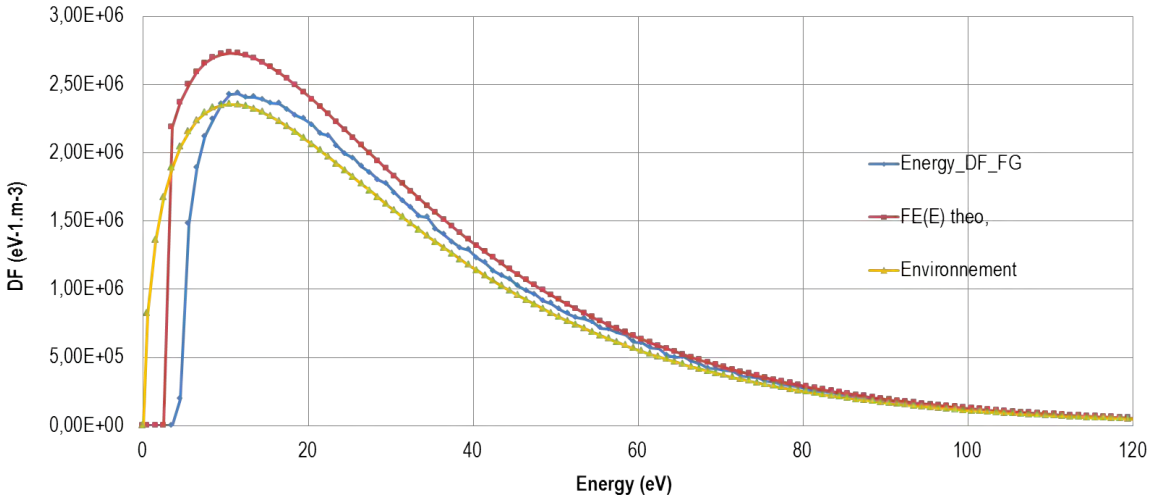

Figure 6.41: SOLO@0.28 AU - Energy distribution functions of thermal electrons on EAS.

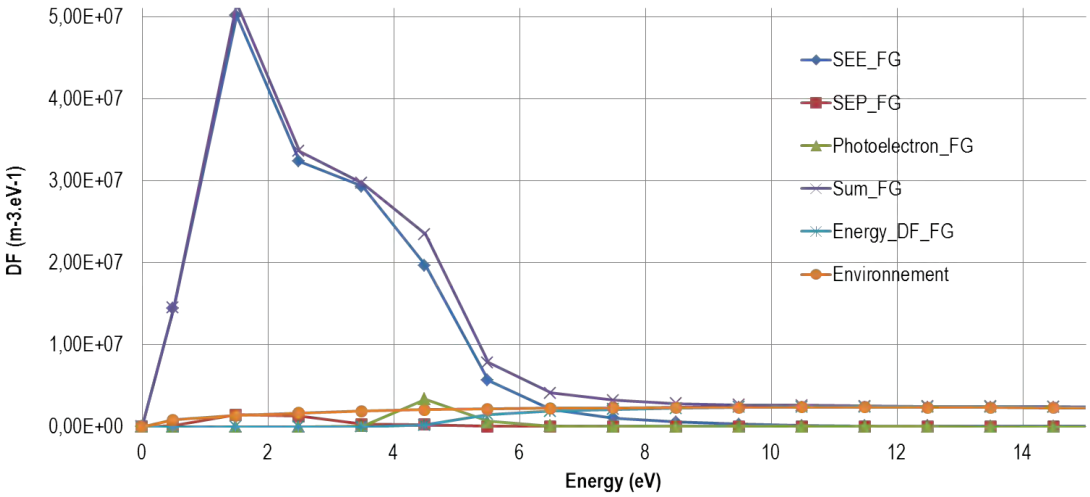

Figure 6.42: SOLO@0.28 AU - Energy distribution functions of all electrons on EAS.

- Undisturbed environment (yellow): $N_0 = 1.04 \times 10^8\,\mathrm{m}^{-3}$ for the same background density (Table 6.1). Same values are found as this model is practically not truncated (the highest temperature considered is 200 eV *i.e.* almost 10 times the thermal electrons temperature modelled),
- Theory (orange): $N_{\mathrm{theo}} = 1.16 \times 10^8\,\mathrm{m}^{-3} > N_0$ because of EAS potential (+3.16 V)
- Measurements (blue): $N_{\mathrm{meas}} = 1.01 \times 10^8\,\mathrm{m}^{-3} < N_{\mathrm{theo}}$ because of the spacecraft charged structure and the plasma disturbances (ion wake, solar panels, HGA, potential barriers).

It can be noticed that the simulated electron measurements (blue curve) is lower than the theoretical red curve (analytical model): it sounds like low energy electrons (visibly between 3 and 5 eV) are missing. This contrasts with respect to the results obtained for the SOLO@1 AU case. The explanation is that the EAS instrument is here surrounded by negative potential barriers between -1.5 and -2.5 V: they filter the low energy electrons. The particles which cross those barriers are then accelerated by EAS potential. The minimum energy of those elements becomes: $1.5 + 3.1 = 4.6$ eV. Negative potentials around the particle detector increase the SEEE densities through electron impacts, which appears in Figure 6.42 where the maximum DF reaches $5 \times 10^7\,\mathrm{m}^{-3}.\mathrm{eV}^{-1}$ for SEEE and $2.5 \times 10^6\,\mathrm{m}^{-3}.\mathrm{eV}^{-1}$ for the primary electrons (factor 20). For the SOLO@1 AU-FW case it was $5 \times 10^6\,\mathrm{m}^{-3}.\mathrm{eV}^{-1}$ for SEEE and $8 \times 10^4\,\mathrm{m}^{-3}.\mathrm{eV}^{-1}$ for the primary electrons (factor 75). This is due to the negative potentials.

The simulated measurements of thermal electrons give a discrepancy of 2.8% regarding N_0. Adding to the measurements photoelectrons, SEEE and SEEP (Figure 6.42) gives a total density of measured electrons (the purple "Sum" curve) of $N_{\mathrm{total}} = 2.42 \times 10^8\,\mathrm{m}^{-3}$ (a difference of 132% regarding N_0). The low energy ranges are highly dominated by SEEE.

In the next Figures 6.43 and 6.44 are presented the maps of respectively counting and deflection of thermal electrons detected by EAS for SOLO@0.28 AU, for electrons of energy lower than 15 eV. The same observations as for SOLO@1 AU can be made here: physical blockade of particles due to the spacecraft body (AZ $\sim 0°$) plus the decrease of visibility for AZ $\sim 90°$ and AZ $\sim 270°$ due to the absence of common views between the two EAS sensors. At null AZ and

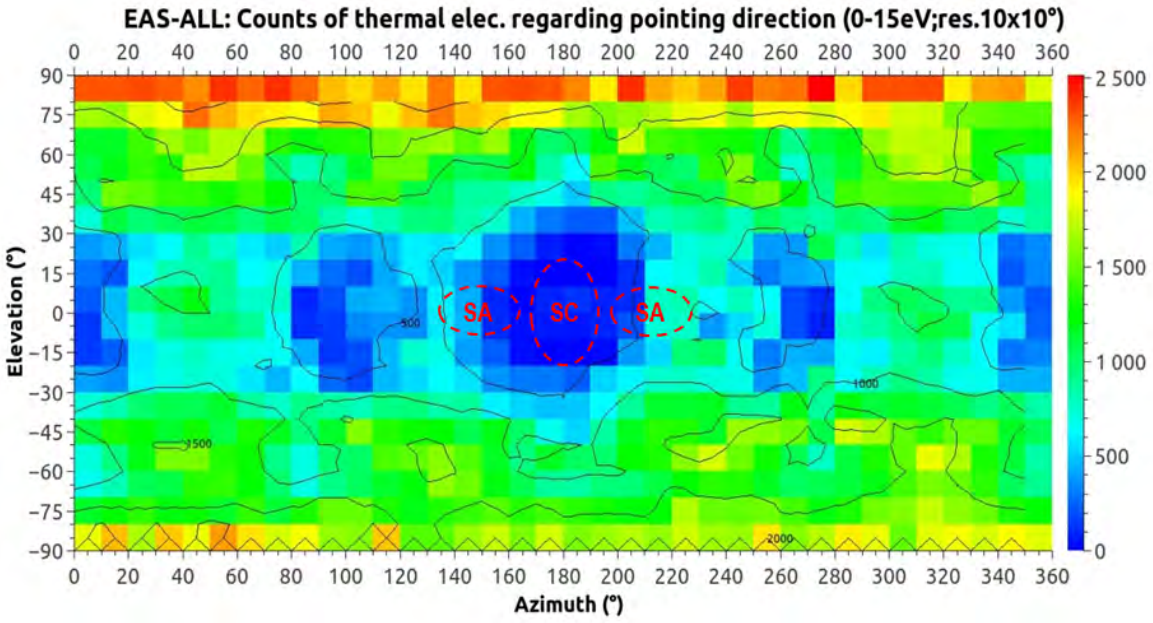

Figure 6.43: SOLO@0.28 AU - Counting map of thermal electrons detected by EAS. The estimated positioning of the Solar Orbiter elements are indicated with red dashed lines, the colour scale indicates the average number of superparticles collected per angular bins.

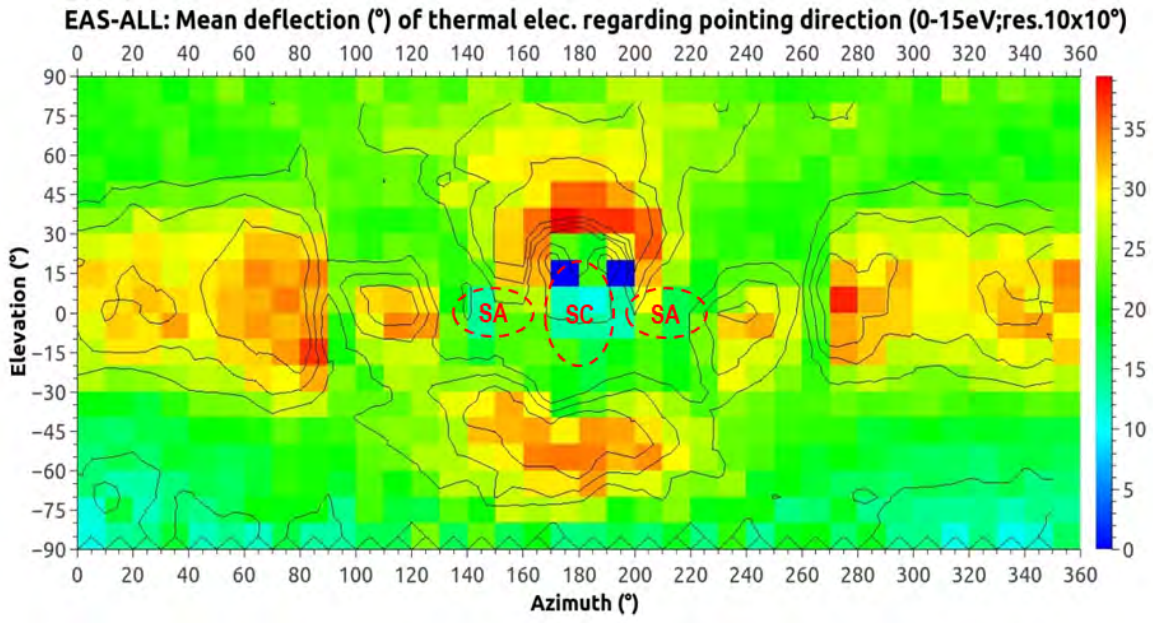

Figure 6.44: SOLO@0.28 AU - Deflection map of thermal electrons detected by EAS. The estimated positioning of the Solar Orbiter elements are indicated with red dashed lines, the colour scale indicates the average angular deflection (in degrees) of superparticles collected per angular bins.

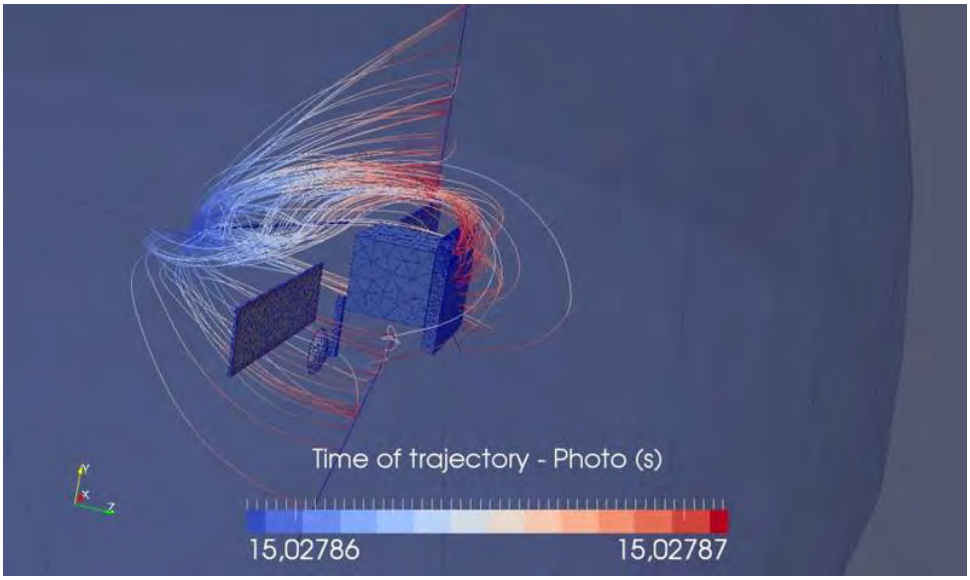

Figure 6.45: SOLO@0.28 AU - Trajectories of some photoelectrons detected by EAS. Most of them come from sunlit surfaces with the less attracting potentials, *i.e.* the conducing elements at +3.16 V (sunshield, RPW antennas) as the solar panels and the HGA are more positively charged and recollect more photoelectrons.

EL between ± 30° the decrease of thermal electron detection is a combination of two factors: first this pointing direction also corresponds to the connection between the two sensors limit acceptance angles (see Figure 6.9), which local effect has already been noticed in the previous results obtained for SOLO@1 AU (on the counting map 6.29). The second reason which makes the electron decrease more important than the one observed locally in SOLO@1 AU is that with SOLO@0.28 AU the rear wake, combined with the important secondary electron population within the ion depletion, digs the local electrostatic potentials down to -2.7 V (see Figure 6.37). This repulsive potential represents only 12.6% of the electron temperature (21.37 eV) but it is sufficient to deviate a non negligible proportion of the particle distribution, thus increasing the loss of the low energy electrons.

This analysis is confirmed by the deflection map (Figure 6.44) for electrons of energy lower than 15 eV. Indeed when pointing the large rear part of the environment (for AZ between 270° and 90°), behind the Solar Orbiter body, it corresponds to directions where particles have been quite deflected (around 30-40°). It indicates that incoming electrons arriving on the EAS sensors with this orientation of their velocity vector, were initially injected in another direction. The rear plasma sheath and its disturbed potential pattern modified the low energy electron trajectories. Indeed the potential map (Figure 6.37) shows the EAS instrument surrounded by a negative potential contour (of -1.5 V) over a large azimuthal range. For AZ closer to 120 and 240° the positively charged solar arrays effects are visible, through several bins of directions corresponding to deviated fluxes. Finally the spacecraft body accelerated its upward and downward fluxes of particles, through the positive potentials on its conductive parts (body, upper RPW antenna and the HGA below). Both spacecraft potentials (body, solar panels, HGA and RPW antennas), surrounding environment potentials and EAS characteristics emphasise their influence on the low energy electron measurements.

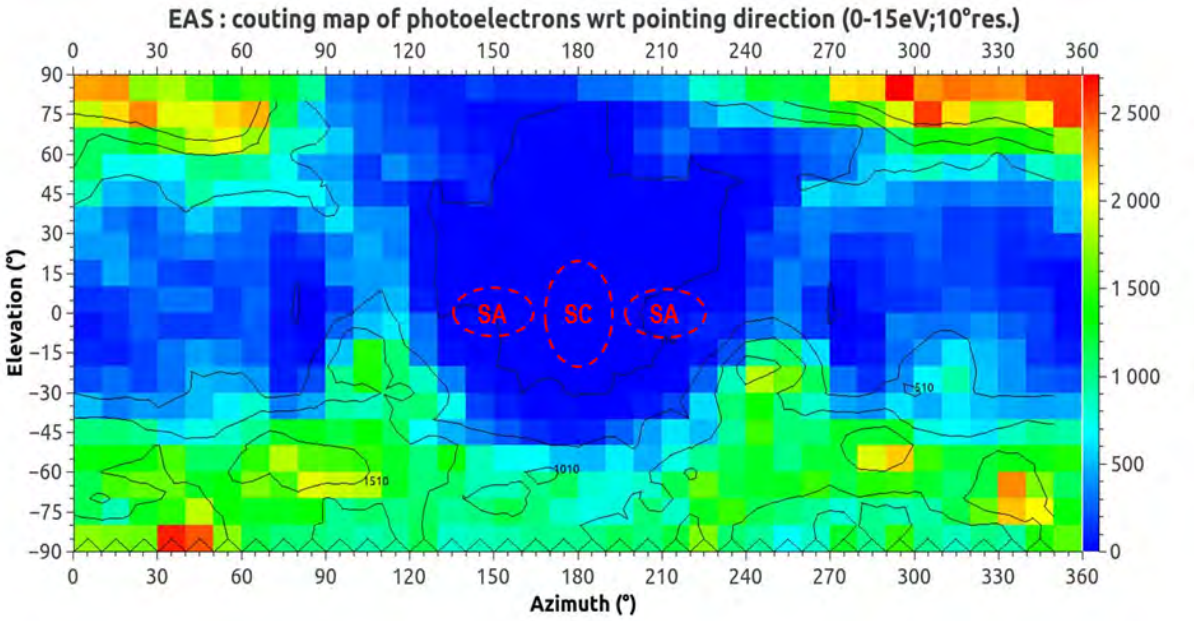

Figure 6.46: SOLO@0.28 AU - Counting map of photoelectrons detected by EAS. The estimated positioning of the Solar Orbiter elements are indicated with red dashed lines, the colour scale indicates the average number of superparticles collected per angular bins.

Some secondary and photoelectrons come from the sunlit faces of Solar Orbiter and escaped the attracting potentials of their originate materials (the recollection rate is of 86.5%). Figure 6.45 shows that EAS collects photoelectrons mostly from sunshield and RPW antennas since their potential is of "only" +3.16 V which makes the particle escaping more feasible than from the HGA and the front solar panels. The corresponding photoelectron fluxes obtained on EAS regarding its pointing direction are presented on the maps 6.46 for the counting of superparticles and 6.47 for the deflections. It can thus be verified that practically no photoelectrons come directly from the shadowed satellite surfaces or from the wake. The few arriving from pointing directions around the satellite body have been highly deflected. The HGA visibly impacted the photoelectron trajectories from the negative elevation incoming direction.

This methodology allows to identify the main sources of disturbing effects within EAS outputs as the originating surfaces of the detected photoelectrons or the preferred trajectories of those biasing particles. Secondary electrons remain the most important pollution in electron measurements. This can be used to develop further filtering technical methods to avoid considering any supposed polluted measurements within a dataset (as an instantaneous measure or for a certain period due to the Sun orientation with respect to the spacecraft attitude).

6.1.4.4 Investigations on numerical parameters

In the VTR - Part I produced for ESA I proceeded to simulation comparisons using different numerical inputs. Several values of SPIS numerical parameters such as, for example, the automatic control of simulation time steps used by the implicit circuit solver have been tested. Those studies refer to advanced ways to optimize SPIS simulations, by improving duration of computation and precision. Results are detailed in the VTR but they will not be presented

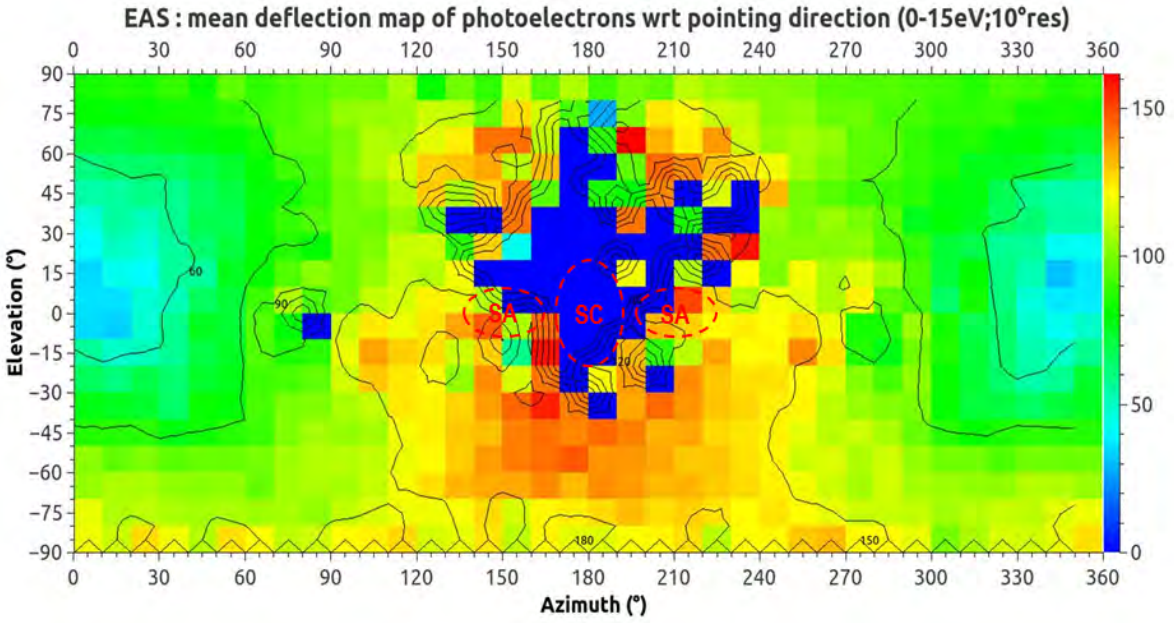

Figure 6.47: SOLO@0.28 AU - Deflection map of photoelectrons detected by EAS. The estimated positioning of the Solar Orbiter elements are indicated with red dashed lines, the colour scale indicates the average angular deflection (in degrees) of superparticles collected per angular bins.

here because of the very specific numerical aspect of this phase. However one global result is synthesized in the following.

For instance, concerning the meshing issue explained in section 6.1.4, two cases of SOLO@0.28 AU were run. One was using the "old" mesh deployed in the SOLO@1 AU simulation (with too large tetrahedra on the external boundary for the environment at 0.28 AU) and another case used the "new" mesh presented in the previous section, which has a meshing grid better adapted to the Debye length at this short heliocentric distance.

The first difference appears in plasma potential regularity and smoothing. Indeed the first Figure 6.48 displays the plasma potential around Solar Orbiter for both meshes. The two Figures 6.49 and 6.50 present the potential values on respectively axes Z and X for the two grids (those axes are represented in Figure 6.48). We remind that the two simulation boxes do not have the same dimensions. The new mesh (that takes into account the Debye length for the environment at 0.28 AU) allows a better computation of plasma potential. The smoother and more regular potential appears on this map and on the potential profiles. Those differences, that are represented by low potential variations in the plasma, will essentially affect secondary and photoelectrons that are the less energetic particles.

We also notice that enhancing the potential contours (obtaining a smoother and more symmetric plasma potential) did not change final charging on spacecraft elements. The potentials obtained on the satellite for both cases are presented in Table 6.2, with the associated uncertainty regarding the most adapted new mesh (around 1% of difference).

We can also compare the EAS measurement precision obtained using the old and new mesh (Table 6.3). Secondary electrons and photoelectrons are the most affected by this mesh enhancement, as the plasma potential in the vicinity of EAS and in the ion wake is better resolved. Thermal electrons, hotter than secondary particles, are less influenced by low potential varia-

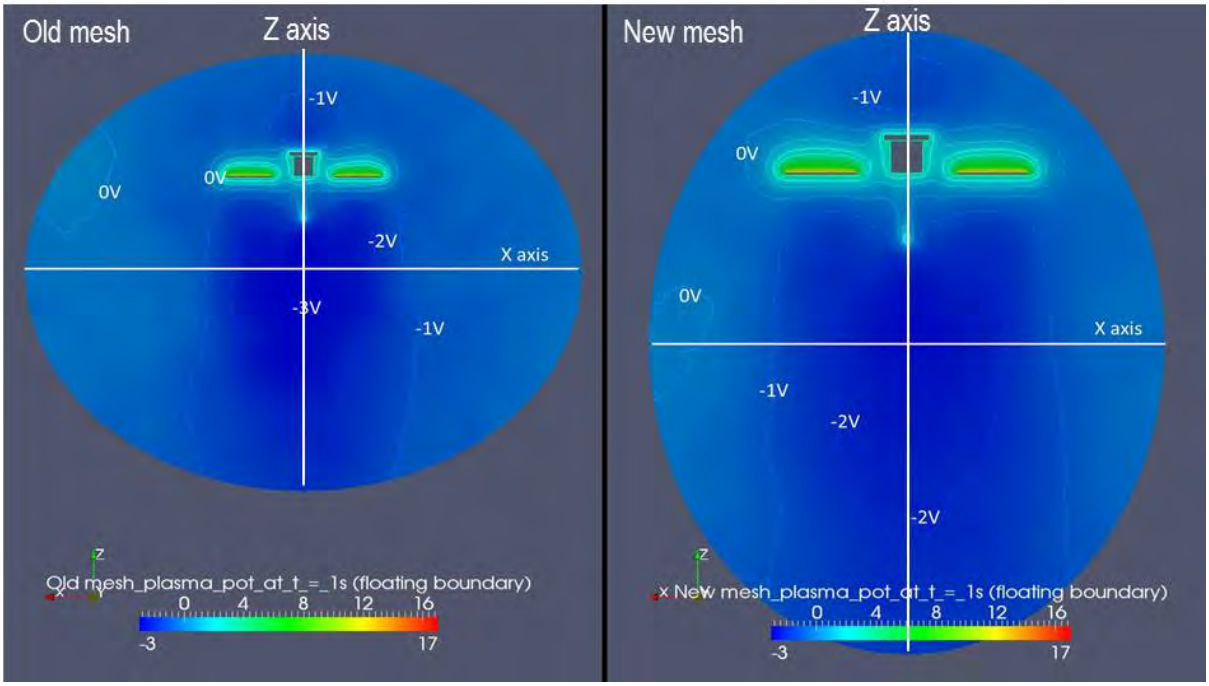

Figure 6.48: SOLO@0.28 AU - Comparison of plasma potential maps obtained with two different meshes (left: old mesh, right: new mesh).

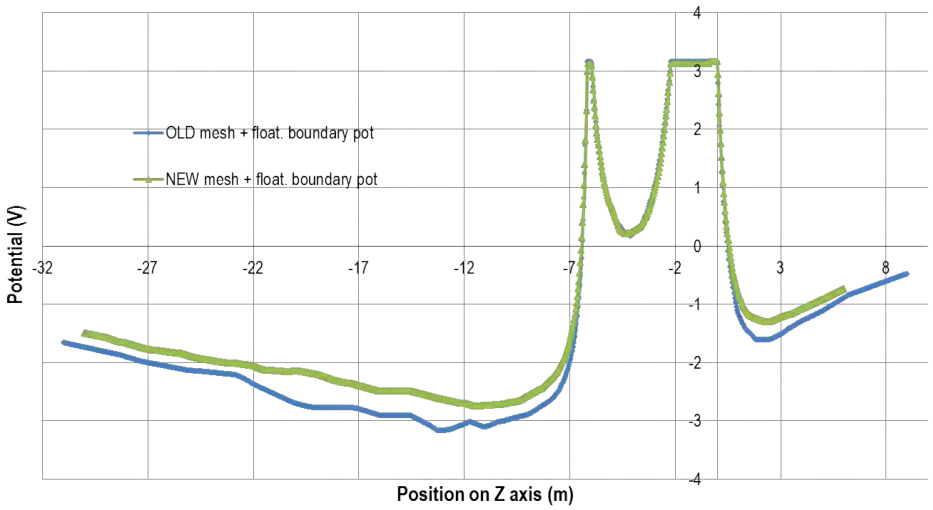

Figure 6.49: SOLO@0.28 AU - Comparison of plasma potential along Z axis obtained with two different meshes (old mesh in blue, new mesh in green).

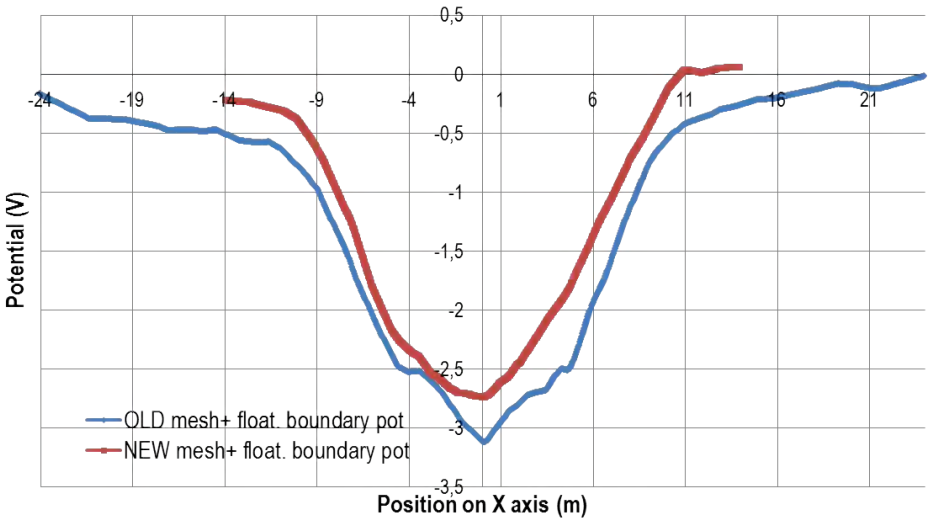

Figure 6.50: SOLO@0.28 AU - Comparison of plasma potential along X axis obtained with two different meshes (old mesh in blue, new mesh in green).

Element potential (V)	SOLO@0.28 AU Old mesh	SOLO@0.28 AU New mesh	Uncertainty obtained
Body	3.12	3.16	1.2%
Solar Panels	13.98	14.10	0.8%
HGA	8.98	9.04	0.6%

Table 6.2: SOLO@0.28 AU - Comparison of satellite potentials obtained using the old and new meshes. The uncertainty is calculated regarding the potentials obtained using the new mesh, more adapted to this environment.

tions in the plasma. Thus their measurement by EAS is practically not affected by the new mesh. However, it appears owing to this comparison that a rigorous calculation of spacecraft/plasma interaction requires a mesh well adapted to the selected environment.

6.1.5 Solar Orbiter cases conclusion

The Solar Orbiter simulation cases provided the expected global results concerning satellite potentials and plasma behaviour (according to the conclusions of [Guillemant et al. (2013)] in Appendix A.5). Depending on the heliocentric distance and the corresponding environment, the cross comparison between the different cases show the results consistency (photo emitted currents, recollection of secondaries, ion wake, potential barriers, *etc*).

They also allowed a better integration of the instrument package within SPIS. It has been fully operated from the configuration of the complex SWA-EAS instrument to the analysis of the particle detector outputs. Several methods have been presented to exploit and combine the instrument outputs and compare the results to theory, with a good consistency between numerical outputs and expectations. The integration of the instrument package to the SPIS software

EAS measurements	Discrepancy between theory and EAS: old mesh	Discrepancy between theory and EAS: new mesh	Numerical uncertainty due to old and new mesh
N Thermal elec. (m^{-3})	3.3%	2.8%	1%
N Total (m^{-3})	137.2%	132%	7%

Table 6.3: SOLO@0.28 AU - Comparison of EAS measurements obtained using the old and new meshes.

multiplies the possibilities of analysing and understanding physical phenomena (identification of SEEE, SEEP and photoelectron sources in the measurements, recollection of secondaries, potential barriers effects on particle measurement, *etc*). The low energy electron measurements polluted by secondary particles (already well known by many instrumentalists) has been reproduced, described and quantified through output post-processing.

Recommendations have been brought on several key considerations that SPIS users have to check before simulating. The choices on meshing, materials, time steps, (and other numerical parameters not described here but in the first part of the Validation Test Report) can be critical and disrupt the precision degree finally obtained on results or dramatically increase the CPU duration of computation. Compromises have to be made between expected numerical precision and CPU duration. Depending obviously on hardware and simulation configurations (number of tetrahedrons in the mesh, number of superparticles, *etc*) The cases presented here have lasted between 9 hours and 2 days (neither considering the particle measurement sequence duration, nor the outputs investigations and post-processing steps).

My simulations indicate that Solar Orbiter shall not be concerned by negative potential charging, even at its perihelion, but small potential barriers for secondaries will affect plasma analyses by deflecting the lowest energetic particles. The low energy electron measurements will be highly polluted by SEEE and photoelectrons, and the Solar arrays, which are directly in sight of the EAS instrument, will affect the electron detection (as they constitute a physical and electrostatic obstacle to thermal electron trajectories, and a source of SEEE, SEEP and photoelectrons). Questions remain on definitive spacecraft covering materials (especially on the HGA coating layer) which will affect the SEEE and charging. It also appear that the 4 m long rear boom supporting at its extremity the SWA-EAS instrument would be too short to carry out the particle measurements outside of the sheath and wake region.

6.2 Cluster

The ESA/NASA Cluster mission (see Figure 6.51) provides in-situ investigation of the Earth's magnetosphere (using four identical probes). Cluster allows the understanding of 3D and time-varying phenomena within several environments such as: solar wind and bow shock, magnetopause, polar cusp, magnetotail and auroral zone. Those satellites are spinning at one rotation every 4 seconds.

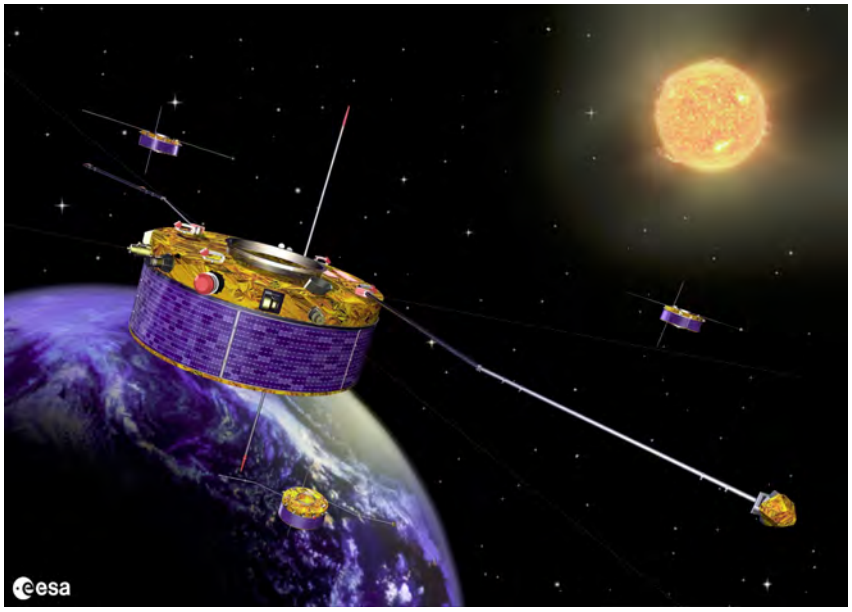

Figure 6.51: The Cluster fleet. *Image credit: ESA*.

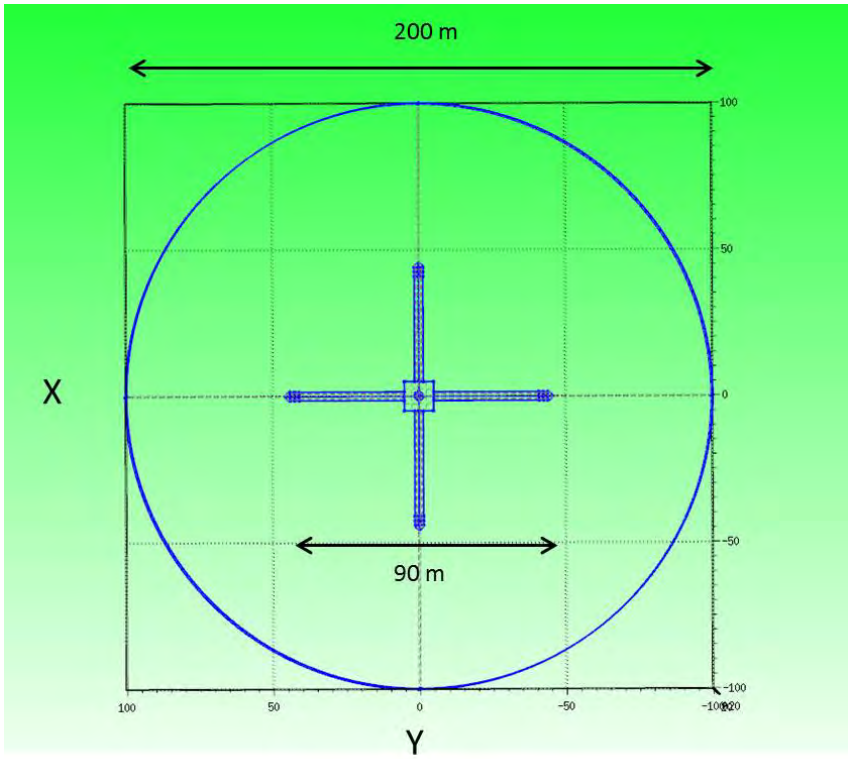

Figure 6.52: GMSH model of Cluster within its simulation box, top view.

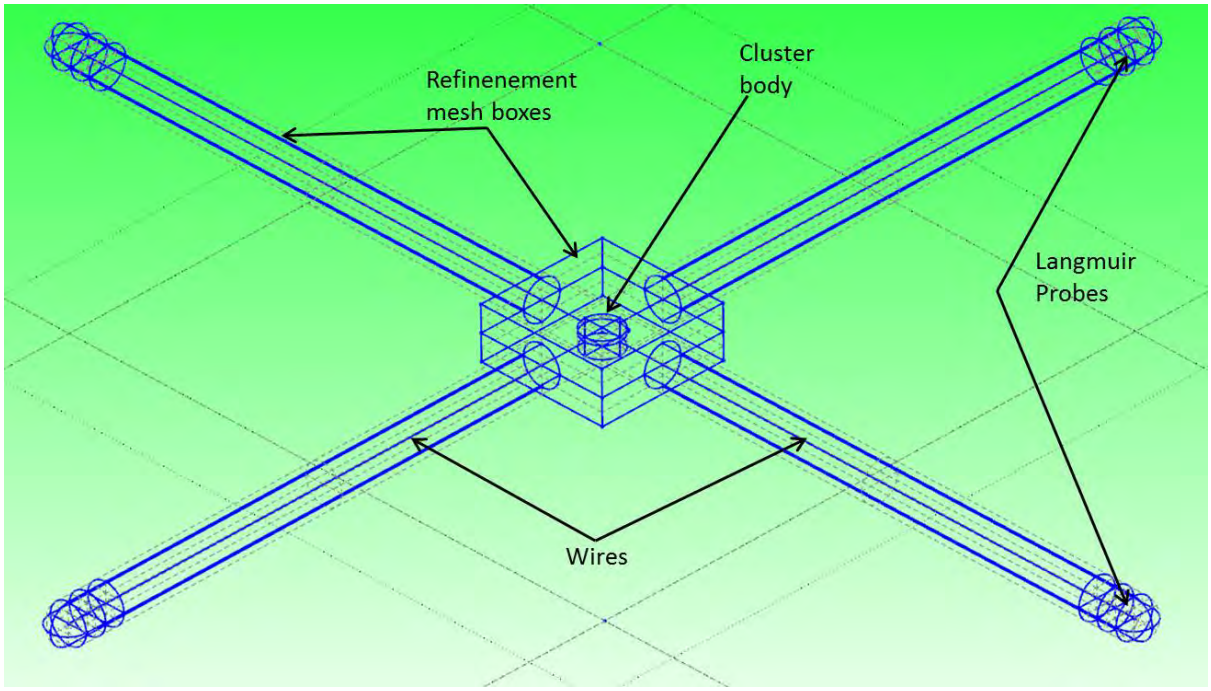

Figure 6.53: GMSH model - Frame of Cluster geometry using *Cassandra* viewer.

6.2.1 Cluster simulation: configuration of the CLUS@1 AU case

6.2.1.1 Cluster spacecraft geometry and materials

The Cluster spacecraft GMSH model has been provided by IRF. This geometry model has been adapted to include the electron instrument LEEA which will be presented in a following section. The simulation box is a "flat cylinder" of 200 m diameter and 40 m height, with Cluster at its center (see Figure 6.52 for the frame view with the refinement mesh boxes, Figure 6.54 for the plain view). The spacecraft is equipped with 4 antennas, extended by Langmuir probe systems at their ends.

The main spacecraft dimensions are (Figures 6.53 and 6.55):

- Body: diameter = 2.9 m; height = 1.3 m
- 4 wires: length = 40.93 m, considered in this model as thin wires
- 4 extensions of wires:
  1. Guard wire: length = 1.5 m
  2. Puck cylinder: diameter = 0.08 m, thickness = 0.03 m
  3. Probe wire: length = 1.5 m
  4. Langmuir Probe sphere (LP): diameter = 0.08 m

The spacecraft is considered as fully conductive, entirely covered with ITOC material, except for the detector surfaces of LEEA which, as for SWA-EAS in the Solar Orbiter cases, replace the existing particles entrances and are covered with the *Steel for detectors* layer. Material properties are displayed in Figure 6.56. The solar panels are placed on the side of the Cluster

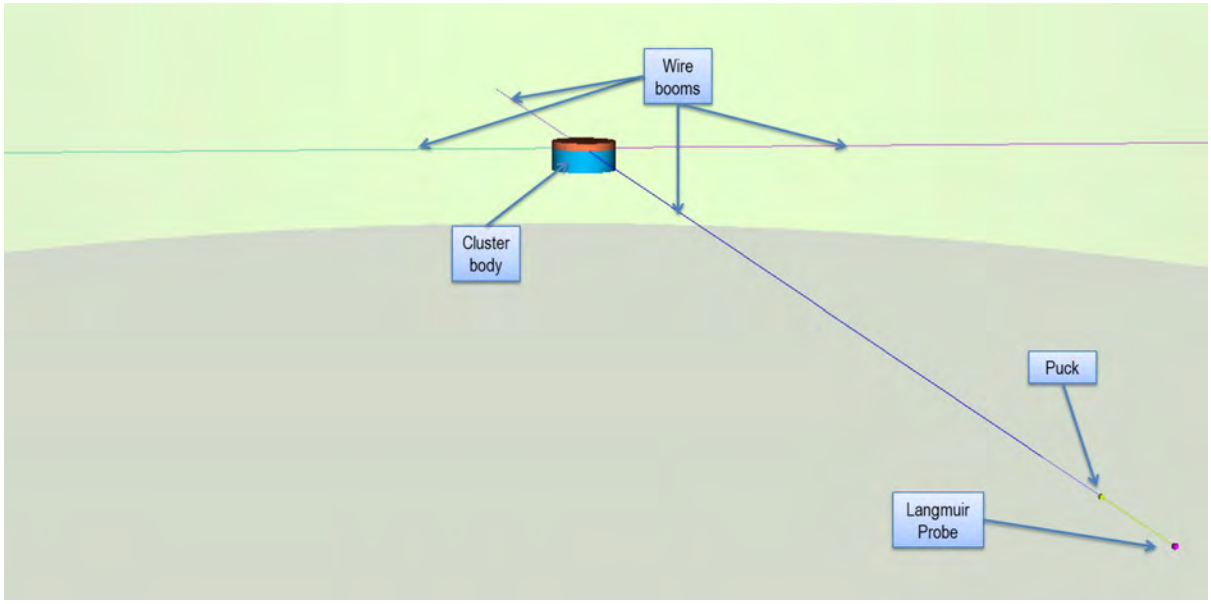

Figure 6.54: GMSH model - Cluster geometry, plain view.

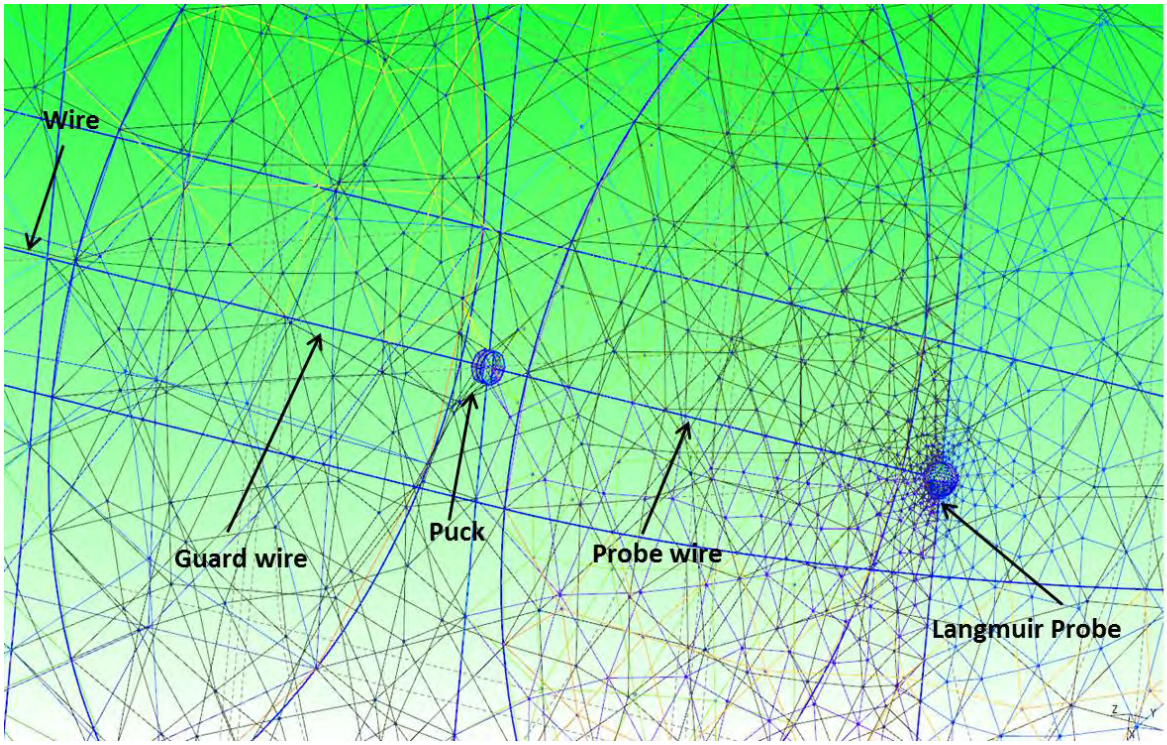

Figure 6.55: GMSH model - extension of wires with the pucks and Langmuir probes.

cylindrical body. This "ring" surface has been designed on the GMSH model, even though the entire spacecraft is here considered to be fully covered with ITOC, but materials might be changed for future simulations.

6.2.1.2 The PEACE-LEEA particle detector

The Plasma and Electron Current Experiment (PEACE) set of instruments is composed of: the High Energy Electron Analyzer (HEEA) and the Low Energy Electron Analyzer (LEEA) which are positioned symmetrically on each sides of the Cluster body. In the CL case only LEEA is simulated, as the interest if focused on the low energy particles. The position of this instrument is indicated on Figure 6.57 and its geometry on Figure 6.58 (Photography) and 6.59 (GMSH model).

On the same principle as for the SWA-EAS detector on Solar Orbiter, this semi-circular particle entrance has to be divided into 4 detection surfaces to define LEEA acceptance angles (see the Table on Figure 6.60 for the main characteristics of the instrument and Figure 6.59 for its geometry). In this last Figure the (X_D, Y_D, Z_D) basis to define acceptance angles is represented. The LEEA acceptance angle in elevation EL is extremely reduced since Cluster is a spinning structure and PEACE instruments scan the entire environment during each rotation. For this CLUS@1 AU Validation Case, Cluster rotation is not taken into account so in order to have enough information during plasma measurements the EL angle has been doubled. Finally for each detector surface the acceptance angle AZ is set to $\pm 90°$ (with respect to $-Z_D$ axis, in the $X_D - Z_D$ plane) and EL to $\pm 5.15°$ (with respect to $-Z_D$ axis, in the $Y_D - Z_D$ plane). The reference basis (X_0, Y_0, Z_0) in which LEEA outputs are provided is showed in Figure 6.61.

Studies are focused on the spacecraft-plasma interaction effects on low energy particle measurements: this is why the entire energy range of electrons (0.56 eV – 26.4 keV) will not be measured but only particles with less than few hundreds of eV, to cover the considered environment.

6.2.1.3 Simulation box and meshing

The refined meshing of LEEA (0.005 m sized cells) is represented in the previous Figure 6.61. The Figure 6.62 illustrates the meshing on the refinement mesh box around Cluster (0.5 m cells) and Cluster itself (0.3 m). The cells of the outer boundary of the simulation box have a size of 10 m. The entire simulation volume contains ~ 252000 tetrahedra.

6.2.1.4 Environment of CLUS@1 AU

The main global parameters used in the CLUS@1 AU simulation is presented in Table 6.4. Other main global parameters for the SPIS software are set as follows:

- Ions: $H+$ are modeled with a full Particle in Cell method, with a Maxwellian distribution and a drifted velocity of 440 km/s along the -X direction
- Photoelectrons: PIC modelling of a Maxwellian distribution, Temperature $kT_{ph} = 3$ eV
- Secondary electrons: PIC modeling of a Maxwellian distribution, Temperature $kT_{\mathrm{SEEE}} = 2$ eV, backscattered electrons simulated (with 2/3 of their primary energy). No secondary under proton impact.
- External boundary conditions : Fourier, $1/R^2$ decrease of potential

Characteristics		Material	
Name	***Description***	**ITOC**	**Steel for detectors**
BUC	Bulk conductivity (/ohm/m)	N/A	N/A
PEE	Primary elec. Energy for max SEE yield (keV)	0.30	0.25
IPE	Proton energy for max SEP yield (keV)	123	140
SRE	Surface resistivity (ohm)	N/A	N/A
PEY	Photoelectron current at 1AU (A/m2)	3.19E-5	0.00
RPR1	Range parameter r1 (Angstrom)	50	70
RPR2	Range parameter r2 (Angstrom)	100	150
MSEY	Max. SEE yield	2.50	0.00
SEY	2^{nd} electron yield due to impact of 1keV protons	0.49	0.00
RPN1	Range parameter n1	0.60	0.60
RPN2	Range parameter n2	1.60	1.79
RDC	Relative dielectric constant	1.00	1.00
Thick.	Material thickness (m)	1.25E-4	1.25E-4

Figure 6.56: Cluster model - material properties.

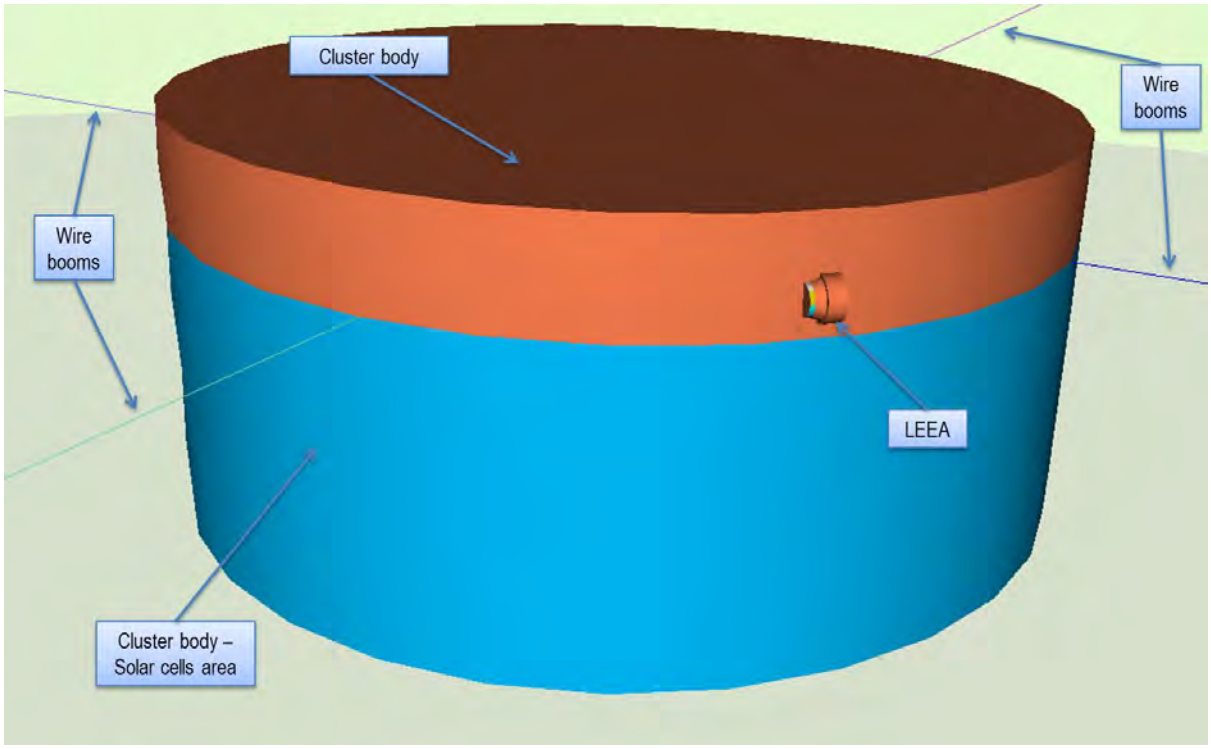

Figure 6.57: GMSH model - Postion of LEEA detector using *Cassandra* viewer.

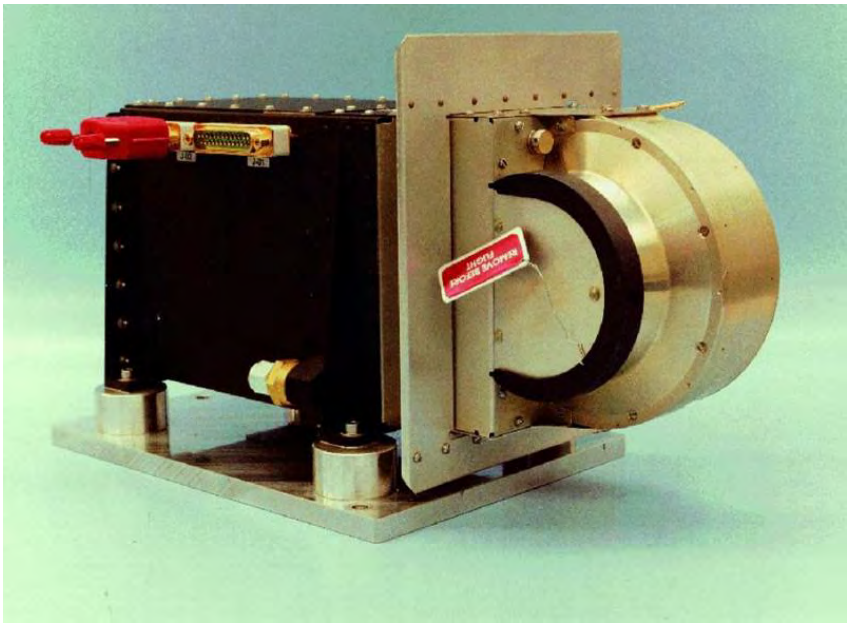

Figure 6.58: Photography of PEACE-LEEA (*source*: Mullard Space Science Laboratory).

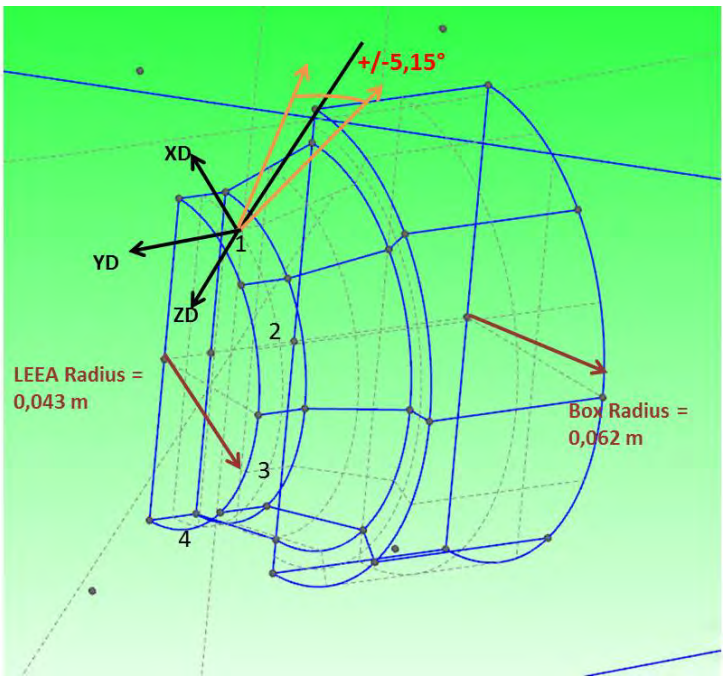

Figure 6.59: GMSH model of LEEA with main instrument dimensions, (X_D, Y_D, Z_D) basis for detector 1 and acceptance angle $EL = \pm 5.15°$.

Sensor characteristics

Sensor	LEEA	HEEA	
Energy range	0.59 eV–26.4 keV	0.59 eV–26.4 keV	
Energy resolution (FWHM)	0.127 ± 0.006	0.165 ± 0.007	
Energy sweeps per spin	16, 32, or 64	16, 32, or 64	
Field of view, polar	179.4°	179.4°	
azimuthal	2.79° ± 0.14°	5.27° ± 0.20°	
Angular resolution polar	3.75°, 15°	3.75°, 15°	
Geometric factor, per 15° zone	1.6×10^{-8}	6.0×10^{-8}	m^2 sr eV/eV
Maximum total count rate over all anodes	$>10^7$	$>10^7$	s^{-1}

Figure 6.60: Main scientific performances of PEACE detectors (*source: "PEACE: a plasma electron and current experiment"* - Mullard Space Science Laboratory).

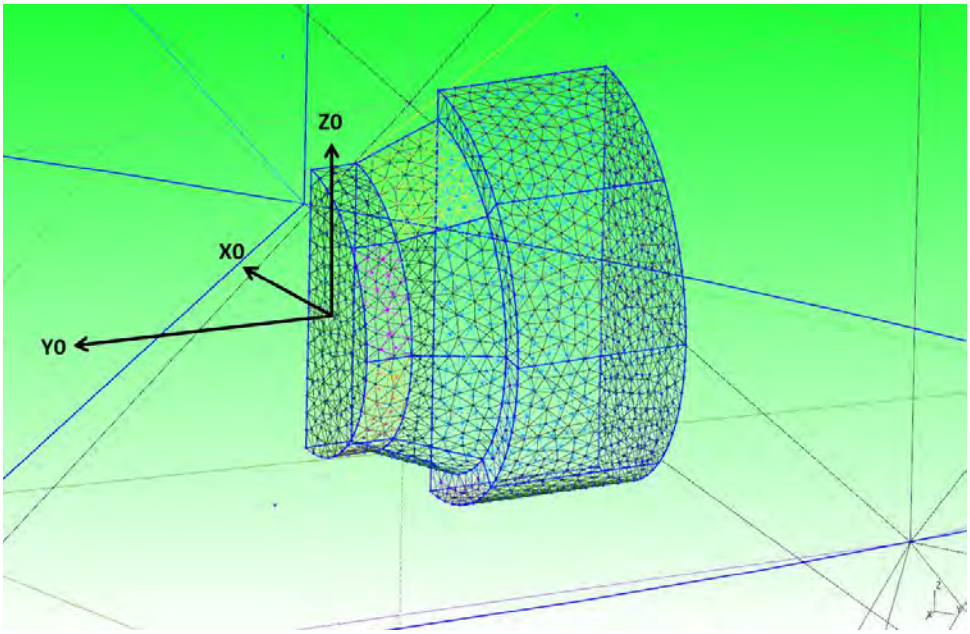

Figure 6.61: GMSH LEEA model - Reference output basis basis (X_0, Y_0, Z_0) and meshing (0.005 m).

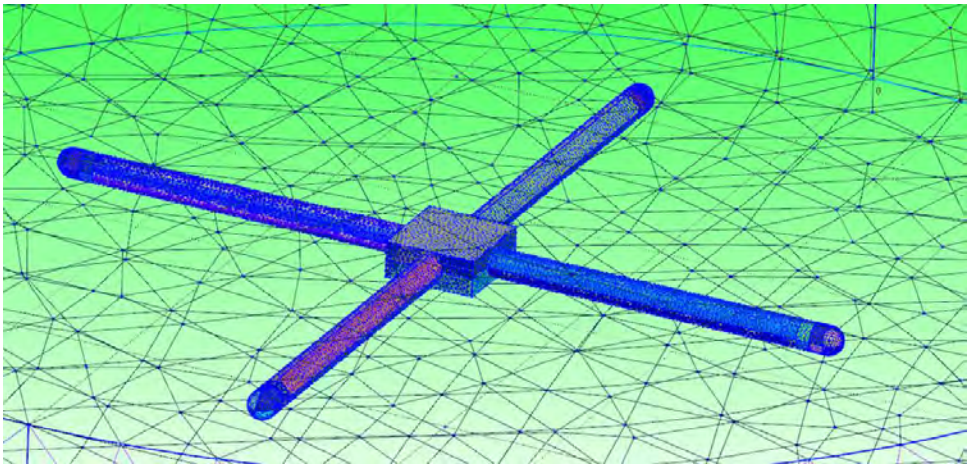

Figure 6.62: GMSH model of Cluster - Meshing.

Simulation ID	CLUS@1 AU
Distance (AU)	1.00
Distance (R_s)	215
Sun Flux (# 1AU)	in X=0.98
	in Y=0.17
Thermal elec. density N_e (m^{-3})	1.8×10^6
Thermal elec. temperature kT_e (eV)	17
Ion density N_i (m^{-3})	1.8×10^6
Ion temperature kT_i (eV)	10
Ion ram speed (km/s): V_X	-440
Mach number	14.21
Debye length (m)	22.8
Debye length photoelec (m)	0.98

Table 6.4: CLUS@1 AU main parameters for SPIS.

- LEEA measurements are activated for thermal electrons, SEEE and photoelectrons

- No magnetic field considered (estimated gyroradii are larger than the simulation box)

This environment has been deduced from real Cluster measurements, provided by LEEA and the *Cluster Ion Spectrometry* experiment (CIS). The spacecraft floating potential was then at +11 V, generating biases in the electron spectra. So using CIS results on the less disturbed ions it provided N_i and T_i reported in Table 6.4, the electron density could therefore be estimated assuming a neutral plasma: $N_i = N_e$.

For CLUS@1 AU: the simulation is based on the *VTR - Part II* results. This work was provided by the *IRFU* team who determined at equilibrium the *I.V* curves of the Cluster Langmuir probes in this CLUS@1 AU environment. Considering the different elements of the satellite (SC = spacecraft body, LP = Langmuir Probes, and the guards and pucks represented on Figure 6.55):

- $U_{\mathrm{SC}} = +9.96\,\mathrm{V}$

- $U_{\mathrm{LP}} = +1.96\,\mathrm{V}$

- $U_{\mathrm{Puck}} = U_{\mathrm{LP}} + 1.30\,\mathrm{V} = +3.24\,\mathrm{V}$

- $U_{\mathrm{Guard}} = U_{\mathrm{LP}} - 6\,\mathrm{V} = -4.04\,\mathrm{V}$

The spacecraft initial potential is thus set to $U_{\mathrm{SC}} = +9.96\,\mathrm{V}$ and the electrical circuit file is configured to respect the relations between the different electrical nodes. All initial potentials are set at the values listed above. The potentials are however allowed to float in order to double-check the consistency of IRFU results.

In this case, the SPIS software has generated the following number of particles (approximately):

- electrons = 4300000

- ions = 1300000

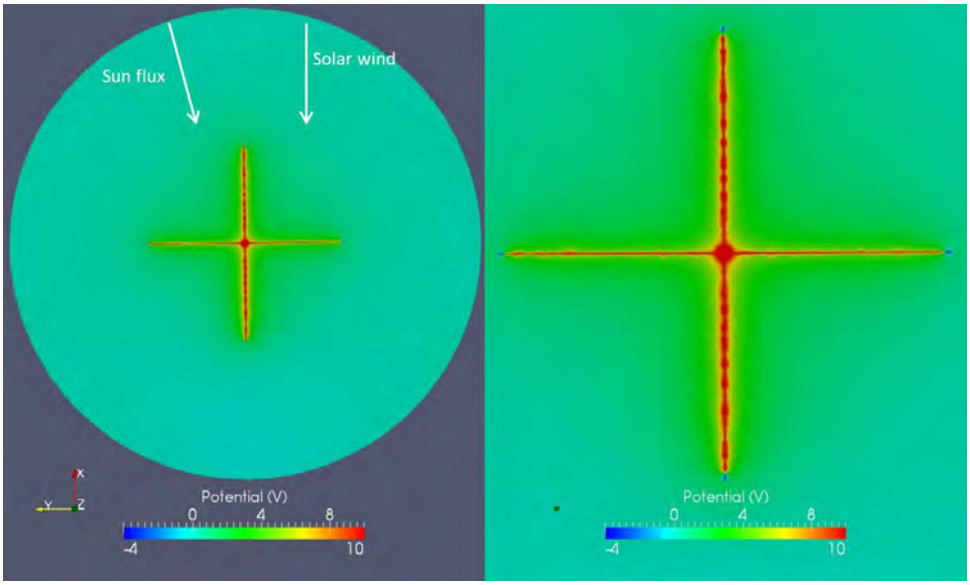

Figure 6.63: CLUS@1 AU - Potential around Cluster in the $X-Y$ plane (left) and zoom on Cluster in the same plane (right).

- photoelectrons = 7000000
- SEEE = 2500000

6.2.2 Results analysis of CLUS@1 AU

6.2.2.1 Satellite potential equilibrium

The steady state spacecraft potentials obtained by the end of the simulation CLUS@1 AU (after a duration set at 5 ms) practically not varied regarding initial values, confirming IRFU results:

- $U_{SC} = U_{LEEA} = +10.01\,V$
- $U_{LP} = +2.02\,V$
- $U_{Puck} = +3.30\,V$
- U_{Guard} = -4.03 V

The recollection rates of secondary and photoelectrons are important (*resp.* 89.24 and 92.20%) and the photoelectron net current is dominant (10^{-5} A) over the one of thermal electrons (8.5×10^{-6} A) and SEEE (7.7×10^{-7} A).

6.2.2.2 Plasma

The plasma potential is represented in Figures 6.63, 6.64 and 6.65. The plasma potential presents negative values only around the guard wires. No potential barriers appear in those outputs.

The attracting potential of Cluster (except the guard wires at -4 V) visibly increases thermal electron density around the structure (Figure 6.66). The LEEA detector, on the side of Cluster,

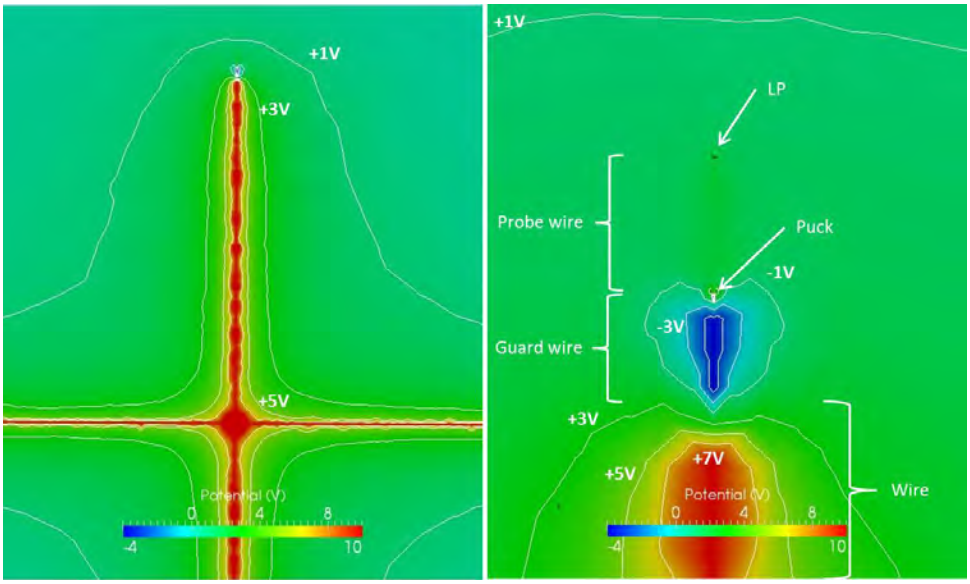

Figure 6.64: CLUS@1 AU - Potential around the wires in the $X-Y$ plane (zoom) and contours of potentials.

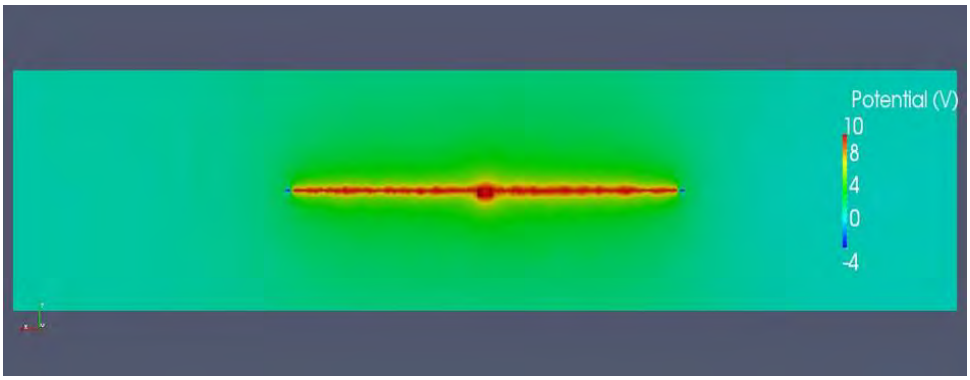

Figure 6.65: CLUS@1 AU - Potential around Cluster in the $X-Z$ plane.

is immersed in this charge density. The ion wake is clearly visible but very thin (Figure 6.67). The spacecraft body and the thin wires constitute a small physical blockage of ions but there is also the electrostatic effect of positive potentials on those elements that generate an ion wake enlargement. Photoelectrons and SEEE are highly present in the vicinity of the spacecraft, all around the body, the wires and the LP (Figure 6.68 and 6.69). LEEA is completely immersed in high densities of those parasite particles.

In Figure 6.70 photoemission generated by the wires, Langmuir probes and pucks is illustrated with shadowing phenomena of the LP and puck on the wire. Figure 6.71 shows that photoelectrons created by the LP and the puck remain relatively confined around those objects and the Probe wire between them. Indeed the LP and Probe wire are positively charged at +2 V and the puck at +3.3 V, which attracts photoelectrons (emitted with a characteristic temperature of 3 eV). Besides the guard wire behind the puck is negatively charged at -4 V which repels photoelectrons and prevents them from stretching along the wires up to the LEEA. However

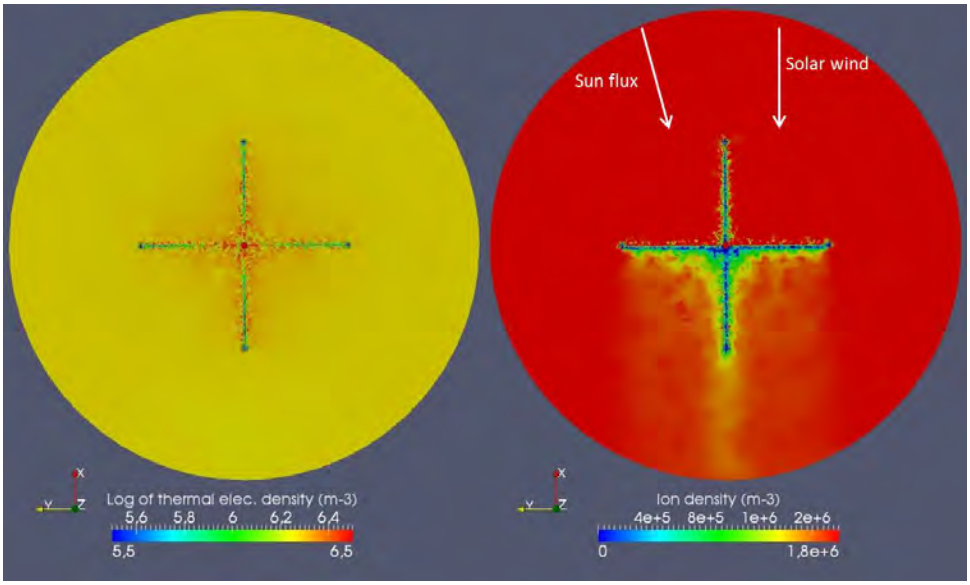

Figure 6.66: CLUS@1 AU – Thermal electron density around Cluster (left) and ion density in the $X - Y$ plane (right).

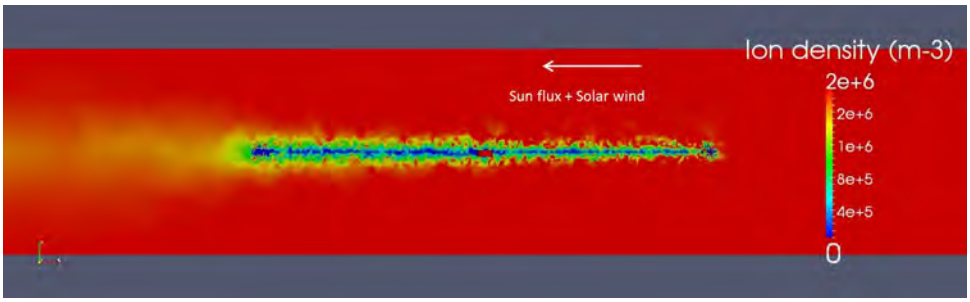

Figure 6.67: CLUS@1 AU – Ion density around Cluster in the $Z - X$ plane.

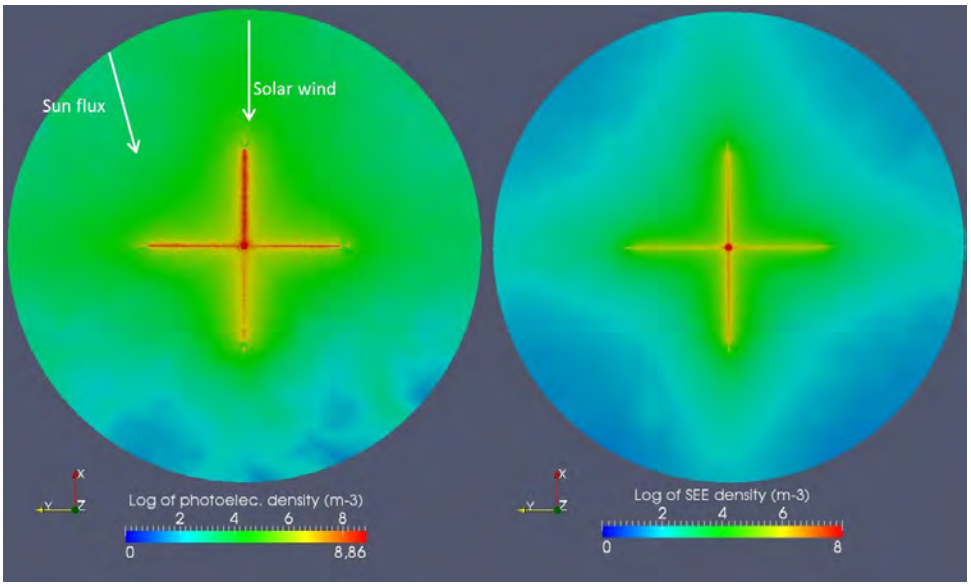

Figure 6.68: CLUS@1 AU – Photoelectron density around Cluster (left) and SEEE density in the $X - Y$ plane (right).

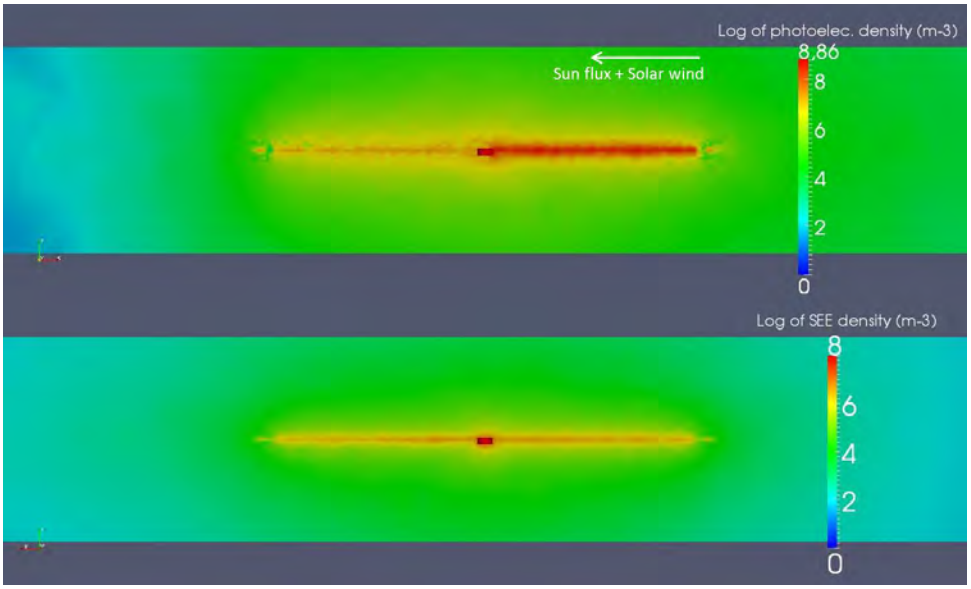

Figure 6.69: CLUS@1 AU – Photoelectron density around Cluster (top) and SEEE density in the $Z - X$ plane (bottom).

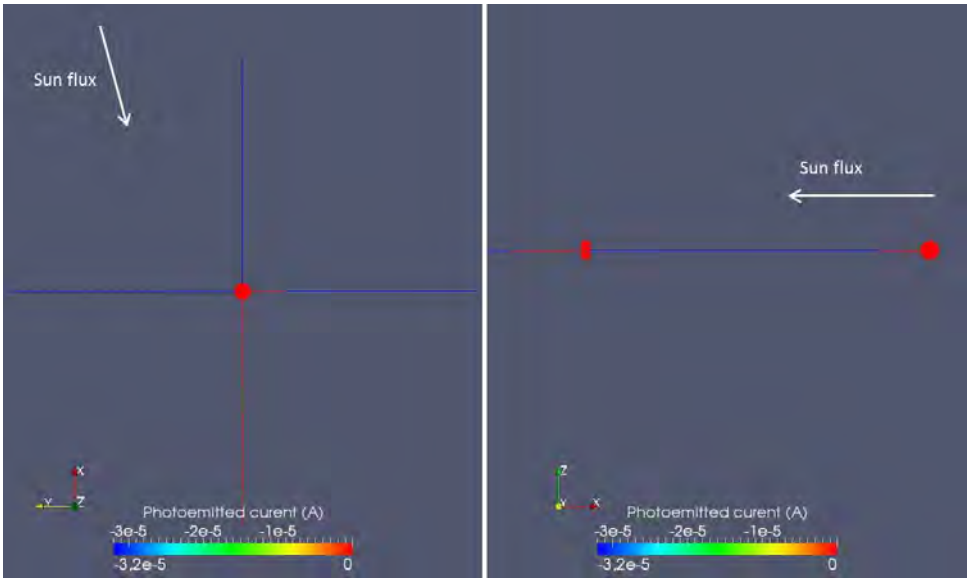

Figure 6.70: CLUS@1 AU - Photoemission on wires (left - top view) and on LP and puck (right).

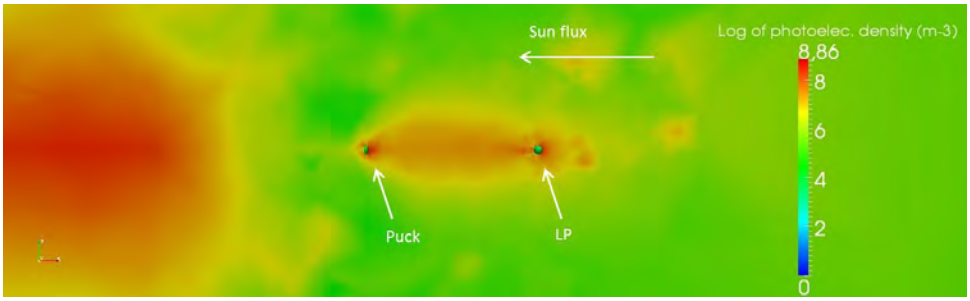

Figure 6.71: CLUS@1 AU - Photoelectron density around LP, puck and wire in the $Z-X$ plane.

the wires do emit photoelectrons (except the one along the -X axis for which photoemission is highly reduced by shadowing), as it appears in Figures 6.68 and 6.68 but it is also showed in those Figures that SEEE are created from all surfaces and wires.

6.2.2.3 LEEA measurements

Energy distribution functions measured by LEEA for CLUS@1 AU are displayed in Figure 6.72 (for thermal electrons only). In this Figure, the yellow curve represents the ambient electron population injected, as described in Table 6.4, and the one that LEEA should measure if there were no plasma disturbances due to spacecraft/plasma interactions. The orange curve represents the environment that should be theoretically measured by LEEA if there were only this instrument charged at its potential of +10 V in the simulation box, with no spacecraft, no wake or any potential barriers and if LEEA had a full field of view on 4π sr (calculated analytically using Liouville's theorem). The green curve represents the measurement provided by LEEA, without any correction concerning the geometric factor, thus the DF is significantly reduced since the acceptance angle EL is small ($\sim 10°$). Finally, the blue curve represents the simulated measurement of thermal electrons corrected by the geometric factor ($\sim 1/36$). This

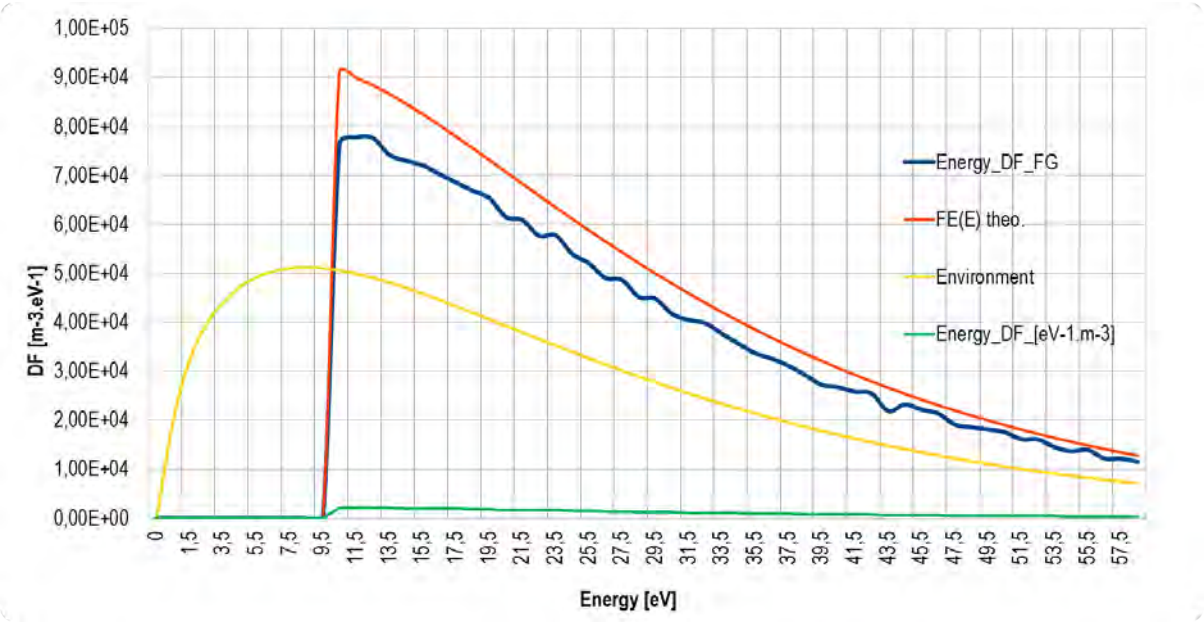

Figure 6.72: CLUS@1 AU - Energy distribution functions of thermal electrons on LEEA.

results in a combination between the true environment and the theoretical measure of LEEA alone.

The corresponding densities calculated through integration of thermal electrons DF (Figure 6.72) are:

- Undisturbed environment (yellow): $N_0 = 1.67 \times 10^6\,\mathrm{m}^{-3}$ for a density of the unperturbed plasma of $1.8 \times 10^6\,\mathrm{m}^{-3}$ (Table 6.4). The difference is due to the truncated integration in our model represented on Figure 6.72.

- Theory (orange): $N_{\mathrm{theo}} = 2.22 \times 10^6\,\mathrm{m}^{-3} > N_0$ because of LEEA positive potential (+10 V).

- Corrected measurements (blue): $N_{\mathrm{meas}} = 1.90 \times 10^6\,\mathrm{m}^{-3} < N_{\mathrm{theo}}$ because of the spacecraft structure and the plasma disturbances.

The simulated corrected measurements of pure thermal electrons give an a priori good accuracy with less than 14% of difference with the true injected environment. This might be misleading: indeed because of Cluster positive potentials there is an energy cut-off in electron measurements at ∼10 eV (the estimated N_{meas} decreases) but electrons of higher energies are accelerated (the estimated N_{meas} increases). Finally the estimated $N_{\mathrm{meas}} \sim N_0$. Adding the SEEE and photoelectrons (Figure 6.73) leads to a total density of measured electrons (the cyan curve) of $N_{\mathrm{total}} = 4.03 \times 10^8\,\mathrm{m}^{-3}$ which is totally out of range regarding N_0 (more than 240 times the initial density), but this result was expected since the detector LEEA more charged than EAS (+10 V here) and is right next to the Cluster body, immersed in the sheath of secondary and photoelectrons (EAS on Solar Orbiter will at the end of a 4 m long boom, which already reduces the simulated perturbations but without avoiding them completely, see section 6.1).

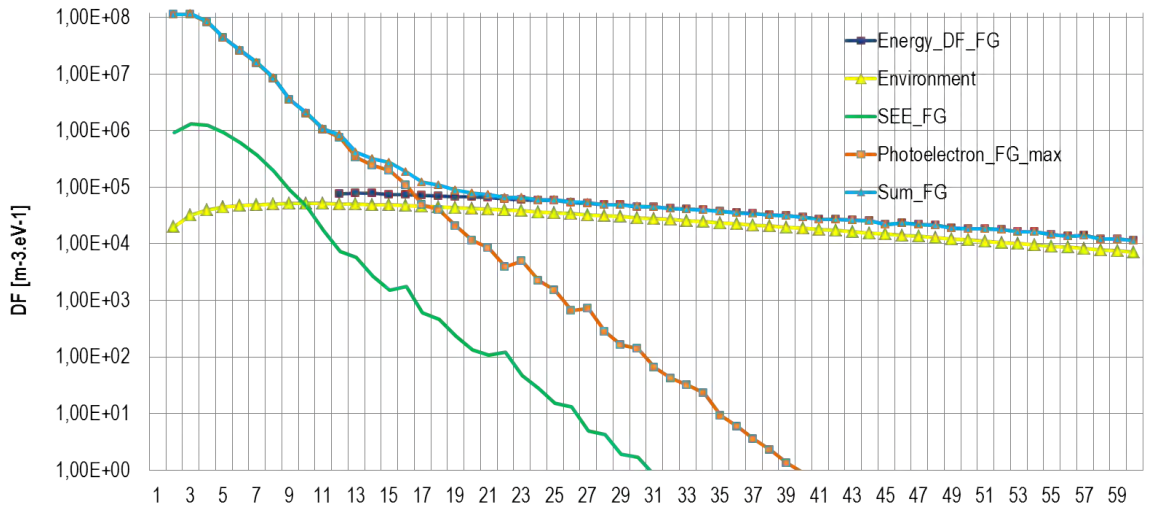

Figure 6.73: CLUS@1 AU - Energy distribution functions of all electrons on LEEA. A logarithmic scale has been used here to distinguish all curves.

6.2.2.4 Comparison of CLUS@1 AU results and real LEEA measurements

It is now possible to compare those simulated results with the real Cluster electron data obtained in 2009 (see data in Appendix A.3), when the probe was immersed in the same environment. At this time period the Cluster spacecraft electrostatic potential was also established at +11 V, meaning that electron measurements were biased (attracting potential effect, secondary and photoelectron pollution). The use of this LEEA data set combined with the CIS instrument outputs for ions at the same period allowed to determine the corrected environment parameters for the real Cluster situation and use them as inputs for our CLUS@1 AU case performed here.

Those data (Appendix A.3) have to be converted into SPIS output format. Indeed output energies are expressed in eV and we actually have from equation 3.45:

$$f_E(E) = f_V(V)\frac{4\pi V}{m}$$

In order to convert Cluster data units $[s^3.km^{-6}]$ into SPIS outputs units of $fE(E)$ $[m^{-3}.eV^{-1}]$, we consider:

$$V = \left(\frac{2Ee}{m}\right)^{\frac{1}{2}} \tag{6.1}$$

with E in eV. Substituting expression 6.1 in 3.45 gives:

$$f_E(E) = 4\sqrt{2}\pi\left(\frac{e}{m}\right)^{\frac{3}{2}} E^{\frac{1}{2}} f_V(V) \tag{6.2}$$

with $f_V(V)$ in $[s^3.m^{-6}]$. Converting $f_V(V)$ in $[s^3.km^{-6}]$ and calculating $4\sqrt{2}\pi\left(\frac{e}{m}\right)^{\frac{3}{2}} = 1.311 \times 10^{18}$ we obtain:

$$f_E(E) = 1.311 \times E^{\frac{1}{2}} f_V(V) \tag{6.3}$$

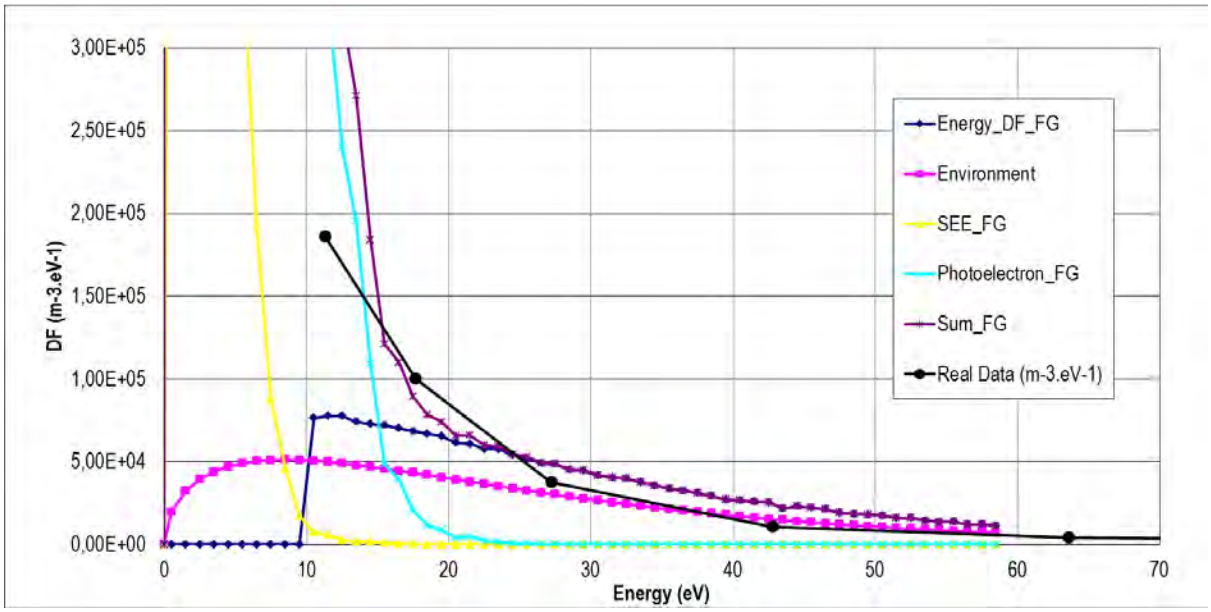

Figure 6.74: CLUS@1 AU - Energy distribution functions of all electrons detected by LEEA, focussed on the real data measurements values (represented by black dots).

with $f_V(V)$ in $[s^3.km^{-6}]$.

Once converted to SPIS output format (using equation 6.3) those data have been plotted in the previous plot 6.73. The result of combining simulated and real LEEA measurements, is presented in Figure 6.74, focussed on the real dataset values, but still in the low-energy range (below 70 eV here).

Using the real data: the environment density calculated is estimated to $2.32 \times 10^6\,\mathrm{m}^{-3}$ (39% of increase regarding the injected N_0 =$1.67 \times 10^6\,\mathrm{m}^{-3}$) and the temperature to 18.3 eV (against the configured kT_e =17 eV). The overestimation of thermal electrons due to parasite populations and of course the satellite electrostatic potential (demonstrated and explained through all SPIS simulations in this thesis) is visibly a phenomenon encountered through in-flight electron detector measurements. It clearly appears that the CIS data were useful to correct the environment parameters estimated only through the biased electron measurements.

The aberrations in the real LEEA outputs should be even greater since here no data below 11 eV were available (probably an energy cut-off set to consider the satellite potential) and it is in this low energy range that the pollution due to secondary and photoelectrons is the most important (which appears clearly thanks to the simulated measurements on Figure 6.74). This is why the SPIS simulated outputs give a total electron calculated density (starting at 0 eV) extremely overestimated regarding the pure thermal electron population injected while real data (with the lower energy cut-off at 11 eV) provide "only" 39% of overestimation. If the simulated distribution function of all electrons is integrated from 11 eV, the estimated density becomes $2.91 \times 10^6\,\mathrm{m}^{-3}$, which is only +25% of difference regarding the real measured data. According to Figure 6.74 this 25% difference resides in the simulated measurements of secondary and photoelectrons, essentially between 11 and ∼15 eV. The photoelectrons in this energy range come from spacecraft elements facing the detector, according to the demonstration made in section 5.5.3.1 showing that the electrons with energies higher than the instrument potential are definitely lost. This time, comparing with the previous SOLO cases, photoelectrons are the

most polluting population as the LEEA instrument can be directly illuminated by the Sun.

This shows that, with this simulation, I could reproduce *beyond the satellite potential threshold* practically the same electron measurement disturbances that were obtained in reality. Furthermore, Figure 6.74 allows to determine the energy cut-off threshold from which the DF should be integrated to provide the measured electron density, liberating the estimate from photoelectrons. Indeed it appears on this Figure that photoelectronic pollution becomes "negligible" after 20 eV. Integrating the DF of all measured electrons from 20 eV leads to a density of $1.32 \times 10^6\,\mathrm{m}^{-3}$: 21% of decrease in comparison to N_0 (due to the truncated integration at low and high energies).

The main difference between the simulated data and the real ones is that those last values have been cumulated over an entire Cluster cycle, which has been "artificially" recreated by multiplying the simulated fluxes on the detectors by the geometric factor value $FG = 36$ (since the LEEA acceptance angle in EL is set in the model to $\sim 10°$). The environment encountered by LEEA during one rotation has been considered as isotropic. The photoelectron collection (quite important as during this simulation LEEA is on the sunlit side) has thus also been multiplied by 36. This constitutes an upper approximation as during the real Cluster spin the LEEA detector might be shadowed. It is difficult to know the exact correction required by the simulated data on secondaries populations but it has to be assumed that our photoelectron energy distribution function is overestimated.

In the next Figures are represented the origin of each particle detected by LEEA (SEEE with green dots, photoelectrons in blue and thermal electrons in red). Those plots have been generated using the *Topcat*[1] tool, a free interactive graphical viewer and editor for tabular data. The simulation box boundary is also partly drawn by thermal electrons origins. Figures 6.75 and 6.76 show that few secondary and photoelectrons detected by LEEA come from the wires, but none originate from the end of wires (LP areas), as suggested in Section 6.2.2.2). Most of the detected SEEE are provided by Cluster body itself. Some photoelectrons detected are also emitted from the wires close to the detector. Many photoelectrons come from the LEEA box, since the instrument is directly exposed to Sunlight. This explains the high proportion of those particles in the measured energy DF (Figure 6.74).

The reduced LEEA field of view clearly appears when looking at detected thermal electrons origins (Figures 6.77 and 6.78). Those electrons come from a somewhat reduced region of the simulation box boundary. The attracting potential of Cluster and its wires deflects remote electrons (the ones which are a priori out of the EL acceptance angle of LEEA) and causes the instrument to collect them with a wider range of angles. We notice that detected thermal electrons also come from above and beyond the Cluster cylinder, in the $\pm Z$ direction, with a greater azimuth angle than accepted by LEEA (180°). It is also due to the attractive surface potential of the spacecraft that attracts particles from beyond the LEEA field of view.

Figure 6.79 displays views of some detected thermal electron trajectories. The attractive phenomenon due to Cluster, wires and LEEA positive potentials is clearly visible on the deviated thermal electron paths, as explained previously.

6.2.3 Cluster simulation conclusion

The Cluster spacecraft and its on-board electron instrument LEEA have been successfully modelled and embedded in the CLUS@1 AU environment, providing consistent results with potentials and plasma behaviour. The LEEA data obtained through this study using the new SPIS-

[1] TOPCAT: Tool for Operations on Catalogues And Tables Web site, *http://www.star.bris.ac.uk/~mbt/topcat/*

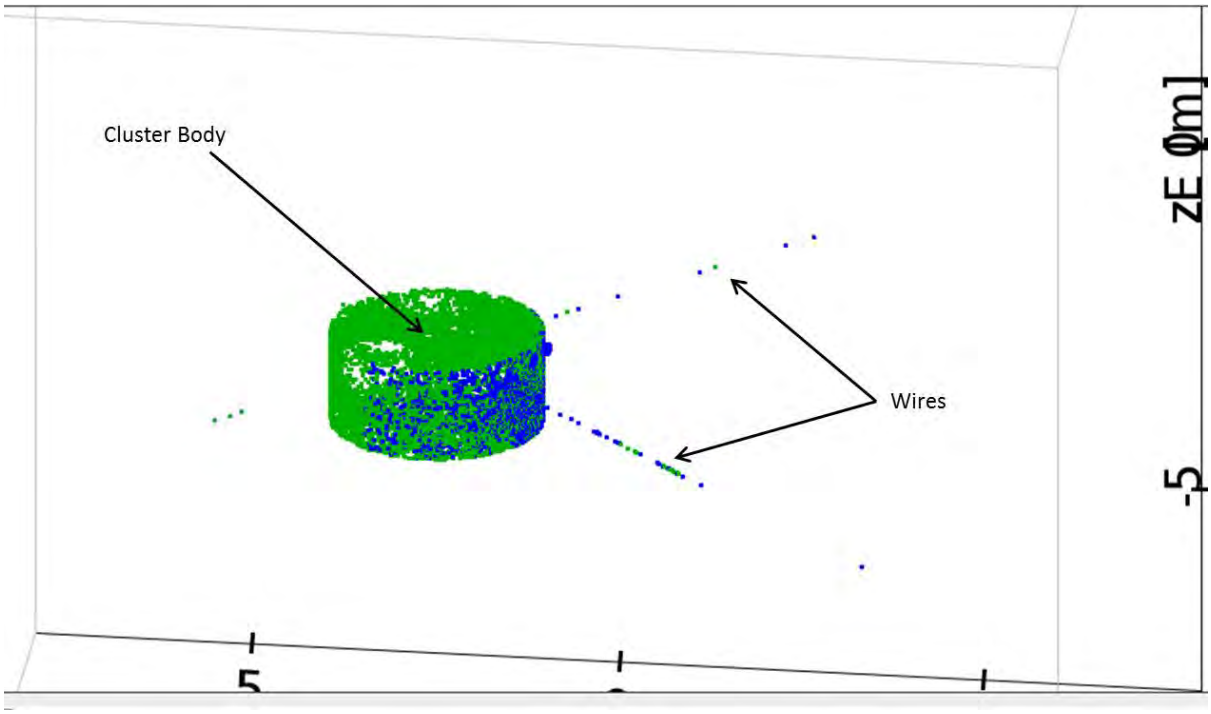

Figure 6.75: CLUS@1 AU - Origin of detected secondary electrons (green dots) and photoelectrons (blue dots) by LEEA.

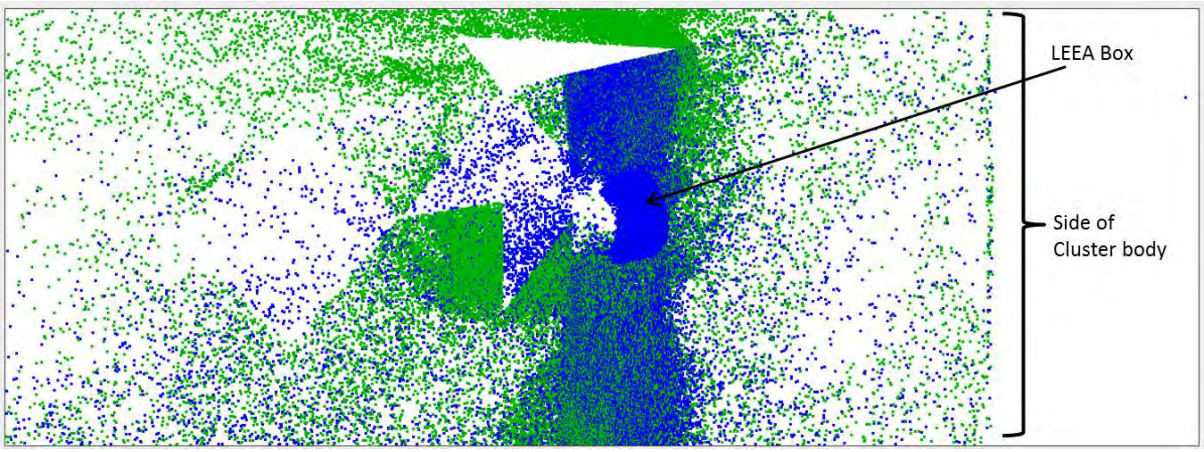

Figure 6.76: CLUS@1 AU - Origin of detected SEEE (green dots) and photoelectrons (blue dots) – Focus on LEEA area.

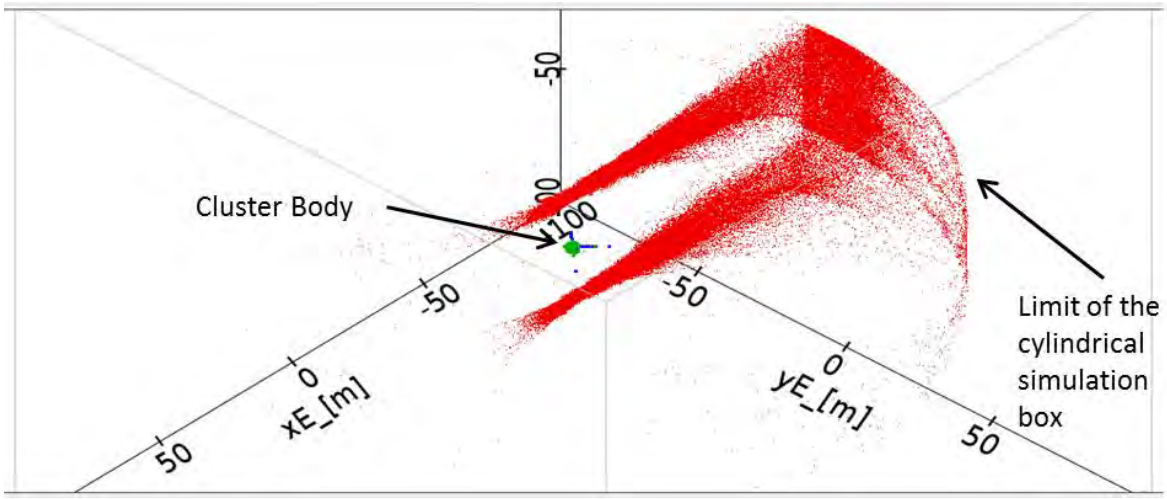

Figure 6.77: CLUS@1 AU - Origin of SEEE (green), photoelectrons (blue) and thermal electrons (red) detected by LEEA. View from top ($+Z$ axis).

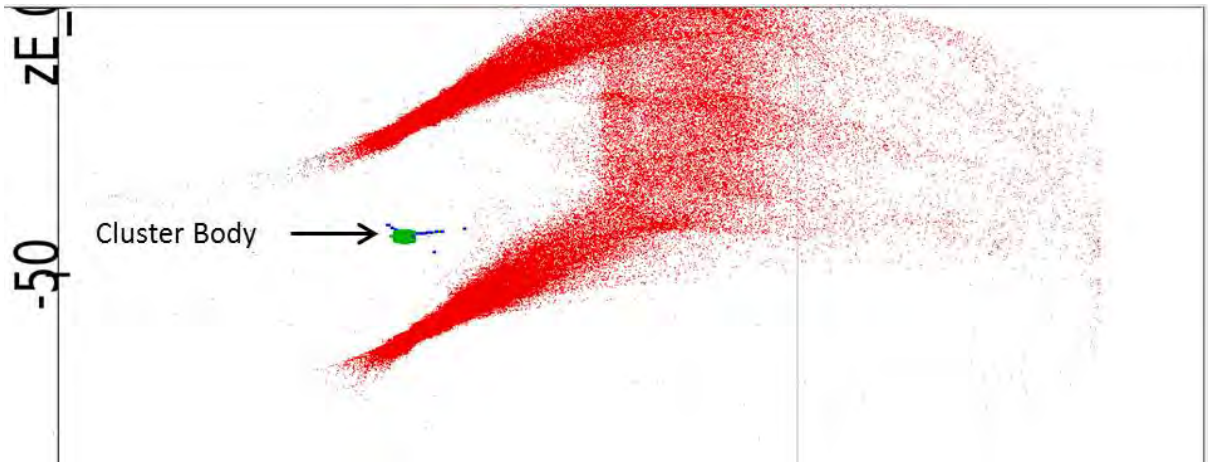

Figure 6.78: CLUS@1 AU - Origin of SEEE (green), photoelectrons (blue) and thermal electrons (red) detected by LEEA. Other view from top ($+Z$ axis).

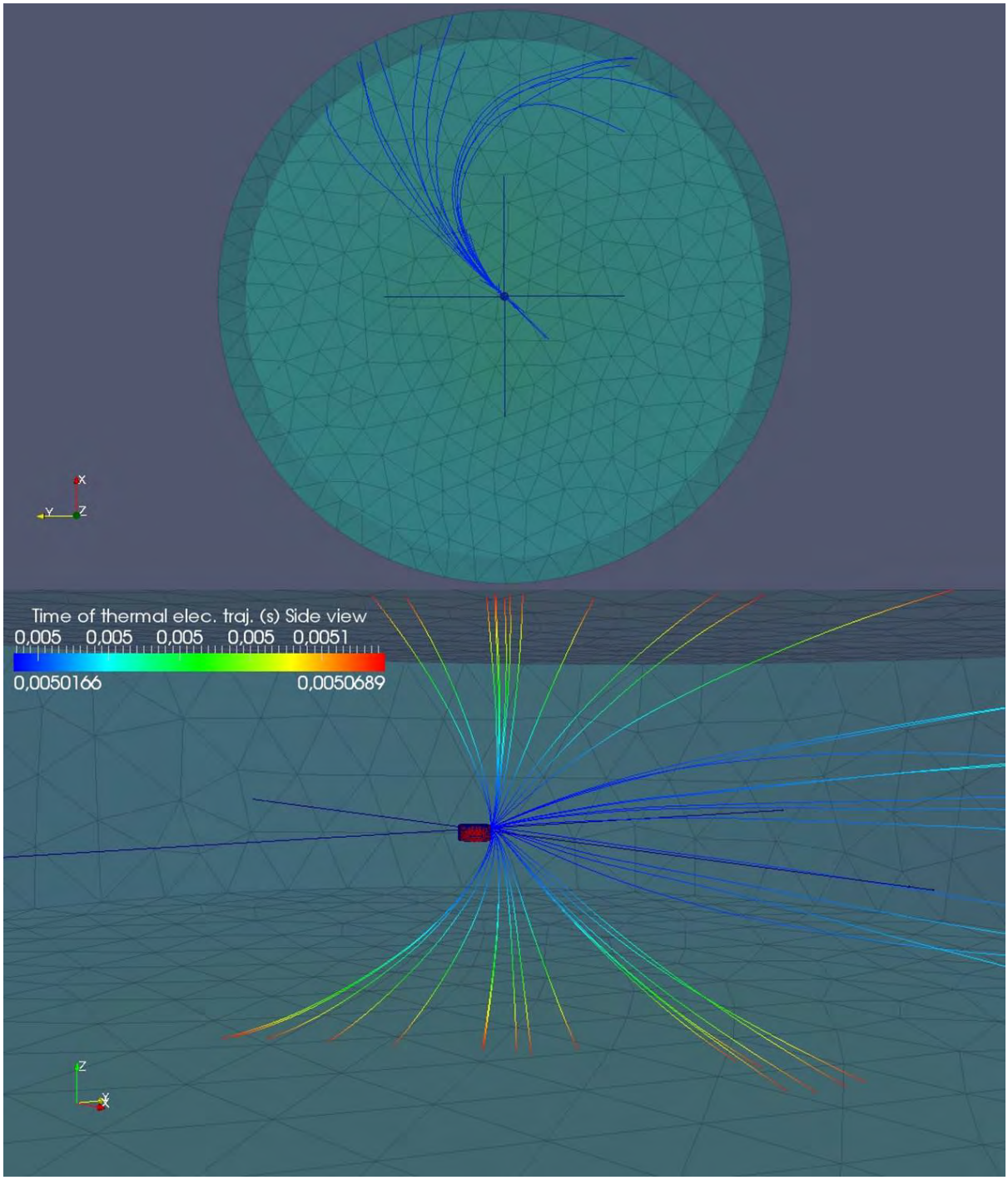

Figure 6.79: CLUS@1 AU - Some trajectories of thermal electrons detected by LEEA (up: top view; bottom: side view).

Science extension give a good match with the input environment, considering that the spinning instrument cannot be simulated and that several approximations have been made to create this numerical model. Furthermore, the comparison of simulated/real data gives a good agreement: indeed the same tendency of overestimating electrons in the low range energies because of the Cluster positive potential and the collection of SEEE and photoelectron has been observed in both datasets.

Despite the several simplifications and approximations inherent in numerical simulations of actual space environment situations, we managed here to reproduce the biased electron measurements performed by the LEEA instrument embedded in the in-flight Cluster probe, using the SPIS-SCI numerical tool. This comparison emphasizes that this methodology including a multi-scale model to simulate spacecraft/plasma interaction effects on low-energy particle measurements is efficient and realistic.

6.3 Conclusion on scientific applications and engineering

The simulations presented in this Chapter constitute complex and complete applications of satellite/plasma interactions studies. The analysis of results obtained on the satellites, around their structures and within the particle measurements provides a large and in-depth overview of the issues encountered by scientific missions in space environments.

The powerful SPIS-SCI software has been tested, optimized and validated with those simulations (plus five others performed but not presented here). It offers various possibilities of performing and analysing numerical simulations of spacecraft/plasma interactions and the associated plasma measurements. Several methods of post-processing simulation outputs have also been developed, allowing to extend the understanding of the interaction processes and consequences.

The complex cases studied in this Chapter demonstrate two facts. First it is possible to predict the interaction between the entire Solar Orbiter structure and the surrounding environments, with a precise quantification of those issues directly on the future particle instrument outputs. Secondly, the comparison of real Cluster measurements with simulated ones demonstrates the accuracy of our simulating methodology. This method seems applicable to analyse future missions. We have shown that the satellite dimensioning and materials can be tested well before in-flight operations, even before its design, in order to optimize the structure and, ultimately, reduce disturbing phenomena on the low energy particle measurements. Designers, engineers, plasma physicists and instrument creators can use this methodology to anticipate and optimize the models, for instance testing various covering materials at different heliocentric distances or varying a scientific instrument location with respect to the spacecraft structure. Those parametric studies would provide a determination of the best possible configuration and of the issues that should be taken into account depending on certain satellite configurations.

Finally, it has been demonstrated that the SPIS-SCI capabilities of simulating particle measurements allow to understand and identify the biasing sources within the measurements, when compared to real in-flight data. This will help in a longer term to develop post-processing correction methods to separate the natural signal from the biased in-flight measurements.

Chapter 7

Conclusion and perspectives

Contents

7.1 Achievements (English) 199
7.2 Critical analysis of this PhD and Perspectives (English) 200
7.3 Conclusion générale (français) 203

7.1 Achievements (English)

The purpose of this work was to study and improve the understanding of the spacecraft/plasma interactions. The final aim was to establish a methodology of configuring and simulating with the SPIS software the various issues related to scientific satellites immersed in space environments and low energy plasma measurements, and analysing the results through different numerical tools, also providing an estimate of results accuracy. I believe these objectives were attained by the end of my PhD study duration.

Indeed after reviewing the different interactions generated by the satellite/plasma systems in the Solar wind, I first started simulating extreme cases the Solar Probe Plus at its perihelion. Those first simulations, considering a conducting cylinder, showed that at this heliocentric distance the final satellite potential will be negative, despite the strong photoelectron and secondary electron currents emitted by the satellite surfaces. The reason for this counter-intuitive equilibrium is the potential barriers generated by the dense electron sheaths surrounding the probe structure, and also the ion wake behind the cylinder. This result consolidated preliminary results provided by [Ergun et al. (2010)] with another numerical code. To go in depth, I initiated a parametric study in this same environment to observe the probe behaviour when varying various characteristics such as the secondary electron emission rate, the photoemission rate, the ion bulk velocity direction or the numerical modelling method of electron population. I published this detailed work in [Guillemant et al. (2012)], (Appendix A.4).

Secondly, based on this statement I started a second parametric study aiming at studying the potential barrier formation depending on the variability of the space environment, and if possible discovering the limit heliocentric distance where potential barriers would disappear, keeping the same numerical satellite. For each of the 10 environments selected, between the Solar Probe Plus perihelion at 0.044 AU from the Sun to the Earth orbit, passing by a location close to the future Solar Orbiter perihelion (0.28 AU), I observed the satellite potential, net currents and plasma behaviour. I highlighted the existence of two distances, proper to this spacecraft geometry and material, where 1/ the surface potential equilibrium changes from negative to positive values (at ∼0.1 AU from the Sun) and 2/ a monotonic decrease of potential from the satellite surface to the neutral plasma is established (beyond ∼0.3 AU). The different proportions of plasma populations collected on the probe have also been quantified. All those

results have been gathered and published in [Guillemant et al. (2013)] (Appendix A.5), also showing that the Solar Orbiter spacecraft at its perihelion would be potentially subject to potential barrier issues, even if its structure will remain positively charged.

Third, I built a parametric study aiming at understanding the sequence of perturbations on particle detection. Logically, the method consisted in modelling initially a simple instrument alone in a plasma, without any disordering phenomena, in order to numerically calibrate my simplified particle detector model by making comparisons between simulated measurements and the results from an analytical model based on Liouville's theory. Step by step, new disturbing phenomena have been included within the simulations, allowing to observe, understand and quantify the aberrations in the instrument outputs. For instance non zero potentials on the detectors, secondary electrons, photoelectrons, non Maxwellian environments have been added and combined within the various cases, giving precise numerical values of biases on electron moments measurements.

The fourth step was the definition, configuration, run and post-processing of the 10 simulations, constituting the test and validation cases for the SPIS-SCI software extension which was being developed at this time by ONERA and ARTENUM. The SPIS-SCI new capabilities were also defined in partnership with the IRAP laboratory (Vincent Génot and myself) to describe the fundamental particle detector principles and the expected measurement output formats. This has been an important task in the frame of the SPIS-SCI ESA study, not only by the time dedicated to this work - almost half of the PhD duration - but also by the level of complexity of the simulations performed. Thanks to the advanced Solar Orbiter and Cluster simulations I detected several numerical bugs allowing their corrections and validated the new capabilities of modelling numerical instruments (particle detectors) and their associated measurements. The multi-scale geometric models (from 1 mm element dimension to tens of meters) generated for the satellites (with a high level of details including: antennas, thin wires, different covering material layers, *etc*) combined with the associated plasma instruments (EAS and LEEA) permitted to go beyond the expected outputs and agreement with the literature. The results, cross-compared with various numerical parameter variations, have been also post-processed outside the SPIS frame thanks to different free numerical tools and self-made Scilab routines, greatly extending the other simulated data interpretation. I could identify the different satellite structure effects directly on the low energy particle measurements (< 100 eV): particle deflection, acceleration, blockade, pollution due to other spacecraft emitted particles, quantification of the biases due to secondary and photoelectrons, the main sources of pollution, efficiency of the boom length supporting EAS, *etc*. Even though the Solar Orbiter simulations remain prospective, the achievement of obtaining simulated electron measurements extremely similar to real Cluster-LEEA data in a similar environment confirmed the validity of our approach using the SPIS software and of the simulation process efficiency developed during this PhD. The corresponding deliverable for this activity was the first part of the Validation Test Report which I produced for ESA, and that may serve as a basis for future missions support.

7.2 Critical analysis of this PhD and Perspectives (English)

One missing point is obviously the magnetic field, not considered in the simulations presented here. It is true that the magnetic field intensity related to the simulated environment was not strong enough to generate ambient electrons gyroradii smaller than the computational volume dimension. Meaning also that the E cross B drift velocity would not be visible in the results.

This assessment has been verified early in the context of the Solar Probe Plus simulations, even though the results have not been presented here. The thermal electron gyroradius was of 15 m, larger than the simulation box. Only secondary particles have a gyroradius of 2.5 m, but a test case showed that considering the magnetic field did not modified the results: neither on the spacecraft (currents and potentials) nor on the plasma sheaths around it. The idea of considering the magnetic field came back with the Solar Orbiter and Cluster simulations, as electron detectors were about to be implemented within the simulations. However again considering the field intensity at those heliocentric distances, not even the low energy particles would have been subject to circular trajectories shorter than the simulation box dimension, and no effects was expected to be noticeable on the instrument outputs. Indeed the magnetic field decreases when getting farther from the Sun (except if we consider the planet magnetosphere environments). Knowing that the calculations in a PIC modelling method of particle transport are much longer when taking B into account, and considering the already long durations of the validation cases computation, it has been decided to neglect it and postpone those studies to a later period. This can however be an interesting perspective for further investigations.

The geometric models that I developed for Solar Orbiter and Cluster (and their respective electron detectors EAS and LEEA), which already set at a high level of details, can still be enhanced. Indeed for Solar Orbiter, information on specific materials and spacecraft dimensions were still missing during the model configuration, but will be rapidly entered when available, for further simulations. The internal electric circuit remains somewhat primitive and would also benefit from new inputs. Specific simulations focused on the Solar Orbiter RPW antennas and the associated electric field measurements are of great interest for the scientific community, and can be rapidly initiated thanks to the material I have developed until now.

The SPIS-SCI package has been fully operational only by the end of this PhD period, and could not be used yet for other investigations than the cases presented here. Yet comparisons of simulated plasma measurements with real in-flight data have been successfully made, showing the efficiency and exactness of the simulations I performed with the SPIS-5 software. However given the existing databases - as the Plasma Physics Data Centre (CDPP[1]), a CNRS/CNES database hosted by IRAP - a considerable amount of measurements can be compared with simulations, only waiting to be configured. This will allow to understand eventual misinterpreted signals, or dubious particle fluxes.

As many software, SPIS is an evolving program always looking for improvements and new functionalities. Several possibilities of enhancement could be studied for future developments, as implementing:

1. Physical models
    - Electric field instrument controlled by user defined current between the Langmuir Probe and the satellite
    - Mobile structures (solar panels) or deformable elements (booms and wire antennas under temperature effects)
    - Propulsion effects on satellite potential and residual neutrals effects
    - Cosmic dust effects: current/voltage peaks on plasma instruments and antennas due to transient plasma generated by impacts
    - Outgassing

[1]CDPP Web site, *http://cdpp.eu*

- Satellite elements carried to strong potentials and exposed to the plasma (for instance solar panels inter-connectors
- Particles carried to higher energies because of electromagnetic waves of the satellite platform
- Induced magnetic field through internal spacecraft currents
- Internal charge of dielectrics

2. Numerical models

- Backup files to relaunch a simulation stopped during computation
- Automatic mesh adaptation during the simulation to refine the local interesting regions of the computational volume
- Multi-scale parallel computation to reduce time of computation for the electric fields

These new functionalities might offer new simulating horizons for spacecraft and instrument designers, as for plasma physicists involved in embedded particle instruments.

Concerning future space missions and embedded plasma instruments: this PhD is particularly relevant to several imminent projects.

- For instance *BepiColombo*, a joint mission between ESA and the Japanese Aerospace Exploration Agency (JAXA), which should reach and begin Mercury study in 2023. Its proximity to the Sun will generate important charging issues, problematic for the satellite, the embedded instrumentation and the associated measurements. Note that BepiColombo will orbit in nearly the same environment that Solar Orbiter at its perihelion, when orbiting in the Solar wind, outside the weak Mercury magnetosphere. This type of environment has already been simulated in this work. The IRAP laboratory is precisely involved in the *Mercury Plasma Particle Experiment* (MPPE) mounted on the *Mercury Magnetospheric Orbiter* (MMO). IRAP will supply the electron spectrum analyser (MEA), scanning the solar wind and planetary plasma from 0.01 eV to 30 keV. Simulations of the MMO system and its electron instrument within its environment might thus be useful.

- The *Particle Environment Package* (PEP), a suite of particle sensors proposed for the ESA *JUpiter ICy moons Explorer* (JUICE) mission, will analyse density and fluxes of positive and negative ions, electrons, exospheric neutral gas, thermal plasma and energetic neutral atoms below 0.001 eV up to energies exceeding 1 MeV, around Jupiter. The composition of the moons' exospheres will also be measured: Ganymede, Europa and Callisto. The simulation methodology presented here should be adapted to the JUICE case, especially when knowing that the JUICE geometry can still evolve, considering the actual state of development of this mission.

- The Juno mission, with an arrival around Jupiter is planned for July 2016, aims at improving the understanding of the solar system's beginnings by revealing the origin and evolution of Jupiter. It will carry plasma and energetic particle detectors (JADE and JEDI): presaging considerable data analyses. It is too late for simulations helping the design optimization, but as demonstrated through the Cluster case in this work, simulations might be of interest for helping at understanding future observations.

A working group "Simulations for Solar Orbiter" is now being set up between IRAP, ESA, MSSL and the Laboratory of Space Studies and Instrumentation in Astrophysics (LESIA). The SOLO simulations presented here will be extended, in particular concerning the electric field measurements of the RPW instrument. New information on the selected Solar Orbiter covering material properties and precise values of the spacecraft element final dimensions should also be available to enhance the realism of my spacecraft model. Note also that future simulations taking into account non-Maxwellian plasma distribution functions, including EAS measurements of the Core, Halo and Strahl electron populations are also planned with the new SPIS-5 completed functionalities (see Section 6).

A paper on Solar Orbiter simulations, based on the VTR Part 1 and 2 produced in the context of the ESA study, is currently in the writing. New thorough simulations will be rapidly performed using the complete SPIS-5 software, an even more realistic spacecraft model and the post-processing numerical tools developed during this PhD.

7.3 Conclusion générale (français)

L'objectif de cette thèse était d'étudier et d'améliorer la compréhension des interactions satellite/plasma. Le but final était d'établir une méthodologie de configuration et de simulation, via le logiciel SPIS, des différents phénomènes liés aux satellites scientifiques immergés dans divers environnements spatiaux et aux mesures des plasmas basses énergies, tout en analysant les résultats aux moyens de différents outils numériques, fournissant également des estimations de la précision des résultats. Je pense avoir atteint cet objectif à la fin de la durée de ma thèse.

En effet après avoir passé en revue les différentes interactions générées par les systèmes satellite/plasma dans le vent solaire, j'ai d'abord simulé des cas extrêmes relatifs à la sonde Solar Probe Plus à son périhélie (à 0,044 UA du soleil). Ces premières simulations, considérant un cylindre conducteur, ont montré qu'à cette distance héliocentrique le potentiel final du satellite serait établi à une valeur négative, malgré les forts courants de photoélectrons et d'électrons secondaires émis par les surfaces du véhicule. La raison de cet équilibre inattendu est l'ensemble des barrières de potentiel générées par les fortes densités d'électrons dans les gaines entourant la structure de la sonde, mais aussi le sillage d'ions à l'arrière de celle-ci. Ce résultat approfondit une précédente étude de [Ergun et al. (2010)], réalisée avec un autre code numérique. Pour approfondir, j'ai mené une étude paramétrique de mon modèle pour observer son comportement en variant certaines caractéristiques telles que les taux d'émission électronique secondaire et de photoémission, la direction de la vitesse moyenne du vent solaire ou encore la méthode de modélisation numérique des électrons ambiants. Ces résultats sont par ailleurs publiés dans [Guillemant et al. (2012)] (Appendix A.4).

En deuxième lieu, à partir de cet état de fait j'ai initié une nouvelle étude paramétrique dont l'objectif était d'étudier la formation et l'évolution des barrières de potentiel en fonction de la variabilité de l'environnement spatial, et si possible de découvrir la distance héliocentrique limite où ces barrières disparaissaient, en gardant le même modèle de satellite. Pour chacun des dix environnements sélectionnés, entre le périhélie de Solar Probe Plus près du soleil et l'orbite terrestre, en passant par la localisation du périhélie de la future mission Solar Orbiter (0,28 UA), j'ai observé le potentiel électrostatique d'équilibre du satellite, les courants nets et le comportement du plasma ambiant. J'ai pu mettre en évidence deux distances, propres à cette structure de satellite et de matériaux, où : 1/ le potentiel d'équilibre de surface du satellite passe de valeurs négatives à positives (autour de 0,1 UA du soleil) et 2/ une décroissance

monotone du potentiel entre les surfaces du satellite et le plasma neutre est établie (à partir de 0,3 UA). Les différentes proportions des populations du plasma collectées par la sonde ont également été décrites. L'ensemble de ces résultats font parties d'une autre publication [Guillemant et al. (2013)] (Appendix A.5), montrant également que Solar Orbiter à son périhélie sera affecté par les phénomènes de barrières de potentiel, même si sa structure restera positivement chargée.

Troisièmement, j'ai mené une autre étude paramétrique visant à comprendre les séquences de perturbations des détections de particules. La méthode a logiquement consisté à modéliser initialement un simple détecteur de particules seul dans un plasma, sans perturbation aucune, pour calibrer numériquement l'instrument simplifié grâce à la comparaison des mesures simulées au modèle analytique basé sur l'équation de Liouville. Etape par étape, de nouvelles perturbations ont été incluses dans les simulations, permettant d'observer, comprendre et quantifier les mauvaises estimations fournies par l'instrument : par exemple des potentiels non nuls sur les détecteurs, la collection d'électrons secondaires, de photoélectrons, des environnements non Maxwelliens ont été ajoutés et combinés dans les différents cas, donnant des valeurs numériques précises sur les biais des moments d'électrons mesurés.

La quatrième étape a été le définition, configuration, simulation et analyse de dix simulations, constituant les cas de validation pour l'extension du logiciel SPIS : Spis-Science, qui était en cours de développement par l'Onera et Artenum. Les nouvelles capacités du logiciel ont été définies en partenariat avec l'IRAP (Vincent Génot et moi-même), pour décrire les principes fondamentaux des détecteurs de particules et le format attendu des mesures produites. Cet ensemble a constitué une tâche importante du cadre de l'étude ESA sur SPIS-SCI, non seulement par rapport au temps dédié – près de la moitié de la durée de la thèse – mais aussi par le degré de complexité des simulations effectuées. Grâce aux simulations avancées des cas Solar Orbiter et Cluster j'ai pu permettre l'amélioration du nouveau code ainsi que la validation des nouveaux outils proposés. Les modèles géométriques multi-échelles de satellites générés (comprenant des éléments d'une dimension de 1 mm jusqu'à plusieurs dizaines de mètres, et un niveau important de détails tels que les antennes, des éléments fins et différents matériaux) ont été combinés aux détecteurs de particules (EAS et LEEA) pour produire des mesures d'électrons allant au delà des résultats attendus et des accords avec d'autres publications. Les résultats ont également été comparés à des post-traitements réalisés aux moyens d'outils externes à SPIS (logiciels gratuits et routines Scilab personnelles), afin d'étendre l'interprétation des données simulées. Nous avons ainsi pu identifier les différents effets des structures des satellites sur les mesures de plasmas basses énergies : déviations de particules, accélérations, blocage, pollution due aux électrons émis par les surfaces, quantification des biais dus aux secondaires et photoélectrons, principales sources de pollution, efficacité de la longueur du mât supportant EAS à son extrémité, *etc.* Même si les simulations Solar Orbiter restent dans le domaine prospectif, l'obtention de mesures d'électrons simulées pour le cas Cluster très proches des données réelles de son instrument LEEA confirme la validité de notre approche avec l'utilisation de SPIS et l'efficacité de notre processus de modélisation développé durant cette thèse.

En perspective, les modèles géométriques développés pour Solar Orbiter et Cluster (et leurs instruments détecteurs d'électrons respectifs EAS et LEEA), déjà grandement détaillés peuvent encore être améliorés. En effet certaines données concernant les matériaux spécifiques de Solar Orbiter et quelques dimensions précises restaient inconnues durant la configuration du modèle, mais pourront y être rapidement intégrées une fois disponibles pour de prochaines simulations. Les comparaisons de données réelles aux données simulées, très encourageantes dans le travail effectué ici, permettent d'envisager de prochaines nouvelles études comparatives. La dernière

version de SPIS-5 sera effectivement disponible à la fin de cette thèse et le Plasma Physics Data Centre (CDPP) – une base de données CNRS/CNES, gérée par l'IRAP – fournit une quantité considérable de mesures pouvant être comparées à des simulations restant à configurer. Cela permettra la compréhension d'éventuels résultats surprenants ou mal compris jusqu'à présent.

Comme tout logiciel, SPIS reste en constante évolution et de nouveaux développements sont actuellement en projets. De nouvelles fonctionnalités pourront dans un avenir proche proposer aux utilisateurs : des structures mobiles sur le satellite (panneaux solaires rotatifs) ou déformables (antennes sous l'effet de chaleurs intenses), d'intégrer les effets des particules neutres résiduelles issues des propulseurs, prendre en compte le dégazage des matériaux, l'effet des poussières cosmiques, les ondes électromagnétiques induites par la structure du satellite, *etc.*

Cette thèse ouvre également de nouvelles perspectives quant aux futures simulations attendues pour les prochaines missions scientifiques s'intéressant aux mesures de plasmas basses énergies. *Bepi Colombo* emportera par exemple autour de Mercure l'analyseur de spectres d'électrons MEA (fournit par l'IRAP). La mission *Jupiter Icy Moons Explorer* (JUICE) effectuera des mesures de particules dès 0,01 eV (grâce à la suite d'instrument Particle Environment Package - PEP) autour de Jupiter, Ganymède, Europe et Callisto. La mission *Juno* emportera également autour de Jupiter les instruments JADE et JEDI, détecteurs de particules à différentes énergies.

Un groupe de travail dédié aux "Simulations pour Solar Orbiter" est par ailleurs en train d'être mis en place entre l'IRAP, l'ESA et le LESIA. Les simulations présentées ici constituent une base essentielle de départ pour ces prochaines études, et pourront ainsi être approfondies grâce aux nouvelles informations bientôt disponibles sur la structure de ce satellite, notamment pour s'intéresser aux mesures de champ électrique via l'instrument RPW déjà modélisé dans nos fichiers.

Appendix

Appendix A

Appendix

A.1 Physical and Geophysical Constants

Constant	*Symbol*	*Value*
Elementary charge	e	-1.602×10^{-19} C
Boltzmann's constant	k	1.3807×10^{-23} m^2.kg.s^{-2}.K^{-1}
Electron rest mass	m_e	9.1094×10^{-31} kg
Proton mass	m_p	1.6726×10^{-27} kg
Permittivity of free space	ε_0	8.8542×10^{-12} F.m^{-1}
Permeability of free space	μ_0	$4\pi \times 10^{-7}$ H.m^{-1}
Electron volt	eV	1.6022×10^{-19} J $= 11605$ K
Gravitational constant	G	6.6726×10^{-11} m^3.s^{-2}.kg^{-1}
Speed of light in vacuum	c	2.9979×10^{8} m.s^{-1}
Earth radius	R_E	6370 km
Sun-Earth distance (Astronomical Unit)	AU	1.496×10^{11} m

Table A.1: Fundamental constants (SI)

A.2 Basic concepts of the distribution function

A distribution of particles can be locally described by the density $n(\mathbf{x})$, $\mathbf{x}$ being the vector of coordinates (x_1, x_2, x_3) defining the position in space. Considering ΔN particles in the differential element of volume $\Delta V = \Delta x_1 \Delta x_2 \Delta x_3$ the local density can be defined as:

$$n(\mathbf{x}) = \lim_{\Delta V \to 0} \frac{\Delta N}{\Delta V} \tag{A.1}$$

To get back to the total number of particles N in the volume V it is necessary to integrate over the three spatial dimensions:

$$N = \int_V n(\mathbf{x}) d^3x \tag{A.2}$$

where d^3x is the differential volume element $dx_1 dx_2 dx_3$.

However, a particle has three position coordinates in the real space and three vector velocities in the velocity space. This leads to a six-dimensional phase space, defined by six coordinates (x_1, x_2, x_3, v_{x1}, v_{x2}, v_{x3}), and that is named the distribution function f of the particles. Thus in the six-dimensional volume element $d^3x d^3v_x$, at time t, there is the number of particles:

$$dN = f(\mathbf{x}, \mathbf{v}_x, t) d^3x d^3v_x \tag{A.3}$$

and the entire volume V:

$$N = \int_V n(\mathbf{x},t)d^3x = \int_V \int_{-\infty}^{\infty} f(\mathbf{x},\mathbf{v}_x,t)d^3x d^3v_x \tag{A.4}$$

Finally the local density $n(\mathbf{x},t)$ is defined as:

$$n(\mathbf{x},t) = \int_{-\infty}^{\infty} f(\mathbf{x},\mathbf{v}_x,t)d^3v_x \tag{A.5}$$

Equation A.5 is the zeroth moment of the distribution function. Higher orders moments are formulated as:

$$M^{(K)}_{xi,xj...xl}(\mathbf{x},t) = \int_{-\infty}^{\infty} \underbrace{v_{xi}v_{xj}...v_{xl}}_{\text{K times}} f(\mathbf{x},\mathbf{v},t)d^3v_x \tag{A.6}$$

Making use of the distribution function integration the average value of any property α(**x**,**v**,t) can be calculated as follow:

$$\langle\alpha(\mathbf{x},t)\rangle = \frac{1}{n(\mathbf{x},t)} \int_{-\infty}^{\infty} \alpha(\mathbf{x},\mathbf{v},t) f(\mathbf{x},\mathbf{v},t)d^3v_x \tag{A.7}$$

A.3 Cluster in-flight data

The following real Cluster electron data has been generated in 2009 (see data below), when the probe was immersed in the same environment. At this time period the Cluster spacecraft electrostatic potential was established at +11 V, meaning that electron measurements were biased (attracting potential effect, secondary and photoelectron pollution). The use of this LEEA data set combined with the CIS instrument outputs for ions at the same period enabled the determination of the corrected environment parameters for the real Cluster situation and their use as inputs for the CLUS@1 AU case performed in Section 6.2.

```
!-----------------------------------------------------------------------|
! Generated by the cl software, developped by Emmanuel Penou, IRAP      |
! For more information, you can send an e-mail to epenou@irap.omp.eu    |
!                                                                       |
! ASCII Format                                                          |
! Blank lines are ignored                                               |
! "!" escapes rest of line as comment                                   |
!-----------------------------------------------------------------------|
!                            Global Metadata                            |
!-----------------------------------------------------------------------|
START_META           = Generation_date
VALUE_TYPE         = ISO_TIME
ENTRY              = 2013-03-22T12:31:40.000Z
END_META             = Generation_date
START_META           = Generated_by
ENTRY              = "cl software"
END_META             = Generated_by

!-----------------------------------------------------------------------|
```

```
!                                Variables                                 |
!--------------------------------------------------------------------------|
START_VARIABLE       = energy
PARAMETER_TYPE     = "Data"
VALUE_TYPE         = FLOAT
UNITS              = "eV"
END_VARIABLE         = energy
START_VARIABLE       = fdist
PARAMETER_TYPE     = "Data"
VALUE_TYPE         = FLOAT
FILLVAL            = -1.000E+31
DEPEND_0           = energy
UNITS              = "s^3/km^6"
FIELDNAM           = "Phase_Space_Density"
!Experiment        = ASCII
!THETA             = All
!PHI               = All
!START_TIME        = 2009-02-01T02:58:00.000Z
!END_TIME          = 2009-02-01T03:02:00.000Z
!MASS              = 1
END_VARIABLE         = fdist
!--------------------------------------------------------------------------|
!                                  Data                                    |
!--------------------------------------------------------------------------|
DATA_UNTIL = EOF
5.51590E+03   2.14243E-04
3.55410E+03   8.02419E-04
2.28050E+03   2.14030E-03
1.45900E+03   3.22675E-03
9.36080E+02   2.29766E-02
6.01690E+02   1.77911E-01
3.85790E+02   1.28238E+00
2.45440E+02   7.14473E+00
1.56080E+02   3.41568E+01
9.87750E+01   1.30944E+02
6.35900E+01   4.02287E+02
4.27630E+01   1.27515E+03
2.72190E+01   5.52964E+03
1.76740E+01   1.82239E+04
1.13080E+01   4.23492E+04
!--------------------------------------------------------------------------|
!--------------------------------------------------------------------------|
```

A.4 Article 1 - Guillemant et al. (2012): Solar wind plasma interaction with Solar Probe Plus spacecraft

Ann. Geophys., 30, 1–18, 2012
www.ann-geophys.net/30/1/2012/
doi:10.5194/angeo-30-1-2012

Annales Geophysicae

Solar wind plasma interaction with solar probe plus spacecraft

S. Guillemant[1,2], V. Génot[1], J.-C. Matéo-Vélez[2], R. Ergun[3], and P. Louarn[1]

[1]IRAP (Institut de Recherche en Astrophysique et Planétologie), Université Paul Sabatier de Toulouse & CNRS, UMR5277, 9 avenue du Colonel Roche, BP 44346, 31028 Toulouse Cedex 4, France
[2]ONERA (Office National d'Études et Recherches Aérospatiales), 2 avenue Édouard Belin, BP74025, 31055 Toulouse Cedex 4, France
[3]The Laboratory for Atmospheric and Space Physics, University of Colorado, Boulder, Colorado 80309, USA

Correspondence to: S. Guillemant (stanislas.guillemant@irap.omp.eu)

Received: 19 March 2012 – Revised: 26 June 2012 – Accepted: 29 June 2012 – Published:

Abstract. 3-D PIC (Particle In Cell) simulations of spacecraft-plasma interactions in the solar wind context of the Solar Probe Plus mission are presented. The SPIS software is used to simulate a simplified probe in the near-Sun environment (at a distance of 0.044 AU or 9.5 R_S from the Sun surface). We begin this study with a cross comparison of SPIS with another PIC code, aiming at providing the static potential structure surrounding a spacecraft in a high photoelectron environment. This paper presents then a sensitivity study using generic SPIS capabilities, investigating the role of some physical phenomena and numerical models. It confirms that in the near- sun environment, the Solar Probe Plus spacecraft would rather be negatively charged, despite the high yield of photoemission. This negative potential is explained through the dense sheath of photoelectrons and secondary electrons both emitted with low energies (2–3 eV). Due to this low energy of emission, these particles are not ejected at an infinite distance of the spacecraft and would rather surround it. As involved densities of photoelectrons can reach 10^6 cm^{-3} (compared to ambient ions and electrons densities of about 7×10^3 cm^{-3}), those populations affect the surrounding plasma potential generating potential barriers for low energy electrons, leading to high recollection. This charging could interfere with the low energy (up to a few tens of eV) plasma sensors and particle detectors, by biasing the particle distribution functions measured by the instruments. Moreover, if the spacecraft charges to large negative potentials, the problem will be more severe as low energy electrons will not be seen at all. The importance of the modelling requirements in terms of precise prediction of spacecraft potential is also discussed.

Keywords. Interplanetary physics (Solar wind plasma) – Space plasma physics (Electrostatic structures; Spacecraft sheaths, wakes, charging)

1 Introduction

Solar Probe Plus (SP+) is a NASA mission which consists in studying the very close environment of the Sun (approaching as close as 9.5 solar radii above the Sun's surface). The in situ measurements and imaging will help to understand the heating process of the Sun corona and the acceleration of the solar wind. The launch is planned for 2018 and the first perihelion in 2021. At such distances from the Sun, the expected environment of Solar Probe Plus should be quite hot and dense, leading the spacecraft and its on board instruments to suffer from high temperatures, charging and erosion. In particular, estimations of the satellite potential behaviour in such plasmas are important to predict the possible biases on plasma and electric measurements. Furthermore, the satellite velocity combined to the relative speed of the solar wind will create an ion wake which will likely increase the disturbances on the near probe environment[1]. In a similar context but with less extreme conditions; the Solar Orbiter spacecraft will reach regions further from the Sun ($\sim$ 0.28 AU). The impact of such conditions will be studied in a further paper.

Following observations of recollected photoelectrons and secondary electrons on the ATS 6 spacecraft, Whipple Jr. (1976) developed a theory for a spherically symmetric photoelectron sheath, including effects of ions, thermal electrons and secondaries. The aim was to determine whether the potential barrier responsible for the secondaries reflection

[1]Solar Probe website, http://solarprobe.jhuapl.edu/

was originating from those same particles or not. However, a comparison with the spacecraft data showed that the observed barrier of potentials is too large to be explained by the model (i.e. a spherically symmetric photoelectron or secondary electron sheath surrounding a uniformly charged spacecraft), and the authors concluded that the most probable explanation is that some portions of the ATS 6 surfaces are charged to different potentials. Actually, this thick sheath approximation is valid for large Debye lengths of emitted electrons, which is not the case for regions as close as 0.044 AU to the Sun. The Debye lengths of all secondaries in this near-Sun environment barely exceed a few centimetres, far from being of the order of the Solar Probe Plus dimensions. Thus the model of Whipple Jr. (1976) is not applicable in the present study.

Following Whipple's analysis and in the context of instruments for active control of the potential, Zhao et al. (1996) proposed an analytical approach to compute the electrostatic barrier and compared to Geotail measurements. However, this analysis is also only relevant in the sheath approximation and does not consider the secondary electronic emission.

Referring to the Helios spacecraft, a paper (Isensee, 1977) presents particle-in-cell simulations of the plasma environment of a spacecraft in the Solar wind, at 0.2 AU from the Sun. Using a certain number of discrete particles, injected at the boundaries of a simulation box with the appropriate distributions, the code moved them in the potentials and calculated the local densities from the number of particles per cell of a mesh. The potential was updated at the next time step by solving Poisson's equation. A two-dimensional model for numerical plasma simulation (9 m $\times$ 19.75 m domain, divided into 0.25×0.25 m cells) with a simplified probe geometry was used. With a conducting spacecraft, the consideration of 1 eV mean energy photoelectrons and the expected Solar wind conditions, the author obtained a lightly positively charged satellite (+2.9 V) surrounded by negative plasma potentials in the wake and in the ram. In front of the sunlit face, due to very high densities of photoelectrons, the local potential reached -1.4 V and in the ion wake behind the probe: -4.5 V. The 1 eV emitted photoelectrons are thus recollected by the surfaces of the probe. The rest of the paper focusses on the consequences in distortions of measured electron distribution functions. Such simple simulations of photoelectron clouds and their effects on spacecraft charging were already of interests for the understanding of plasma measurements disturbances. In these simulations, the secondary electronic emission was not modelled. We can thus easily imagine that with an extra secondary electron cloud surrounding the spacecraft and with a more energetic and concentrated environment that exists closer to the Sun, these simulated effects would be amplified.

Thiébault et al. (2004) studied the potential barrier in the electrostatic sheath around a magnetospheric spacecraft, for cases of conductive spacecraft like Geotail and Cluster. A fully self-consistent analytical model of the plasma around an electron emitting central body in a spherically symmetric geometry was used to analyse the electrostatic sheath around an idealized spacecraft. It was shown by comparison with 3-D PIC simulations that non-monotonic potential with negative potential barrier can exist all around a positively charged spacecraft (with Debye length of the order of the central body radius or more) even in the case of an asymmetric illumination pattern. Those existing potential barriers at distances from the Sun of 1 AU encourage advanced studies for near-Sun environment conditions (where even stronger barriers may exist): the preparation of the Solar Probe Plus mission that may be affected by such potential barriers has naturally been a motivation to perform such study.

Lipatov et al. (2010) studied the interactions of the solar wind with SP+ through 3-D hybrid simulations at a distance of 9.5 R_S. Their simulations are focused on the electric and magnetic fields surrounding the spacecraft. They do not take into account the spacecraft charging, the charge separation effects, the electron dynamics near the spacecraft, or the effects due to photoionization and electron impact ionization near the spacecraft. They demonstrated that the current closure near the spacecraft is very complicated and is directed by the external magnetic field. Some magnetic field barrier forms at the front of the heat shield, whereas strong whistler/Alfvén waves form in both upstream and downstream regions. The values of the electric field oscillations near the spacecraft bus may be of the same order as the maximum of expected electric field at an antenna. Simulated electric field perturbations are comparable to or exceed the maximum electric field expected for the SP+ spacecraft.

Also in the Solar Probe Plus context at 0.044 AU from the Sun, simulation results provided in Ergun et al. (2010) show that a negatively charged satellite is obtained using a PIC code and a simplified geometry model. High potential barriers for emitted photoelectrons and secondary electrons appear in the ram and the wake sides of the probe, due to their high densities in these regions, and make those low energy particles recollected by the spacecraft. The balance of currents is obtained for a negative spacecraft potential. We will cross-compare our numerical tool with the code used in Ergun et al. (2010) and a description of this model is given in Sect. 2.1, the corresponding results are presented in Sect. 2.2.

The simulation tool used in this study is SPIS, a software development project of the European Space Agency (ESA). It is developed as an open source and versatile code with the support of the Spacecraft Plasma Interaction Network in Europe (SPINE) community[2]. The first development phase of the project has been performed by ONERA/DESP, Artenum and University Paris VII (through the ESA contract Nbr: 16806/02/NL/JA). Some developments were funded by the French space agency (CNES). It is a simulation software based on an electrostatic 3-D unstructured particle-in-cell plasma model and consisting of a

[2]SPIS web site, http://dev.spis.org/projects/spine/home

JAVA based highly modular object oriented library, called SPIS/NUM. More accurate, adaptable and extensible than the existing simulation codes, SPIS is designed to be used for a broad range of industrial and scientific applications. The simulation kernel is integrated into a complete modular pre-processing/computation/postprocessing framework, called SPIS/UI, allowing a high degree of integration of external tools, such as CAD, meshers and visualization libraries (VTK), and a very easy and flexible access to each level of the numerical modules via the Jython script language. Developed in an open source approach and oriented toward a community based development, SPIS is available for the whole community and is used by members of the European SPINE network. SPIS should address a large majority of the new challenges in spacecraft plasma interactions, including the environment of electric thruster systems, solar arrays plasma interactions, and modelization of scientific plasma instruments.

The numerical core and the user interface have been developed by ONERA and the Artenum company, respectively (Roussel et al., 2008a). Recent enhancements have consisted in improving multi time scale and multi physics capabilities (Roussel et al., 2012). One first paper on a real engineering application, SMART-1 by Hilgers et al. (2006), studied the electrostatic potential variation of the probe and the first SPIS validations by comparison with theoretical models are presented in Hilgers et al. (2008). The effect of in-orbit plasma on spacecraft has been modelled in a wide range of configurations: geosynchronous (GEO) spacecraft charging (Roussel et al., 2012), electric propulsion (Roussel et al., 2008b), barrier of potential at millimetre scale (Roussel et al., 2008a) and electrostatic discharge onset on GEO solar panels (Sarrailh et al., 2010). The ONERA plasma chamber, named JONAS, was simulated and the results compared to experiments in Matéo-Vélez et al. (2008). It has also been compared with other numerical models (Roussel et al., 2012; Matéo-Vélez et al., 2012a).

The objective of this paper is to estimate the disturbances on near-Sun probe measurements using the SPIS software. Section 2 presents the cross-comparison of SPIS software and the code described in Ergun et al. (2010). Results using SPIS with more complete modelling and a parametric study are described in Sect. 3. Conclusion and perspectives are presented in Sect. 4.

2 Cross-comparison of the two codes

In this section, we present a simplified model of Solar Probe Plus in a near-Sun environment using two codes: SPIS and the code described in Ergun et al. (2010). It aims at cross-comparing these codes with an identical set of parameters. We describe first the approach used in both codes in Sect. 2.1 and provide the results in the next one.

2.1 Models

The comparison is performed on the same case as in Fig. 5 of Ergun et al. (2010). The corresponding code is used here with modifications regarding the previously published paper. The mesh has been refined (1 cm instead of 2 cm) and the photoemission has been changed (maxwellian photoelectrons of temperature 3 eV instead of the double Maxwellian of temperatures 2.7 eV and 10 eV). Concerning the SEEY (Secondary Electronic Emission Yield) it is assumed to be equal to 1, instead of the BeCu SEEY properties reported previously in Ergun et al. (2010) (referenced in Lai, 1991). A higher order calculation of thermal electron trajectories has been implemented and finally, the scattered thermal electrons (15 %) that were not included in the electron density calculation are now taken into account. This simulation is referred to as simulation A in the following. For the sake of completeness, we remind the reader of some details in the following paragraph.

This code is a Poisson solver and electron tracing program considering a 3-D cylindrically symmetric domain on a two dimensional (2-D) grid. The numerical architecture has two parts, which (1) determine the potential structure (ϕ) surrounding the spacecraft via a Poisson solver (given a charge distribution) and (2) determine the charge distribution via particle tracing performed in 3-D (given ϕ). The domain is a 5 m (in R) $\times$ 10 m (in X) cylinder with 500×1000 2-D grid. The grid spacing is 1 cm in both X and R. The space environment is taken from Lipatov et al. (2010) and Ergun et al. (2010) and presented in Table 1. The spacecraft is assumed to be a fully conducting cylinder, 1 m in radius and 2 m long, with one end allowed to emit photoelectrons. Ambient electrons follow a Maxwell-Boltzmann equilibrium distribution. Ion drift velocity is $-300\,\mathrm{km\,s^{-1}}$ in the direction down the z-axis that reproduces a Solar wind bulk speed estimated at $200\,\mathrm{km\,s^{-1}}$ from the Sun, added to the relative probe velocity of $100\,\mathrm{km\,s^{-1}}$ toward the Sun. Ion modelling is very simple since it is assumed that their density is uniform, except behind the cylinder (in the -z direction) where their density is null. 10^6 photoelectrons are randomly created on the sunlit surfaces, along isotropic directions, with a Maxwellian energy distribution and a 3 eV mean energy (Ergun et al., 2010; Pedersen, 1995). A rather high photoelectron current at 1 AU of J_{ph} of $57\,\mu\mathrm{A\,m^{-2}}$ is scaled to the position of the spacecraft (0.044 AU), giving an injected current density J_{ph} of $29\,\mathrm{mA\,m^{-2}}$. The Debye length λ_{ph} for photoelectrons is ~ 3 cm. Secondary electron emission under ion impact (SEI) efficiency is assumed arbitrarily to be 100 % (each impacting ion liberates one secondary electron). Secondary electron emission under electron impact (SEE) is modelled by creating electrons randomly over the spacecraft surfaces with a 2 eV characteristic energy. The thermal efficiency ϵ_{the} (i.e. the fraction of electrons that strike the surface and are absorbed) arbitrarily equals to 0.85. Those that are not absorbed (0.15) are assumed to be scattered without

Table 1. Input parameters for the cross-comparison test case.

Parameter	Value (Ergun et al., 2010)	Value (R. E. Ergun, unpublished data, 2012) Simulation A	Value (SPIS) Simulation B
Thermal electron/ion density $n_{e,i}$	$7 \times 10^9\,m^{-3}$	$7 \times 10^9\,m^{-3}$	$7 \times 10^9\,m^{-3}$
Thermal electron temperature T_e	85 eV	85 eV	85 eV
Electron modelling	Maxwell-Boltzmann	Maxwell-Boltzmann	Maxwell-Boltzmann
Ion modelling	uniform (null in wake)	uniform (null in wake)	PIC (with no deflection)
Ion temperature T_i	N/A	N/A	0.01 eV
Ion velocity	$V_Z = -300\,km\,s^{-1}$	$V_Z = -300\,km\,s^{-1}$	$V_Z = -300\,km\,s^{-1}$
Ion type	H^+	H^+	H^+
Material	Conductive	Conductive	Conductive
Photoelectron temperature T_{ph}	95 % at 2.7 eV + 5 % at 10 eV	3 eV	3 eV (+ case with 10 eV)
J_{ph} ($mA\,m^{-2}$)	29	29	29
SEE Distribution	maxwellian, 2 eV	maxwellian, 2 eV	maxwellian, 2 eV
True Secondary Emission Yield	curves of BeCu in Lai (1991)	1	2.47
Backscattered Electron Yield	0.15	0.15	0.17
Meshing	2 cm	1 cm	from 2 to 50 cm
External boundary conditions	0 V	0 V	0 V

energy loss. The yield of electron secondary emission under absorbed electrons is arbitrarily 1. The potential at the limits of the simulation box is set at 0 V.

SPIS uses an unstructured tetrahedral mesh that allows it to refine spatial resolution near regions of interest. The plasma model treats ions fully kinetically with realistic masses. Electrons can be treated fully kinetically (full PIC) or as a fluid, like in the Maxwell-Boltzmann statistics equilibrium model approximation. A multi-zone modelling combines fluid and PIC description of electrons. Particle sources from ambient environment are modelled by a Maxwellian distribution for electrons and ions (a drift can be added for ions); up to two populations per species can be considered. The electric field is computed from a finite element discretization of Poisson's equation and solved with an iterative conjugate gradient solver. An implicit Newton-type solver is used for a non-linear Poisson equation, in the case of Boltzmann distributions for ambient electrons. The boundary condition on an external boundary is a mixed Dirichlet-Neumann. The boundary condition on a spacecraft is Dirichlet and based on the spacecraft surface potential evolution. Finally, it handles spacecraft geometrical singularities (wires, plates) by extracting the singular part of the field. The charge exchange volume interaction is modelled by a Monte Carlo model. The spacecraft material properties considered are: secondary emission (under electron/proton/UV), conductivities (surface/volume, intrinsic/radiation induced), electron field emission, sputtering (recession rate, product generation and transport). The spacecraft equivalent circuit is composed of dielectric coatings, user-defined discrete components and is solved using an implicit solver, with auto-adaptive time step.

In the SPIS simulation, referred to as simulation B in the following, the 3-D domain is 5 m (in R) × 10 m (in X), with a progressive refinement of the mesh (until 2 cm on the sunlit face of the cylinder); see Fig. 1 showing the Gmsh model for the satellite (Gmsh is an automatic 3-D finite element mesh generator with build-in pre- and post-processing facilities). An intermediate cylinder has been created to limit a fast enlargement of the mesh near the satellite. It is forced to have a 15 cm grid spacing on the sun side and 30 cm on the other side. This intermediate cylinder has no physical existence, its aim is to control the meshing growth. The input parameters are presented in Table 1 in comparison to those used with the other code. Some parameter differences exist. First, the generic PIC (Particle In Cell) modelling used in SPIS was adapted for ions in order to fit the modelling used in the other code: ions are emitted at the boundary with a velocity of $-300\,km\,s^{-1}$, a temperature of 0.01 eV and they are not deflected. Second, the material used has complete curves of SEE yield and backscattering yield versus incident electron energy, see Fig. 2. For the isotropic ambient electron with energy of 85 eV, the backscattering yield is 0.17 and the true secondary emission yield is 2.47. So comparing to the simulation with the other code, this SPIS simulation will generate more secondary electrons. Third, no SEI is modelled.

Plasma frequency associated to thermal and photoelectrons are 748 kHz and 2069 kHz, respectively. Debye length associated to ambient and photo electrons are 80 cm and 3 cm, respectively. That means that photoelectrons should rule the plasma behaviour around the satellite, at least on the

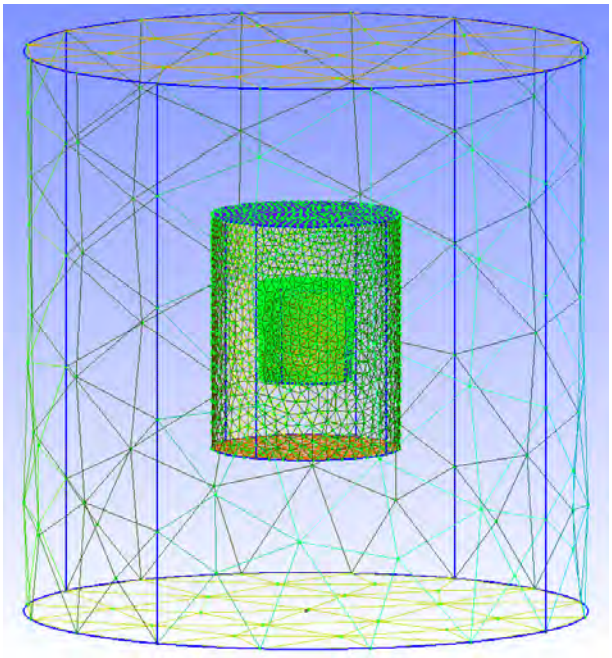

Fig. 1. The GMSH model of the simplified Solar Probe Plus spacecraft used in SPIS simulations with the associated meshing grid. The z-axis described in the text is the vertical axis in this figure. From the outside to the inside the boundary of the simulation box, the intermediate meshing cylinder (which has no physical meaning) and the satellite cylinder can be distinguished.

sun-side face. This induces the necessity to have very small grids and time steps. The simulation duration is set to 40 µs, with time steps of 50 ns.

2.2 Results

Results obtained with simulation A are presented in Fig. 3. Results are qualitatively comparable to those previously obtained in the Fig. 5 of Ergun et al. (2010), except that the spacecraft floats at −15.5 V instead of −4.15 V. This is mainly due to the refined mesh used to simulate the secondary electron barrier, the changes in the SEEY and the consideration of the scattered electrons in the electron density calculation (see Sect. 2.1). Those changes deepened the barrier around the satellite and caused a significant change in the floating potential.

Table 2 shows all net currents on the spacecraft. Concerning simulation A, the total thermal electron current arriving on the spacecraft I_{the} reaches −25.6 mA. Due to ϵ_{the} (i.e. the fraction of electrons that strike the surface and are absorbed), which equals 85 %, there are −21.8 mA effectively absorbed by the structure and −3.8 mA of electron current that is backscattered without energy loss. For secondary electron currents, the account leads then to 21.8 mA emitted, 3.8 mA backscattered, 1.0 mA due to ion impact, and −10.2 mA rec-

Table 2. Comparison of net currents on spacecraft for simulations A and B.

Net current (mA)	Simulation A SC at −15.5 V	Simulation B (SPIS) SC at −20 V
I_{the}	−25.6	−25.2
I_{ion}	1.0	0.7
I_{ph}	8.1	6.6
I_{se}	16.4	17.7
$\sum I$	−0.1	−0.2

ollected, giving a net current I_{se} of 16.4 mA. The net current for photoelectrons equals 8.1 mA.

Results obtained in simulation B with SPIS are qualitatively the same, with the formation of a photoelectron barrier and a negative spacecraft, floating at −20 V. Figure 4 shows the evolution of currents on the spacecraft and of the surface potential versus time. After a transient regime, where the potential grows until 3.9 V due to strong photoemission, the spacecraft then reduces to a permanent −20 V voltage. At that time, collected and emitted currents are balanced.

The collected currents from thermal electrons and ions reach −25.2 mA and 1.0 mA, respectively. The photoelectronic emission is constant over time (−91 mA during a constant solar flux) while the emission of secondary electrons depends on the spacecraft potential: when ϕ_{SC} is highly positive at the first steps of the simulation, the structure collects a high current density of thermal electrons and emits consequently many secondary electrons. Once the spacecraft potential reached equilibrium, the emitted current from secondary electrons sets to a value of 105.3 mA. Large recollected currents of SEE and photo electrons (−87.5 mA and −84.4 mA, respectively) are observed. Thus, those two last populations have a larger impact than the ambient plasma populations. The net SEE current I_{se} is 17.7 mA and the net photoelectron current I_{ph} is 6.6 mA. All net current values are visible in Table 2. 83 % of emitted secondary electrons are recollected and this ratio goes up to 93 % for photoelectrons, even if the spacecraft is negative. This is a clear effect of potential barriers represented in Fig. 5, that shows the plasma potential around the spacecraft.

Figure 6 indicates that the ram barrier has a dimension of a few cm, which correctly fits with $\lambda_{\mathrm{ph}} = 3$ cm and $\lambda_{\mathrm{se}} = 6$ cm and a height of −11 V (−20 V on SC compared with −31 V at the barrier maximum). The wake barrier is larger (1 m) due to the absence of ions in this region. The potential barrier is −25 V (−45 V at the barrier maximum). Figure 7 reveals the existence of a −4 V potential barrier facing the side of the cylinder. The isocontour line at −20 V is 60 cm from the spacecraft in the x-direction. This potential barrier leads to SEE electrons recollection too.

Concerning populations, both simulations A and B exhibit the same global behaviour, as seen in Fig. 3 and in Fig. 8.

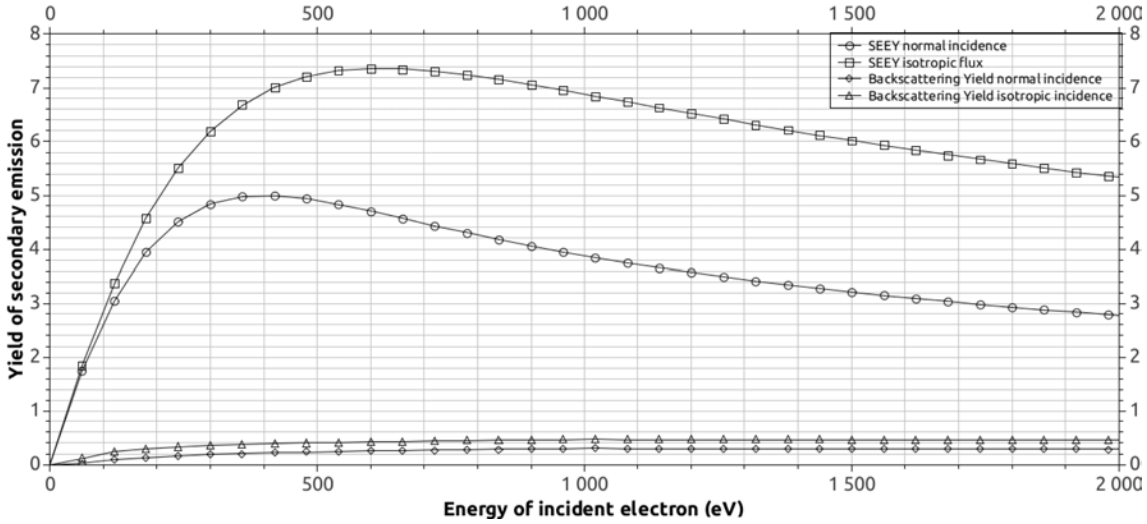

Fig. 2. Cross comparison simulation B (SPIS): Secondary Electron Emission Yield (SEEY) and the backscattering yield vs. incident electron energy (with a normal or isotropic incoming flux).

The diminution of the electron density due to the high negative potential from the structure and the potential barriers (at the front and the back of the cylinder) fits the Boltzmann distribution used. The ion wake is similarly solved, with a small ion non-null thermal velocity effect in simulation B with SPIS.

The most dense population of plasma are photoelectrons, emitted here from the sunlit face at densities of about $10^{11}\,\mathrm{m}^{-3}$ and they are spreading around as far as the wake zone. As they are emitted from the sunlit face and depending on their energies and potential barriers, photoelectrons can move as far as the side of the cylinder that explains the density of particles in this region even though this circular face does not emit photoelectrons. The highly negative potential present in the wake prevents photoelectrons from penetrating this area.

The same effect of a near-sun environment on a spacecraft appears: its structure tends to settle at a negative potential, due to surrounding electrostatic barriers that originate from secondary electrons and photoelectrons. In the wake, negative potentials are somewhat different: $-32\,\mathrm{V}$ and $-45\,\mathrm{V}$ in simulation A and B, respectively. At the front, $-22\,\mathrm{V}$ and $-31\,\mathrm{V}$ maximum potentials are obtained in simulation A and B, respectively. However, looking at the effective potential barrier values, simulation B results in ram and wake barriers of $-11\,\mathrm{V}$ and $-25\,\mathrm{V}$ while simulation A results in $-7\,\mathrm{V}$ and $-17\,\mathrm{V}$. Furthermore, comparing the plasma potential maps for both cases, simulation B provides a more developed potential barrier on the side of the cylinder. This seems to be a direct effect of the higher SEY used in simulation B (2.47 instead of 1). In Fig. 8, SEE electron density of $\sim 10^{11}\,\mathrm{m}^{-3}$ is observed over all surfaces of the spacecraft. It is large compared to that of thermal electrons around the cylinder ($5.5 \times 10^{9}\,\mathrm{m}^{-3}$). In that case, a potential barrier due to SEE electrons ($-4\,\mathrm{V}$) is added to that of photoelectrons. Density values above those faces and especially in the wake are the lowest ($10^{6}\,\mathrm{m}^{-3}$). It is through the sides of the cylinder that SEE electrons mostly escape.

All net currents are similar, except a 2 mA gap for photoelectron currents (8.1 mA and 6.6 mA for simulation A and B, respectively) due to a higher front potential barrier. This difference may be assigned to differences in meshing or photoelectrons dynamics. Concerning the SEE electron current, net values are also similar (16.4 and 17.7 mA for simulation A and B, respectively), but the main difference lies in the emitted current: $I_{\mathrm{the}} = -25.2\,\mathrm{mA}$ and I_{se} (emitted) $= 105.3\,\mathrm{mA}$ for SPIS simulation B, and $I_{\mathrm{the}} = -25.6\,\mathrm{mA}$ and I_{se} (emitted) $= 21.8\,\mathrm{mA}$ for simulation A. The higher emission within SPIS leads to higher potential barriers facing the entire spacecraft surface which become locally one dimensional. Thus, a higher recollection rate of 83 % is obtained. In simulation A, SEE electrons have more opportunities to escape through the side of the cylinder as in this region the potential barrier is visibly thinner (explaining a recollection rate of 45 %). Furthermore, the current I_{se} gathers both secondary and backscattered electrons. Through a certain yield depending on the incident particle energy, the SPIS backscattered particles will get out of the structure with 2/3 of their initial energy (regarding to the other code where the backscattered keep all their energy). In SPIS simulation B, the recollection of the backscattered is thus higher.

Lastly, in simulation A, it is assumed that 100 % of impacting ions emit one secondary electron, which has however only a small impact on the total emitted current.

Finally, given the differences of modelling of the 2 simulations, the results are in good agreement. Possible negative charging of spacecraft in near-Sun conditions is obtained in this cross-comparison study.

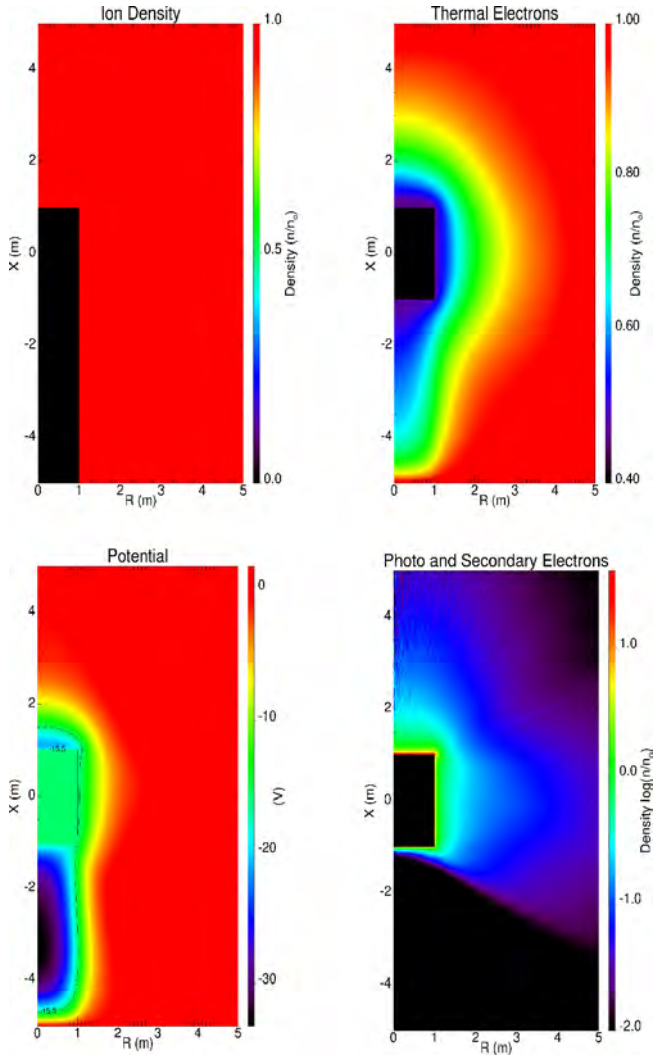

Fig. 3. Cross comparison simulation A. From the upper left to the bottom right of the picture: Ion density; Thermal electron density; SC potential. Photoelectron and SEE densities. n_0 is the plasma density: $7.10^9\,\mathrm{m}^{-3}$.

2.3 Photoelectron energy

As discussed previously, the photoelectron and SEE electron models impact a lot the spacecraft potential. In this paragraph, a simulation C is run using SPIS in the same configuration as in simulation B, except the photoelectron temperature of 10 eV (instead of 3 eV). The spacecraft potential is now -9.7 V, explained by the fact that photoelectrons have more energy to spread further and escape the ram potential barrier, see Fig. 9. The position of the barrier gets further from the surface, as seen on Fig. 6. The barrier structure possibly gets closer to a three dimensional barrier compared to the previous case (almost one dimensional). The amount of photoelectrons emitted is the same but the position of the maximum is further. It has a strong impact close to the side of the sunlit disk.

Table 3. Parameters used for the nominal simulation S1.

Parameter	Value
Thermal electron density n_e	$7 \times 10^9\,\mathrm{m}^{-3}$
Thermal electron temperature T_e	85 eV
Ion density n_i	$7 \times 10^9\,\mathrm{m}^{-3}$
Ion temperature T_i	82 eV
Ion type	H^+
Ion modelling	PIC
Backscattered electron	Active
Photoelectron temperature T_ph	3 eV
Debye length for thermal electrons λ_the	0.8 m
Material	Conductive
Meshing	from 5 cm to 2 m
Number of tetrahedrons	$\sim 158\,000$
External boundary conditions	Fourier: $1/r^2$ decrease of potential

3 Parametric study using SPIS

The need for complementary simulations comes from three points: (1) the necessity of a full PIC description of the environment, (2) the uncertainty on the secondary electron emission (linked to the chosen material coating the probe), and (3) an ion temperature more relevant to the one expected at this distance to the Sun.

In this section, SPIS capabilities are used to simulate the same near-Sun environment with the same spacecraft geometry as in simulation B to perform a parametric study both on numerical and physical parameters. The model and simulations are defined in Sect. 3.1, the results in Sect. 3.2.

3.1 Model

The same geometry is used as in Fig. 1, except a larger external box of dimensions $R = 6$ m and $X = 12$ m. The grid spacing is 5 cm on the sunlit face (toward the z-axis), 15 cm on the other side and 2 m all over the domain limits. The whole meshed volume contains $\sim 158\,000$ tetrahedrons. The same environment is used. However, the genericity of SPIS permits to change the hybrid model (PIC for ions and Maxwell Boltzmann for electrons) to full PIC. It must be noticed that the Maxwell-Boltzmann distribution is exact when the satellite potential is negative and if no potential barrier exists. The Boltzmann model is only approximate if a potential barrier exists and is more negative: the less energetic electrons of the distribution should not be able to cross this barrier, so the Boltzmann model is overestimating the particles arriving on the satellite. Of course, it becomes completely wrong if potential barriers are large or if the spacecraft is significantly positive. In the simulations presented below, the full-PIC

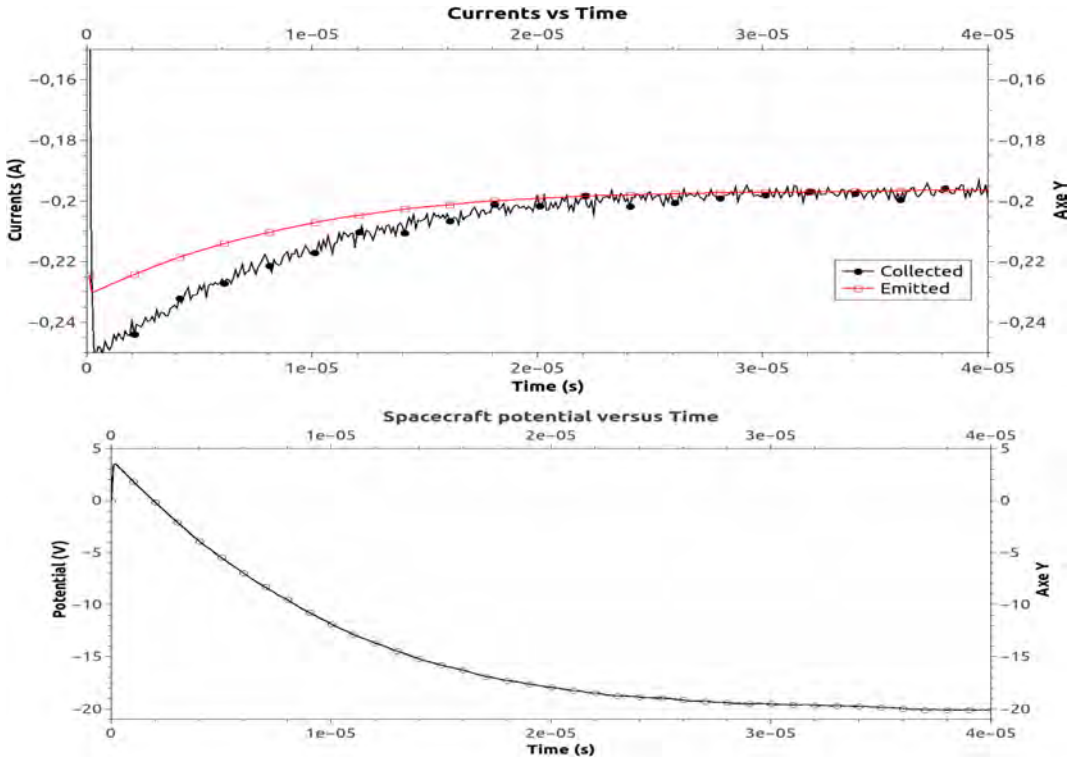

Fig. 4. Cross comparison simulation B (SPIS). Evolution versus time of all collected and emitted currents (on top) and of spacecraft average surface potential (on the bottom).

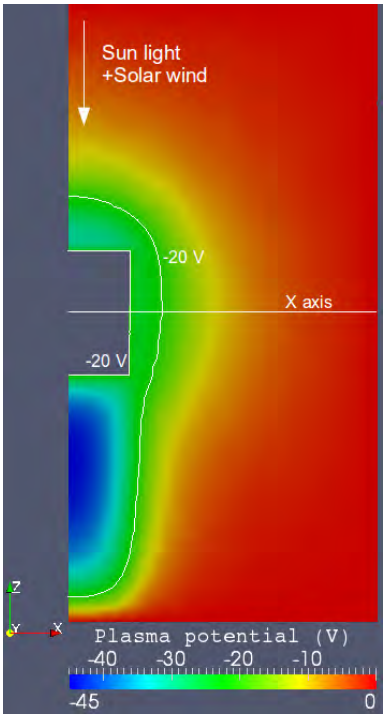

Fig. 5. Cross comparison simulation B (SPIS): Plasma potential in a $X = 0$ plane.

model has been chosen except for a comparison case that permits to determine the impact of using Boltzmann distribution instead of PIC modelling for electrons. For the ions, the PIC model is used to inject particles following a Maxwellian with an energy of $T_i = 82$ eV and a drift velocity of $-300\,\mathrm{km\,s^{-1}}$ in the z-direction. This permits to have a more consistent calculation of the plasma state.

The material covering the Solar Probe Plus model is now a conductive layer quite similar to ITO (Indium Tin Oxide). Its SEEY is presented on Fig. 10. Particularly for thermal electrons at 85 eV, the backscattering yield of ITO for an isotropic incident flux is 0.18 and the SEE (Secondary Electron Emission) yield of ITO for an isotropic incident flux is 1.63. The secondary electron emission is set with a characteristic energy of 2 eV (Maxwellian distribution). The backscattered electrons are emitted with 2/3 of their initial energy. For photoelectrons and secondary electrons, Debye lengths are expected to be smaller than 5 cm. These conditions justify our choices for the meshing: (1) the smallest grid spacing possible on the sunlit side of the cylinder to compute properly these populations with a PIC model and (2) the intermediate meshing cylinder at 1 m around the satellite (bigger than λ_{the}).

The boundary condition mimics a $1/r^2$ decrease of the potential, which is simulated by a Fourier (or mixed

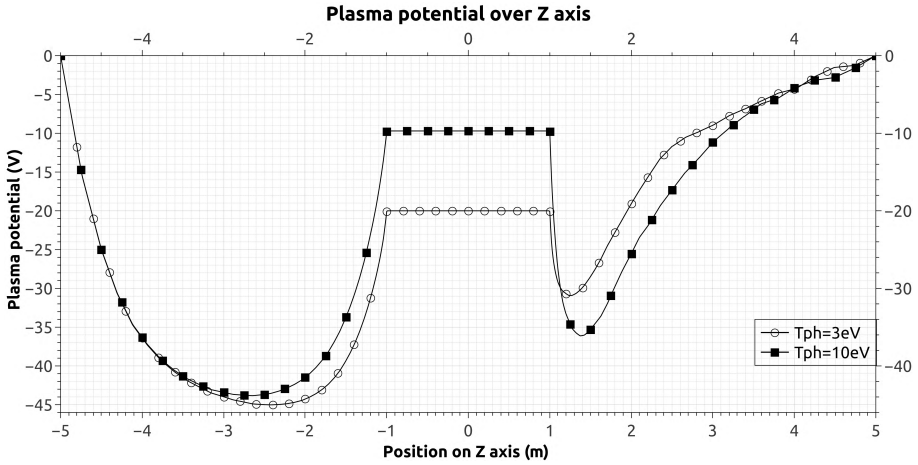

Fig. 6. Cross comparison simulation B (SPIS): plot along the z-axis of the plasma potential. The circled line represents the potential for a photoelectron emission temperature centered on 3 eV, the squared line is for a temperature of 10 eV.

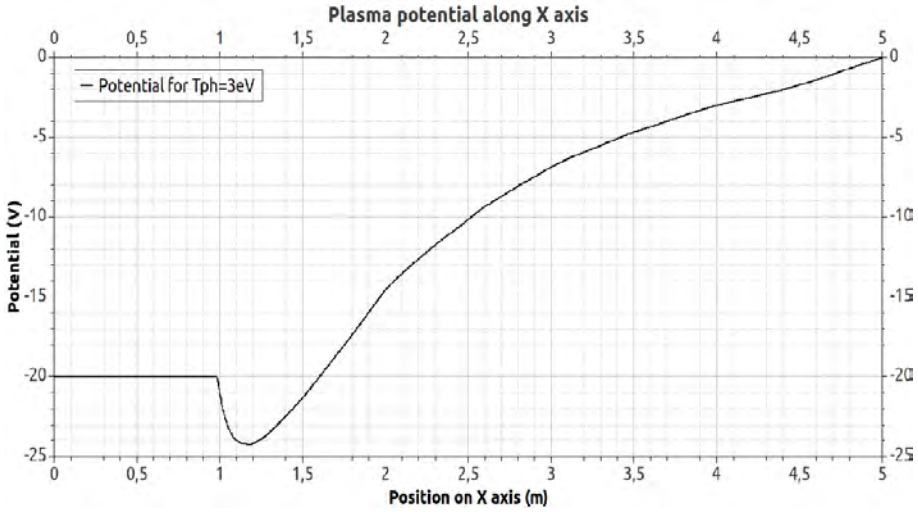

Fig. 7. Cross comparison simulation B (SPIS): plasma potential along the x-axis, showing the existence of a −4 V potential barrier on the side of the spacecraft.

Dirichlet-Neuman) type condition:

$$\alpha\phi + \nabla\phi \times \boldsymbol{n} = \beta \tag{1}$$

$$\alpha = \frac{2\boldsymbol{r} \times \boldsymbol{n}}{r^2} \tag{2}$$

with $\beta = 0$, $\boldsymbol{r}$ is the vector field of boundary mesh surface positions with origin at the spacecraft mesh barycentre, and $\boldsymbol{n}$ is the vector field of the outgoing normals to the external boundary mesh.

The parameters common to all simulations (S1 to S5, S1 being the nominal case) are presented in Table 3. The parameters specific to each case are presented in Table 4. Each non-nominal case (S2 to S5) has only one change with respect to S1.

3.2 Results

The collected, emitted and net final currents of all cases are summarized in Table 5, with all final spacecraft potentials and potential barriers values. In each case the photoemission is constant over time. Figure 11 displays for all cases the plasma potential along the z-axis (for S5: the z-axis is not crossing the center of the wake as a perpendicular spacecraft speed has been added regarding to the Sun-SP+ direction).

3.2.1 S1: nominal case

The final spacecraft potential sets up in this S1 case around −14.5 V (the plasma potential map is represented on Fig. 12). As previously, two major negative potential barriers for secondary particles are visible: −10.5 V in the ram and −15 V

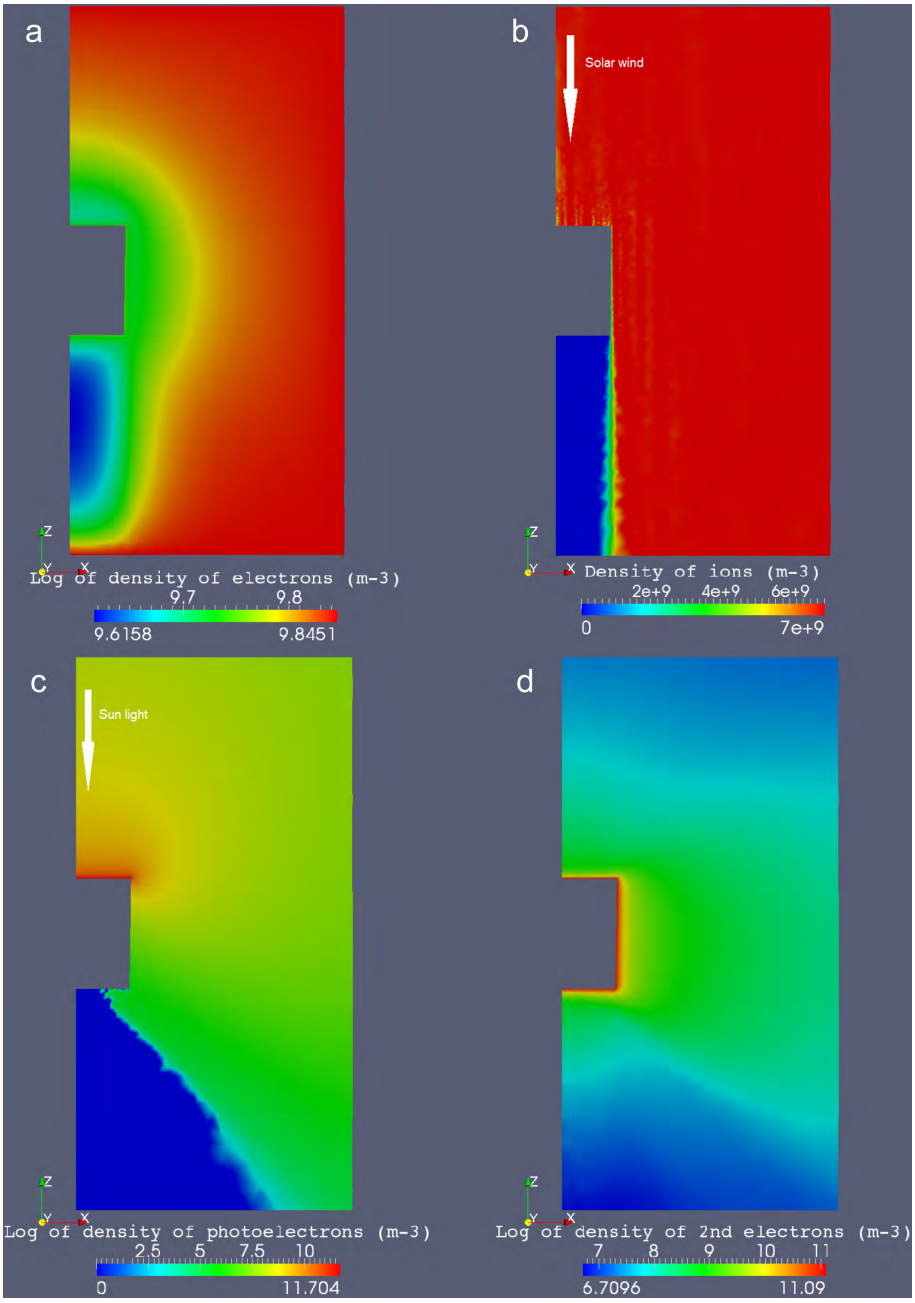

Fig. 8. Cross comparison simulation B (SPIS): population density maps ($T_{ph} = 3$ eV): **(a–d)** from the upper left figure to the lower right figure. **(a)** Thermal electrons, **(b)** Ions, **(c)** Photoelectrons, **(d)** Secondary electrons.

in the wake. Once the potential is stabilized 76 % of emitted secondary electrons are recollected and this ratio goes up to 92 % for photoelectrons (see Table 5). Globally, the same comments as in the previous section can be made.

The maps in a $X = 0$ plane of the particle densities obtained through the S1 simulation are displayed on the Fig. 13. The thermal electron density is almost constant over the simulation box except near the satellite where it goes to 3.16×10^9 m^{-3}. The ion wake is reduced by the thermal energy of these particles and by ion focussing by the negative potential. Local striations of the ion density plot at the front are due to statistic noise in the ion PIC approach caused by a reduced number of superparticles per cell in this region (it decreases until less than 5). However, that does not impact the results since the space charge is ruled by photoelectron density in the sheath (the space charge used in Poisson solver is computed using charge deposit of ions along their trajectory and not at the end of each time step). Photoelectrons are

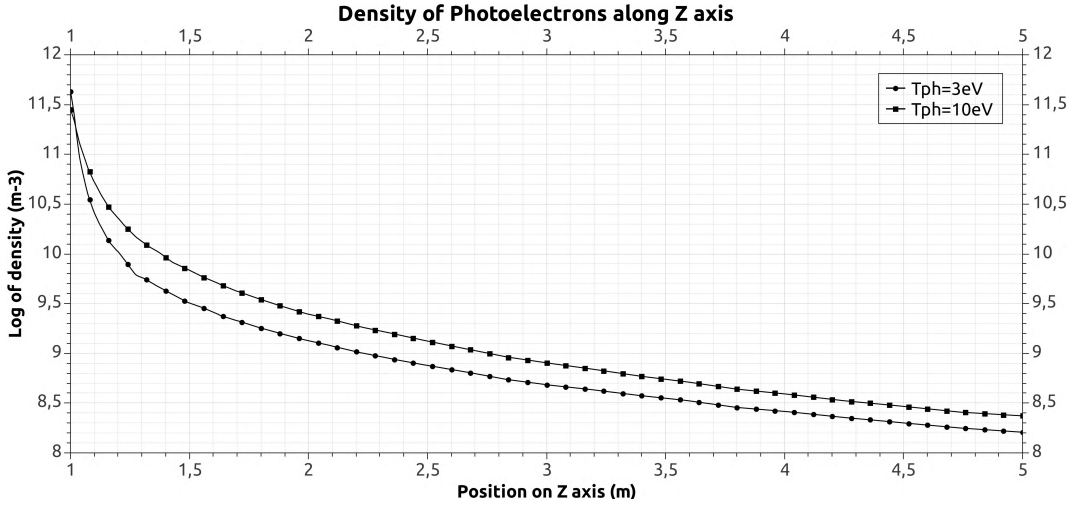

Fig. 9. Cross comparison simulation B (SPIS): plot along the z-axis of the photoelectron density, from the center of the heatshield to the upper boundary of the simulation box. The circled line represents the density for a photoelectron emission temperature of 3 eV, the squared line is for a temperature of 10 eV.

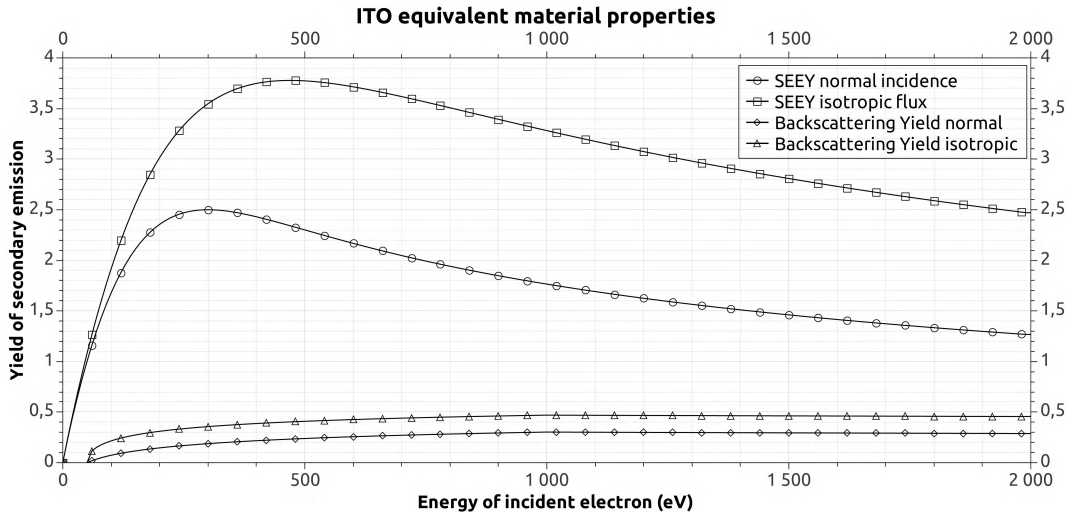

Fig. 10. Secondary electron emission yield (SEEY) and the backscattering yield of ITO material (used in parametric study) vs. incident electron energy (with a normal or isotropic incoming flux).

the denser population: they are emitted from the sunlit face at densities of about 10^{11} m^{-3} and they are spreading around until the wake zone. The photoelectron wake is also visible on the rear side of the cylinder, and the highly negative potential present there prevents photoelectrons from penetrating this area and from being recollected on this face. Secondary electrons are highly present over all surfaces of the spacecraft, as in the simulation B. The potential barriers still have a great influence by preventing secondary electrons from escaping the front and the back faces of the spacecraft.

Figure 14 shows the ratios of thermal, photo and secondary electrons densities over the plasma density ($n_0 = 7 \times 10^9$ m^{-3}), the final blue curve being the sum of those contributions over n_0. The photoelectrons and secondary electrons dominate over thermal electrons in the ram, with a higher density of photoelectrons over secondary electrons. Thermal electrons are predominant over secondary electrons ~ 10 cm further from the front face and over photoelectrons ~ 50 cm further. At the back side of the cylinder, the photoelectrons are not visible because of their extremely low densities with respect to the scale of the plot. The secondary electrons are dominant over thermal ones by ~ 25 cm.

This S1 simulation demonstrates that the same phenomena showed in the Sect. 2 occur in a more complex and realistic simulation. One major difference here is the reduced wake dimension due to the considered ion temperature and their

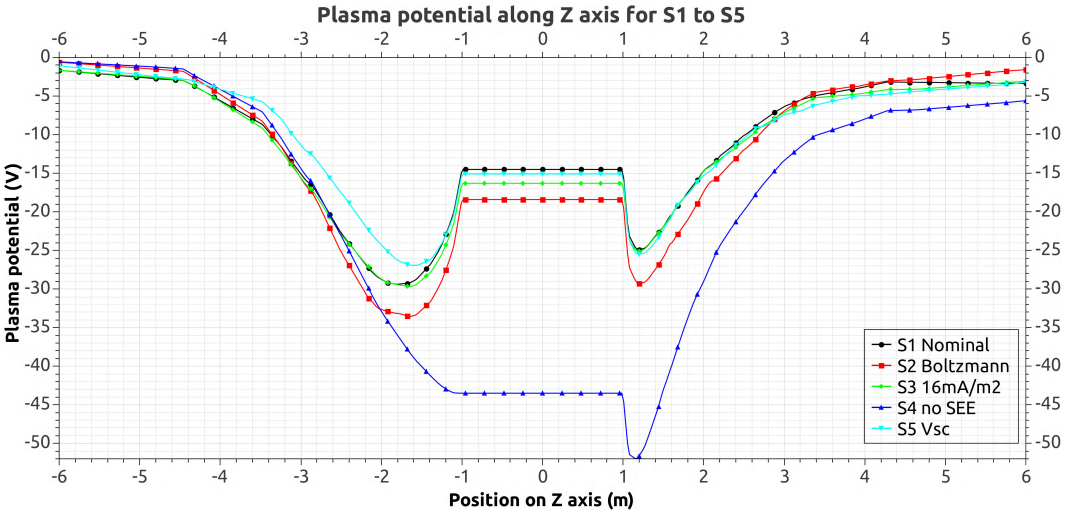

Fig. 11. Plot along the z-axis of the plasma potential for all SPIS simulations (parametric study).

Table 4. Specific inputs for the parametric study.

Simulation	Description	Electron modelling	Ion velocity	J_{ph} (mA m^{-2})	2nd emission
S1	Nominal	PIC	$V_Z = -300\,\mathrm{km\,s^{-1}}$	29	Active
S2	Boltzmann	Boltzmann fluid	$V_Z = -300\,\mathrm{km\,s^{-1}}$	29	Active
S3	$J_{ph} = 16$	PIC	$V_Z = -300\,\mathrm{km\,s^{-1}}$	16	Active
S4	No SEE	PIC	$V_Z = -300\,\mathrm{km\,s^{-1}}$	29	Disabled
S5	Ion drift	PIC	$V_Z = -300\,\mathrm{km\,s^{-1}}$	29	Active
			$V_X = -180\,\mathrm{km\,s^{-1}}$		

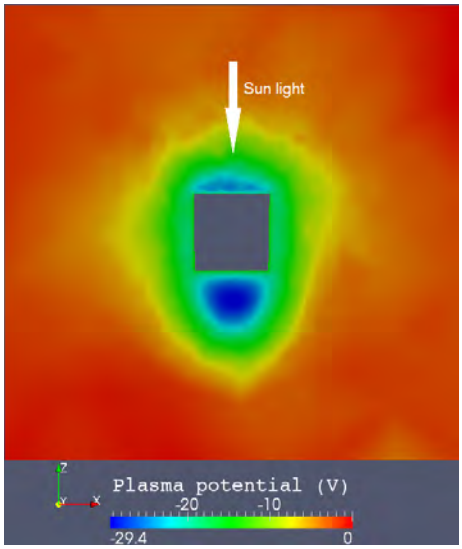

Fig. 12. Simulation S1: map of the plasma potential in a $X = 0$ plane.

true PIC model: the deflection of their trajectories is possible in this case compared to the previous simulations (A and B). Ions are thus able to spread more efficiently and resettle the wake faster. The reduced wake increases the final probe potential. The ITO coating produces less secondary electrons than the previous material but sufficiently to contribute with photoelectrons to the formation of the potential barriers. Finally, PIC electrons permit to properly account for potential barriers, as it will be demonstrated in the next paragraph.

3.2.2 S2 simulation: Boltzmann thermal electrons model

In this S2 simulation the final spacecraft potential sets up around -18.4 V, instead of -14.5 V. Two major negative potential barriers for secondary particles are present (Fig. 11): -10.6 V in the ram and -16.1 V in the wake. The Boltzmann model for thermal electrons did change the final ϕ_{SC} but not the values of the potential barriers: the whole plasma and satellite potentials have been dug negatively by about 4 V. Indeed the Boltzmann analytical model can not fully describe the physics of potential barriers since it makes the assumption of local thermal equilibrium with ϕ. The shielding of the low energy thermal electron is however not modelled. The

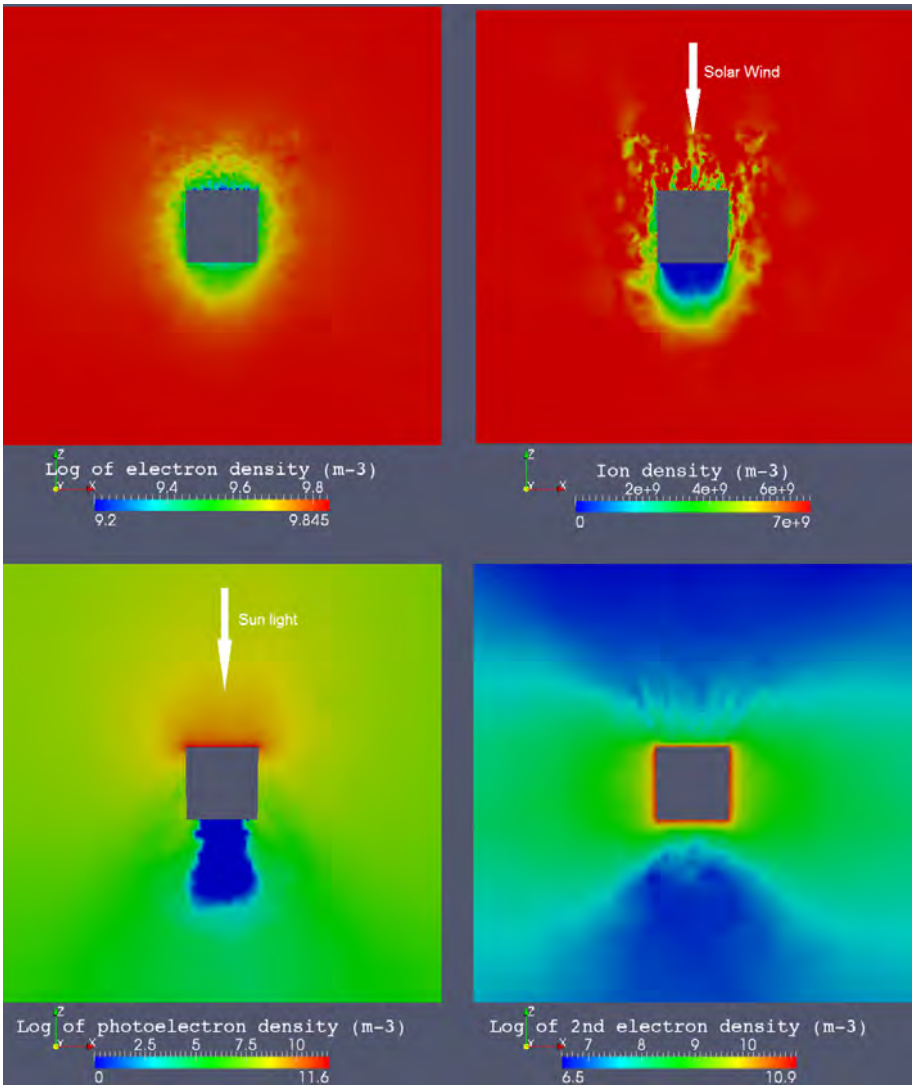

Fig. 13. Simulation S1 population density maps: **(a–d)** from the upper left figure to the lower right figure. **(a)** Thermal electrons, **(b)** Ions, **(c)** Photoelectrons, **(d)** Secondary electrons.

surrounding plasma is more negative, which increases the photoelectron recollection and decreases slightly the thermal electron collection (see Table 5). The reduced disturbance on thermal electrons can be seen on Fig. 15.

This type of near-Sun environment requires a PIC thermal electron model for reliable results with precisions under the Volt. The Boltzmann model can be used to get approximate levels of potentials in a shorter computation duration (a gain of time of $\sim 50\,\%$ with this simulation), in order to prepare full PIC simulations.

3.2.3 S3 simulation: effect of reduced photoemission

As discussed previously, Ergun et al. (2010) simulations are based on a photoelectron emission yield of $29\,\mathrm{mA\,m^{-2}}$. An equivalent material has been previously chosen as conductive layer covering the satellite structure and the solar flux intensity was adapted to reach this photoelectron yield. However, with the solar flux intensity at 0.044 AU and a ITO surface, SPIS computes a J_{ph} of $\sim 16\,\mathrm{mA\,m^{-2}}$, almost half of the rate supposed in the previous A and B cases. The S3 simulation checks the potential barriers settlement in case of this reduced photoemission.

The final ϕ_{SC} is set at $-16.3\,\mathrm{V}$, which is 2 Volts lower than for S1. However, the plasma potential around the probe is unchanged regarding to the S1 case (see Fig. 11), the ram and wake barriers for particles are thus slightly inferior than in S1 but the recollection rates are similar: 88 % for photoelectrons and 74 % for secondary electrons. The immediate effect of $J_{\mathrm{ph}} = 16\,\mathrm{mA\,m^{-2}}$ instead of $29\,\mathrm{mA\,m^{-2}}$ is that emitted and recollected currents due to photoelectrons are divided by almost 2: respectively -44 and $-50\,\mathrm{mA}$ (instead of

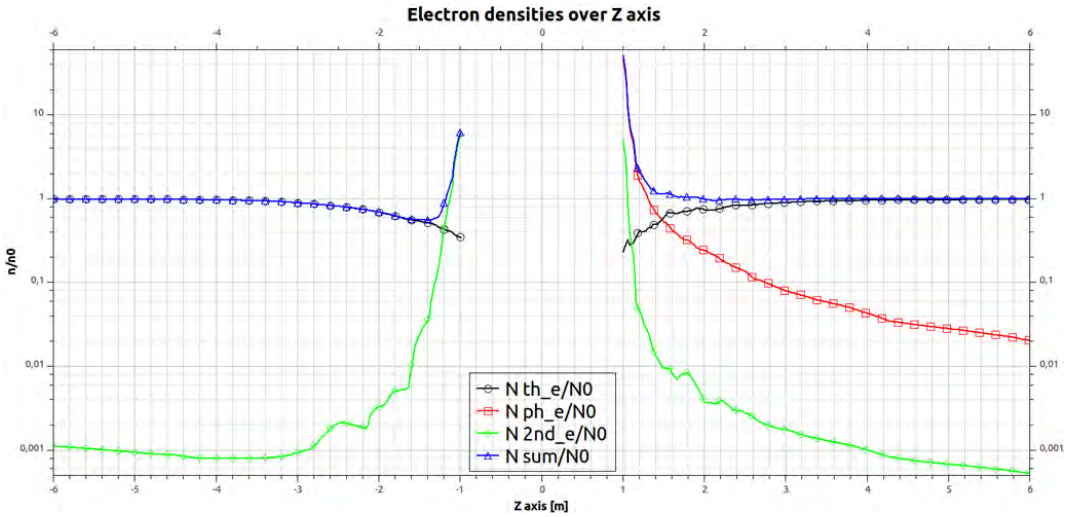

Fig. 14. Simulation S1: plot along the z-axis of electrons over n_0, the plasma density: $7 \times 10^9\,\mathrm{m}^{-3}$.

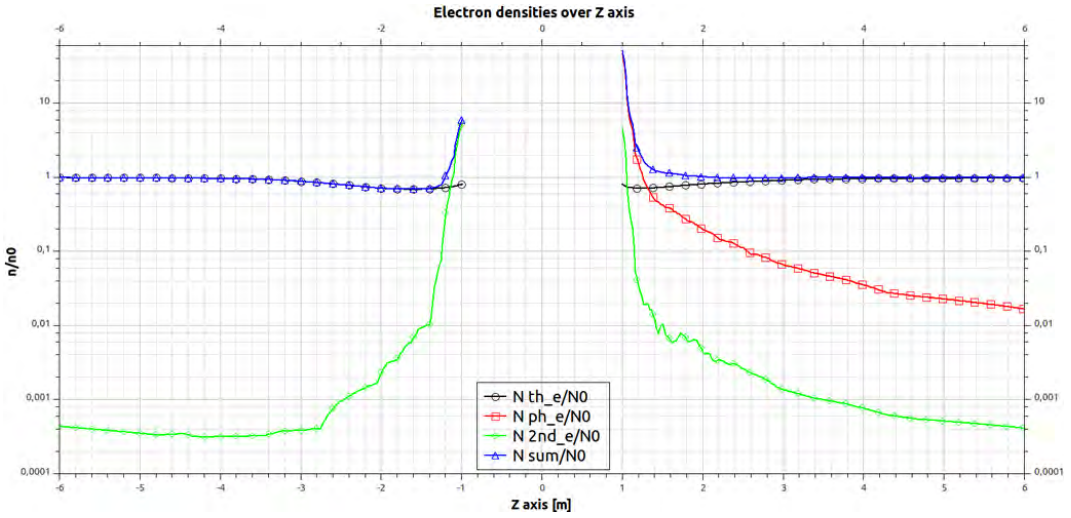

Fig. 15. Simulation S2: plot along the z-axis of electrons over n_0, the plasma density: $7 \times 10^9\,\mathrm{m}^{-3}$.

−84 and −91 mA for S1). Other currents are almost not affected (Table 5). This 2 Volts lower final ϕ_{SC} (12 % of difference regarding the S1 ϕ_{SC} of −14.5 V) is a consequence of a 50 % reduced photoemission. The conclusion, based also on the cross-comparison simulation results, is that the photoemission yield and the characteristic emission temperature of photoelectrons are highly important in this specific environment.

3.2.4 S4 simulation: no secondary electronic emission

As the emission of secondary electrons under thermal electron impact is highly dependent on the type of materials covering the satellite, a S4 simulation was generated with no secondary emission to observe the behaviour of the spacecraft and its close environment in this extreme situation. In previous simulations each thermal electron impact liberates in average ∼ 1.5 secondary electron.

This time ϕ_{SC} sets up at −43.5 V (because the spacecraft is not emitting electrons anymore), and the surrounding plasma is also highly affected by this changed parameter: ram and wake regions reach values of −52 and −43.5 V (Fig. 11), respectively. The thermal electron collection is thus decreased (−19 mA compared to ∼ −26 mA before), and the reduced ram barrier for photoelectrons (−8.5 V) allows them to escape more efficiently (recollection rate of 79 % instead of about 90 % in previous simulations). The population maps for S1 on Fig. 13 showed that those particles should be present in this region with densities between 10^9 and $10^6\,\mathrm{m}^{-3}$, digging the plasma potential and generating a wake barrier for secondaries. Here there is no SEE to produce a potential barrier anymore (see Fig. 11).

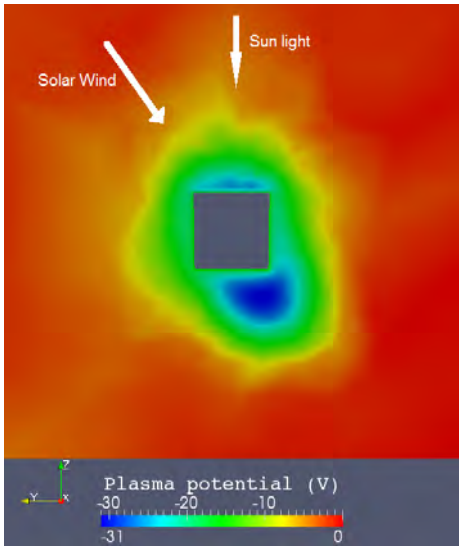

Fig. 16. Simulation S5: map of the final plasma potential in a $X = 0$ plane.

This extreme case showed that the secondary emission yield has a great influence on the spacecraft and surrounding plasma potential. As Solar Probe Plus will not be covered with only one single material with a specific emission yield, more precise information on the different layers properties are needed to investigate properly the effects of the near-Sun environment on the electric fields and secondary particles.

3.2.5 S5 simulation: spacecraft drift velocity

In this S5 case, a spacecraft speed component perpendicular to the solar wind speed is added (simulating an ion velocity of $-180\,\mathrm{km\,s^{-1}}$ in the y-direction.) to verify the effects of an aside shifted wake behind the spacecraft. This corresponds to one part of the predicted orbit of Solar Probe Plus at this distance to the Sun.

The spacecraft potential decreases until $-15.1\,\mathrm{V}$, instead of $-14.5\,\mathrm{V}$ for the S1 case. This result is practically the same for S1 (showing that the final spacecraft potential is not really affected by a perpendicular ion velocity of $180\,\mathrm{km\,s^{-1}}$). The global values of plasma potential and barriers are practically unchanged, it is just the position of the wake that is shifted aside, as represented on the plasma potential map Fig. 16. The values for S5 plasma potentials in Table 5 are truly measured along the wake axis and are practically equal to the values for S1. In the center of the ion wake the potential is $4\,\mathrm{V}$ lower than on the z-axis in this region. Neither the front area potential nor the final currents are affected by the spacecraft drift velocity. But the shifted wake is setting up an asymmetry of the plasma potential against the z-axis, as it appears clearly on Fig. 18, representing the plasma population map densities. The plasma populations densities are matching the plasma potential map and the shifted ion wake, except for thermal electrons. Looking at the secondary electrons, the shifted wake and the higher potential barrier set on the $-$Y side of the spacecraft enhance the acceleration process: the emitted particles that were not recollected could spread along the structure in the +Z region leading to densities of $\sim 10^9\,\mathrm{m^{-3}}$ near the side of the spacecraft. However, on the $-$Y side, those secondary electrons encounter a local potential of $-21\,\mathrm{V}$ that rejects them (density in this region reach $\sim 10^7$–$10^8\,\mathrm{m^{-3}}$). In Fig. 11, the z-axis is not crossing the center of the shifted wake so the real potential along the wake axis is deeper. Further analysis of the potential map shows that the potential barrier by the $-$Y side of the cylinder (the one non impacted by ion side) is deeper: $\delta\phi_{2\mathrm{nd}}(-\mathrm{Y}) = -5\,\mathrm{V}$ while $\delta\phi_{2\mathrm{nd}}(+\mathrm{Y}) = -3\,\mathrm{V}$ due to the arrival of positively charged ions. This is showed on Fig. 17, which displays the plasma potential over the y-axis (from +6 to $-6\,\mathrm{m}$ with respect to the potential map Fig. 16): the ions have a Y velocity component from the left side of the plot to the right. Thus, the recollection of secondary electrons on the $-$Y side of the satellite is slightly enhanced. Comparing to S1 this time the negative wake is reducing the possibility of secondaries to escape through the $-$Y side. A wider and bigger flux of those particles can be seen on the +Y side of SP+ on the Fig. 18. This effect appears less clearly for photoelectrons but it also exists.

The shifted wake did not change significantly the spacecraft potential. However, the global plasma behaviour lost its symmetry around the z-axis and the near plasma potential is different whether we look on the exposed to ions side of the spacecraft or not. A shifted wake may potentially complicate particle measurements, as electron instruments are indeed placed on the side of Solar Probe Plus.

4 Conclusion and perspectives

The near-Sun environment effect picture is confirmed in this paper. Indeed, main phenomenon previously predicted and simulated with simple models are here achieved through different PIC numerical codes: the spacecraft structure tends to settle at a negative potential (of typical -10 to $-20\,\mathrm{V}$), due to the surrounding presence of electrostatic barriers – originating from secondary electrons and photoelectrons – which bring back the secondary particles to the spacecraft. A more realistic modelling gives better accuracy on the spacecraft charging levels obtained. The parametric study using SPIS achieved the same phenomena and furthermore emphasises the importance of key parameters, that heavily affect, respectively, the final Solar Probe Plus potential and the surrounding plasma potential near the probe. The photoelectron emission temperature and yield are important for the final spacecraft potential. The three controlling parameters that require more investigations are (1) the photoelectron temperature, (2) the secondary electron emission yield (also depending on the coating materials) and (3) the orientation of

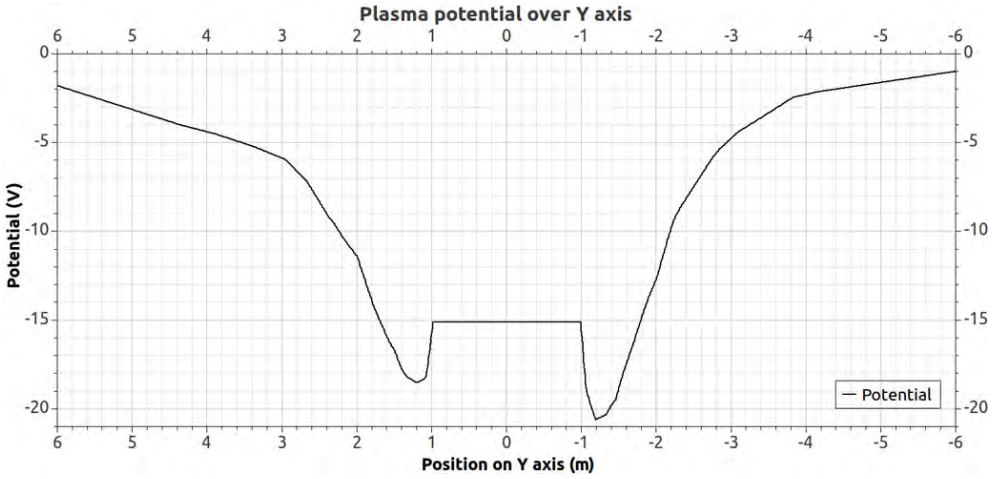

Fig. 17. Simulation S5: plot along the y-axis of the plasma potential. From +6 to −6 m with respect to the potential map Fig. 16: the ions have a Y velocity component from the left side of the plot to the right.

Table 5. Final currents and potentials for all S cases. Potential barriers are calculated for secondary particles emitted from the spacecraft (photoelectrons and secondary electrons).

Currents (mA)	Studied Value	S1 Nominal	S2 Boltzmann	S3 $J_{ph}/2$	S4 No SEE	S5 V_{sc}
Ions	Collected	2.1	2	1.3	1.7	1.7
Electrons	Collected	−26.7	−25.5	−26.2	−19.2	−26.5
Photoelectrons	Collected	−84.1	−85.2	−44.3	−72.4	−83.8
	Emitted	−91.1	−91.1	−50	−91.1	−91.1
	Net (% recollection)	7 (92 %)	5.9 (93 %)	5.7 (88 %)	18.7 (79 %)	7.3 (92 %)
2nd electrons	Collected	−52.3	−49.1	−49.4	0	−52.8
	Emitted	−68.6	−65.6	−67.2	0	−68
	Net (% recollection)	16.3 (76 %)	16.5 (75 %)	17.8 (74 %)	0	15.2 (78 %)
All populations	Collected	−161	−157.8	−118.6	−89.9	−161.4
	Emitted	−159.7	−156.7	−117.4	−91.1	−159.1
	Net	−1.3	−1.1	−1.2	1.2	−2.3
ϕ(V)	Spacecraft	−14.5	−18.4	−16.3	−43.5	−15.1
	Ram	−25	−29	−25	−52	−25.5
	Wake	−29.5	−34.5	−29.5	−43.5	−31
	Ram barrier	−10.5	−10.6	−8.7	−8.5	−10.4
	Wake barrier	−15	−16.1	−13.2	0	−15.9

the wake (potentially modifying the plasma measurements depending on the position of the instruments regarding to the ion flux). This is necessary to at least take into account full PIC modelling and good models of photoelectron and secondary SEEE. The photoelectron temperature study will need a more realistic model of photoemission to be implemented in the SPIS numerical core. The secondary particles recollection is problematic for the plasma instruments, especially the secondary electrons recollection which can occur all around the spacecraft, as it was demonstrated in all previous SPIS simulations. Those final negative spacecraft potentials will definitely affect low energy plasma measurements, and further investigations are needed to quantify precisely the fraction of the ambient Solar wind electrons that will be missed by the electron instruments and the impacts of this charging on the onboard plasma moment computation.

To reach very good previsions, SPIS new developments will focus on: ambient population distributions, material data, detector modelling and boundary conditions (presentation of new SPIS capabilities are displayed in Matéo-Vélez et al., 2012b). In this context, further studies with more complex models of Solar Orbiter are now under way. Indeed, it was showed in Isensee (1977) that regions as far as 0.2 AU from the Sun are not spared by the ram and wake potential

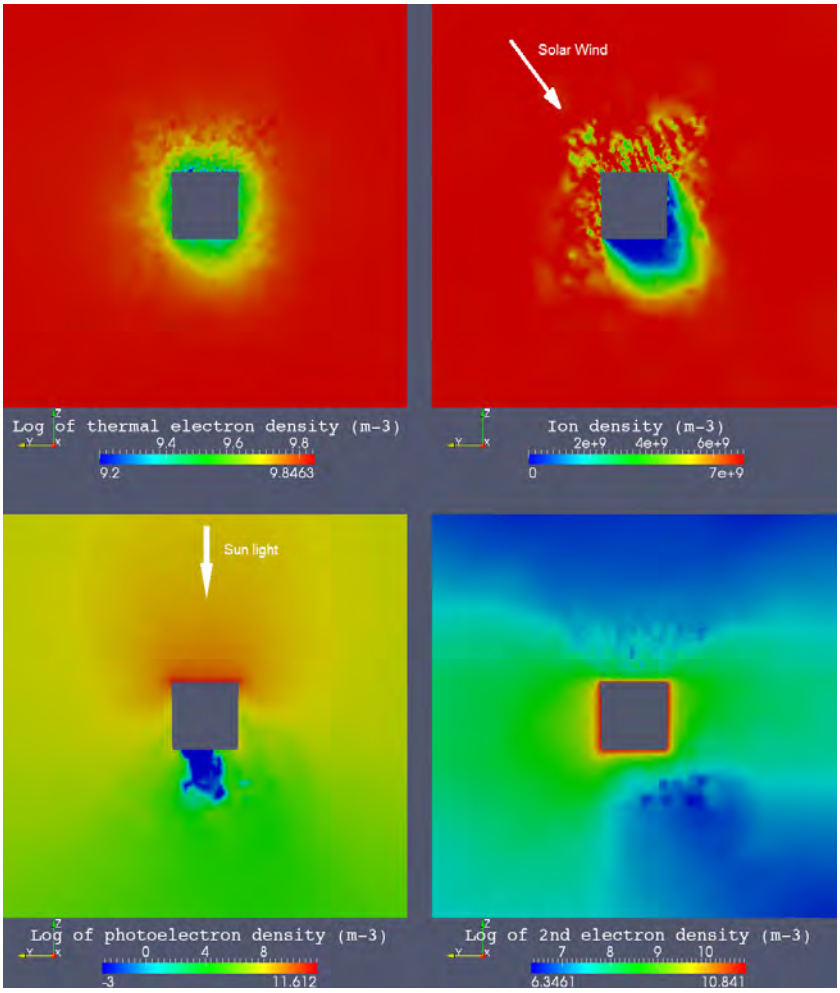

Fig. 18. Simulation S5 population density maps: **(a–d)** from the upper left figure to the lower right figure. **(a)** Thermal electrons, **(b)** Ions, **(c)** Photoelectrons, **(d)** Secondary electrons.

barriers, even if their depths are less important. Preliminary results (Guillemant et al., 2012) show that ram/wake potential barriers can also appear between 0.25 and 0.3 AU from the Sun, leading to investigate the Solar Orbiter perihelion (at 0.28 AU). An other important development would consist in modelling a hot electron population within the plasma (the so called Solar wind non thermal populations "Halo" and "Strahl"), and check the potentially increasing charging effects on the spacecraft. Indeed using data from Helios (M. Maksimovic, personal communication, 2011) and associated modelling (Stverak et al., 2009), it is possible to obtain the different electron population contributions in the distribution function by extrapolating results at Helios orbit to other distances from the Sun. We will use this analysis to set up SPIS with a more detailed distribution function for the ambient electron at the Solar Orbiter perihelion. The onboard instruments, especially the SWA-EAS (Solar Wind Analyser-Electron Analyser System), will be modelled and simulated. The associated measurements will be also simulated to determine the impacts of the possible potential barriers and charging effects on the particle moments calculation.

Acknowledgements. The authors wish to thank Alain Hilgers (ESA, ESTEC) for being one of the initiator of the SPIS concept and project at ESA, for giving useful advice at the beginning of this work, and finally for reviewing the manuscript. We also acknowledge the support of the ISSI (International Space Science Institute) team "Spacecraft interaction with space environment", led by Richard Marchand (University of Alberta, Canada) and its members for their interest and precious advices for our work. We also thank the French Centre National d'Etudes Spatiales (CNES) and the Région Midi-Pyrénées for providing the scholarship for this Ph.D.

Topical Editor R. Nakamura thanks C. Cully and M. Maksimovic for their help in evaluating this paper.

The publication of this article is financed by CNRS-INSU.

References

Ergun, R. E., Malaspina, D. M., Bale, S. D., McFadden, J. P., Larson, D. E., Mozer, F. S., Meyer-Vernet, N., Maksimovic, M., Kellogg, P. J., and Wygant, J. R.: Spacecraft charging and ion wake formation in the near-Sun environment, Phys. Plasmas, 17, 1134–1150, 2010.

Guillemant, S., Génot, V., Matéo-Vélez, J.-C., and Louarn, P.: Scientific spacecraft cleanliness: influence of heliocentric distance, in: Proceedings of 12th Spacecraft Charging Technology Conference, Kitakyushu, Japan, 14–18 May 2012.

Hilgers, A., Thiébault, B., Estublier, D., Gengembre, E., Gonzalez, J., Tajmar, M., Roussel, J.-F., and Forest, J.: A simple model of SMART-1 electrostatic potential variation, IEEE Trans. Plasma Sci., 34, 2159–2165, doi:10.1109/TPS.2006.883405, 2006.

Hilgers, A., Clucas, S., Thiébault, B., Roussel, J.-F., Matéo-Vélez, J.-C., Forest, J., and Rodgers, D.: Modelling of Plasma Probe Interactions With a PIC Code Using an Unstructured Mesh, IEEE Trans. Plasma Sci., 36, 2319–2323, doi:10.1109/TPS.2008.2003360, 2008.

Isensee, U.: Plasma disturbances caused by the Helios spacecraft in the Solar Wind, J. Geophys., 42, 581–589, 1977.

Lai, S. T.: Theory and Observation of Triple-Root Jump in Spacecraft Charging, J. Geophys. Res., 96, 19269, doi:10.1029/91JA01653, 1991.

Lipatov, A. S., Sittler, E. C., Hartle, R. E., and Cooper, J. F.: The Interaction of the Solar Wind with Solar Probe Plus – 3D Hybrid Simulation, Report 2: The study for the distance 9.5R_S, NASA/TM 2010-215863, 2010.

Matéo-Vélez, J.-C., Roussel, J.-F., Sarrail, D., Boulay, F., Inguimbert, V., and Payan, D.: Ground Plasma Tank Modeling and Comparison to Measurements, IEEE Trans. Plasma Sci., 36, 2369–2377, doi:10.1109/TPS.2008.2002822, 2008.

Matéo-Vélez, J.-C., Roussel, J.-F., Inguimbert, V., Cho, M., Saito, K., and Payan, D.: SPIS and MUSCAT software comparison on LEO-like environment, IEEE Trans. Plasma Sci., 40, 177–182, 2012a.

Matéo-Vélez, J.-C., Sarrailh, P., Thiebault, B., Forest, J., Hilgers, A., Roussel, J.-F., Dufour, G., Rivière, B., Génot, V., Guillemant, S., Eriksson, A., Cully, C., and Rodgers, D.: SPIS Science: modelling spacecraft cleanliness for low-energy plasma measurement, in: Proceedings of 12th Spacecraft Charging Technology Conference, Kitakyushu, Japan, 14–18 May 2012b.

Pedersen, A.: Solar wind and magnetosphere plasma diagnostics by spacecraft electrostatic potential measurements, Ann. Geophys., 13, 118–129, doi:10.1007/s00585-995-0118-8, 1995.

Roussel, J.-F., Rogier, F., Dufour, G., Mateo-Velez, J.-C., Forest, J., Hilgers, A., Rodgers, D., Girard, L., and Payan, D.: SPIS Open Source Code: Methods, Capabilities, Achievements and Prospects, IEEE Trans. Plasma Sci., 36, 2360–2368, doi:10.1109/TPS.2008.2002327, 2008a.

Roussel, J.-F., Tondu, T., Matéo-Vélez, J.-C., Chesta, E., D'Escrivan, S., and Perraud, L.: Modeling of FEEP Electric Propulsion Plume Effects on Microscope Spacecraft, IEEE Trans. Plasma Sci., 36, 2378–2386, doi:10.1109/TPS.2008.2002541, 2008b.

Roussel, J.-F., Dufour, G., Matéo-Vélez, J.-C., Thiébault, B., Andersson, B., Rodgers, D., Hilgers, A., and Payan, D.: SPIS multitime scale and multi physics capabilities: development and application to GEO charging and flashover modeling, IEEE Trans. Plasma Sci., 40, doi:10.1109/TPS.2011.2177672, in press, 2012.

Sarrailh, P., Matéo-Vélez, J.-C., Roussel, J.-F., Dirassen, B., Forest, J., Thiébault, B., Rodgers, D., and Hilgers, A.: Comparison of numerical and experimental investigations on the ESD onset in the Inverted Potential Gradient situation in GEO, IEEE Trans. Plasma Sci., 40, 368–379, 2010.

Štverák, Š., Maksimovic, M., Trávníček, P. M., Marsch, E., Fazakerley, A. N., and Scime, E. E.: Radial evolution of nonthermal electron populations in the low-latitude solar wind: Helios, Cluster, and Ulysses Observations, J. Geophys. Res., 114, A05104, doi:10.1029/2008JA013883, 2009.

Thiebault, B., Hilgers, A., Sasot, E., Laakso, H., Escoubet, C. P., Génot, V., and Forest, J.: Potential barrier in the electrostatic sheath around a magnetospheric spacecraft, J. Geophys. Res., 109, A12207, doi:10.1029/2004JA010398, 2004.

Whipple Jr., E. C.: Theory of spherically symmetric photoelectron sheath: a thick sheath approximation and comparison with the ATS 6 observation of a potential barrier, J. Geophys. Res., 81, 601–607, 1976.

Zhao, H., Schmidt, R., Escoubet, C. P., Torkar, K., and Riedler, W.: Self-consistentdetermination of the electrostatic potential barrier due to the photoelectron sheath near a spacecraft, J. Geophys. Res., 101, 15653–15659, 1996.

A.5 Article 2 - Guillemant et al. (2013): Simulation study of spacecraft electrostatic sheath changes with the heliocentric distances from 0.044 to 1 AU

Simulation Study of Spacecraft Electrostatic Sheath Changes With the Heliocentric Distances from 0.044 to 1 AU

Stanislas Guillemant, Vincent Génot, Jean-Charles Matéo Vélez, Pierre Sarrailh, Alain Hilgers, and Philippe Louarn

***Abstract*— In this paper, the electrostatic sheath of a simplified spacecraft is investigated for heliocentric distances varying from 0.044 to 1 AU, using the 3-D Particle in Cell software Satellite–Plasma Interaction System. The baseline context is the prediction of sheath effects on solar wind measurements for various missions, including the Solar Probe Plus mission (perihelion at 0.044 AU from the sun) and Solar Orbiter (SO) (perihelion at 0.28 AU). The electrostatic sheath and the spacecraft potential could interfere with the low-energy (a few tens of eV) plasma measurements, by biasing the particle distribution functions measured by the detectors. If the spacecraft charges to large negative potentials, the problem will be more severe as low-energy electrons will not be seen at all. The Solar Probe Plus and SO cases will be presented in details and extended to other distances through a parametric study, to investigate the influence of the heliocentric distance to spacecraft. Our main result is that, for our spacecraft model, the floating potential is a few volts positive from 1 AU to about 0.3 AU, while below 0.3 AU, the space charge of the photoelectrons and secondary electrons create a potential barrier that drives the spacecraft potential negative.**

***Index Terms*— Potential barriers, photoelectron sheath, simulation software, spacecraft charging.**

I. Introduction

SEVERAL upcoming scientific space missions consist of probes immersed in the solar wind, at relatively close distances to the sun. One example is the Solar Probe Plus (SP+) NASA mission that aims to study the close environment of the sun (approaching as close as 9.5 solar radii above the sun's surface). The launch is planned for 2018 and the first perihelion for 2021. At such distances, the expected environment of the probe should be quite hot and dense, leading the spacecraft and its onboard instruments to be affected by surface charging. In particular, estimations of the satellite potential behavior in such plasmas are important to predict the possible biases on plasma and electric measurements. Furthermore, two phenomena will increase the disturbances on the near probe environment: behind the probe, the satellite velocity combined with the speed of the solar wind will create an ion wake, and high densities of photoelectrons and secondary electrons will generate a potential barrier for those particles and force their recollection by the front surfaces. Another mission is the European Space Agency (ESA) spacecraft: Solar Orbiter (SO). Less extreme conditions are expected in this case since the spacecraft will remain farther from the sun, with a closest perihelion at 0.28 astronomical unit (AU). However the impact of such conditions also need to be studied to avoid biases on plasma measurements as the SO mission at perihelion will be immersed in a region where the average solar photon flux is 13–16 times more intense than at 1 AU. The Bepi-Colombo mission will also cruise in this region.

Potential barriers in electrostatic sheath have already been discussed in many analytical or numerical studies in the past 40 years, in particular to explain observations on different satellites. One of the first is Guernsey and Fu (1970) [1], which introduces a calculation of the potential distribution in the neighborhood of a photo-emitting plate immersed in a plasma. Considering thermal electrons, photoelectrons, and flowing ions, it is shown that two steady state potential distributions can exist: the first with a monotonically decreasing potential from its plate value to zero, and the second with a decreasing potential from its plate value until a (negative) minimum and then an increase to zero. This minimum negative potential, due to a high local density of photoelectrons, can prevent those particles from escaping the surrounding region of the emitting plate and force their recollection.

Potential barriers were primarily inferred around earth-orbiting satellites (they were not directly measured). Following observations of recollected photoelectrons and secondary electrons on the Applications Technology Satellite (ATS)-6 spacecraft, Whipple (1976) [2] developed a theory for a spherically symmetric photoelectron sheath, including effects of ions, thermal electrons and secondaries. The aim was to determine whether the potential barrier responsible for the secondaries reflection was originating from those same particles or not. A comparison with the spacecraft data showed that the observed barrier of potentials was too large to be explained by the model

Manuscript received October 5, 2012; revised December 5, 2012; accepted January 15, 2013. This work was supported in part by the European Space Agency Contract 4000102091/10/NL/AF, a Centre National des Etude Spatiales Grant, and a Région Midi-Pyrénées Grant. This work was performed in the context of a Ph.D. cursus in cosupervision between the Research Institute in Astrophysics and Planetology and the National Office of Aerospatial Studies and Research.

S. Guillemant, V. Génot, and P. Louarn are with IRAP, Toulouse 31028, France (e-mail: stanislas.guillemant@irap.omp.eu; vincent.genot@irap.omp.eu; philippe.louarn@irap.omp.eu).

J.-C. Matéo-Vélez and P. Sarrailh are with ONERA/DESP, Toulouse 31055, France (e-mail: jean-charles.mateo_velez@onera.fr; pierre.sarrailh@onera.fr).

A. Hilgers is with the European Space Research and Technology Centre, European Space Agency, AG Noordwijk 2200, The Netherlands (e-mail: alain.hilgers@esa.int).

Color versions of one or more of the figures in this paper are available online at http://ieeexplore.ieee.org.

Digital Object Identifier 10.1109/TPS.2013.2246193

(i.e., a spherically symmetric photoelectron or secondary electron sheath surrounding a uniformly charged spacecraft), and the authors concluded that the most probable explanation was that some portions of the ATS-6 surfaces were charged to different potentials.

In the context of instruments for active control of spacecraft potential, Zhao *et al.* (1996) [3] proposed an analytical approach to compute the electrostatic barrier and compared to Geotail measurements. However this analysis is only relevant in the thick sheath approximation and does not consider the secondary electronic emission.

Thiébault *et al.* (2004) [4] studied the potential barrier in the electrostatic sheath around a conductive magnetospheric spacecraft, for cases of conductive spacecraft such as Geotail and Cluster. A fully self-consistent analytical model of the plasma around an electron-emitting central body was used to analyze the electrostatic sheath around an idealized spacecraft. It was shown by comparison with 3-D Particle in Cell (PIC) simulations that nonmonotonic potential with negative potential barrier can exist all around a positively charged spacecraft (with Debye length of the order of the central body radius or more). This barrier may still surround the entire spacecraft even in the case of asymmetric illumination pattern with induced photoemission on only one side of the central body.

Referring to a near sun environment mission—the Helios spacecraft — Isensee (1977) [5] presented 2-D simulations of the plasma environment of the probe in the solar wind, at 0.2 AU from the sun. With a simplified conducting spacecraft, the consideration of 1 eV mean energy photoelectrons and the expected solar wind conditions, the author obtained a slightly positively charged satellite (+2.9 V), surrounded by negative plasma potentials in the wake and in the ram. In front of the sunlit face, due to high densities of photoelectrons, the local potential reached −1.4 V, and in the ion wake behind the probe, it reached −4.5 V. The 1eV emitted photoelectrons are thus recollected by the surfaces of the probe.

Ergun *et al.* (2010) [6], through a 3-D self-consistent code, solved the static potential structure surrounding a spacecraft in a high-photoelectron environment (the SP+ context at 0.044 AU to the sun), and showed that a negatively charged satellite is obtained through high densities of secondary electron and photoelectron both emitted as Maxwellian functions with low temperatures (2 and 3 eV, respectively). The photoelectron densities in that study reached 10^6 cm^{-3} (compared to ambient ions and electrons densities of about 7×10^3 cm^{-3}) and decreased the potential surrounding the spacecraft enough to create a barrier for low-energy electrons. Once this barrier is set up, it will bring the next emitted secondary and photoelectrons back to the spacecraft materials, leading them to decrease the spacecraft potential (Φ_{SC}), even after the structure is charged negatively. The secondary particles recollection is problematic for the plasma instruments, especially the secondary electron recollection that can occur all around the spacecraft.

Those phenomena have been studied in detail in Guillemant *et al.* (2012) [7] using the Spacecraft–Plasma Interaction System (SPIS) software, through simulations with more realistic physical and numerical processing, in particular using full PIC instead of hybrid populations modeling. To widen the perspectives, a parametric study considered more realistic parameters for this near sun environment. The potential barriers were always present, with an intensity depending on the varying input conditions.

Those publications encourage advanced studies on the formation and profile of the potential barriers depending on the heliocentric distance, and the effects on the satellite floating potential. In this paper, the limits of this so-called "near sun environment" will be studied: the evolution of the potential barriers farther from the sun, the critical distance for their existence, and the situation at the orbit of SO (at 0.25 AU). This is achieved through a parametric study where only the distance to the sun varies (and consequently the local plasma parameters and sun flux for ten distances between 0.044 AU to 1 AU), but keeping the same geometry model.

Section II presents the physics involved in the simulated environments, the SPIS tool for the parametric study and the simulations set up. Section III presents the simulation results for: 1) the SP+ case at 0.044 AU (closest approach distance), 2) the SO case at 0.25 AU (closest approach distance), and 3) an overview of all the results for the ten different positions.

II. Modeling

A. Environments, Spacecraft Dimensions, and Covering Material

The heliocentric distances selected for this parametric study are presented in Table I. It gathers the essential physical environment parameters that have to be considered for such simulations. Plasma characteristics are derived from Helios data (V. Krasnoselskikh and M. Maksimovic, private communications). The solar wind velocity is discretized for the different positions between earth and 0.044 AU from the model of Parker (1958) [8]. The spacecraft geometry used for all simulations is a cylinder (1-m radius and 2-m length), covered with indium tin oxide (ITO) conducting material.

In this paper, below 1 AU, the emitted photoelectron current is always the largest compared with others (see the estimated photo-emitted current density J_{ph} given on Table I). At first order, neglecting the ions and secondary electrons, the currents on spacecraft will be balanced when the net photoelectron current I_{ph} equalizes the collected thermal electron current I_{the}. Consequently, at the equilibrium state, a large proportion of photoelectrons is recollected. Assuming a Maxwell–Boltzmann regime

$$I_{the} = I_{ph}\,(\text{emitted})\ \exp\left(\frac{-e\Phi_{SC}}{k_B T_{ph}}\right). \tag{1}$$

with k_B the Boltzmann constant, T_{ph} the photoelectron temperature and e the photoelectron charge, therefore the spacecraft potential is *a priori* expected to be of a few times $(k_B T_{ph}/e)$ in order to recollect the fraction of photoelectrons necessary to equalize the other current.

However, Ergun *et al.* (2010) [6] and Guillemant *et al.* (2012) [7] showed in a similar geometry (a cylinder) that negative charging is possible at 0.044 AU from the sun due

TABLE I

DATA OF SPIS SIMULATIONS FOR THE PARAMETRIC STUDY. SHADED LINES ARE THE INPUT PARAMETERS ENTERED IN THE SOFTWARE (PERI = PERIHELION, APH = APHELION, SCI OPS = SCIENCE OPERATIONS ORBIT)

PLASMA	Earth	Venus	Mercury Aph	Mercury Peri	SO peri	SP+ 1st Peri	0,11 UA	SP+ Sci ops	0,067 UA	SP+ Last Peri
Distance (AU)	1	0,72	0,46	0,3	0,25	0,162	0,11	0,093	0,067	0,044
Distance (Rs)	215	154,8	98,9	64,5	53,75	34,83	23,65	19,995	14,405	9,46
Sun Flux (#1AU)	1,00	1,93	4,73	11,11	16,00	38,10	82,64	115,62	222,77	516,53
Ne = Ni (m-3)	6,93E+06	1,35E+07	3,67E+07	8,85E+07	1,19E+08	3,10E+08	8,03E+08	1,14E+09	1,94E+09	7,00E+09
Te (eV)	8,14	10,41	14,52	19,80	22,95	31,77	41,50	48,33	59,25	84,47
Ti (eV)	8,00	11,21	17,00	25,00	30,76	39,90	49,00	55,82	67,00	87,25
V ram protons (km/s)	430,00	429,50	400,00	395,00	401,40	366,00	355,00	350,00	335,00	300,00
J_ph emitted on ITO (A/m2)	3,21E-05	6,19E-05	1,52E-04	3,57E-04	5,14E-04	1,22E-03	2,65E-03	3,71E-03	7,15E-03	1,66E-02
J_the collected (A/m2)	5,30E-07	1,17E-06	3,75E-06	1,06E-05	1,52E-05	4,68E-05	1,39E-04	2,13E-04	4,00E-04	1,72E-03
J_ion collected (A/m2)	4,77E-07	9,30E-07	2,35E-06	5,60E-06	7,63E-06	1,82E-05	4,57E-05	6,41E-05	1,04E-04	3,36E-04
Mach number	15,53	13,11	9,91	8,07	7,39	5,92	5,18	4,79	4,18	3,28
Debye length (m)	8,06	6,52	4,67	3,51	3,27	2,38	1,69	1,53	1,30	0,82
Debye length photoelec (m)	0,98	0,71	0,45	0,29	0,25	0,16	0,11	0,09	0,07	0,04
SEEY (at Te)	0,28	0,35	0,45	0,65	0,7	0,95	1,2	1,32	1,55	1,92
Thermal elec. Gyroradius (m)	1,66E+03	1,12E+03	4,76E+02	2,73E+02	2,41E+02	1,21E+02	5,50E+01	4,93E+01	1,88E+01	1,47E+01
Proton Gyroradius (m)	7,05E+04	4,98E+04	2,21E+04	1,31E+04	1,20E+04	5,82E+03	2,56E+03	2,27E+03	8,58E+02	6,42E+02
Magnetic field (T)	5,80E-09	9,72E-09	2,70E-08	5,50E-08	6,70E-08	1,57E-07	3,95E-07	4,76E-07	1,38E-06	2,10E-06

to potential barriers induced by large densities of photoelectrons (see Section I). Indeed in the ram region, below 1 AU, the UV flux generates densities of photoelectrons that locally surpass thermal electrons. The plasma potential in the region close to the sunlit surface is ruled by photoelectrons and their Debye length λ_{ph} (smaller than that of thermal electrons λ_{the}). Different possibilities arise, depending on the distance between the satellite and the sun. First, in a very close case like 0.044 AU, λ_{ph} is much smaller than the spacecraft size which makes the local potential barrier very close to the surface and the space charge may be considered as 1-D. In this case the "thin sheath" approximation is valid, and the Child-Langmuir's law for space-charge limited flow is applicable. The photoelectron recollection is in this case very efficient through the space charge and the spacecraft is not necessarily positively charged. Second, in a farther case, when λ_{ph} is comparable to the size of the spacecraft: the sheath becomes 3-D, the barrier is farther from the emitting surface, decreasing the recollection rate of photoelectrons. This is the "thick sheath" approximation for which the spacecraft floating potential increases consequently. There is no significant effect of the space-charge and it is the positive spacecraft floating potential that makes the photoelectrons to be recollected. In this paper, we examine where the transition between these two regimes occurs for the given spacecraft geometry and material.

The ion wake geometry is also important for the overall potential distribution. Depending on the Mach number, the ion temperature, and the spacecraft geometry and potential, the ion wake will follow different morphologies. Typical wake geometries are sketched in Engwall *et al.* (2006) [18], concerning a spherically shaped and positively charged spacecraft. If the ion flow energy is much higher than the probe potential, the wake will be cylindrically shaped (narrow wake case); if it is not, ions will scatter off the positive electrostatic potential from the spacecraft (creating an enhanced wake). In the simulations presented hereafter, we extend Engwall *et al.* (2006) [18] with a negatively charged satellite regime. The environment closest to the sun will generate another ion wake morphology: a "bubble wake" (in hot and dense plasma regions, when the ion depletion is quite efficiently repopulated by ions). The "cylinder wake" will be encountered farther from the sun (in colder plasmas, with an enhanced or narrowed extremity depending on the sign of Φ_{SC}). The wake geometry will constrain the minimum potential at its center, leading to different depths of potential barriers and recollection rates for secondary electrons. This wake represents a potential barrier for secondary electrons that are emitted from all exposed faces of the satellite even from the rear side, different from photoelectrons.

B. SPIS Tool for Simulations

The simulation tool used in this paper is SPIS, a software development project of the ESA. It is developed as an open-source and versatile code with the support of the Spacecraft–Plasma Interaction Network in Europe (SPINE) community. The first development phase of the project was performed by ONERA/DESP, Artenum, and University Paris VII (through the ESA Contract Nbr: 16806/02/NL/JA). Some developments were funded by the French space agency (CNES). It is a simulation software based on an electrostatic 3-D unstructured PIC plasma model and consisting of a JAVA-based highly modular objectoriented library, called SPIS/NUM. More accurate, adaptable, and extensible than the existing simulation codes, SPIS is designed to be used for a broad range of industrial and scientific applications. The simulation kernel is integrated into a complete modular preprocessing/computation/postprocessing framework, called SPIS/UI, allowing a high degree of integration of external tools, such as CAD, meshers and visualization libraries (VTK), and a very easy and flexible access to each level of the numerical modules via the Jython script language. Developed using an open-source approach and oriented toward community-based development, SPIS is available for the whole community and is used by members of the European SPINE network. SPIS should address a large majority of the new challenges in spacecraft–plasma interactions, including

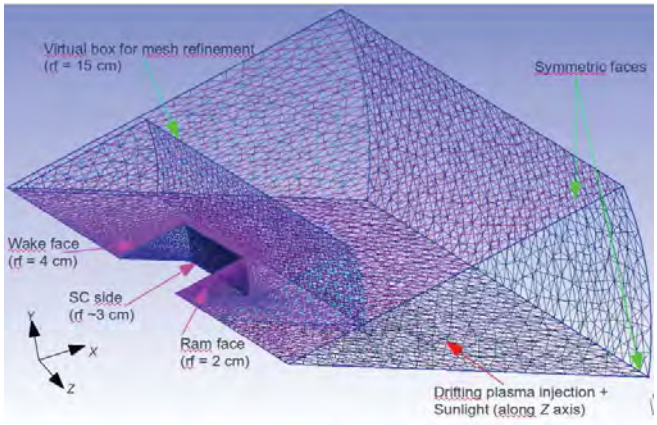

Fig. 1. Geometry cut model of the cylinder (covered with ITO material) and the simulation box + the associated mesh ("rf" = mesh refinement).

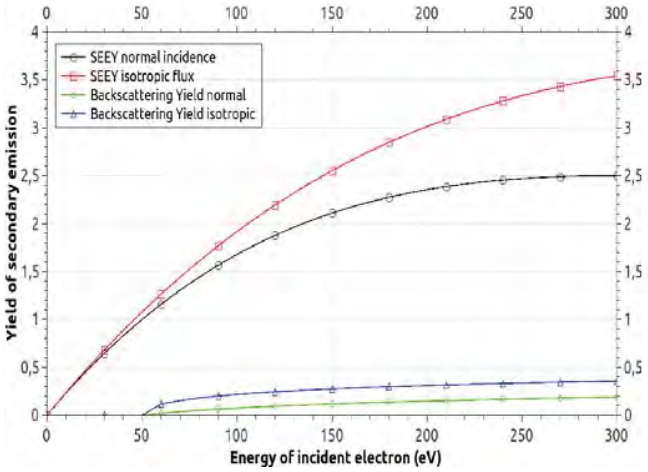

Fig. 2. SEEY and the backscattering yield for ITO material versus incident electron energy (with a normal or isotropic incoming flux).

the environment of electric thruster systems, solar array-plasma interactions, and modeling of scientific plasma instruments.

The numerical core and the user interface have been developed by ONERA and the Artenum company, respectively (Roussel *et al.*, 2008) [9]. Various applications to spacecraft and ground experiments were performed by them and the ESA (Roussel *et al.*, 2010 [10]; Hilgers *et al.*, 2006 [11]; Hilgers *et al.*, 2008 [12]; Roussel *et al.*, 2008 [13]; Sarrailh *et al.*, 2010 [14]; Matéo-Vélez *et al.*, 2008 [15]; and Matéo-Vélez *et al.*, 2012 [16]).

The SPIS-Science extension, performed under ESA Contract (N# 4000102091/10/NL/AF) by ONERA and Artenum, aims at extending the capabilities of SPIS modeling framework for accurate evaluation of low-level surface electrostatic charging of science missions with low-energy plasma instruments. It also improves the code efficiency through multithreading of PIC particle pusher (Matéo-Vélez *et al.*, 2012) [17]. This evolution has been used in this paper.

C. Simulations Set Up

The spacecraft geometry model used for all simulations is a cylinder (1-m radius and 2-m length) in a cylindrical simulation box. The whole system thus presents a symmetry of revolution around the Z axis. SPIS handles the symmetries of fluxes and electric field. For a gain of CPU time, a cut geometry model is used with a 30° angle around the Z axis. The domain is a 5 m (in X) x 10 m (in Z) box, containing the satellite portion, with an unstructured meshing refined at 2 cm on the sunlit face of the satellite (4 cm on the rear side) and 50 cm on the edges of the simulation box (Fig. 1). The external boundary conditions are set to a "Fourier" type (a $1/r^2$ decrease of potential, r being the distance to the spacecraft surface) where particles are injected and to a "mirror" type for the two symmetric faces (see Fig. 1) which means that particles cannot cross those faces and are reflected into the simulation box.

The varying parameters between the simulations are: plasma properties (densities, temperatures, and solar wind velocity), the sun flux (that varies as $1/R^2$, R being the distance to the sun) and the time steps used in SPIS to compute every plasma population transport. To solve the equivalent electrical circuit representing the satellite the spacecraft capacitance is estimated at $C = 1.9\ 10^{-10}$ Farad for a surface entirely covered with the conducting ITO material. The value of this parameter is however not important in this paper since we are interested here in the steady state, rather than the transient phase.

All species (protons, thermal electrons, secondary electrons and photoelectrons) are computed using a PIC model. In Table I, the values in gray are directly entered in SPIS as input parameters. The secondary electron emission (SEE) is set with a characteristic energy of 2 eV (Maxwellian velocity distribution function). The secondary emission yield (SEEY) curves (for true and backscattered electrons) are presented on Fig. 2. The backscattered electrons are emitted with 2/3 of their initial energy, however at those incoming energies the rates of backscattering are quite low (0 for $T_{the} < 50$ eV and 20% for $T_{the} = 80$ eV). Photoelectrons are emitted with a Maxwellian energy profile with temperature of 3 eV. Actually, measured interplanetary photoelectron spectra have sometimes higher energy components. A comparison test was provided by Guillemant *et al.* (2012) [7] and showed that photoelectrons with a Maxwellian energy profile with temperature of 10 eV (instead of 3 eV) lead (in a near sun environment) to a more positive spacecraft potential (+6 V of difference) as photoelectrons have more energy to spread further and escape the ram potential barrier. That is why in further work some more realistic distribution functions of photoelectrons should be considered. The satellite is considered static with respect to the solar wind so only the proton population speed (that depends on the distance to the sun) is simulated. This velocity is considered to be only along the -Z axis as we neglect the spacecraft orbital motion. This approximation has only a minor impact on the results as the ion Mach number would be of $\sim$4 instead of $\sim$ 3.3 and I_i would slightly increase but stay the lowest current. The magnetic field is not taken into account, as proton and electron gyroradii are much greater than the simulation box, even at 0.044 AU (see Table I).

TABLE II
COMPARISON OF INPUTS AND OUTPUTS FOR TWO SIMILAR SIMULATIONS (AT 0.044 AU, FROM GUILLEMANT *et al.*, (2012) [7] AND THIS PAPER)

Simulation Name	S3	Case at 0.044 AU
Source	Guillemant *et al.* 2012	This paper
INPUTS		
Distance from the sun (AU)	0,04	0,044
Sun flux (#1AU)	500,00	516,53
Photoelectron yield J_ph (mA/m2)	16,00	16,60
Ne = Ni (m−3)	7,00E+09	7,00E+09
Te (eV)	85,00	84,47
Te (eV)	82,00	87,25
V ram protons (km/s)	300,00	300,00
Debye length (m)	0,82	0,82
Debye length photoelec (m)	0,04	0,04
SEEY	1,92	1,92
Geometry SC	ITO cylindrical 1 m radius × 2 m long	ITO cut cylinder 1 m radius × 2 m long
Geometry Simulation box	cylindrical 6 m radius × 12 m long	cut cylinder 5 m radius × 10 m long
Meshing (sunlit face → boundary)	5 cm → 2 m	2 cm → 50 cm
OUTPUTS		
Recollection – photoelectrons (%)	88,00	86,99
Recollection – 2nd electrons (%)	74,00	75,24
Spacecraft potential (V)	−16,30	−16,20
Ram min value (V)	−25,00	−25,42
Wake min value (V)	−29,50	−31,30
Ram barrier (V)	−8,70	−9,19

III. SIMULATION RESULTS

A. SP+ at 0.044 AU

In this section are presented and discussed the results of the 0.044 AU case. All population and potential maps are presented in a $X-Z$ plane. The solar wind direction is toward the bottom of each map (in the -Z direction).

This simulation is very similar to the case called "S3" in Guillemant *et al.* (2012) [7], studying the spacecraft-plasma interactions for a cylindrical conducting satellite at the perihelion of SP+ (the other "S1,2,4,5" cases use a higher photoelectron emission yield). Both cases have been run using the SPIS software, with practically the same input parameters and identical covering material on the spacecraft (see Table II). The main difference is the geometry model: in S3 it is an entire cylindrical satellite placed in a cylindrical simulation box, while in this paper the whole geometry model has been cut with a 30° angle around the Z axis (see Section II.C). This cut allowed a considerable meshing refinement for the latest simulation of about a factor 4 on all the grids compared to S3 and the value of 30° was in this case a good compromise to keep enough meshing elements in the corners of the simulation box (avoiding risks of statistical issues in PIC modeling in those regions). Table II presents the inputs/outputs for the two simulations. Minor differences (particle temperatures, sun flux) reflect that the parametric study requires more precision on input data interpolation at several distances from the sun. Results are however very much comparable. However the meshing refinement plays an essential role for the numerical precision in the areas where the space charge is large (the ram and the wake).

For this latter case, the satellite potential converges to −16.2 V. Fig. 3 is a plot of the plasma potential map and the population densities (thermal electrons, ions, photoelectrons and secondary electrons) around the spacecraft. Looking at the potentials, the lowest in the ram is at −25.4 V. With respect to the satellite, it corresponds to a potential barrier for photoelectrons and secondary electrons of −9.2 V. In the ion wake a minimum of −31 V is reached, which corresponds to a potential barrier for all secondaries of about −15 V. On the side of the cylinder a −3 V barrier also forces the recollection of a fraction of secondaries. Those barriers are generated through the high densities of photoelectrons and secondary electrons in the front, and the high densities of secondary electrons added to the lack of ions at the rear. Looking at the positions of those plasma potential minimum values, in the ram it is located at 0.23 m from the sunlit face, which corresponds to five times the Debye length of photoelectrons ($\lambda_{ph} = 0.04$ m). In the wake the minimum is at 0.84 m which corresponds to the thermal electron and secondary electrons Debye length (0.8 m), which are predominant at this location. The level of the potential barrier in the ram is consistent with the photoelectron temperature.

An important parameter is the ratio between the dimension $L$of the wake and $\lambda_{D,the}$: if $L \sim \lambda_{D,the}$ the potential may be scaled at a fraction of $\sim k_B T_e/e$ in the wake. Indeed in the wake the minimum potential which can be obtained (using both Poisson's equation and Gauss's flux theorem), depending on the wake geometry (perfectly spherical or perfectly cylindrical), is, respectively, Φ= *(0.5* or *0.25)* $(L/\lambda_D)^2(-k_B.T_e/e)$. With L the radius of the wake ($\sim$ 0.8 m) and $\lambda_D$the Debye length ($\sim$ 0.8 m),

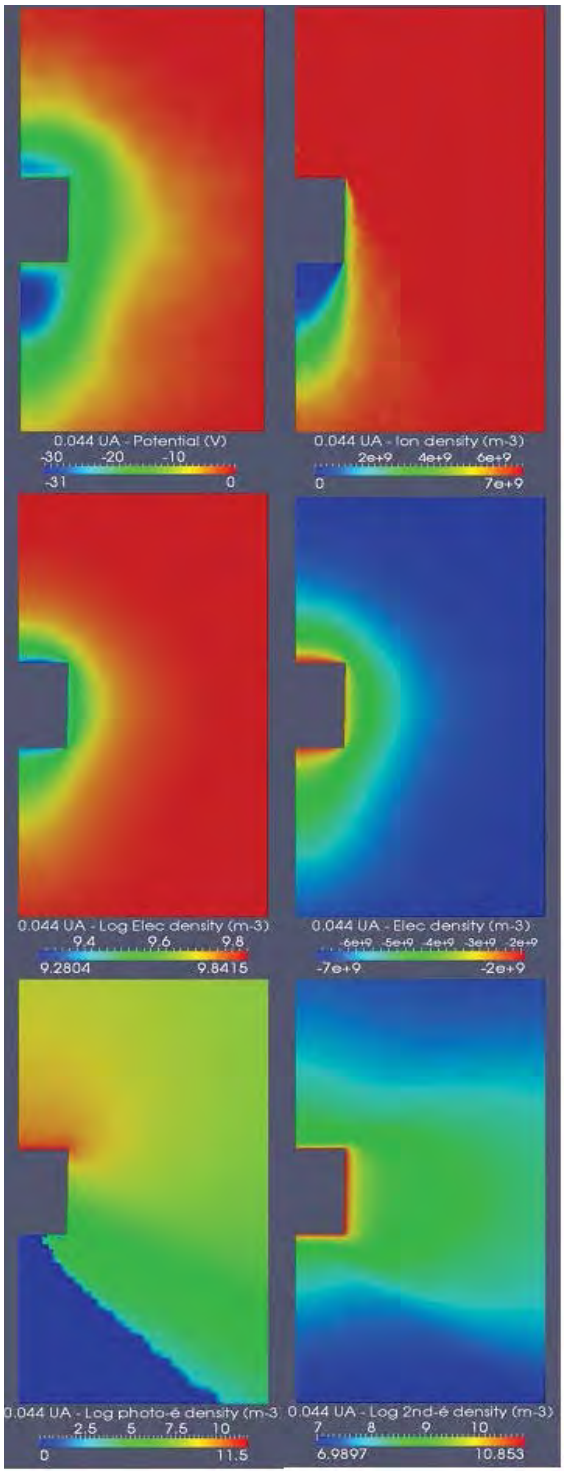

Fig. 3. Simulation results for the 0.044 AU case in a X-Z plane (sun in the +Z direction).

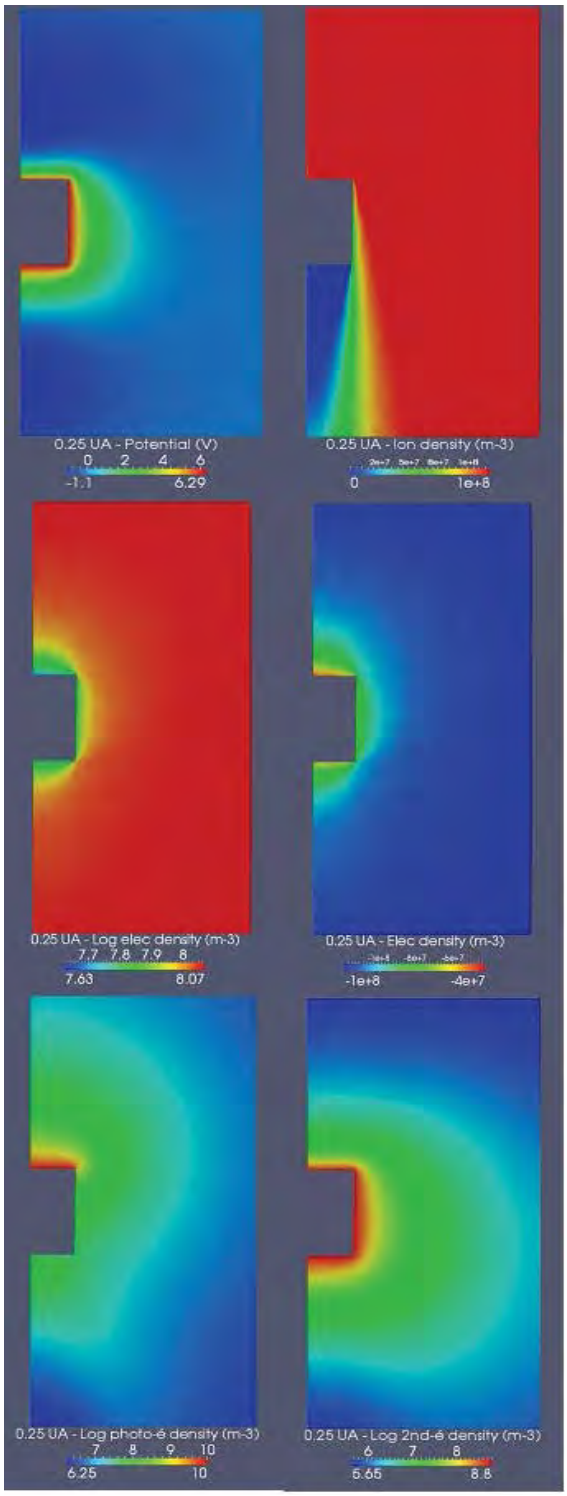

Fig. 4. Simulation results for the 0.25 AU case in a X-Z plane (sun in the +Z direction).

we have in this case Φ between ~ -40 V and -20 V. This simulation gives a wake minimum at -31 V, which seems like an intermediate case between the "bubble wake" and the "cylinder wake".

The potential surrounding the satellite is between -25 and -31 V. Those barriers represent about 1/3 of the thermal electron temperature of $\sim$ 85 eV so it affects their densities close to the spacecraft structure, as only 30% of the initial thermal electron density ($n = 7.\times 10^9$ m^{-3}) populates the region close to SP+ (see the thermal electron map). The ion wake is clearly visible and varies between no particles near the rear face of the cylinder (in the wake) to n around. The ion vacuum is reduced by the thermal diffusion of these particles and by ion focusing through the negative Φ_{SC}. Local disturbances of the

ion density at the front are due to statistic noise in the full PIC approach (the figure is not averaged enough such as to reduce noise). However, that does not impact the results since the problem is ruled by photoelectron density in the sheath. The denser plasma populations are still photoelectrons, emitted from the sunlit face at densities of about 10^{11} m^{-3}, and they are spreading around until the wake region. The photoelectron reduction is also visible on the rear side of the cylinder, highly negative potential present there prevents photoelectrons from penetrating this area. Secondary electrons are dense over all surfaces of the spacecraft. The potential barriers have a great influence by preventing secondary electrons from escaping the front and the back faces of the spacecraft.

Table III shows all net currents on SP+ for all simulations. Concerning this first case, the total thermal electron current arriving on the spacecraft I_{the} reaches 24.6 mA and for ions 1.5 mA. Assuming thermal electrons treated as a fluid, like in the Maxwell–Boltzmann statistics equilibrium model approximation, theoretical net I_{the} should reach $J_{the,0} \times S_{SC} \times exp(e\Phi_{SC}/k_B.T_e)$=26.8 mA (according to $J_{the,0}$ in Table I and the spacecraft total surface of $S_{SC} \sim 18.9$ m^2). Of the 51.9 mA of photoelectron current emitted, -45.2 mA is collected, for a net current of 6.7 mA (87% of recollection). For secondary electrons, 61.4 mA are emitted and -46.2 mA collected, leading to a net current of secondaries of 15.2 mA (75% of recollection, all over the spacecraft surfaces). Plots of all currents are presented in Fig. 7.

Those high rates of secondary and photoelectron recollection will definitely affect the low-energy plasma measurements, especially the secondary particles whose recollection can occur all around the spacecraft. Those potential barriers also disturb the near environment of the spacecraft by filtering the thermal electrons and biasing the measurements. In this case, incoming thermal electrons with energies lower than $\sim$ 31 eV will barely reach the satellite (for example those coming in the wake direction). Between the minimum potential position in the surrounding plasma and the spacecraft itself, electrons will be accelerated by an amount that depends on the height of the barrier (until 9 eV in the ram and 15 eV in the wake).

B. Solar Orbiter at 0.25 UA

We consider now a case in the region of SO closest perihelion at 0.25 UA to the sun. Results for plasma potential and population densities are presented in Fig. 4. The final Φ_{SC} is now set at +6.30 V. This is due to the larger Debye length of photoelectrons: the barrier has changed from a 1-D geometry at 0.044 AU to a 3-D geometry here. The recollection is thus less important and mainly due to the positive satellite potential. However, negative potential values are still present around the spacecraft: -1.1 V at 1.6 m in front of the sunlit face in the ram (at $\sim$ 6 times the photoelectron Debye length of 0.25 m), and -1 V at 2.9 m of the rear face in the wake (close to λ_{the} which equals 3.27 m for ambient electrons). For secondary and photoelectrons, it represents respectively -7.4 and -7.3 V barriers, added to the positively charged satellite which will thus attract them more efficiently. Incoming thermal electrons from environment encounter a -1 V barrier ($\sim$ 4% of their mean kinetic energy of 23 eV) so they are not as much repelled as previously. However the distribution at the spacecraft surface is truncated at $\Phi_{SC} = +6.30$ V: electrons have at least a 6.30eV energy on spacecraft.

Concerning the cylindrical ion wake obtained here, the minimum potential expected at its center (using the numerical application in Section III.A with $L \sim 1$ m and $\lambda_{D,the} \sim 3.27$ m) should be between -1.2 V and -0.6 V. We effectively obtain -1 V.

Looking at plasma population densities, the major difference with the former simulation is the plasma potential structure around the cylinder. In the 0.25 AU case it is more symmetric around the satellite body, less disturbed by the ion wake. This wake is more elongated along the Z axis than before, as the ion speed is increased of $\sim$ 100 km/s, T_i is divided by 4, and there is no focusing of those particles as Φ_{SC} is now positive. As $\lambda_{the} = 3.27$ m (larger than the spacecraft dimension) the space charge in the wake only slightly modifies the potential (of about 1/10). The global behavior of photoelectrons and secondaries is identical to the first case, except that they are less dense than previously and they can spread farther from the cylinder because of the reduced potential barriers.

The recollection of secondary electrons reaches 80.8% and practically the same (78%) for photoelectrons (Table III). Here the recollection of secondaries, which is the condition for equilibrium, is achieved by a positive Φ_{SC} , and a small barrier of potential due to space charge.

At 0.044 AU collected photoelectrons represented $\sim$40% of all collected currents on spacecraft, and the same proportion was reached for secondaries. At 0.25 AU the collected photoelectron current is now 60% of all collected currents while secondaries represent $\sim$ 20%. This is due to the lower SEY at 23 eV with respect to the SEY at 85 eV: a lower emission leads to a lower recollection.

C. Results Between 1 AU and 0.044 AU

The same simulation was performed for several additional distances from the sun, using the input parameters in Table I. All the corresponding results (currents and potentials values) are displayed in Table III. Plasma potential profiles along $Z$and X axis are displayed in Figs. 5 and 6. Values of satellite potentials are plotted in Fig. 7, and location of minimum potentials is plotted in Fig. 8

Looking at the plasma potential profiles along the Z axis, Fig. 5 shows that for this type of model, below $\sim$ 0.3 AU from the sun, a nonmonotonic evolution of potential is obtained, due to secondary electron and photoelectron space charge. Further, the space charge becomes less important. The transition between negative and positive satellite equilibrium potential is reached between 0.093 and 0.11 AU, but it has to be emphasized that this situation depends on the total spacecraft surfaces exposed to the environment and the type of covering materials.

The farther from the sun, the farther the ram and wake minimum potential positions are located from the spacecraft surfaces. After 0.3 AU, the plasma potential profile is decreas-

TABLE III
PARAMETRIC STUDY RESULTS, MAIN OUTPUT VALUES

PLASMA	Earth	Venus	Mercury Aph	Mercury Peri	SO peri	SP+ 1st Peri	0,11 UA	SP+ Sci ops	0,067 UA	SP+ Last Peri
CASE (AU)	1	0,72	0,46	0,3	0,25	0,162	0,11	0,093	0,067	0,044
CURRENTS on SC (A)										
Thermal electrons net	-2,55E-05	-4,98E-05	-1,30E-04	-2,68E-04	-4,76E-04	-9,39E-04	-2,63E-03	-3,78E-03	-6,41E-03	-2,46E-02
Ions net	1,52E-06	3,08E-06	8,05E-06	2,07E-05	2,93E-05	6,61E-05	1,73E-04	2,37E-04	4,00E-04	1,56E-03
Photoelectrons										
Collected	-7,89E-05	-1,53E-04	-3,73E-04	-9,00E-04	-1,25E-03	-3,16E-03	-7,01E-03	-9,89E-03	-1,96E-02	-4,52E-02
Emitted	1,01E-04	1,94E-04	4,75E-04	1,12E-03	1,61E-03	3,83E-03	8,31E-03	1,16E-02	2,24E-02	5,19E-02
Net	2,17E-05	4,05E-05	1,02E-04	2,17E-04	3,54E-04	6,75E-04	1,30E-03	1,73E-03	2,77E-03	6,75E-03
2nd electrons										
Collected	-1,19E-05	-2,59E-05	-8,18E-05	-2,11E-04	-3,89E-04	-1,07E-03	-3,16E-03	-5,01E-03	-8,71E-03	-4,62E-02
Emitted	1,41E-05	3,18E-05	1,02E-04	2,40E-04	4,82E-04	1,26E-03	4,24E-03	6,74E-03	1,29E-02	6,14E-02
Net	2,27E-06	5,97E-06	1,99E-05	2,86E-05	9,26E-05	1,87E-04	1,08E-03	1,73E-03	4,15E-03	1,52E-02
All populations										
Collected	-1,15E-04	-2,26E-04	-5,77E-04	-1,36E-03	-2,09E-03	-5,10E-03	-1,26E-02	-1,84E-02	-3,43E-02	-1,14E-01
Emitted	1,15E-04	2,26E-04	5,77E-04	1,36E-03	2,09E-03	5,08E-03	1,25E-02	1,84E-02	3,53E-02	1,13E-01
Net	-3,60E-09	-1,75E-07	1,31E-07	-1,55E-06	-2,46E-07	-1,02E-05	-8,67E-05	-7,72E-05	9,09E-04	-1,07E-03
Recollection (%)										
Photoelectrons	78,44	79,11	78,54	80,59	77,99	82,38	84,39	85,08	87,61	86,99
2nd electrons	83,97	81,24	80,40	88,09	80,79	85,07	74,59	74,34	67,74	75,24
POTENTIALS										
Spacecraft (V)	13,53	13,89	13,39	7,91	6,29	5,21	1,22	-0,69	-4,26	-16,23
Ram min position (m)	NA	NA	NA	3,02	1,66	0,99	0,56	0,44	0,37	0,23
Wake min position (m)	NA	NA	NA	3,41	2,93	2,16	1,65	1,52	1,13	0,84
Ram min value (V)	NA	NA	NA	-0,23	-1,13	-2,84	-7,23	-8,88	-13,13	-25,42
Wake min value (V)	NA	NA	NA	-0,47	-1,07	-3	-7,06	-9,39	-14,01	-31,3
Potential barriers for secondaries (V)										
Ram	13,53	13,89	13,39	-8,14	-7,42	-8,05	-8,45	-8,19	-8,87	-9,19
Wake	13,53	13,89	13,39	-8,38	-7,36	-8,21	-8,28	-8,70	-9,75	-15,07
OTHER VALUES										
Rate 2nd-emission/the-coll	-0,56	-0,64	-0,78	-0,90	-1,01	-1,34	-1,61	-1,78	-2,00	-2,50
Coll-The/Coll-ALL (%)	22,21	22,01	22,51	19,70	22,78	18,42	20,85	20,48	18,68	21,49
Coll-2nd/Coll-ALL (%)	10,35	11,44	14,17	15,55	18,62	20,95	25,02	27,17	25,36	40,40
Coll-photo/Coll-ALL (%)	68,77	67,91	64,71	66,27	60,00	61,92	55,50	53,63	57,13	39,48

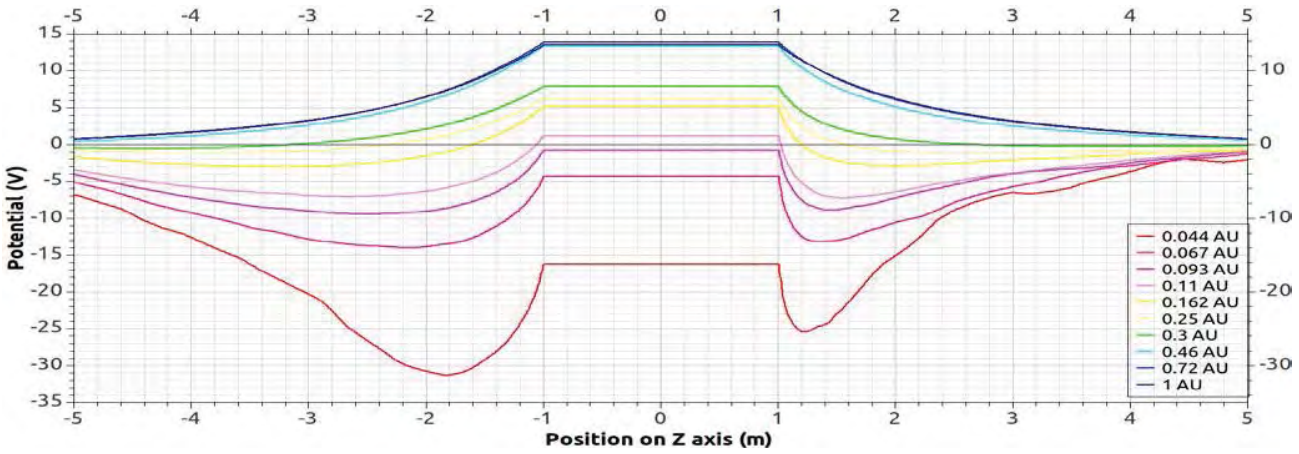

Fig. 5. Plasma potential along Z axis for all simulations (the heliocentric distance is monotonically increasing with spacecraft potential).

ing monotonically while looking farther from the cylinder. It is here visible for the cases at 0.46, 0.72 and 1 AU to the sun. Thus recollection of secondary particles in these regions is simply due to spacecraft positive potential. It can be noticed in Fig. 7 that the simulation box almost reaches the limit of the sheath in each case. The plots of ram and wake minimum potentials should reach 0 V far enough from the body after 0.3 AU, but are slightly larger due to the simulation box boundaries that are still in the sheath. This restriction was necessary for reasons of CPU time consumption, and slightly affects the potential profiles in the surrounding plasma.

The transition between positively and negatively charged spacecraft is linked to the geometry of the sheath. It changes from a 3-D sheath far from the sun (farther than 0.11–0.093 AU, where thermal and photoelectrons Debye lengths are long) to a thin 1-D sheath closer (with short Debye length of photoelectrons). In all cases the emitted-collected current equilibrium is reached once a significant part of photoelectrons is recollected, as it is the most important current. Far from the sun, with no blocking from a potential barrier, the current balance is reached for a positive spacecraft potential (it is easier for photoelectrons to escape a 3-D sheath). In the second case, the limitation from charge space is a 1-D phenomena: the photoelectron recollection is extremely efficient (the net current being approximately given by the Child-Langmuir's law), and we

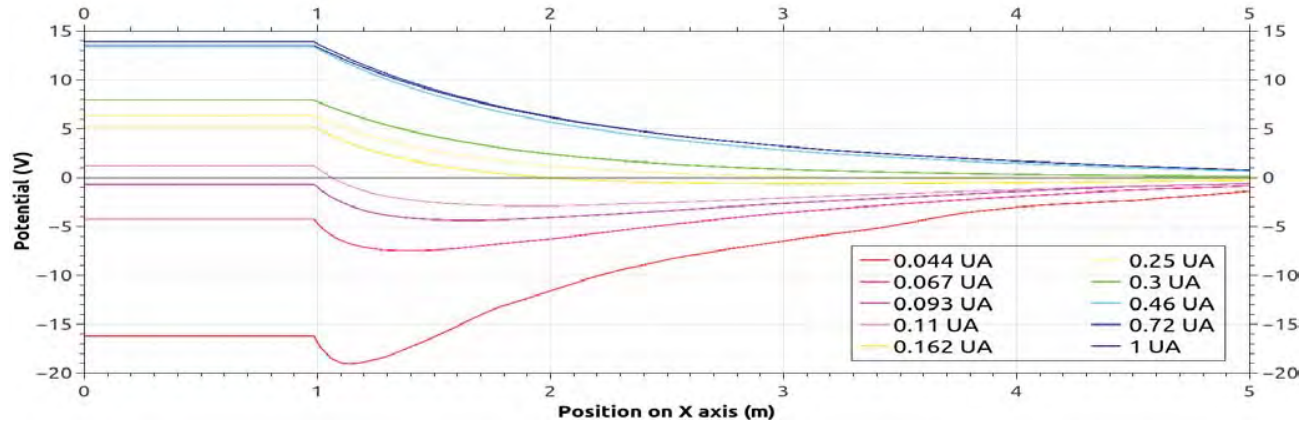

Fig. 6. Plasma potential along X axis for all simulations (the heliocentric distance is monotonically increasing with spacecraft potential).

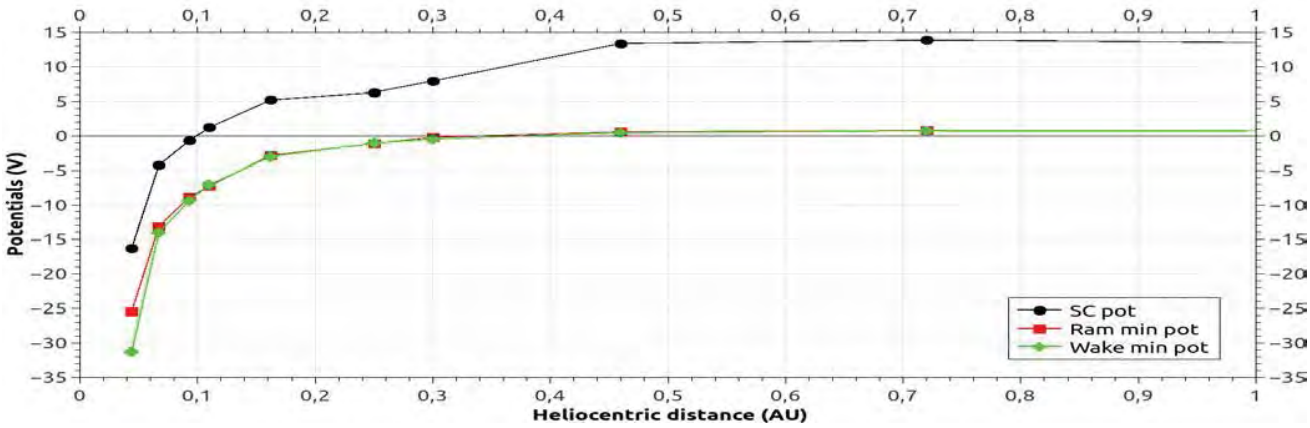

Fig. 7. Potentials versus heliocentric distance.

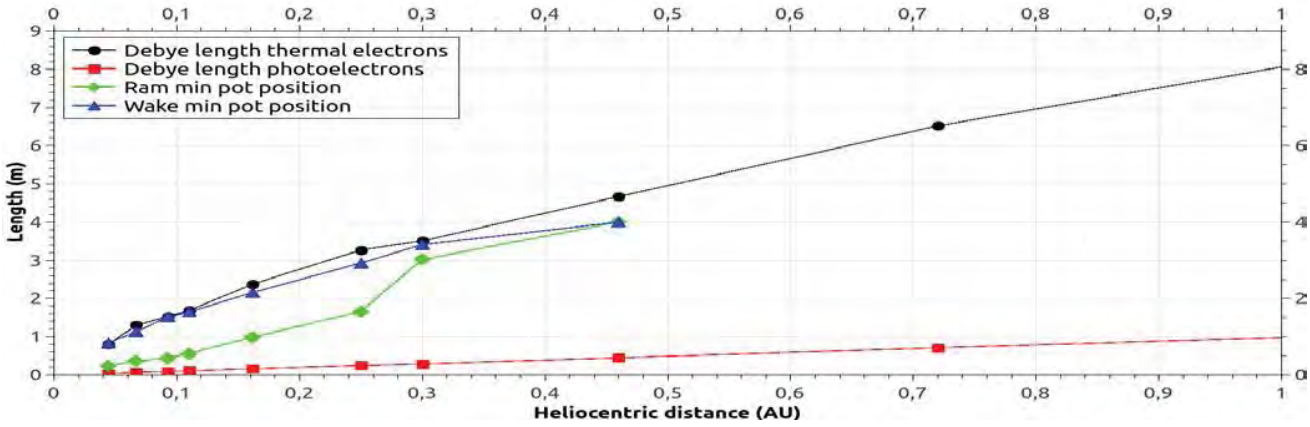

Fig. 8. Comparison of Debye lengths and locations of minimum potentials in plasma versus heliocentric distance.

can obtain the current balance with a negative spacecraft potential.

In Fig. 8, we notice a difference in positioning of the minimum plasma potentials: below $\sim$ 0.3 AU the wake potential barrier is farther from the spacecraft than the ram barrier. After 0.3 AU, the positions of the barriers regarding the facing surfaces are similar in the ram and in the wake. This also corresponds to regions where the potential along Z axis evolves nonmonotonically. More precisely, Fig. 8 suggests that below 0.093 AU the ram barrier position regarding the sunlit face follows the photoelectron Debye length (which is much smaller than λ_{the}). Indeed when closer than 0.093 AU the extreme near sun UV flux generates high densities of photoelectrons that seem to influence most the plasma behavior in the ram. Until 0.25 AU the ram barrier position is at about 5–6 times λ_{ph} to the sunlit face. After that, as it appears in Fig. 8, the ram barrier distance to spacecraft is similar to the wake barrier distance and is comparable to

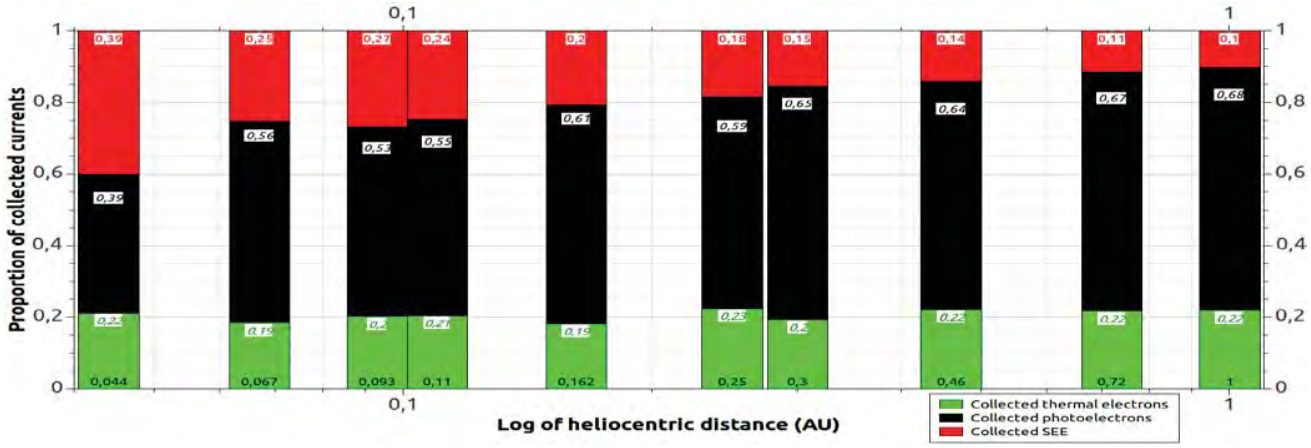

Fig. 9. Proportion of particles among collected electrons versus heliocentric distance.

the thermal Debye length. Within 0.25–0.3 AU the emitted secondary electron current becomes lower than the collected thermal current. In Fig. 8 photoelectron and thermal electron Debye lengths as a function of heliocentric distance appear to be the two asymptotes between which are contained the ram and wake barriers position curves. As in the wake the plasma seems to be more influenced by thermal and secondary electrons (which are there present in quite similar densities), the potential barrier is controlled by the thermal electron Debye length and temperature, the spacecraft size and the ion Mach number.

Fig. 9 makes explicit the part of secondary particles (both photoelectrons and SEE) among collected electrons on the spacecraft. In each case, between 0.044 and 1 AU, those nonenvironmental particles represent ~ 80 % of the collection. Photoelectrons are more and more important in the recollection while looking farther from the sun. This seems paradoxical but can be understood as the SEE is highly reduced with increasing distance to sun (because of the decreasing mean energy of the thermal electrons reducing consequently the secondary emission rate, see Fig. 2). Fortunately, photoelectron recollection occurs essentially on the sunlit face and they will affect the detector entrance areas less than secondary electrons will.

IV. Conclusion

The simulations performed in this paper showed the variation of space charge potential barriers around a spacecraft depending on its distance to the sun. At less than 0.3 AU for this geometry model, the plasma potential around the spacecraft decreases nonmonotonically. Potential barriers for secondary and photoelectrons thus appear and force their recollection to lower Φ_{SC} (even at negative values below 0.11 AU to the sun). The barriers were created by high densities of secondary particles that control the surrounding plasma and are dominant in the collected particles.

The specific case studied at 0.25 AU showed that SO near its perihelion may be affected by those phenomena, even if they are less pronounced than at 0.044 AU as the SP+ perihelion. The measurement errors on low-energy plasma measurements are possible but depend on the size of the spacecraft and its covering materials which will control secondary particles emission. At SO perihelion the low-energy plasma measurements will be disturbed: high rates of secondary particles recollection can still occur and potential barriers still affect the surrounding plasma. A small fraction of incoming thermal electrons (with energies ≤ 1 eV) will be filtered and particles emitted from the satellite surfaces might be measured as noise by the onboard detectors, and thermal electrons arriving on the detectors will be accelerated (as $\Phi_{SC} > 0$) at 6.3 eV.

Generally, the SO case requires further simulations, with a more precise geometry and physical model to anticipate the disturbances: more detailed geometry, exact material properties (solar panels materials, heat shield properties, taking into account thin wires and locations of plasma instruments...) and possibly electrical properties (equivalent resistors and capacitors inside the spacecraft and between the electrical nodes). The magnetic field was not considered in this paper but might play a role in the plasma behavior (especially on the secondary particles trajectories) and the final Φ_{SC}. This will be investigated in a forthcoming paper. We emphasized that the model used here has no link with the real SO geometry, but this simulation gives a first hint of the global plasma behavior in this region that SO will travel through. Actually, given the size of the real SO probe, sunshield and solar arrays, the created ion wake should be bigger and the corresponding potentials more negative, increasing the potential barriers and the biasing phenomena. However the electron instrument (SWA/EAS) was located at the end of a 4–5 m boom, behind the spacecraft, which might limit the influence of Φ_{SC} Moreover, the exposed covering materials (conductors and dielectrics) will generate different level of secondary particles. This subject will be studied in a forthcoming paper.

Concerning further developments, more relevant electron distribution functions of the solar wind need to be considered and their effects on spacecraft charging assessed. They might lead to much different results than obtained with Maxwellian distribution functions, and increase the disturbances of low-energy particles measurements, as more high-energy particles may generate higher SEY. This could be achieved by modeling the hot electron populations of the ambient plasma environment (the socalled solar wind “Core, Halo and Strahl”).

Indeed extrapolating data from Helios to SO (M. Maksimovic, private communication) and using associated modeling (Stverak *et al.*, 2009) [19] it is possible to obtain the different electron population contributions. We will use this approach to set up SPIS with more detailed distribution functions for the ambient plasma. Concerning photoelectrons the use of a 3 eV spectrum limits the positive charging and more realistic energy distribution functions should be investigated. Finally the implementation of virtual particle detectors within the simulations will give direct access to the plasma flux measured by instruments and enable a better assessment of biasing effects.

ACKNOWLEDGMENT

The authors wish to thank BenoîtLavraud (IRAP) and M. Maksimovic (LESIA) for useful discussions.

REFERENCES

[1] R. L. Guernsey and J. H. M. Fu, "Potential distribution surrounding a photo-emitting, plate in a dilute plasma," *J. Geophys. Res.*, vol. 75, no. 16, pp. 3193–3199, 1970.

[2] E. C. Whipple, "Theory of spherically symmetric photoelectron sheath: A thick sheath approximation and comparison with the ATS 6 observation of a potential barrier," *J. Geophys. Res.*, vol. 81, no. 4, pp. 601–607, Jan. 1976.

[3] H. Zhao, R. Schmidt, C. P. Escoubet, K. Torkar, and W. Riedler, "Self-consistent determination of the electrostatic potential barrier due to the photoelectron sheath near a spacecraft," *J. Geophys. Res.*, vol. 101, no. A7, pp. 15653–15659, Jan. 1996.

[4] B. Thiébault, A. Hilgers, E. Sasot, H. Laakso, C. P. Escoubet, V. Génot, and J. Forest, "Potential barrier in the electrostatic sheath around a magnetospheric spacecraft," *J. Geophys. Res.*, vol. 109, no. A12, p. A12207, Dec. 2004.

[5] U. Isensee, "Plasma disturbances caused by the HELIOS spacecraft in the Solar Wind," *J. Geophys.*, vol. 42, no. 6, pp. 581–589, 1977.

[6] R. E. Ergun, D. M. Malaspina, S. D. Bale, J. P. McFadden, D. E. Larson, F. S. Mozer, N. Meyer-Vernet, M. Maksimovic, P. J. Kellogg, and J. R. Wygant, "Spacecraft charging and ion wake formation in the near-Sun environment," *Phys. Plasmas*, vol. 17, no. 7, pp. 072903-1–072903-9, May 2010.

[7] S. Guillemant, V. Génot, J.-C. Matéo-Vélez, R. E. Ergun, and P. Louarn, "Solar Wind Plasma Interaction with Solar Probe Plus Spacecraft," *Annales Geophysicae*, vol. 30, no. 7, pp. 1075–1092, Jul. 2012.

[8] E. N. Parker, "Dynamics of the interplanetary gas and magnetic fields," *Astrophys. J.*, vol. 128, p. 664, Nov. 1958.

[9] J.-F. Roussel, F. Rogier, G. Dufour, J.-C. Mateo-Velez, J. Forest, A. Hilgers, D. Rodgers, L. Girard, and D. Payan, "SPIS open-source code: Methods, capabilities, achievements, and prospects," *IEEE Trans. Plasma Sci.*, vol. 36, no. 5, pp. 2360–2368, Oct. 2008.

[10] J.-F. Roussel, G. Dufour, J.-C. Matéo-Vélez, B. Thiébault, B. Andersson, D. Rodgers, A. Hilgers, and D. Payan, "SPIS multi time scale and multi physics capabilities: Development and application to GEO charging and flashover modeling," *IEEE Trans. Plasma Sci.*, vol. 40, no. 2, pp. 183–191, Feb. 2012.

[11] A. Hilgers, B. Thiébault, D. Estublier, E. Gengembre, J. Gonzalez, M. Tajmar, J.-F. Roussel, and J. Forest, "A simple model of SMART-1 electrostatic potential variation," *IEEE Trans. Plasma Sci.*, vol. 34, no. 5, pp. 2159–2165, Oct. 2006.

[12] A. Hilgers, S. Clucas, B. Thiébault, J.-F. Roussel, J.-C. Matéo-Vélez, J. Forest, and D. Rodgers, "Modeling of plasma probe interactions with a PIC code using an unstructured mesh," *IEEE Trans. Plasma Sci.*, vol. 36, no. 5, pp. 2319–2323, Oct. 2008.

[13] J.-F. Roussel, T. Tondu, J.-C. Matéo-Vélez, E. Chesta, S. D'Escrivan, and L. Perraud, "Modeling of FEEP electric propulsion plume effects on microscope spacecraft," *IEEE Trans. Plasma Sci.*, vol. 36, no. 5, pp. 2378–2386, Oct. 2008.

[14] P. Sarrailh, J.-C. Matéo-Vélez, J.-F. Roussel, B. Dirassen, J. Forest, B. Thiébault, D. Rodgers, and A. Hilgers, "Comparison of numerical and experimental investigations on the ESD onset in the inverted potential gradient situation in GEO," *IEEE Trans. Plasma Sci.*, vol. 40, no. 2, pp. 368–379, Feb. 2010.

[15] J.-C. Matéo-Vélez, J.-F. Roussel, D. Sarrail, F. Boulay, V. Inguimbert, and D. Payan, "Ground plasma tank modeling and comparison to measurements," *IEEE Trans. Plasma Sci.*, vol. 36, no. 5, pp. 2369–2377, Oct. 2008.

[16] J.-C. Matéo-Vélez, J.-F. Roussel, V. Inguimbert, M. Cho, K. Saito, and D. Payan, "SPIS and MUSCAT software comparison on LEO-like environment," *IEEE Trans. Plasma Sci.*, vol. 40, no. 2, pp. 177–182, Feb. 2012.

[17] J.-C. Matéo-Vélez, P. Sarrailh, B. Thiebault, J. Forest, A. Hilgers, J.-F. Roussel, G. Dufour, B. Riviére, V. Génot, S. Guillemant, A. Eriksson, C. Cully, and D. Rodgers, "SPIS science: Modelling spacecraft cleanliness for low-energy plasma measurement," in *Proc. 12th Spacecraft Charging Technol. Conf.*, Kitakyushu, Japan, May 2012.

[18] E. Engwall, A. I. Eriksson, and J. Forest, "Wake formation behind positively charged spacecraft in flowing tenuous plasmas," *Phys. Plasmas*, vol. 13, no. 6, pp. 062904-1–062904-10, Apr. 2006.

[19] Š. Štverák, M. Maksimovic, P. M. Trávnícek, E. Marsch, A. N. Fazakerley, and E. E. Scime, "Radial evolution of non-thermal electron populations in the low-latitude solar wind: Helios, cluster, and ulysses observations," *J. Geophys. Res.*, vol. 114, pp. 1–15, May 2009.

Stanislas Guillemant received the Master's degree in space technologies and instrumentation from Université Paul Sabatier, Toulouse, France, in 2008.

He was with Atos Origin as a Study Engineer on several centers of space mechanics to control satellite orbits from 2009 to 2010.

Vincent Génot received the Ph.D. degree in particle acceleration applied to terrestrial auroral regions from the Université of Versailles Saint-Quentin, France, in 1999.

He became a Scientific Director of CDPP, the French Plasma Physics Data Centre, in 2012.

Jean-Charles Matéo-Vélez received the Ph.D. degree in fluid dynamics from SUPAERO (ISAE), Toulouse, France, in 2006.

He has been a Research Scientist with the Space Environment Department, ONERA, the French Aerospace Lab, since 2007.

Pierre Sarrailh, photograph and biography not available at the time of publication.

Alain Hilgers received the Ph.D. degree in astrophysics from University Paris VII, Paris, France, in 1992.

He has been with the European Space Agency and European Space Agency Headquarters in space environment modeling since 1993.

Philippe Louarn photograph and biography not available at the time of publication.

Bibiography

Bibliography

[Baglin et al. (2000)] Baglin V., Bojko J., Gröbner O., Henrist B., Hilleret N., Scheuerlein C., Taborelli M. *The secondary electron yield of technical materials and its variation with surface treatments.* Proceedings of EPAC 2000, Vienna, Austria. (Cited on pages 50 and 52.)

[Balcon et al. (2012)] Balcon N., Payan D., Belhaj M., Tondu T. and Inguimbert V. *Secondary Electron Emission on Space Materials: Evaluation of the Total Secondary Electron Yield From Surface Potential Measurements.* IEEE Transactions on Plasma Science, Vol. 40, N. 2, 2012. (Cited on pages 49, 50 and 51.)

[Besse et al. (1980)] Besse A. L. and Rubin A. G. *A simple analysis of spacecraft charging involving blocked photoelectron currents.* J. Geophys. Res., Vol. 85, Issue A5, pp. 2324–2328, 1980. (Cited on page 60.)

[Bittencourt (1986)] Bittencourt J. A. *Fundamentals of Plasma Physics.* Pergamon Press, New York, 1986 (Cited on pages 19 and 22.)

[Carlson et al. (1983)] C. W. Carlson C. W., Curtis D. W. , Paschmann G. and Michael W. *An instrument for rapidly measuring plasma distribution functions with high resolution.* Adv. Space Res., Vol.2, No.7, pp. 67-70, 1983. (Cited on page 8.)

[Chen (1965)] Chen, F. F. *Electrical probes.* Chapter 4 in *Plasma Diagnostic Techniques*, eds. R. H. Huddlestone and S. L. Leonid, pp. 113-200, Academic Press, New York, 1965. (Cited on page 33.)

[Child (1911)] Child C. D. *Discharge from hot CaO.* Phys. Rev., vol. 32, no. 5, pp. 492–511, 1911. (Cited on page 42.)

[Engwall (2006)] Engwall E., Eriksson A. I. and Forest J. *Wake formation behind positively charged spacecraft in flowing tenuous plasmas.* Physics of Plasmas, 13, 062904, 2006. (Cited on pages 13, 56 and 58.)

[Ergun et al. (2010)] Ergun R. E., Malaspina D. M., Bale S. D., McFadden J. P., Larson D. E., Mozer F. S., Meyer-Vernet N., Maksimovic M., Kellogg P. J. and Wygant J. R. *Spacecraft charging and ion wake formation in the near-Sun environment.* Phys. Plasmas, 17, 1134–1150, 2010. (Cited on pages 60, 65, 80, 199 and 203.)

[Feldman et al. (1975)] Feldman W. C., Asbridge J. R., Bame S. J., Montgomery M. D. and Gary S. P. *Solar wind electrons.* J. Geophys. Res., 80(31), 4181–4196, doi:10.1029/JA080i031p04181, 1975. (Cited on page 21.)

[Geach et al. (2005)] Geach J., Schwartz S. J., Génot V., Moullard O., Lahiff A. and Fazakerley A. N. *A corrector for spacecraft calculated electron moments.* Ann. Geophys., 23, 931–943, 2005. (Cited on page 13.)

[Génot et al. (2004)] Génot V. and Schwartz S. J. *Spacecraft potential effects on electron moments derived from a perfect plasma detector.* Ann. Geophys., 22, 2073–2080, 2004. (Cited on pages 13 and 14.)

[Guillemant et al. (2012)] Guillemant S., Génot V., Matéo-Vélez J.-C., Ergun R. and Louarn P. *Solar wind plasma interaction with solar probe plus spacecraft.* Ann. Geophys., 30, 1–18, 2012. (Cited on pages 80, 86, 89, 90, 92, 100, 199 and 203.)

[Guillemant et al. (2013)] Guillemant S., Génot V., Matéo-Vélez J.-C., Sarrailh P., Hilgers A. and Louarn P. *Simulation Study of Spacecraft Electrostatic Sheath Changes With the Heliocentric Distances from 0.044 to 1 AU* . Plasma Science, IEEE Transactions on, Volume:PP, Issue: 99, 2013. (Cited on pages 90, 92, 99, 100, 145, 157, 165, 174, 200 and 204.)

[Hanna et al. (2011)] Hanna R., Paulmier T., Belhaj M., Molinie P., Dirassen B., Payan D. and Balcon N. *Characterization of charge carrier lateral conduction in irradiated dielectric materials.* J. Phys. D: Appl. Phys. 44, 445402, 2011. (Cited on page 37.)

[Hastings and Garret (1996)] Hastings D. and Garrett H. *Spacecraft/Environment Interactions.* Cambridge University Press, 1996. (Cited on pages 42, 50, 54 and 55.)

[Hastings and Chang (1989)] Hastings D. and Chang P. *The physics of positively biased conductors surrounded by dielectrics in contact with a plasma.* Physics of Fluids B, 1:1123-32, 1989. (Cited on page 64.)

[Hilgers et al. (2006)] Hilgers A., Thiébault B., Estublier D., Gengembre E., Gonzalez J., Tajmar M., Roussel J.-F. and Forest J. *A simple model of SMART-1 electrostatic potential variation.* IEEE Trans. Plasma Sci., 34, 2159-2165, doi:10.1109/TPS.2006.883405, 2006. (Cited on page 66.)

[Hilgers et al. (2008)] Hilgers A., Clucas S., Thiébault B., Roussel J.-F., Matéo-Vélez J.-C., Forest J. and Rodgers, D. *Modelling of Plasma Probe Interactions With a PIC Code Using an Unstructured Mesh.* IEEE Trans. Plasma Sci., 36, 2319-2323, doi:10.1109/TPS.2008.2003360, 2008. (Cited on page 66.)

[Isensee (1977)] Isensee, U. *Plasma disturbances caused by the Helios spacecraft in the Solar Wind.* J. Geophys., Volume 42, 581-589, 1977. (Cited on pages 60 and 165.)

[Issautier et al. (2001)] Issautier K., Skoug R. M., Gosling J. T., Gary S. P. and McComas D. J. *Solar wind plasma parameters on Ulysses: Detailed comparison between the URAP and SWOOPS experiments.* J. Geophys. Res., Vol. 106,NO. A8, PAGES 15665-15675, DOI:10.1029/2000JA000412, 2001. (Cited on page 6.)

[Katz et al. (1977)] Katz I., Parks D. E., Mandell M. J., Harvey J. M., Wang S. S., Roche J. C. *NASCAP, a three-dimensional Charging Analyzer Program for complex spacecraft.* IEEE Transactions on Nuclear Science, vol. NS-24, p. 2276-2280, Dec. 1977. (Cited on pages 49, 50, 53 and 54.)

[Laframboise and Parker (1973)] Laframboise J. G. and Parker L. W. *Probe design for orbit-limited current collection.* The Physics of Fluids, Vol. 16, N. 5, 1973. (Cited on pages 40 and 45.)

[Langmuir (1913)] Langmuir I. *The effect of space charge and residual gases on thermionic currents in high vacuum.* Phys. Rev., vol. 2, no. 6, pp. 450–486, Dec. 1913. (Cited on page 42.)

[Langmuir (1960)] Langmuir I. *Collected Works of Irvin Langmuir*. Pergamon Press, New York, 1960. (Cited on page 33.)

[Langmuir and Blodgett (1924)] Langmuir I. and Blodgett K. B. *Currents limited by space charge between concentric spheres*. Phys Rev., vol. 24, no. 1, pp. 49–59, 1924. (Cited on page 41.)

[Lucas (1973)] Lucas A. A. *Fundamental processes in particle and photon interactions with surfaces*. In R. J. L. Grard (ed.), *Photon and Particles Interactions with Surfaces in Space*, pp. 3-21, Reidel, 1973. (Cited on page 54.)

[Maksimovic et al. (2005)] Maksimovic M., Zouganelis I., Chaufray J.-Y., Issautier K., Scime E.E., Littleton J. E., Marsch E., McComas D. J., Salem C., Lin R. P. and Elliott H. *Radial evolution of the electron distribution functions in the fast solar wind between 0.3 and 1.5 AU*. J. Geophys. Res., 110, A09104, doi:10.1029/2005JA011119, 2005. (Cited on pages 21 and 133.)

[Marchand (2012)] Marchand R. *Ptetra, a tool to simulate low orbit satellite-plasma interaction*. IEEE Trans. Plasma Sci. (USA), 40 (2), 217 – 29, 2012. (Cited on page 65.)

[Markidis et al. (2009)] Markidis S., Lapenta G. and Rizwan-uddin *Multi-scale simulations of plasma with iPic3D*. Math. Comput. Simul. 80 (7), 1509 – 19, 2009. (Cited on page 65.)

[Matéo-Vélez et al. (2008)] Matéo-Vélez J.-C., Roussel J.-F., Sarrail D., Boulay F., Inguimbert V. and Payan D. *Ground Plasma Tank Modeling and Comparison to Measurements*. IEEE Transactions on Plasma Science, Vol. 36, N. 5, 2008. (Cited on pages 66 and 105.)

[Matéo-Vélez et al. (2012)] Matéo-Vélez J.-C., Roussel J.-F., Inguimbert V., Cho M., Saito K. and Payan D. *SPIS and MUSCAT software comparison on LEO-like environment*. IEEE Trans. Plasma Sci., 40, 177-182, 2012. (Cited on page 66.)

[McFadden et al. (2005)] McFadden J. P., Carlson C. W., Larson D., Ludlam M., Abiad R., Elliott B., Turin P., Marckwordt M. and Angelopoulos V. *The THEMIS ESA Plasma Instrument and In-flight Calibration*. Space Sci Rev, 141, 277–302, 2008. (Cited on page 10.)

[Meyer-Vernet (1999)] Meyer-Vernet N. *How does the solar wind blow ? A simple kinetic model*. Eur. J. Phys., 20, 167–176, 1999. (Cited on page 26.)

[Meyer-Vernet (2007)] Meyer-Vernet N. *Basics of the Solar Wind*. Cambridge Atmospheric ans Space Science Series, 2012. (Cited on pages 27, 28 and 29.)

[Miyake and Usui (2009)] Miyake Y. and Usui H. *New electromagnetic particle simulation code for the analysis of spacecraft-plasma interactions*. Phys. Plasmas (USA), 16 (6), 062904 (11 pp.), 20096. (Cited on page 65.)

[Montgomery et al. (1968)] Montgomery M. D., Bame S. J. and Hundhausen A. J. *Solar wind electrons: Vela 4 measurements*. J. Geophys. Res., 73(15), 4999–5003, doi:10.1029/JA073i015p04999, 1968. (Cited on page 21.)

[Mott-Smith and Langmuir (1926)] Mott-Smith H. M. and Langmuir I. *The theory of collectors in gazeous discharges*. Phys. Rev., 28: 727-763, 1926. (Cited on pages 38, 39 and 40.)

[Parker (1958)] Parker E. N. *Dynamics of the Interplanetary Gas and Magnetic Fields.* Astrophysical Journal, vol. 128, p.664, DOI: 10.1086/146579, 1958. (Cited on pages 25, 26 and 90.)

[Parker (1980)] Parker L. W. *Plasmasheath–photosheath theory for large high-voltage space structures.* in Space Systems and Their Interactions With Earth's Space Environment, vol. 71, H. B. Garret and C. P. Pike, Eds. New York:Amer. Inst. Aeronautics Astronautics, 1980. (Cited on page 41.)

[Paulmier et al. (2009)] Paulmier T., Dirassen B., Payan D. and Van Eesbeek M. *Material Charging in Space Environment: Experimental Test Simulation and Induced Conductive Mechanisms.* IEEE Transactions on Dielectrics and Electrical Insulation, Vol. 16, No. 3, 2009. (Cited on page 37.)

[Pedersen (1995)] Pedersen A. *Solar wind and magnetosphere plasma diagnostics by spacecraft electrostatic potential measurements.* Ann. Geophys., 13, 118-129, 1995. (Cited on page 55.)

[Pfaff et al. (1998)] Pfaff F., Borovsky E. and Young T. *Measurement Techniques in Space Plasmas: Particles.* Geophys. Monogr. Ser., vol. 102, 355 pp., AGU, Washington, D. C., doi:10.1029/GM102., 1998. (Cited on page 10.)

[Pierrard and Lazar (2010)] Pierrard P. and Lazar M. *Kappa distributions: theory and applications in space plasmas.* Solar Physics, Volume 267, Issue 1, pp.153-174, 2010. (Cited on page 21.)

[Pneuman and Kopp (1971)] Pneuman G. W. and Kopp R. A. *Gas-Magnetic Field Interactions in the Solar Corona.* Solar Physics, Volume 18, Issue 2, pp.258-270, 1971. (Cited on page 27.)

[Prokopenko and Laframboise (1980)] Prokopenko S. M. L. and Laframboise J. G. *High-Voltage Differential Charging of Geostationary Spacecraft.* J. Geophys. Res., Vol. 85, N. A8, P. 4125-4131, 1980. (Cited on page 40.)

[Roussel et al. (2008-a)] Roussel J.-F., Rogier F., Dufour G., Matéo-Vélez J.-C., Forest, J., Hilgers A., Rodgers D., Girard L. and Payan D. *SPIS Open Source Code: Methods, Capabilities, Achievements and Prospects.* IEEE Trans. Plasma Sci., 36, 2360–2368, doi:10.1109/TPS.2008.2002327, 2008. (Cited on page 66.)

[Roussel et al. (2008-b)] Roussel J.-F., Tondu T., Matéo-Vélez J.-C., Chesta E., D'Escrivan S. and Perraud L. *Modeling of FEEP Electric Propulsion Plume Effects on Microscope Spacecraft.* IEEE Trans. Plasma Sci., 36, 2378–2386, doi:10.1109/TPS.2008.2002541, 2008. (Cited on page 66.)

[Roussel et al. (2010)] Roussel J.-F., Dufour G., Matéo-Vélez J.-C., Thiébault B., Andersson B., Rodgers D., Hilgers A. and Payan D. *SPIS multi time scale and multi physics capabilities: development and application to GEO charging and flashover modeling.* IEEE Trans. Plasma Sci., 40, doi:10.1109/TPS.2011.2177672, in press, 2012. (Cited on page 66.)

[Salem et al. (2001)] Salem C., Bosqued J.-M., Larson D. E., Mangeney A., Maksimovic M., Perche C. , Lin R. P. and Bougeret J.-L. *Determination of accurate solar wind electron*

parameters using particle detectors and radio wave receivers. J. Geophys. Res., Volume 106, Issue A10, p. 21701-21717, 2001. (Cited on page 13.)

[Sarrailh et al. (2010)] Sarrailh P., Matéo-Vélez J.-C., Roussel J.-F., Dirassen B., Forest J., Thiébaultt B., Rodgers D. and Hilgers A. Comparison of numerical and experimental investigations on the ESD onset in the Inverted Potential Gradient situation in GEO. IEEE Trans. Plasma Sci., 40, 368-379, 2010. (Cited on page 66.)

[Scime et al. (1994)] Scime E. E., Phillips J. L. and Bame S. J. *Effects of spacecraft potential on three-dimensional electron measurements in the solar wind.* J. Geophys. Res., Volume 99, Issue A8, p. 14769-14776, 1994. (Cited on page 14.)

[Sherman et al. (1971)] Sherman C. and Parker L. *Potential due to a Circular Double Disk.* J. Appl. Phys. 42, 870, 1971. (Cited on page 60.)

[Shukla and Mamun (2002)] Shukla P. K. and Mamun A. A. *Introduction to Dusty Plasma Physics.* Institute of Physics, Series in Plasma Physics, IOP, 2002. (Cited on page 63.)

[Song et al. (1997)] Song P., Zhang X. X. and Pashmann G. *Uncertainties in plasma measurements: effect of lower cutoff energy and spacecraft charge.* Planet. Space Sci., 45, 2, 255, 1997. (Cited on page 13.)

[Sternglass (1954)] Sternglass E. J. *Theory of secondary electron emission.* Westinghause Research Laboratories, Pittsburgh, PA, 1957. (Cited on page 50.)

[Štverák et al.(2009)] Štverák Š., Maksimovic M., Trávníček P. M., Marsch E., Fazakerley A. N., and Scime E. E. (2009), Radial evolution of nonthermal electron populations in the low-latitude solar wind: Helios, Cluster, and Ulysses Observations, *J. of Geophys. Res., Vol. 114*, Issue A5, CiteID A05104, 2009. (Cited on pages 21 and 22.)

[Summers and Thorne (1991)] Summers D. and Thorne R. *The modified plasma dispersion function.* Physics of Fluids B (ISSN 0899-8221), vol. 3, no. 8, pt. 1, p. 1835-1847, 1991. (Cited on page 21.)

[Szita et al. (2001)] Szita S., Fazakerley A. N., Carter P. J., James A. M., Trávníček P. M., Watson G., André M., Eriksson A. and Torkar K. *Cluster PEACE observations of electrons of spacecraft origin.* Ann. Geophys., 19, 1721–1730, 2001. (Cited on pages 13, 55 and 56.)

[Thiébault et al. (2004)] Thiébault B., Hilgers A., Sasot E., Laakso H., Escoubet C. P., Génot V. and Forest J. *Potential barrier in the electrostatic sheath around a magnetospheric spacecraft.* J. Geophys. Res., 109, A12207, doi:10.1029/2004JA010398, 2004. (Cited on pages 12 and 60.)

[Vincenti and Kruger (1965)] Vincenti W. G. and Kruger C. H. *Introduction to Physical Gas Dynamics.* Krieger, Malabar, FL, 1965. (Cited on page 19.)

[Wang et al. (1994)] Wang J., Leung P., Garrett H. and Murphy G. *Multibody-plasma interactions - Charging in the wake.* Journal of Spacecraft and Rockets, Vol. 31, No. 5 (1994), pp. 889-894, 1994. (Cited on page 56.)

[Whipple (1976)] Whipple E. C. *Theory of spherically symmetric photoelectron sheath: a thick sheath approximation and comparison with the ATS 6 observation of a potential barrier.* J. Geophys. Res., 81, 601–607, 1976. (Cited on pages 12 and 60.)

[Whipple (1981)] Whipple E. C. *Potentials of surfaces in space.* Reports on Progress in Physics, vol. 44, Nov. 1981, p. 1197-1250, 1981. (Cited on pages 35, 47, 50, 53, 54 and 55.)

[Zhao et al. (1996)] Zhao H., Schmidt R., Escoubet C. P., Torkar K. and Riedler W. *Self-consistent determination of the electrostatic potential barrier due to the photoelectron sheath near a spacecraft.* J. Geophys. Res., 101, 15653–15659, 1996. (Cited on page 12.)